Terms and Conditions of Use of Digitised Theses from Trinity College Library Dublin

Copyright statement

All material supplied by Trinity College Library is protected by copyright (under the Copyright and Related Rights Act, 2000 as amended) and other relevant Intellectual Property Rights. By accessing and using a Digitised Thesis from Trinity College Library you acknowledge that all Intellectual Property Rights in any Works supplied are the sole and exclusive property of the copyright and/or other IPR holder. Specific copyright holders may not be explicitly identified. Use of materials from other sources within a thesis should not be construed as a claim over them.

A non-exclusive, non-transferable licence is hereby granted to those using or reproducing, in whole or in part, the material for valid purposes, providing the copyright owners are acknowledged using the normal conventions. Where specific permission to use material is required, this is identified and such permission must be sought from the copyright holder or agency cited.

Liability statement

By using a Digitised Thesis, I accept that Trinity College Dublin bears no legal responsibility for the accuracy, legality or comprehensiveness of materials contained within the thesis, and that Trinity College Dublin accepts no liability for indirect, consequential, or incidental, damages or losses arising from use of the thesis for whatever reason. Information located in a thesis may be subject to specific use constraints, details of which may not be explicitly described. It is the responsibility of potential and actual users to be aware of such constraints and to abide by them. By making use of material from a digitised thesis, you accept these copyright and disclaimer provisions. Where it is brought to the attention of Trinity College Library that there may be a breach of copyright or other restraint, it is the policy to withdraw or take down access to a thesis while the issue is being resolved.

Access Agreement

By using a Digitised Thesis from Trinity College Library you are bound by the following Terms & Conditions. Please read them carefully.

I have read and I understand the following statement: All material supplied via a Digitised Thesis from Trinity College Library is protected by copyright and other intellectual property rights, and duplication or sale of all or part of any of a thesis is not permitted, except that material may be duplicated by you for your research use or for educational purposes in electronic or print form providing the copyright owners are acknowledged using the normal conventions. You must obtain permission for any other use. Electronic or print copies may not be offered, whether for sale or otherwise to anyone. This copy has been supplied on the understanding that it is copyright material and that no quotation from the thesis may be published without proper acknowledgement.

Declaration

I declare that this work has not been submitted as an exercise for degree at this or any other university, and that it is entirely my own work. Due acknowledgements and references are given to the work of others. The library is granted permission to lend or copy this thesis upon request.

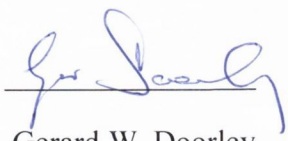

Gerard W. Doorley

Summary

The work described herein encompasses two distinct areas of chemistry. The first of these involved the time resolved study of ultrafast relaxation processes in DNA following UV excitation (chapters 1-5). The nature of the electronic excited states of DNA is today an ever expanding area of scientific curiosity. Exposure of DNA to UV radiation can result in deleterious effects with profound biological consequences. Our goal is to understand the excited states formed and their subsequent reaction or relaxation dynamics. To this end, we have embarked on a systematic study from simple nucleotide units to dinucleotide, polynucleotide and finally biologically relevant systems using picosecond time resolved infrared spectroscopy (ps-TRIR).

In chapter 2 the relaxation dynamics of a family of cytosine derivatives was probed. A new species was identified having a strong infrared absorption at 1574 cm^{-1}, with lifetimes of 33 and 37 ps for 5′-dCMP and dCyd respectively. Interestingly, the long-lived species was not found for 1-MeCyt and Cyt, suggesting that substitution at the 1-position by 2′-deoxyribose had a major effect on the photophysical properties of the nucleobase. The species was assigned to the dark $^1n_N\pi^*$ state, and this study represented the first direct observation of such a dark state.

The next study, chapter 3, encompassed a comprehensive review of A-T containing systems, from mono- to di- and finally polynucleotide systems. Long-lived species (hundreds of picoseconds) were found in dApdA and TpT that are most likely due to excimer-like states. A detailed study of the structural isomers dApT and TpdA was undertaken, including for the first time, variable temperature time resolved infrared measurements. Long-lived species lifetimes of 70 and 50 ps were found for dApT and TpdA respectively. Most significantly the thymine dominated regions were found to have a higher contribution from the long-lived species than the adenine dominated regions, and at long time delays the TRIR profile of the dinucleotides resembled that of thymine. We hypothesize that the long-lived state is localized on thymine, due to the fingerprint information afforded with infrared spectroscopy.

A study of DNA secondary structure of $[poly(dG\text{-}dC)]_2$ is described in chapter 4. Two relaxation processes were found for the B form (τ_1 = 7 ps, τ_2 = 30 ps). The long-lived species was found to have a well-defined absorption band at 1597 cm^{-1} and was assigned to

the $^{1}n_{N}\pi^{*}$ state of the cytidine moiety. Sensitivity of the G-C base-pairs in the polymer to secondary structure was confirmed when only a single species, having a broad transient absorption at 1600 cm^{-1} and lifetime of 16 ps was found for the Z form and was assigned to a localized exciplex state.

The final TRIR chapter focussed on biologically relevant systems – mixed-base duplex, triplex and quadruplex DNA. The mixed-base study affirmed that base-stacking and hydrogen-bonding interactions facilitate energy delocalization and hence are directly linked to the formation of long-lived states in DNA. Triple-stranded DNA was found to have monoexponential kinetics. This suggested that incorporation of the third strand, which introduces extra hydrogen-bonding in the structure, was responsible for the increased rate of energy dissipation. A cation-dependent TRIR investigation of the human telomeric sequence was performed and interestingly mode specific relaxation behaviour was found in the case of the divalent strontium cation induced quadruplex structure.

The second field of research explored in this thesis was toward the next generation of 'smart' nanoparticles. Synthetic approaches toward novel bifunctional nanoparticles for biomedical applications are described. Magnetic separation and fluorescent labelling are the two most widely used techniques used in bioscience today, and this work aims to combine both techniques to make the next generation of nanocomposites. The syntheses of polypyridyl ligands are described en route to ruthenium metal complexes capable of covalent binding to the nanoparticle surface. An alternative strategy described herein, involved the design and realization of a dopamine modified metal complex capable of strong binding to metal oxide surfaces. Iron oxide nanoparticles with coupling functionalities were successfully synthesized and characterized. Particles were successfully coated with silica and this was shown to prevent quenching of luminophore emission. Finally, a novel linker capable of conjugating oligonucleotides to nanoparticles surfaces was designed and synthesized. This molecule combined a functionality capable of strong bonding to metal oxide nanoparticles - an enediol, and a functionality that affords high conjugation efficiencies in conjugation reactions - an oxyamine. This linker, in principle, may act as a robust anchor of oligonucleotides to nanoparticles surfaces, such as Fe_3O_4 and TiO_2 coated Fe_3O_4.

Ar son mo thuismitheoirí, Liam agus Marie,

is mo dheirféar, Caroline.

Míle buíochas daoibh as bhur ngrá is as bhur dtacaíocht.

ps-TRIR Investigations of DNA Systems and Toward Bimodal Nanoparticles for Biomedical Applications

A thesis submitted to the University of Dublin for the degree of Doctor of Philosophy

by

Gerard W. Doorley B.A. (Mod.), P. Grad. Dip. Stat.

Under the supervision of

Prof. John M. Kelly

School of Chemistry
Trinity College Dublin

2009

Acknowledgements

First and foremost, I would like to thank my supervisor Prof. John M. Kelly for affording me the opportunity to work within his research team, for all that he has taught me and for his guidance throughout this work. I thank Prof. Yurii Gun'ko for his help, advice and funding. Dr. Susan Quinn is gratefully acknowledged for her unflagging enthusiasm and drive. I am indebted to Prof. Tony Parker of the Rutherford Appleton Laboratories for his support, encouragement and encyclopaedic knowledge.

The experimental TRIR work described in the thesis was carried out at the Lasers for Science Facility in the Rutherford Appleton Laboratories. This facility provides equipment and personnel that are unique, world-leading and frankly unparalleled. I wish to express my most sincere gratitude to the talented team at RAL that supported us over the past number of years. The team, headed by Prof. Tony Parker, with Dr. Mike Towrie, Dr. Ian Clark and Dr. Kate Roynane were adept at solving all our technical problems and were only too willing to answer any queries no matter how trivial. I would also like to express my gratitude to Prof. Mike George of Nottingham University for his contribution to the TRIR studies.

There are many people who supported the experimental work carried out in TCD and the following are thanked for their respective parts: Dr. Martin Feeney for mass spectral analysis, Patsy Greene for his help with all things, Dr. John O'Brien and Dr. Manuel Ruether for NMR spectra, Dr. Robbie Gunning for XRD spectra, Mr. Neal Leddy for TEM and Dr. Yurii Rakovich for confocal microscopy.

Finally, I would like to thank all the members of the Kelly group, past and present. Science Foundation Ireland and Trinity Foundation are gratefully acknowledged for funding.

Summary

The work described herein encompasses two distinct areas of chemistry. The first of these involved the time resolved study of ultrafast relaxation processes in DNA following UV excitation (chapters 1-5). The nature of the electronic excited states of DNA is today an ever expanding area of scientific curiosity. Exposure of DNA to UV radiation can result in deleterious effects with profound biological consequences. Our goal is to understand the excited states formed and their subsequent reaction or relaxation dynamics. To this end, we have embarked on a systematic study from simple nucleotide units to dinucleotide, polynucleotide and finally biologically relevant systems using picosecond time resolved infrared spectroscopy (ps-TRIR).

In chapter 2 the relaxation dynamics of a family of cytosine derivatives is described. A new species was identified having a strong infrared absorption at 1574 cm^{-1}, with lifetimes of 33 and 37 ps for 5′-dCMP and dCyd respectively. Interestingly, the long-lived species was not found for 1-MeCyt and Cyt, suggesting that substitution at the 1-position by 2′-deoxyribose had a major effect on the photophysical properties of the nucleobase. The species was assigned to the dark $^1n_N\pi^*$ state, and this study represented the first direct observation of such a dark state.

The next study, chapter 3, encompassed a comprehensive review of A-T containing systems, from mono- to di- and finally polynucleotide systems. Long-lived species (hundreds of picoseconds) were found after excitation of dApdA and TpT that are most likely due to excimer-like states. A detailed study of the structural isomers dApT and TpdA was undertaken, including for the first time, variable temperature time resolved infrared measurements. Long-lived species lifetimes of 70 and 50 ps were found for dApT and TpdA respectively. Most significantly the thymine dominated regions were found to have a higher contribution from the long-lived species than the adenine dominated regions, and at long time delays the TRIR profile of the dinucleotides resembled that of thymine. We hypothesize that the long-lived state is localized on thymine, due to the fingerprint information afforded from infrared spectroscopy.

A study of DNA secondary structure of $[poly(dG\text{-}dC)]_2$ is described in chapter 4. Two relaxation processes were found for the B form (τ_1 = 7 ps, τ_2 = 30 ps). The long-lived species was found to have a well-defined absorption band at 1597 cm^{-1} and was assigned to

the $^1n_N\pi^*$ state of the cytidine moiety. Sensitivity of the G-C base-pairs in the polymer to secondary structure was confirmed when only a single species, having a broad transient absorption at 1600 cm^{-1} and lifetime of 16 ps was found for the Z form and this species was assigned to a localized exciplex state.

The final TRIR chapter focussed on biologically relevant systems – mixed-base duplex, triplex and quadruplex DNA. The mixed-base study affirmed that base-stacking and hydrogen-bonding interactions facilitate energy delocalization and hence are directly linked to the formation and subsequent relaxation of long-lived states in DNA. Triple-stranded DNA was found to have monoexponential kinetics. This suggested that incorporation of the third strand, which introduces extra hydrogen-bonding in the structure, was responsible for the increased rate of energy dissipation. A cation-dependent TRIR investigation of the human telomeric sequence was performed and interestingly mode specific relaxation behaviour was found in the case of the divalent strontium cation induced quadruplex structure.

The second field of research explored in this thesis was toward the next generation of 'smart' nanoparticles. Synthetic approaches toward novel bifunctional nanoparticles for biomedical applications are described. Magnetic separation and fluorescent labelling are two of the most widely employed techniques in biosciences today, and this work aims to combine both techniques to make the next generation of 'smart' nanocomposites. The synthesis of polypyridyl ligands is described en route to ruthenium metal complexes capable of covalent binding to nanoparticle surfaces. An alternative strategy described herein, involved the design and realization of a dopamine modified metal complex capable of strong binding to metal oxide surfaces. Iron oxide nanoparticles with coupling functionalities were successfully synthesized and characterized. Particles were successfully coated with silica and this was shown to prevent quenching of fluorophore emission. Finally, a novel linker capable of conjugating oligonucleotides to nanoparticles surfaces was designed and synthesized. This molecule combined a functionality capable of strong bonding to metal oxide nanoparticles - an enediol, and a functionality that affords high conjugation efficiencies in conjugation reactions - an oxyamine. This linker, in principle, may act as a robust anchor of oligonucleotides to nanoparticles surfaces, such as Fe_3O_4 and TiO_2 coated Fe_3O_4.

List of Figures and Schemes

List of Tables

List of Abbreviations

1-MeCyt	1-methylcytosine
2D-IR	2 dimensional infrared
3D ps-TRIR	3 dimensional picosecond time resolved infrared
5′-dAMP	2′-deoxyadenosine 5′-monophosphate
5′-dCMP	2′-deoxycytidine 5′-monophosphate
5′-dGMP	2′-deoxyguanosine 5′-monophosphate
5′-TMP	2′-deoxythymidine 5′-monophosphate
A	adenine
ADC	analogue-to-digital converter
APTES:	3-aminopropyltriethoxy silane
bipy	2,2′-bipyridine
C	cytosine
CD	circular dichroism
CI	conical intersection
COSY	correlated spectroscopy
CPD	cyclobutane pyrimidine dimer
Cyt	cytosine
dApdA	2′-deoxyadenyl-(3′-5′)-2′-deoxyadenosine
dApT	2′-deoxyadenyl-(3′-5′)-thymidine
dApU	2′-deoxyadenyl-(3′-5′)-uridine
DCC	N,N′-dicyclohexylcarbodiimide
DCM	dichloromethane
dCyd	2′-deoxycytidine
DFG	difference frequency generation
DIPEA	diisopropylethylamine
DMF	dimethylformamide
DMSO	dimethyl sulfoxide
DNA	deoxyribonucleic acid
EDC	1-ethyl-3-(3-dimethylaminopropyl)carbodiimide
emf	electromagnetic field
endo	endocyclic
ES	excited state
exo	exocyclic
FC	Franck-Condon
fcc	face centred cubic
FRET	fluorescence resonant energy transfer
FTIR	fourier transform infrared
FWHM	full width half maximum
G	guanine
GS	ground state
HA	hexanoic acid
HY	hexylamine

IC	internal conversion
IR	infrared
IRF	instrument response function
ISC	intersystem crossing
IVR	intramolecular vibrational redistribution
LC	ligand centred
LM	Levenberg-Marquardt
LSF	Lasers for Science Facility
MADA	magnetically amplified DNA assay
MCT	mercury cadmium telluride
MIR	mid infrared
MLCT	metal to ligand charge transfer
MRI	magnetic resonance imaging
N	north
NHS	N-hydroxysuccinimide
NMR	nuclear magnetic resonance
OA	oleic acid
OD	optical density
ODN	oligodeoxynucleotide
O_h	octahedral
OPA	optical parametric amplifier
OY	oleylamine
PEG	polyethylene glycol
phen	1,10-phenanthroline
phen′	5-(4-carboxybutanamido)-1,10-phenanthroline
PIRATE	Picosecond InfraRed Absorption and Transient Excitation
PL	photoluminescence
poly(dA)	polyadenylic acid
poly(dT)	polythymidylinic acid
ps-TRIR	picosecond time resolved infrared
pu	purine
py	pyrimidine
RAL	Rutherford Appleton Laboratory
RNA	ribonucleic acid
S	south
SPC	single photon counting
T	thymine
TA	transient absorption
T_d	tetrahedral
TD-DFT	time dependent density functional theory
TEM	transmission electron microscopy
TEOS	tetraethyl orthosilicate

TFA	trifluoroacetic acid
TFO	triplex forming oligonucleotide
TLC	thin layer chromatography
TMA	tetramethyl ammonium hydroxide
TOCSY	total correlation spectroscopy
TpdA	thymidylyl-(3′-5′)-2′-deoxyadenosine
TpT	thymidylyl-(3′-5′)-thymidine
TRIR	time resolved infrared
TSU	N,N,N′,N′-tetramethyl(succinimido)uronium tetrafluoroborate
ULTRA	Ultra-sensitive Life science Time-Resolved Analysis
UpA	uridylyl-(3′-5′)-2′-deoxyadenosine
UV	ultraviolet
VC	vibrational cooling
VT-NMR	variable temperature nuclear magnetic resonance
VT ps-TRIR	variable temperature picosecond time resolved infrared
W-C	Watson-Crick
XRD	X-ray diffraction

List of Presentations

Date/Event/Venue	Title	Type
Mar. 07 Supramolecular Chem. TCD	Picosecond Transients from Oxidation of Guanine by a Ruthenium Complex Intercalated in Double-Stranded DNA	Poster
May 07 Seminar TCD	Ultrafast IR spectroscopy of the short-lived transients formed by UV excitation of cytosine derivatives	Oral
June 07 ISPPCC TCD	Picosecond Transients from Oxidation of Guanine by a Ruthenium Complex Intercalated in Double-Stranded DNA	Poster
July 07 Femto8 Oxford, UK.	Ultrafast IR spectroscopy of the short-lived transients formed by UV excitation of cytosine derivatives	Poster
Sept. 07 COST Meeting Messina, Italy.	Development of "2 in 1" Magnetic and Fluorescent Nanocomposites	Oral
Dec 07 CSCB TCD	Ultrafast IR spectroscopy of the short-lived transients formed by UV excitation of cytosine derivatives	Poster
Mar. 08 Oxidative Damage DCU	Ultrafast IR spectroscopy of the short-lived transients formed by UV excitation of cytosine derivatives	Poster
April 08 IRDG DCU	Ultrafast IR spectroscopy of the short-lived transients formed by UV excitation of cytosine derivatives **Awarded the best poster prize**	Poster
June 08 UP2008 Stresa, Italy.	A Time-Resolved Vibrational Spectroscopy Study on Adenine/Thymine Based Nucleic Acid Systems	Poster

List of Publications

(1) Picosecond Processes in DNA Monitored by Transient Infra-red Absorption Spectroscopy.
G. W. Doorley, J. M. Kelly, D. A. McGovern, S. Quinn and A. M. Whelan and K. L. Ronayne.
Central Laser Facilities Annual Report 2005/2006 **2006**, 129-132.

(2) Ultrafast IR Spectroscopy of the Short-Lived Transients Formed by UV Excitation of Cytosine Derivatives.
S. Quinn, G. W. Doorley, G. W. Watson, A. J. Cowan, M. W. George, A. W. Parker, K. L. Ronayne, M. Towrie and J. M. Kelly.
Chemical Communications **2007**, 2130-2132.

(3) Picosecond Infrared Probing of the Vibrational Spectra of Transients Formed Upon UV Excitation of Stacked G-Tetrad Structures.
D. A. McGovern, S. Quinn, G. W. Doorley, A. M. Whelan, K. L. Ronayne, M. Towrie, A. W. Parker and J. M. Kelly.
Chemical Communications **2007**, 5158-5160.

(4) Photooxidation of Guanine by a Ruthenium Dipyridophenazine Complex Intercalated in a Double-Stranded Polynucleotide Monitored Directly by Picosecond Visible and Infrared Transient Absorption Spectroscopy.
B. Elias, C. Creely, G. W. Doorley, M. M. Feeney, C. Moucheron, A. Kirsch-DeMesmaeker, J. Dyer, D. C. Grills, M. W. George, P. Matousek, A. W. Parker, M. Towrie and J. M. Kelly.
Chemistry - A European Journal **2008**, *14*, 369-375.

(5) Picosecond Transient Infrared Study of the Ultrafast Deactivation Processes of Electronically Excited B-DNA and Z-DNA Forms of $[poly(dG\text{-}dC)]_2$.
G. W. Doorley, D. A. McGovern, M. W. George, M. Towrie, A. W. Parker, J. M. Kelly and S. J. Quinn.
Angewandte Chemie International Edition **2009**, *48*, 123-127.

(6) A Study of the pH Dependence of Electronically Excited Guanosine Compounds by Picosecond Time-Resolved Infrared Spectroscopy.
D. A. McGovern, G. W. Doorley, A. M. Whelan, A. W. Parker, M. Towrie, J. M. Kelly and S. J. Quinn.
Photochemical and Photobiological Sciences, **2009**, *8*, 542-548.

(7) ps-TRIR Covers All the Bases - Recent Advances in the Use of Transient IR for the Detection of Ultrafast Species in DNA.
M. Towrie, G. W. Doorley, M. W. George, A. W. Parker, S. J. Quinn and J. M. Kelly.
The Analyst, **2009,** DOI: 10.1039/b902108f.

(8) A Time-resolved Vibrational Spectroscopy Study on Adenine/Thymine Based Nucleic Acid Systems.
G. W. Doorley, D. A. McGovern, R. J. H. Davies, M. Towrie, A. W. Parker, J. M. Kelly and S. J. Quinn
Springer Chemical Physics, Proceedings of Ultrafast Phenomena XVI, **2009**, in press

(9) UV Excitation of DNA Dinucleotides dApT and TpdA Results in a Long-lived Excited State Localized on Thymine.
G. W. Doorley, M. Wojdyla, D. A. McGovern, M. Towrie, A. W. Parker, J. M. Kelly and S. J. Quinn.
Journal of the American Chemical Society, in preparation.

Table of Contents

Chapter 1

Introduction to Nucleic Acids and the ps-TRIR Technique

1.1 General Introduction

The nature of the electronic excited states of DNA is currently a rapidly expanding area of scientific curiosity. Not just mere subjects of academic interest, DNA excited states play a pivotal role in DNA damage. Unravelling the complex nature of DNA photophysics has been the motivation of many research groups for years but as yet the complete picture has not been fully revealed. A lot of experimental work has emerged throughout the last half century or so since Watson and Crick revealed the true structure of genomic DNA.[1] With each new generation of results from new and superior techniques, have come additional insights into the electronic properties of the DNA bases upon excitation. However, the jigsaw puzzle is far from complete.

Exposure of DNA to ultraviolet (UV) radiation can result in deleterious effects with profound biological consequences.[2-10] Solar UV radiation is the primary cause of non-melanoma skin cancers, and with the continued depletion of the ozone layer, incidences of skin cancers are ever-rising. Photocarcinogenesis, which is today a major growing health concern, results from photochemical damage to DNA caused by the direct absorption of UV light. The nucleobases absorb strongly in the UV and this facilitates the production of excited states, which are the first step in the complex chain of events which may or may not culminate in photolesions/photodamage. Understanding the excited states formed and their subsequent reaction or relaxation dynamics is of fundamental importance but it is not a trivial issue. One goal of photophysical investigations has been to appreciate how electronic excited states produce photochemical outcomes. This is complicated by the fact that in order to counteract the potentially harmful effects of UV radiation exposure, organisms have developed highly sophisticated and complex mechanisms to dissipate the excess energy.

However, there are still numerous questions that remain unanswered with regards to the remarkable stability of DNA toward harmful external influences, and this study seeks to unravel some of these secrets using the relatively new and sophisticated technique of picosecond time resolved infrared (ps-TRIR) spectroscopy.

1.2 Structure of the Nucleic Acids

Deoxyribonucleic acid (DNA) is a long linear chain polymer, encoding genetic information, that is comprised of just four subunits, the nucleotides. These units were isolated in the early twentieth century by chemical degradation studies and today their structure is known.[11] Figure 1.1 shows the four bases of DNA: adenine, thymine, guanine and cytosine. The bases are planar and are divided into two sub-groups, the pyrimidine (py) bases {cytosine (C) and thymine (T)} and the purine (pu) bases {adenine (A) and guanine (G)}. Substitution at the 1-position (py) / 9-position (pu) with a hydrogen atom is termed the free base, while substitution with a ribose ring (figure 1.1) is termed a nucleoside. Individual nucleoside units are joined together in a nucleic acid in a linear manner through a negatively charged phosphate backbone. Substitution of the base with a ribose and phosphate results in a nucleotide unit. Watson-Crick hydrogen bonding occurs between the complementary base (A:T ; G:C), and this plays an integral part in the stability of DNA structures.[1] There are two hydrogen bonds between the A:T base-pair and three between the G:C base-pair.

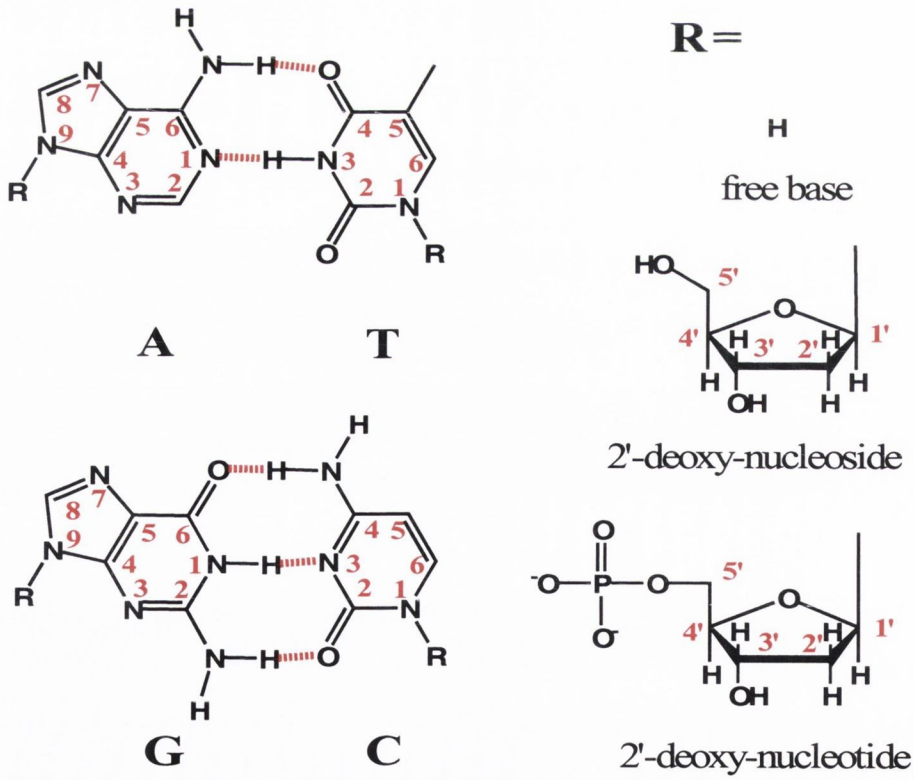

Figure 1.1 The nucleobases, adenine (A), thymine (T), guanine (G) and cytosine (C) with Watson-Crick hydrogen bonding shown and the ribose and ribosyl phosphate groups.

The non-planarity of the sugar is referred to as the pucker. Due to the sugar ring's desire to attain the most energetically stable conformation either the C2′ or C3′ will pucker out of the plane of the sugar. In practice, both carbon atoms are found to shift geometry to a certain extent and form a 'twist' conformation. The resulting structures are termed C2′-*endo*, C3′-*exo* (South (S) conformer) and C3′-*endo*, C2′-*exo* (North (N) conformer), where *endo* and *exo* are endocyclic and exocyclic respectively. Direct correlations have been found between the observed sugar pucker and backbone secondary structure conformation in oligo- and polynucleotide systems.

A final important structural consideration of the nucleotides is the conformation about the glycosidic bond. This is the bond between the nucleobase and the 1′-position of the deoxyribose. The glycosidic torsion angle, χ, is defined in terms of four atoms for the bases: O4′-C1′-N9-C4 for purines and O4′-C1′-N1-C2 for pyrimidines. This angle defines whether a base is in the *anti* or *syn* conformation, where *anti*: $-120 > \chi > 180°$ and *syn*: $0 < \chi < 90°$. The anti conformation is preferred for A, T and C nucleotides, whereas a G nucleotide unit displays a small preference for the *syn* conformation. In the *anti* conformation the base is directed away from the sugar, while in the *syn* arrangement the sugar and base overlap. Unsurprisingly, there are correlations between the sugar pucker and torsional angle. *Syn* glycosidic angles are not found with C3′-*endo* puckers due to steric interactions between the base and the sugar.

As previously mentioned, the nucleotide units are joined together through the negatively charged phosphodiester backbone linkage. The bases are attached to the 3′ or 5′ positions of the sugar. Figure 1.2 shows an example of this linkage for a short strand containing the four DNA bases. Chain direction is frequently expressed with the 5′ or 3′ labels so as to eliminate ambiguity when describing a sequence. The complementary strand forms hydrogen bonds to the first strand and the linkage runs 5′-3′ to 3′-5′, as illustrated in figure 1.2. In the double-stranded form, DNA adopts a helical structure. The right-handed form, known as the B form, is the most common. However, conformational changes can be induced, for example conversion into the left-handed Z form upon addition of salt. Metal cations interact with the negatively charged phosphate backbone and can stabilize the helix. There are base-stacking interactions between adjacent bases (separated by 3.4 Å in B-DNA) in the helical structure, and these interactions are thought to be key to electron and charge distribution within the helical polymer. Higher order multi-stranded structures such as triplex and quadruplex DNA are

also found in biological systems, and base-stacking and hydrogen-bonding motifs are central to the stability of such architectures.[11,12] These structures will be considered further in chapter 5.

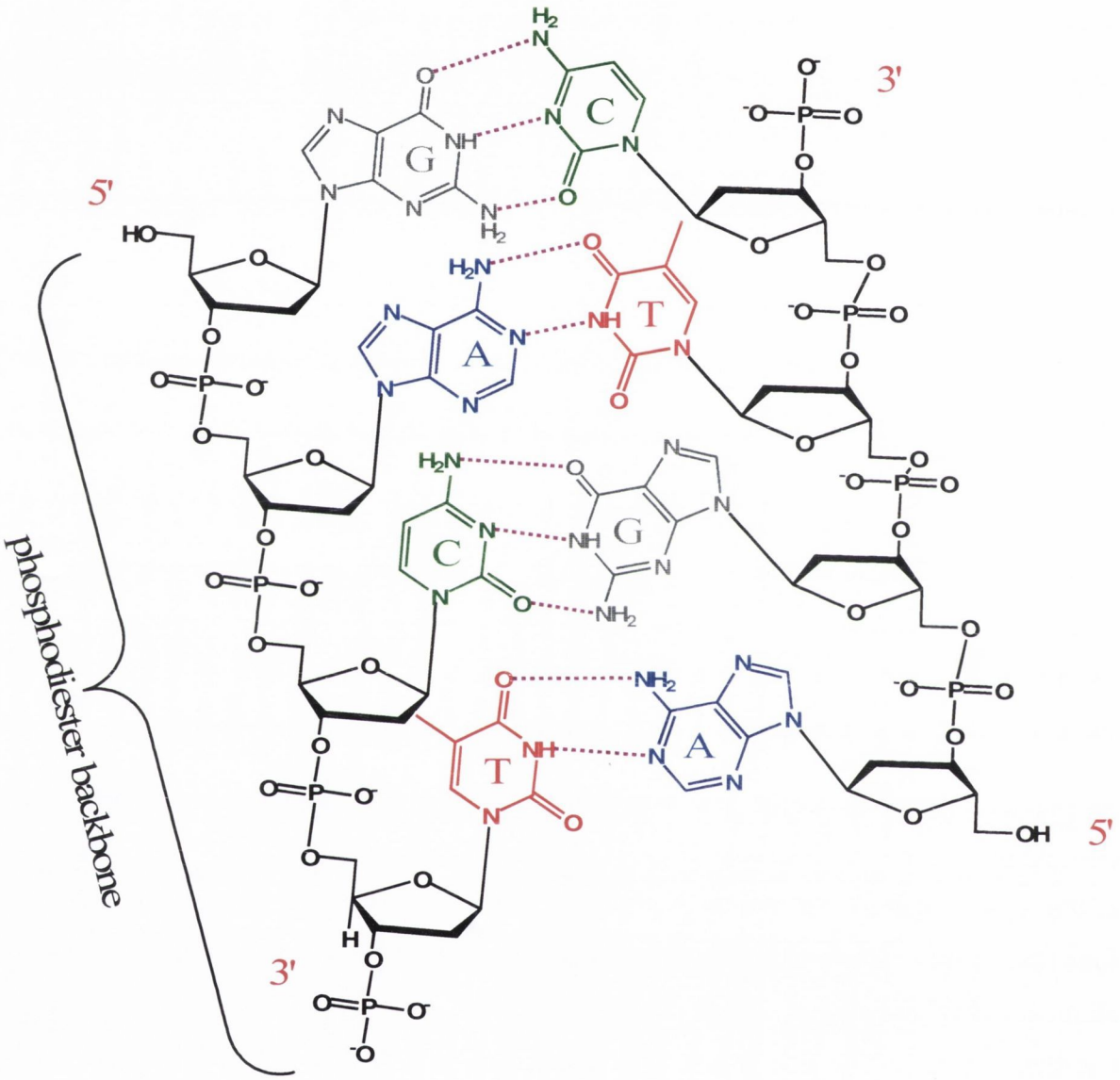

Figure 1.2 Complementary DNA strands showing the phosphodiester backbone, base-pairing, and hydrogen bonding (purple dashes).
Non exchangeable hydrogen atoms have been omitted for clarity.

1.3 Photophysics and Photochemistry of Nucleic Acids

It is well established that exposure of DNA to UV light can result in photoadducts,[2-10] with the prevalence and distribution of such photoproducts being dependent on the intensity and wavelength of the incident radiation. Figure 1.3 gives the absorption spectrum of DNA, with maximum absorbance at 260 nm, and indicates that the excited state(s) that may be produced and subsequent photoreactivity is indeed a function of the wavelength of the incident light. In the UVA region (320-380 nm) there is no absorption. The higher energy, UVB radiation (290-320 nm), is absorbed to a greater degree, but the majority of DNA absorptions occur in the UVC region (190-290 nm).

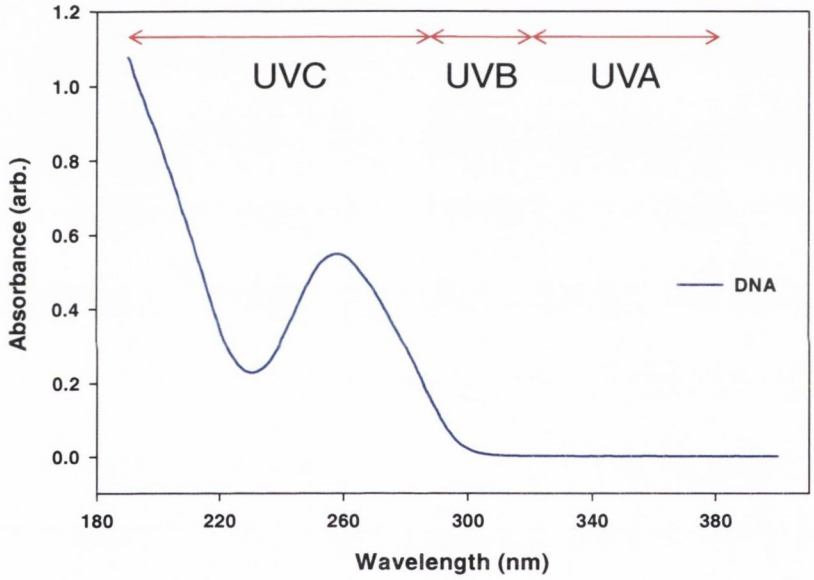

Figure 1.3 UV absorption spectrum of DNA.

Upon absorption of a photon by a pyrimidine or purine base, there are several possible outcomes, some of which are illustrated in figure 1.4. Initially, a Franck-Condon excited state is produced. Ultrafast internal conversion of the nucleobases is the predominant nonadiabatic process facilitating recovery to the ground state with theoretical studies emphasising the importance of this processes.[13,14] The nucleobases fluoresce extremely weakly with very low quantum yields, and this has led to the conclusion that their excited states must be very short-lived.[15] In recent years, ultrafast laser spectroscopy has provided many new insights into the excited states of the nucleic acids. Femtosecond transient visible absorption[5,16,17] and fluorescence upconversion[18,19] measurements have shown sub-picosecond excited state lifetimes for the bases and mononucleotides despite the

> 4 eV gap between the vibrationless levels of the electronic ground state, S_0, and the emitting state. The intrinsic photostability provided by such short excited singlet state lifetimes of the DNA and RNA bases, may be responsible for their selection as the building blocks of the genetic code.

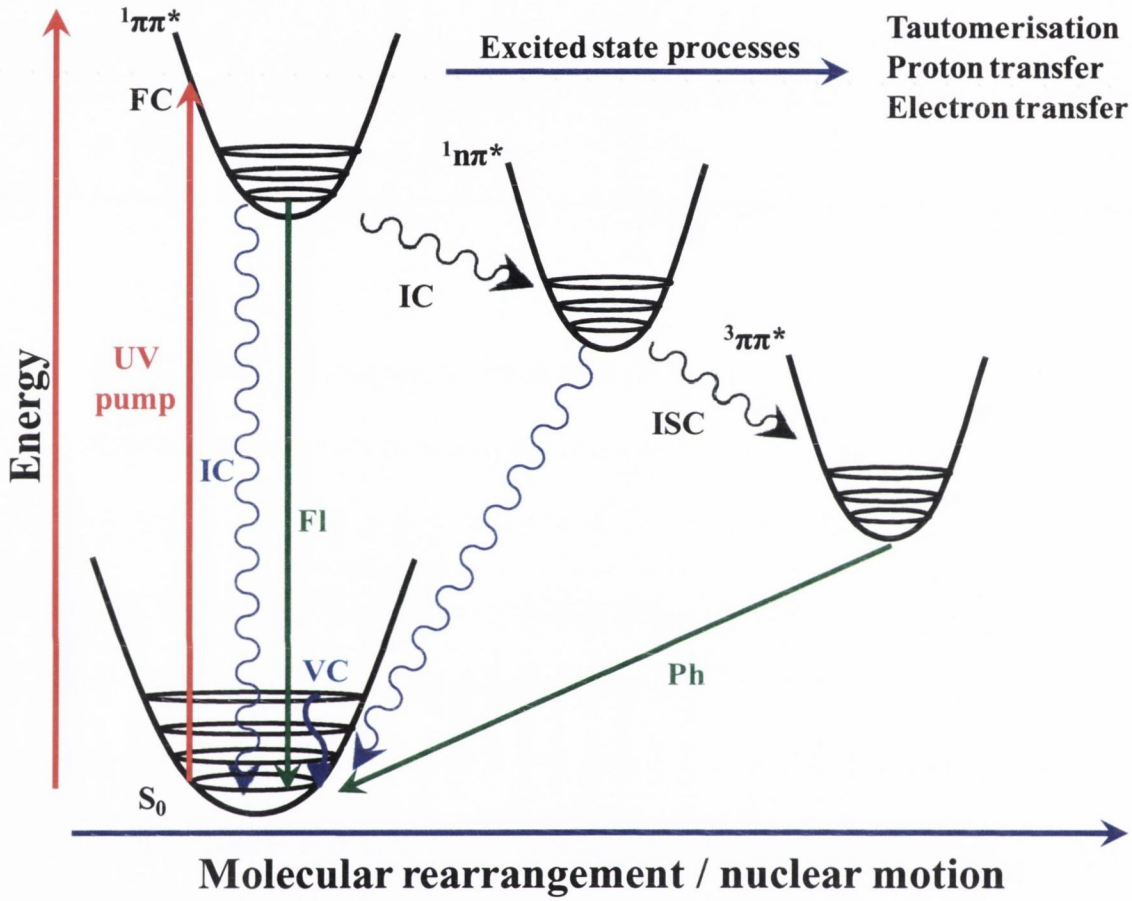

Figure 1.4 State diagram illustrating possible ultrafast processes in DNA following UV excitation. Key: FC – Franck-Condon, IC – Internal Conversion, ISC – Intersystem Crossing, VC – Vibrational Cooling, F – Fluorescence and P – Phosphorescence.

Strong vibronic coupling between the $^1\pi\pi^*$ and $^1n\pi^*$ states may occur if the energy gap between the states is small enough so that the states are almost considered to be degenerate. The strong coupling of electronic and nuclear motions results in internal conversion through a conical intersection into the $^1n\pi^*$.[16] In recent years, conical intersections have been proposed in many studies as facilitating ultrafast nonradiative decay in DNA.[13,14,16,20-40]

Intersystem crossing (ISC) to the triplet state is expected to occur in very low yield ($\Phi_{ISC} < 0.01$) as a result of the rapid single-state(s) dynamics.[41] Triplet states in DNA have been known to exist for many years[42] and have more recently been successfully sensitized for the nucleotides using high energy triplet sensitizers, that facilitate triplet-triplet energy transfer and hence generate the state in high yields.[43] It is now suggested that the triplet state may be a precursor to or directly involved in DNA damage, more specifically the production of cyclobutane pyrimidine dimers.[5,8,39,40,44-47]

In addition to electronic transitions nucleic acids also undergo vibrational cooling. Vibrational cooling is the process by which the molecule after returning to the ground state (S_0) dissipates the excess vibrational energy in order to return to the lowest vibrational level. Redistribution of the energy among the available vibrational modes, known as intramolecular vibrational redistribution (IVR), and intermolecular vibrational energy transfer to solvent molecules, returns the 'vibrationally hot' molecule to thermal equilibrium with the surrounding solvent. This process was first identified for the nucleotides by transient absorption (TA) methods[17,37] and later characterized by picosecond time resolved infrared (ps-TRIR).[48] Recently, the solvent dependency of this process was probed for the nucleobases, and it was clearly demonstrated that the efficiency with which the molecule vibrationally cools was greatest for solvents with a dense network of hydrogen bonds.[49] This is presumably due to the fact that the hydrogen bonded solvent molecule, interacting with the polar groups of the nucleobases, is adept at intermolecularly transferring the excess energy to neighbouring hydrogen bonded solvent molecules.

Once formed, an excited state species may undergo reaction, either inter- or intramolecularly. Tautomerization has been widely proposed for both isolated bases and base-pairs with single and double proton transfer and charge transfer states all being considered.[28,31,32,50-77] As we shall see later in chapter 2, tautomerization is particularly important for the reactions of the pyrimidines such as cytosine. Theoretical studies have argued that tautomerization is critical to relaxation mechanisms of the excited states. Proton and electron transfer processes are also important excited state practices and may at least be partly responsible for the inherent stability of DNA.[13,22,33,50,53,54,68,71,78-85] Proton transfer in the excited state of G-C base-pairs has recently been offered as a mechanism for the ultrafast relaxation observed,[85] and this process of proton transfer (both forward and

backward) has been calculated to occur on a 200 fs timeframe.[22] This matter is relevant to our study of [poly(dG-dC)]$_2$ and will be considered in more detail in chapter 4.

Until recently, most photophysical studies of DNA were by transient absorption and fluorescence methods.[17,37] An excellent review of the area by the Kohler research group, published in 2004, summarized the field at the time. Problems associated with these techniques include the extremely low quantum yield of the nucleobases and their inability to directly observe dark states. Major advances have occurred since 2004, and now techniques such as TRIR are proving very useful for the characterization of ultrafast relaxation behaviour in DNA. The first TRIR study of DNA relaxation behaviour was published in 2005 and involved a collaborative effort between groups from Trinity College Dublin, the University of Nottingham and the Rutherford Appleton Laboratory.[48] In fact, the Kohler group have themselves realized the potential of TRIR spectroscopy and have complemented their significant body of transient absorption work with TRIR investigations in the last two years.[44,86]

1.4 Vibrational Spectroscopy of Nucleic Acids

The biological functionality of the nucleic acids is very much dependent on their structure and geometry. Nucleic acid structures have been studied by a wide variety of techniques such as X-ray diffraction (XRD), ultraviolet (UV), circular dichroism (CD) and nuclear magnetic resonance (NMR) spectroscopies. However, one technique that provides clear spectroscopic signals relating to structure and geometrical orientation in solution is infrared (IR) spectroscopy. While NMR is a powerful technique to study nucleic acid structure, it is limited by the concentration and size of the entities that can be studied and is best applied to smaller fragments. IR can investigate highly complex and large systems such as native DNA and can be applied not only to the solution phase samples but also to hydrated films and crystalline states. The technique is non-destructive and the effect of variation of external parameters such as ionic strength, nature of counterion, pH, hydration and temperature can be easily varied and followed. Information of sugar conformation (C2′-*endo* ; S type vs. C3′-*endo* ; N type), helical sense (B-DNA vs. Z-DNA) base-pairing motif (Watson-Crick, Hoogsteen) and even higher order structures such as triplex or quadruplex DNA can all be gleaned from vibrational spectroscopy (chapter 5).

Figure 1.5 represents the infrared spectral window that provides the vast majority of structural information for nucleic acids. Each domain, as divided up in the figure, has the ability to provide key structural information relating to distinct parts of the nucleic acids. Region I (1800-1500 cm^{-1}) contains the vibrations from the nucleobases, and each nucleobase has its own distinct fingerprint within this region. Peaks corresponding to in-plane double bond stretching vibrations, C=O, C=N and C=C, all occur in this domain. Band positions are characteristic of secondary structure and base-pairing schemes. Water absorbs strongly in this region and therefore when studying nucleic acids in this region, it is necessary to use D_2O (which absorbs at lower wavenumbers). Region II (1500-1250 cm^{-1}) is sensitive to the sugar conformation about the glycosidic bond and reports the presence of an *anti* or *syn* conformation for the purines. This region, for example, has the ability to distinguish between quadruplex DNA in the parallel (all guanines are *anti*) or antiparallel (mixture of *anti* and *syn*) conformation. Region III (1250-1000 cm^{-1}) can provide information on the secondary structure, for example B-DNA versus Z-DNA. Intense phosphate vibrations occur here, with the antisymmetric (~1230 cm^{-1}) and symmetric (~1089 cm^{-1}) vibrations of the DNA backbone. The antisymmetric band is a very sensitive reporter of DNA secondary structure. Finally, region IV (< 1000 cm^{-1}), contains diagnostic absorptions from the phosphodiester chain, pucker specific vibrations of the sugar (C2′-*endo* ; S type vs. C3′-*endo* ; N type) and out-of-plane double bond vibrations of the nucleobases.

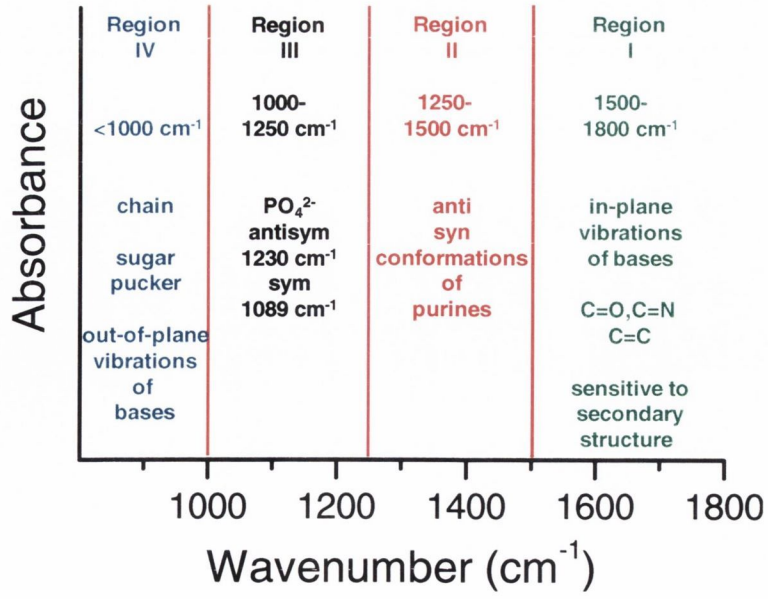

Figure 1.5 Infrared spectrum with assignment of the fingerprint regions for DNA.

1.5 The TRIR Measurement

The following is a brief description of the Picosecond Infrared Absorption and Transient Excitation (PIRATE) instrument at the Lasers for Science Facility (LSF) in the Rutherford Appleton Laboratories (figure 1.6). A more detailed explanation of the apparatus can be found in the experimental section and in reference 87.

TRIR is a pump-probe technique. For DNA studies a pump pulse having a wavelength of 267 nm (150 fs, repletion rate of 0.5 kHz and energy of 1-2 μJ) is generated from the third harmonic of the 800 nm output from a regenerative amplifier (150 fs, 1 mJ). As mentioned earlier, the DNA bases absorb strongly in the UVC region and consequently 267 nm excitation is employed. An infrared probe beam (FWHM ~ 150 cm^{-1}) is generated using difference frequency generation (DFG) methods. The spot size of the pump and probe beams at the sample are 200 and 150 μm respectively. To avoid pumping the same position and hence minimize sample degradation, the sample cell is randomly oscillated in both x and y directions. Mercury cadmium telluride (MCT) detectors monitor the change in transmittance and a digital signal is fed to a computer that generates a difference spectrum. Samples concentrations in the low mM range are required, typically 10-20 mM, in order to obtain a good signal-to-noise ratio. All samples are prepared in D_2O as water absorbs strongly in the mid infrared.

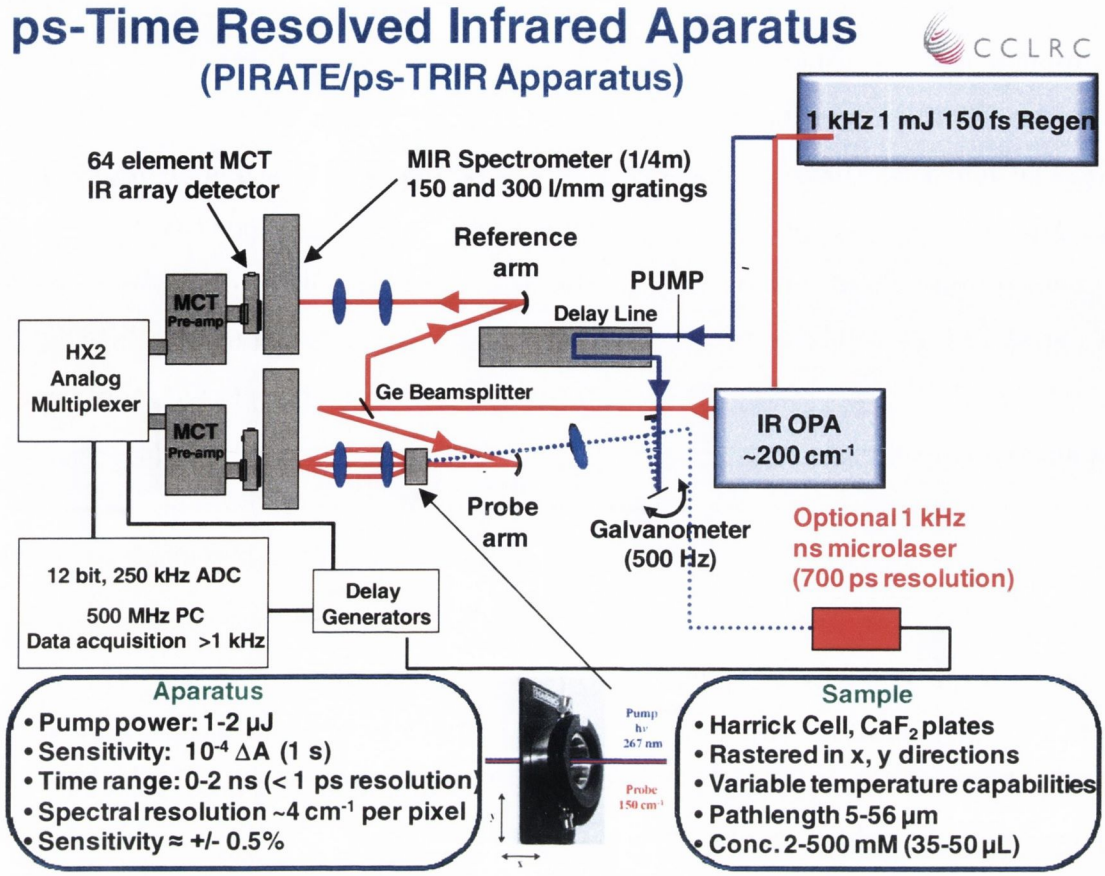

Figure 1.6 Setup of the ps-TRIR apparatus at the Rutherford Appleton Laboratory.

1.6 The TRIR Difference Spectrum Explained

With difference spectroscopy it is possible to monitor small differences in the ground and excited state populations. The spectrum obtained in our TRIR measurements is essentially the excited state absorption minus the depleted ground state absorption at a particular time, Δt, after the pump pulse (t = 0), i.e. $A_{diff.} = A_{E.S.} - A_{G.S.}$. Figure 1.7 demonstrates pictorially how the difference spectrum is generated. In figure 1.7 (a) the depleted ground state absorption is centred at 1600 cm^{-1} with the excited state absorption being centred at 1550 cm^{-1}. The resulting difference spectrum shows that the transient absorption and ground state bleaching are sufficiently separated that the band structures do not change, i.e. at 1550 cm^{-1}, $A_{diff.} = A_{E.S.} - 0$, as there is no contribution in this region from the depleted ground state. At 1600 cm^{-1}, $A_{diff.} = 0 - A_{G.S.}$, as there is no absorption from a transient species at this wavenumber. This represents the simplest case where there is no overlapping of transient absorption and ground state bands.

The reality is that in most cases there will be overlapping between the bands and figure 1.7 (b) illustrates the case where the ground state depletion band is still centred at 1600 cm^{-1} but now the transient absorption is centred at 1590 cm^{-1}. In this case of overlapping absorptions the bands are no longer symmetrical in the difference spectrum, and this is most obvious for the transient absorption band. This represents the type of spectra that will be presented throughout this thesis, where there is overlap between the bands. As this overlap increases, band structure deviates more and more from symmetrical Gaussian-type shape.

The final case, figure 1.7 (c) illustrates what the difference spectrum would look like if both the transient absorption and ground state depletion bands absorb at 1600 cm^{-1}. This represents an unusual case, and one that mistakenly may be interpreted as having no transient absorption in the sample.

One important point to note is that with increasing delay times the signal of the bleaching band becomes smaller and smaller, and recovers to the baseline (as the transient absorption decays). In the TRIR spectrum we are monitoring the extent of ground state depletion, and therefore at longer times, all molecules have recovered to the ground state and the TRIR shows no absorbance at this position.

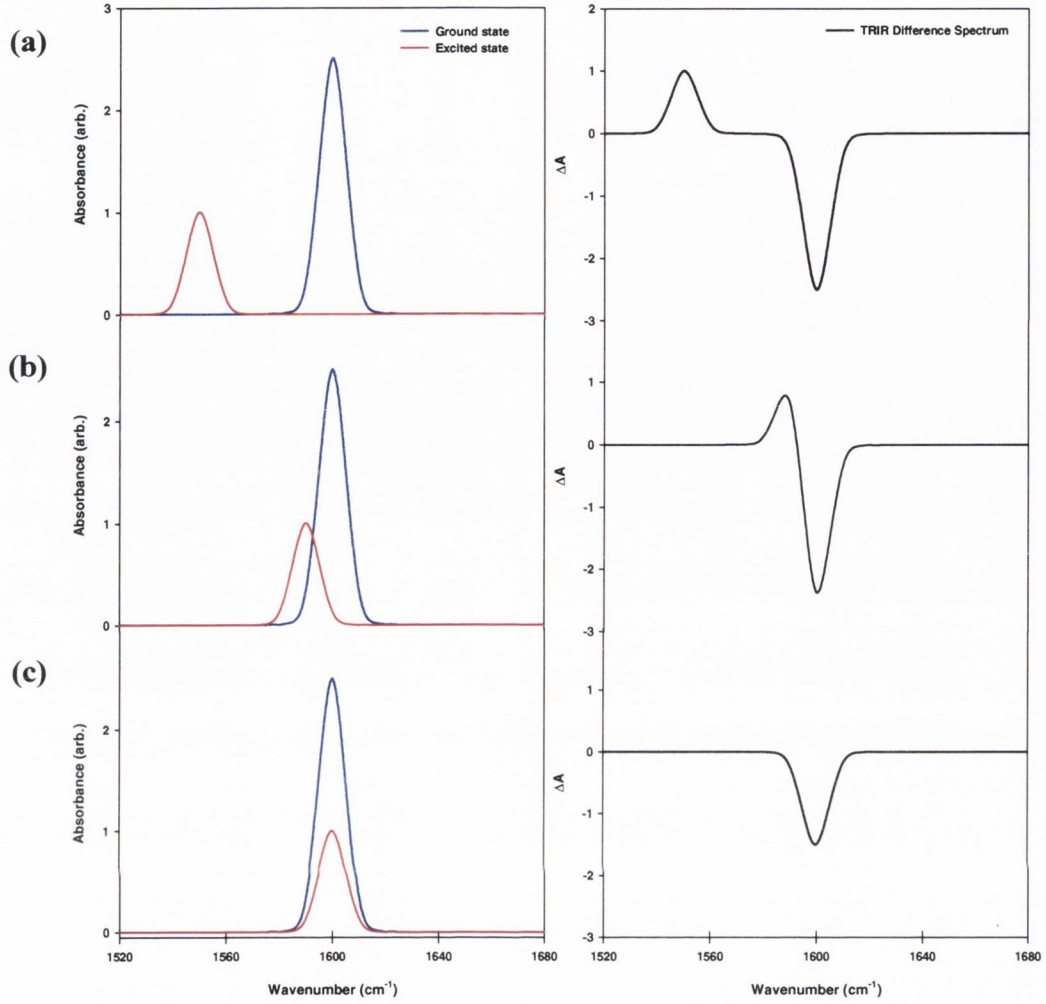

Figure 1.7 Modelled ground and excited state absorption and TRIR difference spectra at time Δt after the pump pulse. Ground state absorption is centred at 1600 cm^{-1} in all cases and the transient absorption is centred at (a) 1550, (b) 1590 and (c) 1600 cm^{-1}. All bands are Gaussian.

1.7 Analysis of the TRIR Spectrum

Analysis of the relaxation behaviour is achieved by fitting the rate of decay of the transient absorption band or the ground state bleaching band recovery to an exponential model. In the cases of a mono- and biexponential recovery the data is fitted to the functions $y = A_1*\exp(-x/\tau_1) + y_0$ and $y = A_1*\exp(-x/\tau_1) + A_2*\exp(-x/\tau_2) + y_0$, where the A terms are the pre-exponential factors or amplitude factors and y_0 is the y offset constant. The result of the fitting, say for the case of a biexponential model results in two lifetimes, τ_1 and τ_2 and the contribution from these two lifetimes is directly proportional to the magnitude of the A terms.

OriginPro uses the non-linear least squares fitter (NLSF) to fit exponential functions to a given dataset. This nonlinear regression method is based on the Levenberg-Marquardt (LM) algorithm and is the most widely used algorithm in nonlinear least squares fitting. The LM algorithm is an iterative technique that locates the minimum of a multivariate function that is expressed as the sum of squares of non-linear real-valued functions.[88,89] It has become a standard technique for non-linear least-squares problems, widely adopted in a broad spectrum of disciplines. LM can be thought of as a combination of the steepest descent and the Gauss-Newton methods. When the current solution is far from the correct one, the algorithm behaves like a steepest descent method: slow, but guaranteed to converge. When the current solution is close to the correct one, it becomes a Gauss-Newton method. A detailed analysis of the LM algorithm is beyond the scope of this thesis with more comprehensive treatments being described for the interested reader elsewhere.[90-92] The goodness of the fit of the model to the observed data at each iteration is determined by the value of the statistically determined coefficient, R^2, and the value of Chi-squared, χ^2. χ^2 is essentially a sum of the differences between the observed (O) and expected (E) outcome frequencies, each squared and divided by the expectation ($\chi^2 = \sum\{(O-E)^2/E)\}$). R^2 is a measure of the variability of the data set with the applied model and is measured through examining how the residual sum of squares vary with the total sum of squares (which is proportional to the sample variance). If the residual sum of squares is small in comparison to the total sum of squares then R^2 approaches one. Both R^2 and χ^2 are in the range 0-1. Successive iterations seek to reduce the discrepancy between the observed values and those predicted by the model. R^2 approaches unity and χ^2 is minimized with each successful iteration. The program terminates when no further

reduction in χ^2 is achievable, and the values obtained at this final iteration are those presented throughout this thesis.

A simulated TRIR difference spectrum is given figure 1.8 (a). The pixel at 1600 cm^{-1} has been highlighted at all delays. The single pixel fitting procedure involves plotting the ΔA at each time delay against the time delay as a scatter plot. The next step is to fit the scatter plot to either a mono- or biexponential model. Figure 1.8 (b) illustrates the result of this fitting for the simulated spectrum where both mono- and biexponential functions were used. It is evident upon examining the fitted models that a monoexponential model is inappropriate in this case, while the biexponential function appears to provide a good fit to the data points. The goodness of both fits can be assessed by examining the parameters R^2 and χ^2 as mentioned above. Table 1.1 provides a summary of these parameters as well as the results of the fitting procedures for both models. The table shows that the R^2 values were 0.94638 and 0.99811 for the mono- and biexponential models respectively. The respective χ^2 values were determined to be 0.26976 and 0.01332 for the mono- and biexponential models. These values confirm that the monoexponential model is an inappropriate one whereas the biexponential model fits well to the data points. The lifetimes obtained from the models are 14 ± 4 ps for the monoexponential model and 5 ± 1 ps (71%) and 143 ± 27 ps (29%) for the biexponential model. Taking into account the values of the 'goodness-of-fit' parameters, the recovery of the simulated bleaching band occurs with two lifetimes as predicted by the biexponential model.

An alternative approach and one that can be useful in certain instances is to analyze how the area of a band decays/recovers with time (double headed arrow in figure 1.8 (a) illustrates this). This method is employed to gain an overall kinetic picture for a particular band as it is essentially taking the average over a number of pixel points. This method involves plotting say a 2 ps TRIR delay over the particular wavenumber range of interest. The integral of this plot is calculated, resulting essentially in the area under the curve/TRIR profile. The procedure is then repeated for all time delays. A scatter plot of the area against time delay results in a plot that can now be fitted to an exponential model, as per the single pixel fitting case outlined above. OriginPro 7.5 was used for the fitting of all experimental data presented in this thesis with the parameters in the exponential models left unconstrained.

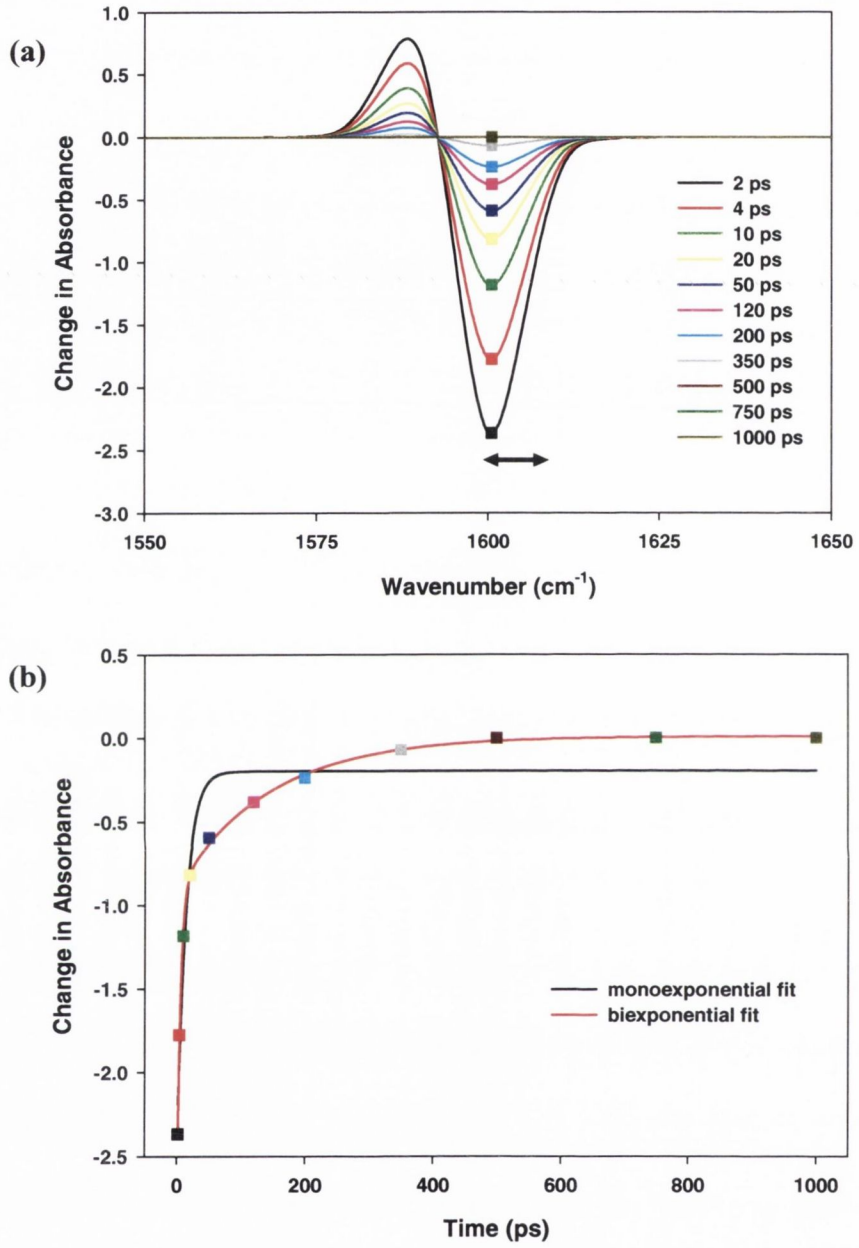

Figure 1.8 Illustration of the kinetic fitting process.

(a) Simulated TRIR spectrum with delays at 2, 4, 10, 20, 50, 120, 200, 350, 500, 750 and 1000 ps and (b) Kinetic analysis of the 1600 cm^{-1} pixel position.

Model	ExpDec1		ExpDec2	
Equation	$y = A_1*\exp(-x/\tau_1) + y_0$		$y = A_1*\exp(-x/\tau_1) + A_2*\exp(-x/\tau_2) + y_0$	
χ^2	0.26976		0.01332	
R^2	0.94638		0.99811	
Iterations	40		40	
	value	±	value	±
y_0	-0.19622	0.08971	0.01055	0.03831
A_1	-2.30458	0.25571	-2.16294	0.11952
τ_1	13.89804	3.687969	5.02084	0.64858
A_2	-	-	-0.90339	0.06662
τ_2	-	-	143.34966	26.69565

Table 1.1 Summary of the results obtained when mono- and biexponential models were fit to the bleach recovery at 1600 cm^{-1} from figure 1.8 (a).

1.8 Aims and Objectives of this Work

To gain insight into the extremely complex nature of DNA photophysics, we have started with simple units. It is hoped that an understanding of the dynamics on a simple monomeric level will result in the ability to make inferences about the higher order structures, facilitating an easier interpretation, with the ultimate goal of understanding ultrafast relaxation processes in native DNA. It is from a primary understanding of the processes on a molecular level that insight will be gained into the very complex bigger picture. IR methods, including 2D-IR, are proving an increasingly valuable tool for the study of DNA systems.[93-96] Time-resolved Infrared (TRIR) absorption spectroscopy[87] is an ideal technique to elucidate such intricacies as it not only provides ultrafast kinetic information but also affords important structural information. An important contribution from previous work within the group allowed for the observation of the vibrationally excited ground states formed from nucleotides excited at 267 nm.[48] Subsequently the method has been used to identify the products of the photoionization of 5′-GMP after excitation at 200 nm[97] and very recently the formation of thymine dimers.[86]

This work represents a comprehensive survey of the relaxation behaviour in a multitude of nucleic acid systems. Aspects such as solvation, hydrogen-bonding, base-stacking, extent of overlap in stacked systems, temperature, sequence composition, secondary structure, base-pairing motif, cation size and charge and resultant secondary structure conformation

are all examined in the context of the excited state(s) produced and their subsequent relaxation dynamics.

This study involved probing the transient species formed following UV excitation of :

- mononucleotides (chapters 2, 3 and 4) : effect of substitution at the 1-position is examined for cytosine derivatives in chapter 2,
- dinucleotides (chapter 3) : a family of dinucleotides, dApT, TpdA, dApdA and TpT are studied with particular emphasis on the role of stacking and the extent of overlap in the systems,
- isomeric but conformationally diverse polynucleotides (chapter 4) : [poly(dG-dC)$_2$] in both the B- and Z-DNA forms are examined and
- finally biologically relevant systems such as mixed-base double-stranded, triplex and quadruplex DNA (chapter 5) : architectures that are found in mammalian systems are investigated with a view to understanding how secondary structure modulates ultrafast relaxation processes.

Chapter 2

ps-TRIR Investigation of Cytosine Derivatives

2.1 Introduction

This first study is of cytosine derivatives. DNA is intrinsically photostable and this is perhaps the reason that evolution has chosen the two pyrimidines (C and T) and purines (A and T). This said, photodamage/photolesions may and have been shown to occur.[2-10] Cytidine in a polymer arrangement is known to form mutagenic products, for example cyclobutane pyrimidine dimers (CPDs) have been shown to form upon exposure to UVC and even lower energy UVB radiation.[2] However, it is not clear what factors are important in favouring or disfavouring the proliferation of such harm.

2.2 Motivation for this Study

We wish to understand what excited state(s) are formed in cytosine derivatives and if substitution at the 1-position of the nucleobases is a governing factor. The vast majority of photoexcitations result in nonradiative relaxation of the excited state, with ultrafast internal conversion being the predominant mechanism.[13,14] It has been suggested that dark states may also be very important in facilitating the removal of potentially harmful energy, and one such state, the $^1n_N\pi^*$ state, has been predicted to be very close in energy to the $^1\pi\pi^*$ state of cytosine.[14] If such states exist, TRIR in principle, should be able to monitor the relaxation from the dark excited state to the ground state (assuming of course the relaxation occurs on a ps timescale). With this study, we have taken cytosine (and its derivatives) in the simplest context, in the hope of unravelling the fundamental processes that are specific to this base. To this end, we have probed the excited state relaxation dynamics of a family of cytosine derivatives, 2′-deoxycytidine 5′-monophosphate (5′-dCMP), 2′-deoxycytidine (dCyd), 1-methylcytosine (1-MeCyt) and cytosine (Cyt) using vibrational spectroscopy.

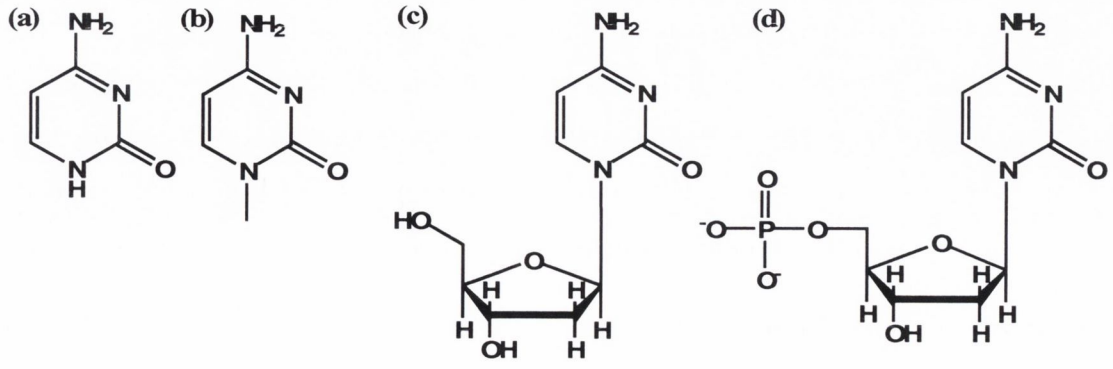

Scheme 2.1 Structures of (a) Cyt, (b) 1-MeCyt, (c) dCyd and (d) 5′-dCMP.

2.3 Results

2.3.1 2′-deoxycytidine 5′-monophosphate (5′-dCMP)

The ps-TRIR difference spectrum of 5′-dCMP in buffered D_2O solution (pH 7) following UV excitation (150 fs, 267 nm) is given in figure 2.1. For clarity, early time delays are shown in red (2-10 ps) with the later time delays in black (15-1000 ps). The spectrum was recorded in two spectral windows at various delays between 2 and 1000 ps. Depletion bands centred at 1507, 1524, 1613 and 1649 cm^{-1} correspond to ground state absorptions, as is evidenced by the agreement with the FTIR. Transient absorptions are seen at 1490, 1574 and 1630 cm^{-1}.

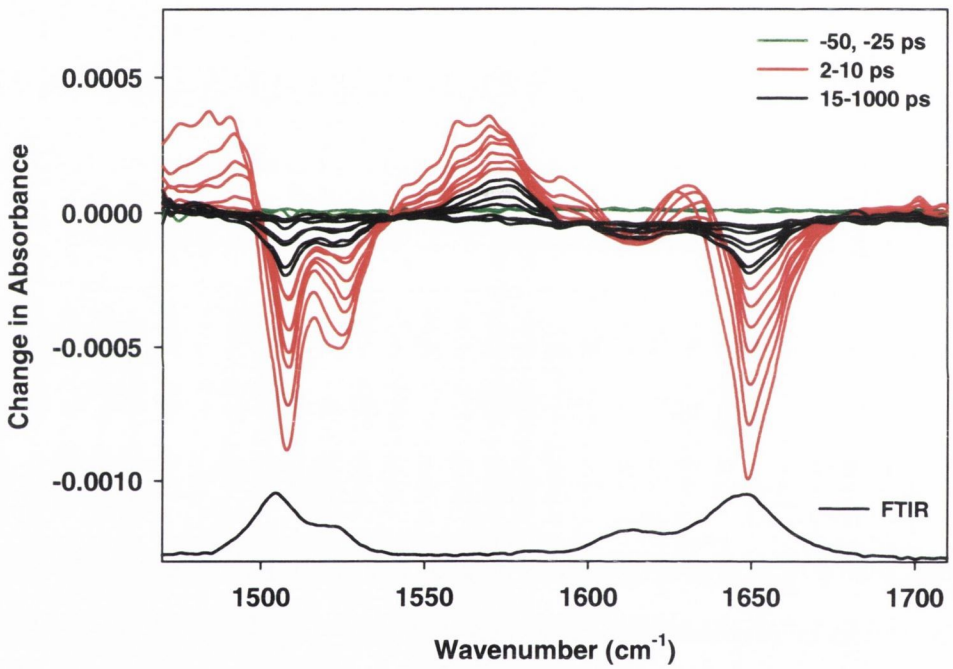

Figure 2.1 ps-TRIR of 10 mM 5′-dCMP in 50 mM potassium phosphate D_2O buffer (pH 7) with FTIR below (baseline adjusted). Delays are at -50, -25 (green), 2, 3, 4, 5, 6.5, 8, 10 (red), 15, 20, 35, 50, 100, 500 and 1000 ps (black).

The high wavenumber bleach corresponds to carbonyl stretching with the lower wavenumber bleach being the in-plane ring vibrations. Transient features are observed on the low wavenumber side of each bleaching band and with early time delays these bands simultaneously narrow and shift to higher wavenumber. This behaviour is consistent with cooling of the vibrationally hot ground state as previously seen for the mononucleotides.[48] However, intriguingly in this system, the transient band centred at 1574 cm^{-1} was found to

persist for tens of picoseconds. The transient absorption decay (and the ground state recovery) is essentially complete over the 1000 ps timescale of the experiment.

The kinetics of the system were found to be distinctly biphasic (see figure 2.2). Kinetic analysis of both the bleaching bands and the transient band region 1550-1590 cm^{-1} revealed lifetimes of 2.6 ± 0.3 ps and 33 ± 4 ps. The first of these lifetimes is ascribed to vibrational cooling. The second species, characterized by a broad transient absorption band, centred at 1574 cm^{-1}, had not previously been observed for 5′-dCMP. This band is the only one observable in the IR absorption spectrum in the region 1450–1750 cm^{-1} (assuming that there is no accidental overlap of other bands with those of the ground state).

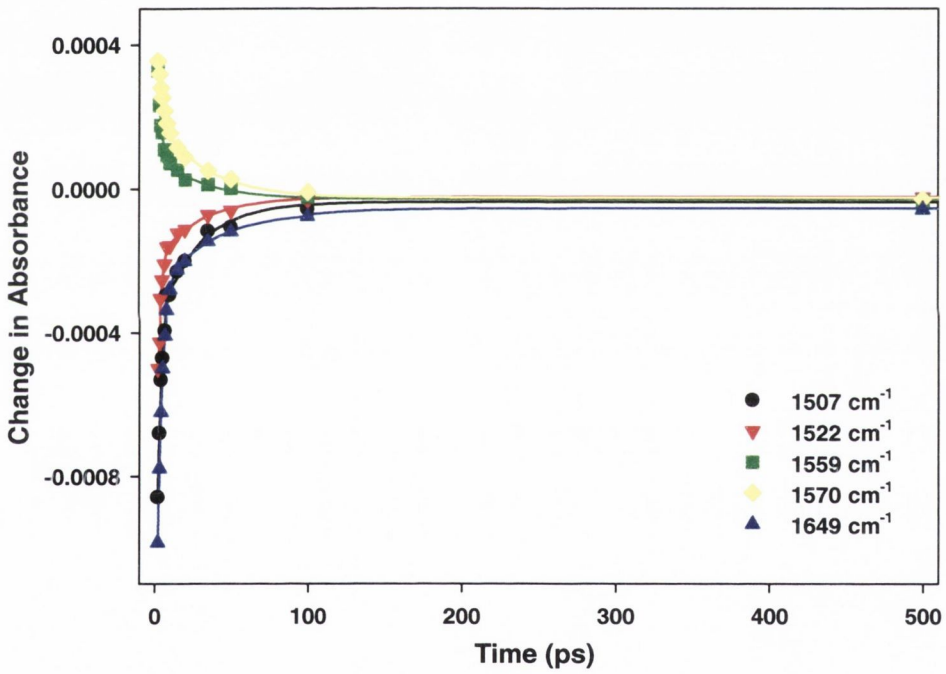

Figure 2.2 Kinetic analysis of 10 mM 5′-dCMP in 50 mM potassium phosphate D_2O buffer (pH 7) at 1507, 1522, 1559, 1570 and 1649 cm^{-1}.

2.3.2 2′-deoxycytidine (dCyd)

The ps-TRIR difference spectrum of dCyd in buffered D_2O solution (pH 7) following UV excitation (150 fs, 267 nm) is shown below (figure 2.3). Bleaching bands occur at 1507, 1529, 1616 and 1653 cm^{-1} with transient absorption bands present at 1482, 1572 and 1630 cm^{-1}. The spectrum is similar to that of 5′-dCMP in that the strong transient absorption at 1574 cm^{-1} is also present in this system. The nucleoside shows behaviour indicative of intramolecular vibrational cooling as was expected. But the presence of this long-lived species once again was intriguing.

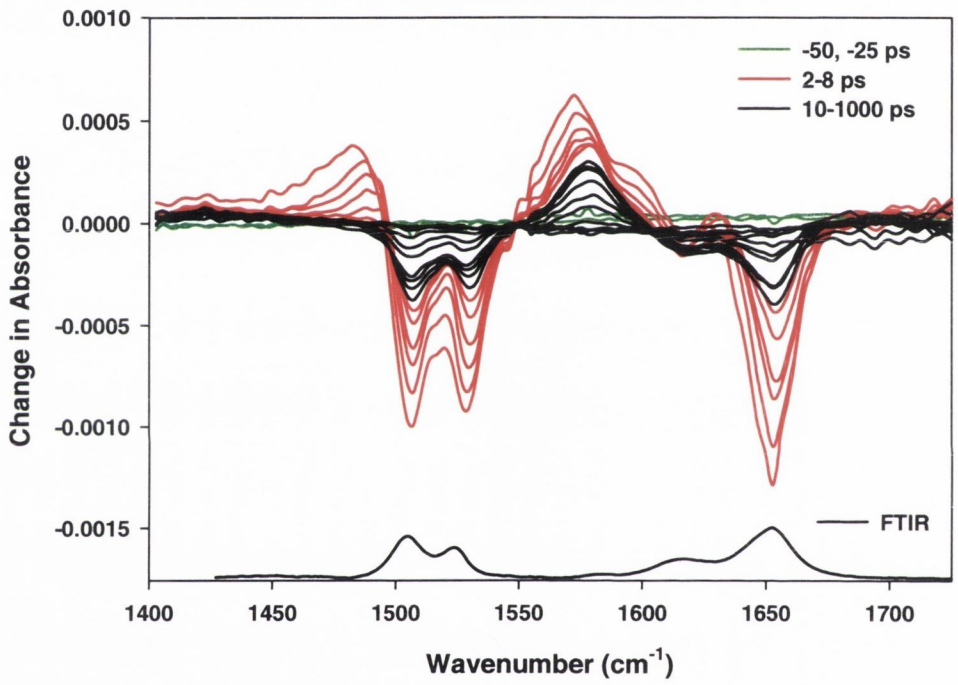

Figure 2.3 ps-TRIR of 20 mM dCyd in 50 mM potassium phosphate D_2O buffer (pH 7) with FTIR below (baseline adjusted). Delays are at -50, -25 (green), 2, 3, 4, 5, 6.5, 8 (red), 10, 12.5, 15, 20, 35, 50, 100, 200, 500 and 1000 ps (black).

Complete recovery of the system was found over the 1000 ps timescale of the experiment. Kinetic analysis of the the transient decay and bleach recoveries was carried out and once again biexponential kinetics were observed (figure 2.4). Cooling of the vibrationally hot ground state occurred with $\tau = 2.6 \pm 0.3$ ps. The presence of the second lifetime, $\tau = 37 \pm 4$ ps, coupled with the fact that this species had an absorption in the same region as for the 5′-dCMP case, led us to believe we were essentially observing the same species in both the nucleoside and nucleotide.

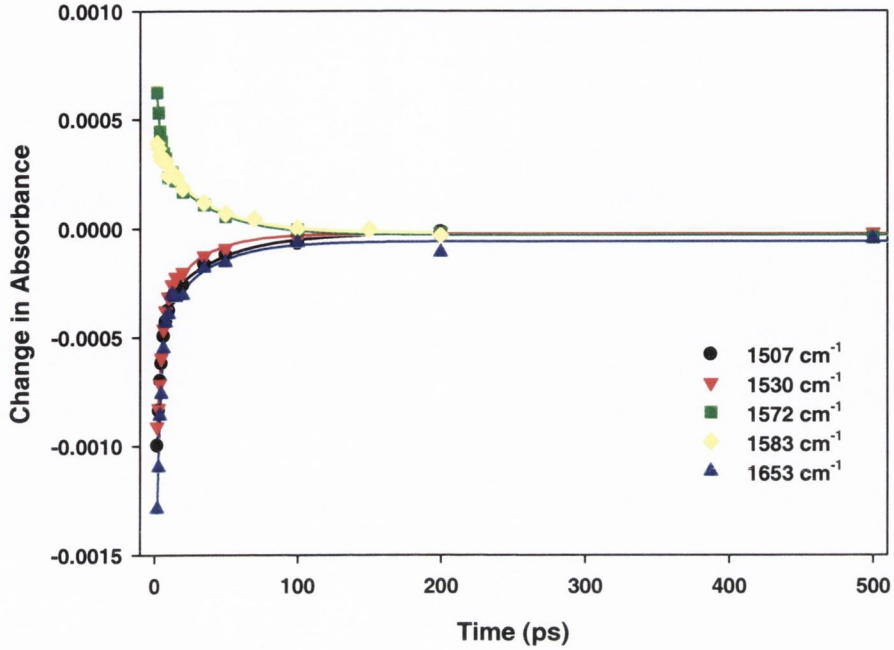

Figure 2.4 Kinetic analysis of 20 mM dCyd in 50 mM potassium phosphate D_2O buffer (pH 7) at 1507, 1530, 1572, 1583 and 1653 cm^{-1}.

2.3.3 Cytosine (Cyt)

Figure 2.5 shows the ps-TRIR of the Cyt nucleobase studied under identical conditions to that of the dCyd nucleoside (20 mM in 50 mM potassium phosphate D_2O buffer, pH 7). In this system bleaching bands occur at 1506, 1520, 1590, 1610 and 1645 cm^{-1}. There are transient absorption bands at 1483, 1566, 1599 and 1629 cm^{-1}. Most strikingly, there is no indication for a long-lived species in this system (see figure 2.6 below). The persistent transient absorption that was seen in the 5′-dCMP and dCyd cases is absent. The transient species was found to undergo rapid single exponential decay with a lifetime of 4.4 ± 0.4 ps, with no significant (i.e. > 5%) longer-lived component being detectable.

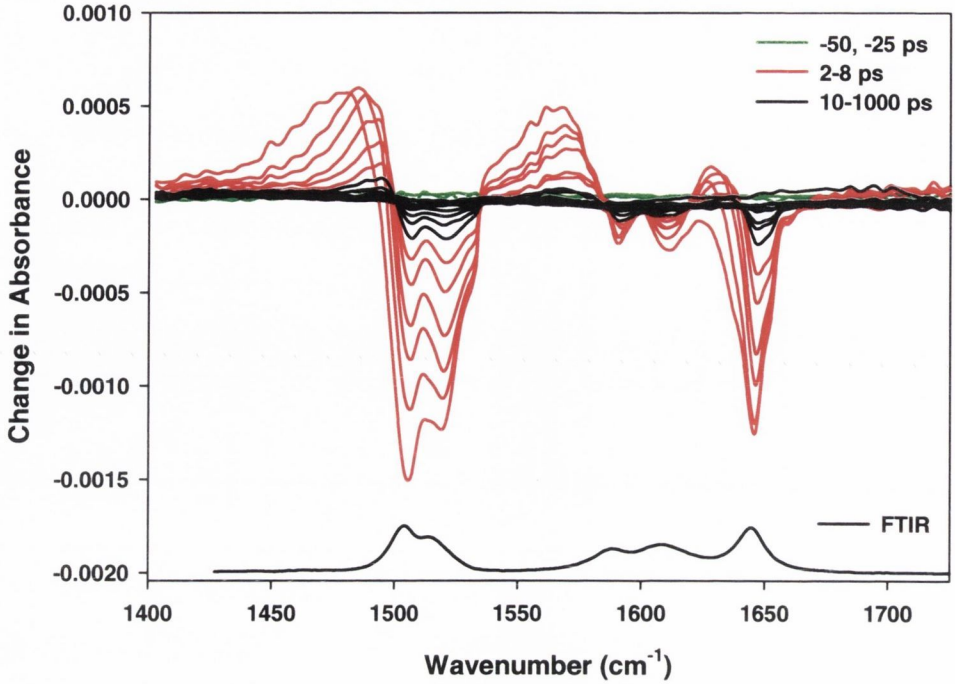

Figure 2.5 ps-TRIR of 20 mM Cyt in 50 mM potassium phosphate D_2O buffer (pH 7) with FTIR below (baseline adjusted). Delays are at -50, -25 (green), 2, 3, 4, 5, 6.5, 8 (red), 10, 12.5, 15, 20, 35, 50, 100, 200, 500 and 1000 ps (black).

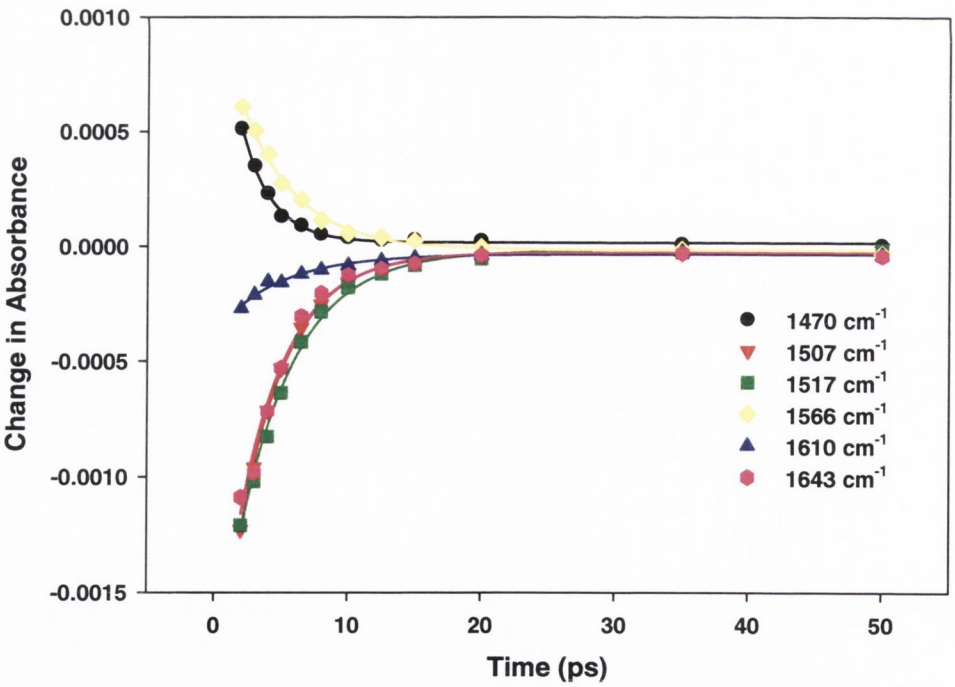

Figure 2.6 Kinetic analysis of 20 mM Cyt in 50 mM potassium phosphate D_2O buffer (pH 7) at 1470, 1507, 1517, 1566, 1610 and 1643 cm^{-1}.

The difference in recovery of the three cytosine derivatives is shown in figure 2.7. A representative transient decay and bleach recovery is presented for each case. Excellent recovery is seen for all three systems. There is a clear difference in behaviour of the nucleotide and nucleoside to that of the nucleobase. The amount of long-lived species produced was determined by examining the amplitude of the pre-exponential factors of the biexponential functions and was found to be in the range of 20-25%.

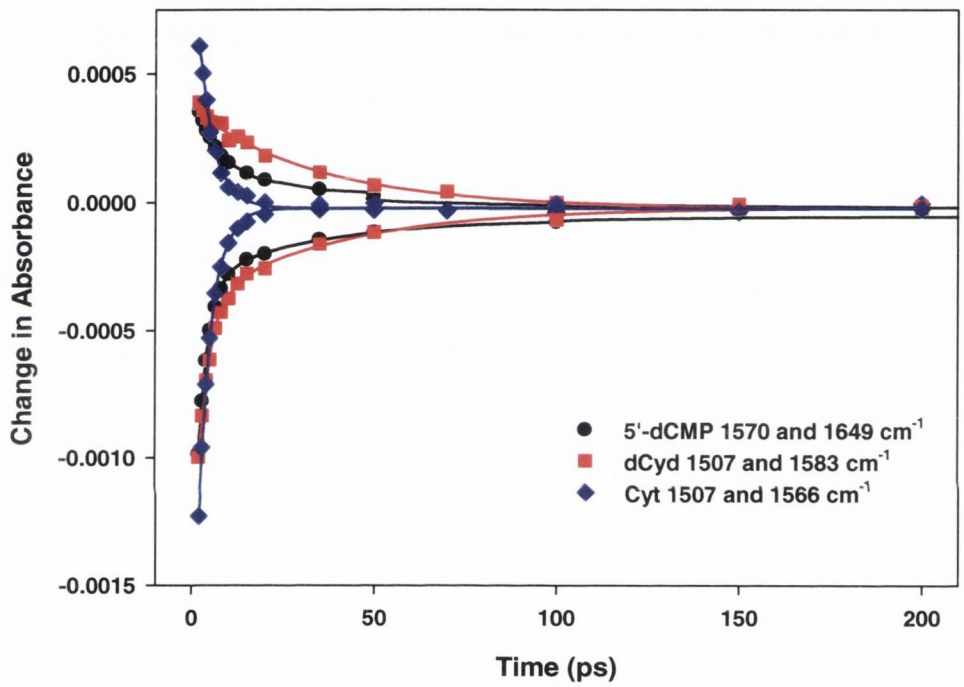

Figure 2.7 Comparative kinetic analysis of 10 mM 5′-dCMP at 1570 and 1649 cm^{-1} (black), 20 mM dCyd at 1507 and 1583 cm^{-1} (red) and 20 mM Cyt at 1507 and 1566 cm^{-1} (blue).
All compounds were studied in 50 mM potassium phosphate D_2O buffer (pH 7).

2.3.4 1-Methylcytosine (1-MeCyt)

To investigate the effect of substitution of cytosine at the 1-position, the ps-TRIR of the simplest substitution product, 1-methylcytosine was recorded. The ps-TRIR difference spectrum of 1-MeCyt in buffered D_2O solution (pH 7) following UV excitation is given below (figure 2.8). Ground state depletion bands centred at 1506, 1525, 1585, 1611 and 1654 cm^{-1} correspond to the ground state absorptions (see FTIR below TRIR in figure 2.8). Transient absorption bands are found at 1481, 1564, 1593 and 1640 cm^{-1}. As with the other cytosine derivative samples, this spectrum is comprised of two interleaved spectral windows. Noticeably, there is an absence of long-lived species in the system.

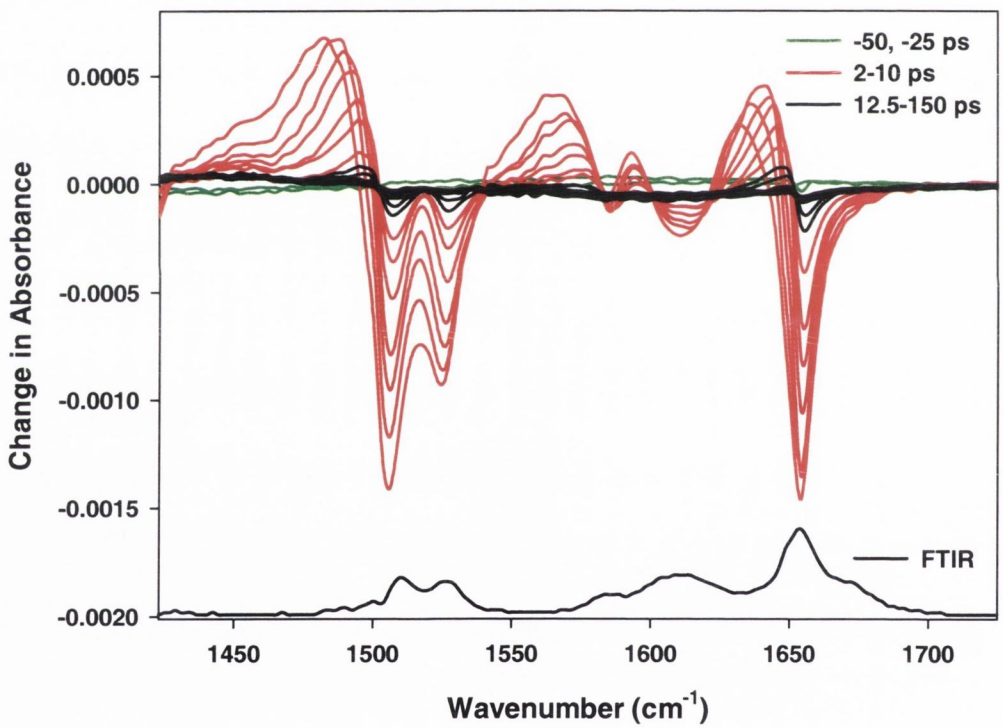

Figure 2.8 ps-TRIR of 10 mM 1-MeCyt in 50 mM potassium phosphate D_2O buffer (pH 7) with FTIR below (baseline adjusted).
Delays are at -50, -25 (green), 2, 3, 4, 5, 6.5, 8, 10 (red),
12.5, 15, 20, 25, 35, 40, 50, 75, 100, 130 and 150 ps (black).

The kinetics of the system were examined at a number of points throughout the spectrum and figure 2.9 shows the results of this analysis at all the main band positions. The results confirm that the kinetics of both the transient absorption and bleaching bands are monoexponential. For example, the transient absorption band at 1478 cm^{-1} gave a lifetime of 3.1 ± 0.2 ps, with the depletion band at 1506 cm^{-1} displaying a lifetime of 4.3 ± 0.2 ps. This result is in contrast to that found for the nucleotide and nucleoside, where a second long-lived species was detected, but in excellent agreement with that of the free base.

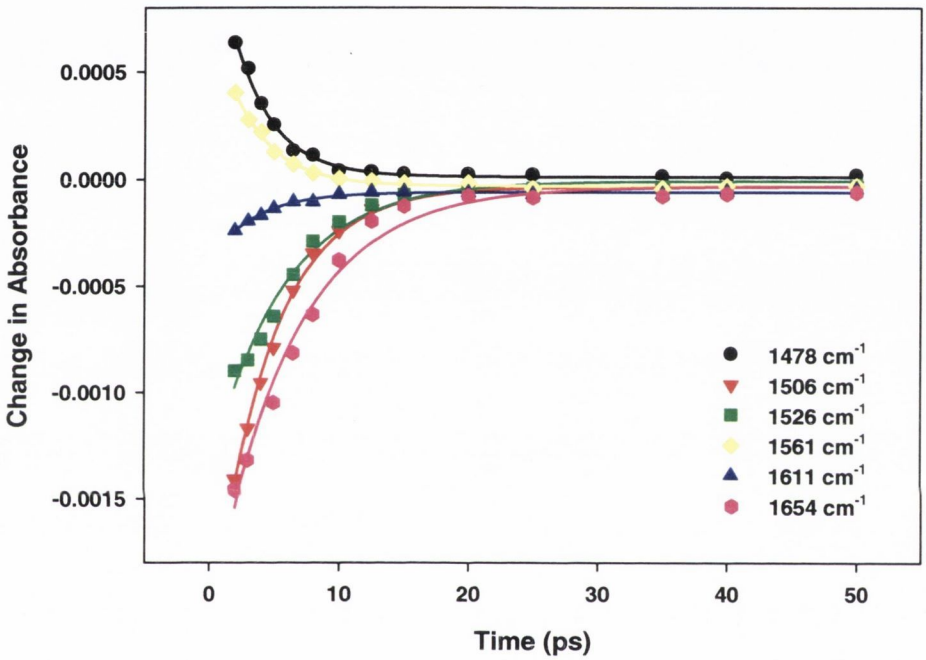

Figure 2.9 Kinetic analysis of 10 mM 1-MeCyt in 50 mM potassium phosphate D_2O buffer (pH 7) at 1478, 1506, 1526, 1561, 1611 and 1654 cm^{-1}.

2.4 Discussion

2.4.1 Possibilities for the long-lived species.

Upon absorption of a UV photon there are many processes that can occur (figure 2.10). Initially following 267 nm excitation the Frank Condon $^1\pi\pi^*$ state will be populated and this process will occur on a femtosecond timescale. Ultrafast internal conversion to the ground state may occur but this would not account for the presence of the transient absorption in our system. A systematic consideration of the possibilities for the assignment of the long-lived transient species was undertaken. All options, including the possibilities of an excited state, tautomers or another photoproduct(s) were examined.

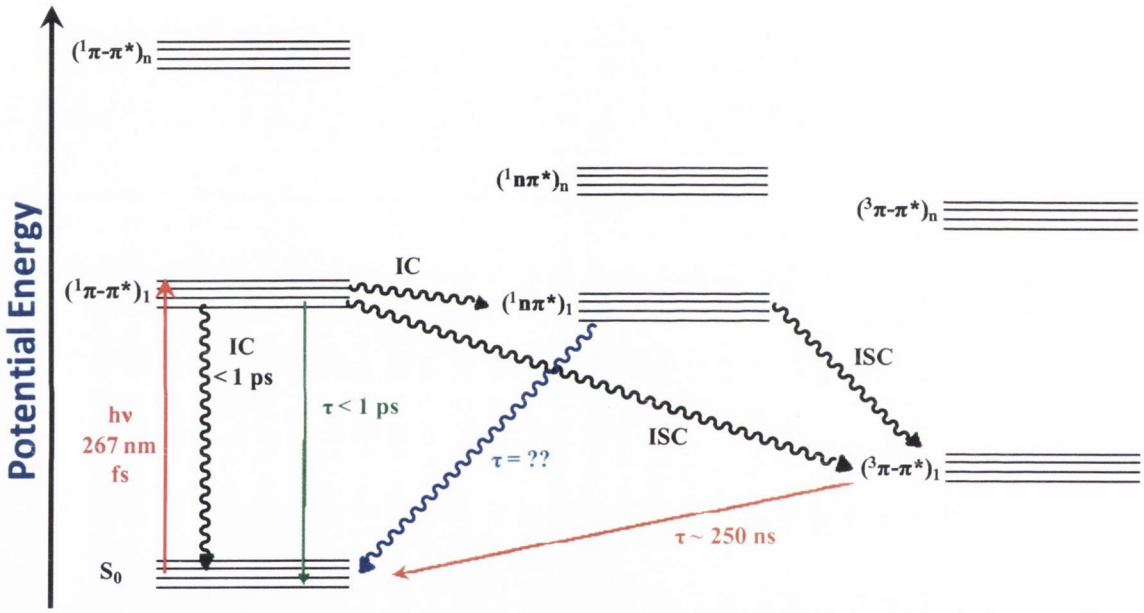

Figure 2.10 Jablonski diagram for Cytidine derivatives.

2.4.1.1 Excited states

It is known that the fluorescence quantum yield of 5′-dCMP is very low (1.15 (±0.06) x10^4) with very fast return to the S_0 ground state being reported.[19,98] Lifetimes of 0.53 (±0.02) ps and 0.27 (±0.02) and 1.38 (±0.11) ps were found when fluorescence decays at 330 nm were fitted to mono- and biexponential kinetics respectively.[19] Therefore the transient species observed in our systems cannot be a $^1\pi\text{-}\pi^*$ singlet state. Furthermore, the triplet state is known to be relatively long-lived and at the concentrations used in our experiments, a lifetime of the order of 250 ns is expected.[43,99]

2.4.1.2 Transient Photoproducts

The possibility of formation of a short-lived photoproduct which could relax to the ground state canonical form was also investigated. Proton transfer in the excited state, base ionization, photohydrate, dimer and tautomer formation were all considered as possible candidates. Protonation and deprotonation of 5′-dCMP and dCyd in the ground state is known to occur as per scheme 2.2 Deprotonation does not actually occur on the nucleobase but on the sugar.[100] Consequently the region we are probing would not provide any spectral signatures from sugar vibrations and a spectrum similar to that at neutral pH might be expected.

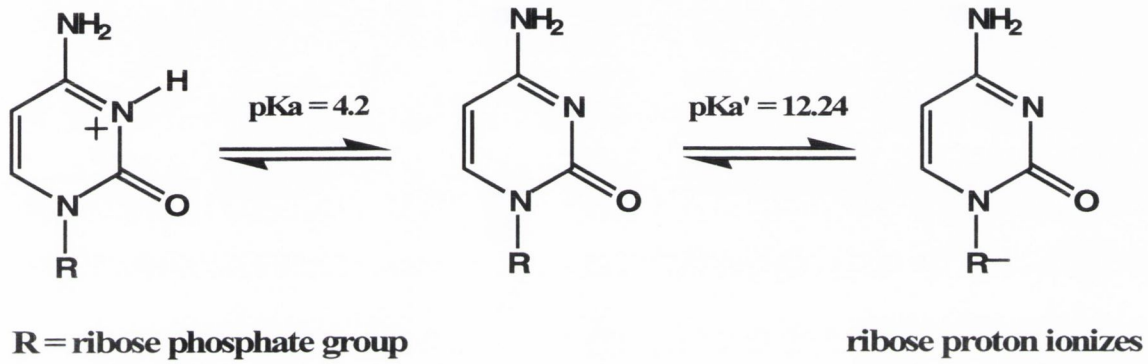

Scheme 2.2 Ionic forms of dCyd and 5′-dCMP.

The ps-TRIR of 5′-dCMP at pH 8.5 was recorded (figure 2.11) and transient behaviour was found to be the same as for the nucleotide in neutral conditions. The kinetics of the system were essentially identical to that of the neutral case, with lifetimes of 3.6 (± 0.3) and 38 (± 3) ps being measured (inset figure 2.11).

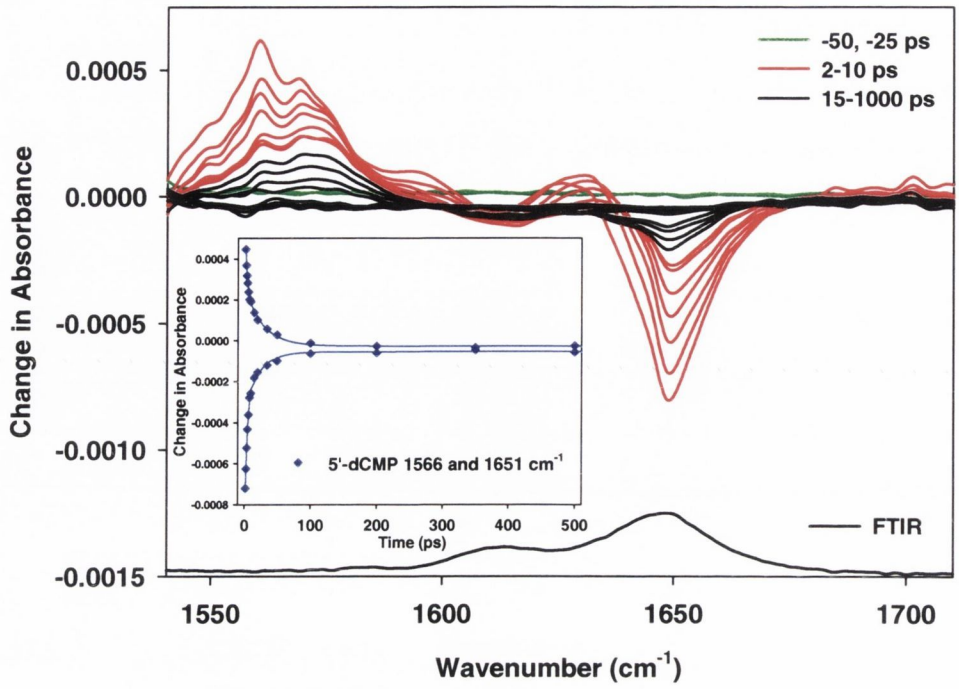

Figure 2.11 ps-TRIR of 10 mM 5′-dCMP 50 mM K_2HPO_4 in D_2O (pH 8.6). Delays are at -50, -25 (green), 2, 3, 4, 5, 6.5, 8, 10 (red), 15, 20, 35, 50, 100, 500 and 1000 ps (black). Inset: Kinetic analysis at 1566 and 1651 cm^{-1}.

Both the ground state bleaching and transient absorption behaviour for 5′-dCMP in 0.132 M H_3PO_4 acid are quite different from that recorded in neutral solution (figure 2.12). Here the transient absorption band shifts to higher wavenumber as the signal decays and shows a single exponential rapid recovery of the ground state ($\tau = 4.0 \pm 0.4$ ps) – behaviour consistent with vibrational relaxation (figure 2.12 inset). Protonation results in a new absorption band above 1700 cm^{-1}, as is clearly seen from both the bleaching band and the FTIR. Bleaching at this position was not observed under neutral conditions for 5′-dCMP and dCyd. At low pH, formation of the 1574 cm^{-1} transient appears to be suppressed and an efficient route(s) for radiationless deactivation dominates with no long-lived species being detectable. Therefore, a protonated excited-state species was discounted as a possible origin for the long-lived species found in 5′-dCMP and dCyd.

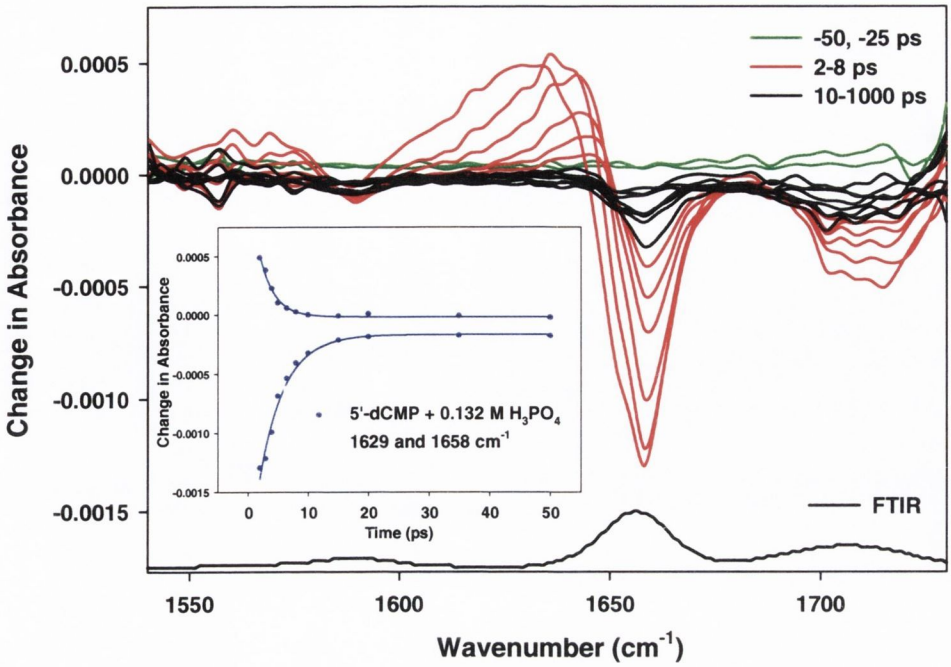

Figure 2.12 ps-TRIR of 10 mM 5′-dCMP + 0.132 M H_3PO_4 in D_2O (pH 2.0) with FTIR below (baseline adjusted). Delays are at -50, -25 (green), 2, 3, 4, 5, 6.5, 8 (red), 10, 15, 20, 35, 50, 100, 500 and 1000 ps (black). Inset: Kinetic analysis at 1629 and 1658 cm^{-1}.

Photoionization energies for cytosine (and derivatives) in aqueous solution have been calculated to be in the range 4.8 - 5.5 eV, with the value fluctuating depending on the level of the theoretical calculations.[101,102] Given our pump wavelength (267 nm = 4.6 eV) and the low quantum yield of formation of photoionized species for 5′-dCMP (0.0018 with 5 MW/cm^2) photoionization was not expected to play a major part.[103] However, in principle multiphoton absorption events could result in the generation of an ionized species. Power dependence measurements were performed with the beam power being varied between 0.6 and 1.6 μJ. Linear variation of bleach and transient intensities were found with power, indicating that photoionization of the cytosine derivatives was not occurring in our system.

Other photoproducts that can form after exposure to UV radiation include cyclobutane dimers (scheme 2.3) and to a lesser extent the dewar isomer and 6,4-photoproduct.[2,6,8,9,104] Pyrimidine dimers are more prevalent in T-T than C-C systems due to a difference in the ordering of the two lowest excited states.[105] Given the unconstrained nature of the mononucleotide unit compared to the pre-orientated polymer case, and at the

concentrations used in our experiments such photoproducts are unlikely. The so-called cytosine photohydrate, 6-hydroxy-5,6-dihydrocytosine (scheme 2.3), is known to be stable on a ps timescale.[106-108]

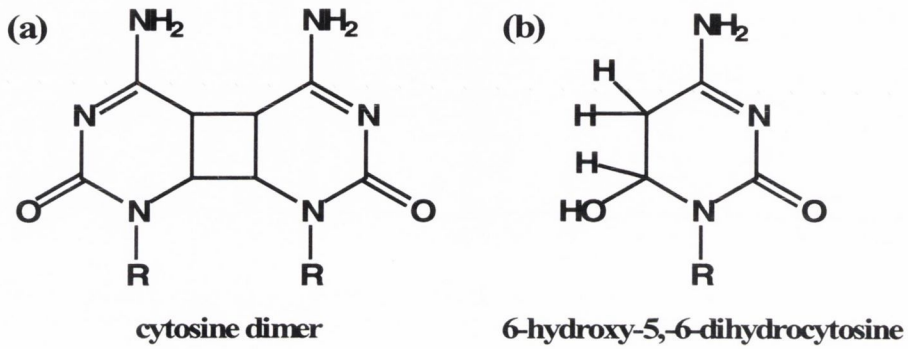

Scheme 2.3 (a) Cytosine cyclobutane dimer and (b) cytosine photohydrate.

We considered the possibility of this species being a tautomer as there have been a number of theoretical studies of the tautomers of cytosine derivatives.[28,51,52,57,60,63,65,70,75,77,109,110] For dCyd and 5′-dCMP the most stable tautomers are the iminooxo (I) or the iminohydroxy (H) (scheme 2.4) and a recent theoretical study[60] indicated that the iminooxo isomer I.H_2O can rapidly revert to its canonical form C.H_2O.

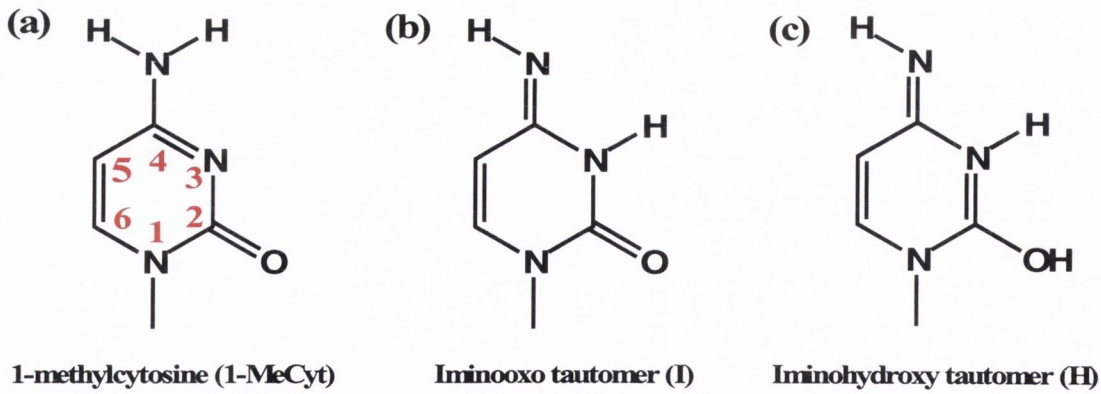

Scheme 2.4 Structure of (a) 1-MeCyt, (b) I tautomer and (c) H tautomer.

To identify whether the transient species could be one of these tautomers we performed optimisations and vibrational frequency calculations at the B3LYP and MP2 levels with a 6-311+G(2d,p) basis set in the Gaussian 03 package. Frequency scaling factors of 0.9679

and 0.9427 were applied for B3LYP and MP2 results respectively.[111,112] For these preliminary studies calculations were performed on 1-methylcytosine (and its hydrate C.D_2O). The individual and difference spectra between the 1-methylcytosine and its tautomers were determined. The simulated spectra were obtained using the calculated intensity and a Gaussian distribution with a standard deviation of 15 cm^{-1}. The calculations indicated that species I (or its hydrate I.D_2O) should have a strong IR absorption band at higher frequency than dCyd/5′-dCMP, in contrast with what was found experimentally. (Table 2.1 and figure 2.13 B3LYP (a) and (b); MP2 (c) and (d)). The absence of this band in the experiment therefore speaks against this tautomeric form. Calculations on species H gave rise to spectra that do not have this high frequency peak but agreement with the experimental spectra was still not satisfactory. However, given the limitations of the calculations, e.g. explicit consideration of only a single water molecule bound as shown, we were unable to unequivocally rule out the formation of the imino-enol tautomer H. Further calculations (B3LYP) were carried out using the entire nucleotide (5′-dCMP) in place of just the methyl substituted nucleobase to see if this had any further effect on the calculated frequencies. (figure 2.13 (e) and (f)) No significant improvement leading to better agreement with the experimental result was found.

1-MeCyt (cm^{-1})	Principal Components	Tautomer I (cm^{-1})	Principal Components	Tautomer H (cm^{-1})	Principal Components
1678	C2-O	1700	N3-C2	1656	C5-C6, C2-N3
1621	C5-C6, C4-NH_2	1633	C5-C6, C4-NH	1596	C4-NH, C2-N3
1505	C4-C5 C5-C1 C4-NH_2	1566	C4-NH, C5-C6	1531	C4-NH, C2-N3 C5-C6

Table 2.1 B3LYP calculated IR vibrational frequencies with principal mode assignment. A scaling factor of 0.96790 has been applied to all frequencies.

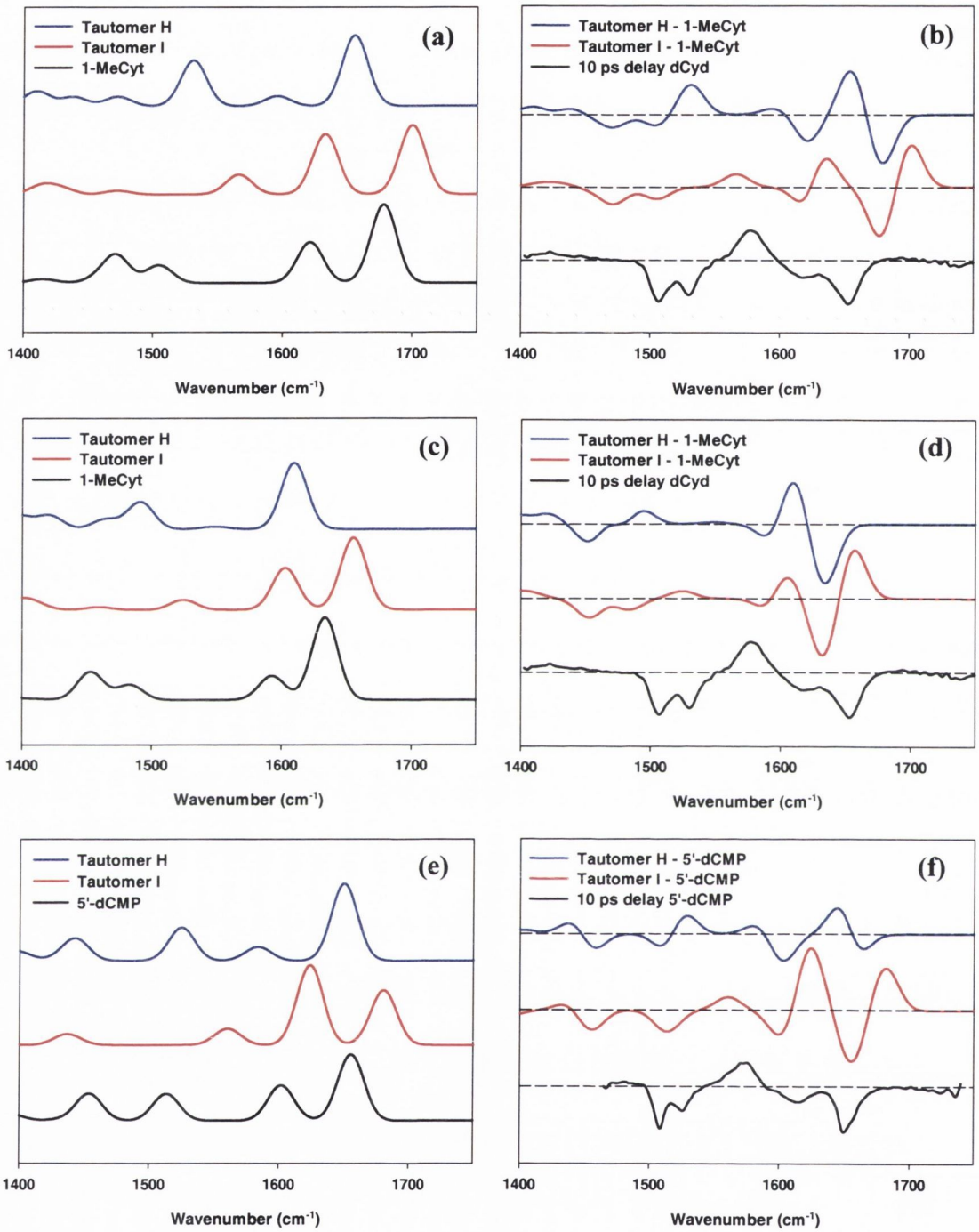

Figure 2.13 Calculated IR spectra of 1-MeCyt and tautomers I and H (a) and (c), and difference spectra of tautomers I and H compared to 1-MeCyt, with experimental data for dCyd at 10 ps (b) and (d). (B3LYP spectra (a) and (b) and MP2 spectra (c) and (d). Calculated B3LYP IR spectra of 5′-dCMP and tautomers I and H (e), and difference spectra of tautomer I and H compared to 5′-dCMP, with experimental data for 5′-dCMP at 10 ps (f). (Scaling factors of 0.96790 and 0.9427 were applied to B3LYP and MP2 calculations respectively).

Having shown that the 1574 cm^{-1} transient was unlikely to be a transient photoproduct we then considered the possibility of the new species being a 'dark' excited state of dCyd, even though these states had not been observed by detailed transient absorption studies.[16,17,43,99]

Dark states have been known to exist for the nucleobases or derivatives of the bases and have been the subject of both theoretical[14,23,25,26,32,35,69,113-115] and experimental studies.[36,39,40,116] Their role as facilitators of ultrafast relaxation dynamics is vital, as they undoubtedly contribute to DNA photostability. But the exact ordering of such states and the precise role played, at least in the cytosine case, has in the past been the subject or debate.

Owing to $^1\pi\pi^*$ transitions being highly allowed most theoretical studies predict transition energies that are close to those measured experimentally. However, in the $^1n\pi^*$ case, the experimental evidence and theoretical predictions are sometimes conflicting. Detection of such dark states with the traditional techniques such as transient absorption and fluorescence methods can be difficult. Low oscillator strength of these states, coupled with possible overlap of stronger transitions has meant that such states were not as intensively studied and hence readily identified.

$^1n\pi^*$ states have a greater solvent sensitivity than their $^1\pi\pi^*$ counterparts.[25] This can lead to changes in the ordering of states and indeed this has been shown this to be the case for uracil and thymine derivatives.[117] Shukla and Leszczynski also observed an inversion of states of Cyt upon solvation,[64] with Rachofsky *et al.* concluding that dipolar interactions were responsible for such an effect.[118]

Coincidentally, after our experimental work was complete, the existence of such an intermediate dark state of 5′-dCMP was suggested from kinetic analysis of the transient bleaching behaviour at 250 nm.[39] The authors tentatively assigned the species to a $^1n\pi^*$ state and in the case of 5′-dCMP the lifetime was reported to be 34 ± 3 ps in H_2O, in excellent agreement with the results observed in our ps-TRIR experiments. However, the authors did not state explicitly which of the two possible $^1n\pi^*$ states the non-radiative decay was arising from.

Two possible $^1n\pi^*$ excited states (the $^1n_O\pi^*$ and $^1n_N\pi^*$) should be considered for cytosine derivatives, the energetics of which have been the subject of theoretical studies.[14,35,114,119] Ismail *et al.* calculated energetics of both the $^1n_O\pi^*$ and $^1n_N\pi^*$ states for cytosine and concluded that both states were very close in energy to the $^1\pi\pi^*$ state. However, in our experiments, the presence of a strong band at 1574 cm^{-1} in the TRIR spectra is a distinguishing feature, as valence bond treatment[14] of the two states (scheme 2.5) predicts that the carbonyl bond has substantial double bond character in the $^1n_N\pi^*$ but not in the $^1n_O\pi^*$. In the case of $^1n_O\pi^*$ the valence bond treatment indicates substantial single bond character for the carbonyl bond and therefore its vibration is not expected to be close to the carbonyl bleaching band in our system at 1650 cm^{-1}. This strongly suggests that we are dealing with the $^1n_N\pi^*$ as a large shift of the transient carbonyl absorption from the parent ground state band was not observed.

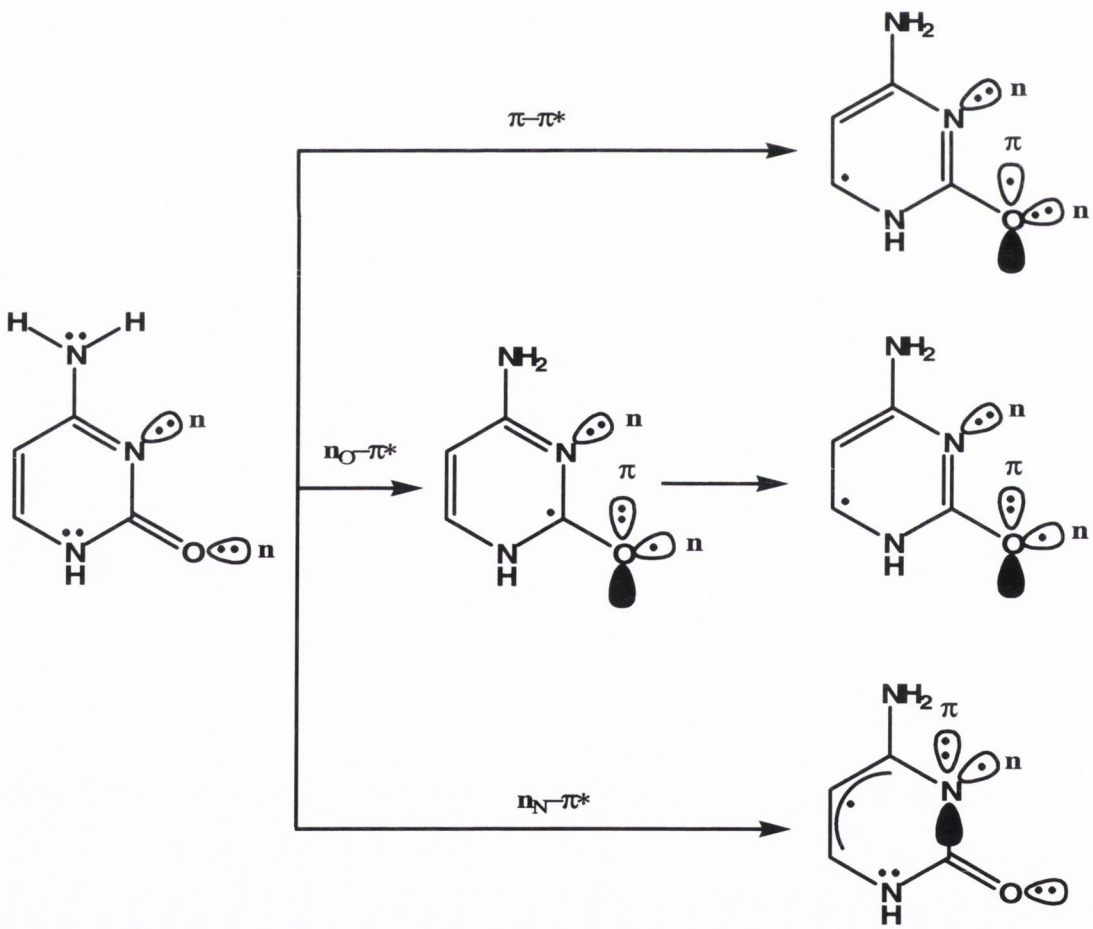

Scheme 2.5 Valence bond representation of singlet excited states of Cyt (after Ismail *et al.*).[14]

The observation of a single strong IR band in the transient spectra between 1500 and 1700 cm^{-1} is quite striking given the presence of multiple bands in the ground state in the same spectral window. In the ground state these bands correspond to vibrations of the carbonyl bond, ring double bond stretches and NH_2 bending vibrations.[110,120,121] The simplicity of this transient spectrum may be due to a variety of structural and electronic changes. Such changes may result from the destruction of the π-conjugated bonding network in the dCyd atomic frame causing loss of IR activity in this spectral region. While at present a definitive identification of the 1574 cm^{-1} transient band is not possible, we have provisionally assigned it to the C_2=O mode. Confirmation of this will require isotopic (^{18}O) substitution measurements.

Computational analysis to assist our assignment of the 1574 cm^{-1} requires the calculation of the second derivative matrix at an optimized excited-state geometry and requires substantial computational resources. It is hoped that we may perform such a calculation in the future.

Pecourt *et al.* first proposed that conical intersections were responsible for ultrafast internal conversion in DNA bases.[17,37] Conical intersections occur at points of nuclear coordinate space where there is strong coupling between nearby/quasidegenerate states. Vibronic interactions increase as the energy gap between nonadiabatically coupled electronic states is reduced. At conical intersections, electronic and nuclear motions are very strongly coupled and changes in molecular geometry can take place. Optimization of excited state geometries have shown that non-planar distortions may occur.[14,33,70,122] Such distortions, can result in small potential barriers being overcome and ultimately in a reordering of the states.

In the cytosine case, the state switch takes place via a transition structure (i.e. fully avoided crossing), and the nuclear coordinate is an out-of-plane bending of the amino group with a distortion of the ring. The NH_2 inversion and the pyrimidine ring distortion, minimizes repulsion between the π orbital of N3, which is doubly occupied in the excited state, and the π orbital of C4, and increases the stabilizing effect of the lone-pair orbital of the amino group. We believe that upon excitation, the Franck-Condon $^1\pi\pi^*$ state is initially populated. Subsequent coupling of excited state levels and nuclear rearrangement allows

for the deactivation of the $^1n_N\pi^*$ state to the ground state through a conical intersection as per scheme 2.6.

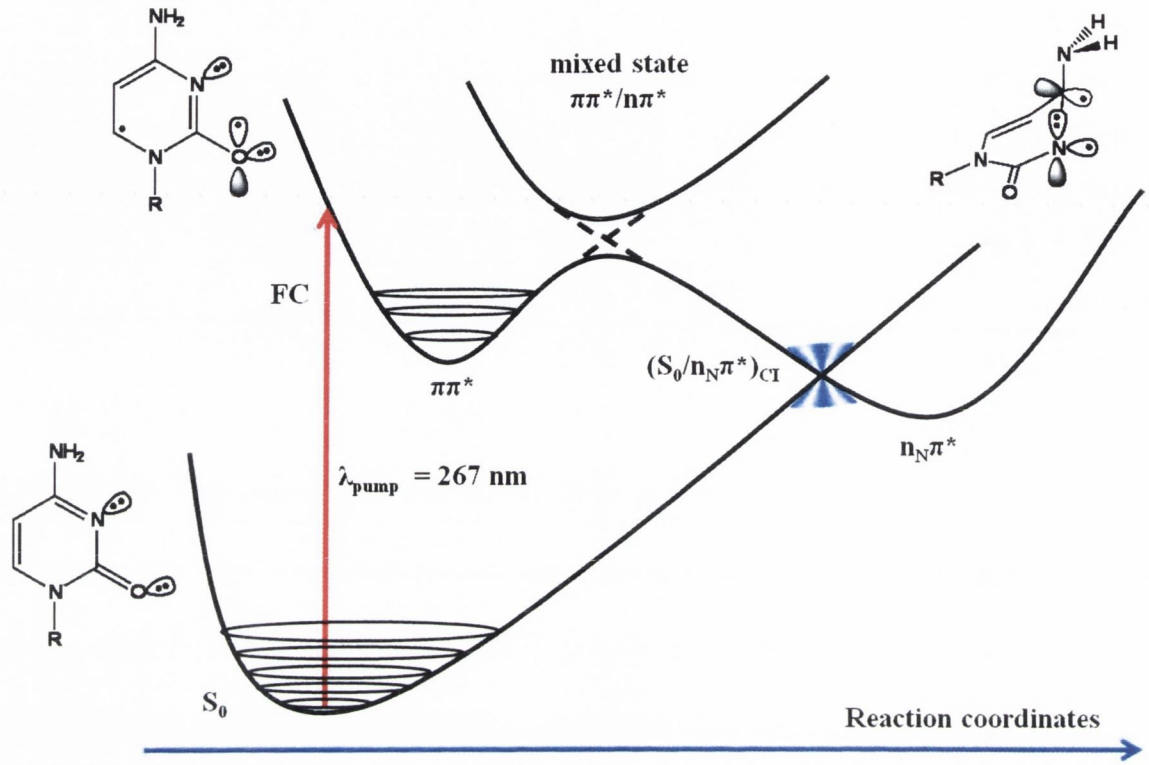

Scheme 2.6 Schematic representation of the proposed deactivation pathways for the excited state of cytidine derivatives.

2.5 Conclusions

In summary, we propose that the deactivation of 5′-dCMP and dCyd can proceed by at least two routes. The first of these involves the rapid formation of the vibrationally excited ground state, which then relaxes with a lifetime of 2.6 ps to the 'cooled' ground state. The second process that competes with the cooling, proceeds via a species possessing a strong vibrational band at 1574 cm^{-1}. If this species is a tautomer our calculations suggest that it is very unlikely to be the iminooxo isomer I. Although at this stage, we cannot exclude the possibility that this species is the iminohydroxy isomer H, we assign the species to the $^1n_N\pi^*$ state. The fact that no analogous species is formed upon excitation of the nucleobase cytosine, or 1-MeCyt, demonstrates that substitution at the 1-position by 2′-deoxyribose has a major effect on the photophysical properties and probably on the photochemical reactivity. This work represents the first direct observation

of such a state for a nucleotide. More routinely employed spectroscopies have only seen these states indirectly, i.e. bleaching at 250 nm due to the presence of such a species.[39] Dark states are immensely important when one considers that the quantum yields of the DNA bases are so low, so that other deactivation mechanisms have to dissipate the majority of the potentially harmful energy in an efficient manner.

Future work will include the investigation of the solvent dependence of the $^1n_N\pi^*$ state. Solvent variation may modulate the energy of the excited states that are very close together and this may switch the ordering of the dark $^1n\pi^*$ states, with the possibility of non-radiative decay from the $^1n_O\pi^*$. The behaviour of the $^1n_N\pi^*$ state in stacked systems, such as dinucleotides and polynucleotides (both single- and double-stranded), also warrants study. This initial study has not considered stacking or interbase hydrogen-bonding interactions and one might well expect these factors to influence the relaxation dynamics.

Chapter 3

ps-TRIR Study of a Family of Adenine and Thymine Containing Dinucleotides

3.1 Introduction

This chapter focuses on A-T containing systems and aims to build on the monomer studies in chapter 2. A complete and comprehensive study is presented with progression from the simpler monomer units 2′-deoxyadenosine 5′-monophosphate (5′-dAMP) and 2′-deoxythymidine 5′-monophosphate (5′-TMP) to the more complex dinucleotide units of 2′-deoxyadenyl-(3′-5′)-thymidine (dApT), thymidylyl-(3′-5′)-2′-deoxyadenosine (TpdA), 2′-deoxyadenyl-(3′-5′)-2′-deoxyadenosine (dApdA) and thymidylyl-(3′-5′)-thymidine (TpT) (see scheme 3.1). Dinucleotide units represent the smallest oligomer units possible and the photophysical behaviour of each nucleotide will now be affected/influenced by the neighbouring nucleotide. The hetero- (dApT and TpdA) and homodinucleotides (dApdA and TpT) represent the simplest repeating units of the higher order double stranded polymeric structures of poly(dA-dT).poly(dA-dT) and poly(dA).poly(dT) respectively. Understanding the building blocks of the polymer may allow for inferences to be made in relation to the polymer.

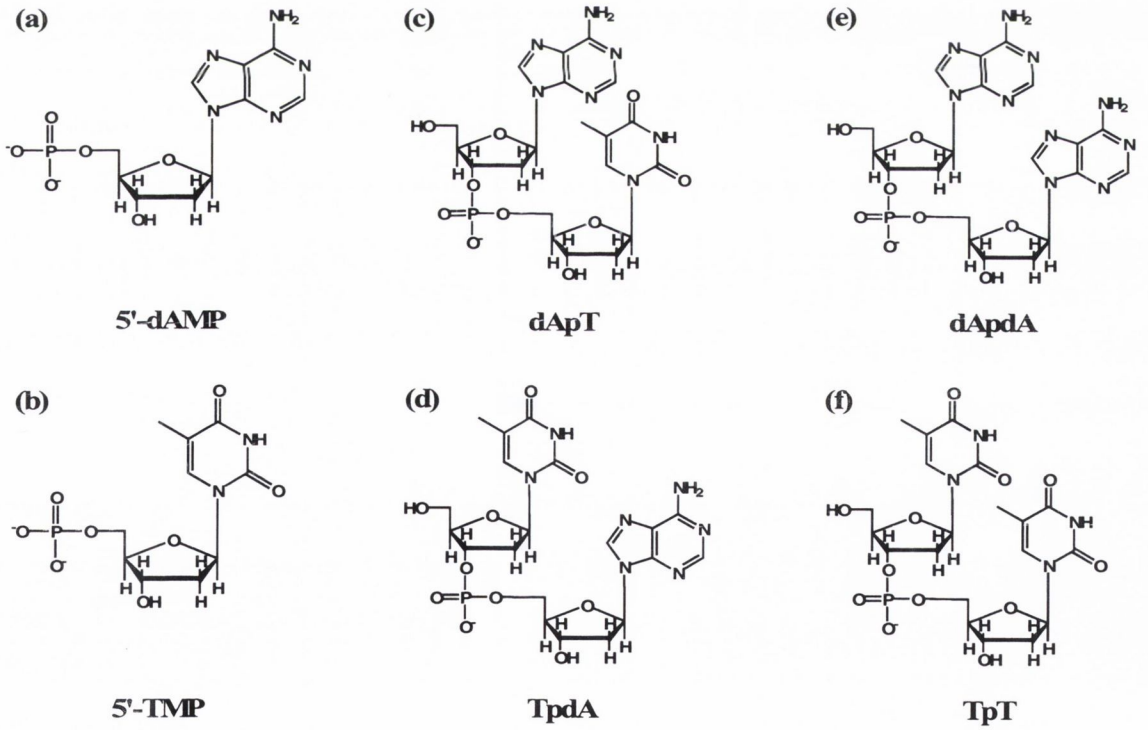

Scheme 3.1 Structures of (a) 2′-deoxyadenosine 5′-monophosphate (5′-dAMP), (b) 2′-deoxythymine 5′-monophosphate (5′-TMP), (c) 2′-deoxyadenyl-(3′-5′)thymidine (dApT), (d) thymidylyl-(3′-5′)-2′-deoxyadenosine (TpdA), (e) 2′-deoxyadenyl-(3′-5′) 2′-deoxyadenosine (dApdA) and (f) thymidylyl-(3′-5′)- thymidine (TpT).

3.2 Motivation for this Study

The photoactivity of DNA is the subject of great scientific curiousity, the results of which impact greatly on our understanding of processes contributing to photoinduced damage in DNA.[2,6,8,123] The absorption of UV light is a process of prime biophysical interest as it is known that harmful photochemical consequences can result. While the cause and subsequent end result are recognized, the processes between the absorption of the photon and production of photoproducts are still not fully appreciated.

Genomic DNA is inherently stable and this stability is due to its ability to redirect or dissipate excess energy very quickly. Many factors can influence the delocalization of such energy and excited state dynamics, with the two most important of these being base-stacking and hydrogen-bonding. Such noncovalent interactions are mainly responsible for nucleic acid secondary structure, but the extent to which either or both mediate relaxation processes is a matter of debate.[124-126]

Base composition (i.e. pyrimidine or purine), sequence position and conformation dictate the electronic coupling between adjacent bases in polymeric strands and hence the possible photodynamics.[16,19,124,127-129] Conformational changes occurring on picosecond (ps) and nanosecond (ns) timescales are controlled by an ensemble of interactions involving not only the bases but also the backbone, counterions and water molecules. Excited state dynamics are also expected to be sensitive to the local environment within the particular structural conformation present.[130-132] Relaxation processes occur extremely fast. Internal conversion, accounting for the majority of relaxation processes occurs on a sub picosecond timescale. Other processes that can occur on a picosecond timeframe include intramolecular vibrational relaxation of the hot ground state,[48] proton and or electron transfers,[84] and temporary or permanent photoproduct formation.[4,5,86,133-135] Stability in simple mononucleotide units is attributed to the extremely short singlet excited state lifetimes of the bases.[16,17,98] These short-lived states have been characterised by femtosecond transient visible absorption[17] and fluorescence upconversion[98] measurements (though it should be noted that the individual bases exhibit very low quantum yields). Of course stacking interactions are not a factor in mononucleotide relaxation processes where the predominant process on a ps timescale is found to be vibrational relaxation.[16,48]

By contrast, oligo- and polynucleotides (both single- and double-stranded) exhibit longer-lived excited states that are not typically observed for the constituent monomer bases.[5,124,136-138] Compelling and often conflicting arguments have been proposed as to the identity of the overriding factor contributing to the occurrence of long-lived states in oligo- and polynucleotide systems, with arguments being put forward for base-stacking and hydrogen-bonding interactions or a combination of both.[124-126,129]

It has been shown that purine nucleotides decay more rapidly than their pyrimidine counterparts.[39,139] But as previously noted, electronic coupling between stacked bases leads to additional photophysical processes. Of note, is the fact that G-C homopolymers decay over shorter times than the corresponding A-T containing DNA systems.[16,19] Whether the difference in behaviour is due to hydrogen-bonding (3 H bonds in G-C vs. 2 H bonds in A-T) poses an interesting question. Recently, thymine dimer formation was reported for $(dT)_{18}$ oligonucleotides[86] and in several A-T mixed composition hairpins[133] following UV irradiation, highlighting the role of short-lived excited states in photochemical damage.

Long-lived states in polymers are often rationalized as being of excimer/exciplex nature.[115,124,126,138] The existence of excimers in poly A (but not poly T) and their contribution to the long-lived species was recently examined by Santoro *et al.*[115] In this study, base-stacking was found to tune the delocalization of energy after photoexcitation and thus influence deactivation pathways. Two scenarios were proposed: firstly, that the excitation is delocalized over different bases and secondly, that it is localized on an individual base. Researchers have for many years,[140-142] and continue to do so today,[137] offer excimer/exciplex formation as the origin of long-lived excited states in dinucleotide units that are not readily identifiable as originating from other states. In most cases, owing to the technique being used, it is impossible to make a discrimination between which base may be causing the state, and so on this basis these states are routinely assigned as originating from a collective excited state of the two constituent parts.

Crespo-Hernandez *et al.* have concluded from their transient absorption measurements on A-T systems that long-lived intrastrand excimer states are present in oligonucleotide systems where A is stacked with A or T but not in T stacked systems and have therefore

dismissed the possibility that hydrogen-bonding controls excited-state dynamics in A-T systems.[124,126] The inferences made by the authors from the interpretation of their experimental data has been questioned by Markovitsi and co-workers, who believe that hydrogen-bonding is the mitigating factor in deactivation processes.[125]

This study seeks to gain an understanding of the excited dynamics of a family of A-T DNA systems using picosecond ultrafast transient infrared (ps-TRIR), which has the benefit of providing structural as well as kinetic details for the transient species. It is envisaged that in progressing from simple mononucleotides, to dinucleotides and finally polynucleotides, further insight can be gained into the factors modulating the furcation (bi- or poly-) of reaction dynamics. Elucidating the vibrational spectra, ground-state and transient, of complex biomolecules such as DNA is a challenging process. However, it may be aided by the study of short sequences and the constituent dinucleotide components. For instance, in the mixed monomer building block dinucleotide units, stacking interactions may be monitored in the absence of Watson-Crick (W-C) hydrogen-bonding interactions. As such they may provide insight into the role of stacking interactions in facilitating the long-lived species observed for A-T rich DNA. With the absence and existence of long-lived states in mononucleotide and polynucleotide systems respectively, it begs the question as to what is the minimum number of bases required before evidence of a long-lived species is found. If base-stacking is indeed responsible for the production of such states, then one would expect a long-lived component in dinucleotide systems, as they exist in both stacked and unstacked conformers. Thus dinucleotide units can be considered as the simplest repeating units of the higher order polymeric structures. In these polynucleotides, the dynamics will be influenced by both base stacking and interbase hydrogen-bonding. As previously mentioned, excimer/exciplex formations are frequently suspected as being responsible for long-lived states. ps-TRIR may be able to address this issue, as it has been successfully used to gain not only kinetic information of ultrafast processes occurring in DNA but also to provide a fingerprint of transient species.[44,48,84,97,130,131,143] While the more routinely employed fluorescence methods provide information of decay pathways taken by excess electronic energy in DNA, it must be pointed out that less than 0.1% of all excitations in DNA decay by photon emission.[16] Utilizing ps-TRIR means that both emissive and non-emissive pathways can be detected.

3.3 Results

3.3.1 Mononucleotide systems: 5′-dAMP and 5′-TMP

The ps-TRIR difference spectrum following UV excitation of 5′-dAMP in buffered D_2O solution (pH 7) is shown in figure 3.1. Depletion bands centred at 1578 and 1623 cm^{-1} originate from the ground state ring vibrations. Transient features are observed on the low wavenumber side of the parent bleach band. The maximum of the transient is found to shift to higher wavenumbers with time and this is characteristic behaviour for the cooling of the vibrationally hot electronic ground state as previously discussed in chapter 2 for the cytosine derivatives. The kinetics (inset figure 3.1) show that both the recovery of the bleach band and the decay of the transient band fit to monoexponential functions with a lifetime of 2.7 ± 0.2 ps (2.2 ± 0.1 ps at 1594 cm^{-1} and 3.3 ± 0.2 ps at 1623 cm^{-1}).

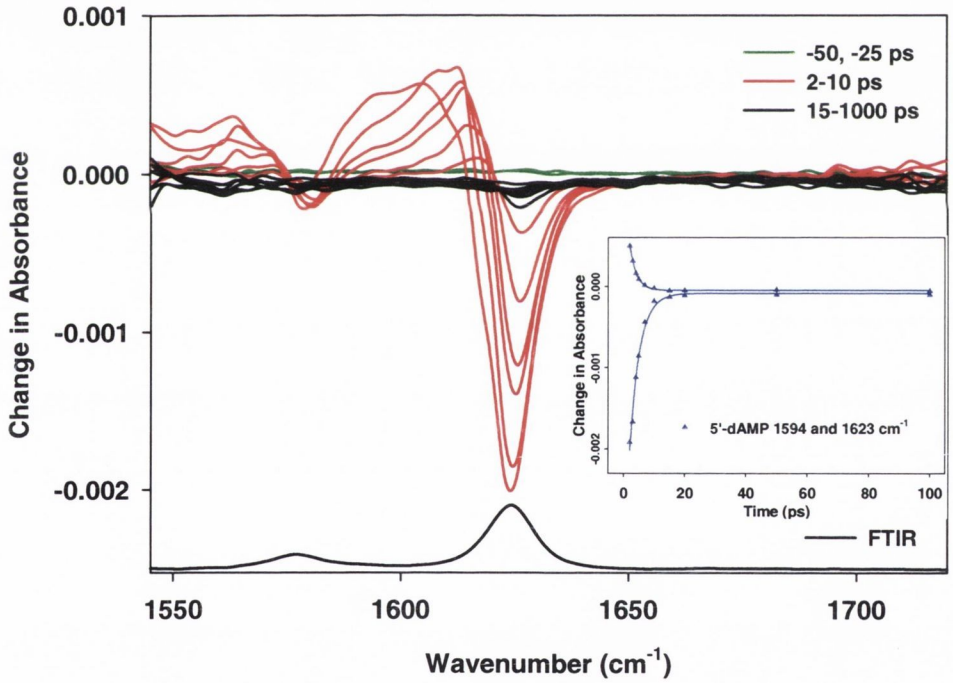

Figure 3.1 ps-TRIR of 10 mM 5′-dAMP in 50 mM potassium phosphate D_2O buffer (pH 7) with FTIR below (baseline adjusted). Delays are at -50, -25 (green), 2, 3, 4, 5, 7, 10 (red), 15, 20, 50, 100, 200, 500, 750 and 1000 ps (black).
Inset: Kinetic analysis at 1594 and 1623 cm^{-1}.

Similar behaviour was seen for the 5′-TMP nucleotide (figure 3.2). Strong depletion bands at 1664 and 1693 cm^{-1} correspond to the C_4O and C_2O carbonyl stretching frequencies respectively with the remaining bleaching band at 1632 cm^{-1} being

assigned to the in-plane ring vibration. Two weaker transient features were evident, again on the low wavenumber side of the bleaching band. The first was centred at 1645 cm^{-1} and the second was a very broad band spanning in excess of fifty wavenumbers below 1600 cm^{-1}. The reversibility of the system was poor, at least up to 1 ns, as the bleaching bands had not fully recovered to the baseline by this time. Both the bleaching and transient bands conformed to monoexponential kinetics with a lifetime of 2.6 ± 0.3 ps (2.5 ± 0.2 ps for the transient absorption at 1602 cm^{-1} and 2.7 ± 0.3 ps for the bleaching band at 1661 cm^{-1}). The UV spectrum of the sample after irradiation suggested that photodamage/photoproduct formation had taken place as the absorbance had decreased significantly (see appendix figure A3.1).

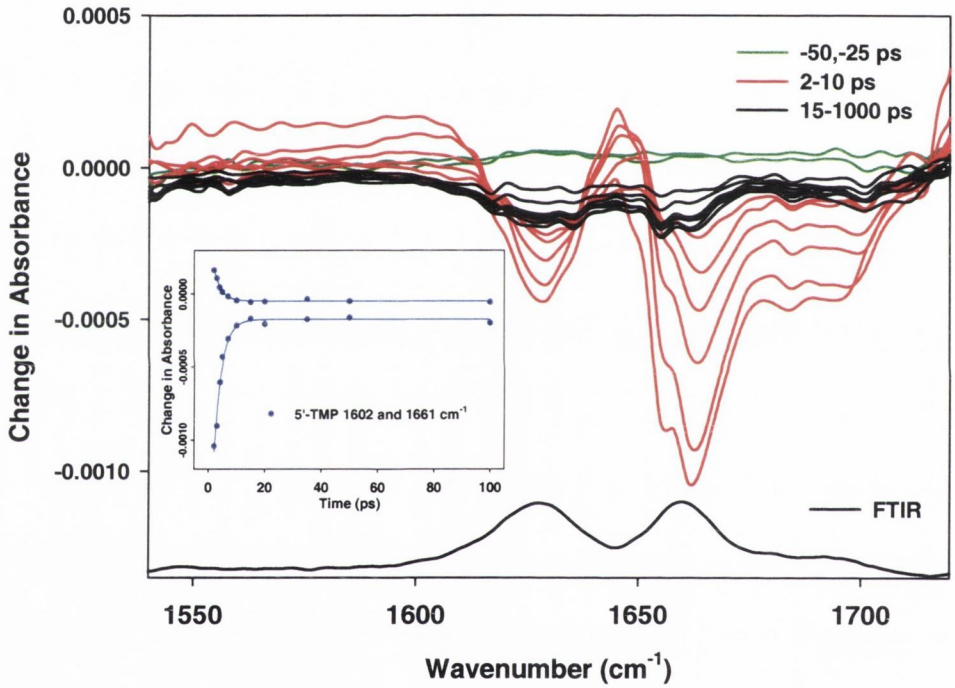

Figure 3.2 ps-TRIR of 10 mM 5′-TMP in 50 mM potassium phosphate D_2O buffer (pH 7) with FTIR below (baseline adjusted). Delays are at -50, -25 (green), 2, 3, 4, 5, 7, 10 (red), 15, 20, 35, 50, 100, 200, 500 and 1000 ps (black).
Inset: Kinetic analysis at 1602 and 1661 cm^{-1}.

3.3.2 Homodinucleotide systems: dApdA and TpT

Figure 3.3 shows the ps-TRIR difference spectrum of dApdA in buffered D_2O solution (pH 7) after UV excitation. The spectral features of the homodimer is almost identical to that of the parent nucleotide 5′-dAMP. The dominant bleaching band occurred at 1626 cm^{-1} with a minor band at 1577 cm^{-1}. The characteristic vibrational cooling

behaviour of the transient band, i.e. shifting to higher wavenumbers with time was clearly seen. Intriguingly, the main bleaching band at 1626 cm^{-1} undoubtedly displayed a long lived component. This is clearly discernable by the red and black colouring scheme (red = 2-10 ps with black = 15-2000 ps) and the kinetic profile of the band shown in figure 3.4. However, the transient bands in this spectral window did not display biphasic behaviour and have fully recovered on the vibrational cooling timescale (~3 ps). Attempts were made to locate a long-lived transient band for this compound in both higher and lower wavenumber spectral windows but no such species was found.

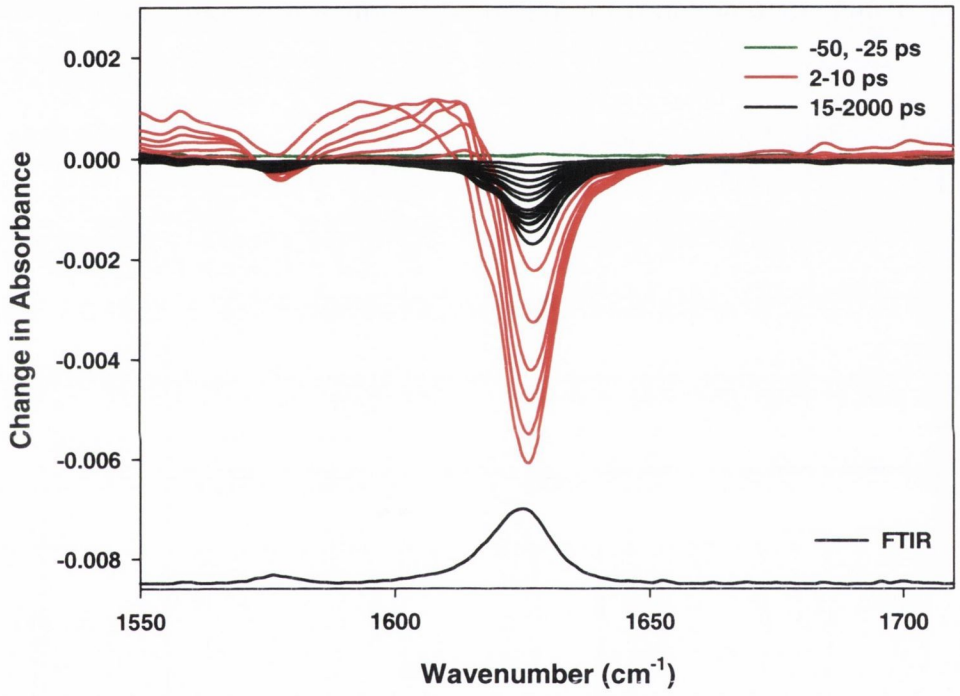

Figure 3.3 ps-TRIR of 10 mM dApdA in 50 mM potassium phosphate D_2O buffer (pH 7) with FTIR below (baseline adjusted). Delays are at -50, -25 (green), 2, 3, 4, 5, 7, 10 (red), 15, 20, 35, 50, 75, 100, 150, 200, 350, 500, 750, 1000, 1500 and 2000 ps (black).

Fitting single exponential functions to the transient bands at at 1561 and 1593 cm^{-1} gave a lifetime of 3.1 ± 0.1 ps (figure 3.4). The bleaching band at 1626 cm^{-1} was found to have a short lifetime of 5 ± 0.5 ps, and a significant (~15%) long-lived component in the range of 600-800 ps. The shorter lifetime component is assigned to intramolecular vibrational cooling, with the longer component arising from some as yet unknown excited state. Possible origins of this long-lived species will be discussed later.

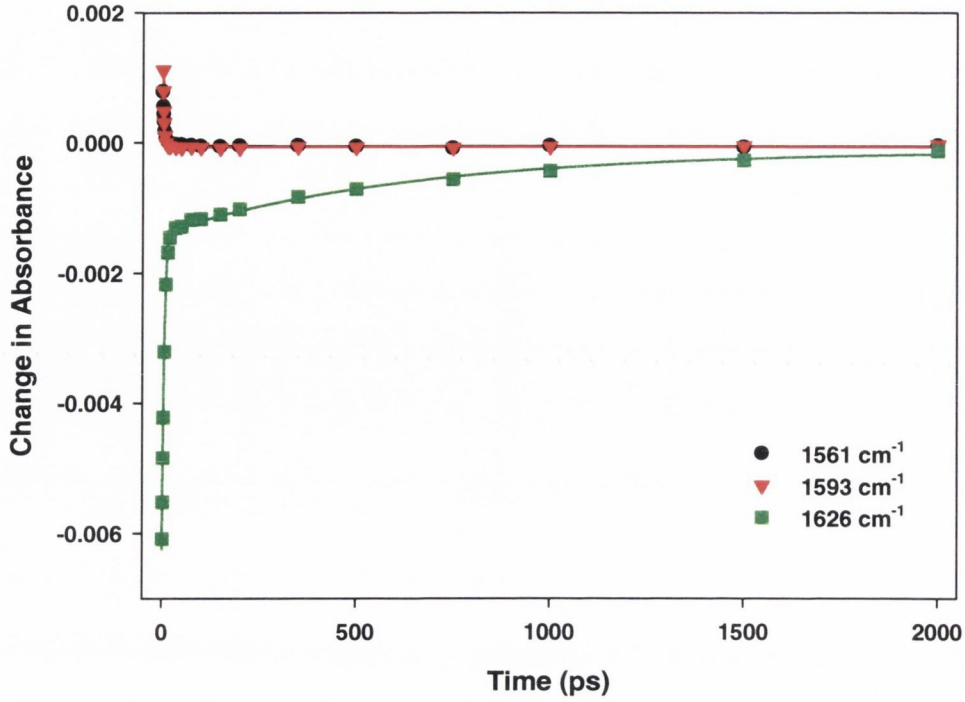

Figure 3.4 Kinetic analysis of 10 mM dApdA in 50 mM potassium phosphate D_2O buffer (pH 7) at 1561, 1593 and 1626 cm^{-1}.

The ps-TRIR difference spectrum of TpT in buffered D_2O solution (pH 7) after UV excitation is shown in figure 3.5. Again the homodimer exhibits a profile similar to that of the monomer nucleotide 5′-TMP unit. Bleaching bands are present at 1629, 1665 and 1696 cm^{-1} with transient features at 1647 and below 1600 cm^{-1}. Vibrational cooling was evident in this system and kinetic analysis revealed that this process occurred over a 2-4 ps time frame. Incomplete recovery of the bleaching bands was found over the 1000 ps timescale of the experiment. Examination of the UV spectrum of the sample after irradiation revealed that the absorbance at 266 nm had decreased by 20% (see appendix figure A3.2). Given that the transient bands display excellent recovery, it is plausible a permanent photoproduct (that does not have an absorption in this spectral window) was possibly formed in a moderate yield.

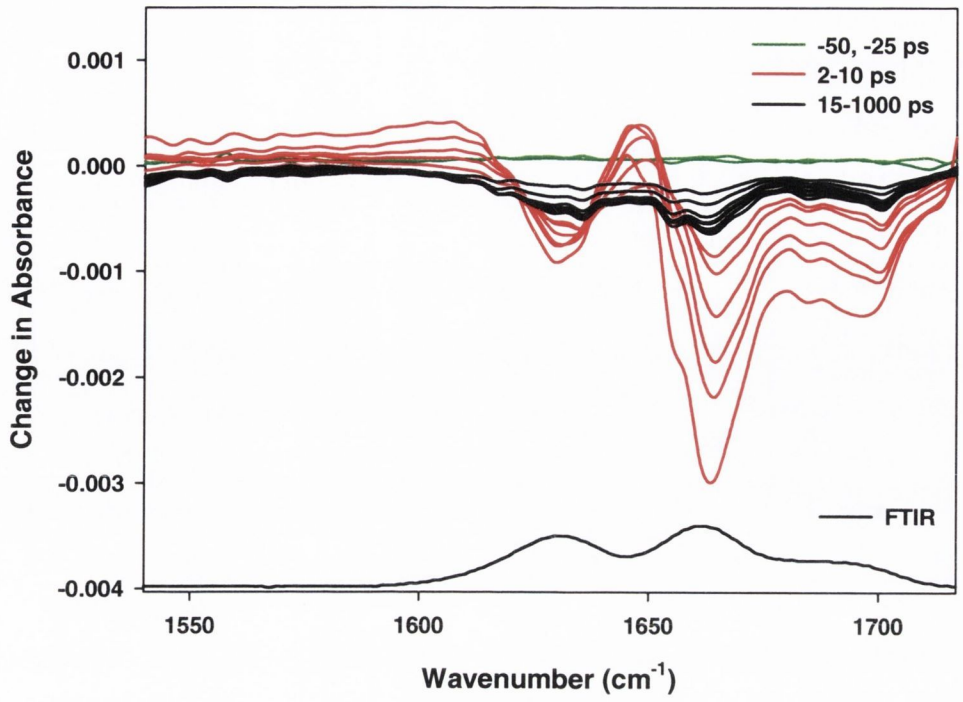

Figure 3.5 ps-TRIR of 10 mM TpT in 50 mM potassium phosphate D_2O buffer (pH 7) with FTIR below (baseline adjusted). Delays are at -50, -25 (green), 2, 3, 4, 5, 7, 10 (red), 15, 20, 35, 50, 100, 200, 500 and 1000 ps (black).

The kinetic analysis of the system is shown in figure 3.6. The broad transient band exhibits biexponential kinetics with lifetimes of 2.0 ± 0.2 ps (86%) and 34 ± 10 ps (14%) being found at 1572 cm^{-1}. The bleaching band at 1629 cm^{-1} gave a short lifetime of 3.8 ± 0.4 ps (65%), and a long-lived species of the order of several of hundreds of picoseconds (35%). At 1668 cm^{-1} the majority (92%) of the bleach decayed with a lifetime of 3.8 ± 0.3 ps, but there was also a long-lived contribution (8%) having a lifetime of approximately 400 ± 100 ps. At the high wavenumber region, 1694 cm^{-1}, monoexponential behaviour was predominately found with a lifetime of 4.0 ± 0.6 ps. The long-lived species is very poorly defined in this system as there are very few data points at the longer time delays. Efforts were made to improve on the characterization of this long-lived species by calculating the area for a particular region for each delay and plotting this against delay time and this suggested that the long-lived component had a lifetime in the region of 300 ps. There may also be some evidence of another lifetime, of ~8-10 ps but further experimentation would be required to investigate the legitimacy of this.

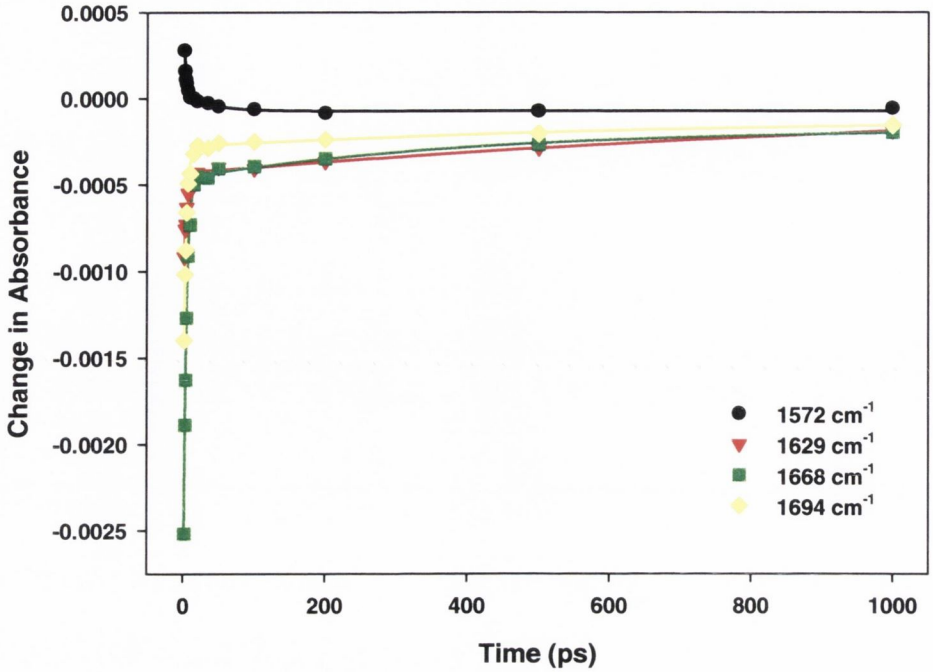

Figure 3.6 Kinetic analysis of 10 mM TpT in 50 mM potassium phosphate D_2O buffer (pH 7) at 1572, 1629, 1668 and 1694 cm^{-1}.

3.3.3 Heterodinucleotide systems: dApT and TpdA

In the case of the heterodimers dApT and TpdA, the spectra exhibit common features, typical of the constituent nucleotides. The spectrum of dApT (figure 3.7) exhibits bleaches at 1575 cm^{-1} (A), 1620 cm^{-1} (A and T, C=C, C=N stretching vibrations), 1658 cm^{-1} (T, C_4=O stretch) and 1688 cm^{-1} (T, C_2=O) cm^{-1} and transient features (A and T) in the region 1530-1610 cm^{-1}.

The time resolved infrared difference spectrum of dApT is shown in figure 3.7. This dimer, in contrast to both dApdA and TpT, displayed a very strong and broad transient absorption. An equimolar mix of the constituent nucleotides was also investigated and as expected, this sample did not show such a long-lived transient feature (see appendix figure A3.3). This suggests that that stacking interactions in the dimer play a pivotal role in the generation of such long-lived species and a detailed study on such interactions is presented later in this chapter.

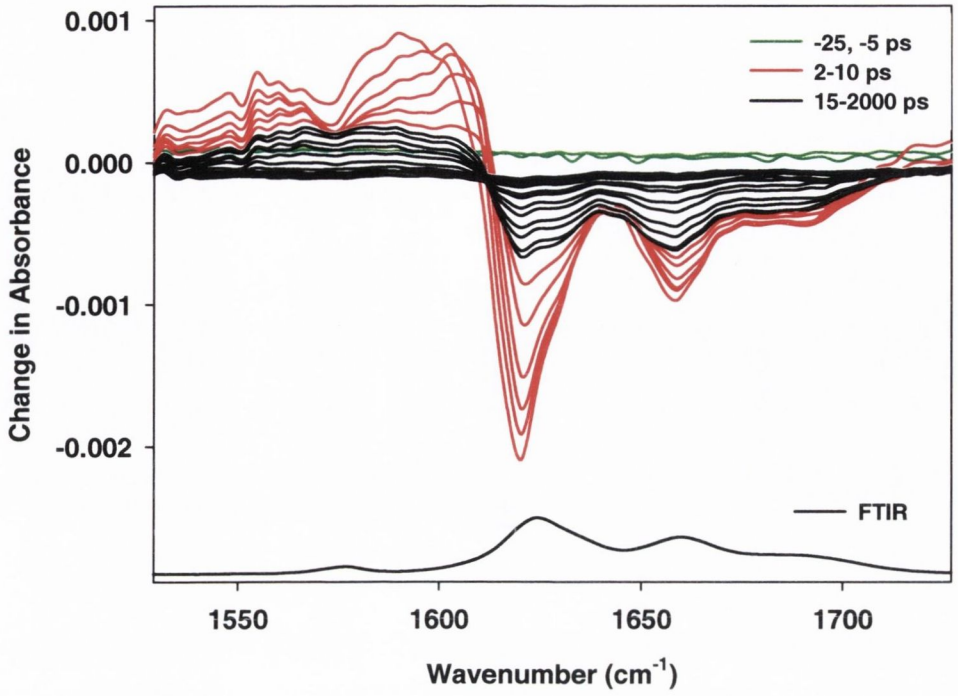

Figure 3.7 ps-TRIR of 10 mM dApT in 50 mM potassium phosphate D_2O buffer (pH 7) with FTIR below (baseline adjusted). Delays are at -50, -25 (green), 2, 3, 4, 5, 7, 10 (red), 15, 20, 35, 50, 75, 100, 150, 200, 350, 500, 750, 1000, 1500 and 2000 ps (black).

Fitting of both bleaching and transient bands to a biexponential model revealed second order kinetics with a short lifetime component (2-6 ps) assigned to vibrational relaxation of the vibrationally hot ground state and a longer component of ~70 ps (figure 3.8 (a)). Variation in the lifetime of the fast process was found across the spectrum due to the presence of overlapping transient and ground state absorptions and also in the main 1620 cm^{-1} band due to the overlapping of both A and T absorptions. Both the short and long lifetimes were found to decrease slightly, while the percentage of long-lived species was found to increase, upon radiating out in both directions from the central 1620 cm^{-1} bleach. (see figure 3.8 (b)) This phenomenon of varying lifetime for the long-lived species depending on the position considered was found in several samples and the reader is directed to the appendix (Tables A3.1 and A3.2) where detailed tabular analysis of several samples by both single pixel and area analysis is given, with each region of the spectrum being carefully considered.

Interestingly, when the ps-TRIR of dApT was examined under acidic conditions (0.132 M H_3PO_4, pH 2) there was no detectable long-lived species present (see appendix figure A3.4). As was the case for 5′-dCMP (chapter 2) protonation

either shuts off a pathway or opens the possibility of an alternative (faster) route. In the case of dApT, protonation would occur at the amino group of adenine (pKa 3.45), with no analagous site on the thymine base moiety. Therefore, changing the photophysical properties of the adenine moiety, affects the ability of the dinucleotide system to form the long-lived species.

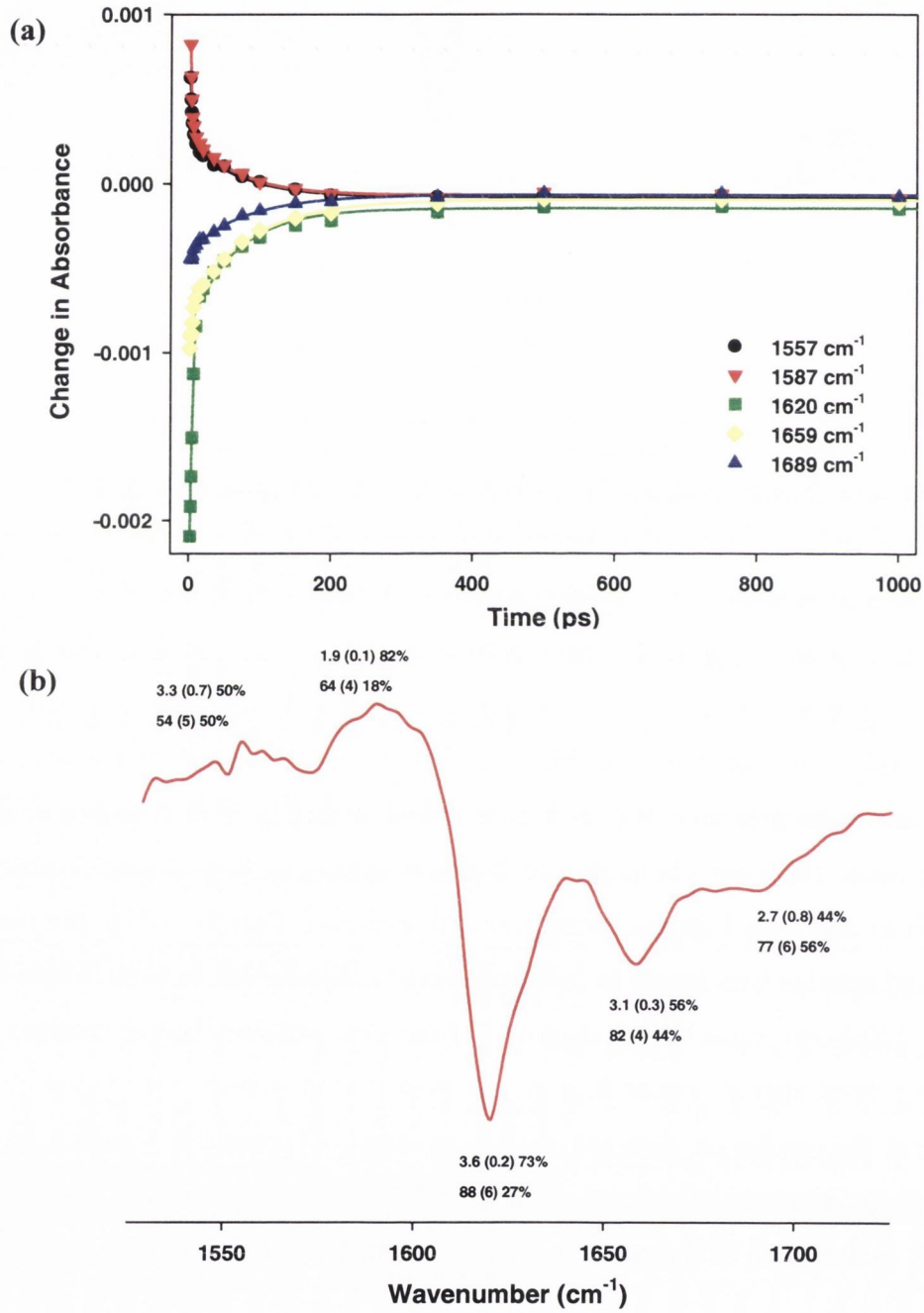

Figure 3.8 (a) Kinetic analysis of 10 mM dApT in 50 mM potassium phosphate D_2O buffer (pH 7) at 1557, 1587, 1620, 1659 and 1689 cm^{-1} and (b) summary of how the lifetimes vary with band position. Trace profile is the 2 ps delay.

A similar result was obtained for TpdA with bleaches centred at 1623 cm^{-1} (ring deformation of thymine base and C=C, C=N stretching vibrations in the purine ring deformation mode), 1661 cm^{-1} (C_4=O stretch) and 1694 cm^{-1} (C_2=O stretch) and a broad transient spanning from 1530-1612 cm^{-1} (figure 3.9). The transient band is notably less intense than the coresponding transient in dApT.

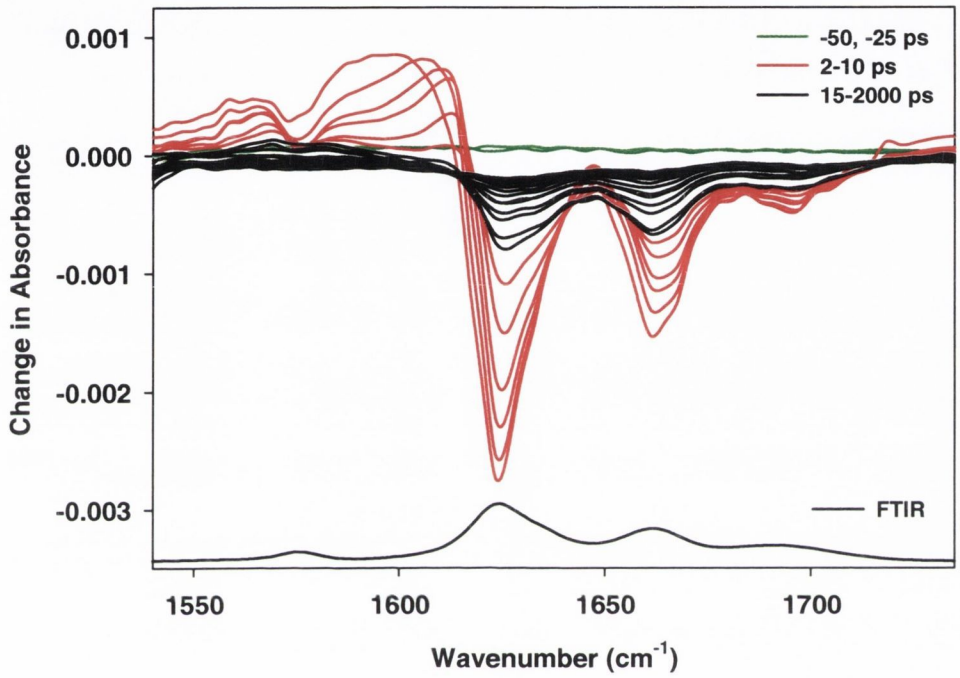

Figure 3.9 ps-TRIR of 10 mM TpdA in 50 mM potassium phosphate D_2O buffer (pH 7) with FTIR below (baseline adjusted). Delays are at -50, -25 (green), 2, 3, 4, 5, 7, 10 (red), 15, 20, 35, 50, 65, 80, 100, 150, 225, 325, 450, 650, 850, 1000, 1500 and 2000 ps (black).

Analysis of the recovery of the bleaching bands and transient decay in TpdA revealed biexponential behaviour, with a similar trend to that found in the dApT case. However, while vibrational cooling dynamics are comparable to the dApT system, the lifetime of the long-lived species is now of the order of 50 ps. Figure 3.10 (a) shows the kinetic profiles of five pixel points in the five main regions of the spectrum, with figure 3.10 (b) being a graphical representation of the overall averaged kinetic picture. Again, a comprehensive account of the kinetics for multiple samples is provided in the appendix (Tables A3.3 and A3.4), with emphasis placed on the variation of the long-lived species' lifetime with band position. As for the dApT case, excellent recovery was observed in this system with no indication of sample degradation. This indicates that the normally susceptible thymine moiety is somehow protected or stabilized by the presence of the

adenine and thus does not form photoproducts (either very long-lived or permanent) upon UV excitation.

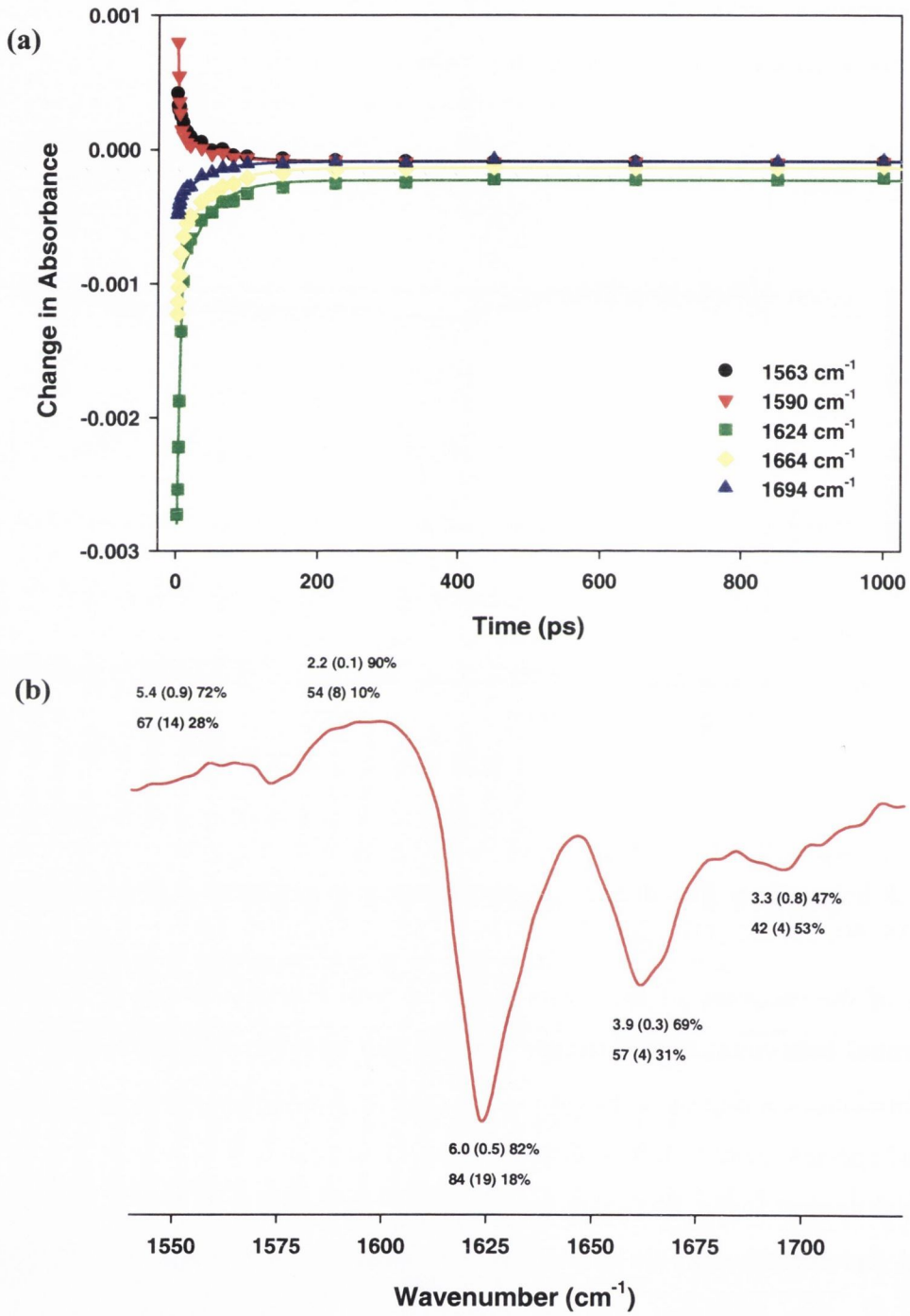

Figure 3.10 (a) Kinetic analysis of 10 mM TpdA in 50 mM potassium phosphate D_2O buffer (pH 7) at 1563, 1590, 1624, 1664 and 1694 cm^{-1} and (b) summary of how the lifetimes vary with band position. Trace profile is the 2 ps delay.

3.3.4 Stacking Studies

The stacking interactions in DNA are very important and there is considerable debate in the literature as to whether base-stacking[124,126] or hydrogen-bonding[125] interactions have the overriding influence on the relaxation dynamics of DNA. In our family of dinucleotides the amount of stacked species follows the order dApdA, dApT, TpdA and finally TpT. Given that the relaxation dynamics were found to vary in the structural isomers, dApT and TpdA, a more comprehensive study of these two dinucleotides was warranted.

Three techniques that are sensitive to the amount of stacked species were employed, namely circular dichroism (CD), nuclear magnetic resonance (NMR) and picosecond time resolved transient infrared spectroscopy (ps-TRIR). With two of these techniques, NMR and ps-TRIR, we also have the capability of performing variable temperature experiments. As the amount of stacking changes upon heating, this was also expected to change the relaxation behaviour.

3.3.4.1 Circular Dichroism Measurements

The CD spectra obtained for the dinucleotides (under the same conditions as the ps-TRIR measurements) is given in figure 3.11. For comparison the spectra of the constituent mononucleotides (in isolation and in an equimolar mixture) is also shown. Instantly significant differences between the mono- and dinucleotides, and even between the two dinucleotides can be seen. CD is very sensitive to secondary structure in solution and with dApT being the most stacked of the two dinucleotides, it exhibited the strongest CD signal. The spectrum of dApT displayed local minima at 208 and 252 nm and local maxima at 220 and 272 nm. Local maxima occur at 218 and 271 nm with a local minimum at 251 nm in the case of TpdA. Exciton bands are present at 263 and 262 nm for dApT and TpdA respectively. Both dinucleotides have positive signals at long wavelength with negative signals at shorter wavelength. This indicates that both compounds are in a right-handed stacked conformation.

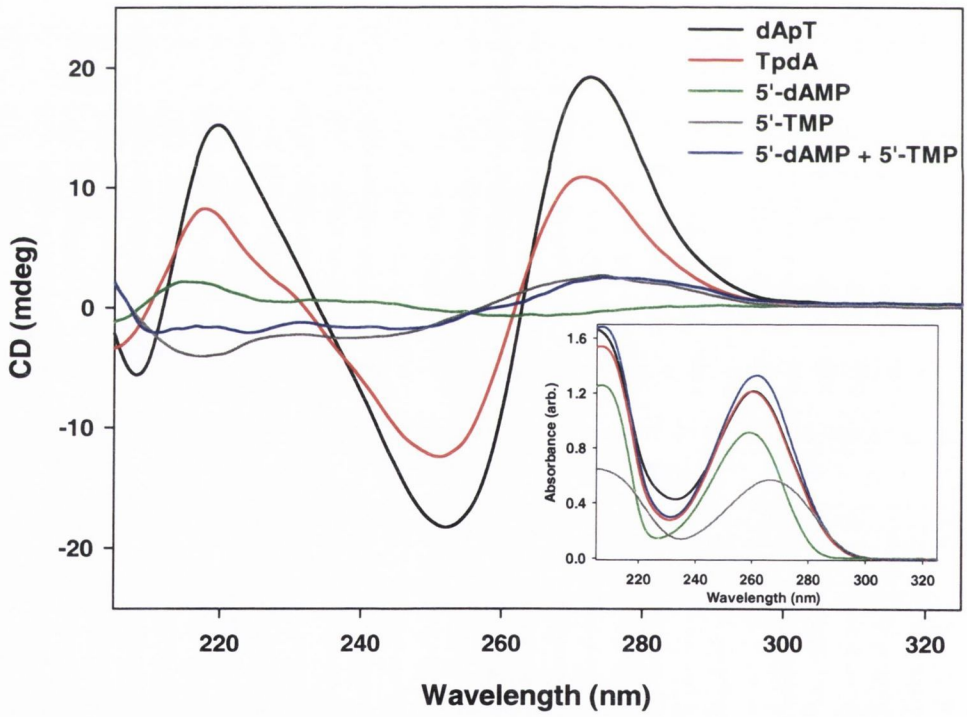

Figure 3.11 CD spectra of dApT (black), TpdA (red), 5′-dAMP (green), 5′-TMP (gray) and an equimolar mixture of 5′-dAMP and 5′-TMP (blue). Inset: UV spectrum for all five cases. All samples were 10 mM in 50 mM potassium phosphate D_2O buffer (pH 7).

3.3.4.2 Variable Temperature Nuclear Magnetic Resonance Studies of dApT and TpdA

^{1}H NMR was used to study the structural conformations of the dinucleotides, dApT and TpdA. However, before assignment of the more complex dinucleotides, the simplier mononucleotide units were characterized (scheme 3.2 and Table 3.1). Spectra were recorded under identical experimental conditions (10 mM DNA in 50 mM potassium phosphate buffer, pH 7) as that of the CD and ps-TRIR measurements (spectra of 5′-dAMP and 5′-TMP are provided in appendix figure A3.5, with assignments summarized in Table 3.1 below). Unambiguous assignment of the signals was achieved using ^{1}H, ^{13}C, ^{1}H-^{1}H COSY and ^{13}C-^{1}H COSY spectroscopy.

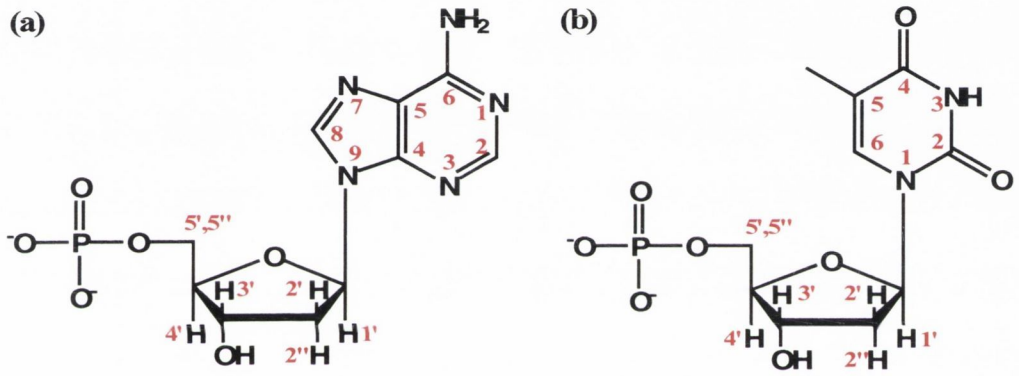

Scheme 3.2 Structures of (a) 5′-dAMP and (b) 5′-TMP with the numbering system for the bases and ribose included.

^{1}H NMR Chemical Shifts of the Mononucleotides 5′-dAMP and 5′-TMP at 20 °C									
DNA	H8/H6	H2/CH_3	1′	2′	2′′	3′	4′	5′	5′′
5′-dAMP	8.41	8.11	6.38	2.71	2.46	4.60	4.14	3.84	3.84
5′-TMP	7.69	1.81	6.23	2.30	2.21	4.46	4.03	3.85	3.85

Table 3.1 Proton assignments of 5′-dAMP and 5′-TMP both in 50 mM potassium phosphate D_2O buffer (pH 7).

Assignment of the dinucleotide units was then successfully completed employing ^{1}H and ^{1}H-^{1}H COSY techniques. In the case of dApT all signals except that of the 3′ of the adenine ribose (obscured by the residual H_2O peak at 4.7 parts per million (ppm)) were identified (^{1}H spectrum in figure 3.13 (20 °C)). All signals in TpdA were also clearly identifiable and the ^{1}H-^{1}H COSY is shown below in figure 3.12 (^{1}H spectrum is in figure

3.14 (20 °C)). The number of cross peaks in the spectrum indicates that there are complex coupling events in the ribose protons.

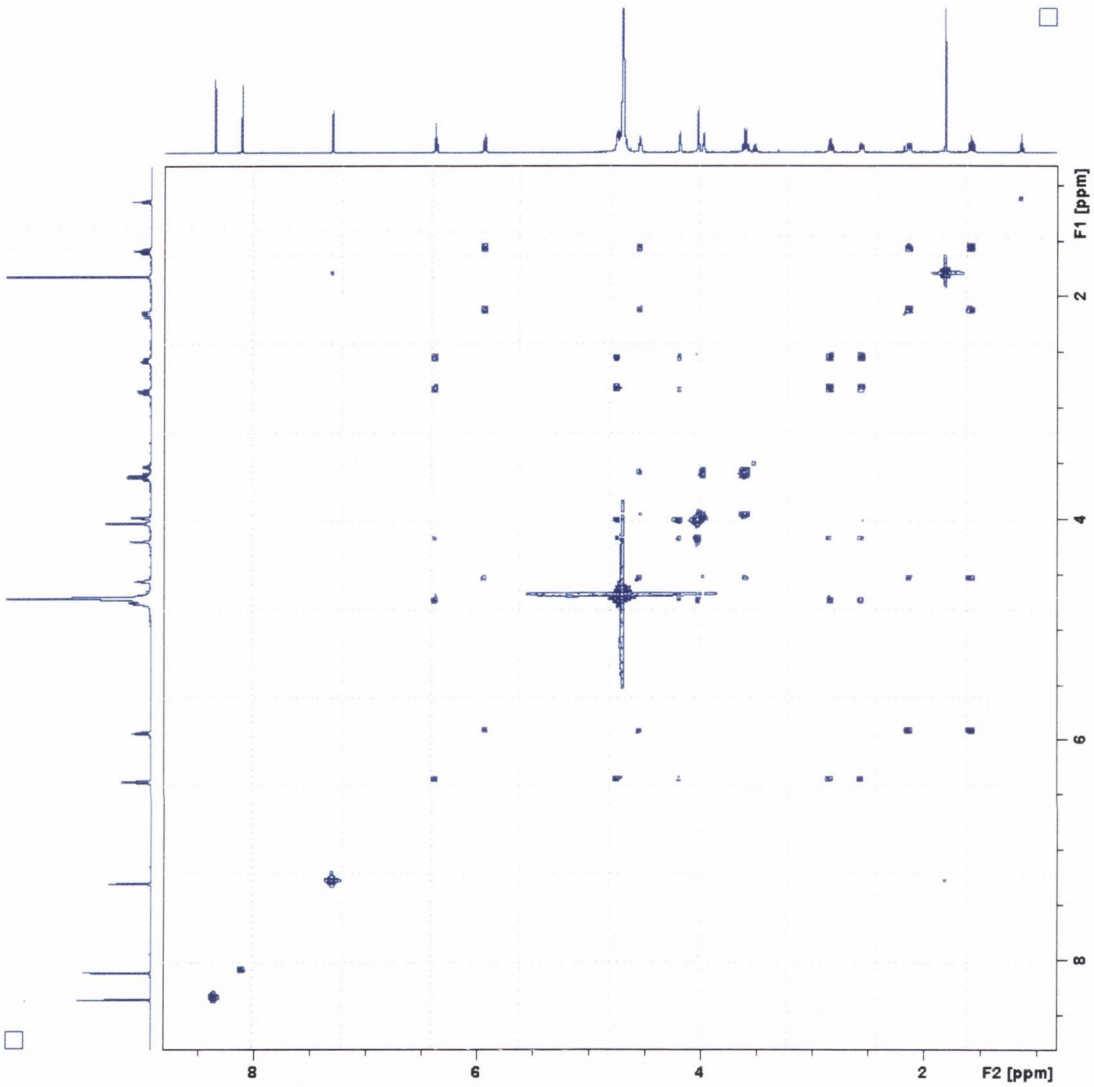

Figure 3.12 ^{1}H-^{1}H COSY of 10 mM TpdA in 50 mM potassium phosphate D_2O buffer, (pH 7).

Variable temperature spectra were recorded for the dinucleotides at temperatures of 20, 50 and 70 °C. The ^{1}H NMR spectra obtained for dApT at all three temperatures is shown in figure 3.13 and as the dinucleotide unit is heated all resonances shift to higher ppm. The residual water peak's resonance is found to shift with increasing temperature and the elevated temperature spectra were calibrated using the sodium salt of 3-(trimethylsilyl)-1-propane sulphonic acid.

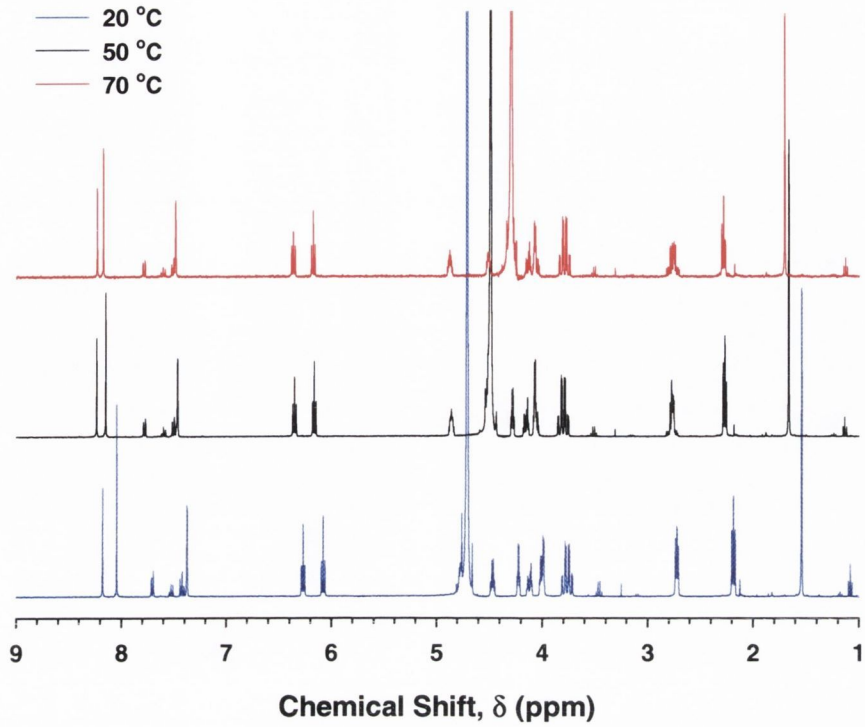

Figure 3.13 Variable temperature ^{1}H NMR spectra of dApT at 20 °C (blue), 50 °C (black) and 70 °C (red).

Assignment of the peaks for all three temperatures is given in table 3.2. Some protons could not be assigned due to their masked by the residual H_2O peak. As evidenced by the values in the table, the greatest shift in ppm occurs between 20 and 50 °C, with there being only slight changes on going from 50 to 70 °C.

dApT ^{1}H NMR Chemical Shifts at 20 °C, 50 °C and 70 °C									
DNA	H8/H6	H2/CH_3	1′	2′	2′′	3′	4′	5′	5′′
3′-dAp	8.15	8.02	6.25	2.71	2.71	obs*	4.20	3.74	3.74
pT-5′	7.35	1.52	6.05	2.16	2.16	4.44	4.11	3.99	3.99
3′-dAp	8.23	8.15	6.35	2.77	2.77	4.86	4.28	3.80	3.80
pT-5′	7.47	1.66	6.16	2.27	2.27	obs*	4.16	4.06	4.06
3′-dAp	8.23	8.17	6.36	2.76	2.76	4.87	obs*	3.79	3.79
pT-5′	7.48	1.70	6.18	2.28	2.28	4.51	4.13	4.06	4.06

Table 3.2 Proton assignments of dApT in 50 mM potassium phosphate D_2O buffer (pH 7) at 20, 50 and 70 °C. * obscured peak by the residual H_2O peak.

Figure 3.14 shows the ^{1}H NMR spectra of TpdA at 20, 50 and 70 °C and as for the case of dApT all signals shift to higher ppm with the increase in temperature.

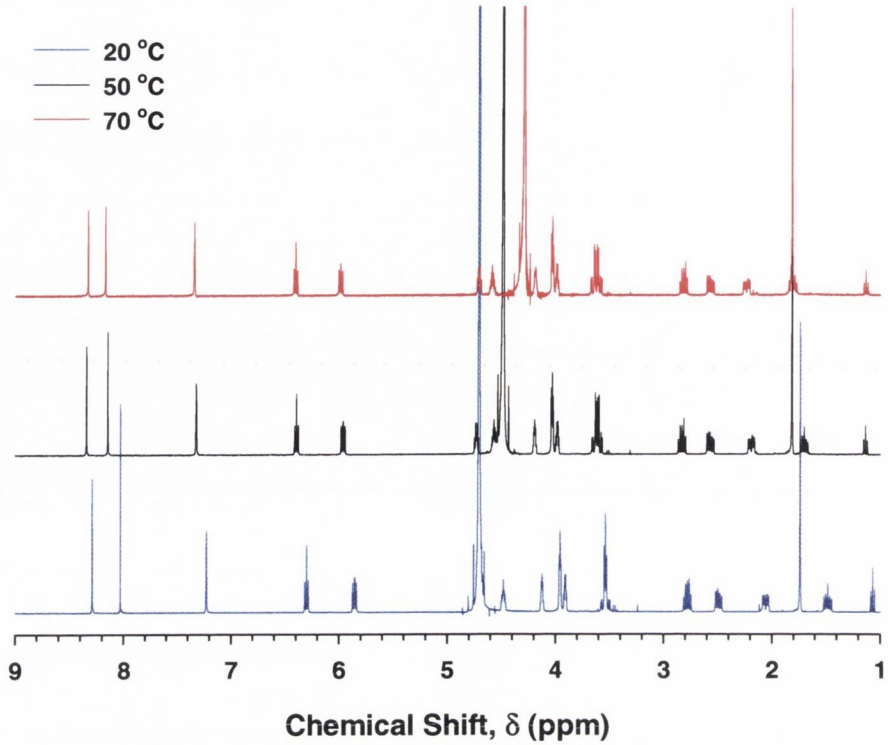

Figure 3.14 Variable temperature ^{1}H NMR spectra of TpdA at 20 °C (blue), 50 °C (black) and 70 °C (red).

The variable temperature peak assignments for TpdA are summarized below in table 3.3. All signals are discernable except for that of the 2′ thymine ribose at 70 °C as it overlaps with that of the thymine methyl peak. As for the dApT case, the largest change in ppm was observed between 20 and 50 °C.

dApT ^{1}H NMR Chemical Shifts at 20 °C, 50 °C and 70 °C									
DNA	H8/H6	H2/CH_3	1′	2′	2′′	3′	4′	5′	5′′
3′-Tp	7.21	1.73	5.84	1.46	2.04	4.47	3.90	3.50	3.50
pdA-5′	8.28	8.01	6.29	2.48	2.77	4.67	4.11	3.95	3.95
3′-Tp	7.32	1.82	5.96	1.70	2.19	4.57	3.98	3.62	3.62
pdA-5′	8.34	8.15	6.40	2.57	2.83	4.73	4.19	4.03	4.03
3′-Tp	7.34	1.82	5.99	obs*	2.24	4.59	3.99	3.62	3.62
pdA-5′	8.33	8.17	6.41	2.57	2.82	4.71	4.19	4.03	4.03

Table 3.3 Proton assignments of TpdA in 50 mM potassium phosphate D_2O buffer (pH 7) at 20, 50 and 70 °C. * obscured peak by the thymine methyl peak at 1.82 ppm.

Decoupling experiments were performed in order to evaluate the sum of the coupling of the 2′ and 2′′ protons to the 1′ proton. Figure 3.15 shows the result of decoupling

experiments for both dApT and TpdA. The 3′ proton of both the A and the T portion were selectively decoupled and hence the splitting at the 2′ and 2′′ positions was simplified, allowing for an accurate determination of the coupling to the 1′ proton to be made.

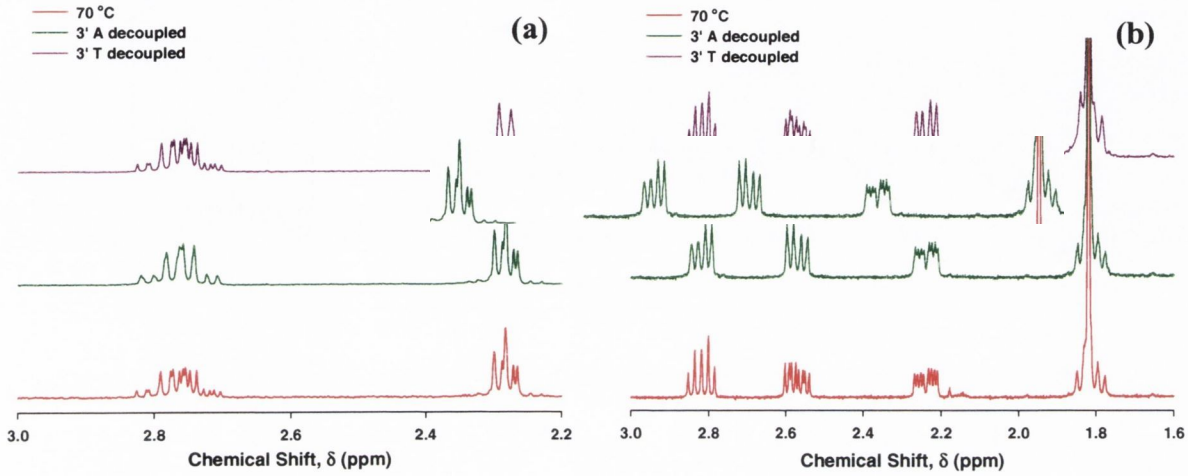

Figure 3.15 Selective TOCSY ^{1}H NMR spectra of (a) dApT and (b) TpdA at 70 °C. Normal ^{1}H spectrum (red), 3′ adenine ribose decoupled (green) and 3′ thymine ribose decoupled (purple).

The work of Isaksson *et al.*[144] had shown that evaluation of the total 1′ coupling with subsequent substitution into formula 3.1 gave a reliable evaluation of the stacking in DNA systems. The total coupling to the 1′ position for both dinucleotide systems was substituted into the formula derived by Rinkel *et al.*[145]:

$$\% \text{ N} = 100(1-(\textstyle\sum J_{\text{H1}'} - 9.8)/5.9) \qquad (3.1)$$

$$\text{where } \textstyle\sum J_{\text{H1}'} = J_{1'2'} + J_{1'2''}$$

The result is the percentage north conformer of the sugar, which can be used as a direct measurement of the extent of stacking within DNA systems. This approach when applied to our systems at 20 °C, gave good agreement for the percentage stacking for both dApT and TpdA with that previously reported in the literature.[146] Upon heating to 50 °C, it was found that the equilibrium between stacked and unstacked changed for the dApT case but not to any appreciable degree within the TpdA dinucleotide. Further heating to 70 °C appeared to shift the equilibrium for both dinucleotides where appreciable differences in the amount of stacking compared to that of the 20 °C spectra were found. The results of this NMR stacking study are summarized below in Table 3.4.

dApT			TpdA		
Temperature (°C)	**$\sum J_{1'}$ (Hz)**	**% stacked**	**Temperature (°C)**	**$\sum J_{1'}$ (Hz)**	**% stacked**
20	13.45	38	20	14.51	20
50	13.72	34	50	14.53	20
70	13.85	31	70	14.91	13

Table 3.4 Summary of the ^{1}H NMR study to evaluate extent of base-stacking for dApT and TpdA at 20, 50 and 70 °C.

3.3.4.3 Variable Temperature Time Resolved Infrared (VT ps-TRIR)

The ps-TRIR spectrum of dApT at 70 °C in buffered D_2O solution (pH 7) after UV excitation is shown in figure 3.16. Inspection of the spectral features revealed some differences from that of the 20 °C described earlier (figure 3.7). Most notably the amount of long-lived species (black delays) relative to the short-lived species (red delays) is less. Another key observation is that the main 1620 cm^{-1} band, which has contributions from both A and T (~4:1 ; A:T), now shows better resolution, with the shoulder at 1630 cm^{-1} being more pronounced at the elevated temperature. Both observations can be explained in terms of the difference in the stacking of the system at the elevated temperature. The variable temperature ^1H NMR results presented above indicate that the amount of stacking in the system changes from 38% at 20 °C to 31% at 70 °C. As the bases unstack, they behave more akin to the constituent monomers, and hence less long-lived species was observed with the band positions starting to resemble more closely that of the monomers.

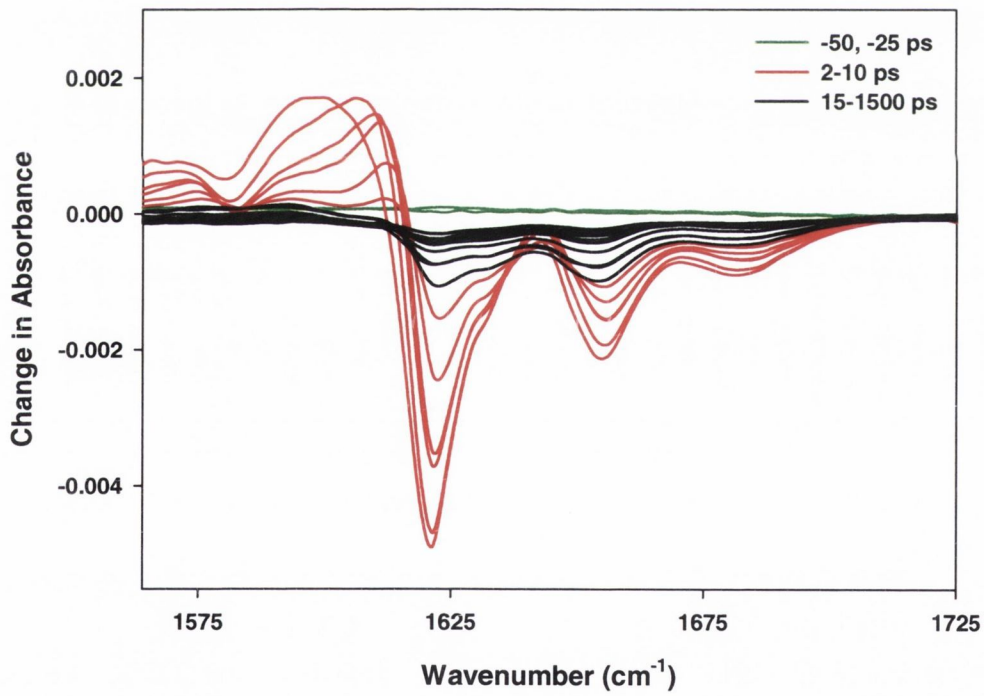

Figure 3.16 ps-TRIR of 10 mM dApT at 70 °C in 50 mM potassium phosphate D_2O buffer (pH 7). Delays are at -50, -25 (green), 2, 3, 4, 5, 7, 10 (red), 15, 20, 35, 50, 75, 100, 150, 200, 250, 350, 500, 750, 1000 and 1500 ps (black).

Analysis of the relaxation dynamics following excitation is given in figure 3.17. The kinetics of the system are still biexponential but now there is less of a contribution from the long-lived state. For instance the transient band at 1588 cm^{-1} had a long lifetime of 73 ± 4 ps that accounted for 15% of the decay at 20 °C, and now at the same position the transient was found to have a lifetime of 44 ± 6 ps with a 9% contribution from the long-lived species. A similar trend was found along all transient and bleaching bands and once again a full treatment is provided in the appendix (tabular analyses A3.5) for the different regions at both 20 and 70 °C. The long-lived species was found for both transient and bleaching bands to have reduced by *ca.* 40% from 70 ps to 40 ps.

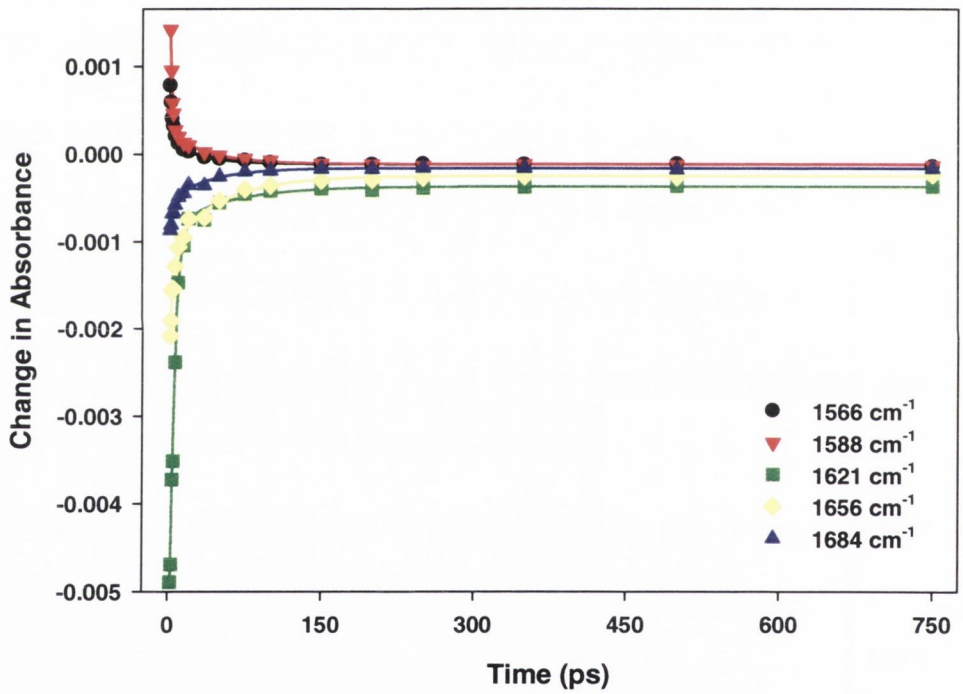

Figure 3.17 Kinetic analysis of 10 mM dApT at 70 °C in 50 mM potassium phosphate D_2O buffer (pH 7) at 1566, 1588, 1629, 1656 and 1684 cm^{-1}.

Variable temperature ps-TRIR measurements were also made for TpdA and the spectrum obtained at 70 °C is given in figure 3.18. Once again, as for the dApT case, spectral differences are immediately recognizable between this spectrum and that recorded at 20 °C (figure 3.9) - there is less long-lived species present and the shoulder at 1630 cm^{-1} is more aparent. From the variable temperature ^{1}H NMR measurements it is predicted that the percentage stacking in the system has changed from 20% at 20 °C to 13% at 70 °C.

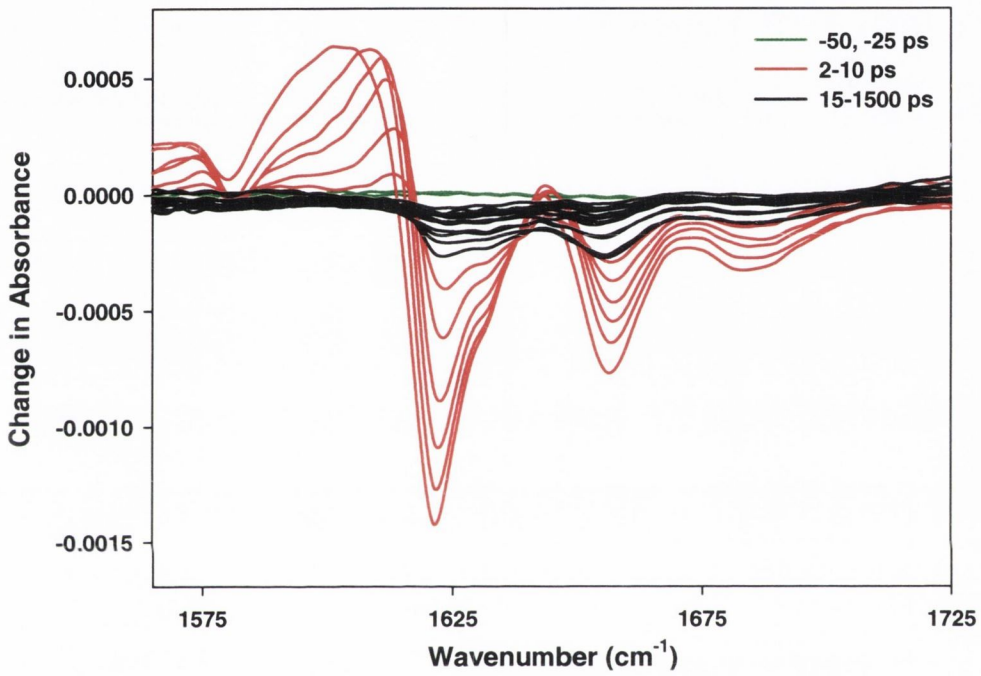

Figure 3.18 ps-TRIR of 10 mM TpdA at 70 °C in 50 mM potassium phosphate D_2O buffer (pH 7). Delays are at -50, -25 (green), 2, 3, 4, 5, 7, 10 (red), 15, 20, 35, 50, 75, 100, 150, 200, 250, 350, 500, 750, 1000 and 1500 ps (black).

Analysis of the relaxation processes is given in figure 3.19. The kinetics of the system are still biexponential and unsurprisingly both the percentage contribution and lifetime of the long-lived state have decreased (see appendix, tabular analysis A3.6). For example the transient absorption decay at 1591 cm^{-1} had a long-lived species lifetime of 37 ± 6 ps (11%) at 20 °C, that has now become 19 ± 6 ps (9%) at 70 °C. However, it must be noted that the error associated with the long-lived species is relatively large. The quality of the fit is probably a consequence of a couple of factors: (i) The signal at 70 °C was not as strong as that at 20 °C and thus the signal to noise ratio is increased – especially at the longer time delays. (ii) With there being a smaller/reduced contribution from the long-lived species at the elevated temperature the fitting model struggles to attain an accurate fit,

therefore the error associated with the lifetime becomes larger. In an effort to characterize the long-lived species' lifetime better, the long time delays were fit to single exponential functions and this suggested that the lifetime of the long-lived species was in the range of 25-30 ps (appendix tabular analysis A3.6). This would appear to be a more accurate assessment of the lifetime.

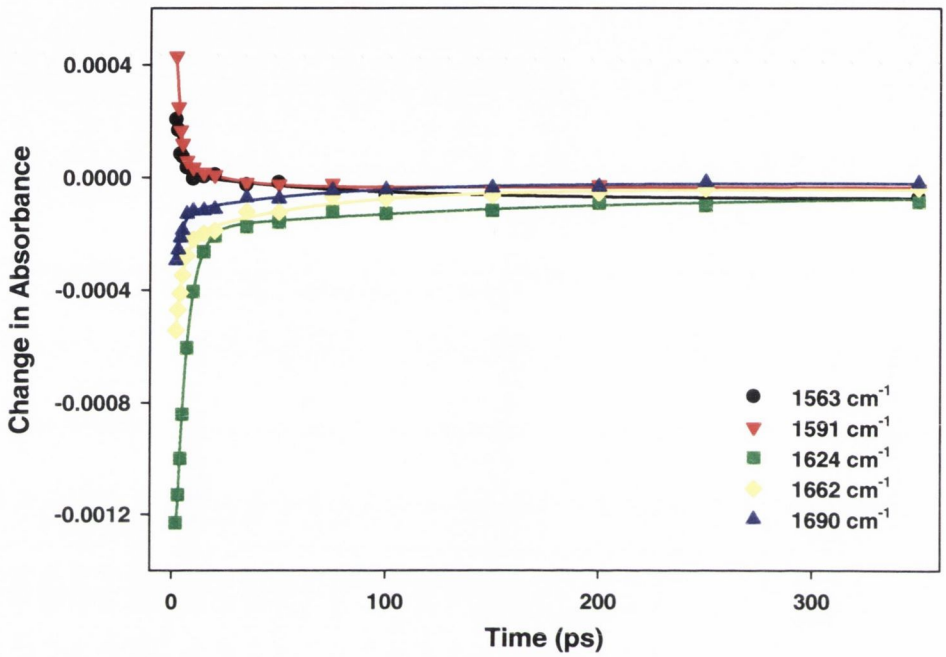

Figure 3.19 Kinetic analysis of 10 mM TpdA at 70 °C in 50 mM potassium phosphate D_2O buffer (pH 7) at 1563, 1591, 1624, 1662 and 1690 cm^{-1}.

The final temperature dependent ps-TRIR spectrum for TpdA was recorded at 90 °C and is shown in figure 3.20. The signal at this temperature was poor and it must be noted that the data in figure 3.20 was only accumulated over two cycles whereas all other data was recorded over four cycles. Although there was a poor signal-to-noise ratio, the spectrum does confirm that an insignificant amount (if any at all) of long-lived species was present. This is due to the dinucleotide being predominately in the unstacked conformation.

The kinetics of this system are distinctly first order and fit to a lifetime in the range of 2-4 ps (figure 3.21). At 90 °C, cooling of the vibrationally hot ground state is the only discernable process (full single pixel analysis of the sample is provided in the appendix, tabular analysis A3.6).

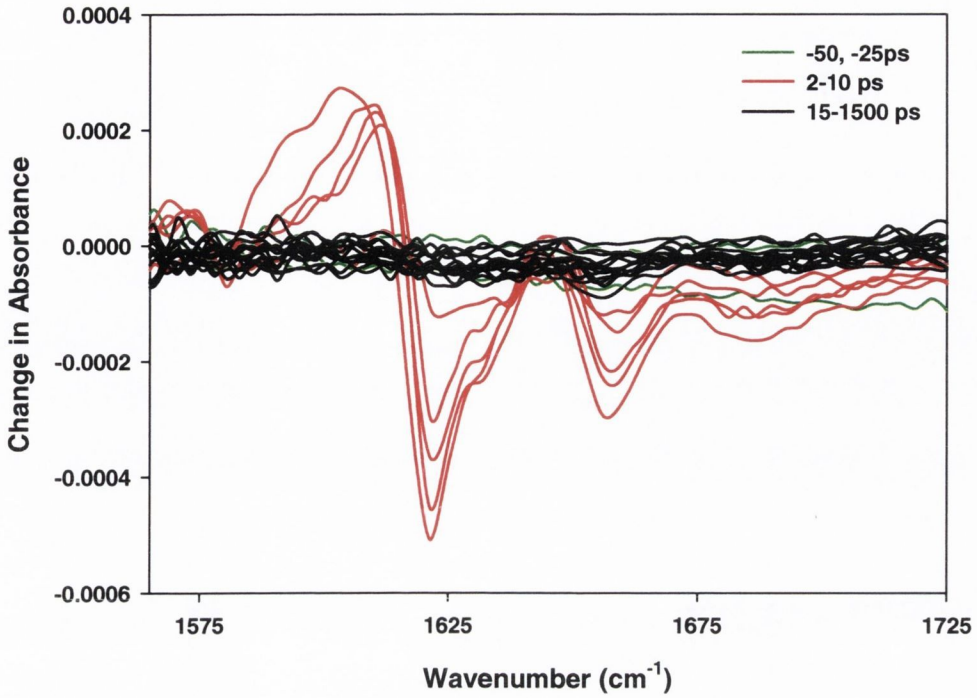

Figure 3.20 ps-TRIR of 10 mM TpdA at 90 °C in 50 mM potassium phosphate D_2O buffer (pH 7). Delays are at -50, -25 (green), 2, 3, 4, 5, 7, 10 (red), 15, 20, 35, 50, 75, 100, 150, 200, 250, 350, 500, 750, 1000 and 1500 ps (black).

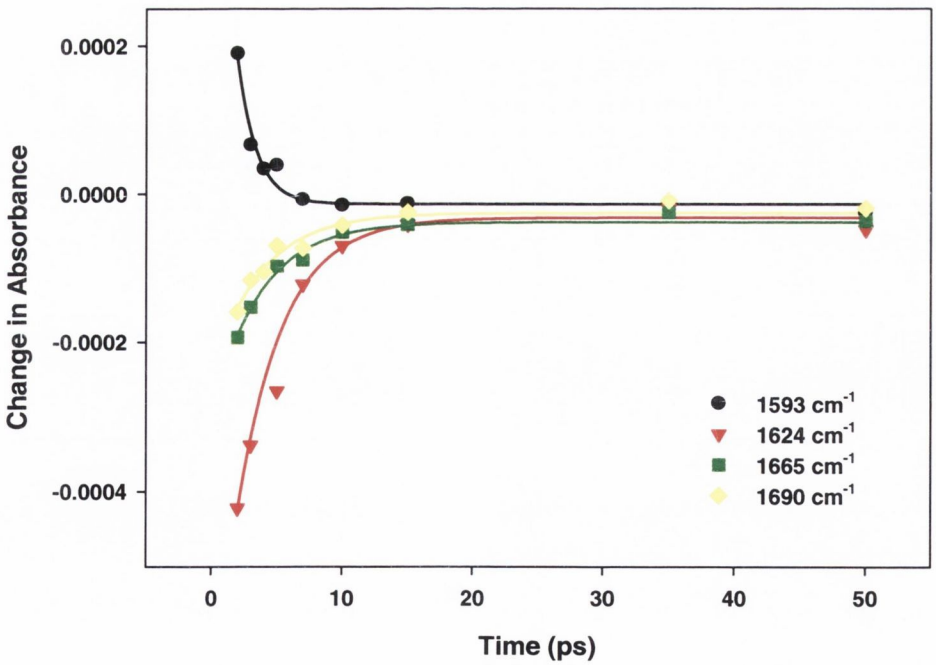

Figure 3.21 Kinetic analysis of 10 mM TpdA at 90 °C in 50 mM potassium phosphate D_2O buffer (pH 7) at 1593, 1624, 1665 and 1690 cm^{-1}.

3.3.5 Alternating Polynucleotide System: poly(dA-dT).poly(dA-dT)

The ps-TRIR spectrum of poly(dA-dT).poly(dA-dT) obtained following UV excitation is shown in figure 3.22. In the ground state the effect of base-pairing has caused the bands at 1661 cm^{-1} and 1695 cm^{-1} to be of comparable intensity. This is also reflected in the transient spectrum. There are five bleaches located at 1570, 1617, 1637, 1665 and 1692 cm^{-1}. The depletions at 1570 and 1637 cm^{-1} are masked by the overlap with strong transient bands, but the FTIR (below the TRIR in figure 3.22) confirmed the positions of these ground state absorptions. A broad transient was observed once again in the range 1530-1605 cm^{-1} with more transient species present in the range 1625-1650 cm^{-1}. There are clearly two processes evident in the system with the presence of long-lived transient species similar to those seen for the repeating dinucleotide units of the polymer dApT and TpdA. Noticeably, the characteristic tracking behaviour of the transient band at early time delays associated with vibrationally cooling is less pronounced in the polymer system.

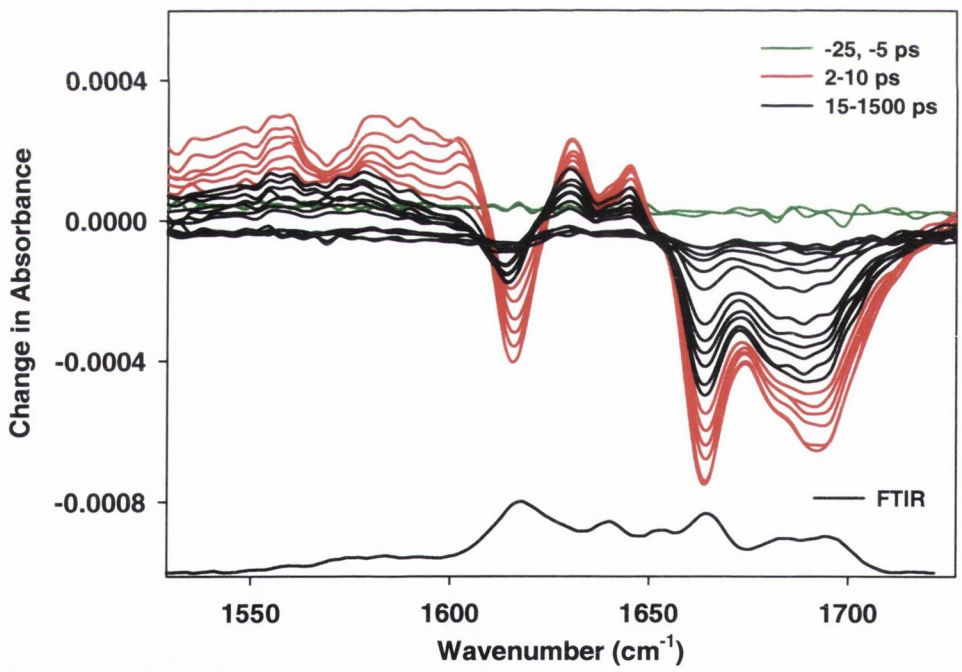

Figure 3.22 ps-TRIR of 10 mM $[poly(dA\text{-}dT)]_2$ in 50 mM potassium phosphate D_2O buffer (pH 7) with FTIR below (baseline adjusted). Delays are at -25, -5 (green), 2, 3, 4, 5, 7, 10 (red), 15, 20, 35, 50, 75, 100, 200, 350, 500, 750, 1000 and 1500 ps (black).

Single pixel analysis of the main transient and bleaching bands is given in figure 3.23. Excellent results were obtained when a biexponential function was applied to the data.

The first process is attributed to vibrational cooling and occurs in the time range of 3-7 ps. This range is slightly larger than that seen for the mono- or dinucleotides and suggests that the cooling process is slightly slower in the polymeric structure. The second process, which contributes significantly, has a lifetime of *ca.* 150 ps and is likely to originate from an electronic excited state.

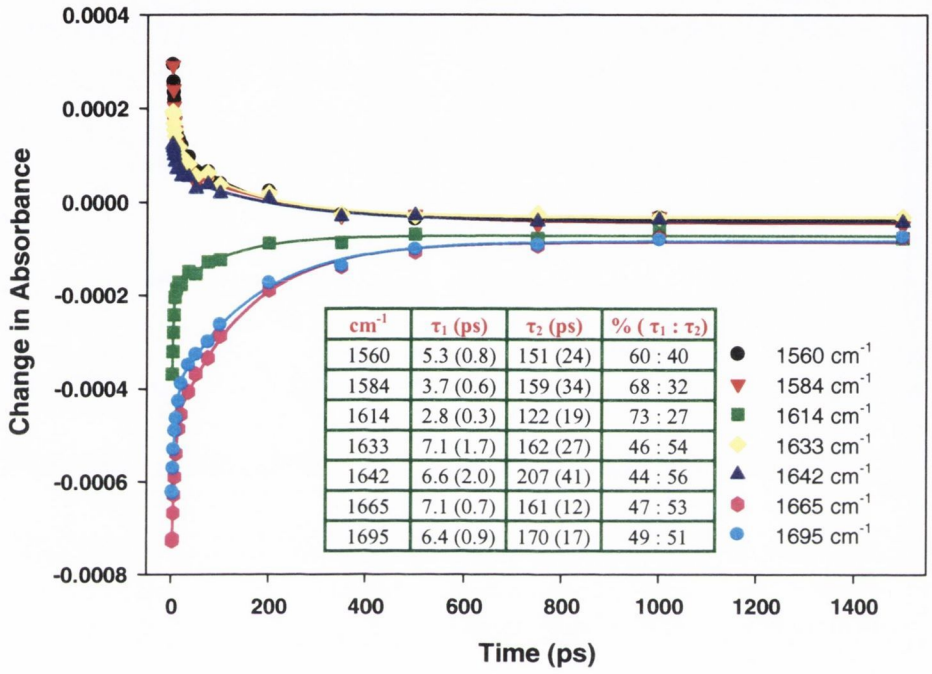

cm^{-1}	τ_1 (ps)	τ_2 (ps)	% (τ_1 : τ_2)
1560	5.3 (0.8)	151 (24)	60 : 40
1584	3.7 (0.6)	159 (34)	68 : 32
1614	2.8 (0.3)	122 (19)	73 : 27
1633	7.1 (1.7)	162 (27)	46 : 54
1642	6.6 (2.0)	207 (41)	44 : 56
1665	7.1 (0.7)	161 (12)	47 : 53
1695	6.4 (0.9)	170 (17)	49 : 51

Figure 3.23 Kinetic analysis of 10 mM $[poly(dA\text{-}dT)]_2$ in 50 mM potassium phosphate D_2O buffer (pH 7) at 1560, 1584, 1614, 1633, 1642, 1665 and 1695 cm^{-1} with lifetime table inset.

3.3.6 Non-Alternating Polynucleotide System: poly(dA).poly(dT)

The ground state IR and ps-TRIR spectra of poly(dA).poly(dT) is striking with four distinct and discrete absorption bands (figure 3.24). The bands at 1641, 1662 and 1696 cm^{-1} are associated with the C=C/C=N, C_4=O, C_2=O vibrations of the thymine moiety respectively. The remaining band at 1622 cm^{-1} arises from the adenine ring vibration involving C=C and C=N stretching. The recovery, in contrast to the heteropolymer $[poly(dA\text{-}dT)]_2$, was found to be dominated by a short process, with some evidence for a longer process observed when analysis was performed on the thymine C_2=O stretch.

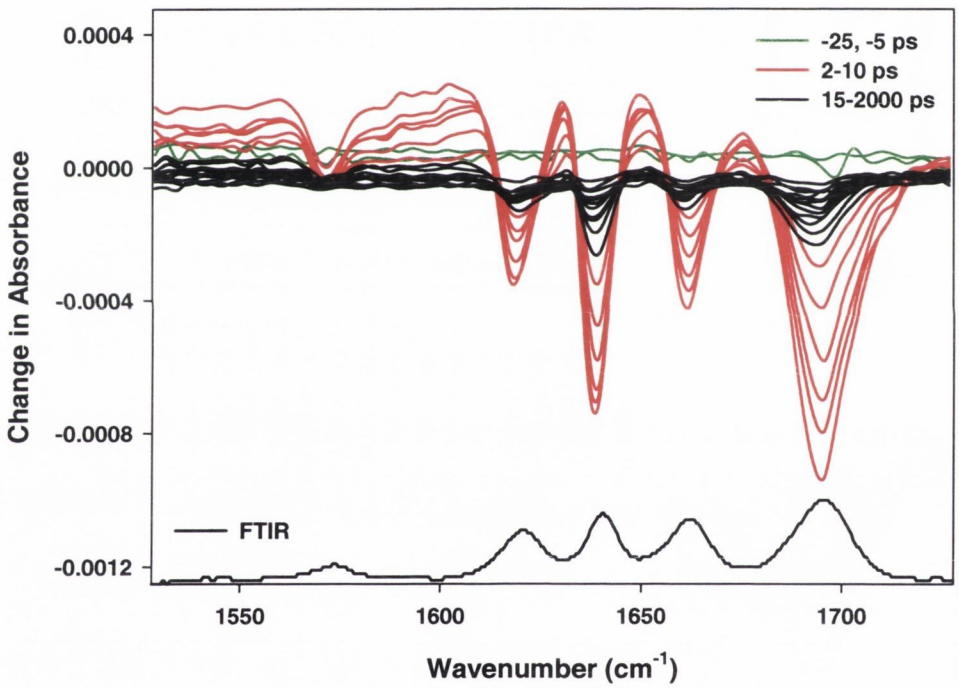

Figure 3.24 ps-TRIR of 10 mM poly(dA).poly(dT) in 50 mM potassium phosphate D_2O buffer (pH 7) with FTIR below (baseline adjusted). Delays are at -25, -5 (green), 2, 3, 4, 5, 7, 10 (red), 15, 20, 35, 50, 75, 100, 200, 350, 500, 750, 1000 and 2000 ps (black).

Analysis of the kinetic behaviour of the system revealed the presence of two lifetimes, with the majority of the signal amplitude arising from the faster process (figure 3.25). As noted for the case of $[poly(dA\text{-}dT)]_2$, the dynamics of the vibrational cooling is slightly slower (~5 ps) than that of the constituent mono- or dinucleotides. Also the tracking behaviour

was found to be less pronounced in this polymer, compared to the mono- and dinucleotides. The contribution from the long-lived component accounts for ~10% of the relaxation process, and as such errors in the fitting of this lifetime are quite large. Also as the spectrum contains multiple bleaching and transient absorption bands there are varying degrees of overlap in different regions of the spectral window and this further complicates the fitting. However, despite such difficulties, a lifetime of ~90 ps seemed to be prevail.

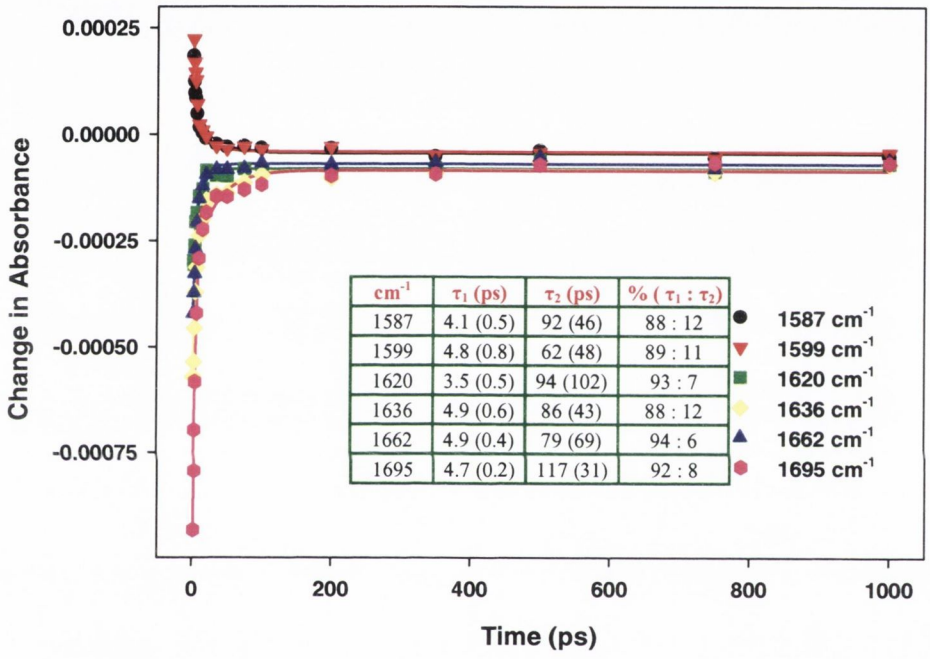

cm^{-1}	τ_1 (ps)	τ_2 (ps)	% (τ_1 : τ_2)
1587	4.1 (0.5)	92 (46)	88 : 12
1599	4.8 (0.8)	62 (48)	89 : 11
1620	3.5 (0.5)	94 (102)	93 : 7
1636	4.9 (0.6)	86 (43)	88 : 12
1662	4.9 (0.4)	79 (69)	94 : 6
1695	4.7 (0.2)	117 (31)	92 : 8

Figure 3.25 Kinetic analysis of 10 mM poly(dA).poly(dT) in 50 mM potassium phosphate D_2O buffer (pH 7) at 1587, 1599, 1620, 1636, 1662 and 1695 cm^{-1} with lifetime table inset.

3.4 Discussion

3.4.1 Mononucleotides

The singlet excited state lifetime of the individual bases is known to be sub-picosecond, thymine (720 ± 40 fs) and adenine (290 ± 40 fs).[3] Thus the short-lived species observed for the mononucleotides are attributed to the relaxation of the vibrationally hot ground state, formed after subpicosecond internal conversion from the $^1\pi$-π^* (S_1) excited state.[11] The cascading of the transient maxima with time toward higher wavenumbers is characteristic of vibrational cooling[48] and is clearly seen in the 3D and contour plots below (figure 3.26). There was no evidence for a second long-lived species when the kinetics of 5′-TMP were analyzed, though as mentioned in the results section, incomplete recovery was observed on the timescale of the experiment (1 ns). This is presumably a result of photodamage to the base and thymine is known to be particularly susceptible to photoproduct formation.[86]

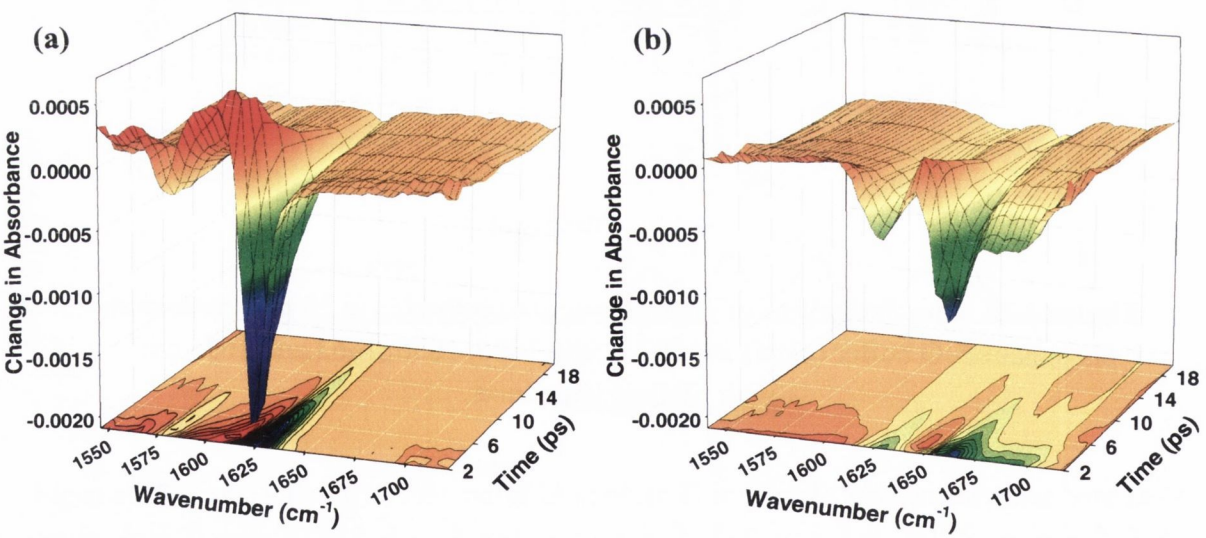

Figure 3.26 3D ps-TRIR spectra with contour plots of (a) 5′-dAMP and (b) 5′-TMP at delays between 2 and 20 ps. Both compounds are 10 mM in 50 mM potassium phosphate D_2O buffer (pH 7).

3.4.2 Dinucleotides

All four dinucleotides used in this A-T study are presented in scheme 3.3 below. The molecules are drawn so that the differences in the overlap of the bases can be seen. It is known that on progressing from monomer to polymer units that long-lived species are found. In such polymer structures there are additional interactions present that are not found in the mononucleotide units, namely hydrogen-bonding and stacking interactions. Dinucleotide units represent the smallest repeating units of the polymeric structures and exhibit stacking interactions (but not the exact same interbase stacking interactions found in the polymers). These molecules exist in equilibrium between stacked and unstacked forms. Therefore, such units represent a middle ground between the monomer and polymer unit and are an excellent candidate to study how stacking interactions (both extent of stacking and overlap) modulate ultrafast relaxation mechanisms following UV excitation.

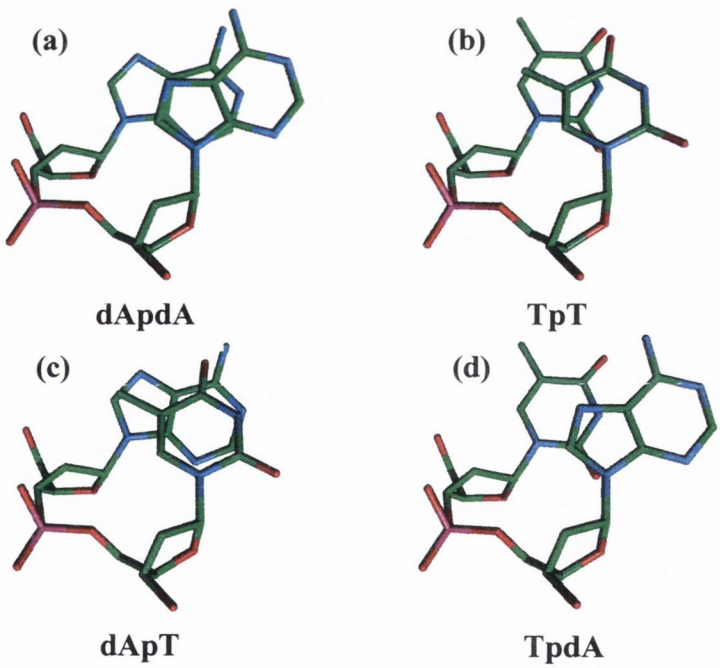

Scheme 3.3 Overlap in the stacked form of (a) dApdA, (b) TpT, (c) dApT and (d) TpdA. Atoms are carbon (green), nitrogen (blue), oxygen (red) and phosphorus (purple). Hydrogen atoms have been omitted for clarity. Molecules were drawn using the ChemSW® package.

3.4.2.1 Homodinucleotides: dApA and TpT

The 3D ps-TRIR and contour plots of dApdA and TpT are shown in figure 3.27. It is striking that on progressing from the single bases to dimeric units, long-lived species are immediately evident. Presumably the emergence of a second species is a result of the introduction of stacking interactions.

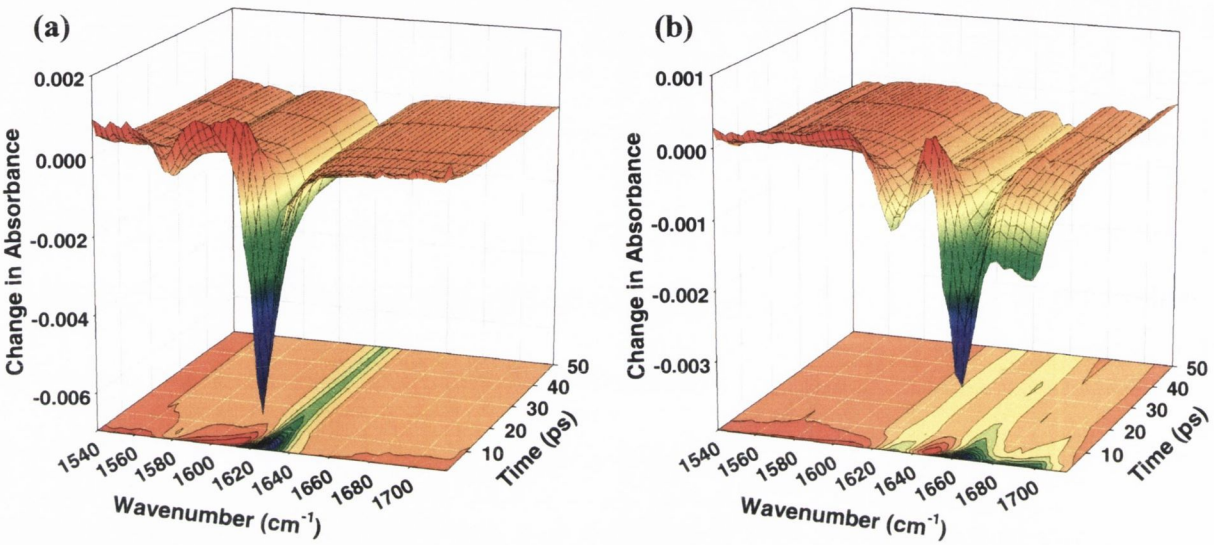

Figure 3.27 3D ps-TRIR spectra with contour plots of (a) dApdA and (b) TpT at delays between 2 and 50 ps. Both compounds are 10 mM in 50 mM potassium phosphate D_2O buffer (pH 7).

It has been reported in the literature that dApdA exhibits strong excitonic coupling[147,148] while TpT does not.[16,149] The long-lived species in dApdA was attributed as originating from an excitonic state with faster processes being associated with monomer-like excited states in both dinucleotides. Recent transient absorption measurements by Takaya *et al.*[137] on the RNA equivalent, ApA, monitored the bleaching at 252 nm after 267 nm excitation. Fitting gave two lifetimes of 2 ps (91%) and 105 ± 30 ps (9%). The authors attributed the long-lived species as originating from an exciplex state. Previously reported results from the same group on ApA reported lifetimes of 0.5 ± 0.1 ps and 60 ± 16 ps when the transient absorption signals at 570, 600 and 630 nm were recorded.[16] Our results for dApdA suggest that while the amount of long-lived species (15%) is similar to their more recent RNA study, the long-lived species' lifetime is significantly longer, of the order of 600-800 ps. This is not surprising as the excited states produced in RNA and DNA are

expected to be different, a function of overlap, and as such one might expect different relaxation dynamics.[115,126,150] Takaya also performed experiments on a short RNA strand, $(A)_4$, and mentioned that the long-lived species' lifetime is the same as that of ApA within experimental uncertainty. We performed measurements on $(dA)_6$ (see appendix figure A3.6 for ps-TRIR and kinetic analysis) and found the long-lived component to account for 23% of excited state deactivation with a lifetime of the order of 435 ± 60 ps. An interesting yet somewhat perplexing result in our measurements, is that neither dApdA nor $(dA)_6$ showed any evidence of a long-lived state in the transient absorption bands. This could happen if the transient absorption of the long-lived state was outside our spectral window (i.e. 100 cm^{-1} or more from the parent bleaching band, this is unlikely) or if the absorption lay directly over the bleaching band, therefore being masked. Further experimentation and analysis is required to unequivocally resolve this issue.

In the case of TpT, our results indicate the presence of long-lived species. Lifetimes of *ca.* 34 ps in the broad transient region and *ca.* 400 ps in the bleaching bands were found. Admittedly, there was an indication of permanent damage to the system after irradiation and to what extent this will affect the kinetic fitting (which is applied to the result of the accumulation of four eight minute cycles) is unclear. Crespo-Hernandez *et al.* reported a single lifetime of 680 ± 40 fs for TpT when monitoring the transient absorption signals produced at 570, 600 and 630 nm.[16]

3.4.2.2 Heteordinucleotides: dApT and TpdA

Figure 3.28 shows the 3D ps-TRIR and contour plots of dApT and TpdA. Immediately one can see that there is different behaviour in the two systems. The difference in the contour plots illustrates how the broad transient takes longer to recover in dApT than in TpdA. This is also clearly reflected in the thymine based bands and may be somewhat harder to notice for the adenine band. Vibrational cooling's signature cascade is also aparent at early times.

Although these molecules are structural isomers, the extent of overlap in the two systems is different with greater overlap for ApT (see scheme 3.3 for comparison). The amount of stacked species in solution is also different with an approximate 2-fold

difference between the two dunucleotides at room temperature. Both of these factors contribute to the photophysical behaviour of the dimers. Long-lived states are found for both dimers that are not present in the equimolar mixture of the constituent mononucleotides (see appendix figure A3.3 for ps-TRIR of equimolar mix of 5′-dAMP and 5′-TMP), proving that the long-lived species form only when two bases are in close spatial proximity. Simply put, the presence of the stacked form of the dinucleotide is responsible for the production of such long-lived states but the origin of the state is not necessarily from the two bases as will be argued later.

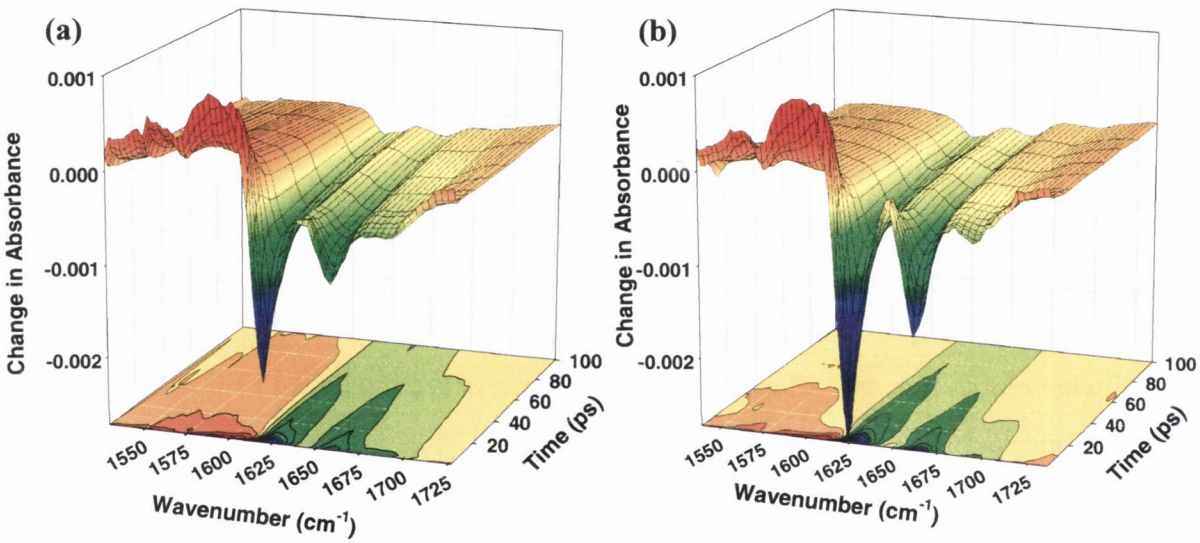

Figure 3.28 3D ps-TRIR spectra with contour plots of (a) dApT and (b) TpdA at delays between 2 and 100 ps. Both compounds are 10 mM in 50 mM potassium phosphate D_2O buffer (pH 7).

The analysis of these two mixed monomer dinucleotide systems revealed complex behaviour. The lifetime of the long-lived species and the amount of contribution from this species varied in our spectral window and depended on the dominant base contributing to a particular band, i.e. the base that was absorbing more at a particular wavelength. The differing dynamics observed by ps-TRIR for dApT and for TpdA can be rationalized in terms of stacking interactions. In both systems, the short 5 ps component is attributed to the vibrationally hot ground state. The lifetime and the yield of formation of the long-lived component is related to the extent of the stacked conformation. In the recent femtosecond transient study of dinucleotide systems by Takaya *et al.*, the presence of long-lived species were also noted.[137] The authors

concluded that this was due to the formation of an exciplex-type species, caused by electron transfer within the dinucleotide. Transient absorption measurements, such as those of Takaya, are routinely employed to study such systems and give the global kinetic picture of the molecule. However, with our technique, the added benefit of structural information can lead to fingerprint identification of species responsible for certain events.

In our measurements, profiling of the delays between 20-1000 ps in the regions characteristic of adenine and thymine allows for the identification of the long-lived species (see figure 3.29 below). The profiles of the bleaching and broad transient absorption bands are found to evolve with time. The key observation is the change in profile structure of the bleaching bands with time. Initially at 2 ps, the ratio of the bleach at 1620 cm^{-1} which is dominated by adenine (4:1 ; A:T), to the solely thymine based bleach (1661 cm^{-1}) was 2:1. However, once the fast vibrational cooling process was over, i.e. from 20 ps on, the ratio of these bleaching bands was found to have changed to 1:1, and it remained so at all delays to 1000 ps.

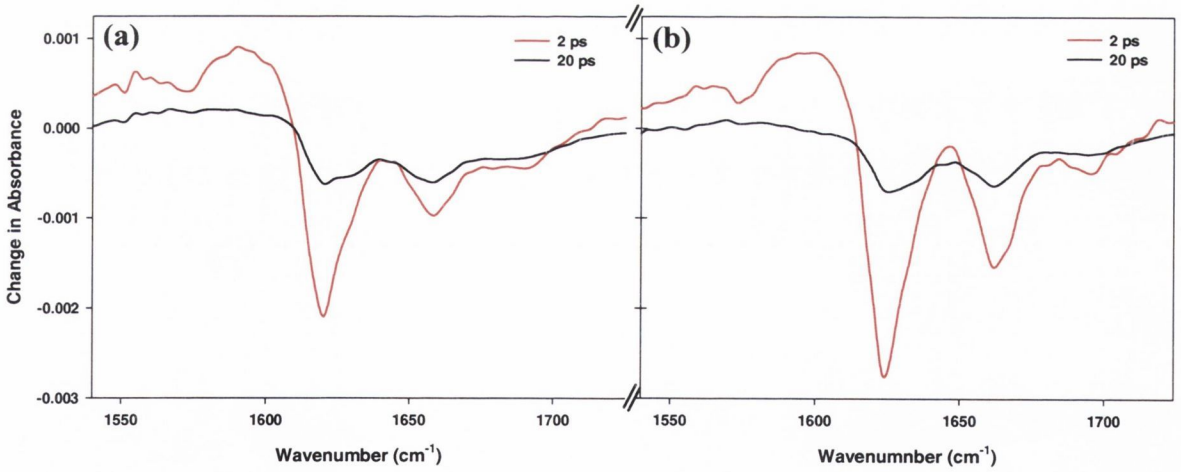

Figure 3.29 Comparison of the 2 ps (red) and 20 ps (black) delays for (a) dApT and (b) TpdA.

From this profile it is apparent that the change in the ratio of the band structure is linked to a more rapid removal of the adenine based species than that of thymine. The 1575 cm^{-1} adenine mode is not present in the 20 ps profile of either dinucleotide and the transient absorption profile that remains is very similar to those observed in the

5′-TMP and TpT experiments. The profile at long delay times in dApT and TpdA is remarkably similar to the TRIR profile of 5′-TMP and TpT after 10 ps (the reader is referred back to figures 3.2 and 3.5). There is a broad transient absorption (1550-1600 cm^{-1}) and bleaching bands at 1632 cm^{-1} and 1664 cm^{-1} that have an intensity of ~1:1, and there is the high wavenumber *ca.* 1692 cm^{-1} band. This is incredibly similar to the profiles of dApT and TpdA at long time delays.

This hypothesis was further tested by subtracting the characteristic ps-TRIR spectra of an equimolar mixture of 5′-dAMP and 5′-TMP at all time delays from that observed for dApT and TpdA. The result (figure 3.30) shows that the long-lived species possesses the TRIR fingerprint of thymine, as described in the previous paragraph. We consider this to be further powerful and convincing evidence that the long-lived species is disproportionally or solely located on the thymine residue. This assignment is in contrast to the exciplex rationalization of Takaya *et al.* on RNA dinucleotides. However, the structural information afforded by TRIR allows for the structural signatures to be observed and as such the elucidation of structural nuances.

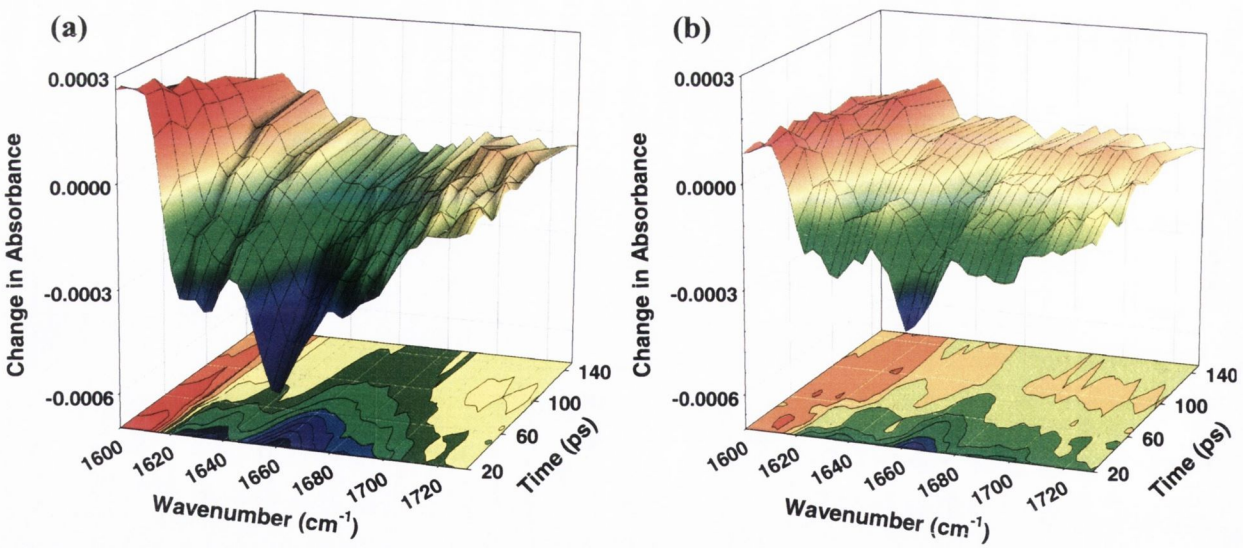

Figure 3.30 Result of subtraction of the ps-TRIR spectrum of an equimolar mixture of 5′-dAMP and 5′-TMP from the ps-TRIR spectrum of (a) dApT and (b) TpdA. Delays are between 20 and 150 ps.

3.4.3 Stacking studies on the heterodinucleotides dApT and TpdA

In light of the interesting ps-TRIR results of the heterodinucleotides a more comprehensive study of how base stacking influences the excited state dynamics was undertaken. To successfully study the effect of one factor it is desirable to keep all or as many other factors as possible constant. Structural isomers such as dApT and TpdA are ideal model compounds for such a study, as they allow for the different stacking environments to be probed. As previously eluded to, the amount of stacked species and the overlap of the bases in the stacked conformation is different in the two dinucleotides. The nature of the 3′-5′ phosphodiester linkage is known to alter the stacking and flexibility so that under our experimental conditions both the stacked and unstacked (open) forms are present in solution. To this end, we have utilized three techniques that are sensitive to stacking interactions, namely circular dichroism, nuclear magnetic resonance and transient infrared spectroscopy.

3.4.3.1 Circular Dichroism Measurements

The extent of hypochromicity observed in the UV is proportional to the number of stacked bases and increases with the number of nucleotides in a given stack. Comparison of the hypochromicity at 260 nm for dApT and TpdA reveals values of 4.8% and 2.4%.[151] This suggests a 2-fold difference in the extent of stacking of dApT and TpdA in solution.

Circular dichroism measurements were performed under identical conditions of those of our ps-TRIR measurements. CD in particular is very sensitive to the secondary structure of DNA and this had been exploited to good use in many publications in the literature.[131,148,151-158] The signal obtained in CD measurements is directly related to the extent of nucleobase overlap. Our measurements confirm that both dinucleotides are stacked at 20 °C and that dApT exhibits a greater extent of stacking as there was greater absorption of the circularly polarized light compared to that of TpdA. The band pattern of the exciton bands indicates that both dinucleotides are in right-handed stacked conformations. The magnitude of the bands suggests that the stacking in dApT is 1.8 times greater than that of TpdA. Unfortunately, a temperature dependent CD study was not possible.

3.4.3.2 ^{1}H NMR Measurements

DNA has a number of resonances in the range 9-1 ppm. Those protons directly attached to the rings of the nucleobases resonate at higher field, typically between 7 and 9 ppm. The seven-proton deoxyribose spin system in DNA typically covers a chemical shift range of *ca.* 4 ppm. Fortuitiously, the proton resonances in DNA are separated to a sufficient degree to allow for individual assignment.

NMR spectra were recorded under identical conditions as the ps-TRIR and CD studies. Assignment of the dinucleotides was facilitated by firstly assigning the spectra of the constituent mononucleotides. Splitting patterns in the dinucleotides are complex as there are multiple coupling contributions to each proton's splitting pattern. Selective decoupling experiments were performed in order to pick out distinct coupling and make definitive assignments.

In the dinucleotide systems an equilibrium exists between stacked and unstacked forms. With the emergence of new NMR techniques almost 40 years ago, came a plethora of studies of dinucleotide systems. They were seen as ideal models for unravelling stacking interactions in DNA.[146,159-170] These works endeavoured to elucidate the conformations present and stacking equilibria by analysing complicated splitting patterns and analysing coupling interactions within the ribose ring. For example previous NMR experiments have found the extent of stacking to be 34% in ApU and 15% in UpA. The extensive NMR study by Ezra *et al.*[146] on the conformational properties of purine-pyridine (pu:py) and pyridine-purine (py:pu) dinucleosides observed that the extent of stacking followed the trend pu:py> pu:pu> py:py≥ py:pu.

These somewhat complex approaches to analyses, which involve calculating the coupling constants to all ribose protons, were attempted for our spectra but did not prove very successful. In certain cases, it was not possible to measure all the individual coupling constants. An alternative approach, proposed by Rinkel *et al.*[145] involved calculating the sum of the coupling constants to the 1′ position with subsequent substitution into their derived equation. The result, the percentage of North conformer, is a direct measure of the extent of stacking in the system. When applied to our dinucleotide systems, the amount of stacked species at 20 °C was found to be 38% for dApT and 21% for TpdA. This

corresponds to a difference of 1.9 times, which is in good agreement with that estimated from our CD measurements.

Variable temperature ^{1}H NMR spectra were recorded for the heteordinucleotides at temperatures of 20, 50 and 70 °C. This confirmed the expected shift in equilibria, with the percentage of stacked species at 70 °C estimated to be 31% and 13% for dApT and TpdA respectively.

3.4.3.3 Variable Temperature Time Resolved Infrared Measurements

The results of the variable temperature ps-TRIR are very interesting and represent the first such measurements. The 3D and contour plot for dApT at 70 °C is given in figure 3.31 and immediately recognizable is the fact that there is not as much long-lived species present in comparison to that of the 20 °C spectrum (figure 3.28(a)).

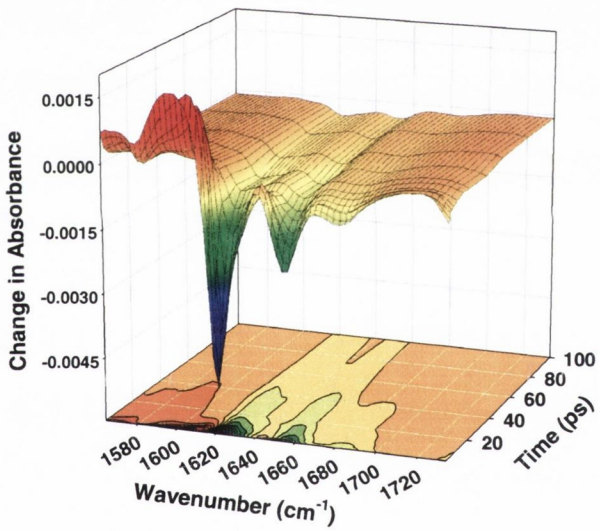

Figure 3.31 3D ps-TRIR spectrum with contour plot of 10 mM dApT in 50 mM potassium phosphate D_2O buffer (pH 7) at 70 °C. Delays are between 2 and 100 ps.

A comparison of the lifetime fitting results across the spectral window at both 20 and 70 °C is given in figure 3.32. The figures quoted represent the general picture observed i.e. an average reflection of a number of single pixel fits at any given point, and the values found at each individual pixel point are provided in the appendix tabular analysis A3.5. Both the lifetime and the amount of the long-lived species have decreased at the elevated temperature. The reduction in the amount of long-lived species is *ca.* 30% in the thymine dominated regions (the transient below 1575 cm^{-1} and the bleaching bands at 1665 and 1690 cm^{-1}) and greater in the adenine dominated regions, *ca.* 50%. The lifetime of the

long-lived species is found to have reduced in all regions of the spectrum by ~43%. Both trends are consistent with what might be predicted although the reduction of 30% in the amount of long lived species at first may seem slightly larger than what was expected from the ^{1}H NMR result. However, this can be rationalized in the following way. At 70 °C there is more open than closed form of dApT. The extinction coefficient of the bands of the open form is greater than those of the closed form. Therefore, at higher temperature, the magnitude of the open form contribution to the overall bleach or transient intensity is greater and upon fitting may seem to be slightly greater, thus making the percentage of stacked species contributing to the decay seem slightly smaller.

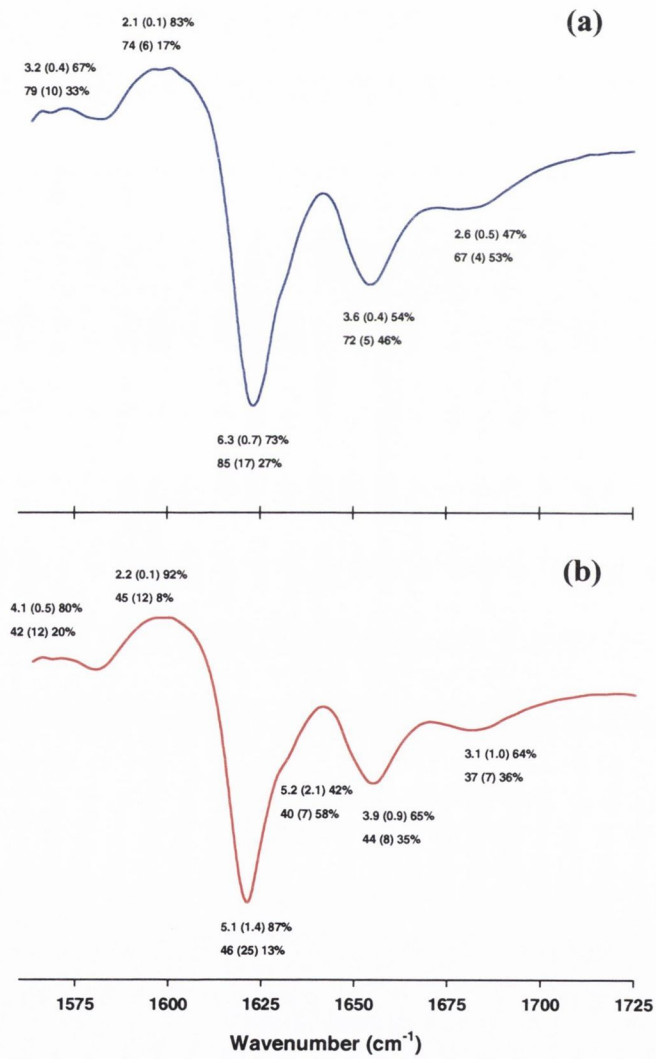

Figure 3.32 Variation in the kinetic behaviour of dApT at (a) 20 °C (blue) and (b) 70 °C (red).

Finally, a comparison of the decay profiles for dApT at both temperatures for the transient band at 1588 cm^{-1} and bleaching bands at 1629, 1656 and 1688 cm^{-1} is given in figure 3.33. The profiles have been normalized and this allows for an easy visual comparison to be made. All four plots clearly show that both the lifetime and contribution from the long-lived species has diminished upon heating the sample to 70 °C.

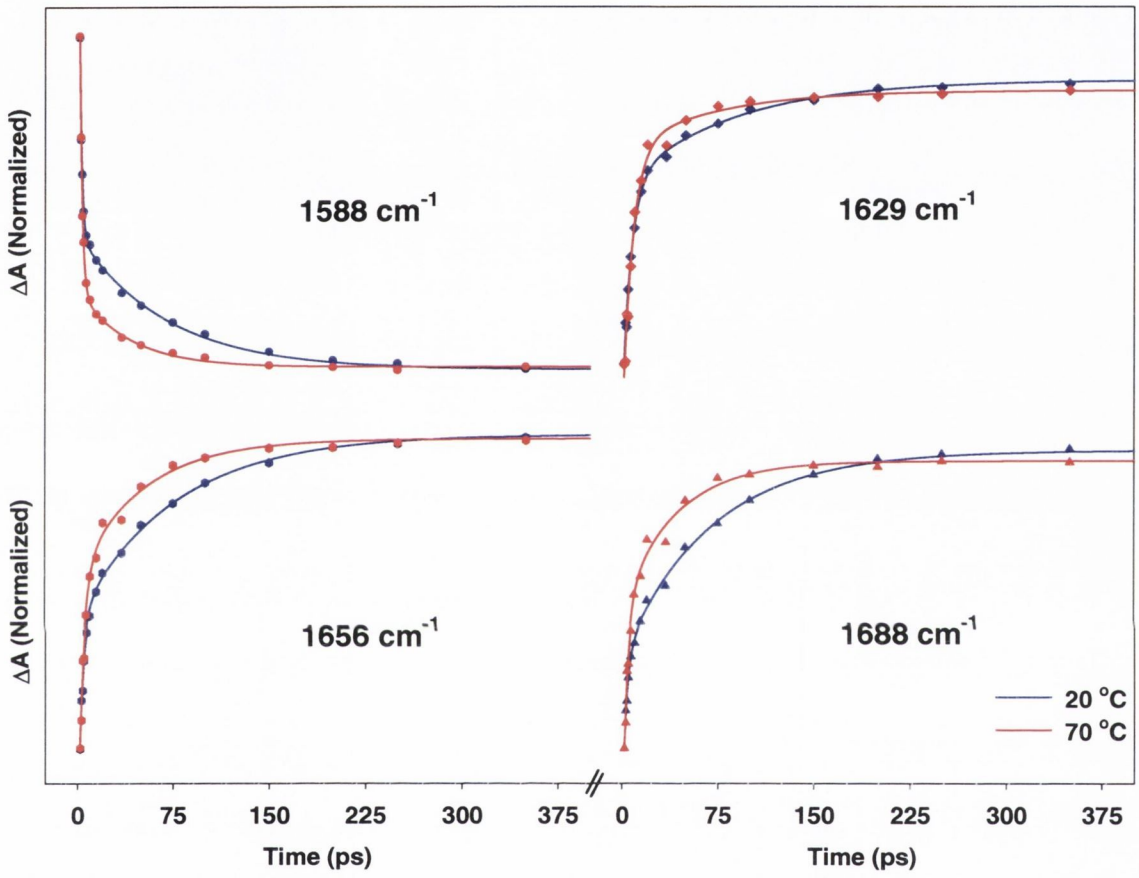

Figure 3.33 Comparison of the kinetic behaviour of dApT at the transient absorption band at 1588 cm^{-1} and bleaching bands at 1629, 1656 and 1688 cm^{-1} at temperatures of 20 (blue) and 70 °C (red).

The 3D and contour plots of the variable temperature ps-TRIR of TpdA are shown in figure 3.34. Once again, clear differences in behaviour are instantly obvious. In the case of TpdA elevated temperature spectra were recorded at two temperatures, those being 70 and 90°C. As expected the contribution from the long-lived state is less as the temperature increases. At 90 °C only evidence for fast decay was found indicating that a very high percentage if not all of the dinucleotide was in the open form.

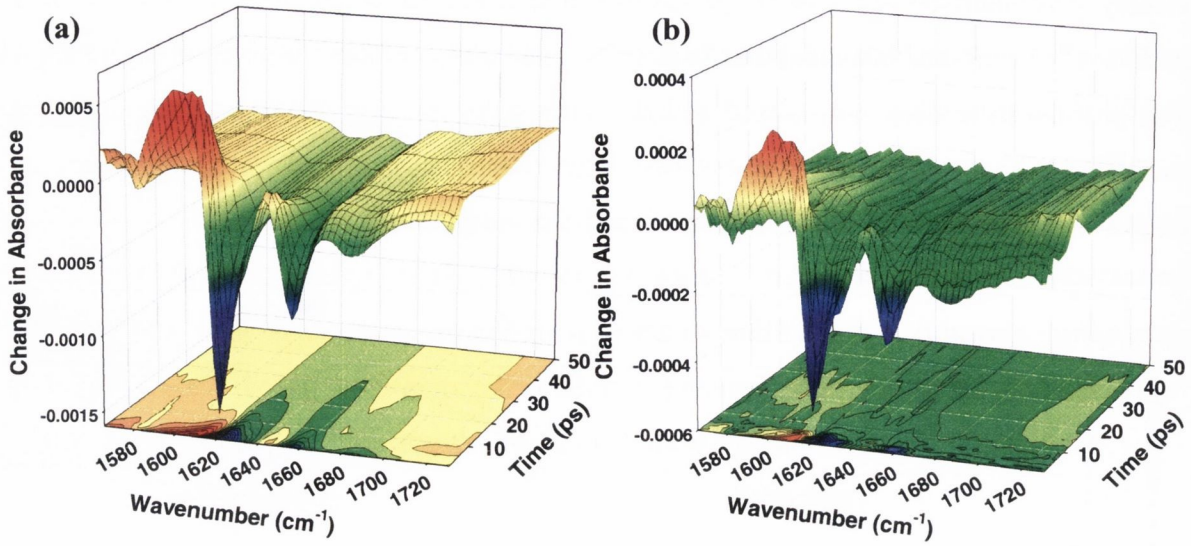

Figure 3.34 3D ps-TRIR spectra with contour plots of 10 mM TpdA in 50 mM potassium phosphate D_2O buffer (pH 7) at (a) 70 °C and (b) 90 °C at delays between 2 and 50 ps.

Comparison of the kinetic behaviour at all three temperatures of 20, 70 and 90 °C is summarized in figure 3.35. The trend in behaviour is somewhat less clear than in the dApT case. The amount of long-lived species does reduce consistently across the spectrum by ~50% on heating from 20 to 70 °C. However the trend in the lifetime variation of the long-lived species is not immediately apparent. There is a large error associated with the long lived species so that in order to get a reliable estimation of the lifetime, it was necessary to fit just the longer time delays to single exponential decay (as previously mentioned in the results section). Upon applying this strategy, a reduction of *ca.* 40% was found for the lifetime of the long-lived species. This is very similar to that seen for dApT. At 90 °C there was evidence of one process only, i.e. vibrational cooling. However, the fit to the data gave lifetimes that in some regions were slightly longer than the same points at 70 °C. However, it must be noted that the data obtained at 90 °C had a poor signal-to-noise ratio and was accumulated over two cycles only.

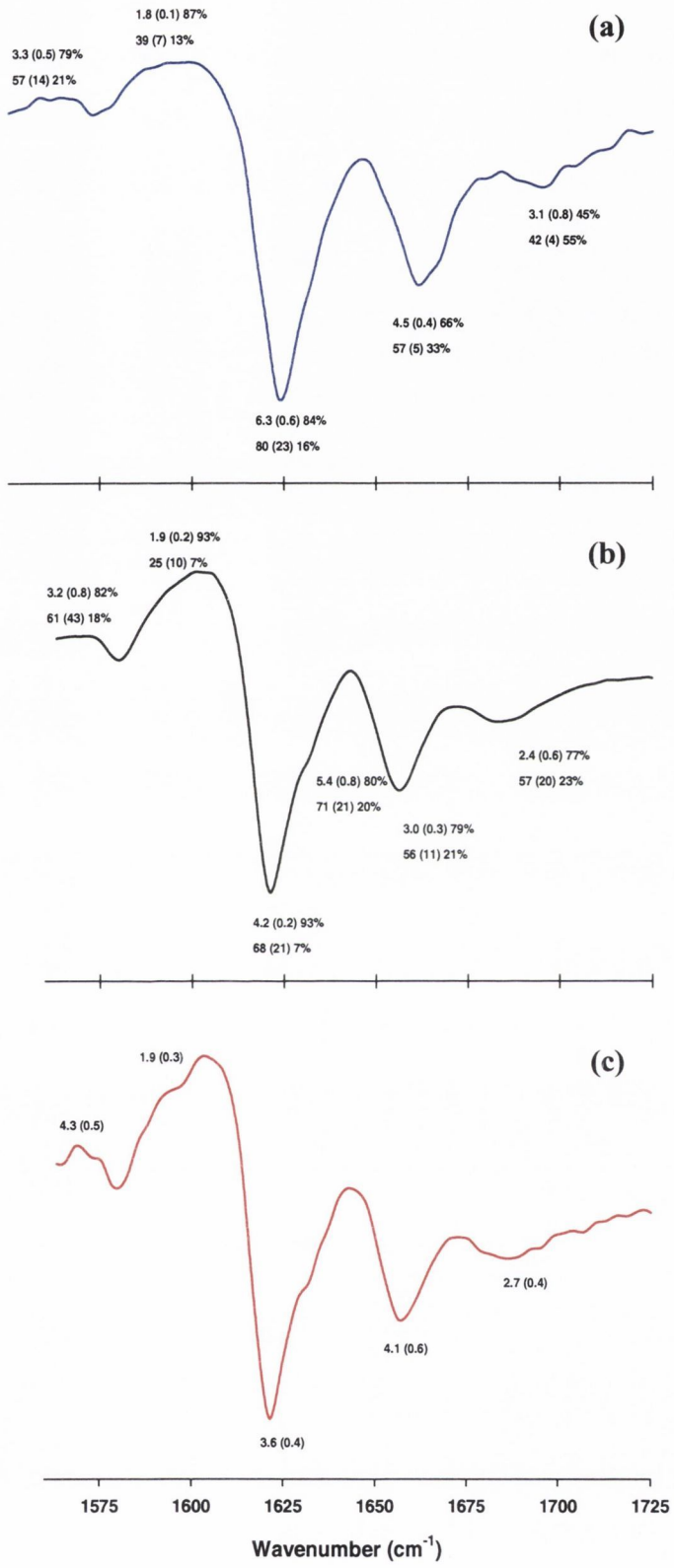

Figure 3.35 Variation in the kinetic behaviour of TpdA at (a) 20 °C (blue), (b) 50 °C (black) and (c) 90 °C (red).

Comparison of the kinetic profiles of TpdA at the transient 1590 cm^{-1} and bleaching regions of 1624, 1665, and 1690 cm^{-1} at all three temperatures is provided in figure 3.36. The striking differences in decay behaviour can be clearly seen. As for the dApT case, all four plots illustrate how the lifetime and contribution from the long-lived state lessened with increasing temperature, until finally at 90 °C, only a very fast decay was apparent.

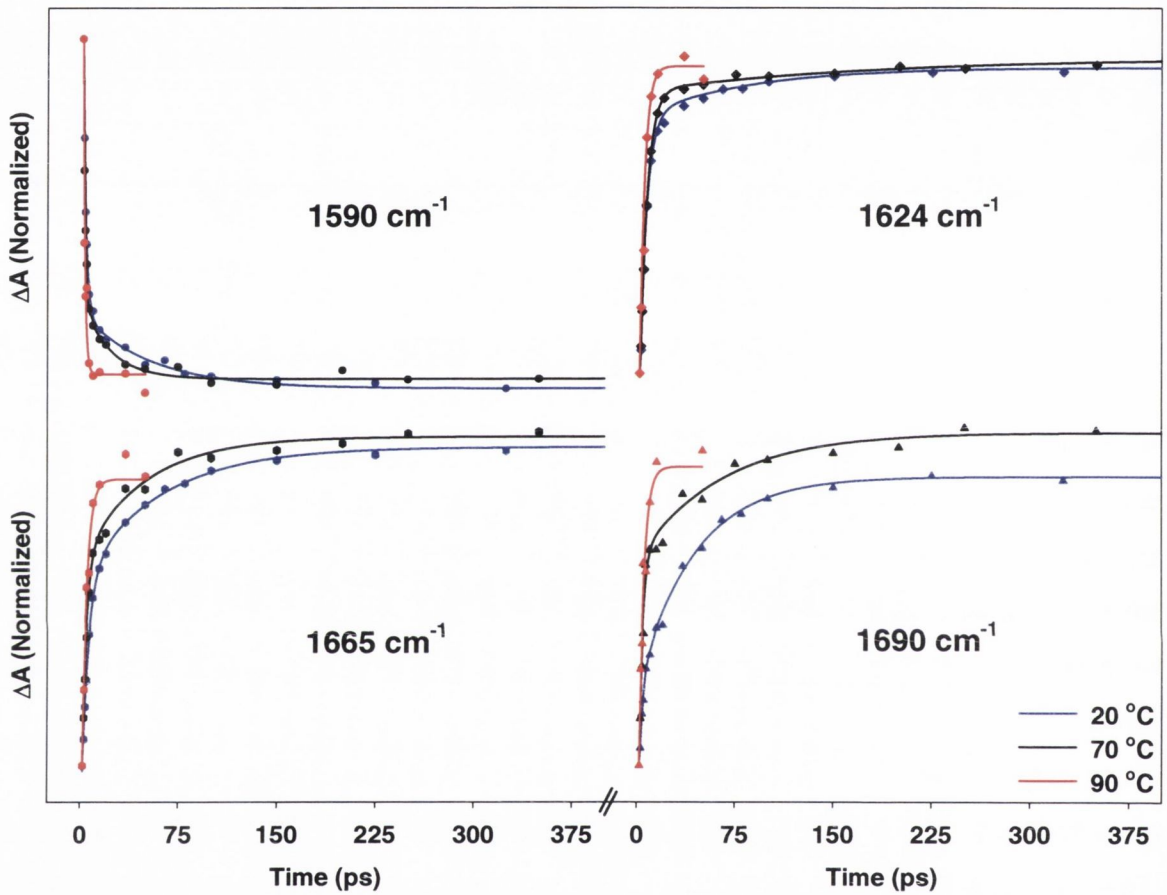

Figure 3.36 Comparison of the kinetic behaviour of TpdA at the transient band at 1590 cm^{-1} and bleaching bands 1624, 1665 and 1690 cm^{-1} at temperatures of 20 (blue), 70 (black) and 90 °C (red).

We propose a mechanism for the excited state deactivation of the heterodinucleotides dApT and TpdA as outlined in scheme 3.4. Excitation of the unstacked form resulted in behaviour characteristic of the constituent monomers. However, excitation of the stacked form resulted in a long-lived species, whose deactivation was dominated by the recovery of thymine. This could arise due to an initially localized excited adenine that transfers energy (sub ps) to thymine, or could arise due to an excited thymine, that in the presence of adenine is stabilized. Two features are particularly striking with regards to the long-lived species observed for either dApT or TpdA – (i) that the excitation is localized on thymine and (ii) that the resulting excited state returns completely to the ground state, in contrast what was found for the 5′-TMP or indeed TpT.

It is known that purine nucleotides decay faster than their pyrimidine counterparts.[39,139] In the case of adenine this is attributed to the fact that the $^1\pi$-π^* and ^{1}n-π^* states are close lying, separated by just 600 cm^{-1}. These adjacent states are readily mixed due to out-of-plane vibrational modes. Electronic coupling between bases can lead to photophysical properties that are not observed for isolated bases and as mentioned earlier this is typically considered in the context of excimer/exciplex formation. [115,124,126,137,138,140-142]

The existence of excimers and their relation to long-lived species was recently examined by Santoro *et. al.* for the case of polyadenine in water.[115] This study proposed that base-stacking tuned the delocalization of energy after photoexcitation and thus influenced deactivation pathways. Two scenarios were proposed: firstly, that the excitation is delocalized over different bases and secondly, that it is localized on an individual base. In the case of dApT or TpdA, it appears that the energy remaining in the system after the vibrationally hot molecules have relaxed, is localized on the thymine moiety. The nature of this excited state produced following UV excitation is obviously quite different from that formed in the free nucleotide, perhaps because the excited state is unable to pucker in a fashion similar to that found for thymine and therefore not able to access a conical intersection. However, the changing profile, revealing the rapid recovery of adenine in conjunction with the prolonged lifetime of thymine implies that energy transfer is possible.

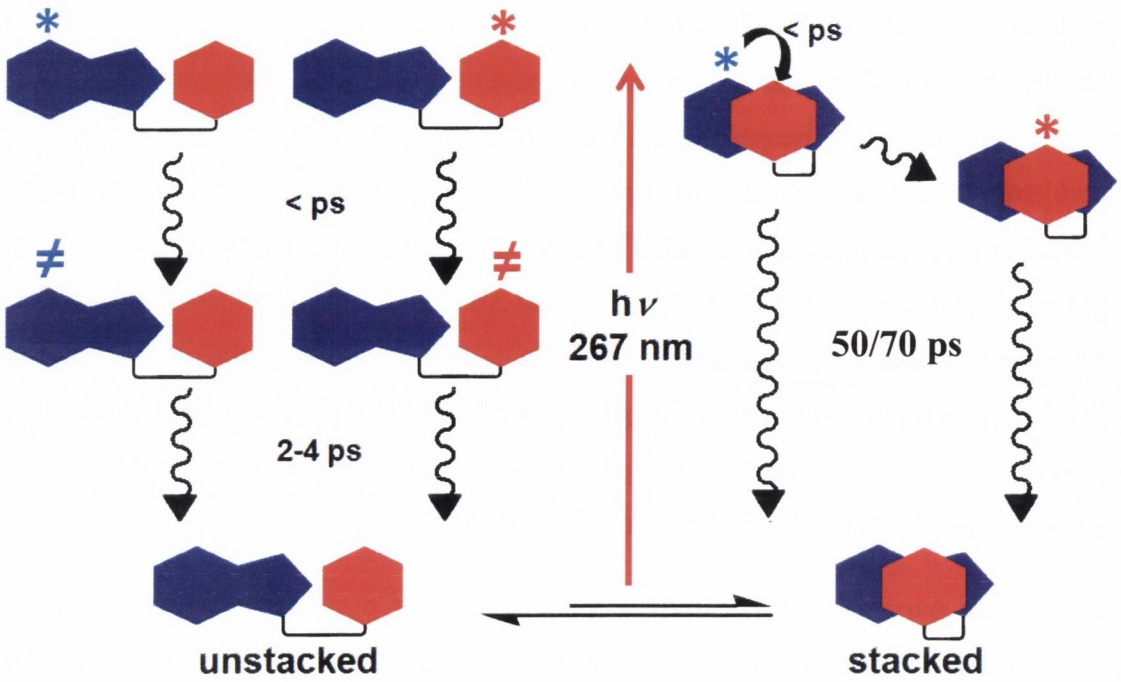

Scheme 3.4 Proposed deactivation mechanism for the heterodinucleotides dApT and TpdA. Key: * = electronic excited state and ≠ = vibrationally hot ground state.

Our hypothesis of energy transfer from the adenine to thymine moiety is interesting when considered in the context of how these long-lived states are normally rationalized in the literature, i.e. described as being of exciplex nature.[137] Recently, the efficiency of energy transfer along several single and double stranded oligonucleotide sequences having a modified 2-aminopurine (2AP) as an energy trap was studied.[171] Adenine was found to be exhibit the highest transfer efficiency and the placement of a different nucleobases (C, G or T) between adenine and 2AP greatly reduced the energy transfer. Ultrafast energy transfer in DNA was studied using femtosecond transient absorption spectroscopy and it was concluded that excitation energy can migrate over distances of ~7 Å in ~300 fs.[172] These results, when considered in light of our "T fingerprint" at long delay time, the result in acidified dApT (appendix figure A3.4), and our ps-TRIR subtractions in figure 3.30, strengthens our argument of energy transfer from adenine to thymine in the mixed dinucleotide systems. Also our result may in some part explain the trend of photoproduct formation observed in the mixed AT hairpins study of Hariharan *et al.*[133].

A summary of the information gained from our ps-TRIR measurements of heterodinucletides dApT and TpdA is shown in figure 3.37. The spectrum has regions where adenine and thymine dominate the absorption and this was reflected in the kinetics.

This dominance is clearest when the extent of stacking is at its greatest and results have shown that upon heating and hence unfolding of the stacked species, resolution of the thymine band under the main adenine bleaching band was found. Our experiments have shown that the presence of a long-lived species can be directly correlated to the stacking in the system. Also the contribution from the stacked species is found to increase in thymine dominated regions. This is due to the adenine absorptions, in the centre of the spectrum contributing predominantely to the short-lived component. The variation in lifetime of both the short and long lifetimes is rationalized in the same way, with the overlapping absorptions being the cause of the observed variations.

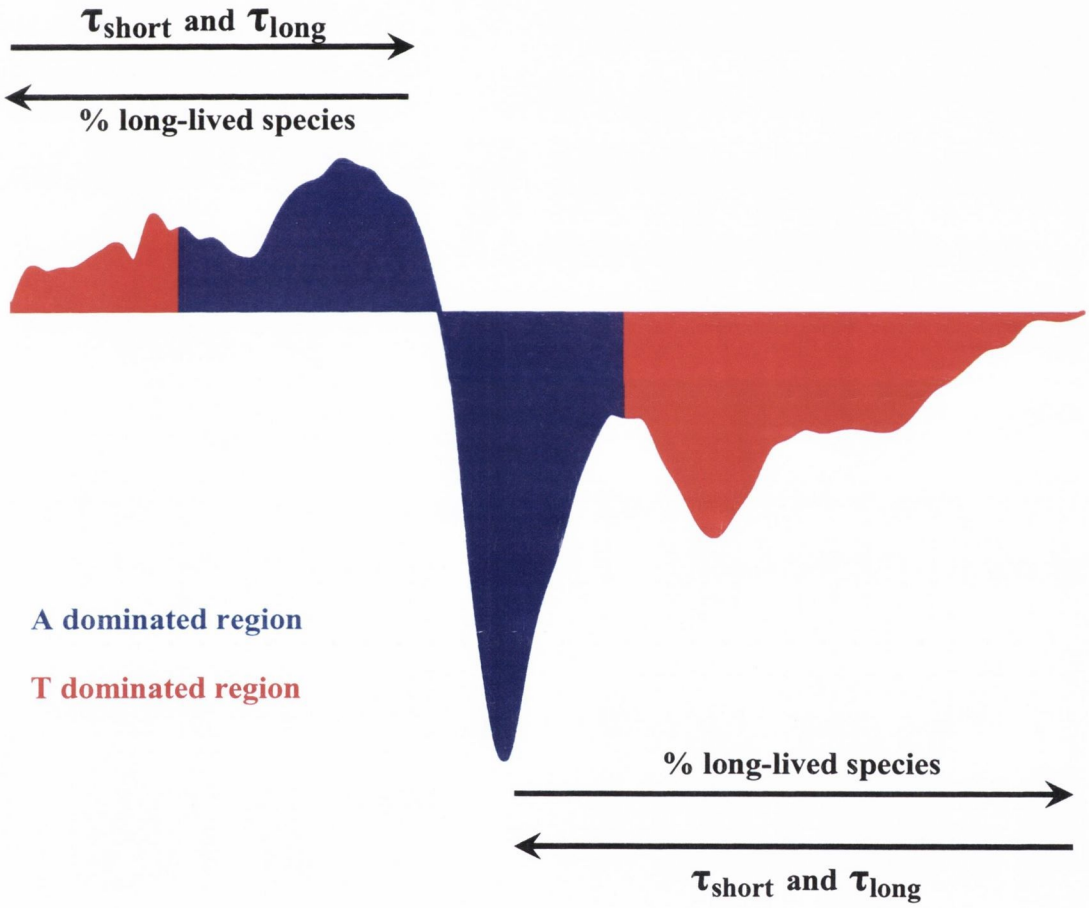

Figure 3.37 Summary of the lifetime trend observed in the heterodinucleotide systems dApT and TpdA.

3.4.4 Polynucleotides: poly(dA).poly(dT) and poly(dA-dT).poly(dA-dT)

The 3D ps-TRIR and contour plots of poly(dA).poly(dT) and poly(dA-dT).poly(dA-dT) are shown in figure 3.38. It is striking that the profiles are so dramatically different even though the constituent bases are the same. Another significant feature is that the cascading effect of the band maxima that is synonymous with vibrational cooling, is less pronounced in the non-alternating than in the alternating polymer. This can be clearly seen in the contour plots that focus on the early time range (2-50 ps). The bands recover in a straight manner in the homopolymer case (indicating little cascading) but are curved in the heteropolymer case. This could be a result of the improved energy transfer with the homopolymer, with the initial excitation energy being rapidly delocalized over a number of bases as has been predicted by exciton theory.[173]

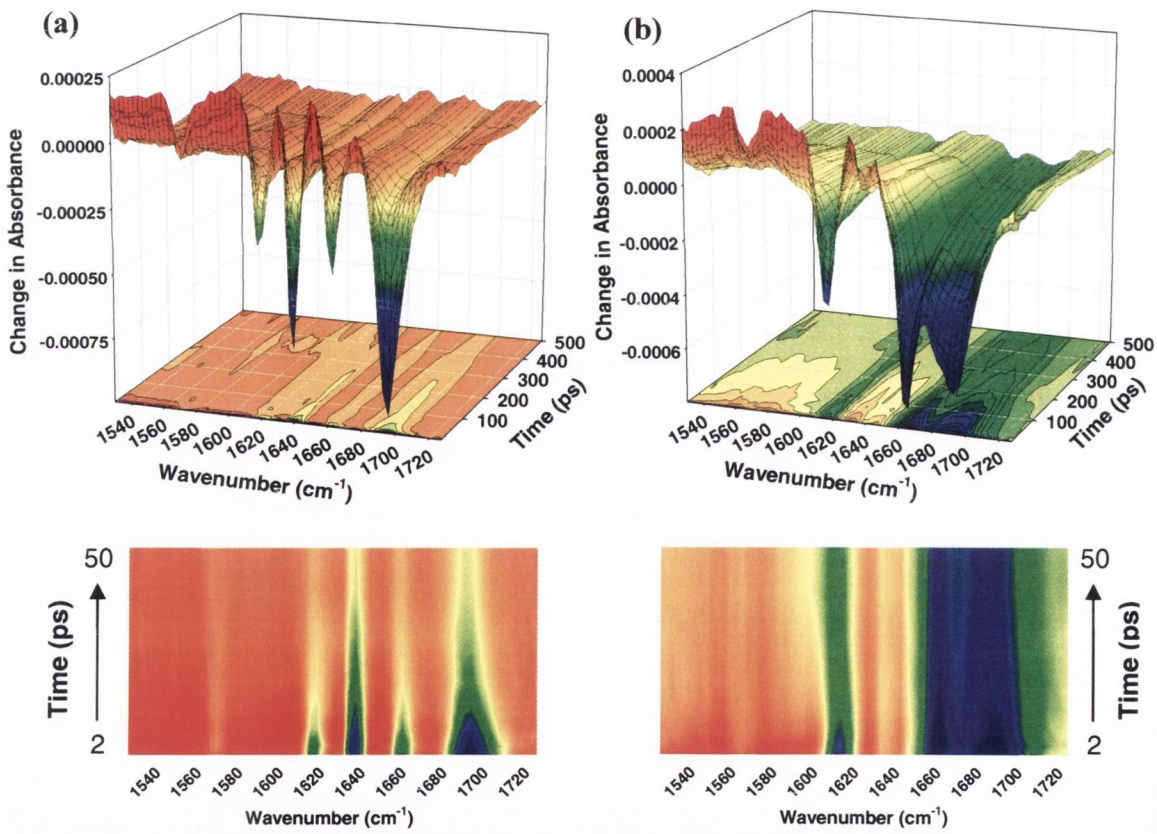

Figure 3.38 3D ps-TRIR spectra with contour plots with focus on the first 50 ps below of (a) poly(dA).poly(dT) and (b) $[poly(dA\text{-}dT)]_2$ at delays between 2 and 500 ps. Both compounds are 10 mM in 50 mM potassium phosphate D_2O buffer (pH 7).

In the polymers, one possibility is that the long-lived state is of an excimer/exciplex, the deactivation of which can be affected by interstrand hydrogen bonding. In our study, the long-lived lifetime was found to be ~90 ps in poly(dA).poly(dT) and ~150 ps in poly(dA-dT).poly(dA-dT). It is important to consider results from single-stranded studies as it is believed that excited state species can be localized on one strand, so as to retain the complementary strands integrity and hence a copy of the genetic information.[173,174] Kwok *et al.* assigned a lifetime of 182 ps in $(dA)_{20}$ to excimer emission formed as a result of excited state charge transfer.[138] A more recent study by the same group has reported a lifetime of 140 ps for $(dT)_{20}$ and have attributed this as the deactivation of the triplet state, which they conclude is the route by which cyclobutane pyrimidine dimers (CPDs) are formed.[5] Crespo-Hernandez *et al.* monitored the bleaching at 253 nm and found lifetimes of 126 ps for $(dA)_{18}$ and 103 ps for $(dT)_{18}$.[124] When monitored at 280 nm a lifetime of 800 ps was found for $(dT)_{18}$. In the base-paired polymers $(dA)_{18}.(dT)_{18}$, lifetimes of 101 ps (at 250 nm) and 150 ps (at 570 nm) were reported. The 150 ps lifetime was attributed as being from an adenine-based excimer state. In the heteropolymer $d(AT)_9.d(AT)_9$, a lifetime of 51 ps was attributed to an A-T excimer. Earlier transient absorption experiments on poly(dA) found a long-lived state, having a lifetime of 154 ps.[175] Another contribution from the Kohler research group stated that long-lived states in $(dT)_{18}$ varied between 100 and 1000 ps "because of $^1n_N\pi^*$ population".[86] Studies in the Markovitsi research group have proposed that delocalization of energy over at least two bases resulting from mixing of different monomer states is responsible for the long-lived state in $(dA)_{10}.(dT)_{10}$.[176] Fluorescence measurements by the same group on poly(dA-dT).poly(dA-dT) and poly(dA).poly(dT) did not find any species greater than a few picoseconds.[127] This may suggest that dark states could be the likely candidate for the long-lived species found in the polymeric structures. Santoro *et al.*[115] also pointed out the possibility of dark excimer states from adenine oligomers having lifetimes of 100 ps.

Along with efforts to address this issue experimentally, much research has been directed into computational modelling of the ultrafast dynamics in polynucleotide DNA following UV excitation. [173,174,177,178] However, a caveat was issued by Scholes *et al.* with regards to modelling energy transfer processes.[179] The authors pointed out that exclusive consideration of a Forster or Dexter type mechanism to describe interchromophore singlet-singlet electronic energy transfer at close separations to be insufficient as it neglects

coulombic interactions. Recent time dependent density functional theory (TD-DFT) calculations on stacked adenine dimers in water found that the charge transfer states lie well above the $^1n_N\pi^*$ and $^1\pi\pi^*$ states at the Franck-Condon point.[177] Our study may lend more weight to involvement of dark $^1n_N\pi^*$ states rather than charge transfer states that lead to excimer/exciplex type complexes. While the conclusions of the computational studies sometimes contradict one another, most agree that delocalization of excitation energy over a number of bases is possible. One study suggested that delocalization is possible over four or more bases[180] while another suggests the excitation energy can spread over up to six adenine and thymine bases in the $A_{12}.T_{12}$ polymer.[181] Rapid energy transfer between exciton states in B form $(dA)_{10}.(dT)_{10}$ has been estimated to occur in less than 100 fs.[178] Calculations by Bittner have suggested that over several hundred femtoseconds, a cohesive excitonic wavepacket remains on the adenine side of an A-T homopolymer, whereas the thymine exciton rapidly decomposes.[173,174] The author suggests that this isolation of the long-lived excited species is nature's method for limiting photodamage since the complementary chain remains undamaged and therefore a back-up copy of the genetic information is retained.

3.5 Conclusions

In conclusion, we have demonstrated how ps-TRIR is an invaluable tool for investigating the photophysics of DNA dinucleotide species. The photophysical behaviour of the homo- and heterodinucleotides are different from that of the constituent monomers (5′-dAMP and 5′-TMP) as new long-lived species were found in all dinucleotides. The homodinucleotides (dApdA and TpT) showed long-lived species that may be due to excimer formation. However surprisingly in the case of dApdA, a long-lived transient absorption band could not be found even though monitoring the ground state repopulation showed that there was a significant long-lived component.

A comprehensive and detailed study of the structural isomers dApT and TpdA was undertaken, including, for the first time, variable temperature time resolved infrared measurements. Circular dichroism, and variable temperature NMR was used to study the difference in stacking in the dinucleotides to complement the ps-TRIR data. Most significantly in the mixed dinucleotides we hypothesize that the long-lived state is

localized on thymine, due to the fingerprint information afforded with infrared spectroscopy.

Our studies on the polymeric strands have found that long-lived species exist in both the alternating polymer (poly(dA).poly(dT)) and non-alternating polymer (poly(dA-dT).poly(dA-dT)). The long-lived state was found to be slightly longer in the $[(poly(dA\text{-}dT)]_2$ case. The profile of this polymer resembled that of the dinucleotide repeating units while that of the poly(dA).poly(dT) was found to be more complex in nature. While, the study of dunucleotide species is a reasonable model to understand the processes accessible to bases within DNA it must be noted that additional processes and behaviour is observed for polynucleotides that cannot be simply inferred from these basic subunits.

Chapter 4

ps-TRIR Investigation of B- and Z-DNA forms of $[poly(dG\text{-}dC)]_2$

4.1 Introduction

This chapter builds upon the studies of mononucleotide, dinucleotide and polynucleotide systems outlined in the previous two chapters. DNA being a polymorphic molecule can adopt various secondary structures. While such structures have been studied by X-ray crystallography and steady state spectroscopies, the ultrafast dynamics of a structural isomer capable of adopting different secondary structure has until now not been addressed.

As previously stated, the individual base components have very short electronically singlet excited state lifetimes (< 1 ps).[16] We have shown that additional deactivation mechanisms are present on a picosecond timescale in all of the systems that we have studied. UV excitation of the polynucleotide systems, a closer analogue to genomic DNA, produces additional species having much longer lifetimes.[136] In these systems, questions remain as to whether the electronic excited states are localized on a single base or delocalized over a number of bases. Furthermore, the structural features of polymeric DNA raise a number of additional questions, such as the influence of base-stacking, hydrogen-bonding, hydration and conformation on the excited state properties and relaxation dynamics.

To address these questions we have chosen to probe the ultrafast relaxation mechanisms of poly(dG-dC).poly(dG-dC) (see scheme 4.1). Watson-Crick base pairing and stacking interactions within the double-stranded polymer will influence the deactivation pathways. Conversion from right-handed B form to left-handed Z form allows for influences due to the secondary structure on the relaxation mechanisms to be analyzed. ps-TRIR is the ideal spectroscopic technique to probe such complexities, as structural fingerprint information is afforded in addition to the kinetic behaviour of transient species produced upon excitation.

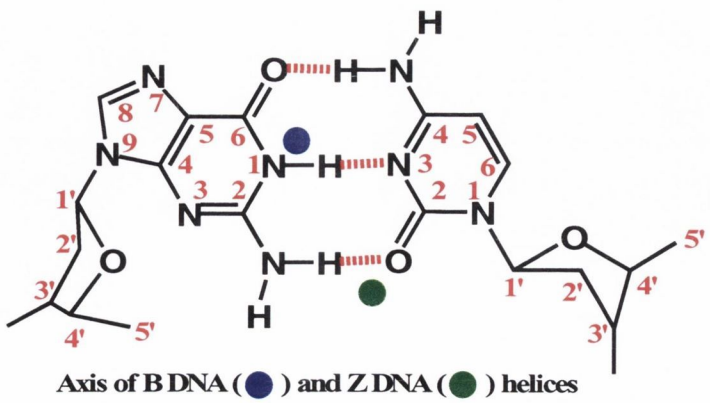

Scheme 4.1 Watson-Crick hydrogen bonded base pairs in $[poly(dG\text{-}dC)]_2$ with the polymer helical axis for B- (blue) and Z-DNA (green).

4.2 Structural Characteristics of B- vs Z-DNA

There are a number of structural differences between the B and Z forms of DNA (see table 4.1). Stacking interactions are altered due to geometrical orientation as well as different intramolecular separation. The bases are in the centre of the helix in B-DNA but are at the periphery in Z-DNA, making them more exposed to solvent molecules. Therefore it is not unreasonable to expect different photophysical behaviour from structural isomers in different geometric orientations. Factors such as base-stacking and solvent interactions are expected to mediate the relaxation mechanisms.

The characteristic UV absorption spectrum of equimolar concentrations of [poly(dG-dC)]$_2$ in both the B and Z form is shown below in figure 4.1. As an absorption spectrum can be viewed as a probability plot of the electronic transitions, one can see that although the two forms are identical in composition, the orientation of the bases has a significant effect on the possible photophysics. The B form has a greater absorption at lower wavelength, while the Z form can absorb photons at higher wavelength. The difference spectrum (figure 4.1 (b)) shows that the Z form exhibits both hypochromism (minimum at 245 nm) and hyperchromism (maximum at 290 nm) when compared to the more common B form. Notably, at our excitation wavelength (267 nm) the absorption of both forms is the same.

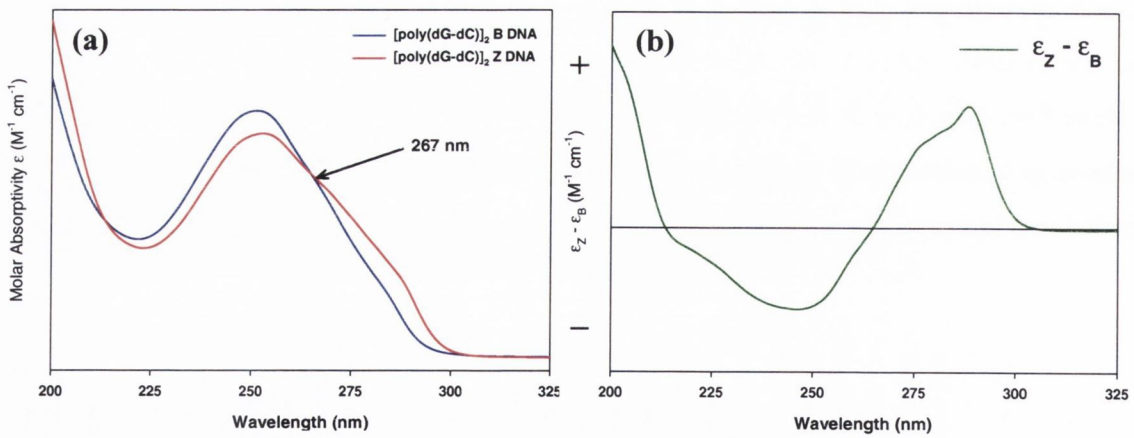

Figure 4.1 (a) UV absorption spectra of equimolar concentrations (10 mM) of [poly(dG-dC)]$_2$ in 50 mM potassium phosphate D_2O buffer (pH 7) in the B (blue) and Z (red) form and (b) difference spectrum ($\varepsilon_Z - \varepsilon_B$) of the two forms.

	B-DNA		Z-DNA	
Helical sense	Right	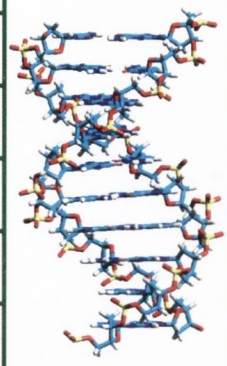	Left	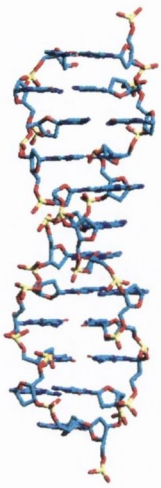
Vertical rise (Å)	3.4 Å		3.7 Å	
Base pairs per turn	10		12	
Helix diameter (Å)	20 Å		18Å	
Rotation per bp (°)	35.9 °		- 30 °	
Helix pitch (Å) per turn	33.2 Å		45.6 Å	
Rise per bp (Å)	3.32 Å		3.8 Å	
Base pairs position	Centred		In groove	
Sugar Puckering in general: both py and pu	*C2′-endo*, C3′-*exo*		pu C2′-*exo*, C3′-*endo* py C2′-*endo*, C3′-*exo*	
Glycosidic bond orientation wrt sugar	*anti*	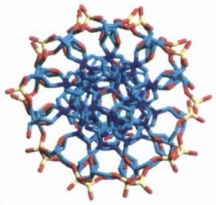	*anti* at C *syn* at G	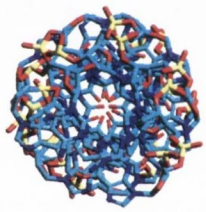
P to P distance (Å)	7 Å		< 7 Å	
P-S-P backbone	Smooth		Zig-Zag	
Propeller twist (°)	+16 °		~0 °	
Overlap in one GC double stranded unit (H atoms omitted for clarity)	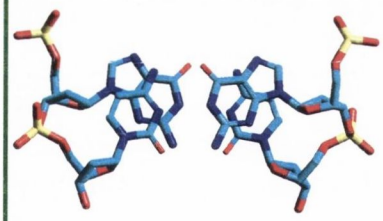		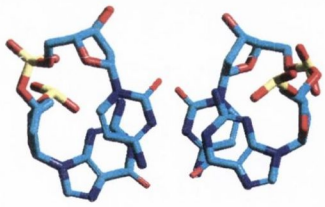	

Table 4.1 Comparison of some of the structural parameters for B and Z DNA. All structures were drawn with HyperChem™ 8.0.5 package.

4.3 Motivation for this Study

This model system is interesting for a number of reasons:- (i) It has recently been shown that the excited states of the bases in $[poly(dG\text{-}dC)]_2$ decay at rates faster than those observed for the individual nucleotides,[182] with a particular role ascribed to charge-transfer states,[22] a process that is predicted to be followed by rapid proton transfer between the G and C units.[22,33,53,85] (ii) If, as predicted, proton transfer acts to modulate the decay of locally excited (LE) states,[22] then the characteristic IR signatures of the deprotonated guanine and protonated cytosine products should be detectable by ps-TRIR, as long as they last for greater than 1 ps. (iii) $[poly(dG\text{-}dC)]_2$ can adopt the unusual left-handed Z-DNA structure.[183] Thus a comparison of how the base stacking arrangements in the structurally distinct right-handed B- and left-handed Z-DNA forms influences the photophysical processes of the G-C base pairs is possible. (iv) The characterization of an $^1n_N\pi^*$ dark state for 5′-dCMP, with a strong IR identifiable transient band at 1574 cm^{-1} (chapter 2) poses questions as to the possible role of this state in C-containing polynucleotide photochemistry.

4.4 Results

4.4.1 Constituent Bases of the Polymer – 5′-dGMP and 5′-dCMP

Figure 4.2 shows the transient IR spectra of the constituent monomers of our model polymer system when studied in isolation. Bleaching regions centred at 1510 cm^{-1} (5′-dCMP) and at 1580 cm^{-1} (5′-dGMP) correspond to ground state ring vibrations while those centred at 1650 cm^{-1} (5′-dCMP) and at 1670 cm^{-1} (5′-dGMP) occur at the carbonyl stretching frequencies of the ground state. Relaxation of the vibrationally hot ground state was observed for both bases. The additional long-lived transient species produced in 5′-dCMP was assigned to the deactivation of the dark $^1n_N\pi^*$ state as discussed in chapter 2.

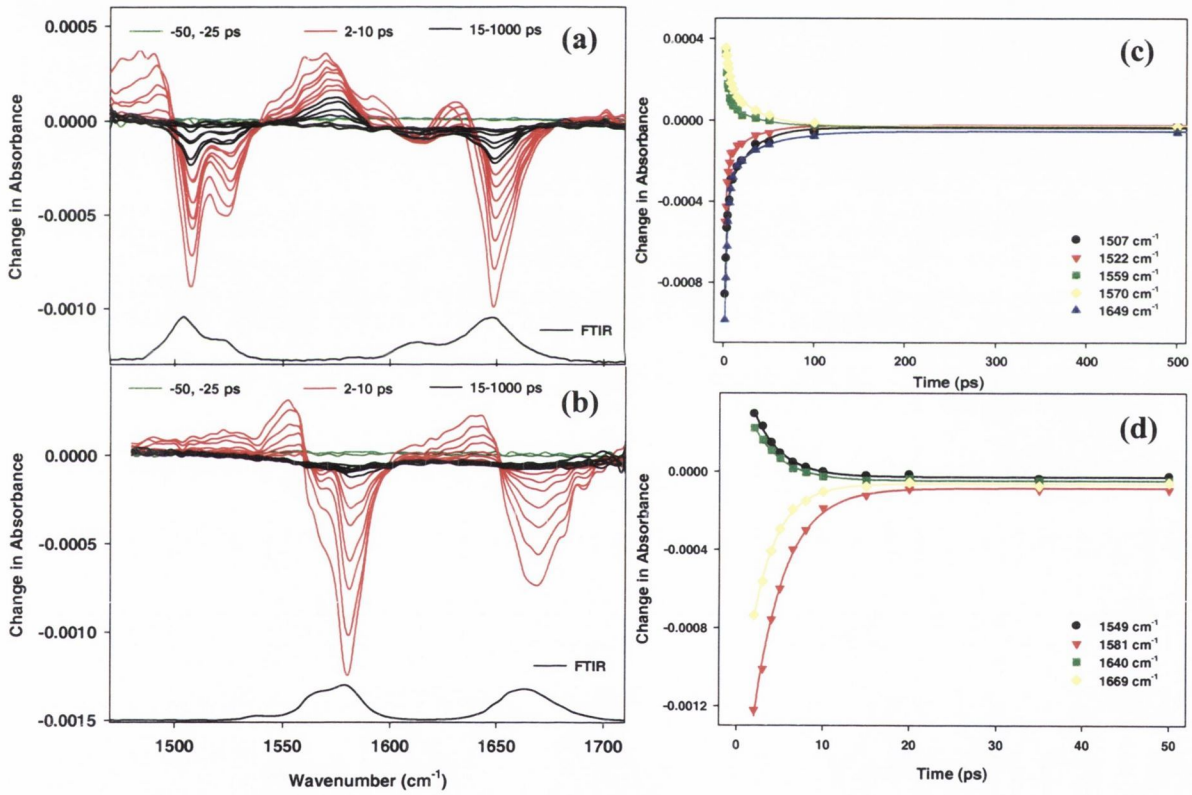

Figure 4.2 ps-TRIR of (a) 10 mM 5′-dCMP and (c) 10 mM 5′-dGMP, both in 50 mM potassium phosphate D_2O buffer (pH 7) with FTIR below (baseline adjusted). Delays are at -50, -25 (green), 2, 3, 4, 5, 6.5, 8, 10(red), 15, 20, 35, 50, 100, 500 and 1000 ps (black) for both spectra. Kinetic analysis of (c) 5′-dCMP sample at 1507, 1522, 1559, 1570 and 1649 cm^{-1} and (d) 5′-dGMP sample at 1549, 1581, 1640 and 1669 cm^{-1}.

4.4.2 B form [poly(dG-dC)]$_2$

The transient IR spectra for double-stranded [poly(dG-dC)]$_2$ (10 mM) in 50 mM potassium phosphate D_2O buffer, where the polynucleotide is in the B form is shown in figure 4.3. This shows strong bleaching and weaker transient absorption features. The ground state IR spectra of the individual bases as previously mentioned can be considered to have three regions with characteristic vibration bands: the carbonyl stretching region (1640-1700 cm^{-1}), where both G and C bases absorb, the G ring region (1550-1600 cm^{-1}) and finally the C ring region (1490-1550 cm^{-1}). The Watson-Crick (W-C) hydrogen bonding and stacking interactions present in double-stranded DNA results in mixing of the vibrational degrees of freedom. This manifests itself in changes in the IR bands compared to those of the mononucleotides 5′-dCMP and 5′-dGMP, resulting in strong suppression of the ring stretches for both C and G.[93]

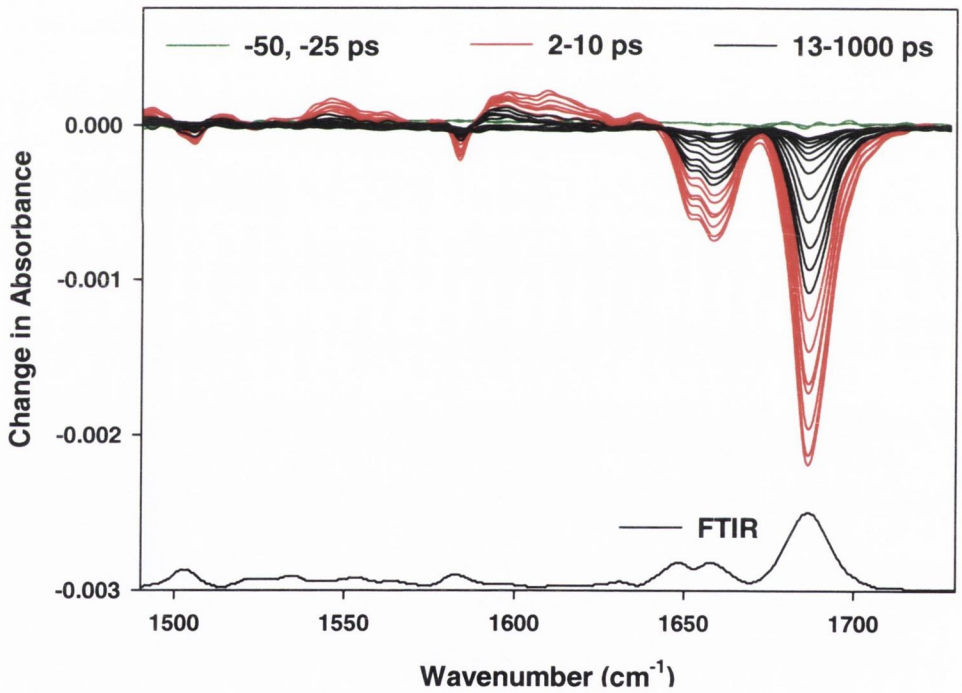

Figure 4.3 ps-TRIR of B form [poly(dG-dC)]$_2$ (10 mM) in 50 mM potassium phosphate D_2O buffer at pH 7 with FTIR below.
Delays are at -50, -25 (green), 2-10 (red) and 13-1000 ps (black).

From analysis of the kinetics of the bleaching in both the C (1657 cm^{-1}) and G (1685 cm^{-1}) carbonyl regions of the double-stranded polynucleotide, it was evident that two processes were occurring (see figure 4.4). These two processes have lifetimes of 7 ± 2 ps and 30 ± 4 ps with approximately the same amplitude (table inset of figure 4.4). As in the first

ps-TRIR study of DNA,[48] the shorter of these lifetimes is ascribed to the relaxation of a vibrationally excited ground state and the longer to the decay of an electronic excited state. However, a comparison with the data from our more recent studies[131,143] of 5′-dCMP and 5′-dGMP reveals significant differences between the fast processes in the mononucleotides and the double-stranded polynucleotide. This is particularly relevant in the regions where transient absorption dominates. Decay in the mononucleotides is accompanied by a shift of the maximum of the absorption band of the vibrationally hot ground state to higher wavenumbers. Strikingly this 'tracking' behaviour was not found for the polynucleotide between 2-10 ps. One possible explanation for this is that in the double-stranded polynucleotide, the vibrational energy is very rapidly (< 1 ps) distributed between the nucleobases, so that on average no base has more than one quantum of vibrational energy, at least in the higher (> 1500 cm^{-1}) modes. This would be expected if very effective phonon coupling exists between the stacked bases and/or it could be due to rapid delocalization of the initially formed Franck-Condon excited state over a number of bases as has been predicted by exciton theory.[173]

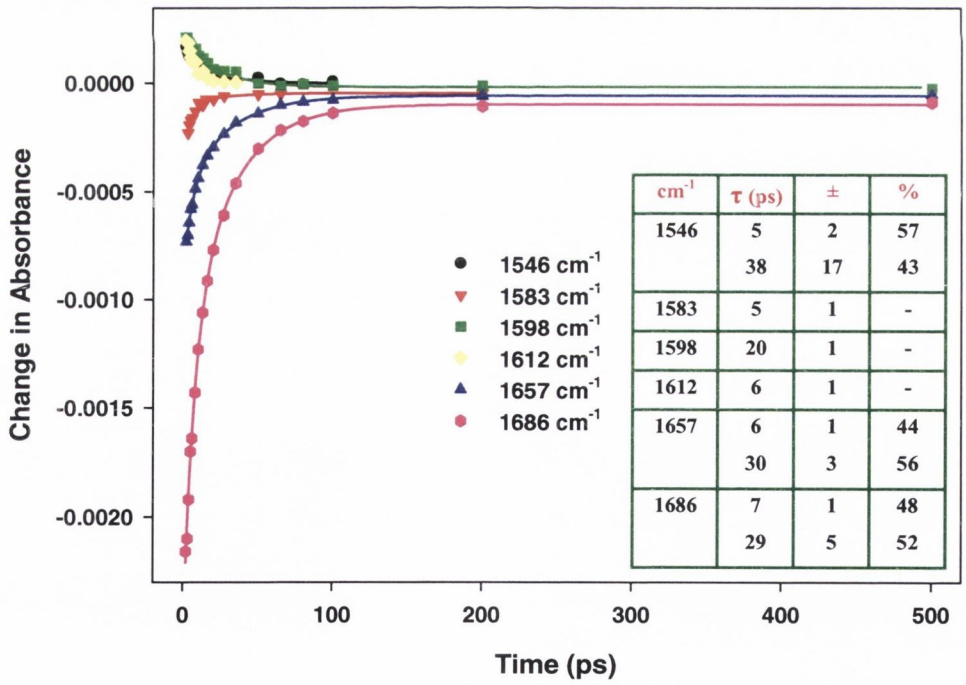

cm^{-1}	τ (ps)	±	%
1546	5	2	57
	38	17	43
1583	5	1	-
1598	20	1	-
1612	6	1	-
1657	6	1	44
	30	3	56
1686	7	1	48
	29	5	52

Figure 4.4 Kinetic analysis of B form $[poly(dG\text{-}dC)]_2$ (10 mM) in 50 mM potassium phosphate D_2O buffer (pH 7) at 1546, 1583, 1598, 1612, 1657 and 1686 cm^{-1} with lifetime table inset.

A second observation is the behaviour of the transient absorption in the region 1590-1625 cm^{-1}, where two bands are discernible at 1598 and 1612 cm^{-1} and different kinetics prevail in these bands. Unlike the bleaches, both of these transient bands are found to obey monoexponential kinetics (20 ± 1 ps at 1598 cm^{-1} and 6 ± 1 ps at 1612 cm^{-1}). From these results we conclude that there are two pathways available for the decay of the excited states.

4.4.3 Z form [poly(dG-dC)]$_2$

DNA is a polymorphic structure and in the presence of 4 M NaCl the left-handed Z conformation of [poly(dG-dC)]$_2$ is obtained.[184,185] The ps-TRIR spectrum of this form is given in figure 4.5. Following the B-Z transition the bleach bands located at 1657 and 1685 cm^{-1} are shifted to 1636 and 1670 cm^{-1} respectively due to the modification of the base-pair stacking and solvation in the ground state.

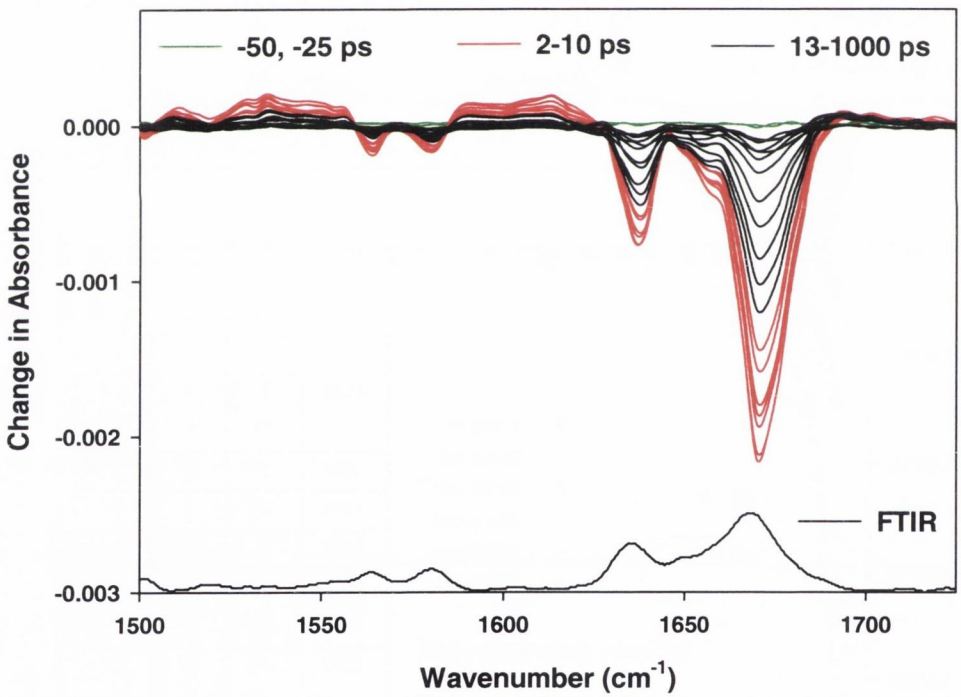

Figure 4.5 ps-TRIR of Z form [poly(dG-dC)]$_2$ (10 mM) in 50 mM potassium phosphate D_2O buffer at pH 7 with FTIR below.
Delays are at -50, -25 (green), 2-10 (red) and 13-1000 ps (black).

Moreover, in contrast to the B form, the recovery kinetics of the ground state monitored at the two dominant bleaches, 1670 cm^{-1} (18 ± 2 ps) and 1636 cm^{-1} (21 ± 2 ps) followed single exponential decay with no significant improvement found for double exponential fitting (see figure 4.6). The transient bands analyzed in the region of 1520-1560 cm^{-1} gave

a single exponential lifetime of 16 ± 2 ps and a similar value was obtained in the region 1587-1605 cm^{-1} (table 4.2) However, some evidence of shorter values was obtained between 1610-1620 cm^{-1}, *e.g.* at 1617 cm^{-1} (the peak maxima in this spectral region) a decay of 10 ± 2 ps was observed.

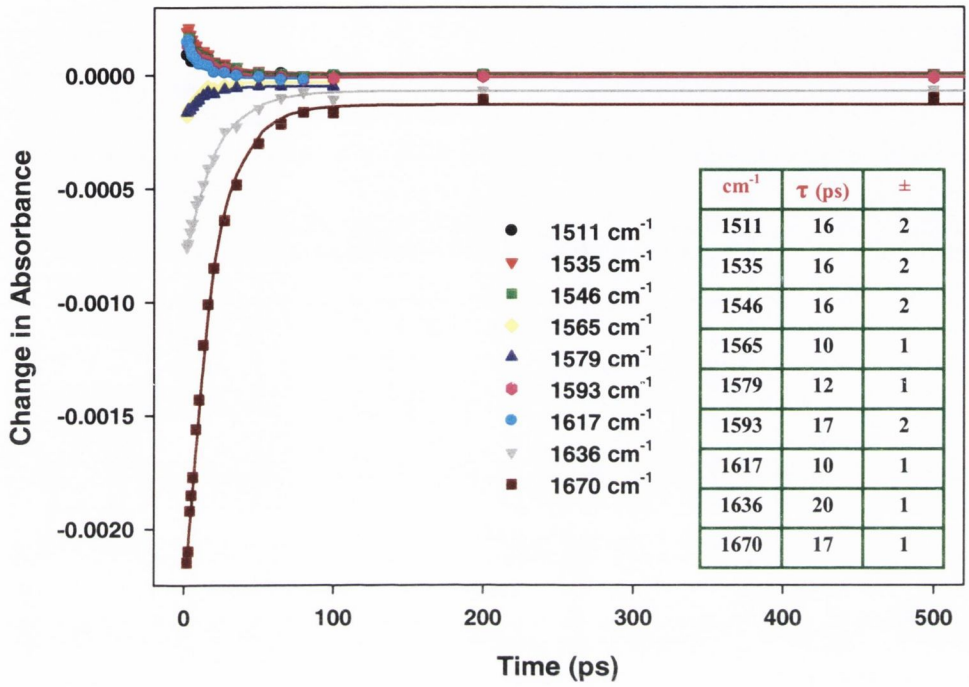

cm^{-1}	τ (ps)	±
1511	16	2
1535	16	2
1546	16	2
1565	10	1
1579	12	1
1593	17	2
1617	10	1
1636	20	1
1670	17	1

Figure 4.6 Kinetic analysis of Z form $[poly(dG\text{-}dC)]_2$ (10 mM) in 50 mM potassium phosphate D_2O buffer (pH 7) at 1511, 1535, 1546, 1565, 1579, 1593, 1617, 1636 and 1670 cm^{-1} with lifetime table inset.

It must be noted that a small signal remains after 1000 ps, which shows depletions at 1636 and 1670 cm^{-1} and transient absorption band at 1695 cm^{-1}. As has been previously reported the production of an IR band in a similar position following direct photoionization[97] or the sensitised photooxidation[84] of B-form $[poly(dG\text{-}dC)]_2$. Possible origins from this species will be discussed further below.

A comparison of the B and Z forms at 2 and 16 ps is shown in figure 4.7. This representation highlights not only the different band structure and position, but perhaps more striking is the difference in the kinetic behaviour can be easily identified. For the B form, on going from 2 to 16 ps, the bleaches have recovered to *ca.* 40% of the initial intensity. Interestingly, there was different behaviour between the transient absorption bands. The broad transient centred at *ca.* 1540 cm^{-1} conformed in a similar manner to the bleaching bands. The transient species centred at *ca.* 1600 cm^{-1} displayed two distinct

regimes. The left hand side exhibited a slower decay of the band (compared to the bleaching bands) while the right hand side revealed a very fast retreat with little or no transient absorption remaining after 16 ps. In contrast, the Z form displayed consistent behaviour in all transient absorption and bleaching bands, with *ca.* 50% of the ground state having being repopulated after 16 ps. Evidence for a transient absorption at 1690 cm^{-1} was observed in the 16 ps spectrum and this absorption has clearly grown in, as it was not present in the 2 ps spectrum. The transient centred at 1600 cm^{-1} does not show different behaviour with time as in the B case. All of these observations will be considered further in the discussion section.

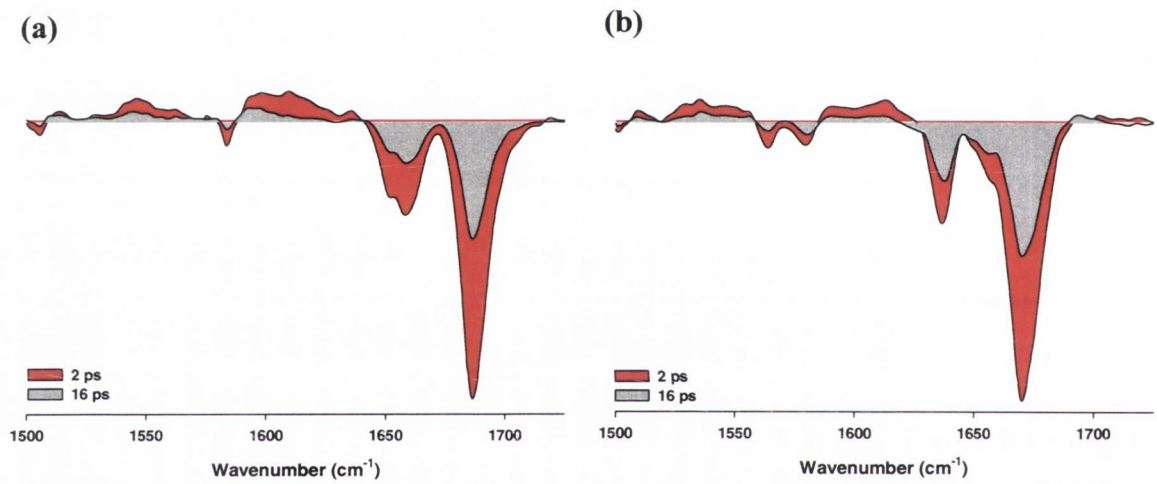

Figure 4.7 Comparison of (a) B form $[poly(dG\text{-}dC)]_2$ at 2 and 16 ps and (b) Z form $[poly(dG\text{-}dC)]_2$ at 2 and 16 ps.

A summary of the kinetics in both the mononucleotide and polynucleotide systems is given in table 4.2. As described earlier in chapter 2, 5′-dCMP exhibits biexponential kinetics with the lifetimes being assigned to vibrational cooling (3 ps) and decay of the dark $^1n_N\pi^*$ state (33 ps). No long-lived species was observed for 5′-dGMP (at 10 mM concentration, pH 7) and the sole lifetime of 3.1 ps is assigned to cooling of the vibrationally hot ground state. In the B form two processes were evident, whereas the Z form results indicated that only one process was occurring. Origins for these lifetimes will be considered in detail in the discussion section.

DNA	IR band position (cm^{-1})	τ (ps)	
5′-dCMP	1574	2.6 (± 0.3) 80%,	33 (± 4) 20%
5′-dGMP	1669	3.1 (± 0.3)	
$[poly(dGdC)]_2$ B form	1598		20 (± 1)
	1612	6 (± 1)	
	1657	6 (± 1) 44%,	30 (± 3) 56%
	1686	7 (± 1) 48%,	29 (± 5) 52%
$[poly(dGdC)]_2$ Z form	1593		17 (± 2)
	1617	10 (± 1)	
	1636		20 (± 1)
	1670		17 (± 1)

Table 4.2 Summary of observed IR bands and kinetics for 5′-dCMP, 5′-dGMP, $[poly(dG\text{-}dC)]_2$ B form and $[poly(dG\text{-}dC)]_2$ Z form.

4.5 Discussion

The steady-state absorption of the non-interacting G and C bases differs from that of the polymeric form and indicates the presence of electronic interactions between the bases that in turn alter the excited state dynamics from that of the parent bases.[182] Recent fluorescence upconversion measurements by Markovitsi and coworkers on the B form of $[poly(dG\text{-}dC)]_2$ revealed that 99% of the emission was lost by 1.4 ps.[182] However, DNA is only weakly emissive and excited state decay occurs predominantly via non-radiative channels. Thus by measuring the ground-state recovery it is possible to estimate the kinetics of the dark processes occurring on the picosecond timescale which are unseen by fluorescence techniques.

In the case of the B form we have observed two species, one of which decays with a lifetime of 7 ps and another which has a clearly defined absorption band at 1597 cm^{-1} (τ = 20 ps). Somewhat contrasting behaviour was found in the Z form where the recovery of the ground state followed single exponential kinetics. The transient absorption predominantly decayed with a comparable lifetime of 16 ps although there was also evidence of a faster decay (*ca.* 10 ps) measured at 1616 cm^{-1}.

A comparison of the transient profiles for both forms is presented in figure 4.8. Immediately it is evident that there are striking differences in the profiles. On the lower wavenumber side (1595 cm^{-1}) both the initial intensity (2 ps) and subsequent decay of the transient bands is comparable in both samples. However, on the higher wavenumber side (1610 cm^{-1}) the transient is found to decay much more rapidly for the B than in the Z case. This is clearly seen in both the 3D and contour plots. The time slice taken at 16 ps (dashed black line on contour plots and profile shown on the top of the contour plots) shows that the high wavenumber region of the transient still persists in the Z form (ratio of 1595 cm^{-1}:1610 cm^{-1} is ~1:1) but has retreated in the B form (ratio of 1595 cm^{-1}:1610 cm^{-1} is ~2:1).

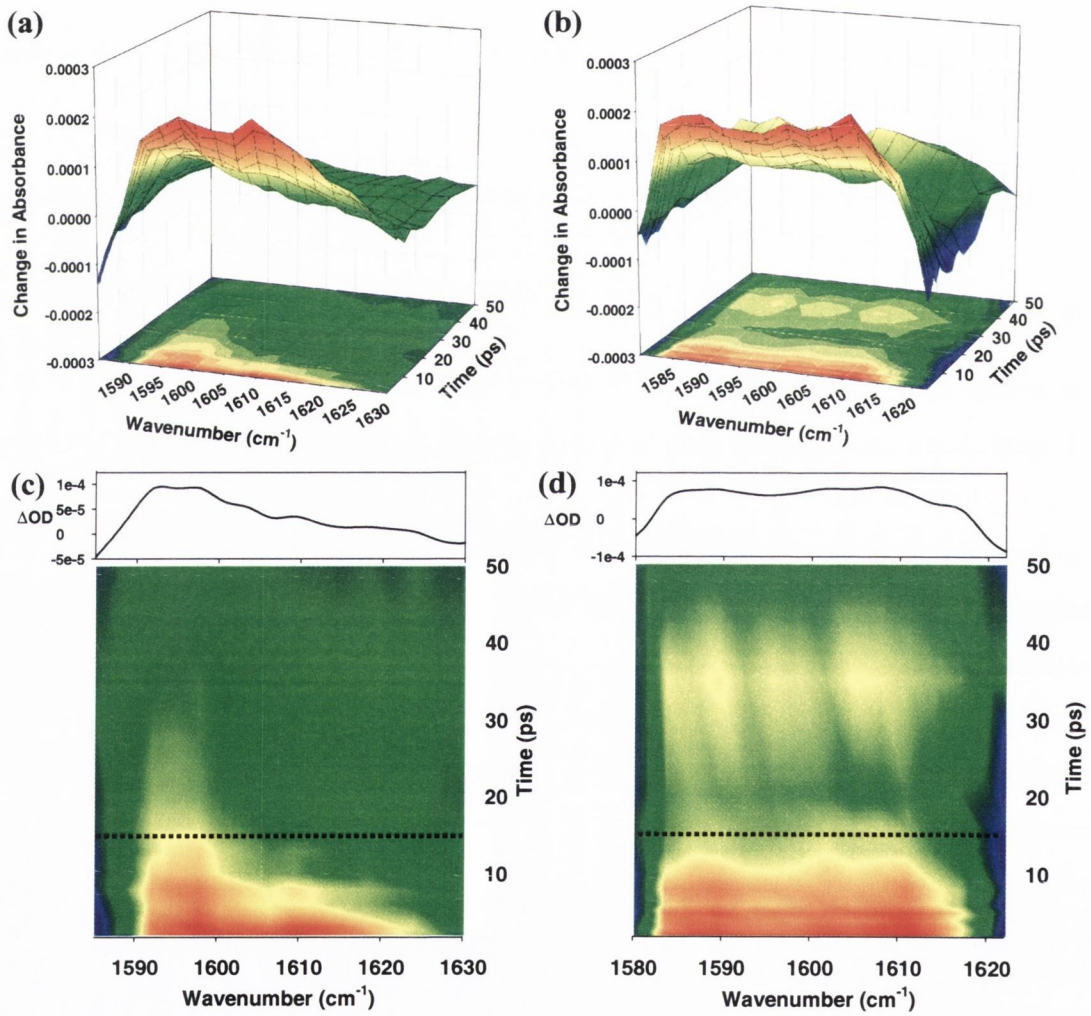

Figure 4.8 Comparative 3D and contour plots for the major transient absorption region for B- (a) and (c) and Z-DNA (b) and (d).
Dashed black lines on and the profile shown above the contours plot are at 16 ps.

The results obtained for the B conformer suggest that there are at least two channels, of roughly equal magnitude, from which the initially formed excited state can decay on the ultrafast timescale. It is worth pointing out that longer-lived species (observed by fluorescence on the nanosecond timescale) have in the past been considered to be due to excited state species, often of an exciplex-type.[186] Our direct monitoring of ground-state recovery by ps-TRIR indicates that nanosecond processes contributing to the relaxation dynamics of this system are small (*ca.* 4%). The 20 ps species has a relatively well-defined infrared absorption feature at *ca.* 1597 cm^{-1}. The location of this band is close to that assigned to the dark $^1n_N\pi^*$ state of 5′-dCMP (1574 cm^{-1}) (chapter 2).[143]

4.5.1 Possibilities for the Lifetimes

A strong candidate for the transient observed in the B-form of [poly(dG-dC)]$_2$ could be the $^1n_N\pi^*$ dark state of the cytidine moiety. However, a number of other possible origins of the 20-30 ps component may also be considered, including tautomers, electron and/or proton transfer products (e.g. guanine radical cation, guanine radical, protonated cytosine etc.) (see scheme 4.2(a-f)) or other dark excited states, as these have previously been proposed as possible routes for the deactivation of excited states. Of the two most likely C-based tautomers (iminooxo and iminohydroxy forms) the first can be ruled out as calculations predict a carbonyl stretch at higher frequency than that of the canonical form (calculations are in chapter 2).[143] Further computation will be required to unequivocally dismiss the imino-enol possibility, as mentioned in chapter 2. Additionally the IR spectra of protonated cytosine or guanine anion, suggest that it is unlikely that either species is responsible for the characteristic absorption at 1597 cm^{-1}.

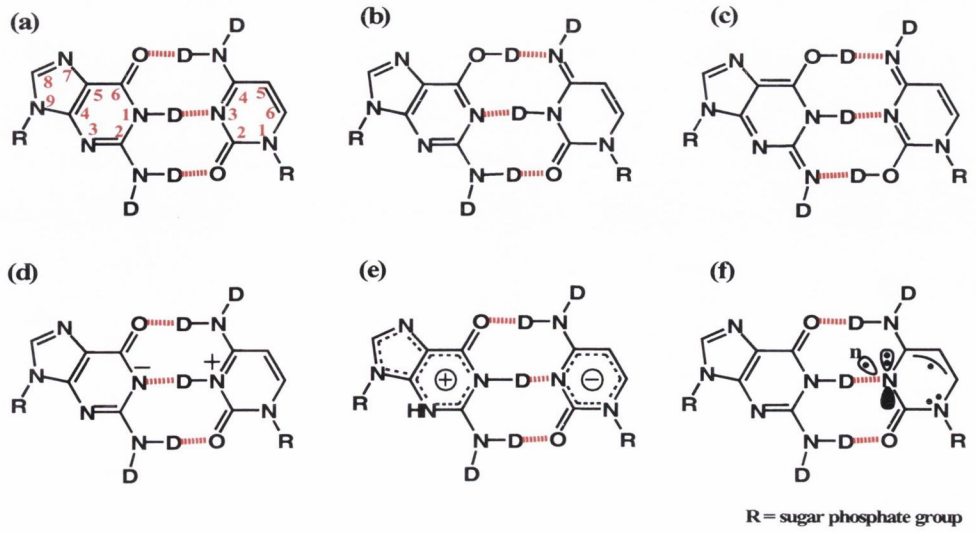

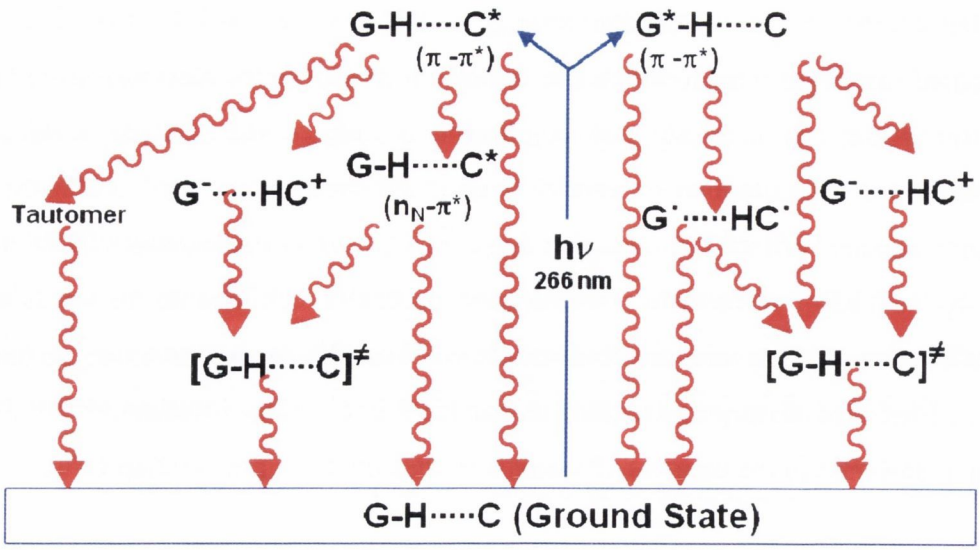

Scheme 4.2 (a) Watson-Crick G-C base-pairing, (b) and (c) tautomeric products, (d) proton transfer (e) charge transfer and (f) $^{1}n_{N}\pi^{*}$ form for the excited state of $[poly(dG\text{-}dC)]_2$. Summary of the possible deactivation pathways for the hydrogen bonded base pairs after 267 nm excitation.

The faster (7 ps) process observed in B form $[poly(dG\text{-}dC)]_2$ is consistent with the formation of a vibrationally excited ground state. This can be accessed by rapid internal conversion from the initially formed excited state (either localized on one of the nucleobases or delocalized over several). As eluded to previously neither the B or Z form show a cascading of transient maximum to higher wavenumber with time (clearly shown with the 3D profile and the contour plots in figure 4.9), something that is associated with vibrational cooling, at least for the smaller mono- and dinucleotide systems. Of course these systems do not have the possibility for distribution of the excess vibrational energy over a number of neighbouring bases. In the polymer systems, there is the possibility that the energy can be delocalized over the neighbouring stacked bases sub-picosecond, so that on our timescale no one base has more than one quantum of vibrational energy and hence there is no cascading effect seen for the subsequent relaxation. Such phenomena has been studied computationally for polymer DNA systems although the studies to date have concentrated on homopolymer B DNA of the A-T [173,174,176,178,181,187] rather than G-C [188] variety.

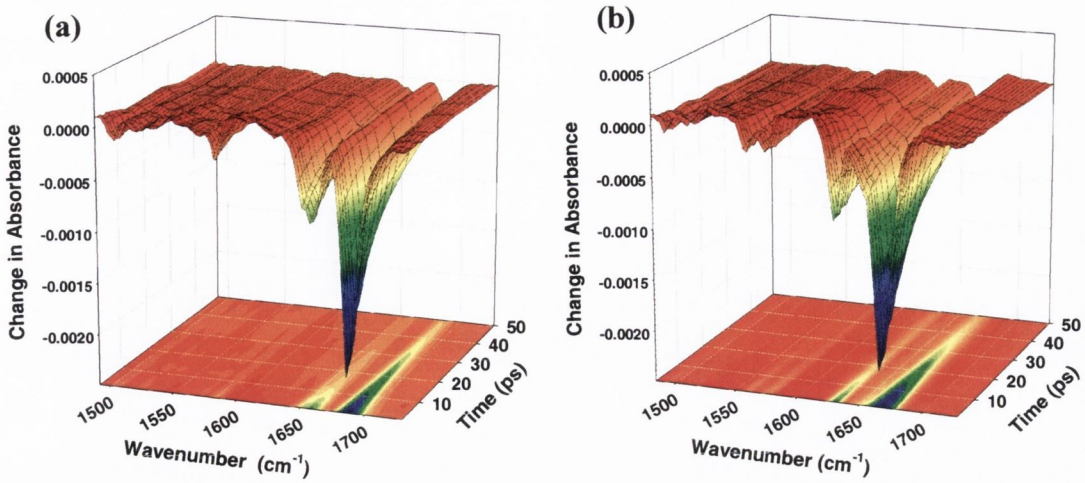

Figure 4.9 3D ps-TRIR spectra and contour plots of (a) B form $[poly(dG\text{-}dC)]_2$ and (b) Z form $[poly(dG\text{-}dC)]_2$ at delays between 2 and 50 ps. Both compounds are 10 mM in 50 mM potassium phosphate D_2O buffer (pH 7).

Alternatively the 'hot' species could in theory result after a subpicosecond back reaction from a rapidly formed photoproduct. One such option is the initial formation of a charge transfer state (CT) (with a single electron moving from the guanine base to the cytosine), which is then followed by the transfer, within tens of femtoseconds, of the imino proton from guanine to cytosine with formation of a neutral radical.[22] Recent fluorescence upconversion measurements of modified G-C pairs H-bonded in chloroform concluded that the enhancement in the decay rate was due to proton transfer in the base-pair – a mechanism not available to the individual base.[85] This overall process is estimated to occur within a 200 fs time frame (much shorter than our time resolution),[22] although structural and hydration effects in polynucleotide systems might prolong this process. The timescale of our measurements do not allow us to say more about the processes leading to the creation of this vibrational energy. In fact in D_2O, our solvent, the dynamics of such proton transfer processes are expected to be perturbed as all exchangeable hydrogen atoms are substituted by the heavier deuterium. Such an effect may well influence the ordering of states and their subsequent deactivation pathways.

There are significant structural differences between the B and Z forms of DNA. For example, in the B form the intrastrand stacking of G-C bases is uniform with a base separation of 3.4 Å while the Z form is characterized by a repeating dinucleotide unit with the spacing being 3.5 Å within and 4.1 Å between such units.[189] There is also improved

overlap of the stacked bases in the dinucleotide unit. The nature of hydration is also very different for the two conformers. The inversion of the helix, from right- to left-handed, results in the location of bases at the periphery of the helix and positions the phosphate groups closer together. The presence of the sodium ions (4 M NaCl) acts to stabilize the resulting electrostatic repulsion between the phosphate groups. These structural differences are expected to influence the excited state dynamics.

The Z form $[poly(dG\text{-}dC)]_2$ results show that the transient absorption predominantly decays with a lifetime of 16 ps although we note some evidence of a faster decay (*ca.* 10 ps) in the 1616 cm^{-1} region. The transient spectra of B- and Z-DNA at 2 ps and 16 ps, are compared in figure 4.10. The intensity of the absorbing species is comparable at both times. As in the case of the B form, the Z form shows absorbance in the region of the spectra associated with the $^1n_N\pi^*$ state but the structured band at 1597 cm^{-1} is replaced by a broader less structured feature in Z-DNA. If this is a single species (e.g. the vibrationally hot ground state) then its decay is significantly slower than in the B conformer. Alternatively, it is possible that two species give rise to this band, with the $^1n_N\pi^*$ being one likely candidate.

Theoretical studies on $(dG\text{-}dC)_5$ in the B form have predicted that 50% of the excited states produced are delocalized over at least two bases.[188] The broad nature of the transient spectrum in Z-DNA could also be consistent with an exciplex species, as the inter-dinucleotide step staggers the bases far enough apart to make electronic communication less efficient than in the B form.[184-186] Thus, in Z-DNA the location of the excitation may be restricted to two bases, whereas in the B form the excitation is more widely delocalized and thus this excited state has a shorter lifetime. There exists considerable speculation regarding the role of base-stacking interactions in the stabilization of the long-lived excited states witnessed in polynucleotide systems. It is worth noting that the common structural feature present in both the B- and Z-DNA forms is W-C hydrogen bonding. This bonding between G and C bases allows coupling of the transition dipoles in the excited state form and this coupling has been predicted to be strong between G and C bases.[187] Furthermore, recent 2D-IR work has focused on the sensitivity of this coupling to the conformation of DNA present.[96] The formation of delocalized excited states due to electronic coupling has been studied in detail in the work of Markovitsi and coworkers.[182,187,188,190]

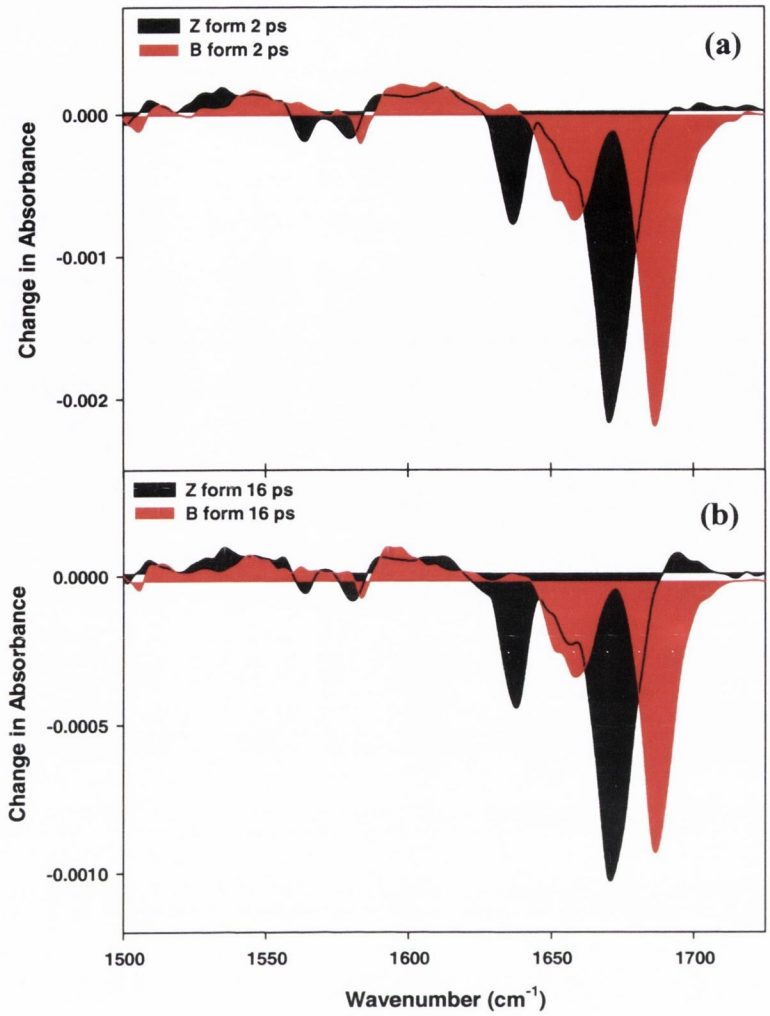

Figure 4.10 Comparison of ps-TRIR spectra of both forms of $[poly(dG\text{-}dC)]_2$ at (a) 2 ps and (b) 16 ps time delays following UV excitation. Both forms (10 mM) in 50 mM potassium phosphate D_2O buffer at pH 7, with 4 M NaCl for the Z case. Note: The thin line shown within the B form spectra represents the peak profile of the Z form.

4.5.2 Deconvolution of High Wavenumber Bleaching Band in Z-DNA

In both systems a small amount of bleaching (*ca.* 4%) was found to persist after 1 ns. However, for the Z-DNA system, the appearance of a transient absorption band at 1695 cm^{-1} was also observed. A band in a similar position from the direct photoionization by 200 nm UV excitation[97] and the sensitised photooxidation[84] of $[poly(dG\text{-}dC)]_2$ in the B conformation have been reported. Thus, this species may be related to direct photoionization of guanine yielding an oxidized guanine photoproduct, but given the early timescale signals it may be related to an excited state charge-transfer transition, from cytosine to guanine identified in recent theoretical reports[22] and/or subsequent H transfer.

Our ability to clearly resolve this band may stem from the shifting of the guanine based carbonyl band in the Z form relative to its position in the B form, where it would most likely be masked.

Deconvolution of the region 1650-1730 cm^{-1} was attempted for both the B and Z forms. The experimental profile obtained at each delay was fitted to two convoluted Lorentzian functions. The procedure applied is outlined for the Z form in figure 4.11 (a) below for the 2 ps case, with figure 4.11 (b) showing the temporal evolution of the Lorentzian fitting.

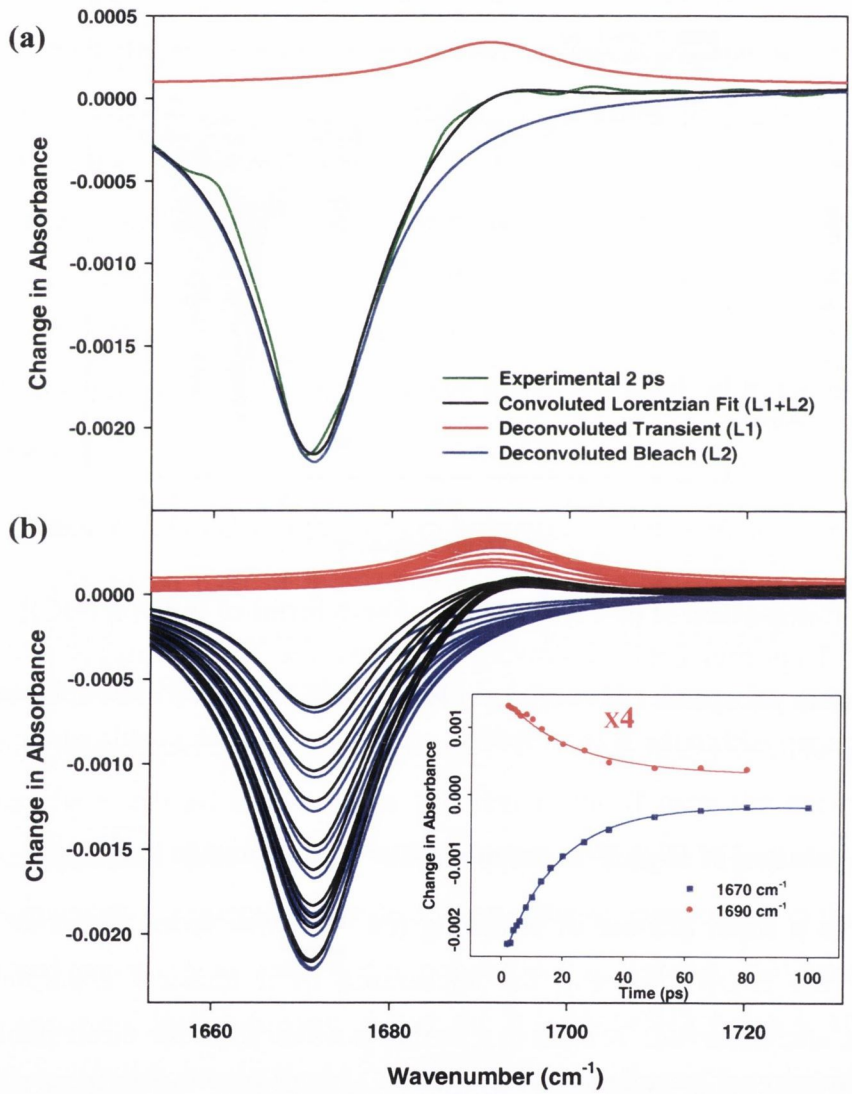

Figure 4.11 (a) Lorentzian convoluted fit (black) to the experimental (green) 2 ps data with the deconvoluted bleach (blue) and transient absorption (red) for Z-DNA and (b) Lorentzian fits through 2-27 ps with inset showing the kinetic fit of the deconvoluted bleach at 1670 cm^{-1} and transient absorption at 1690 cm^{-1} (scaled x4).

In the case of the Z form, where the carbonyl bleaching band is at lower wavenumbers than the B form, it was possible to fit the delays and thus reveal the transient feature at 1690 cm^{-1}. The deconvoluted transient absorption and bleaching bands both fit to single exponential kinetics with lifetimes of 22 ± 2 ps and 18 ± 1 ps respectively (inset figure 4.11 (b)). However, applying the same procedure to the B form did not reveal the presence of a similar transient species. Therefore, in answer to the question posed previously, as to whether a transient band was hidden in the B form due to the carbonyl absorbing at higher wavenumbers than in the Z form, in light of these results it is unlikely that such a transient exists. This implies that the presence of the transient in the Z from may be facilitated by the different secondary structure present and some or all of the different interactions that are present in such a structure.

4.6 Conclusion

In conclusion, we have shown that UV excitation of the Watson-Crick G-C base-pairs in double-stranded DNA produced transient IR absorption signals long after the $^1\pi$-π^* excited state was expected to have decayed. Evidence for two processes that contribute approximately equally to the decay of the initially formed excited state was found for B form $[poly(dG\text{-}dC)]_2$. The first may be rationalized in terms of the decay of a vibrationally excited ground state. Dispersion of excess energy, over a number of base-pairs could account for the absence of the 'tracking' behaviour that is characteristic of vibrational cooling. It is also possible that the 7 ps species in B-DNA could be due to a delocalized exciplex formed over more bases.

However, the second transient in the B form, which has a well-defined band at 1597 cm^{-1} is quite clearly due to a localized excited state (or less likely, a tautomer), and demonstrates that a very significant proportion of the excited states decay by a very different route than that proposed in most recent theoretical treatments.[14,22] We attribute this band at 1597 cm^{-1} to the $^1n_N\pi^*$ state of the cytidine moiety. The formation of this excited state in the polynucleotide is also presumably closely linked to differences in the decay pathways which are governed by the substitution at the N1 (C) or N9 (G) position of the nucleobases, a point which is generally not considered explicitly in most computational approaches.

There was some sensitivity of the decay processes in the G-C base-pair to changes of the structure of DNA. In Z-DNA both the transient absorption and the ground state bleaching

bands conformed very well to a single exponential decay of 16 ps, with some evidence for a faster process. While at present, we cannot rule out the role again here of the $^1n_N\pi^*$, we favour the presence of a dinucleotide-localized exciplex-type excited state manifesting itself as the spectrally broad transient.

The ps-TRIR measurements described in this chapter show that all transients species formed in both B- and Z-DNA [poly(dG-dC)]$_2$ are deactivated much more readily than those found in A-T rich DNA systems (chapter 3).[124] This may be in part due to the extra hydrogen bond in the G-C systems compared to their A-T counterparts, facilitating a faster dissipation of energy. There is still considerable debate in the literature as to whether base-stacking[126] or hydrogen-bonding[125] is the dominant factor in excited state relaxation dynamics. It is striking that the significant structural changes in base-stacking and solvation between the two conformations studied, does not appear to dramatically influence the timescale of the relaxation dynamics. To what extent the hydration and the close proximity of the sodium ions have in influencing the photophysical properties and in controlling the non-radiative decay properties of the excited states including the $^1n_N\pi^*$ state remains to be fully elucidated.

Chapter 5

ps-TRIR Study of Biologically Relevant Systems

5.1 Introduction

Having considered the properties of simple systems, this chapter describes advances on the insights gained in the previous three and aims to look at some biologically relevant systems, albeit in a speculative "first look" manner, that may provide more information as to how factors such as sequence, hydrogen-bonding and secondary structure modulate the ultrafast relaxation dynamics in DNA. In addition to the predominant double-stranded DNA arrangement, there are other non-canonical structures such as triplex and quadruplex DNA that have important biological functions. Examination of these complex motifs will be discussed in this chapter.

The first section focuses on mixed-base double-stranded (duplex) DNA. Since the seminal elucidation of DNA's helical structure by Watson and Crick[1] in the mid twentieth century much research efforts have been invested into understanding this unique structure. While at present there is a greater understanding of the structure and much of the macroscopic behaviour of genomic DNA, the minutiae and intrinsic mechanisms (e.g. electron and proton transfer) of double-stranded DNA that are so important to biological function are poorly understood. To date, investigations into the ultrafast mechanisms in double-stranded DNA have concentrated on simple systems, containing two of the four nucleobases, for which there are a plethora of examples.[86,124,127-129,132,136,150,175,182,188,191-193] Such approaches are entirely understandable as they seek to minimize the number of variables in the system, and therefore facilitate an easier interpretation of results. While these studies are valuable, they are not an accurate reflection of genomic DNA. With this in mind, this study seeks to tackle this intricate issue by investigating the complexity of a mixed-base duplex architecture. We chose complementary non-hairpinning 24-mer oligonucleotides (scheme 5.1 (a)) and studied the relaxation of both the single- and double-stranded forms.

The next section describes a study of triple-stranded (triplex) DNA. Triple-stranded DNA was first described in 1957, not long after the duplex (1953), when polyuridylinic and polyadenylic acid strands were found to form a stable complex when combined in a ratio of 2:1 respectively.[194] Almost twenty years later, the same methodology was applied to oligonucleotides, where the potential therapeutic benefits of sequence specific targeting was eluded to.[195] Today triplex formation is being exploited in so called antisense

strategies where gene translation is inhibited by blocking messenger RNA.[196,197] A long standing goal of molecular medicine has been the ability to selectively modulate/regulate the activity of genes and hence understand the biological consequences and ultimately further therapeutic applications.[198] Triplex-forming oligonucleotides (TFOs) have become an attractive method of sequence specific targeting of DNA and have been utilized both to manipulate gene sequence and ultimately modify the gene expression[199,200] and, when conjugated to photoreactive molecules, induce DNA damage.[200] Without question, further therapeutic strategies and applications will inevitably be developed with regards to triplex DNA because of its specificity,[201] and the reader is directed to an excellent review by Duca *et al.* where the history and evolution of new techniques, such as TFO therapies is discussed.[202] Aside from the therapeutic aspect, triple-stranded DNA formation has been implicated as the root cause of the progressive nervous system disorder, Friedreich's ataxia.[203,204] It is an autosomal recessive neurodegenerative disease (the most common hereditary ataxia) and is caused by the formation of triple-stranded DNA at GAA TTC repeats.[205]

While various macroscopic physical properties of triple-stranded structures have been studied in detail,[197,206-218] there have been no investigations of the ultrafast photophysical behaviour of the motif. This is somewhat surprising as triplex DNA has been reported to be very stable, but the underlying properties that possibly confer this stability (e.g. hydrogen-bonding and base-stacking) have not been probed. The model systems in our triplex study are poly(dA).poly(dT).poly(dT) and $(dA)_{18}.(dT)_{18}.(dT)_{18}$. The third strand (dT) resides in the major groove of the duplex structure and Hoogsteen hydrogen bonds to the dA residue (scheme 5.1 (b)). It is envisaged that with a comprehensive study encompassing the individual single strands, duplex, and finally triplex forms of both the long- and short-chained systems, insight into the fundamental properties of this unique scaffold may be gained.

Finally, the third study presented is this chapter is a TRIR investigation of the quadruplex-forming human telomeric DNA sequence 5′-AGGG$(TTAGGG)_3$-3′ (scheme 5.1 (c)). DNA quadruplex structures first came to attention in the 1980s when it was recognized that such structures were formed from telomeric DNA and that they might possess key biological function.[219,220] Telomers are the structures at the end of eukaryotic chromosomes and play a key role in chromosome stability and complete replication

chromosomal terminus during each cell cycle.[221] These telomere regions were found to be specifically G-rich and were found to form G-tetraplex structures.[222] Normal (healthy) cells undergo a finite number of divisions after which they encounter a proliferative barrier, and they die.[223] Human cancers have been associated with activation of a mechanism to maintain the telomere length, and hence the cancerous cell does not undergo normal replication and becomes immortal.[221,223-228] As a consequence of the biological significance of these regions being recognized focus turned to elucidating the actual scaffold/architecture of these regions as this was thought to be key to the biology expressed. Intramolecular quadruplex structures formed by these telomeres were shown to exhibit a remarkable dependency on alkali metal cations for their formation and stabilization.[229] There have been numerous studies of quadruplex and G-tetrad structures, covering aspects of formation, structure stabilization and therapeutic targeting,[209,230-247] and this is still an emerging area as evidenced by number of related publications this year.[157,206,224,248-257] Given the amount of scientific curiosity, it is surprising that the fundamental photophysics of these structures have not been investigated. We propose in this study to characterize the quadruplex structure of the human telomeric sequence by TRIR and study the effect of metal cation (both mono- and divalent) on the formation and dynamics of the resultant quadruplex scaffold.

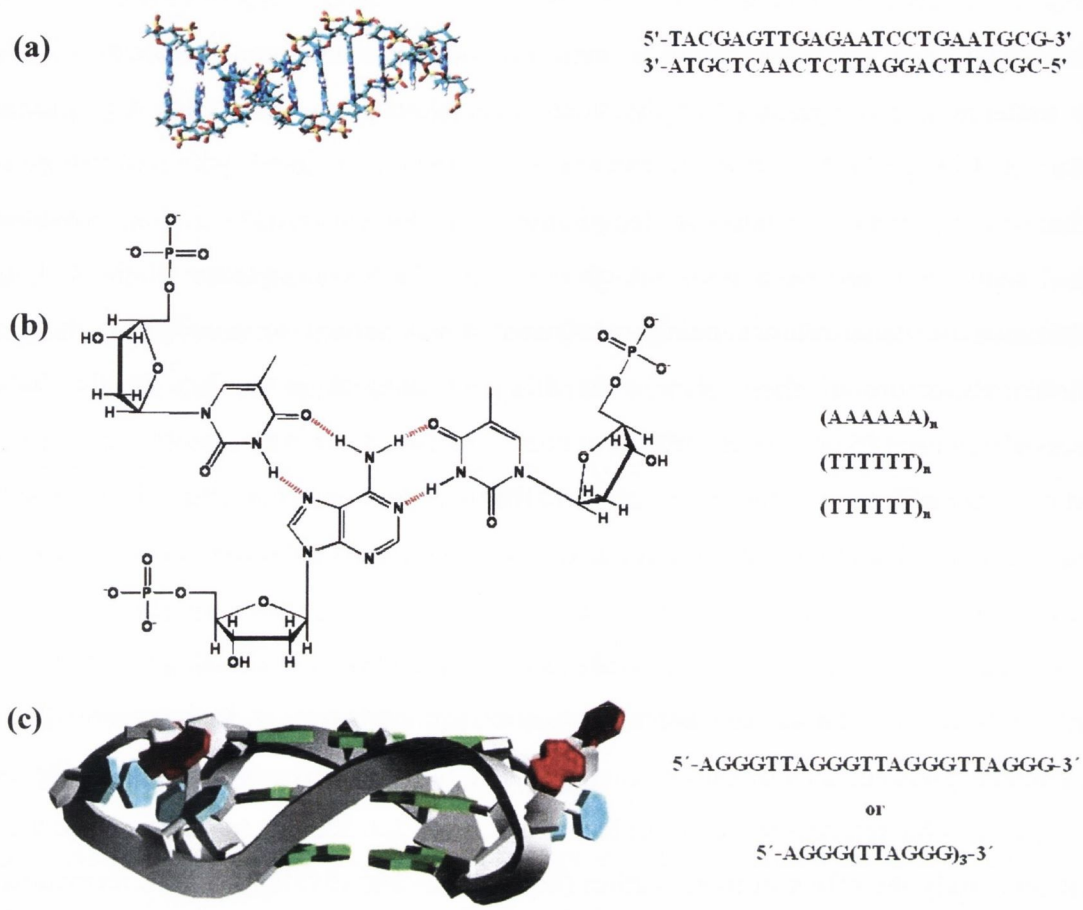

Scheme 5.1 (a) Mixed-base duplex DNA, (b) A:T:T triplex DNA and (c) human telomeric sequence quadruplex DNA. Quadruplex crystal structure taken from reference 250.

5.2 Mixed Base Single- and Double-Stranded Study

5.2.1 Motivation for this Study

This is a brief study of non-hairpinning short oligonucleotide strands in both single- and double-stranded form. To date, all photophysical DNA studies in the literature of oligo- or polynucleotide strands have focussed on simpler systems than genomic DNA. Most experimental studies have examined the homopolymers (i.e. polypurine or polypyrimidine)[86,124,129,132,136,150,175,191-193] in isolation and then possibly the hybridized product of the two strands, while some other studies have considered alternating duplex structures such as $[poly(dG\text{-}dC)]_2$ or $[poly(dA\text{-}dT)]_2$.[127,128,182,188] Computational efforts, also on similar systems, have endeavoured to predict or model the behaviour of excited

states produced following UV excitation.[173,174,176,181,258] The common and ultimate goal of both these practical and theoretical efforts is to gain understanding that may allow for inferences to be made about the biologically relevant genomic DNA. The more routinely employed fluorescence and transient absorption techniques do not allow for the same level of discrimination between the four different DNA bases that infrared spectroscopy does. Each nucleobase has its own particular IR fingerprint and it was envisaged that a study of mixed-base single- and double-stranded oligonucleotide DNA may provide information that would be more relevant and comparable to the actual processes that may occur with human exposure to UV radiation.

5.2.2 TRIR Fingerprint of the Individual DNA Bases

Figure 5.1 shows the TRIR profile of all the individual DNA nucleotides (10 mM in 50 mM potassium phosphate buffer, pH 7) in the spectral region of this study (1580-1723 cm^{-1}) when they are UV pumped in isolation, i.e. without any influence from neighbouring nucleobases. This shows the specific fingerprint for each of the bases and the contributions are summarized in the table below figure 5.1. With the exception of 5′-dCMP (chapter 2), the bases when studied in isolation (under neutral conditions as above) display a single relaxation behaviour on a picosecond timescale, assigned to cooling of the vibrationally excited ground state. When in a polymeric form, if communication occurs efficiently between the bases, one might expect collective relaxation behaviour rather than each of the bases relaxing independently.

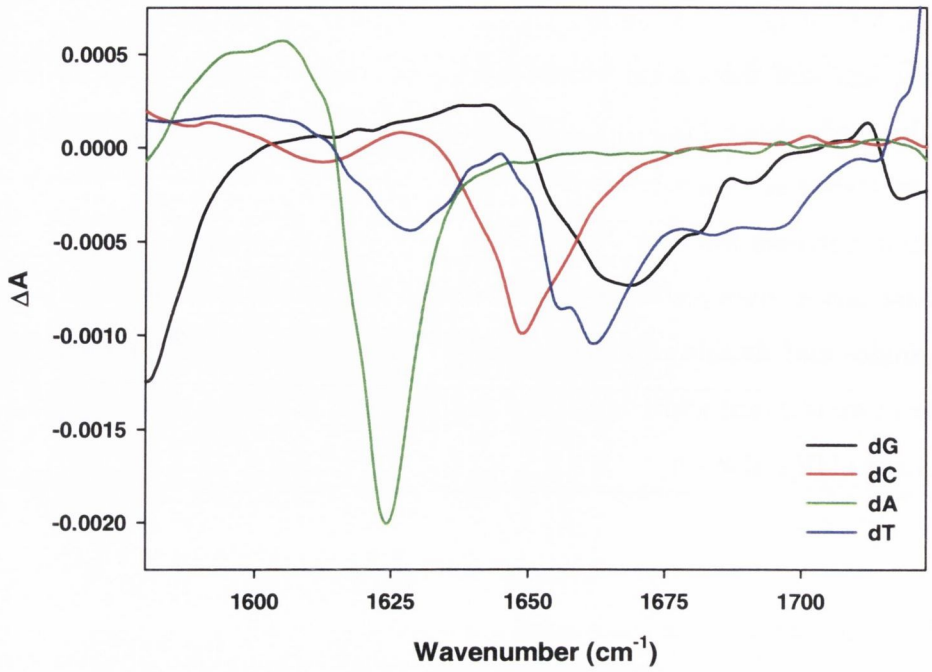

Contributions in 1580-1723 cm^{-1} window		
cm^{-1}	Ground state bleaching	Excited state absorption
1580-1600	dG	dA, dC(s), dT(s)
1600-1615	dC(s)	dA, dT(s)
1615-1635	dA, dT	dG(s), dC(s)
1635-1655	dC, dT(s)	dG
1655-1680	dT, dG, dC(s)	-
1680-1723	dT, dG	-
s = small		

Figure 5.1 ps-TRIR band positions of the mononucleotides (10 mM) in 50 mM potassium phosphate D_2O buffer (pH 7) at 2 ps for the spectral window (1580-1723 cm^{-1}) used in this mixed-base study.
Table summarizes the contributions in various regions of the spectrum.

5.2.3 Results

5.2.3.1 Single-stranded Mixed Base DNA – 5′-TACGAGTTGAGAATCCTGAATGCG-3′ (ODN 1)

The ps-TRIR difference spectrum following UV excitation of the first of two complementary non-hairpinning oligonucleotide strands 5′-TACGAGTTGAGAATCCTGAATGCG-3′ in buffered D_2O solution (pH 7) is shown in figure 5.2. Depletion bands are discernible at 1620, 1642 and 1669 cm^{-1} comprising of contributions from both ring vibration and carbonyl stretching frequencies from all the bases, as discussed earlier. The bleaching band centred at 1620 cm^{-1} is primarily adenine (ring vibration) and thymine (also ring vibration) modes. The higher wavenumber section (1640-1720 cm^{-1}) of the spectrum contains a mixture of four carbonyl stretching frequencies from the cytosine (1), thymine (2) and guanine (1) moieties. The complexity of this spectrum will be discussed later. There is also a broad transient feature (1580-1615 cm^{-1}) in the spectrum that if composed of the individual mononucleotide spectra given earlier, contains excited state absorptions from all the bases, but primarily from the adenine moiety.

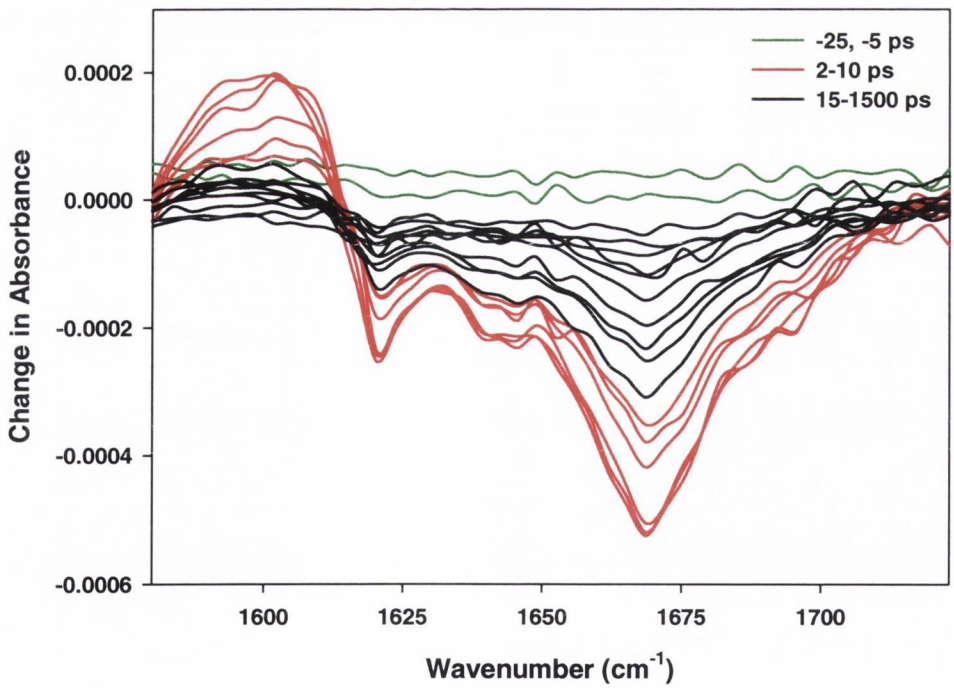

Figure 5.2 ps-TRIR of 5 mM 5′-TACGAGTTGAGAATCCTGAATGCG-3′ in 50 mM potassium phosphate D_2O buffer (pH 7). Delays are at -25, -5 (green), 2, 3, 4, 5.5, 7.5, 10 (red), 15, 20, 35, 50, 75, 100, 200, 500 and 1000 ps (black).

The kinetic behaviour of the oligonucleotide was analyzed (see appendix for analysis at all wavenumbers) and some of the analysis is presented in figure 5.3 below. The results reaffirm the complexity of the convoluted spectrum. In the case of the mononucleotides, relaxation of the electronically excited state is very rapid, in fact sub picosecond. All spectral changes occurring on a picosecond timescale are those of the vibrationally hot ground state (2-4 ps).[48] Following the ultrafast nonradiative internal conversion from the excited state, the immediate surroundings sustain a large temperature rise and a large population of ground state molecules residing in the higher vibrational states ($v > 1$). Spectral broadening and a redshift result. However, as presented in chapter 2, the case of 5′-dCMP is an exceptional one. An additional species having a transient absorption at 1574 cm^{-1}, assigned as the $^1n_N\pi^*$ dark state (33 ps), was detectable. As presented in chapters 3 and 4, stacking between adjacent bases introduces additional long-lived species. At 1596 cm^{-1} (centre of the transient band) lifetimes of 4.3 ± 0.9 ps (77%) and 64 ± 34 ps (23%) were found. As one might expect, there was great variation in the lifetimes obtained at the bleaching bands, with 1620 cm^{-1} giving 4.3 ± 2.2 ps (68%) and 39 ± 27 ps (32%) and 1669 cm^{-1} giving 7.2 ± 1.9 ps (61%) and 83 ± 27 ps (39%). The averaged lifetime values for the transient (1584-1596 cm^{-1}) were found to be 3.9 ± 0.9 ps (73%) and 68 ± 37 ps (32%), while the averaged lifetime of the bleaching bands (1620-1695 cm^{-1}) was found to be 5.2 ± 3.0 ps (52%) and 55 ± 23 ps (48%).

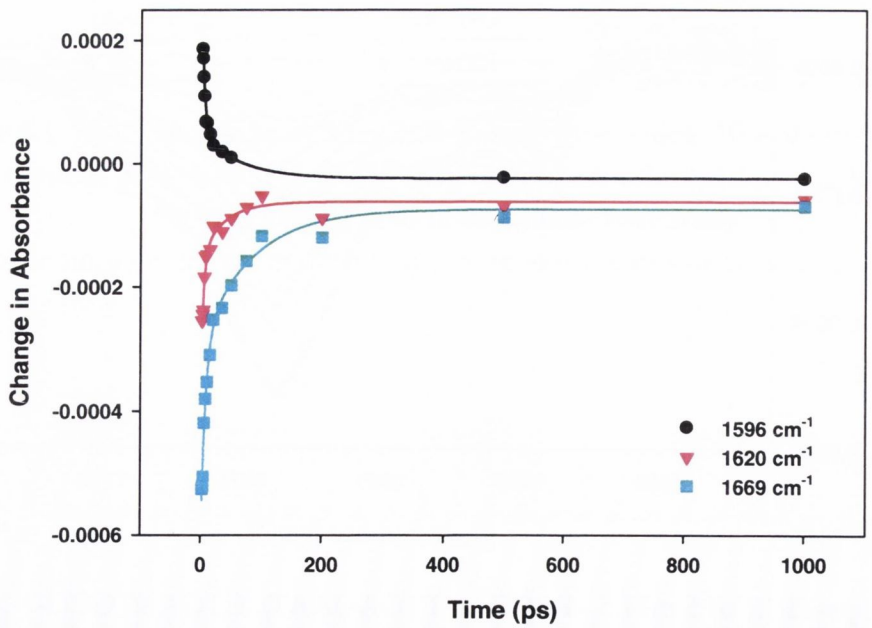

Figure 5.3 Kinetic analysis of 5 mM 5′-TACGAGTTGAGAATCCTGAATGCG-3′ in 50 mM potassium phosphate D_2O buffer (pH 7) at 1596, 1620 and 1669 cm^{-1}.

5.2.3.2 Single-Stranded Mixed Base DNA – 5′-CGCATTCAGGATTCTCAACTCGTA-3′ (ODN 2)

Figure 5.4 shows the ps-TRIR spectrum following UV excitation of the second non-hairpinning 24-mer oligonucleotide 5′-CGCATTCAGGATTCTCAACTCGTA-3′ in buffered D_2O solution (pH 7). The spectrum consists of ground state depletion bands centred at 1626 and 1670 cm^{-1} with a transient absorption dominating in the region 1590-1615 cm^{-1}. Again, due to the mixed nature of the oligonucleotide there are expected to be at least six different contributions from all the bases in this spectral window. The complexity of this system will also be considered later on. Noticeably, there was some imprinting from atmospheric water in the system, with the sharp feature at 1684 cm^{-1} being an example of this.

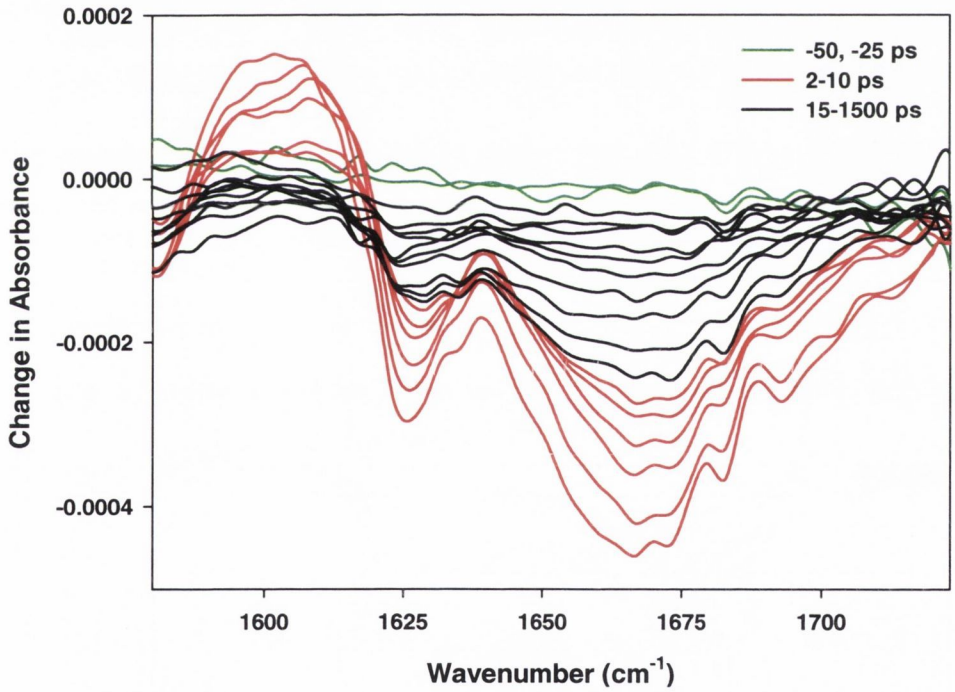

Figure 5.4 ps-TRIR of 5 mM 5′-CGCATTCAGGATTCTCAACTCGTA-3′ in 50 mM potassium phosphate D_2O buffer (pH 7). Delays are at -50, -25 (green), 2, 3, 4, 5.5, 7.5, 10 (red), 15, 20, 35, 50, 75, 100, 200, 500, 1000 and 1500 ps (black).

Representative kinetic behaviour is given in figure 5.5. For analysis at all wavelengths, the reader is referred to the appendix for chapter 5 (mixed base ODN study section). The transient absorption at 1599 cm^{-1} gave a good fit to a single exponential model, lifetime of 6.0 ± 0.7 ps (range of 2-200 ps), and no second lifetime component was discernible. At 1626 cm^{-1} lifetimes of 2.8 ± 0.8 ps (74%) and 64 ± 22 ps (26%) were found. At higher wavenumbers, 1670 cm^{-1}, the contribution from the long-lived state had increased, with the analysis indicating lifetimes of 3.7 ± 0.8 ps (60%) and 57 ± 9 ps (40%).

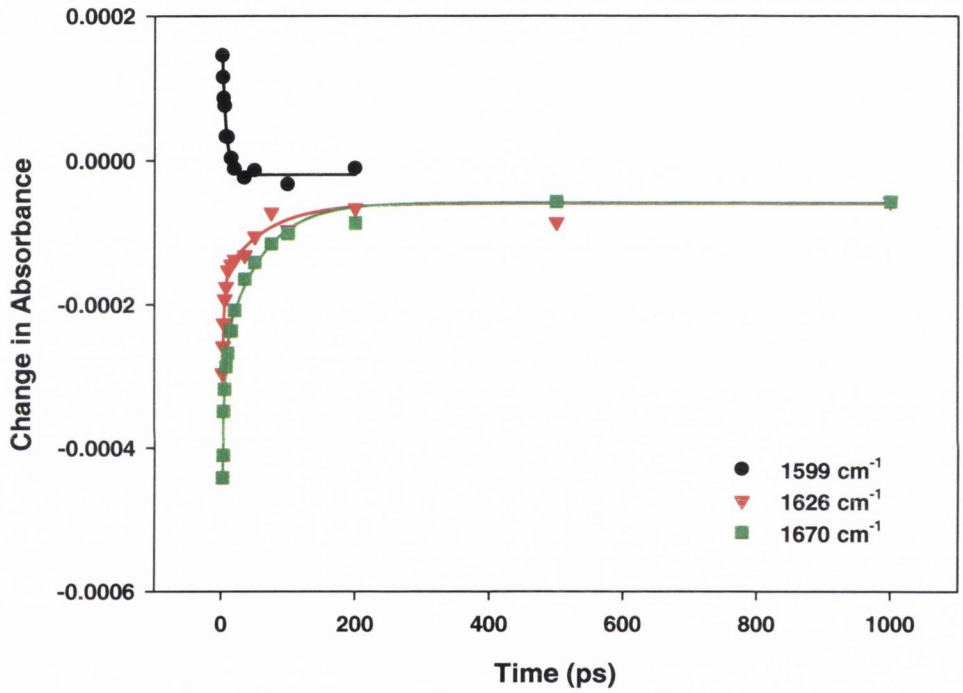

Figure 5.5 Kinetic analysis of 5 mM 5′-CGCATTCAGGATTCTCAACTCGTA-3′ in 50 mM potassium phosphate D_2O buffer (pH 7) at 1599, 1626 and 1680 cm^{-1}.

5.2.3.3 Double-Stranded Mixed Base DNA – 5′-TACGAGTTGAGAATCCTGAATGCG-3′ + 5′-CGCATTCAGGATTCTCAACTCGTA-3′ (ODN 1 + ODN 2)

The ps-TRIR of the double-stranded mixed base DNA after UV excitation is given in figure 5.6. Successful hybridization of the two complementary single strands was confirmed by the suppression of the adenine bleaching band at 1626 cm^{-1}, the improved resolution of the band at 1648 cm^{-1} and the shifting of the carbonyl bands to higher wavenumbers. The spectrum is characterized by bleaching bands at 1626, 1648, 1683 and 1696 cm^{-1} and a transient absorption in the region 1585-1620 cm^{-1}.

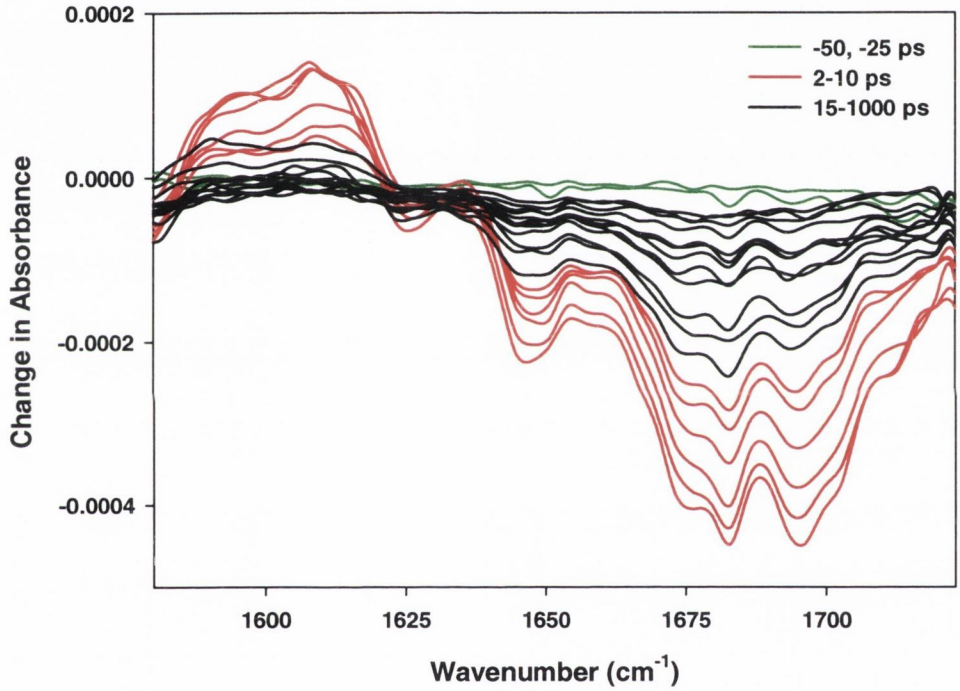

Figure 5.6 ps-TRIR of 5 mM 5′-TACGAGTTGAGAATCCTGAATGCG-3′ and 5′-CGCATTCAGGATTCTCAACTCGTA-3′ in 50 mM potassium phosphate D_2O buffer (pH 7). Delays are at -50, -25 (green), 2, 3, 4, 5.5, 7.5, 10 (red), 15, 20, 35, 50, 75, 100, 150, 200, 300, 500, 750 and 1000 ps (black).

Unsurprisingly, the kinetics of the system were found to be biphasic. A summary of the full analysis is provided in the appendix, with selected traces provided in figure 5.7 below. The kinetics were analyzed over all time delays in the experiment (2-1000 ps) and also over a shorter time range of 2-200 ps, with large variation being found for the long-lived species' lifetime depending on the range employed when fitting. For example, at

1696 cm^{-1} lifetimes of 6.5 ± 0.8 ps (73%) and 101 ± 23 ps (27%) were found using the full range of 2-1000 ps (fit shown in figure 5.7) and the same position gave lifetimes of 5.1 ± 0.8 ps (67%) and 38 ± 9 ps (33%) when a range of 2-200 ps was used. Clearly there is a large discrepancy in the value obtained for the long-lived species. Notwithstanding the fact that the shorter time range provides the lifetime with the smallest associated error, it is more likely that the fit over the entire range is indeed the more accurate fit. This results as the fitting procedure applied to the data relies heavily on the initial and final points in a data set when fitting the entire range. The 200 ps delay intensity appears to be far removed from the fit in the long time range (see all traces below in figure 5.7) so it is likely that when the short range is used, this 200 ps point (now the final point) has an overriding influence on the fit and hence the lifetime is underestimated. This trend was observed for all bleaching bands. At 1648 cm^{-1} lifetimes of 7.1 ± 1.7 ps (73%) and 83 ± 38 ps (27%) were found using the full range of 2-1000 ps (fit shown in figure 5.7). Using the shorter range of 2-200 ps, lifetimes of 2.8 ± 0.7 ps (58%) and 32 ± 6 ps (42%) were found.

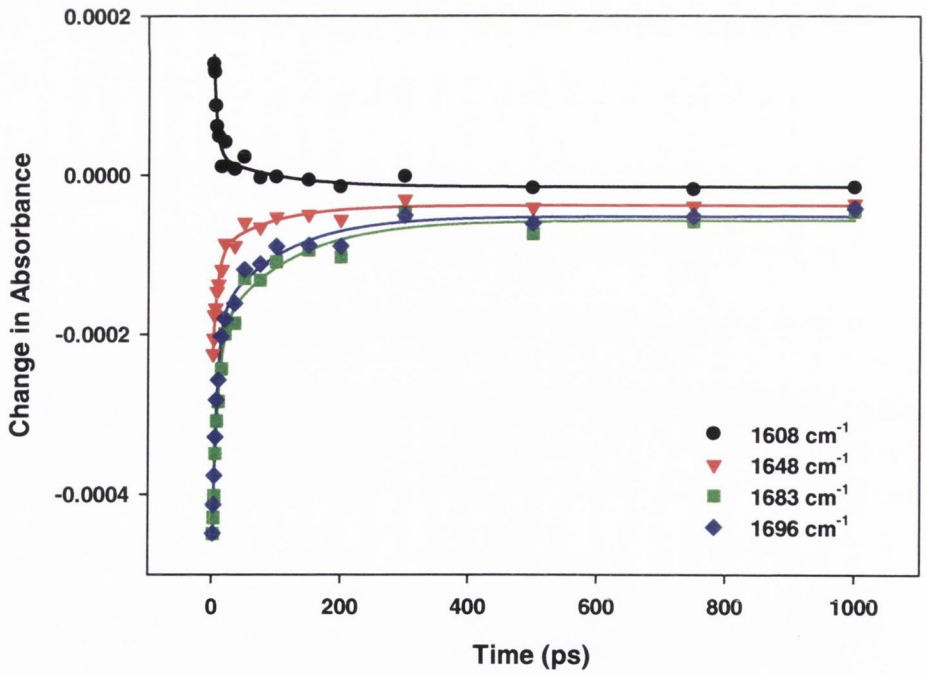

Figure 5.7 Kinetic analysis of 5 mM 5′-TACGAGTTGAGAATCCTGAATGCG-3′ and 5′-CGCATTCAGGATTCTCAACTCGTA-3′ in 50 mM potassium phosphate D_2O buffer (pH 7) at 1608, 1648, 1683 and 1696 cm^{-1}.

A small summary table of the main bands is given in table 5.1 below. The results indicate that the lifetimes for the short-lived species are slightly shorter in the single-stranded ODNs than in the double-stranded polymer. Interestingly, there is an increase in lifetimes with increasing wavenumbers, and this could mean enhanced decoupling of higher modes to lower ones. We have observed mode specific relaxation for guanine [131] and the work of Krummel *et al.* has shown that the ring and carbonyl stretching modes of guanine are not strongly coupled.[259] The trend could simply just be a consequence of there being a number of bands contributing in the high wavenumber region. This matter may in the future be clarified by high-end calculations, where model systems containing contributions from all the nucleobases are considered, although this is something that theoreticians have not yet attempted.

ODN	cm^{-1}	τ_1 (ps)	τ_2 (ps)	% (τ_1 : τ_2)
ODN 1	**1596**	**4.3** ± 0.9	**64** ± 34	**77:23**
	1620	**4.3** ± 2.2	**39** ± 27	**68:32**
	1669	**7.2** ± 1.9	**83** ± 27	**61:39**
ODN 2	**1599**	**6.0** ± 0.7	-	-
	1620	**2.8** ± 0.8	**64** ± 22	**74:26**
	1670	**3.7** ± 0.8	**57** ± 9	**60:40**
ODN 1 + ODN 2	**1608**	**5.3** ± 1.5	**97** ± 79	**82:18**
	1648	**7.1** ± 1.7	**83** ± 38	**73:27**
	1696	**6.5** ± 0.8	**101** ± 23	**73:27**

Table 5.1 Summary of the lifetimes at the main band positions for ODN 1, ODN 2 and ODN 1 + ODN 2.

Returning to the issue of the convoluted nature of all bands, these oligonucleotide systems represent a challenging arrangement to characterize. Upon duplex formation, several changes occurred in our spectral window. The adenine ring band at 1626 cm^{-1} became suppressed, the 1648 cm^{-1} band was found to be better resolved, and there was significant shifting of all other bands (including the transient band) to higher wavenumbers. These changes are illustrated in figure 5.8 where the 2 ps delay of both single-stranded oligos, the annealed duplex and a simple addition of the two constituent oligos in single-stranded form is compared.

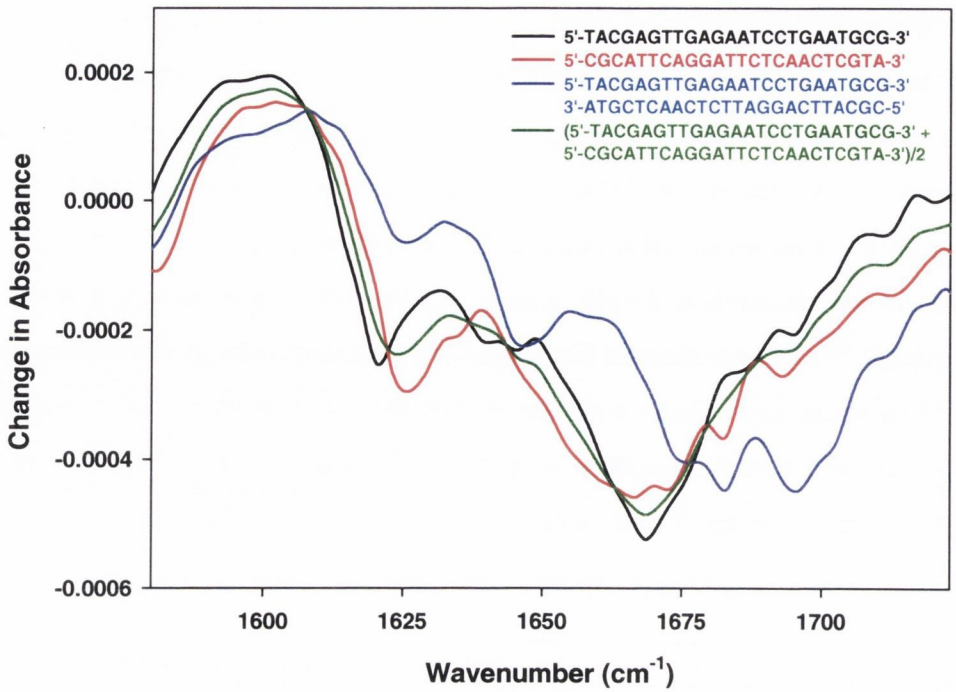

Figure 5.8 Comparison of the 2 ps delay of oligo 1 (black), oligo 2 (red), annealed oligo 1 and oligo 2 (blue) and (oligo 1 + oligo 2)/2 (green).

To appreciate the spectral differences between the 24-mer mixed base systems and their constituent parts, the percentage contribution from each base was calculated and the "convoluted" spectrum was calculated. The composition of 5′-TACGAGTTGAGAATCCTGAATGCG-3′ is dG - 29%, dC - 17%, dA - 29% and dT - 25%. The complementary oligo 5′-CGCATTCAGGATTCTCAACTCGTA-3′ is comprised of dG - 17%, dC - 29%, dA - 25%, and dT - 29%. Using these proportions the 2 ps delay of each of the mononucleotides was scaled and added together to generate a calculated spectrum (figure 5.9). This convoluted spectrum will therefore not take into account stacking interactions (in both the single- and double-stranded cases) and interbase hydrogen-bonding interactions in the case of the duplex. Such factors are expected to and indeed do, affect the observed spectra. The two most striking differences between the experimental and calculated spectra are that the adenine band at *ca.* 1626 cm^{-1} is much less intense in both the single- and double-stranded systems than the calculations would predict and also all other bands are shifted to higher frequency when in the oligomer relative to their mononucleotide counterparts. The degree of shift is greatest in the duplex case, as noted earlier, and presumably this is predominantly (but maybe not exclusively) due to the hydrogen-bonding in the system.

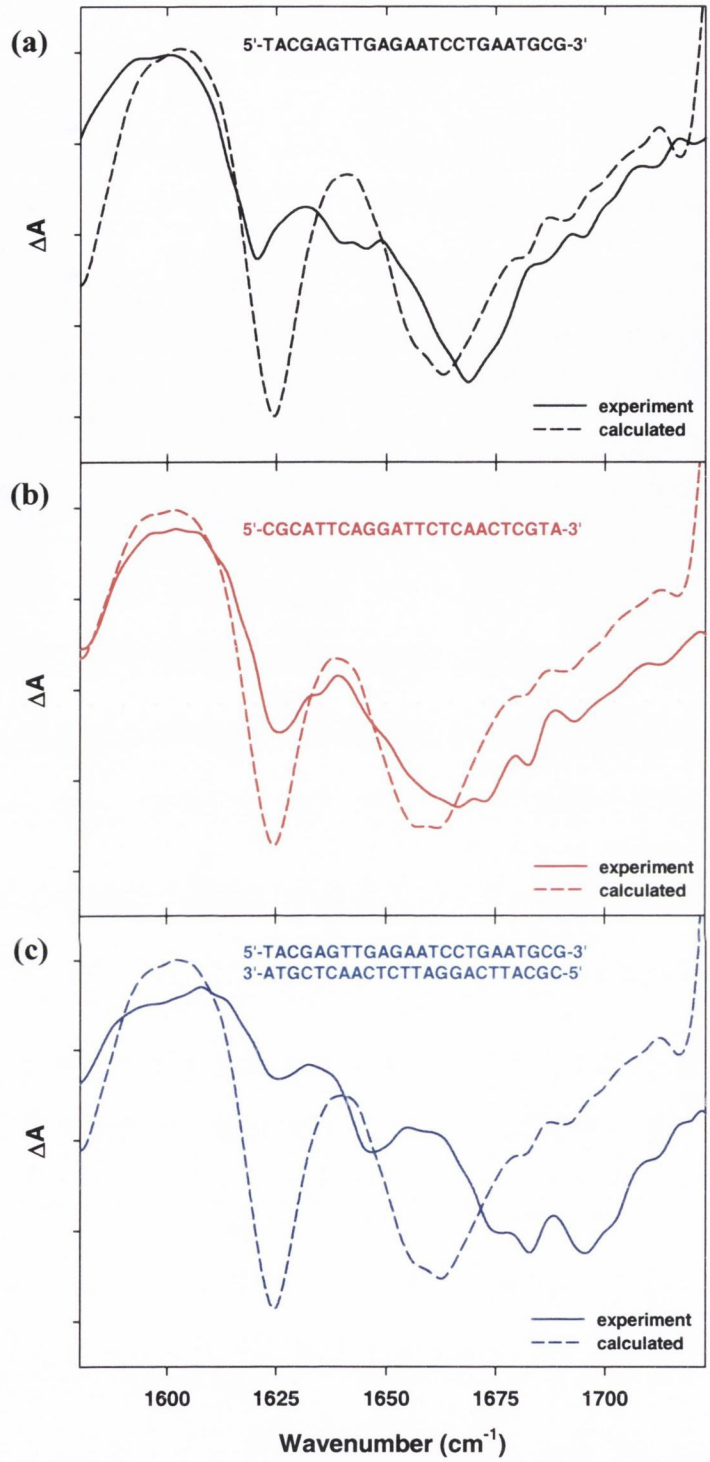

Figure 5.9 Experimental (solid lines) and calculated (dashed lines) TRIR spectra at 2 ps for the single- (a) and (b) and double-stranded (c) mixed-base oligonucleotides.

5.2.4 Discussion

This work represents the first study of the ultrafast relaxation processes in a mixed base oligonucleotide system by any spectroscopic technique. ps-TRIR, in principle, demonstrates tremendous potential to investigate base specific relaxation in mixed polymeric base systems, by virtue of the bases having their own specific infrared fingerprints. However, the region studied was a very congested one with considerable overlap from all four bases (at least above ~1630 cm^{-1}). For follow-up studies, focus on the lower wavenumber region where characteristic bands such as the cytosine $^1n_N\pi^*$ region (1570 cm^{-1}), cytosine ring vibrations (1507 and 1523 cm^{-1}) and guanine ring vibration (1567 and 1579 cm^{-1}) occur may be more useful in ascertaining if independent relaxation behaviour occurs in mixed-base strands (see appendix figure A5.1 for image of the full spectral region 1460-1723 cm^{-1} and table summarizing the contributions).

The results of this study for the single-stranded oligonucleotides indicate that there are two species involved in the ground state depletion recovery bands. The first, having a lifetime of 2-5 ps is assigned to the cooling of the vibrationally excited ground state. The second, having a lifetime of ~55 ps, is provisionally assigned to an electronic excited state. As this lifetime was found to be present across the whole spectrum, it is not possible to discriminate between the four bases so as to identify one or more of them as being responsible for the lifetime over another. In the duplex case, evidence for two processes was also found. A lifetime of 2-6 ps was found for the vibrational cooling in this case. The second process proved more problematic to characterize. As previously alluded to, significant variations were found for the lifetime of the long-lived species depending on the time range employed in the fitting procedure. For example, when analysis was carried out over the entire time range of the experiment (2-1000 ps) a lifetime of 98 ps was found, but when analyzed over a shorter timescale (2-200 ps) this lifetime would now seem to be closer to 37 ps. Without repetition of the experiment, it is difficult to establish the true lifetime of the second process. However, given that fitting over the entire range gave a good distribution of residuals, and the 200 ps delay almost appeared to be an outlier, it is more likely that the results from the entire range fitting are a better reflection of the long-lived state lifetime. A significant shortening of the long-lived species was not seen on going from single- to double-stranded, although the contribution from the long-lived state appeared to be less in the duplex case. In the literature, it has been

proposed that that relaxation rates are increased in duplex systems, due to the hydrogen-bonding facilitating faster relaxations.[85,125,182] Without repetition of the experiments on this system, we are at present unable to verify this hypothesis or provide an antithesis.

5.2.5 Conclusions

This study was an ambitious one as evidenced by the non-existence of literature in this area. As previously mentioned, all accounts of single- and double-stranded ultrafast relaxation studies in the literature have minimized the number of variables in the system by studying polypurine:polypyrimidine type systems. While all studies into DNA photophysics are useful, they do not concentrate on systems that are similar to genomic DNA. However, some rather fundamental points can be taken from this preliminary study: (i) Evidence for two relaxation processes occurring in both the single- and double-stranded systems was found. (ii) Hybridization of two complementary strands of mixed base nature was observed for the first time by TRIR (evidenced by shifting of band frequencies and modulation of band intensities). (iii) The very presence of any long-lived species in a mixed base system suggests that communication/energy delocalization occurs between the stacked bases – i.e. the bases do not behave as their individual components do when they are in a polymeric arrangement. (iv) Adenine ring vibrations are suppressed in the stacked single-stranded system and even more so in the stacked double-stranded conformation. (v) Spectra observed are not simply the sum of their parts – which confirms that additional processes such as stacking and electronic communication plays a role in regulating the relaxation dynamics.

5.3 Triplex Study

5.3.1 Introduction

The following study considers single strands of adenine and thymine, the double-stranded form, and finally the triple-stranded structures. The picosecond relaxation dynamics of all samples following UV excitation was probed. In order to study the effect (if any) of strand length, analogous studies were carried out for polynucleotide samples (~2,000 bases long) and short (18 bases long) oligonucleotides.

5.3.2 Results

5.3.2.1 poly(dA)

The ps-TRIR difference spectrum following UV excitation of poly(dA) in buffered D_2O solution (pH 7) is shown in figure 5.10. Depletion bands originating from ground state ring vibrations are present at 1569 and 1628 cm^{-1}. Broad transient features are found on the low wavenumber side of the parent bleaching band. Initial inspection of the spectrum reveals a similar picture to that for the stacked A systems dApdA and $(dA)_6$ studied in chapter 3. The recovery of the main bleaching band is unquestionably biphasic, while the transient bands appear to exhibit only a single short-lived component. However, upon analysis the transient bands were found to have a very small contribution from a long-lived state. At 1587 cm^{-1} (inset figure 5.10) fitting gave lifetimes of 2.8 ± 0.1 ps (96%) and 244 ± 130 ps (4%). The bleach recovery at 1630 cm^{-1} (inset figure 5.10) gave lifetimes of 7.2 ± 0.4 ps (82%) and 257 ± 47 ps (18%).

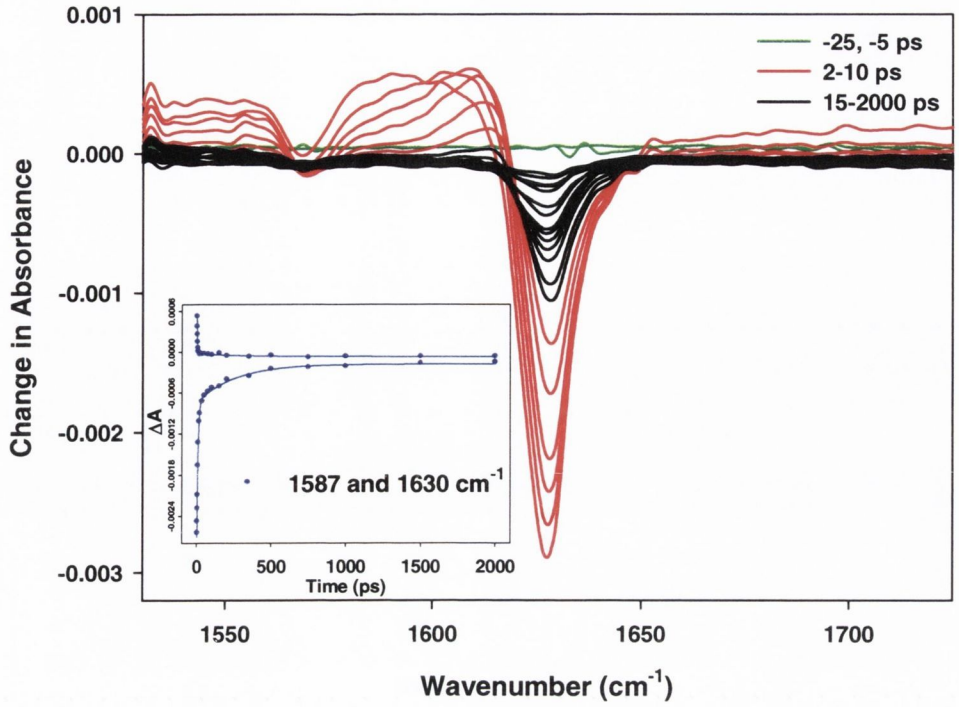

Figure 5.10 ps-TRIR of 10 mM poly(dA) in 50 mM potassium phosphate D_2O buffer (pH 7). Delays are at -25, -5 (green), 2, 3, 4, 5, 7, 10 (red), 15, 20, 35, 50, 75, 100, 150, 200, 350, 500, 750, 1000, 1500 and 2000 ps (black).
Inset: Kinetic analysis at 1587 and 1630 cm^{-1}.

The short lifetime is assigned to cooling of the vibrationally hot ground state, although it must be noted that in this polymeric structure the lifetime is significantly longer than observed in the nucleotide systems (2-4 ps). The origin of the long-lived state as discussed in chapter 3 for the stacked adenine systems is likely to be of an exciplex nature. Efforts were made to obtain an accurate value for the lifetime of the long-lived species employing both single pixel and area analysis. All fits are summarized in the appendix (section A5.1) together with an additional ps-TRIR spectrum that was recorded, specifically focussed on long time delays to achieve a better estimation for the long lived species' lifetime. Considering all of this in-depth analysis, we believe the lifetime of the long-lived species to be 150 ± 30 ps.

5.3.2.2 poly(dT)

Figure 5.11 shows the ps-TRIR spectrum of poly(dT). Bleaching bands occur at 1626, 1661 and 1693 cm^{-1} and correspond to in-plane ring vibrations, C_4O and C_2O carbonyl stretching frequencies respectively (see FTIR in appendix section A5.2). Weaker transient features were also present with a very broad transient centred at 1575 cm^{-1} and a sharp

transient at 1640 cm^{-1}. Our previous measurements on T-containing compounds had revealed that decomposition can be a problem with such systems. This was found to be the case with this sample as is evidenced by the UV and FTIR spectra recorded before and after the ps-TRIR experiments (provided in the appendix section A5.2). The spectrum shown below has poor signal-to-noise as it is only one cycle of all delays.

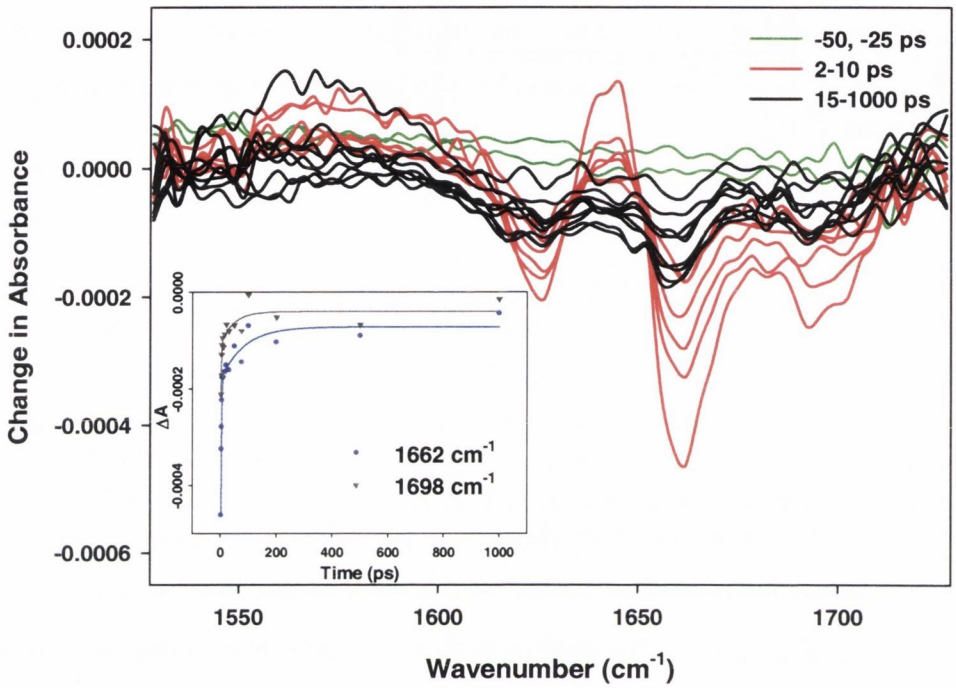

Figure 5.11 ps-TRIR of 10 mM poly(dT) in 50 mM potassium phosphate D_2O buffer (pH 7). Delays are at -50, -25 (green), 2, 3, 4, 5, 7, 10 (red), 15, 20, 30, 50, 75, 100, 200, 500 and 1000 ps (black). Inset: Kinetic analysis at 1662 and 1698 cm^{-1}.

Kinetic analysis of the two carbonyl bleaching bands is given in the inset of figure 5.11. At 1662 cm^{-1} lifetimes of 1.7 ± 0.3 ps (89%) and 83 ± 42 ps (11%) were obtained while at 1698 cm^{-1} fitting gave lifetimes of 1.6 ± 0.9 ps (85%) and 45 ± 41 ps (15%). These results were obtained when all delays from 2-1000 ps were included. However, when analysed using delays from 2-200 ps lifetimes of 1.7 ± 0.4 ps (90%) and 50 ± 40 ps (10%) at 1662 cm^{-1} and 1.9 ± 0.3 ps (90%) and 79 ± 73 ps (10%) at 1698 cm^{-1} were found. The short vibrational cooling component was found to ~ 2 ps in all analyses. However, quite a large variation in the values obtained for the long-lived species was found (see appendix section A5.2 for full analysis). An estimate of 50-90 ps would seem to be the most consistent lifetime range. Due to the problems caused by sample decomposition, and the resulting necessity to analyse over a single cycle a more accurate estimate cannot be given at this time.

5.3.2.3 poly(dA).poly(dT)

The ps-TRIR spectrum of poly(dA).poly(dT) in buffered D_2O solution (pH 7) is shown in figure 5.12. Bleaching bands at 1576 (A), 1623 (A), 1641 (T), 1664 (T) and 1697 (T) cm^{-1} correspond to the ground state absorptions (FTIR is provided in the appendix section A5.3). Weaker transient features are present at 1561, 1598, 1635, 1654 and 1680 cm^{-1}. In the duplex form the A-based ring vibration band at 1623 cm^{-1} is suppressed while the T-based C_2O band at 1697 cm^{-1} is enhanced with respect to their constituent polymers poly(dA) and poly(dT) respectively.

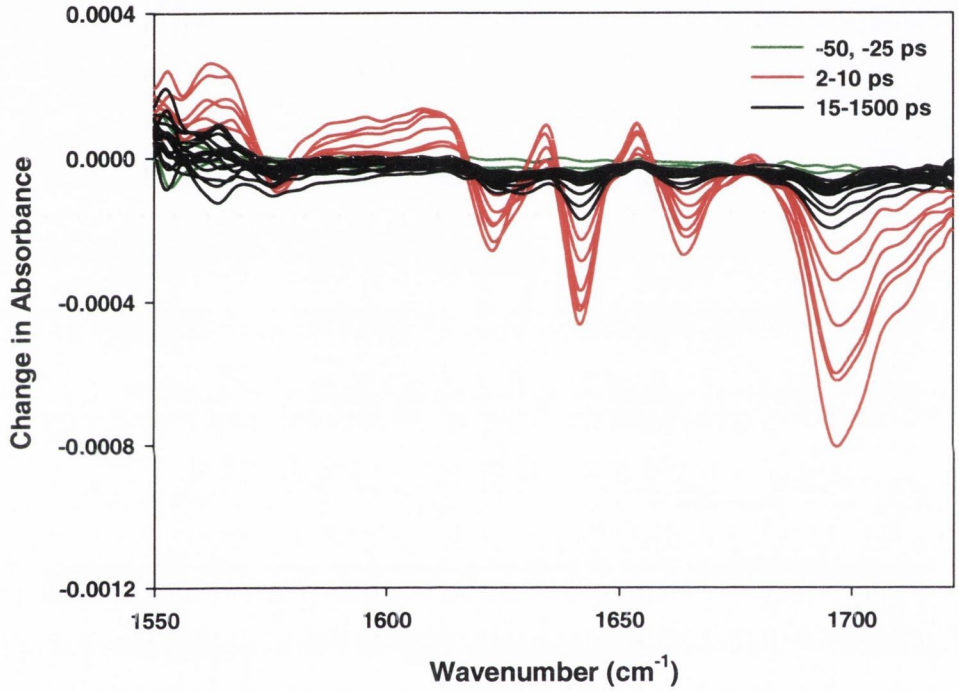

Figure 5.12 ps-TRIR of 6.1 mM poly(dA).poly(dT) in 50 mM potassium phosphate D_2O buffer (pH 7). Delays are at -50, -25 (green), 2, 3, 4, 5, 7, 10 (red), 15, 20, 35, 50, 75, 100, 150, 175, 200, 250, 300, 350, 500, 700, 1000 and 1500 ps (black).

The spectrum in figure 5.12 is the result of the accumulation of 4 cycles of all delays. However, as pointed out previously, T-containing compounds are known to be susceptible to degradation. The data is collected as a moving average over 4 cycles and the analysis software allows for accumulations of cycles to be viewed – i.e. the spectrum after cycle 1, cycle 1 + cycle 2, cycle 1 + cycle 2 + cycle 3 ...etc. The Feitan software (RAL developed software for the TRIR instrument) does not allow for individual cycles to be processed, i.e. cycle 3 independent of cycles 1 and 2. This may be important to see exactly when degradation or possible changes in secondary structure are occurring. Considering this, the individual cycles were calculated by working back from the accumulated cycles.

Figure 5.13 illustrates the differences between the 2 ps delay for the accumulated and individual cycles for the poly(dA).poly(dT) case. Comparison of the profile after the accumulation of two cycles with that of the 2nd cycle profile reveals that there was a major difference between the 1st and 2nd cycles, but because of the averaged nature of the accumulated spectrum this difference is not as striking. Interestingly, although there is variation in the T-based depletion and transient absorption bands, the A-based depletion band at 1623 cm^{-1} does not exhibit the same fluctuations. Also the broad transient band on the low wavenumber side of this A-based band shows little deviation. This is intriguing as this transient band is expected to have contributions from both A and T.

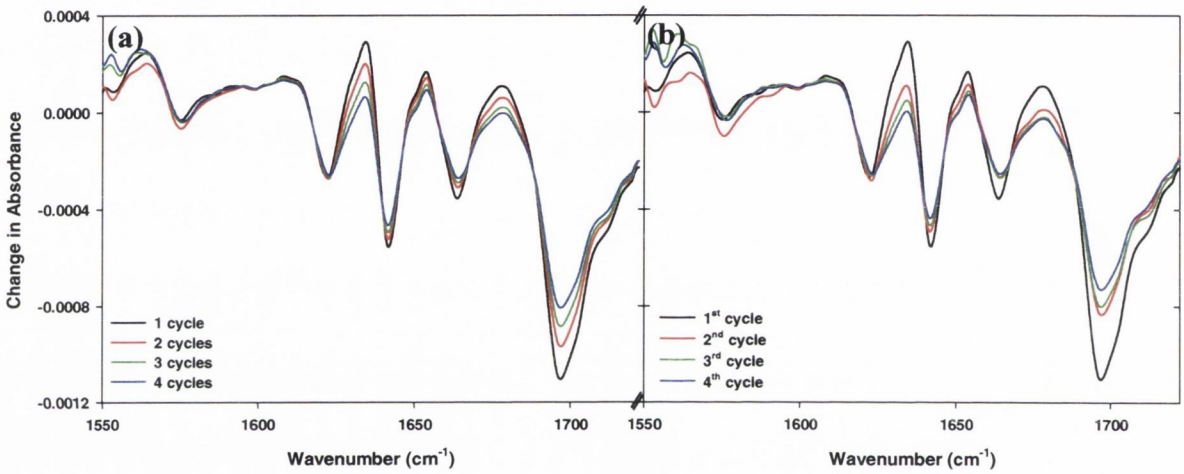

Figure 5.13 Comparison of the 2 ps delay for (a) accumulated and (b) individual cycles of 6.1 mM poly(dA).poly(dT) in 50 mM potassium phosphate D_2O buffer (pH 7) with 50 mM $MgCl_2$.

ps-TRIR spectra (i.e. all delays) for all the accumulated and individual cycles have been calculated and are provided in the appendix, figure A5.3.2. One might observe changes in absorption between cycles and attribute this effect to degradation of the thymine polymer. However, inspection of both the UV and FTIR spectra (appendix figure A5.3.1) recorded before and after the ps-TRIR experiment indicated that the UV absorption was unchanged while the FTIR had changed. The four main bands are not as well resolved, there is a slight shift (~2 cm^{-1}) of the thymine C_2O band at 1664 cm^{-1} (involved in the duplex hydrogen-bonding) and the adenine ring vibration band at 1623 cm^{-1} is now more intense. This would suggest a change in secondary structure - possibly that the helix has unwound to a certain extent with increasing laser exposure. As the UV absorption in this case is unchanged, and as this would be affected by differences in stacking (and not hydrogen-bonding) this unwinding could be a plausible explanation for the trend observed. This also

suggests that the association of the poly(dT) with the poly(dA) confers a stability to the polymer that is not present in the single-stranded form, where decomposition was extensive.

In light of the changing profiles between cycles the kinetics of the system were analysed at the 1st and 4th cycles (figure 5.14) in addition to that after 4 accumulated cycles (appendix section A5.3). Some of the results are shown in the figure below, where a biexponential function was fit to the data. However, in all cases there were large errors associated with the long-lived lifetime e.g. 1st cycle fit of the 1699 cm^{-1} bleach gave lifetimes of 3.4 ± 1.2 ps (80%) and 16 ± 13 ps (20%), and the 4th cycle fit at the same position gave lifetimes of 4.3 ± 0.4 ps (89%) and 34 ± 14 ps (11%). With the contribution from the long-lived state being approximately 20% and the lifetime of same being ~20 ps the data was also fit to a single exponential function (shown in appendix, section A5.3). However, we believe there to be two components present and it seems that owing to the long-lived species being relatively close to that of the short lifetime, the biexponential fitting function has some difficulty in calculating the second lifetime component with a reasonable associated error. What is abundantly clear from the kinetic profiles below is that the transient (1602 cm^{-1}) and A-based ring bleach at 1623 cm^{-1} do not change through the cycles whereas the T-based profiles at 1641 and 1699 cm^{-1} show significantly different signal intensities. Thymine photodegradation was not entirely unexpected, and it had been noted in previous TRIR measurements.[48]

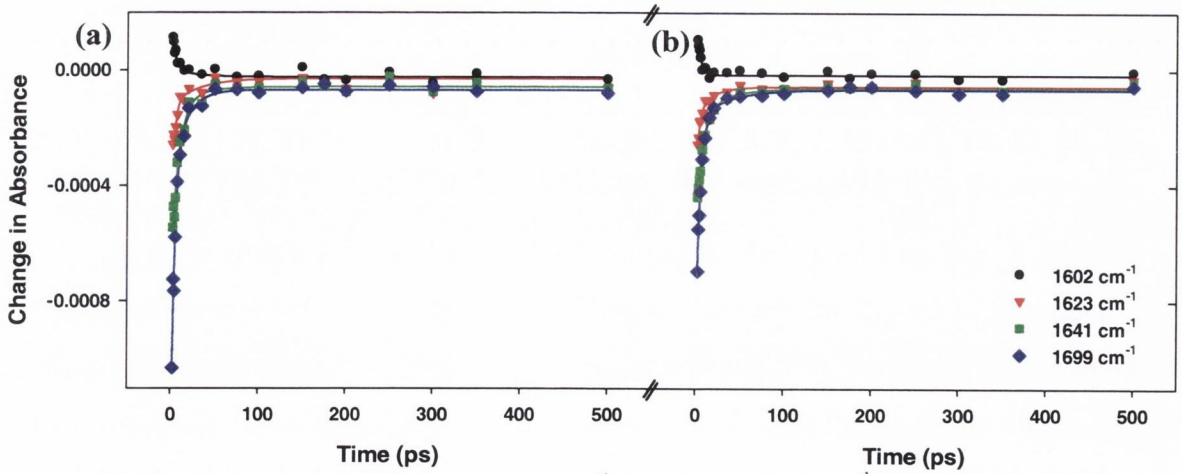

Figure 5.14 Kinetic analysis of (a) the 1st cycle and (b) the 4th cycle of 6.1 mM poly(dA).poly(dT) in 50 mM potassium phosphate D_2O buffer (pH 7) at 1602, 1623, 1641 and 1699 cm^{-1}.

5.3.2.4 poly(dA).poly(dT).poly(dT)

The ps-TRIR spectrum of poly(dA).poly(dT).poly(dT) over **one cycle** is shown in figure 5.15. Bleaching bands are present at 1568, 1615, 1624, 1634, 1655 and 1694 cm^{-1} with transient features at 1550, 1590, 1630, 1645 and 1667 cm^{-1}. The profile is markedly different from that of the duplex form indicating that the triplex had indeed formed. The FTIR spectrum is provided in the appendix figure A5.4.1(b). The C_2O depletion band at high wavenumber has become even more dominant compared to all the other bands, while the A-based band at 1624 cm^{-1} has become so suppressed that it is difficult to identify. This is a result of the engagement of the purine residue in Hoogsteen hydrogen bonding with the additional pyrimidine strand.[94]

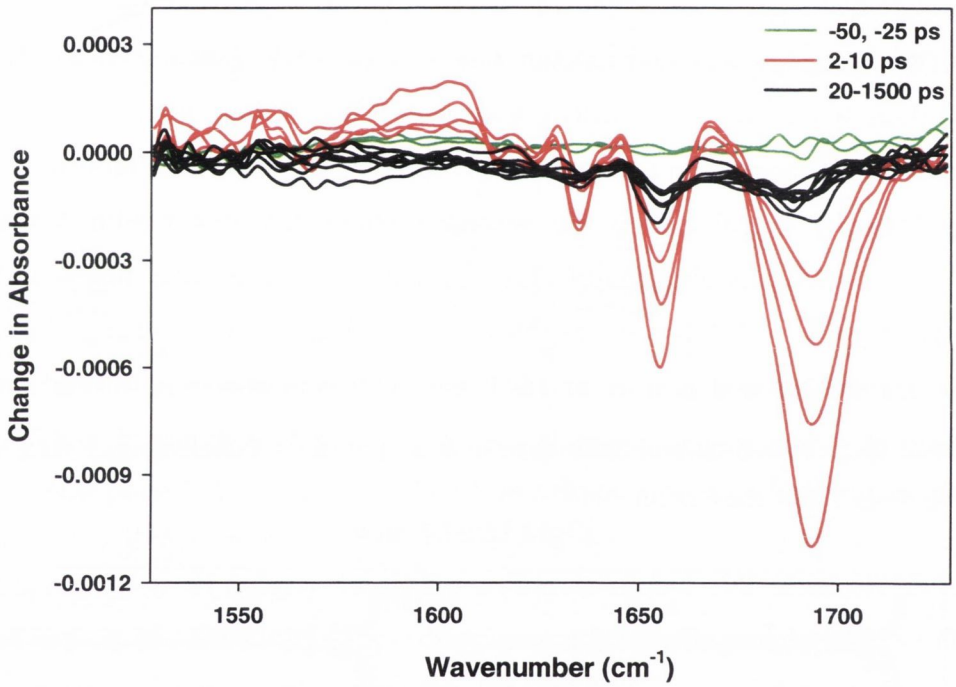

Figure 5.15 ps-TRIR of 6.1 mM poly(dA).poly(dT).poly(dT) in 50 mM potassium phosphate D_2O buffer (pH 7) with 250 mM NaCl (annealed). Delays are at -50, -25 (green), 2, 4, 7, 10 (red), 20, 50, 100, 150, 200, 500, 1000 and 1500 ps (black). Note: after 1 cycle only.

A further **four cycles** were recorded for the same sample and the accumulated result is presented below in figure 5.16. One can immediately recognize that the profile of the spectrum has evolved from that of the first cycle during the subsequent cycles. The adenine-based depletion bands at 1568 and 1624 cm^{-1} are now much more intense. Noticeably the thymine ring vibration at 1634 cm^{-1} has become more intense while the

thymine C_2O depletion band (which is not involved in the triplex hydrogen bonding) is now less intense.

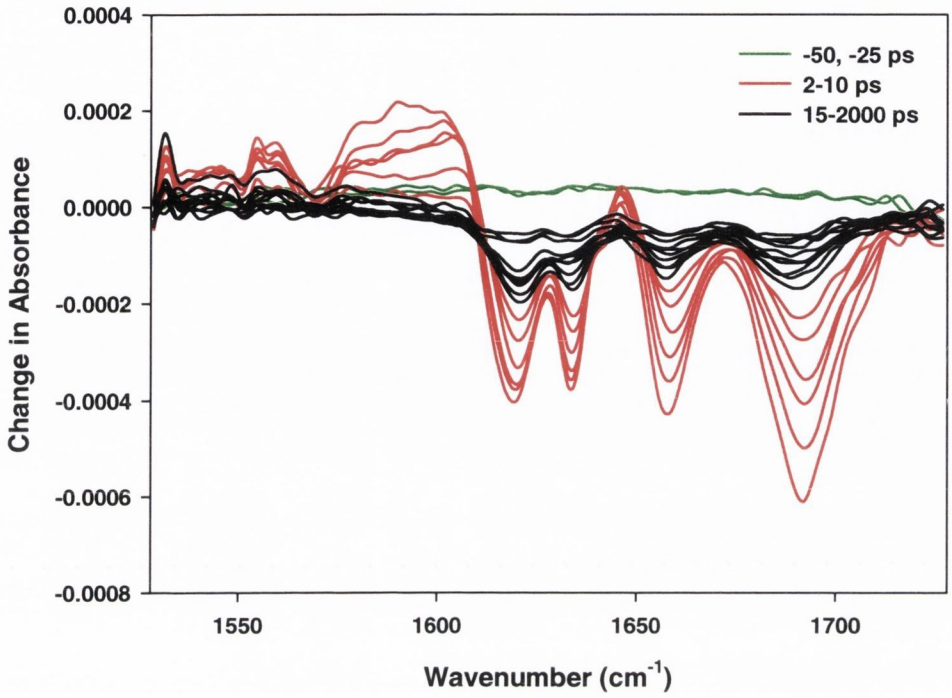

Figure 5.16 ps-TRIR of 6.1 mM poly(dA).poly(dT).poly(dT) in 50 mM potassium phosphate D_2O buffer (pH 7) with 250 mM NaCl (annealed). Delays are at -50, -25 (green), 2, 3, 4, 5, 7, 10 (red), 15, 20, 35, 50, 75, 100, 200, 500, 1000 and 2000 ps (black). Note: after 5 cycles.

To investigate when band intensity fluctuations were taking place in the accumulated spectrum the same procedure of examining the individual cycles used in the duplex case was applied. Figure 5.17 (a) shows the result of this process for the 2 ps delay, while figure 5.17 (b) shows the 2 ps delays for all the individual cycles recorded on the triplex sample i.e. the initial 1st cycle and the subsequent four cycles. Within the accumulated cycles, the results show that the greatest change in intensity of the 1623 cm^{-1} A band occurred between the 1st and 2nd cycle. The retreat of the high wavenumber T band was gradual between cycles with the other two remaining T bands not showing a lot of change through the cycles. Curiously there is no change in the transient centred at 1590 cm^{-1} even though the A ring vibration beside this transient is changing. When compared to the first cycle that was recorded one can see that the transient has shifted slightly and has a different shape. The 1623 cm^{-1} A band region appears to have had two bands initially when in the unperturbed triplex form and it appears that perhaps these bands have coalesced as further cycles were recorded. The FTIR (see appendix figure A5.4.1 (b)) does

show the presence of these two weak bands in the ground state. The T ring vibration at 1634 cm^{-1} showed a major change in signal intensity between the 1st and 2nd cycle as did the C_4O T stretch, and this band also underwent a shift from 1655 to 1659 cm^{-1}.

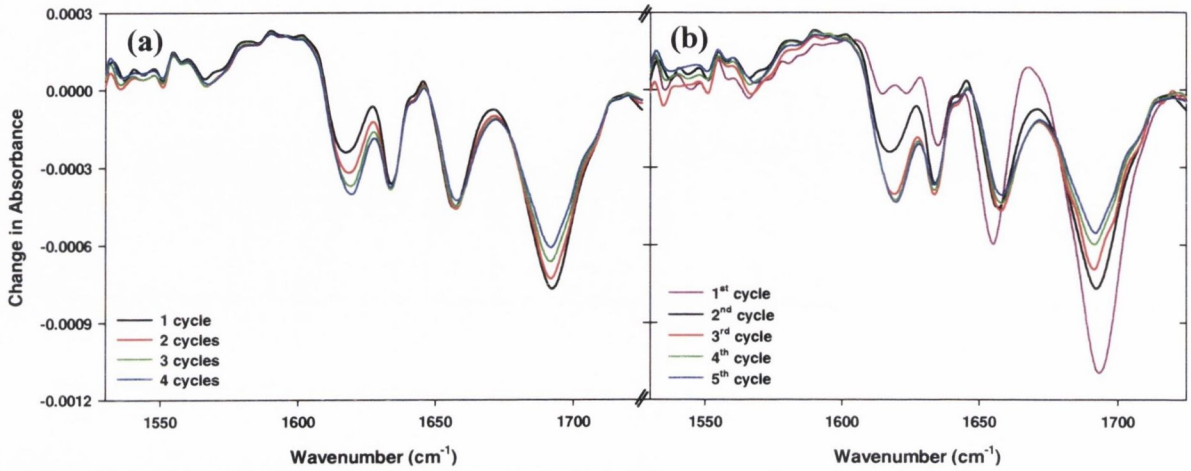

Figure 5.17 Comparison of the 2 ps delay for (a) accumulated and (b) individual cycles of 6.1 mM poly(dA).poly(dT).poly(dT) in 50 mM potassium phosphate D_2O buffer (pH 7) with 250 mM NaCl (annealed).

Figure 5.18 shows the evolution of all accumulated and separated spectra at all time delays. The profile of all delays clearly changes with increasing exposure to the laser beam but interestingly even though the triple stranded helix contains two thymine polynucleotides it appears from the UV and FTIR spectra recorded before and after the TRIR experiments that very little degradation/decomposition had occurred (see appendix figure A5.4.1). The FTIR would suggest that the secondary structure has changed as the intensity ratio of the bands in the ground state was found to be different after irradiation. The C_2O band intensity was found to decrease, while both the A and T ring vibrations band intensities were found to increase with respect to the C_4O band. The greatest shift in band position was seen for the thymine C_4O band – as was observed in the TRIR experiment. The C_4O band in thymine is involved in the hydrogen-bonding. There are of course two thymine strands contributing to this band in the triplex form. However, given the shift observed in this band from the initial and subsequent cycles, coupled with the simultaneous emergence of the adenine based band (this band is suppressed in the triplex form as it is Hoogsteen hydrogen-bonded to the second thymine residue)[94], this would suggest that the third thymine strand may be disassociating itself from the duplex. Notably, the presence/interaction of the poly(dT) with the poly(dA) appears to confer an extra stability on the normally somewhat fragile thymine residue.

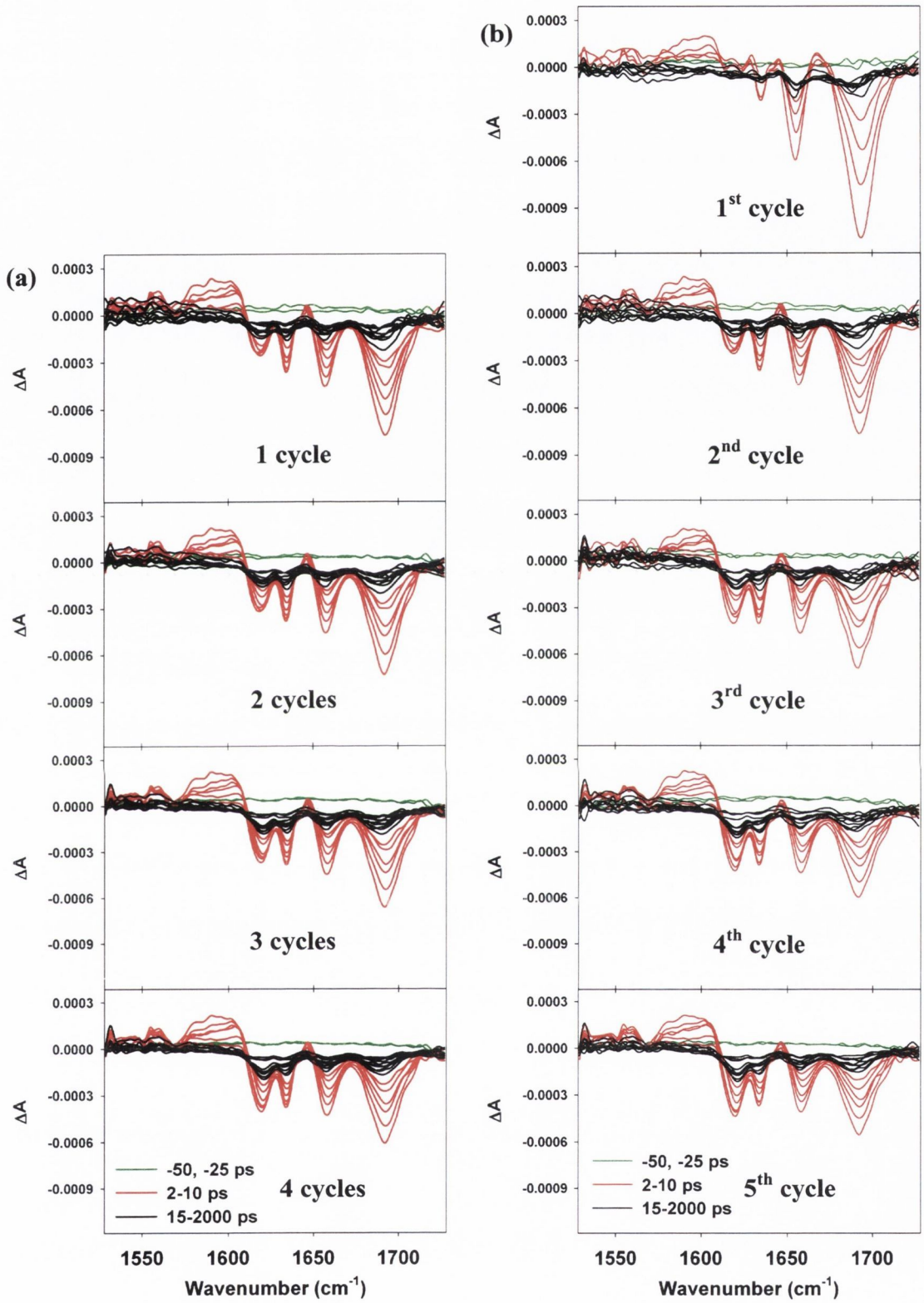

Figure 5.18 Accumulated (a) and separated (b) cycles of 6.1 mM poly(dA).poly(dT).poly(dT) in 50 mM potassium phosphate D_2O buffer (pH 7) with 250 mM NaCl (annealed).

Detailed kinetic analysis was carried out and is summarized in figure 5.19. All five cycles were analysed at the main band positions. Tabulated results for all fits are supplied in the appendix section A5.4. The results suggest that for the 1st cycle, i.e. in the triple-stranded form, the kinetics of the system are very fast and almost exclusively single exponential. Very little reliable evidence for a long-lived state was found, with the 1695 cm^{-1} band suggesting that there was a small (5%) contribution from a long-lived ~200 ps state (analysed by both single pixel and area analysis). The transient band fitted to a single lifetime (4.6 ± 0.8 ps) as did the 1633 cm^{-1} T ring vibration (4.3 ± 1.2 ps). Curiously, the 1659 cm^{-1} C_4O T band showed biexponential behaviour with lifetimes of 3.4 ± 0.3 ps (85%) and 53 ± 20 ps (15%). Due to the suppressed nature of the A band at 1620 cm^{-1} no kinetic information was gleaned from this bleach. Therefore, evidence of a long-lived A state could neither be confirmed nor denied.

Analysis of the subsequent cycles revealed a consistency between the lifetimes in these cycles. When a biexponential function was employed, the transient band showed a moderate contribution (~18%) from a long-lived species with a lifetime of ~20 ps. However, the error associated with this lifetime was similar to the value for the lifetime itself, and this would question the validity of the fit and suggest that there may not be a long-lived species present at all. The 1620 cm^{-1} A signal is now much stronger and a long-lived species with a lifetime of hundreds of picoseconds appeared to be present (~25% contribution), although there were large variations in the lifetime obtained in the different cycles. The thymine ring vibration at 1633 cm^{-1} was found to have a contribution of *ca.* 20% from a long-lived state with a lifetime of somewhere in the region of 100-200 ps. The two thymine carbonyl bands at 1659 cm^{-1} and 1695 cm^{-1} both displayed a ~13% contribution from a long-lived state having a lifetime of approximately 85 ps. These results (2nd to 5th cycles) confirm that a long-lived species is present after the initial triplex structure had changed.

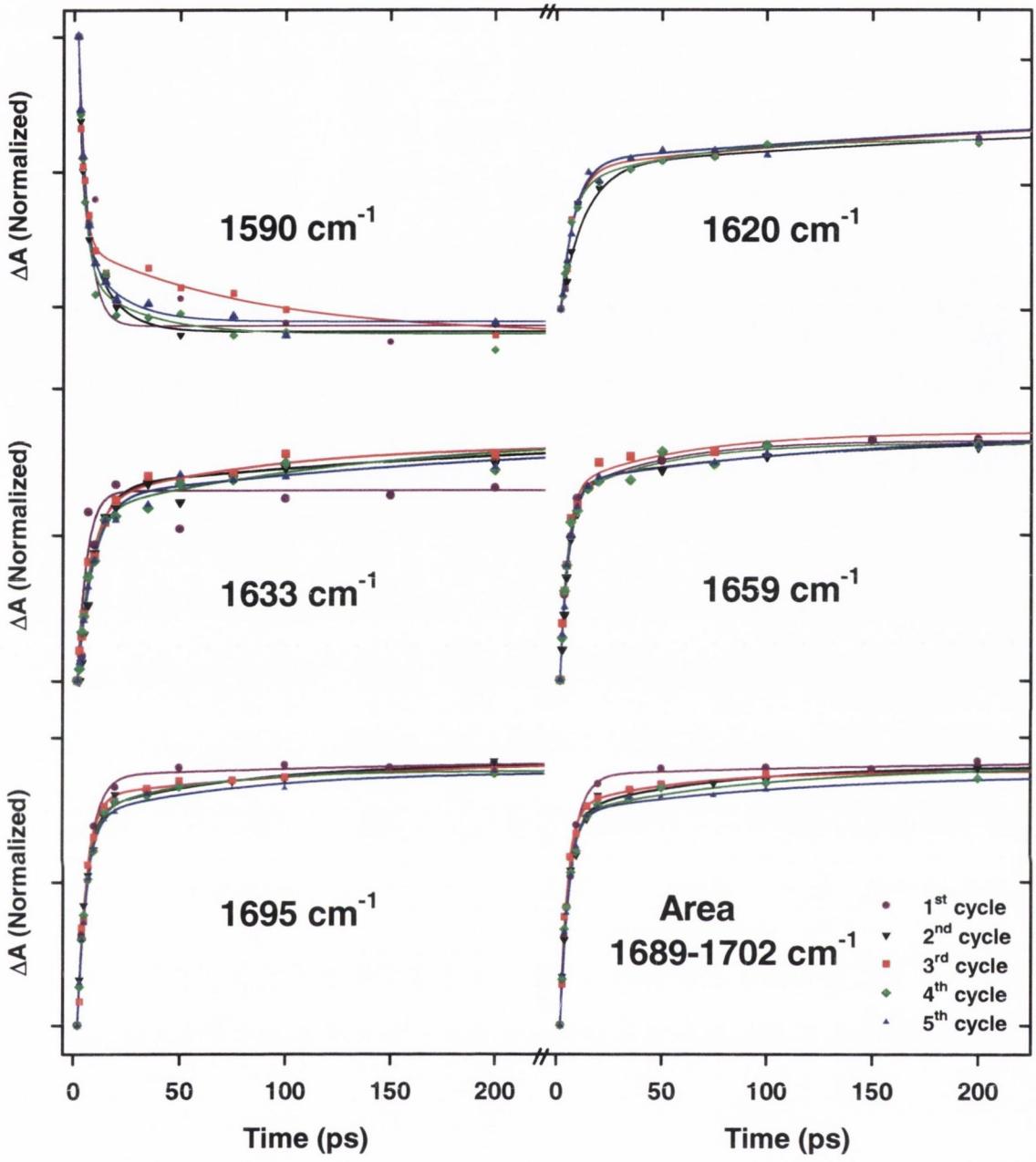

Figure 5.19 Kinetic analysis of the individual cycles of 6.1 mM poly(dA).poly(dT).poly(dT) in 50 mM potassium phosphate D_2O buffer (pH 7) with 250 mM NaCl (annealed) at 1590, 1620, 1633, 1659 and 1695 cm^{-1} and over the range 1689-1702 cm^{-1}.

Interestingly, whilst the kinetics of the system and the secondary structure of the sample were found to change with exposure, not all the band positions were affected to the same extent. The peak intensities at 2 and 20 ps of the transient absorption and bleaching bands over the 5 cycles are plotted in figure 5.20. At 2 ps the transient band signal (1575-1605 cm^{-1}) appeared to be unaltered from cycle to cycle, while all the bleaching

bands were found to undergo change. This would suggest that the transient absorption signal at 2 ps is not sensitive to the secondary structure of the helix. The adenine ring vibration and the thymine C_2O displayed the greatest signal variation. At 20 ps once again the transient band showed little variation and had almost fully decayed to the baseline – as evidenced by the short lifetime of the second species as discussed above (that is if indeed there is a second species, a point that it not fully resolved at this time). As eluded to previously, there is a significant difference in the adenine ring signal (1620 cm^{-1}) and interestingly at this time (20 ps) the thymine ring vibration (1633 cm^{-1}) is found to shift considerably (especially between the 1st and 2nd cycle).

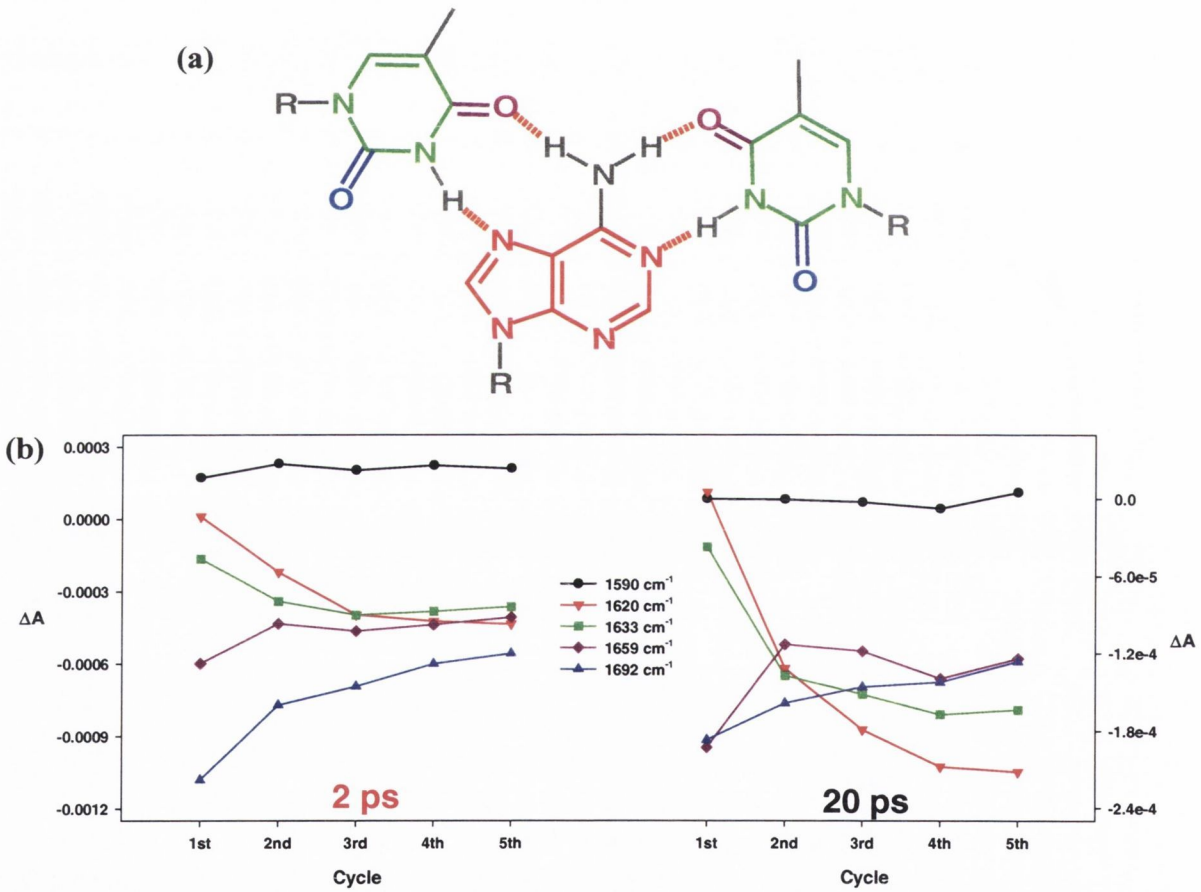

Figure 5.20 (a) Triplex hydrogen-bonding structure with colour coding indicating the vibration that corresponds to the band position in (b). (b) Intensity of the band positions 1590, 1620, 1633, 1659 and 1692 cm^{-1} through all five cycles at 2 and 20 ps.

The experiment was repeated on a fresh sample and an identical trend was observed, from the change in band structure of the ps-TRIR to the kinetic analysis and the FTIR and UV data. All spectra are supplied in the appendix, section A5.4.2. Intriguingly, the UV spectrum of this sample was recorded nine hours after the TRIR experiment and after this period the spectrum was almost identical to that before the experiment. In both the case presented here and the one in the appendix the UV spectra recorded directly after the TRIR measurement showed a slight decrease in absorption at 260 nm and a slight broadening beyond 300 nm. However, the spectrum recorded after nine hours resembles that of the initial UV scan. Therefore, we believe that sometime over the nine hour period, the structural change that had occurred during the experiment had reversed and the sample reverted back to the initial triplex structure. Unfortunately the FTIR was not recorded at this time and obviously this would be required to unequivocally confirm this triplex reformation hypothesis. Next, the oligonucleotide systems are considered.

5.3.2.5 $(dA)_{18}$

The ps-TRIR difference spectrum following UV excitation of $(dA)_{18}$ in buffered D_2O solution (pH 7) is shown in figure 5.21. The spectrum consists of bleaching bands at 1577 and 1629 cm^{-1} corresponding to the ground state ring vibrations and transient bands centred at 1550 and 1596 cm^{-1}. As with the polynucleotide described earlier and the stacked adenine systems described in chapter 3, there was clear evidence for a long-lived state in addition to a fast vibrational cooling process. At 1596 cm^{-1} (inset figure 5.21) fitting gave a single lifetime of 3.6 ± 0.2 ps. The bleach recovery at 1629 cm^{-1} (inset figure 5.21) gave lifetimes of 7.0 ± 0.4 ps (75%) and 515 ± 95 ps (25%). Analysis throughout the spectrum is summarized in the appendix, section A5.5.

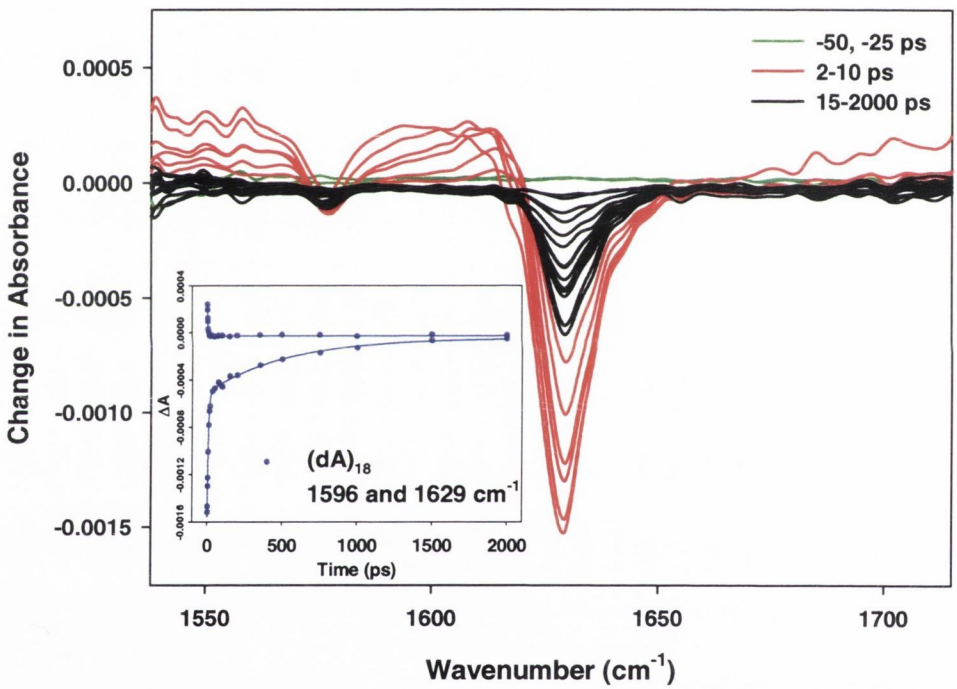

Figure 5.21 ps-TRIR of 5 mM $(dA)_{18}$ in 50 mM potassium phosphate D_2O buffer (pH 7). Delays are at -50, -25 (green), 2, 3, 4, 5, 7, 10 (red), 15, 20, 35, 50, 75, 100, 150, 200, 350, 500, 750, 1000, 1500 and 2000 ps (black). Inset: Kinetic analysis at 1596 and 1629 cm^{-1}.

The kinetics of this system implied that there was a 25% contribution from a long lived state having a lifetime of 500-600 ps. This lifetime is very similar to that found for dApdA (chapter 3), where the bleach recovery was found to have a long-lived component with a lifetime of 600-800 ps. It is however different to the 150 ps lifetime observed for the polymer earlier. The experiment was repeated on a fresh sample and this result suggested that there was a long-lived species (20%) having a lifetime of ~180 ps (see appendix

section, figure A5.5.3 for the ps-TRIR and tabular analysis). The discrepancy between these values will be addressed later in the discussion section.

5.3.2.6 $(dT)_{18}$

The ps-TRIR spectrum of $(dT)_{18}$ is given in figure 5.22. Bleaching bands occur at 1630, 1664 and 1700 cm^{-1} and correspond to in-plane ring vibrations, C_4O and C_2O carbonyl stretching frequencies respectively. A broad transient was present over the range 1550-1600 cm^{-1} and a sharp transient occurred at 1648 cm^{-1}.

As found in the case of the polymer sample there was evidence of decomposition from the UV and FTIR spectra (see appendix figure A5.6.1) recorded after the experiment. Therefore, the kinetic analysis was carried out on the 1st cycle, some of which is shown in the inset of figure 5.22. Both the transient decay and ground state depletion recovery obeyed single exponential behaviour with a lifetime of 3.0 ± 0.9 (at 1593 cm^{-1}) and 3.9 ± 1.2 ps (at 1664 cm^{-1}) respectively. A comparison of the 2 ps delay for accumulated and individual cycles is also provided in the appendix and this showed that the majority of change in the bands occurred between the 1st and 2nd cycles but once again the peak height of the broad transient was virtually unaffected.

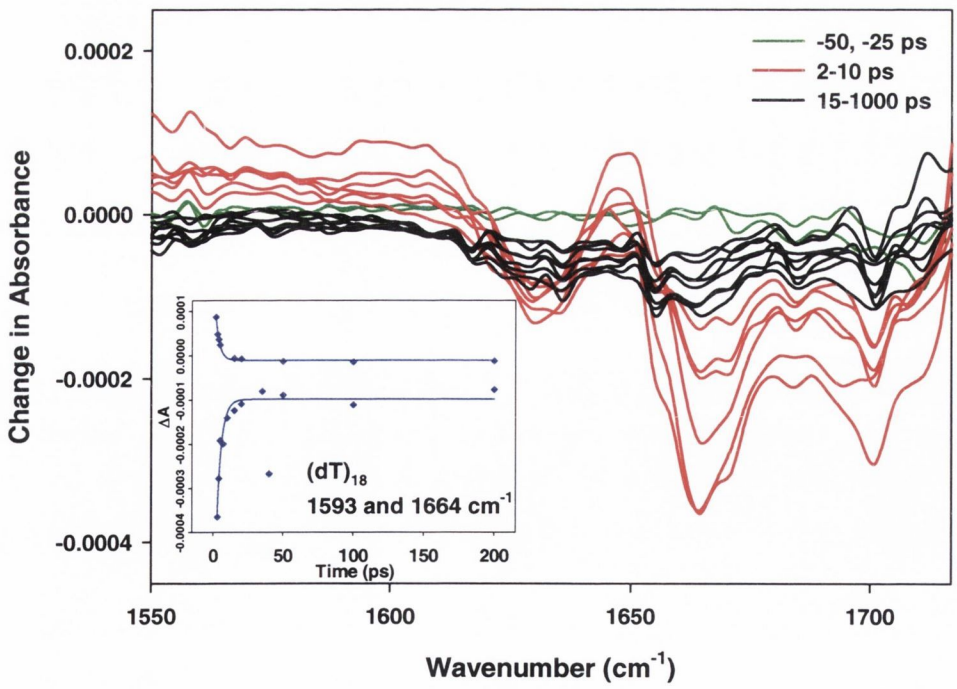

Figure 5.22 ps-TRIR of 5 mM $(dT)_{18}$ in 50 mM potassium phosphate D_2O buffer (pH 7). Delays are at -50, -25 (green), 2, 3, 4, 5, 7, 10 (red), 15, 20, 35, 50, 100, 200, 500 and 1000 ps (black). Inset: Kinetic analysis at 1593 and 1664 cm^{-1}.

5.3.2.7 $(dA)_{18}.(dT)_{18}$

Next the ps-TRIR spectrum of the duplex $(dA)_{18}.(dT)_{18}$ in buffered D_2O solution (pH 7) was recorded and is presented in figure 5.23. Bleaching bands found at 1576 (A), 1623 (A), 1642 (T), 1664 (T) and 1699 (T) cm^{-1} correspond to the ground state absorptions. Weaker transient features are found at 1561, 1599, 1634, 1653 and 1678 cm^{-1}. As for the case of the polymers (figure 5.13) the A-based ring vibration band at 1623 cm^{-1} was suppressed in the duplex form, while the signal of the T-based C_2O band at 1699 cm^{-1} gave a stronger signal, with respect to their constituent oligonucleotides $(dA)_{18}$ and $(dT)_{18}$ respectively.

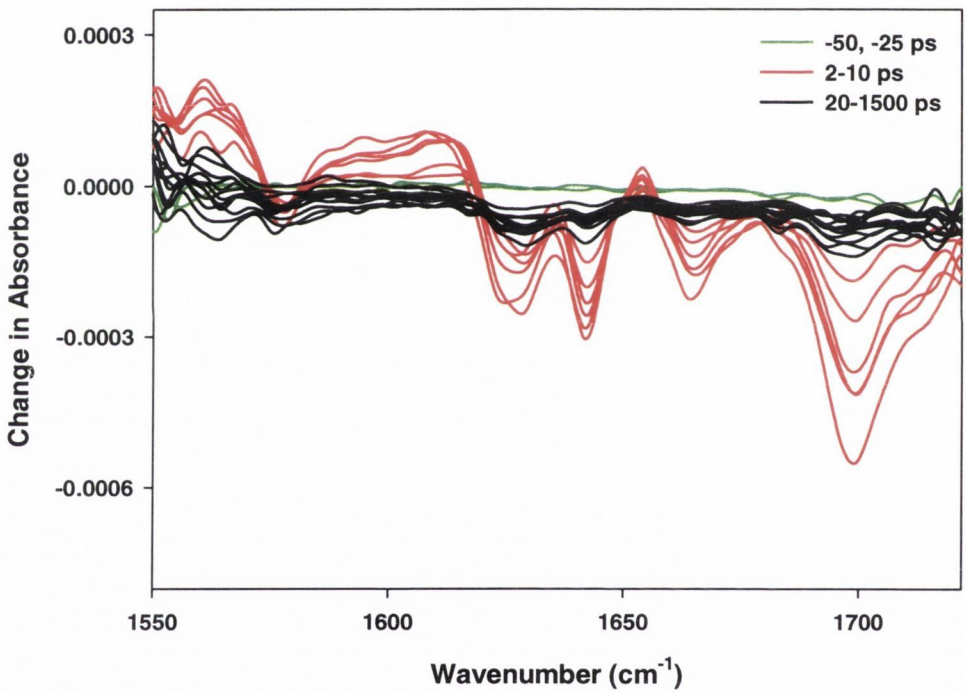

Figure 5.23 ps-TRIR of 5 mM $(dA)_{18}.(dT)_{18}$ in 50 mM potassium phosphate D_2O buffer (pH 7) with 50 mM $MgCl_2$. Delays are at -50, -25 (green), 2, 3, 4, 5, 7, 10 (red), 15, 20, 35, 50, 75, 100, 200, 350, 500, 700, 1000 and 1500 ps (black).

As in the analogous polymer duplex case the spectrum of the sample was found to change over the course of the four cycles that were recorded. Figure 5.24 demonstrates the differences between the 2 ps delay for the accumulated and individual cycles for the $(dA)_{18}.(dT)_{18}$ sample. The separated individual cycles confirmed that the major differences

in signal intensities occurred between the 1st and 2nd cycle. Significant changes arose in all bands throughout the cycles except for the 1642 cm^{-1} thymine ring vibration and the broad transient centred at 1599 cm^{-1}. In the analogous polymer study, it was the A-based band at 1623 cm^{-1} and the broad transient that remained relatively unaffected with increasing cycles. Full ps-TRIR spectra for all the accumulated and individual cycles have been calculated and are provided in the appendix figure A.5.7.2. As observed in the polymer case, the UV spectra recorded before and after the experiment suggested that little degradation had occurred. The FTIR spectra would suggest that a change in secondary structure had occurred, as the ratio of the bands had been altered (appendix figure A.5.7.1). A possible explanation for this could be helical unwinding. Noticeably, as for the polymer case, the presence of the adenine strand appears to lessen the damage that the thymine oligonucleotide suffered.

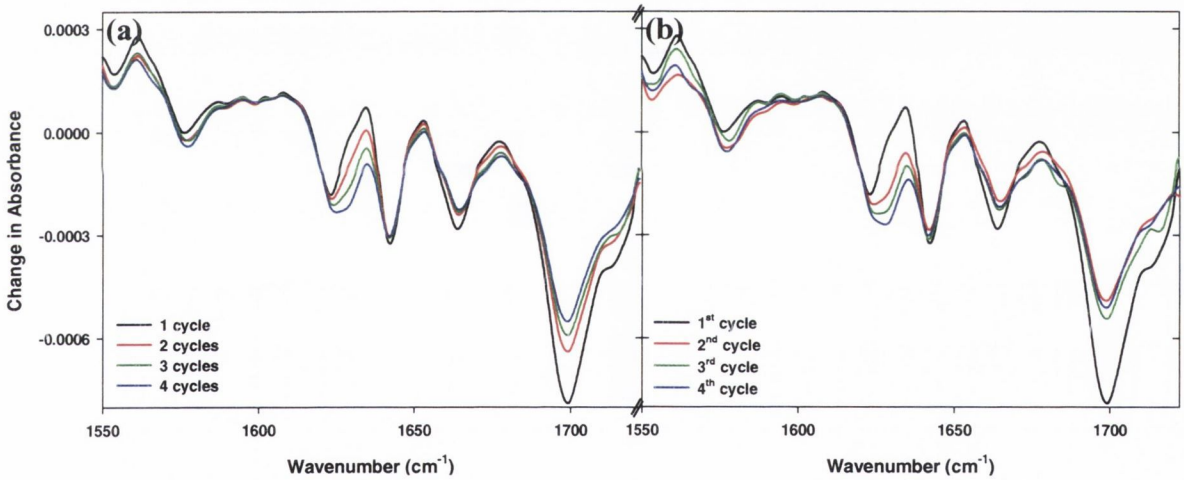

Figure 5.24 Comparison of the 2 ps delay for (a) accumulated and (b) individual cycles of 5 mM $(dA)_{18}.(dT)_{18}$ in 50 mM potassium phosphate D_2O buffer (pH 7) with 50 mM $MgCl_2$.

As the band structure was found to change with increasing cycles the kinetics of the system were examined after the 1st cycle and the decay profiles at the main transient and bleaching bands are shown below in figure 5.25. Tabular analyses for the first and fourth cycles are provided in the appendix, section A5.7. Both single- and biexponential models were used to analyze the data. From this, it was evident that there were indeed two processes occurring. For example the bleaching band at 1699 cm^{-1} (shown in figure 5.25) revealed lifetimes of 4.4 ± 1.5 ps (86%) and 30 ± 21 ps (14%). There were in most cases large errors associated with the fitted lifetimes and this would appear to be a consequence of fitting a single cycle, where the occurrence of any noise or a poor signal can skew the result in a way that an accumulation of many cycles would not.

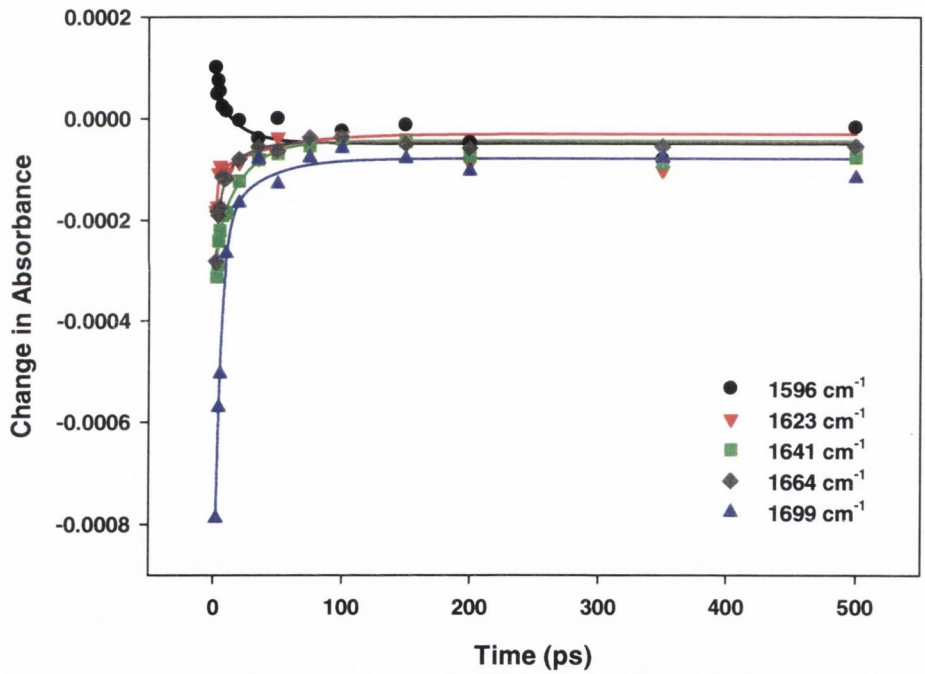

Figure 5.25 Kinetic analysis of the 1st cycle of 5 mM $(dA)_{18}.(dT)_{18}$ in 50 mM potassium phosphate D_2O buffer (pH 7) with 50 mM $MgCl_2$ at 1596, 1623, 1641, 1664 and 1699 cm^{-1}.

5.3.2.8 $(dA)_{18}.(dT)_{18}.(dT)_{18}$

The ps-TRIR spectrum of the triplex form for the oligonucleotides $(dA)_{18}.(dT)_{18}.(dT)_{18}$ in buffered D_2O solution (pH 7) with $MgCl_2$ is shown in figure 5.26. Bleaching bands are present at 1573, 1632, 1642, 1660 and 1696 cm^{-1} with transient features at 1561, 1598, 1636, 1647 and 1673 cm^{-1}. The profile is obviously different from that of the double-stranded structure signifying that the triple-stranded structure had indeed formed. As witnessed in the polymer case, the thymine C_2O depletion band at high wavenumber is the dominant band in the spectrum and the A-based band at 1624 cm^{-1} has practically disappeared in this case. This suppression has been identified before as arising when the purine residue Hoogsteen hydrogen bonds to the second thymine residue that resides in the major groove of the duplex helix.[94] This system displayed excellent reversibility.

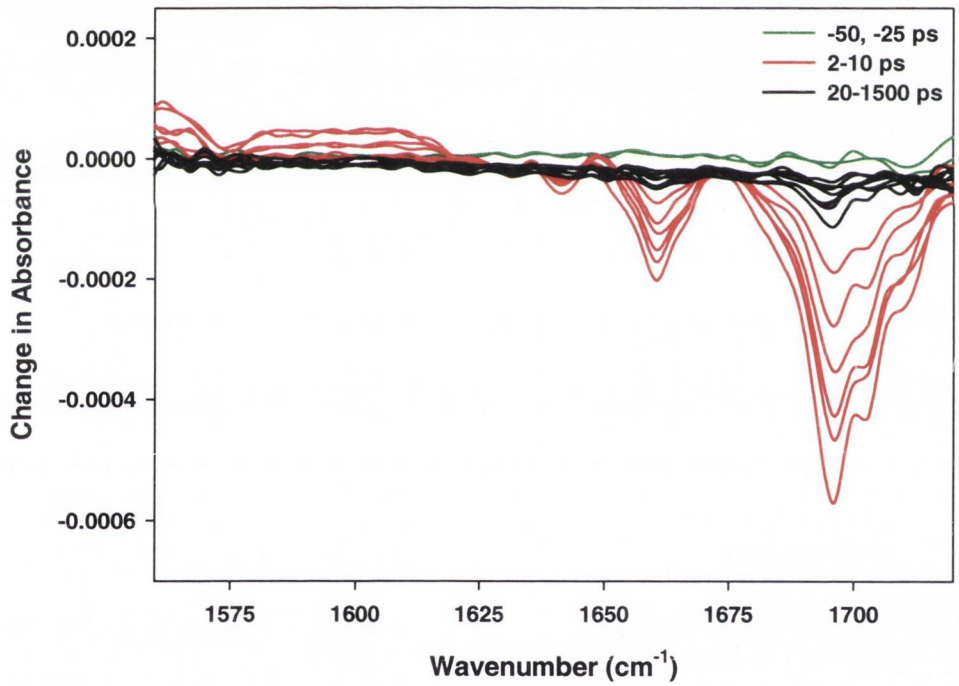

Figure 5.26 ps-TRIR of 5 mM $(dA)_{18}.(dT)_{18}.(dT)_{18}$ in 50 mM potassium phosphate D_2O buffer (pH 7) with 50 mM $MgCl_2$ (annealed). Delays are at -50, -25 (green), 2, 3, 4, 5, 7, 10 (red), 20, 35, 50, 75, 100, 200, 500 and 1000 ps (black).

Surprisingly with this sample, very little variation if any in the signal of the bands was observed with increasing laser exposure. Figure 5.27 illustrates this point and indicates that the only slight exception occurred for the 2nd cycle, which gave a stronger signal at all bleach and transient positions. Interestingly, in this system the adenine band was severely suppressed and only began to emerge in the 3rd and 4th cycles.

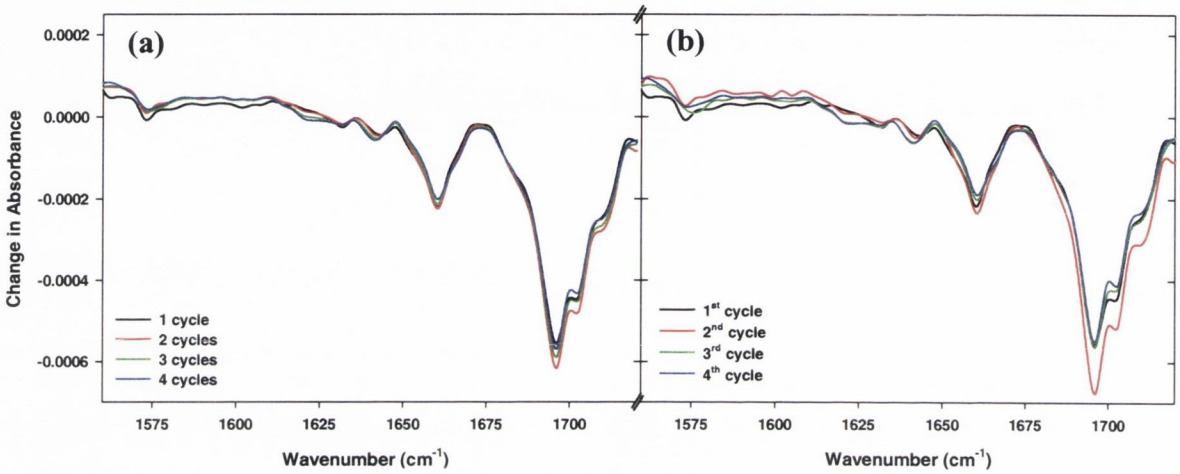

Figure 5.27 Comparison of the 2 ps delay for (a) accumulated and (b) individual cycles of 5 mM $(dA)_{18}.(dT)_{18}.(dT)_{18}$ in 50 mM potassium phosphate D_2O buffer (pH 7) with 50 mM $MgCl_2$.

Figure 5.28 shows the evolution of all accumulated and separated spectra at all time delays. The profile of all cycles is remarkably similar confirming that the secondary structure of the sample was retained throughout the experiment. UV and FTIR measurements carried out before and after the experiment confirmed that very little degradation or change had occurred (see appendix figure A5.8.1). The FTIR showed a slight change but the overall profile was very similar, which is in contrast to what was discovered for the analogous polymer system discussed earlier. Again, it is worth mentioning that the thymine oligonucleotide, which when studied in the absence of another strand is found to undergo irreversible photodamage, has in this multi-stranded structure acquired an increased photostability.

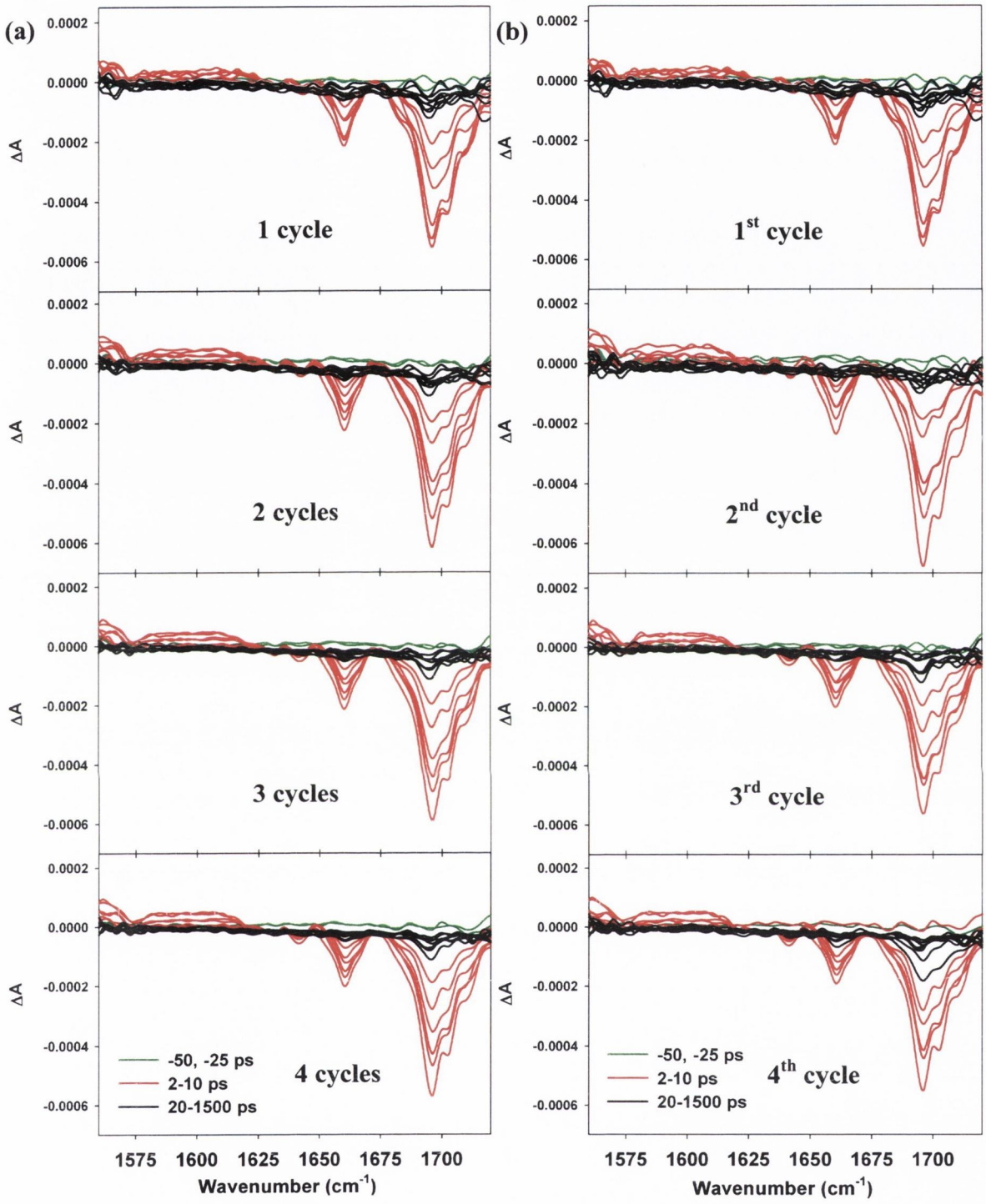

Figure 5.28 Accumulated (a) and separated (b) cycles of 5 mM $(dA)_{18}.(dT)_{18}.(dT)_{18}$ in 50 mM potassium phosphate D_2O buffer (pH 7) with 50 mM $MgCl_2$ (annealed). Delays are at -50, -25 (green), 2, 3, 4, 5, 7, 10 (red), 20, 35, 50, 75, 100, 200, 500 and 1000 ps (black).

Examination of the kinetics using both single and biexponential functions was carried out and is summarized in figure 5.29 (detailed tabular analyses are provided in the appendix section A5.8). There was very little evidence for significant contribution from long-lived states. For example the transient band at 1590 cm^{-1} gave lifetimes of 3.0 ± 0.7 ps (90%) and 52 ± 48 ps (10%) when a biexponential model was applied and a lifetime of 4.0 ± 0.6 ps under a single exponential model fit. Given the error associated with and the small contribution from the long-lived state in the biexponential fit, it is plausible that the kinetics are actually first order and therefore the model struggles to attain a very good fit to second order kinetics. The lifetimes obtained at 1660 cm^{-1} (biexponential lifetimes of 4.9 ± 0.5 ps (89%) and 335 ± 355 ps (11%), single exponential lifetime of 5.6 ± 0.6 ps) and 1690 cm^{-1} (biexponential lifetimes of 5.3 ± 0.4 ps (93%) and 95 ± 62 ps (7%), single exponential lifetime of 6.0 ± 0.4 ps) lend weight to this argument.

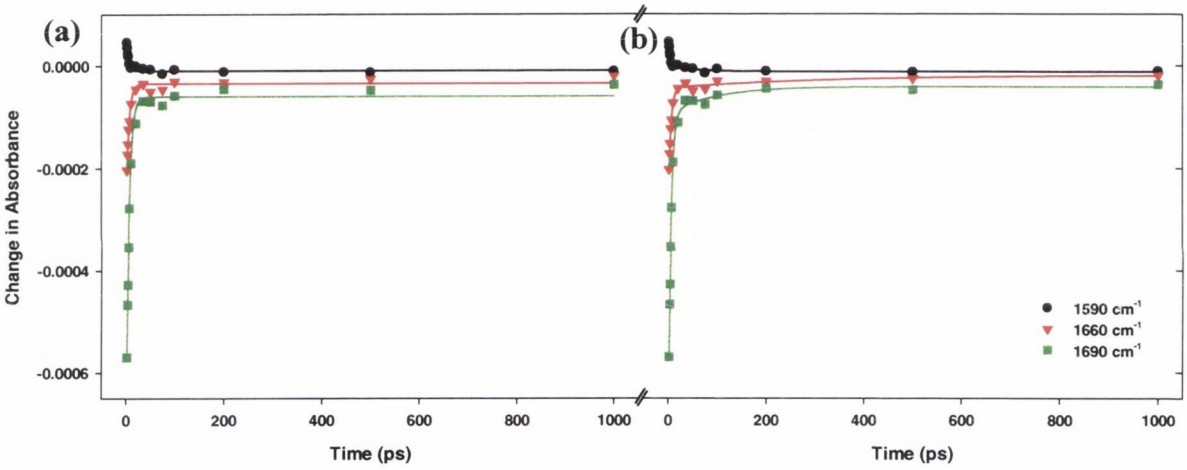

Figure 5.29 Kinetic analysis of the four accumulated cycles of 5 mM $(dA)_{18}.(dT)_{18}.(dT)_{18}$ in 50 mM potassium phosphate D_2O buffer (pH 7) with 50 mM $MgCl_2$ at 1590, 1660 and 1690 cm^{-1} using a (a) single- and (b) biexponential model.

5.3.2.9 Comparison of All Single-, Double- and Triple-Stranded Lifetime Fits

Table 5.2 provides a summary of the results of all the systems studied. There is only one band position given for all samples and the reader is referred to the appendix for this chapter where the results for all samples at a number of band positions is provided. The results indicate that the adenine systems contain a significant (18%) contribution from a long-lived state, while polymeric thymine strands have a lesser contribution from a long-lived state. In the case of $(dT)_{18}$ the data from the first cycle was fit to a single exponential, however the sample was found to show signs of degradation, and the data was rather noisy. In both double-stranded cases there are long-lived states, accounting for 14-20% of the decay – data from the first cycle fits. In the triplex structure the kinetics are predominately single exponential, with the suggestion of a very small (6%) contribution from a long-lived state at 1695 cm^{-1} in the polymer case. The oligonucleotide triplex clearly displayed monoexponential kinetics.

Sample	cm^{-1}	τ_1 (ps)	τ_2 (ps)	% (τ_1 : τ_2)
5′-dAMP	**1623**	**3.3** ± 0.2	-	-
5′-TMP	**1661**	**2.7** ± 0.3	-	-
poly(dA)	**1632**	**3.4** ± 0.4	**236** ± 76	**83:17**
poly(dT)	**1662**	**1.7** ± 0.3	**83** ± 42	**89:11**
poly(dA).poly(dT)	**1669**	**3.4** ± 1.2	**16** ± 13	**80:20**
poly(dA).poly(dT).poly(dT)	**1695**	**5.3** ± 0.3	**189** ± 151	**94:6**
$(dA)_{18}$	**1627**	**5.8** ± 1.1	**215** ± 72	**81:19**
$(dT)_{18}$	**1664**	**3.9** ± 1.2	-	-
$(dA)_{18}.(dT)_{18}$	**1699**	**4.4** ± 1.5	**30** ± 21	**86:14**
$(dA)_{18}.(dT)_{18}.(dT)_{18}$	**1690**	**5.5** ± 0.8	-	-

Table 5.2 Summary of kinetic analysis at selected positions for the constituent mononucleotide units (chapter 3) and all systems studied in this chapter.

5.3.2.10 Comparison of All Single-, Double- and Triple-Stranded Infrared Band Structures

Figure 5.30 shows the profile and band position of all samples involved in the triplex study for the polynucleotide case. This illustrates nicely how the ratio of the bands change with changing secondary structure and also how the ratio of bleaching bands observed in the TRIR spectrum differs from that of the ground state. This, of course, is due to the excited state absorptions. Also noteworthy is the impressive sensitivity of the TRIR technique

with regards to its ability to resolve even minuscule bands, with the suppressed adenine bands at 1623 cm^{-1} in the triplex structure being an excellent example of this.

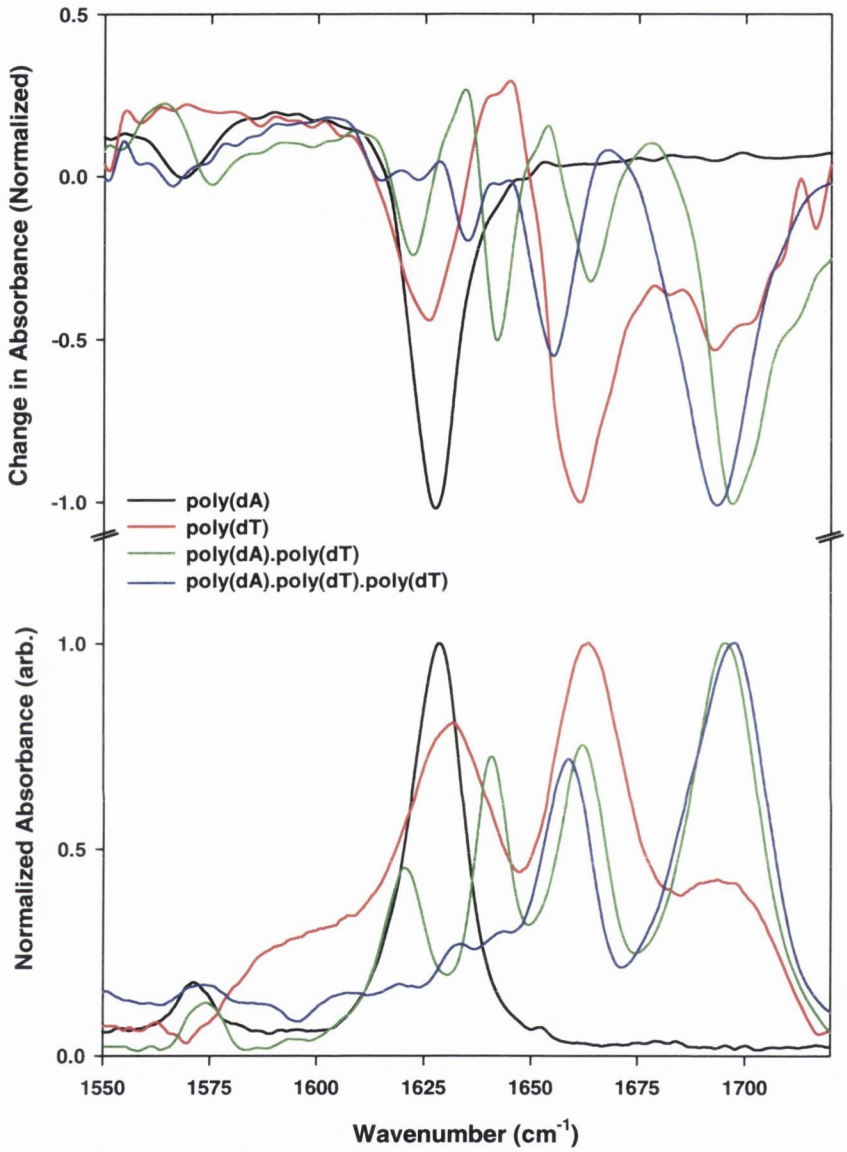

Figure 5.30 Comparison of the TRIR 2 ps delay profiles and FTIR spectra (both normalized) of poly(dA) (black), poly(dT) (red), poly(dA).poly(dT) (green) and poly(dA).poly(dT).poly(dT) (blue).
All spectra were normalized to the dominant peak in each case.

An equivalent image for the oligonucleotide case is given in figure 5.31. Again all bands are clearly resolved. Interestingly, the FTIR of the triple-stranded sample suggests a different ratio between bands than that observed for the polynucleotide case. The adenine band at 1626 cm^{-1} does not appear to be suppressed to the same extent as the polynucleotide case. However, the TRIR spectrum reveals that the adenine ring vibrations

are suppressed, confirming the triplex structure. All oligonucleotide samples were purified using NAP-5 columns. This was necessary as the samples (as received from Sigma Genosys) contained traces of an acetate buffer from their purification procedure. This impurity absorbs at 1670 cm^{-1} (in our spectral window of interest) and so efforts were made to remove it. Our purification, for the most part, worked very well. However, close inspection of the FTIR of the $(dT)_{18}$ sample in figure 5.31, reveals an absorption at 1670 cm^{-1} and this is most likely due to a small trace of the impurity. Fortuitously, the presence of this compound does not appear to encroach into the time resolved spectra.

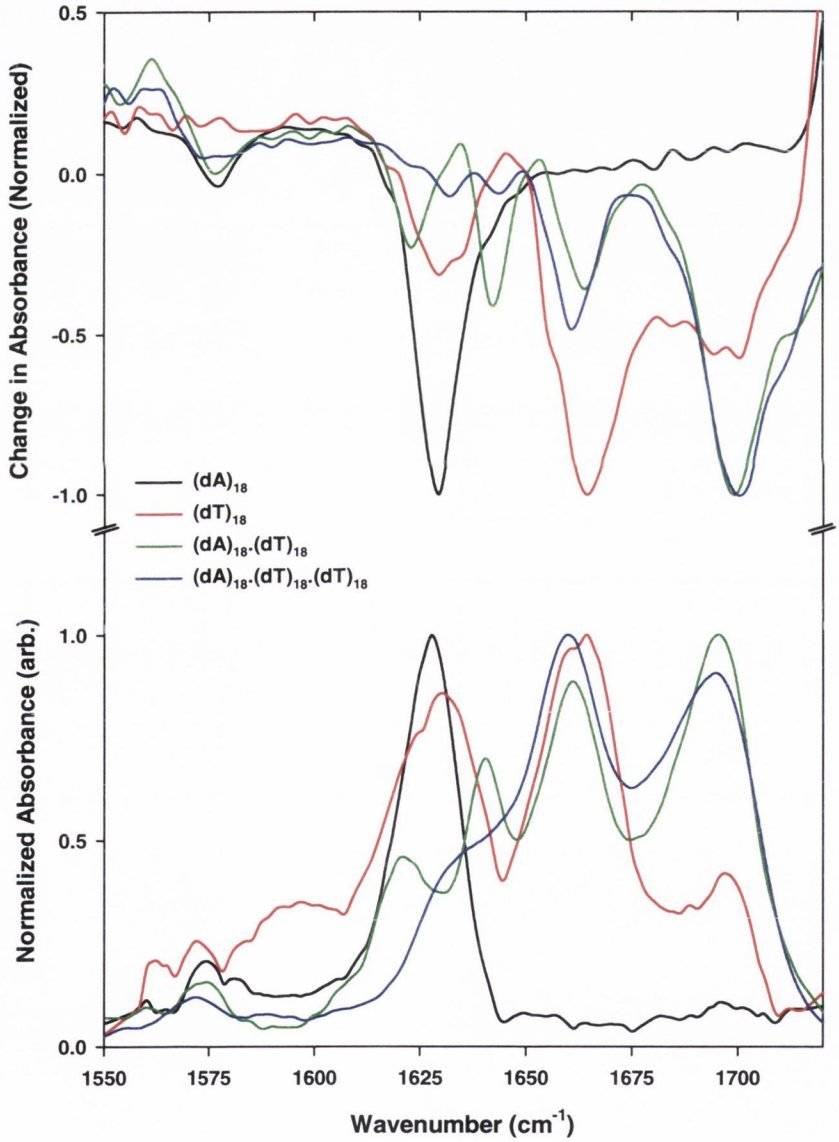

Figure 5.31 Comparison of the TRIR 2 ps delay profiles and FTIR spectra (both normalized) of $(dA)_{18}$ (black), $(dT)_{18}$ (red), $(dA)_{18}.(dT)_{18}$ (green) and $(dA)_{18}.(dT)_{18}.(dT)_{18}$ (blue). All spectra were normalized to the dominant peak in each case.

5.3.3 Discussion

5.3.3.1 Single-Stranded DNA: poly(dA) and $(dA)_{18}$

Our results for both the polymer and oligomer confirm the bifurcation of dynamics upon UV photon absorption. Monitoring the ground state recovery at the dominant bleach reveals the presence of a long-lived component – not seen for the simpler mononucleotide unit. Therefore, as discussed previously in chapter 3 for the case of dApdA and $(dA)_6$, the existence of such long-lived species is undoubtedly linked to the stacked nature of adjacent adenine monomers. However, contrasting behaviour between the oligo- and polynucleotide systems was found in the transient absorption bands. In poly(dA), there was spectroscopic evidence for a long lived state contributing to ~13% of the decay and having a lifetime of 268 ± 130 ps (average lifetime and contribution over 1532-1557 cm^{-1}). In $(dA)_{18}$ there was no such state present in the transient band and this result was akin to that of the other short adenine systems dApdA and $(dA)_6$ studied in chapter 3. This would suggest that the excited state or states (possibly multiple excited states in the polymer, with a spectral signature in our window) produced in the longer polynucleotide system is of a somewhat different nature to that which is found in the other adenine systems. It is possible that the secondary structure of the polymer allows for the production of excited states not possible in shorter adenine systems. With regards to where the long lived transient species absorbs in the shorter systems there are a few possible explanations. The transient could either absorb in a removed spectral region, sit directly over the ground state depletion area (and hence be masked by the bleach) and/or albeit unlikely, it may have an extremely small extinction coefficient (compared to that of the ground state compound). The additional ps-TRIR experiment for the polynucleotide included in the appendix that focussed on just long time delays would seem to favour the argument that the transient absorption does occur directly over the bleaching band as the profile of the band is most definitely different to that of the early time delays where the profile more closely resembles a single Gaussian or Lorentzian function. The same effect was not present in the oligonucleotide sample suggesting perhaps that the identity of the long-lived species is indeed different for both cases. A recent computational report by Hu *et al.*[260] examined helical H-aggregates of adenine and found that photoexcited states of adenine could be described as Frenkel excitons. The computational work showed that the UV absorption spectra of a stack of twenty adenine units displayed a blueshift of 2.6 nm compared to the

isolated unit, confirming the excitonic coupling within the stacked units. Analysis of the UV spectrum of all our adenine systems is given in figure A5.8.5 in the appendix, and this may explain the different behaviour that was observed, not only between, but within systems. The maxima of absorption in the UV, an indication of the excitonic coupling in the sample was found to vary both between and within systems. This would suggest that there are different excited states formed in the samples, possibly as a result of different secondary structure and hence differing relaxation behaviour is found.

The fast decay of the transient (~2-4 ps) in both cases is assigned to cooling of the vibrationally excited ground state and displays the signature cascading of transient maxima to higher frequency with time. Interestingly, for the bleaching bands this short lifetime component is somewhat longer (~7 ps). A recent femtosecond time-resolved fluorescence spectroscopy study by Schwalb and Temps[261] examined $(dA)_{20}$ and found the decay to be comprised of three components: $\tau_1 = 0.63 \pm 0.03$ ps (81%), $\tau_2 = 5.8 \pm 0.4$ ps (13%) and $\tau_3 = 97 \pm 20$ ps (7%). The authors do not explicitly assign each lifetime but rather report that the mean fluorescence lifetime of $(dA)_{20}$ is 8.05 ps. Therefore, it is possible that the lengthening of our short lifetime to ~7 ps is as a result of the TRIR picking up on some amount of an electronic excited state decay in addition to the vibrational cooling.

The lifetime of the second component in our two systems was found to differ. In the polynucleotide the lifetime was found to be 150 ps, being in excellent agreement with transient absorption data.[16,175] The oligomer when analyzed at the bleaching band over all time delays (2-2000 ps) indicated that the lifetime of the long-lived species was ~600 ps. This lifetime is similar to that found for dApdA and $(dA)_6$. However, when another sample (under the same conditions) was analyzed over the same time range a value of 178 ps was obtained for the long-lived species. This lifetime is in excellent agreement with time resolved fluorescence measurements for $(dA)_{15}$ where a lifetime of 150 ps was detected[262] and with that found for $(dA)_{20}$ from femtosecond Kerr-gated time-resolved fluorescence experiments where a lifetime of 182 ps was assigned to an E_2 "excimer-like" emission.[138] Crespo-Hernandez *et al.* monitored the bleaching at 280 nm in femtosecond transient absorption measurements and found a lifetime of 126 ps for $(dA)_{18}$, with an excimer once again being nominated as the likely candidate.[124,126] A recent fluorescence study found a lifetime of 97 ps for $(dA)_{20}$ accounting for just 7% of the decay.[261] Strangely, the authors did not assign the species but rather emphasized the need for further

studies of optically dark intermediate states in their discussion. Finally, Santoro *et al.* carried out TD-DFT calculations and suggested the possibility of dark excimer states from adenine oligomers having lifetimes of 100 ps.[115] Taking all of these contributions into account we assign the long-lived state to that of an excimer. With regards to the discrepancy between our two oligomer samples and indeed the discrepancy between the different stacked systems, and given that there are in theory multiple excimer states accessible to our systems,[138] it is possible that the ~600 ps lifetime is from a different excimer state to that of the ~150 ps decay. The discrepancies in long-lived lifetimes found within our systems can be rationalized in terms of the argument put forward earlier[260] of the existence of different excited states within the adenine systems, and it is suspected that this difference is caused by differing secondary structure and hence differing excitonic coupling between the stacked bases.

5.3.3.2 Single-Stranded DNA: poly(dT) and $(dT)_{18}$

Within the thymine containing compounds poly(dT) and $(dT)_{18}$, different relaxation behaviour was found. Evidence for sample decomposition was apparent for both systems, and as a result the analysis applied was to one cycle of data rather than the normal four accumulated cycles. For the polynucleotide two contributions were detected, the first having a lifetime of 2 ps (90%) and the second lifetime was found to be in the range 50-90 ps (10%). The oligonucleotide displayed a single lifetime of 3 ps. However, owing to the relatively poor data for the $(dT)_{18}$ system, the occurrence of a long-lived state in short oligomers cannot be ruled out by this study. The fast component arises from the vibrationally hot ground state. The long-lived component observed in the poly(dT) case is possibly due to a dark state.

Crespo-Hernandez *et al.* found lifetimes of 103 (14%) and 800 ps (5%) for $(dT)_{18}$ when bleaching signals were monitored at 253 and 280 nm respectively.[124] The authors assigned the 103 ps component to an unidentified singlet intermediate state. As with our experiments the authors found that the UV spectrum after the experiment showed a significant decrease in the absorption at 260 nm, and they concluded that because thymine dimers do not absorb appreciably above 250 nm, that this decrease in absorbance was confirmation that dimerization had indeed taken place in 10-15% of the photoexcitations. However they suggested that the dimerization does not occur via the unidentified

intermediate long-lived state but rather formation of the dimer is complete sub picosecond. A recent and somewhat contradictory report by Kwok *et al.* concluded that upon excitation of $(dT)_{20}$ a lifetime of 140 ps was found, and assigned to the deactivation of the triplet state, which the authors declare is the route by which cyclobutane pyrimidine dimers (CPDs) are formed.[5] The absence of a long-lived state in the recent fluorescence study of Schwalb and Temps[261] on $(dT)_{20}$ would suggest that long-lived states in thymine strands are of a dark nature. Another contribution from the Kohler research group stated that long-lived states in $(dT)_{18}$ varied between 100 and 1000 ps "because of $^1n_N\pi^*$ population".[86] In contrast to the purine case, it would appear that pyrimidine base single strands do not form long-lived exciplex states, but rather decay through either single base localized dark singlet or triplet states.

5.3.3.3 Double-Stranded DNA: poly(dA).poly(dT) and $(dA)_{18}.(dT)_{18}$

Duplex formation was confirmed in both systems by a change in spectra profile. The A-based ring vibration band at 1623 cm^{-1} was suppressed while the T-based C_2O band at 1697 cm^{-1} was enhanced with respect to their constituent single-stranded A and T moieties respectively. The band structure was found to change as the experiment progressed, suggesting a change in the secondary structure. The FTIR spectra recorded after TRIR experiments had altered and as the UV spectra after the experiment were unaffected, the most likely explanation is that the helix may have unwound under continued excitation. It has been postulated by researchers that there may be an inherent mechanism in DNA to limit the potential damage to one sequence in a helix, and in doing so an undamaged copy of the genetic information is retained.[173,174] It is possible, in principle, that unwinding of the helix may, in addition to exciton localization, be one such defence mechanism.

Similar kinetic behaviour was observed for both systems with lifetimes of 3 and ~20 ps. The long-lived species contributes 15-25% in both systems. Intriguingly, the signal of the broad transient band at ~1600 cm^{-1} was found to be invariant throughout the experiments in both the oligo- and polynucleotide cases. A lifetime of 16 ps was recently reported for $(dA)_{20}.(dT)_{20}$ in fluorescence measurements and attributed to exciton or exciplex contributions.[261] Transient absorption measurements on $(dA)_{18}.(dT)_{18}$ by

Crespo-Hernandez *et al.* found a lifetime of 101 ps (at 250 nm) and 150 ps (at 570 nm), with the latter lifetime being attributed to an A-based excimer state.[124,126]

The Markovitsi research group have proposed that delocalization of energy over at least two bases resulting from mixing of different monomer states is responsible for long-lived states in $(dA)_{10}.(dT)_{10}$.[176] They postulate that a large number of excited states are formed initially, with subsequent delocalization over many bases and crucially they suggest that such delocalized states can be either on the same or opposite strands before further energy transfer takes place.[125,191] Other fluorescence upconversion studies by the same group on $(dA)_{20}.(dT)_{20}$ and poly(dA).poly(dT) did not find any species greater than a few ps.[127,136] Their most recent contribution (again by the fluorescence upconversion technique) noted contributions from long-lived states in poly(dA).poly(dT).[129] Fitting of their data to several exponentials (5 in some cases) found lifetimes of 187 ps (at 330 nm), 6.5 and 130 ps (at 380 nm) and 8.3, 101 and 480 ps (at 420 nm) in addition to some very fast (sub ps) and long (~2 ns) decays. Interestingly, where fluorescence upconversion decay measurements are concerned, they conclude that the average decay constants are larger for poly(dA).poly(dT) than that found for $(dA)_{20}.(dT)_{20}$, suggesting that the degree of delocalization increases with increasing duplex size.

There is currently great debate in the literature as to the identity of the single most important or overriding factor controlling relaxation dynamics in DNA. Whether the predominant factor is base-stacking or hydrogen-bonding is still a contentious issue and one which is at present still not resolved. There are several factors within the two main categories above. On the base-stacking side of the argument localized dark states on single bases and delocalized states that form either bright or dark excimer states are all expected to modulate the relaxation dynamics. If hydrogen-bonding is important, then interstrand energy transfer and formation of delocalized exciplex states may be possible. The dissipation of energy in a hydrogen bonded duplex system may be faster if such energy transfer is possible. With reference to our results in this study, the relaxation of both the oligo- and polynucleotide systems were found to be faster than the single-stranded components. Another interesting observation from this study is that the association of the thymine oligomer ($(dT)_{18}$ or poly(dT)) with its complementary adenine oligomer ($(dA)_{18}$ or poly(dA)) somehow confers a stability to the thymine moiety that is not present in the

single-stranded form. Compared to the single-stranded case, the extent of decomposition/photoproduct formation is much less in the duplex systems. At present we are unable to fully explain this observation but perhaps interstrand energy transfer could be involved.

5.3.3.4 Triple-Stranded DNA: poly(dA).poly(dT) .poly(dT) and $(dA)_{18}.(dT)_{18}.(dT)_{18}$

Our TRIR study of triple-stranded structures represents the first investigation of ultrafast relaxation dynamics of such a motif. In the case of the polynucleotides, the band structure was found to dramatically alter after the first cycle and adopt a different secondary structure for the subsequent cycles. Figure 5.32 illustrates this change, where most noticeably the thymine C_2O signal at high wavenumber recedes while the adenine signal at 1623 cm^{-1} is found to increase and adopt a ratio with the other bands in the system that is more akin to the ratio observed in the double-stranded samples. The same effect was not observed in the oligonucleotide sample, and possibly the increased degrees of freedom available to the shorter triplex allows for the dissipation of energy before the need for secondary structure reorganization.

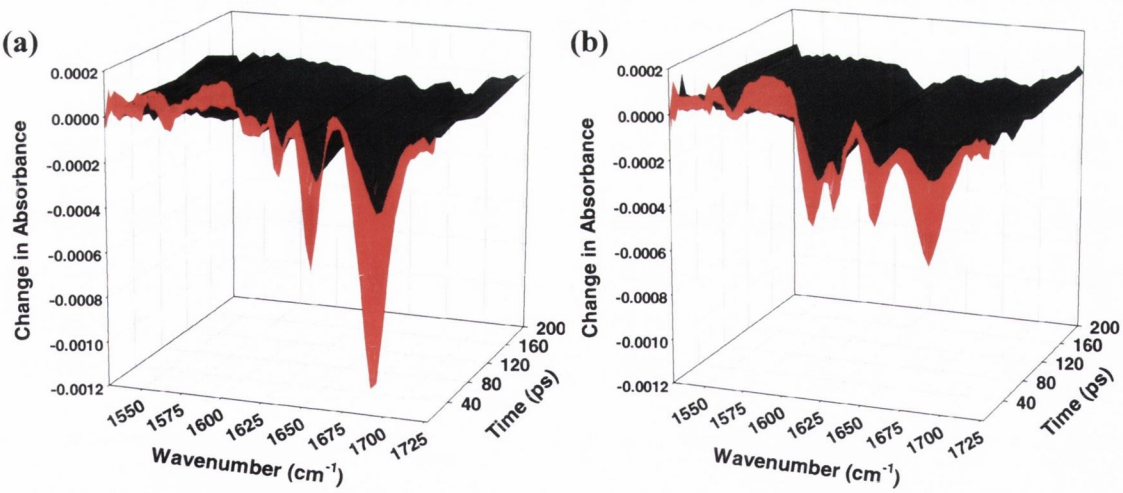

Figure 5.32 3D ps-TRIR plot of 6.1 mM poly(dA).poly(dT).poly(dT) in 50 mM potassium phosphate D_2O buffer (pH 7) with 250 mM NaCl (annealed) after (a) 1st cycle and (b) 5th cycle. 2-10 ps are shown in red with 10-200 ps in black.

The kinetics of both systems are predominately single exponential. This can possibly be rationalized in terms of the increased hydrogen bonding in the triple-stranded systems (compared to the single- and double-stranded cases) allowing for the rapid removal of the

excess energy. Also, the proximity of an additional strand compared to the double-stranded case, could in principle facilitate very rapid and increased **interstrand** delocalization of electronic states, [129,263] and hence relaxation rates are increased, resulting in the absence of long-lived states.

Curiously, for both samples the transient absorption signal centred at 1590 cm^{-1} is found to remain steady, even though in the polynucleotide case the adenine ring vibration beside this transient is found to change over time. This may indicate that there is a limited amount of this transient species which can be produced and therefore the intensity of the transient is found to be invariant to differing ground state depletion behaviour. This may well mean that the decay process involves a cascade of energy flowing from adenine to thymine. However, certain other mechanisms are possible and should be considered at this stage. These include: (i) differential coupling of the high wavenumber modes with low causing non-linear perturbations within the non-Boltzmann distribution populations from significant localization of energy, (ii) exciplex formation and (iii) differences associated with the solvation and/or hydrogen bonding *cf.* C=O vs. ring and NH_2 vs. C=O. Further work isolating each effect is clearly required.

Another crucial observation is the increased stability that the thymine residues exhibit in these systems. Given that the sample consists of two thirds thymine, it is remarkable that there is scant evidence of photodamage. This increased stability of T polynucleotides was also seen in the duplex case. Perhaps this suggests that (a) the adenine is aiding the thymine to dissipate the energy more efficiently before damage can occur and or (b) in order for thymine damage to occur the conformation of the thymine bases must be different to that of a helical arrangement – i.e. maybe the polymer needs to fold into a certain geometry for damage to occur and this is not possible in the rigid helical form. This stabilisation may result from energy delocalization in the multi-stranded arrangements, and perhaps in doing so make specific bond-bond ruptures thermodynamically unfavourable.

A further simple structural consideration is that in the polymeric duplex and triplex structures, there are expected to be flailing ends – that is the average length of the polymers is ~2000 bases. The behaviour of the single-, double- and triple- stranded portions is different. The distribution of lengths within the polymer systems will result in a distribution of secondary structures. With the oligonucleotide systems being so short, it is

expected that full base-pairing has occurred throughout the length of the polymeric structure and so the behaviour might be a truer reflection of the multi-stranded arrangement.

Intriguingly, as mentioned in the results section, another sample of the triple-stranded polymeric structure was examined and behaved in the same manner to the first, save for the UV spectrum recorded some time after the experiment (9 hours) which intimated that the triplex structure may have reformed. If the triplex had undergone secondary structure reorganization in order to minimize potential damage, and then reformed some time after, this would be a very exciting and insightful result. However, without repetition of the experiment this is merely speculation. Elaboration of this point, along with repetition to amass improved kinetic data would be highly desirable. ULTRA (the next generation TRIR apparatus at RAL) with its increased sensitivity, allowing for milder pumping conditions, is the ideal medium with which to further this study.

5.3.4 Conclusions

The TRIR of triplex DNA (both polymer and short oligo) has been recorded for the first time and both systems displayed a single fast species. This result, when viewed in the context of the single- and double-stranded samples having long-lived lifetime components, would imply that the increased hydrogen-bonding in the triplex structure facilitates the rapid removal of the excess energy. In the case of the oligonucleotide sample the triplex remained intact, while the polymer sample was found to regress to the duplex form with increasing laser exposure. Interestingly, one of the polymer samples monitored by UV some time after the experiment appeared to have reverted back to the triple-stranded architecture, although further investigation of this phenomenon is warranted before this can be fully confirmed. Further work is required to fully interpret the precise nature of the different decay mechanisms observed in the various systems investigated. Undoubtedly, excited state formation and subsequent relaxation dynamics play a crucial role in determining the dynamics and reactivity towards mutagenic modification. Whilst this may seem an obvious point, this work demonstrates how ps-TRIR can separate out and resolve such processes, and provide crucial insight into the subtlety of structure, function and stability of DNA.

5.4 Human Telomeric Sequence Quadruplex Study

5.4.1 Motivation

This study aims to characterize the quadruplex structure formed by the biologically relevant human telomeric sequence 5′-AGGG(TTAGGG)$_3$-3′ which has been implicated in the replication and maintenance of chromosomal termini. Whilst this sequence represents a potential drug target for many researchers, we wish to understand some of the basic features of the sequence. TRIR can afford extremely impressive resolution of band structure and to understand how the structure changes/evolves (or not) with time is a very important issue. Characterization of excited state structure produced upon UV excitation is desirable and ps-TRIR offers the added advantage of providing structural information in addition to kinetic data. This could provide insight into the localization or delocalization of excited states. Another aspect this study aims to probe is the effect of salt on the oligonucleotide. It is known that the quadruplex structure is stabilized in a salt environment and we wish to examine the effect of metal cations of different ionic radii and charge. Our results may possibly offer some insight into the structure and excited state behaviour of the human telomeric sequence that may influence future drug targeting strategies.

5.4.2 Results

5.4.2.1 No additional Salt

The ps-TRIR spectrum following UV excitation of the 22-mer human telomeric sequence 5′-AGGG(TTAGGG)$_3$-3′ in buffered D_2O solution (pH 7) is given in figure 5.33 below. Depletion bands centred at 1562, 1584, 1620, 1669 and 1692 cm^{-1} correspond to ground state absorptions, as is evidenced by the agreement with the FTIR. Transient absorption bands are found at 1549, 1566, 1601 and 1639 cm^{-1}. The dominant bleaching bands are those of guanine with the ring vibration occurring at 1584 cm^{-1} and the carbonyl stretching being present at 1669 cm^{-1}. The two adenine ring vibrations are found at 1562 and 1620 cm^{-1} and both appear to be visible at early time delays only. As witnessed in other polymeric structures the 1620 cm^{-1} adenine bleach is clearly suppressed when compared to that of free adenine (chapter 3). Thymine carbonyl and ring bands are masked by the strong guanine carbonyl stretching at 1669 cm^{-1} with the only discernable evidence for thymine being the C_2O stretching that occurs as a shoulder on the high wavenumber side of this band at 1692 cm^{-1}.

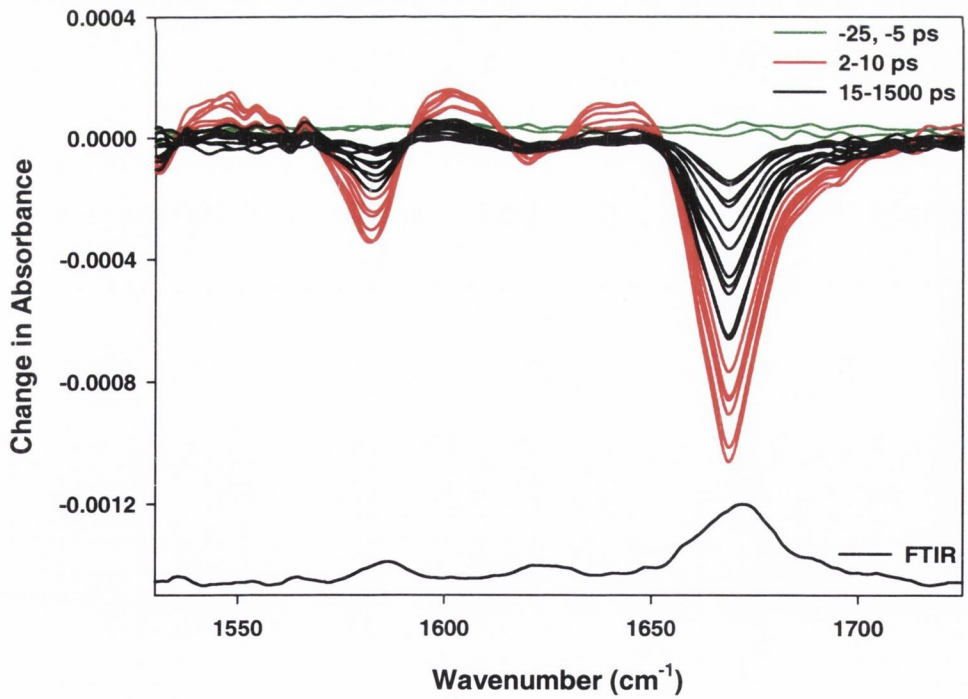

Figure 5.33 ps-TRIR of 5 mM 5′-AGGG(TTAGGG)$_3$-3′ in 10 mM potassium phosphate D_2O buffer (pH 7). Delays are at -25, -5 (green), 2, 3, 4, 5.5, 7.5, 10 (red), 15, 20, 35, 50, 75, 100, 200, 350, 500, 1000 and 1500 ps (black).

Kinetic analysis was performed across all bands in the spectrum. A biexponential model was used and the results of some selected positions are given in figure 5.34. Full analysis at all wavelengths is provided in the appendix. The lifetimes given inset of figure 5.34 show the general spread of values that were obtained. In almost all cases the short lifetime component was found to be slightly longer than that obtained for the mononucleotides (2-4 ps). Values were found to range from 3-9 ps, with the lower bound of this range coming from the transient bands. A typical example of this is the 1596 cm^{-1} fit in figure 5.34 below. With regards to the long-lived species, there was again a large spread of values. At 1596 cm^{-1} the lifetime was found to be 70 ps while at 1672 cm^{-1} analysis gave a lifetime of 155 ps. The results of the fitting are presumably a product of the convoluted nature of the spectrum. Deconvolution of the bands, and fitting of all deconvolved bands (rather than point fitting) might resolve this issue, but this is not a trivial task. TRIR spectra are not normal vibrational spectra. In our systems we generate very hot ground states and at long time delays the changes in structure are slight. The spectral resolution in the crowded region does not permit accurate fitting, making the situation very complicated. An apparent trend from the analysis (clearly seen in the table below and the full table in the appendix) was that the contribution from the long-lived species appeared to increase across the spectrum on traversing from low to high wavenumbers.

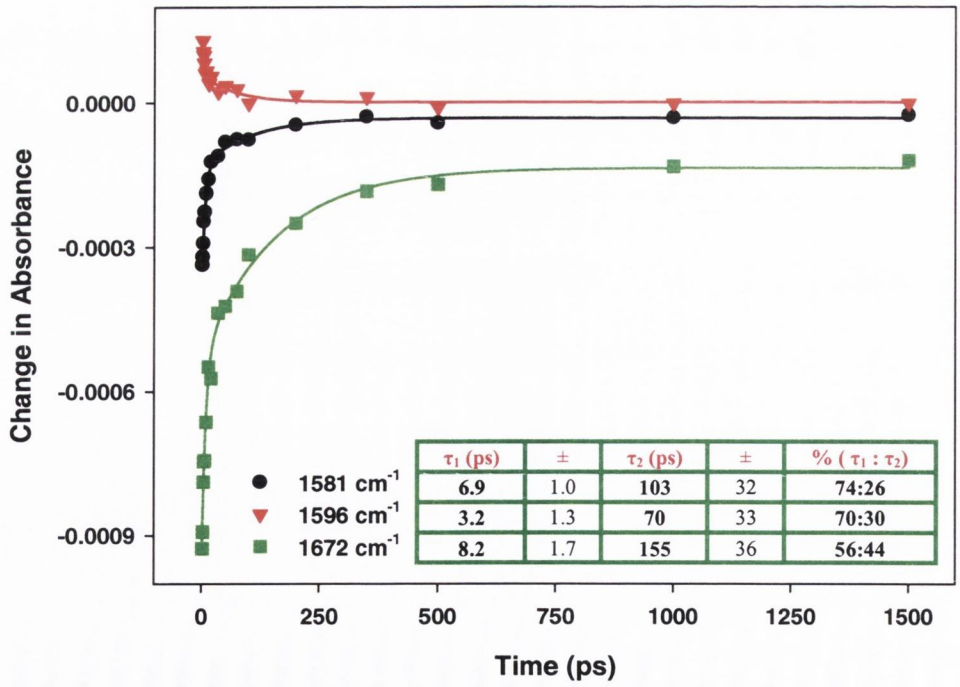

τ_1 (ps)	±	τ_2 (ps)	±	% (τ_1 : τ_2)
6.9	1.0	103	32	74:26
3.2	1.3	70	33	70:30
8.2	1.7	155	36	56:44

Figure 5.34 Kinetic analysis of 5 mM 5′-AGGG(TTAGGG)$_3$-3′ in 10 mM potassium phosphate D_2O buffer (pH 7) at 1581, 1596 and 1672 cm^{-1}.

5.4.2.2 100 mM NaCl

The experiment was repeated on a fresh oligonucleotide sample with 100 mM NaCl added, and the ps-TRIR spectrum following UV pumping is shown in figure 5.35. The spectrum is not dissimilar to the first experiment. Bleaching bands are located at 1551, 1581, 1618, 1662 and 1682 cm^{-1}. Transient absorption bands are present at 1542, 1560, 1599 and 1636 cm^{-1}. Again the dominant bleaching bands in the TRIR are those of the guanine moieties. However, it must be pointed out in this case there is not perfect agreement with the bleaching bands in the TRIR and the FTIR absorption bands. Most noticeably the guanine ring vibration at 1581 cm^{-1} is extremely hard to see in the FTIR. There is a small absorption there but the reason for this band being so suppressed is at present unclear.

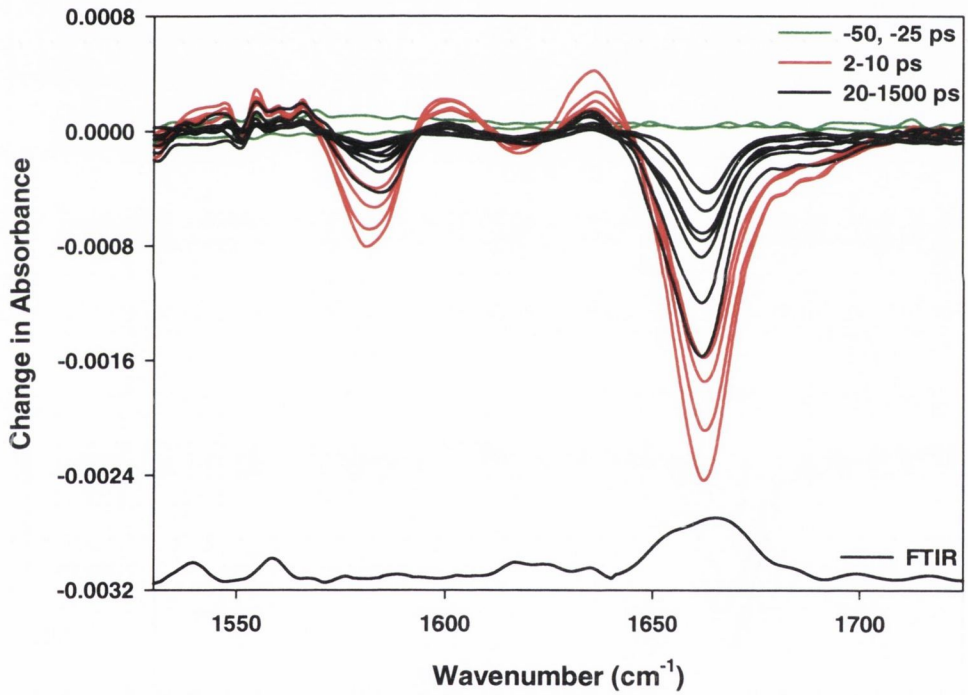

Figure 5.35 ps-TRIR of 5 mM 5′-AGGG(TTAGGG)$_3$-3′ in 10 mM potassium phosphate D_2O buffer (pH 7) with 100 mM NaCl. Delays are at -50, -25 (green), 2, 4, 7, 10 (red), 20, 50, 100, 150, 200, 500, 1000 and 1500 ps (black).

Analysis of this system again revealed biexponential kinetics with similar trends being observed to that of the previous sample. Some of the results are given in figure 5.36 below with a comprehensive analysis supplied in the appendix. The short lifetime component (3-8 ps) was found to be longer than that for the mononucleotides, while the long lifetime was found to show some consistency (90-120 ps), as the values inset of figure 5.37 would indicate. The contribution from the long-lived species was found to be 30-40% with the only notable exception being the transient absorption band at 1636 cm^{-1} which showed on average a contribution of 17% from the long-lived species. However, this is not interpreted as differing behaviour from the rest of the spectrum, as kinetic analysis of a small band such as this one that has many complicated contributions from underlying bleaching bands should not be considered as the definitive measure of lifetime.

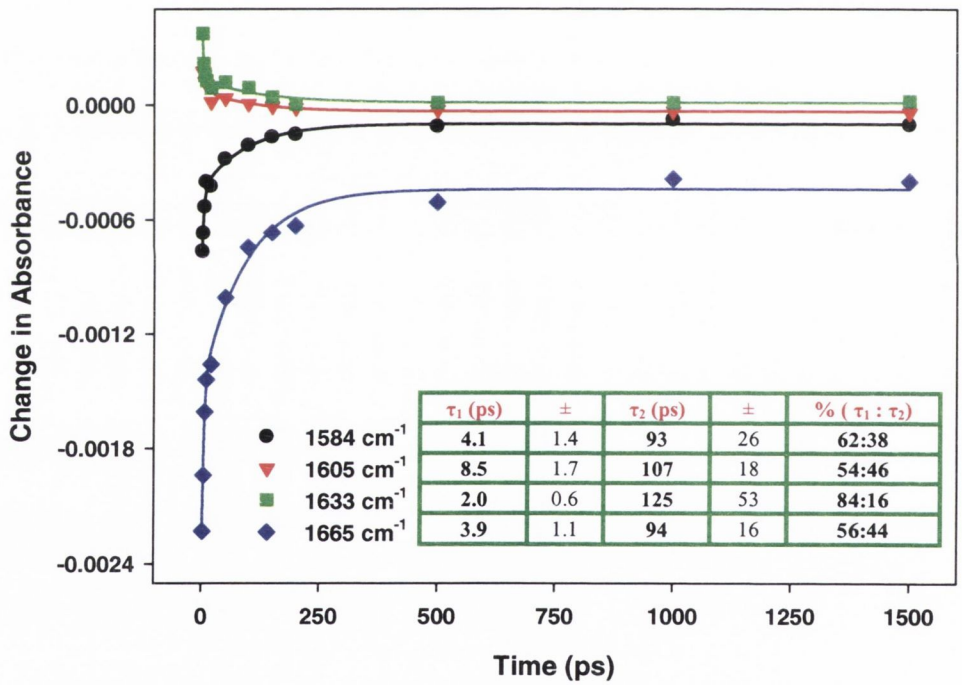

Figure 5.36 Kinetic analysis of 5 mM 5′-AGGG(TTAGGG)$_3$-3′ in 10 mM potassium phosphate D_2O buffer (pH 7) with 100 mM NaCl at 1584, 1605, 1633 and 1665 cm^{-1}.

5.4.2.3 100 mM KCl

Next the ps-TRIR of the human telomeric sequence in 100 mM KCl was recorded and is presented in figure 5.37 below. Structural features include bleaching bands centred at 1551, 1580, 1617, 1665 and 1683 cm^{-1} with transient absorption bands centred at 1543, 1560, 1599 and 1639 cm^{-1}. In this case, compared to that of the 100 mM NaCl case (figure 5.35), the ratio of the bleaching bands is better reflected in the FTIR, with the guanine ring vibration being clearly visible. There are some significant gaps between delays, most evidently in the high wavenumber band. The system had not completely recovered on the timescale of the experiment (1500 ps), and this is clearly seen for the high wavenumber carbonyl bleaching band.

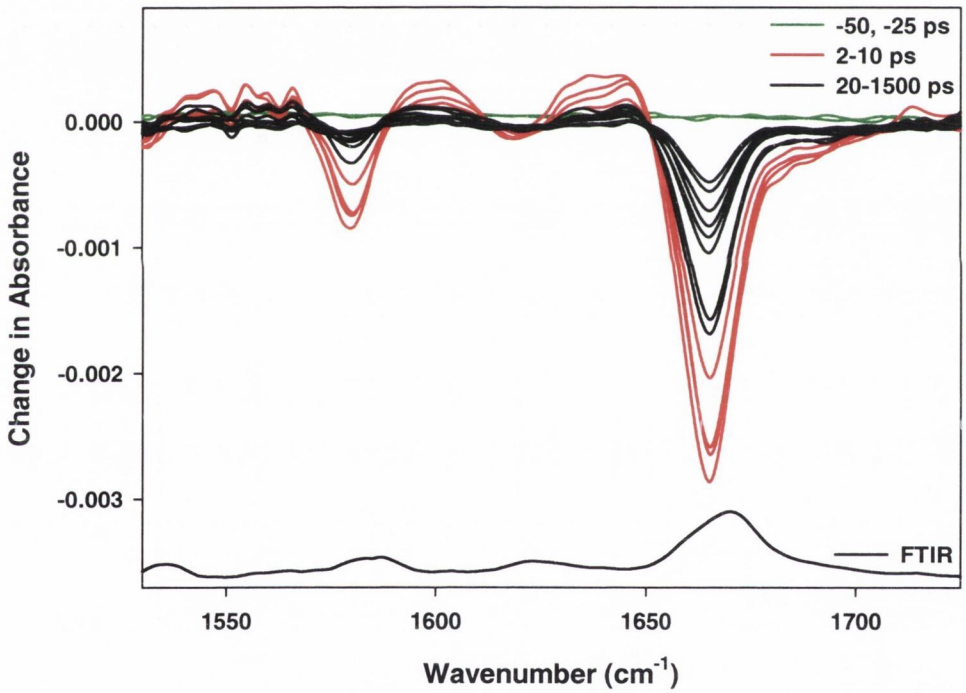

Figure 5.37 ps-TRIR of 5 mM 5′-AGGG(TTAGGG)$_3$-3′ in 10 mM potassium phosphate D_2O buffer (pH 7) with 100 mM KCl. Delays are at -50, -25 (green), 2, 4, 7, 10 (red), 20, 50, 100, 150, 200, 500, 1000 and 1500 ps (black).

The kinetics of the systems were found to be similar to those of the 'no additional salt' and 100 mM NaCl samples. As a consequence of the uneven distribution between the band intensities with delay times, one might expect poor kinetic fits. On the contrary, there was a very good consistency with the values obtained across the spectrum and the kinetics shown in figure 5.38 together with the inset table illustrate this point well. This presumably is a consequence of the delays that coincided with one another, not being at critical points in the decay profile. That is to say the points at the extremities have a greater influence on the lifetime obtained than those in the middle of the decay profile. Full analysis is provided in the appendix. Excellent lifetime agreement was found for both the short and long lifetimes in the transient absorption bands. This is evidenced by the fact that the traces practically sit on top of one another and the analyses suggest a short lifetime of 4 ± 1.5 ps with the long lived species having a lifetime of 155 ± 80 ps.

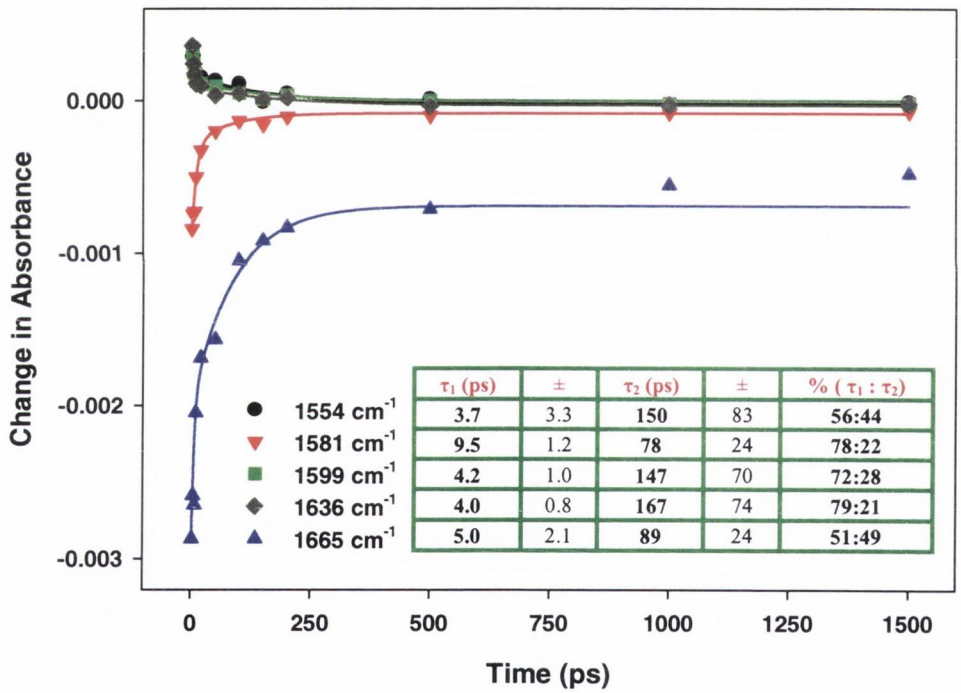

τ_1 (ps)	±	τ_2 (ps)	±	% (τ_1 : τ_2)
3.7	3.3	150	83	56:44
9.5	1.2	78	24	78:22
4.2	1.0	147	70	72:28
4.0	0.8	167	74	79:21
5.0	2.1	89	24	51:49

Figure 5.38 Kinetic analysis of 5 mM 5′-AGGG(TTAGGG)$_3$-3′ in 10 mM potassium phosphate D_2O buffer (pH 7) with 100 mM KCl at 1554, 1581, 1599, 1636 and 1665 cm^{-1}.

5.4.2.4 50 mM $SrCl_2$

The final cation dependent TRIR study on the human telomeric sequence was with $SrCl_2$ and the spectrum is given in figure 5.39. The Sr^{2+} ions are expected to have a strong

interaction with the guanine carbonyls and phosphate backbone, by virtue of their increased charge compared to the Na^+ and K^+ cases. The overall band structure is similar to all the previous samples with bleaching bands occurring at 1551, 1581, 1620 and 1657 cm^{-1} and transient absorption bands occurring at 1543, 1555, 1600 and 1639 cm^{-1}. Again good agreement was found with the ground state band positions from the FTIR. There is however one notable exception in the profile when compared to the other samples. The transient absorption band on the low wavenumber side of the main bleach is extremely sharp and the bleaching band appears more asymmetric in shape than those of the previous three samples. This would suggest that either the transient absorption band has moved to higher wavenumbers or that the bleaching band has moved to lower wavenumbers and the resulting overlap caused by either scenario has increased. As a result of the increased overlap, when the difference spectrum is calculated a sharp feature such as the one found is generated. Analysis of the FTIR answers this question, as the high wavenumber band is centred at 1661 cm^{-1}. This band in the presence of no additional salt (the first TRIR given in this study) was found at 1672 cm^{-1}. The presence of the $SrCl_2$ in this system has caused a shift in the band of 11 cm^{-1} and this shift is responsible for the sharp feature observed.

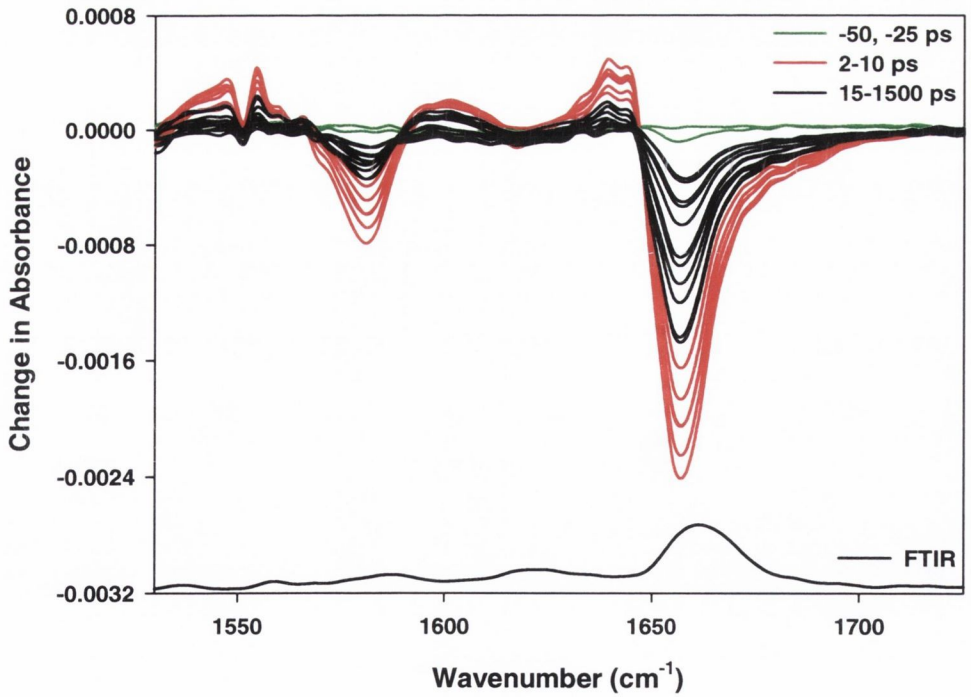

Figure 5.39 ps-TRIR of 5 mM 5′-AGGG(TTAGGG)$_3$-3′ in 10 mM potassium phosphate D_2O buffer (pH 7) with 50 mM $SrCl_2$. Delays are at -50, -25 (green), 2, 3, 4, 5, 7, 10 (red), 15, 20, 35, 50, 75, 100, 200, 350, 500, 1000 and 1500 ps (black).

Figure 5.40 shows some of the kinetic analysis of the system. The reader is referred to the appendix for a summary of the full analysis. Unsurprisingly, biexponential kinetics were found in this system. As with the preceding experiment the short lifetime was found to be slightly elongated when compared to that of the constituent mononucleotide units. This is not an uncommon phenomenon with oligonucleotide systems and the slower rate of vibrational cooling is presumably linked to secondary structure. This system, of all four studied, had the most apparent differences in the lifetime of the long-lived species throughout the spectrum. The guanine ring vibration band (1581 cm^{-1}) and the transient absorption band (1639 cm^{-1}) both gave a lifetime of 80 ± 30 ps for the long-lived species with a contribution of 25%. In contrast the high wavenumber bleaching band gave an average lifetime of 160 ± 36 ps for the long lived species.

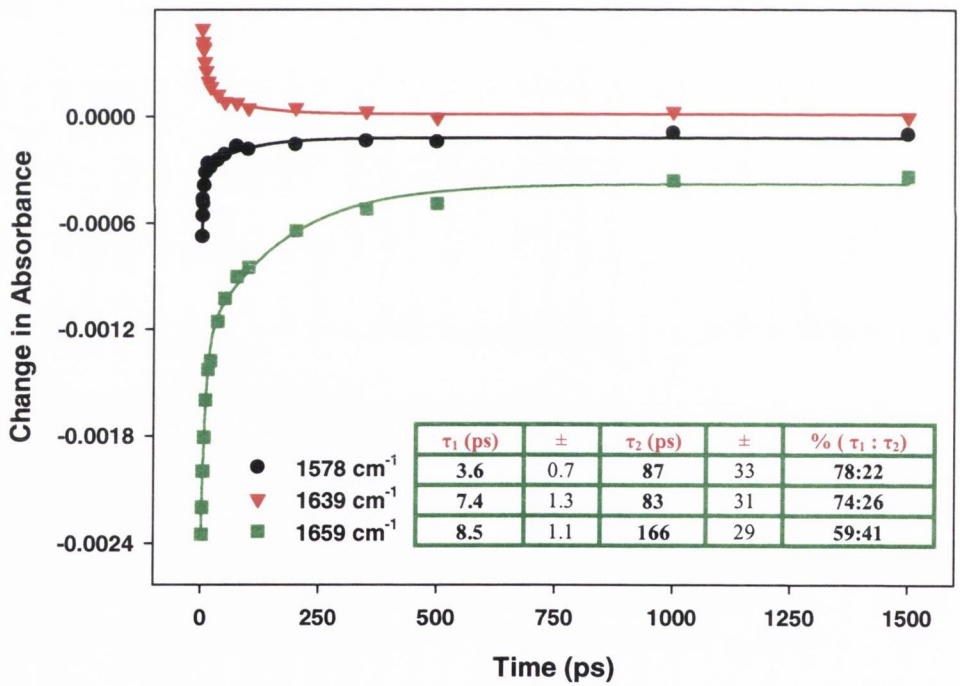

τ_1 (ps)	±	τ_2 (ps)	±	% (τ_1 : τ_2)
3.6	0.7	87	33	78:22
7.4	1.3	83	31	74:26
8.5	1.1	166	29	59:41

Figure 5.40 Kinetic analysis of 5 mM 5′-AGGG(TTAGGG)$_3$-3′ in 10 mM potassium phosphate D_2O buffer (pH 7) with 50 mM $SrCl_2$ at 1578, 1639 and 1659 cm^{-1}.

5.4.3 Discussion

This study represents, to our knowledge, the first ultrafast investigation of the biologically relevant human telomeric sequence. As such, there is no work in the literature to which comparisons can be made. We sought to characterize the ps-TRIR behaviour of the human telomeric sequence and investigate how the addition of metal cations (both mono- and divalent) perturbed the structure and modulated the ultrafast relaxation dynamics following UV excitation.

The presence of excess cations in the sample stabilizes the secondary quadruplex structure as these ions are expected to occupy the central channel. (see scheme 5.2) For instance a sodium ion is known to reside between four guanine units (i.e. ratio of 4:1 ; $dG:Na^+$), while a potassium ion is known to occupy the space between two tetrad units (i.e. ratio of 8:1 ; $dG:K^+$). While the association of metal cations with quadruplex forming strands is not in dispute, the arrangement of the strand is still not wholly understood as the strand can adopt a parallel or antiparallel conformation (see scheme 5.2). Our sequence of choice, 5′-AGGG(TTAGGG)$_3$-3′, has been discussed in a recent article by Neidle and Parkinson.[250] The authors offer crystal structure evidence that in a K^+ environment the sequence adopts an all-parallel fold (this crystal structure was presented earlier in the introduction to this chapter). In solution phase, there is general agreement that in the presence of sodium the antiparallel structure is the dominant one, while in the presence of potassium both parallel and antiparallel structures have been proposed.[222,245,252,264] Other studies on the same 22-mer in presence of potassium have suggested a mixture of parallel and antiparallel exist[233] (Fluorescence Resonant Energy Transfer (FRET) study) and that in conditions of molecular crowding (conditions similar to the crowded intracellular environment), the parallel conformation is preferred (CD study).[243,265] Dai *et al.* proposed that the 22-mer and closely related sequences exhibited a mixture of parallel and antiparallel structures in solution (NMR study).[239] A recent review by the same authors concluded that the 22-mer and similar sequences exhibit polymorphism in solution and they have proposed intermediate "hybrid" states.[256] In the solution phase in presence of Na^+ an antiparallel conformation was assigned to the 22-mer used in our study.

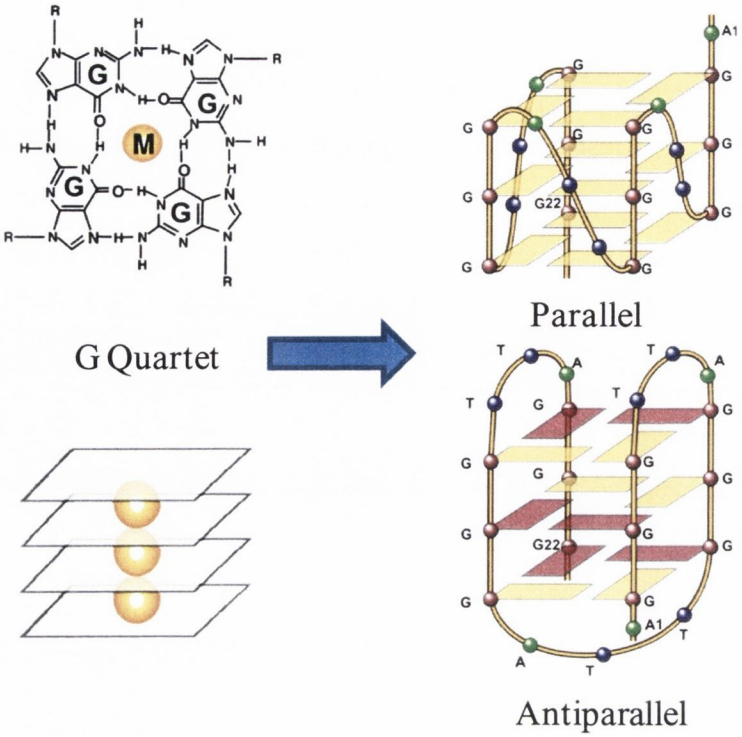

Scheme 5.2 G quartet structure (adapted from reference 265)
and the parallel and antiparallel conformations of the 22-mer human telomeric sequence
5′-AGGG(TTAGGG)$_3$-3′ (adapted from reference 256).
Yellow rectangle - *anti* sugar conformation, red rectangle - *syn* sugar conformation.

Given the similarity of the spectral profiles in our study, it is difficult to assign a conformation. All four samples had similar profiles (see figure 5.41 below for the 2 ps trace) and this would suggest that there is a similarity to the conformation or distribution of conformations within all the samples. The presence of the *anti* or *syn* vibrational bands of the guanine residues would point toward a specific conformation, but this would require a much lower wavenumber spectral window for the TRIR. However, the FTIR spectra were examined in this region and these studies suggested that the antiparallel structure may be dominant, as there were small absorptions at 1408 cm^{-1} (dG *syn*) and 1418 cm^{-1} (dG *anti*).[94] However, adenine anti and syn bands are also expected to contribute here, so this is by no means a definitive assignment.

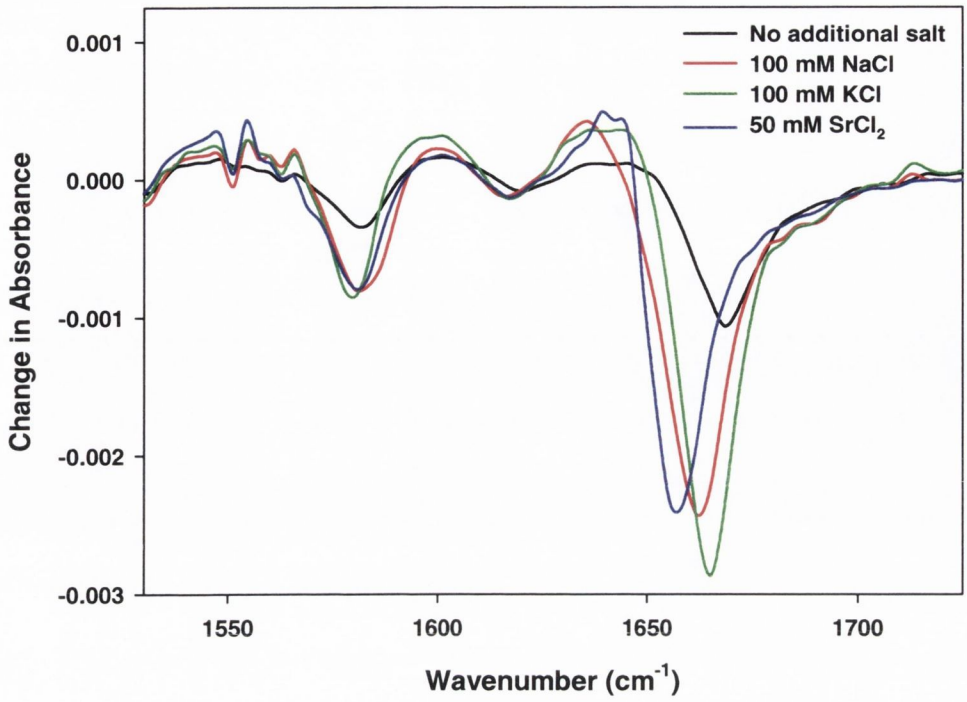

Figure 5.41 Comparison of the 2 ps delay profile of 5 mM 5′-AGGG(TTAGGG)$_3$-3′ in 10 mM potassium phosphate D_2O buffer (pH 7) with no additional salt (black), 100 mM NaCl (red), 100 mM KCl (green) and 50 mM $SrCl_2$ (blue).

Regardless of the conformation present, there are some points of interest with regard to the different ions present. The stabilization of the quadruplex structure is facilitated by the metal ions present. There are two forms of interaction that the ion may have with the oligonucleotide: (i) Non specific interaction of the ion with the negatively charged phosphodiesters on the backbone and (ii) specific coordination of the ion with the guanine carbonyl (C_6O) in the centre of the tetrad structure.[252] It is this second interaction that the TRIR spectrum is most sensitive to. Interaction of an ion with the guanine C_6O perturbs the frequency of this band and also results in a sharpening of structure (or narrowing of the FWHM) of the band – indicative of a more rigid structure with less conformation fluctuations.[230] Considering all four samples were of the same concentration examination of the FWHM would suggest that the Sr^{2+} and K^+ ions had the greatest stabilization of the structure with the Na+ and the 'no additional salt' sample being approximately the same. However, the 'no additional salt' sample did contain 10 mM potassium phosphate buffer and as tetrad structures form in a potassium environment with a ratio of 8:1;dG:K^+, this sample is expected to have more than enough cations present to stabilize the quadruplex structure. When the extent of the shift of the main bleach is examined the trend is

$Sr^{2+}>Na^{+}>K^{+}$. This would imply that the Sr^{2+} has the strongest interaction with the C_6O in the centre of the tetrad. A study by Kankia and Markia on mono- and divalent metal cation induced folding of the Thrombin aptamer into a G quadruplex structure found that Sr^{2+} was the ion that conferred the greatest stability, with K^{+} being the next best candidate. The authors found that the Sr^{2+} aptamer displayed an unfolding temperature that was 18 °C higher than that of the K^{+} aptamer. Earlier work by Hardin *et al.*[229] had shown that the ideal ionic radius of a metal ion for quadruplex stabilization was 1.3-1.5 Å. Sr^{2+} with an ionic radius of 1.13 or 1.27 Å for a coordination number of 8 would appear to be a good candidate for quadruplex stabilization. K^{+} (ionic radius of 1.33 Å) is also well suited, while Na^{+} at 0.95 Å may be too small to maintain a strong interaction with four carbonyls and hence Na^{+} ions are not such efficient stabilizers as their Sr^{2+} and K^{+} counterparts.

The formation of a guanine tetrad is confirmed by the presence of a band at 1537 cm^{-1}. This band arises from the Hoogsteen hydrogen bonding at the N7 position of the moieties.[230] This band is present in the FTIR of all four samples (see figure 5.42 below). Intriguingly, the band does not appear in the TRIR spectrum, at least not at 1537 cm^{-1}. There is an indication that at the edge of our spectral window (1530 cm^{-1}) another bleaching band is present. However, we did not move the spectral window to investigate this further, and in follow-up studies this lower wavenumber region should be explored. Another feature that requires further investigation is the extremely sharp band at 1551 cm^{-1} in the TRIR. This is most likely due to absorption from atmospheric water in the system. The FTIR data reflects quite well with the TRIR spectra in terms of the position of the guanine carbonyl band, but noticeably in the case of the NaCl FTIR, there appears to be a shoulder on the lower wavenumber side of the band. This may suggest a distribution of conformations in the NaCl sample.

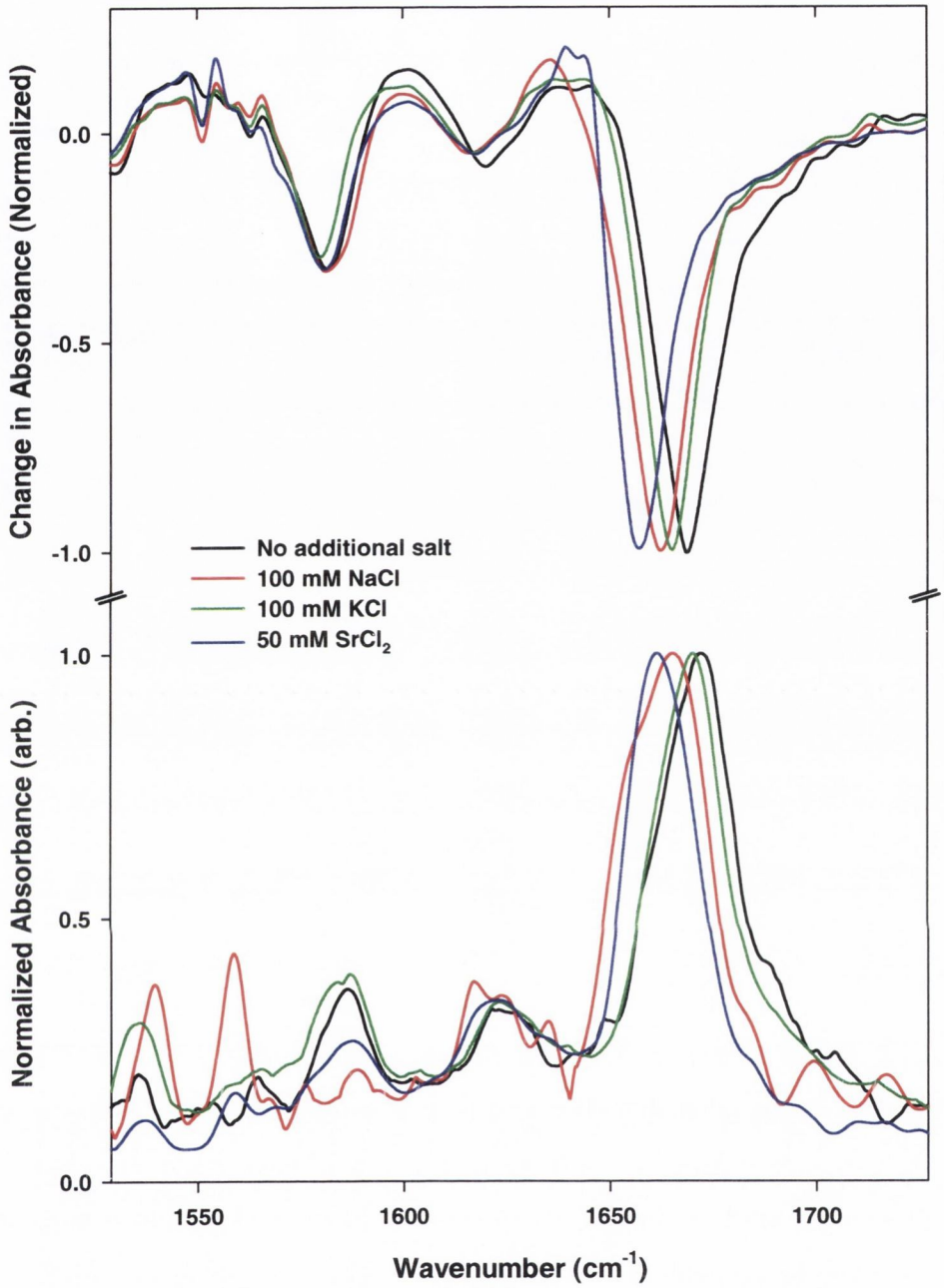

Figure 5.42 Comparison of the TRIR 2 ps delay profiles and FTIR spectra (both normalized) of 5 mM 5′-AGGG(TTAGGG)$_3$-3′ in 10 mM potassium phosphate D_2O buffer (pH 7) with 'no additional salt' (black), 100 mM NaCl (red), 100 mM KCl (green) and 50 mM $SrCl_2$ (blue). All spectra were normalized to the dominant peak in each case.

Finally, with regards to the stability of the oligonucleotide upon laser exposure, the UV spectra before and after all experiments were recorded and are presented in figure 5.43. The results indicate that the greatest decomposition/degradation occurred in the sample with no additional salt, while somewhat surprisingly the $SrCl_2$ sample appeared to be the

next most damaged/altered. The KCl sample showed almost no indication of decomposition. The samples were not measured on the same day. Only the NaCl and KCl samples were recorded sequentially and this may in some part explain the differences in decomposition observed, as the laser power may have been greater for some samples rather than others and hence lead to greater damage. When monitored the laser power was found to be in the range 1-2 μJ. Also, given the low cation concentration in the 'no additional salt' sample (10 mM buffer) compared to the other samples, it is possible that this sample may not have had a predominant preferential structural arrangement, something that the higher salt concentration samples may have had (i.e. stabilization of the structure would be less, and therefore more likely for rearrangement to occur). If this was the case, and there was a greater distribution of structures in this sample, perhaps one structure is more susceptible to damage than another and hence greater sample decomposition was observed.

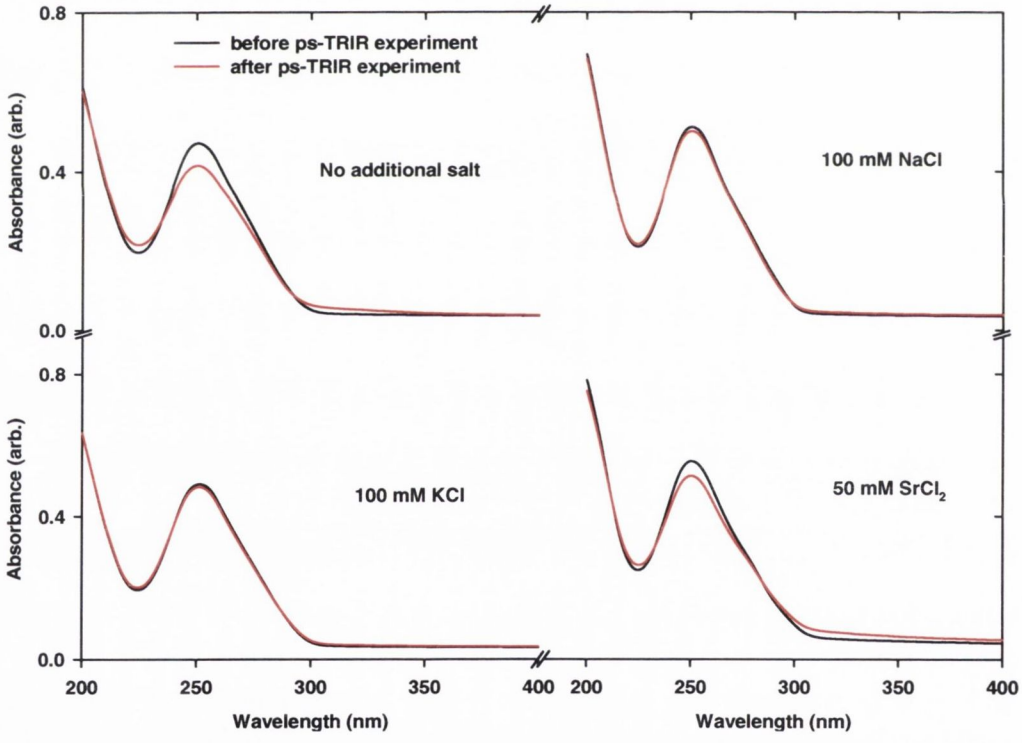

Figure 5.43 UV spectra recorded for all human telomeric sequence measurements before (black) and after (red) ps-TRIR experiments.

The lifetimes observed for all samples were reasonably consistent (see table 5.3 below). The lifetime for the cooling of the vibrationally excited ground state was in all cases found to be slightly longer than for that of the mononucleotides. Vibrational cooling is the

process by which a base dissipates its excess vibrational energy in order to return to thermal equilibrium with the surrounding medium.[17] This process is facilitated by intermolecular energy transfer to the surrounding solvent molecules.[49] The ions in our system occupy the cavity in the centre of the tetrads and in doing so the ions displace D_2O molecules from the centre.[236] This 'structural' water normally interacts with the polar groups of the nucleobases. Therefore, the base cannot perform the vibrational cooling as efficiently (especially as the C_6O which is interacting with the ion cannot transfer energy efficiently to D_2O) as in the mononucleotide case, and hence the cooling rate becomes slower.

Sample	cm^{-1}	τ_1 (ps)	τ_2 (ps)	% (τ_1 : τ_2)
no additional salt	**1581**	**6.9** ± 1.0	**103** ± 32	**74:26**
	1672	**8.2** ± 1.7	**155** ± 36	**56:44**
100 mM NaCl	**1584**	**4.1** ± 1.4	**93** ± 26	**62:38**
	1665	**3.9** ± 1.1	**94** ± 16	**56:44**
100 mM KCl	**1581**	**9.5** ± 1.2	**78** ± 24	**78:22**
	1665	**5.0** ± 2.1	**89** ± 24	**51:49**
50 mM $SrCl_2$	**1578**	**3.6** ± 0.7	**87** ± 33	**78:22**
	1659	**8.5** ± 1.1	**166** ± 29	**59:41**

Table 5.3 Summary of the lifetimes observed for all quadruplex samples at the two main bleaching bands.

The second species present is most likely an electronic excited state. There are a number of possibilities. There could be a number of exciplex type states present between adjacent stacked bases and we are observing the "averaged" behaviour from all contributing states. Energy transfer in DNA has been predicted to be more efficient for intrastrand rather than interstrand transfer.[266,267] Excited states delocalized over a number of bases have been considered in the literature[192], admittedly not in a mixed-base context, but nevertheless excited state delocalization is a possibility. Interstrand excited states have been proposed by the Markovitsi research group[129,187] and others[263] and although we are studying a single strand, the tetrad arrangement is akin to that of a multistranded arrangement. The final possibility could be single base localized excited states that occur due to the stacked environment but remain localized. Whether the state, or indeed states, are localized or delocalized we can report that the lifetime is broadly similar in all four samples (90-160 ps). The contribution from the long-lived state varied significantly from sample to

sample (17-50%). Taking both of these results into consideration, it is possible that the variations observed are the result of different structures and salt environments. It might suggest that the lifetime is not due to the tetrad structure as this is the common feature in all four samples. Perhaps one of the most interesting findings of this study was in the $SrCl_2$ sample that showed a lifetime of 80 ps for the guanine ring vibration and the transient absorption band, while the guanine carbonyl band indicated a 2-fold greater contribution from a species having a lifetime of 160 ps. This carbonyl band is located beside the divalent ion, and this may have an effect on the electron distribution in the excited state, and hence the relaxation rates. Without further experimentation, it is impossible at this time to draw any further conclusions.

5.4.4 Conclusions

The TRIR spectrum of the human telomeric has been recorded for the first time. In addition our study sought to characterize the cation-dependent (both mono- and divalent cations) structure and resulting excited state behaviour following UV photoexcitation. While the overall profiles of the samples were similar the high wavenumber guanine band was found to be sensitive to the cation used to template the scaffold, as evidenced by the shifting of this band in both the FTIR and TRIR spectra. In terms of stability of the samples to laser exposure the sample with no additional salt and the $SrCl_2$ did show signs of degradation, while the NaCl and KCl samples appeared to be unaltered after experiment. The reason for this is at present somewhat unclear, as the laser power for the individual samples was not recorded and any comparison of degradation between samples would have to be made with samples that had experienced the same exposure.

The relaxation dynamics of the samples were broadly similar with two lifetimes apparent in all cases. The first lifetime is assigned to the cooling of the vibrationally hot ground state that results following rapid (< 1 ps) internal conversion to the ground state. This process was found to occur in ~4-8 ps and account for 50-80% (generally speaking) of the decay in the samples. The rate of the cooling is slower than that observed for the constituent mononucleotide units (2-4 ps) and this can be rationalized in terms of some cation-dependent mechanism (i.e. less D_2O to interact with the polar groups of the molecules as they have been displaced by the metal cations, and hence vibrational cooling is less efficient) or in terms of stacking interactions, which we have shown in previous

chapters to elongate the dynamics. The second species detected is assigned to an electronic excited state or states. The lifetime of the long-lived component was found to vary (78-166 ps, upper and lower limits taken from table 5.3) between samples. For the most part, the lifetime observed for the guanine ring vibration and high wavenumber bleaches were within experimental error of one another. The $SrCl_2$ sample was an interesting exception to this where there was a distinct difference in the lifetime of these two bands.

5.5 Overall Conclusion

This chapter represents an ambitious study of the photophysical behaviour of biologically relevant systems. Testament to the challenge of characterizing the ultrafast processes in such systems is the absence of any literature relating to the ultrafast photophysical processes of these systems. As prefaced in the outline of the chapter, this work was an exploratory one, and any insight gained, however small, would indeed be a step forward. As one might expect with preliminary studies, further experimentation will be required to follow up on the initial findings and to uncover the nuances. This study has shown that the behaviour of the samples is much more complex than a collective of the constituent parts, and secondary structure, in addition to interactions such as base-stacking and hydrogen-bonding, was found to have a profound effect on the excited states produced and ensuing relaxation dynamics.

In the first study, an examination of mixed-base duplex DNA, hybridization of two complementary mixed-base strands was characterized by TRIR for the first time and two lifetimes were evident upon photoexcitation. Cooling of the vibrationally hot ground state and electronic excited state or states were proposed as the likely candidates responsible for the lifetimes. Perhaps more importantly the study highlighted some fundamental points. The presence of a long-lived component in a mixed-base system would imply that electronic delocalization occurs between the stacked bases and possibly even across the hydrogen-bonded structures (as the bases, with the exception of 5′-dCMP do not have a long-lived component when studied in isolation). The spectra obtained for both the single- and double-stranded TRIR experiments were not simply the sum of the parts – band

positions were found to shift and band intensities were also modulated. This is another indication that electronic communication occurs in such systems and that relaxation dynamics are heavily dependent on secondary structure.

The next section involved probing the ultrafast relaxation mechanisms in triple-stranded DNA. This represented a comprehensive review of the basic single-stranded elements, to the higher order double stranded B form helix and finally the triplex structure. Both short oligonucleotides (18 bases long) and polymer strands (average ~ 2000 bases long) were studied. Surprising results were found for the adenine single strands, prompting a review of all adenine systems studied in this thesis. It would appear that the lifetime of the long-lived species in adenine stacked systems is dependent on the secondary structure and there are possibly a multitude of states that can be produced, which may account for the somewhat contrasting results found in the literature. Duplex structures, in both the oligo- and polynucleotide cases displayed a contribution from a long-lived state, and there were indications of changes in secondary structure of the sample with increasing laser exposure, as the band structure displayed variations between cycles. Studies on the triple-stranded forms revealed some exciting new results. The kinetics that both systems displayed were predominantly monoexponential. This would imply that the incorporation of the third strand results in faster relaxation dynamics – faster than both the single- and double stranded cases. In the case of the polymer sample, the third strand was found to disassociate with the duplex after one cycle. Intriguingly, in an additional polymer sample tentative evidence was found to suggest that some time (several hours) after the experiment, the third strand may have returned to the major groove of the duplex and reformed the triplex. In contrast the oligonucleotide sample was found to be remarkably stable throughout the experiment. A key observation of all the experiments was that thymine residues in isolation were found to undergo irreversible photodamage upon laser exposure. However, in the presence of the complementary adenine strand (either in the duplex or triplex), this damage appears to be minimized and the thymine strand does not suffer the same fate. Future studies are required before the observations of this study can be corroborated and studied in greater detail.

The third and final study was a TRIR investigation of the human telomeric sequence, a sequence that has been directly linked with the immortality of cancerous cells. The

quadruplex structure that this sequence is known to form is dependent on metal cation and our cation-dependent investigation would suggest that while the guanine carbonyl band position was found to be sensitive, the relaxation dynamics upon excitation did not show a dramatic difference between cations. Some tentative evidence for cation-dependent sample stability was found, however this is offered with the caveat that the laser power may not have been the same for all samples. The relaxation dynamics were found to be biphasic, with the lifetimes being assigned to cooling of the vibrationally hot ground state and an electronic state or more likely states, probably excimer/exciplex in character. Interestingly, the sample that contained the divalent Sr^{2+} cations was the only one to display mode specific long-lived relaxation times in the bleaching bands. Further experimentation is required to address this phenomenon.

Finally, these studies have again shown that ps-TRIR gives direct information relating to structure and dynamics. The goal was to produce proof-of-concept data and this has been achieved. Future work will involve the acquisition of improved measurements and seeking to resolve the transient species. In particular, the behaviour of the 1537 cm^{-1} mode will be investigated as this feature gives a direct insight into the strains taking place within the quadruplex structure. The correlation between the stability of this band under solution phase (biologically relevant) conditions. Another key question is whether the longer lived transients correlate with a tighter structure and/or more delocalized electronic structure. Answering questions such as these may help answer fundamental questions on key issues relating the relative contributions that destabilising the secondary and/or tertiary structure of DNA has in increasing the potential for genetic modification and errors in protein transcription through such change.

Chapter 6

Bimodal Nanoparticles for Biomedical Applications

6.1 Introduction

6.1.1 Nanoscience – The Next Big Thing!

Over the past decade there have been remarkable advances in nanoscience and this is due in no small part to increased investment by both public and private sectors in this emerging science. The National Science Foundation of the U.S.A. recently proclaimed: "nanotechnology has a projected total worldwide market size of over $1 trillion dollars annually in 10 to 15 years."

Nanoscience requires multidisciplinary co-operation and offers researchers the opportunity to collaborate with groups outside of their accustomed field. The fundamental sciences of Biology, Chemistry and Physics converge at the nanoscience interface, and all three are essential to the increased understanding and continued evolution of the subject.

Nanoparticles are unique in that they can have physical and chemical properties that are neither characteristic of their atoms nor their bulk counterparts. The large ratio of surface area to volume contributes to some of the unique properties of nanoparticles. Novel electrical, optical, magnetic, and catalytic properties of particles are constantly being discovered and studied in greater detail in order to exploit these unique properties and develop a new generation of "smart" materials. Understanding and exploring the nano realm requires that existing methods used to characterize such singular materials must be updated and adapted, alongside the emergence of newer and more sophisticated techniques.

The properties of nanoparticles arise from their size, and because of their nanoscopic dimensions, they often behave differently to their bulk counterparts – see figure 6.1 (a) for a comparison of the size of nanoparticles compared to some biological entities.[268] Researchers now have a much greater ability to control the size of nanoparticles, with particles as small as 2-3 nm having been characterized.[269] Such small particles can penetrate through the endothelium of cancerous cells easily, taking advantage of the 'leaky' nature of the blood cell wall and because of this capability, these vehicles offer new possibilities of therapeutic applications. Target specific applications of nanoparticles are constantly increasing and the next generation of 'smart' nanoparticles will possess mutifunctionality – e.g. targeting, imaging, reporting and delivering therapeutic applications (see figure 6.1 (b)). High selectivity and high sensitivity are desirable. The

large ratio of surface area to volume contributes to some of the unique properties of nanoparticles, and the optimal balance between particle size and effectiveness of the particle for biomedical applications must be found. Ideally, the size of the particles should be large enough to allow for multi-ligand docking, for instance if the particles are being used for biomolecule recognition or screening of multiple biomarkers.[270-272] The stability of the particle can also be dependent on the size, and if agglomeration of particles intended for biomedical applications occurs, this has obvious negative consequences. The speed or ability of a particle to move through a biological environment will also be a product of its size as there will be a greater drag on larger particles. Biocompatibility and biodegradability are two other concerns for such particles, as the cure should not cause more harm than the disease.

Magnetic nanoparticles such as magnetite fulfil many of the requirements just outlined. At present particles such as the multifunctional target in figure 6.1 (b) have not been made but researchers are getting ever closer to the ideal particles. With regards to targeting, magnetite by virtue of its magnetic properties can be directed to a specific site with an external magnet.[273] Targeting of cancerous cells has also been achieved by taking advantage of the fact that folate receptors are over-expressed in cancerous cells.[274] Magnetic nanoparticles are ideal imaging agents, and are being used in magnetic resonance imaging (MRI) applications.[275-277] Ferrofluid contrast agents for MRI are commercially available and these particles have many potential applications by virtue of their size and susceptibility towards external magnetically controlled manipulation. As therapeutic agents, magnetite nanoparticles have been shown to be effective in the hyperthermic treatment of cancers.[278] The reporter aspect of magnetite nanoparticles is probably the area that offers most scope to researchers. Electrostatic attachment of fluorophores has been achieved but the ultimate challenge is to covalently attach a reporter unit that will have good reporter efficiency (i.e. good quantum yield of fluorescence); be stable (electrostatically attached fluorophores may not be very stable in highly charged cellular environments); and emissive (avoiding quenching) in a biological environment. This is one of the main targets of this work, as the properties of iron oxide nanoparticles and metal complexes make them ideal candidates for such a magnetic and fluorescent reporter unit.

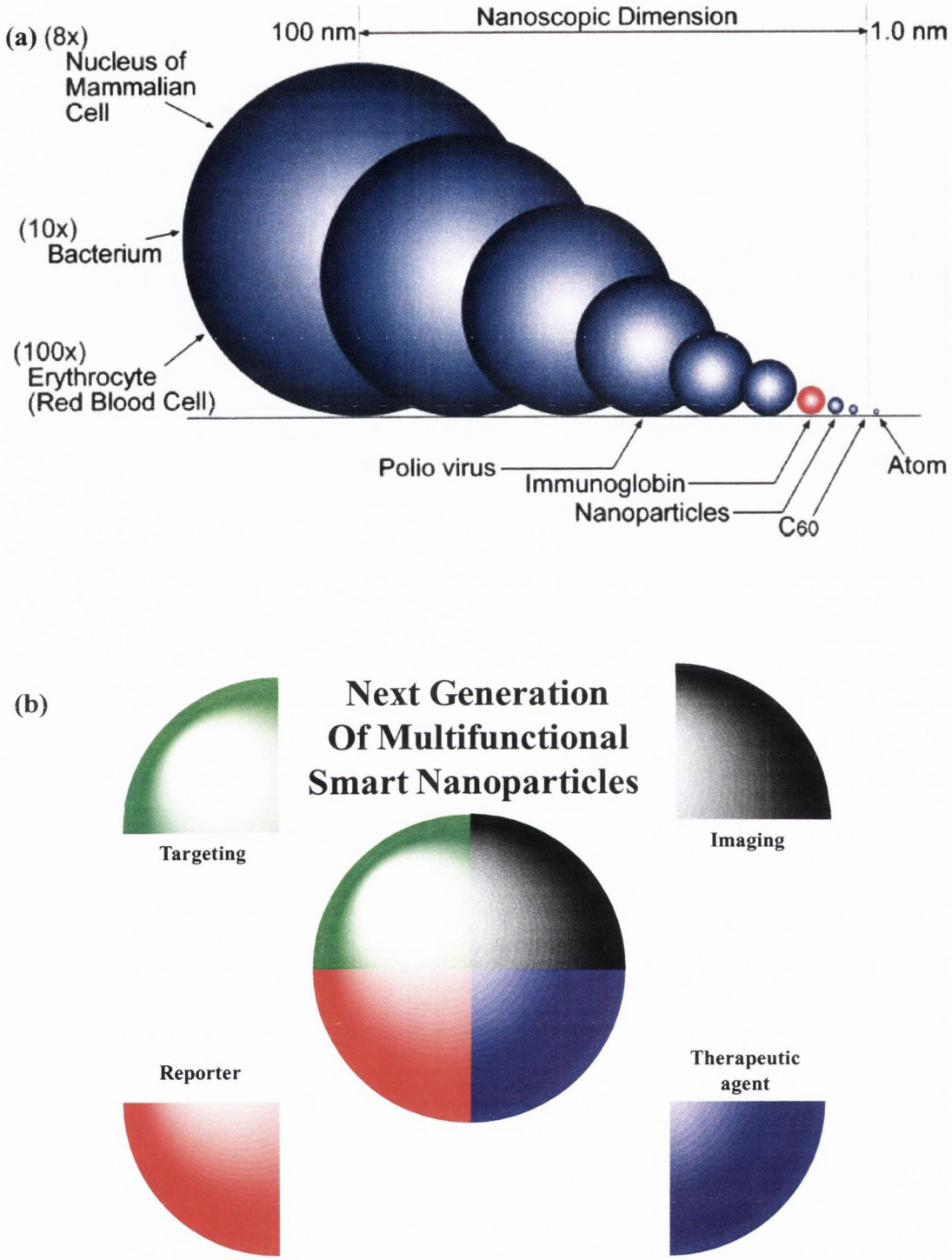

Figure 6.1 (a) Comparison of the size of atoms, nanoparticles and biological entities (reproduced from reference 268) and (b) schematic representation of the next generation of multifunctional 'smart' nanoparticles.

6.1.2 Magnetite – Structure and Magnetic Properties

Magnetite (Fe_3O_4) is the simplest of the so-called ferrites, compounds of the form $X^{2+}(Y^{3+})_2O_4$, crystallising in the spinel structure.[279] Its structure is cubic, having 8 tetrahedral (T_d, A) sites being occupied by ferrous (Fe^{2+}) cations, and 16 octahedral (O_h, B) sites which are occupied by the ferric (Fe^{3+}) cations. The remaining component of the unit cell, the oxygen anions (O^{2-}) form a face-centred cubic (fcc) closed packing arrangement.[280]

However magnetite undergoes a transition, known as the Verwey transition, from a spinel to an inverse spinel structure ($[Fe^{3+}]_{Td}[Fe^{3+},Fe^{2+}]_{Oh}O_4$) at temperatures above 120 K (figure 6.2).[279,281] Tetrahedral sites are now occupied by ferric ions and the octahedral sites now have an equal number of ferric and ferrous ions. This arises from the fact that above this temperature fast electron hopping occurs between the Fe^{2+} and Fe^{3+} ions on the O_h sites.[282,283]

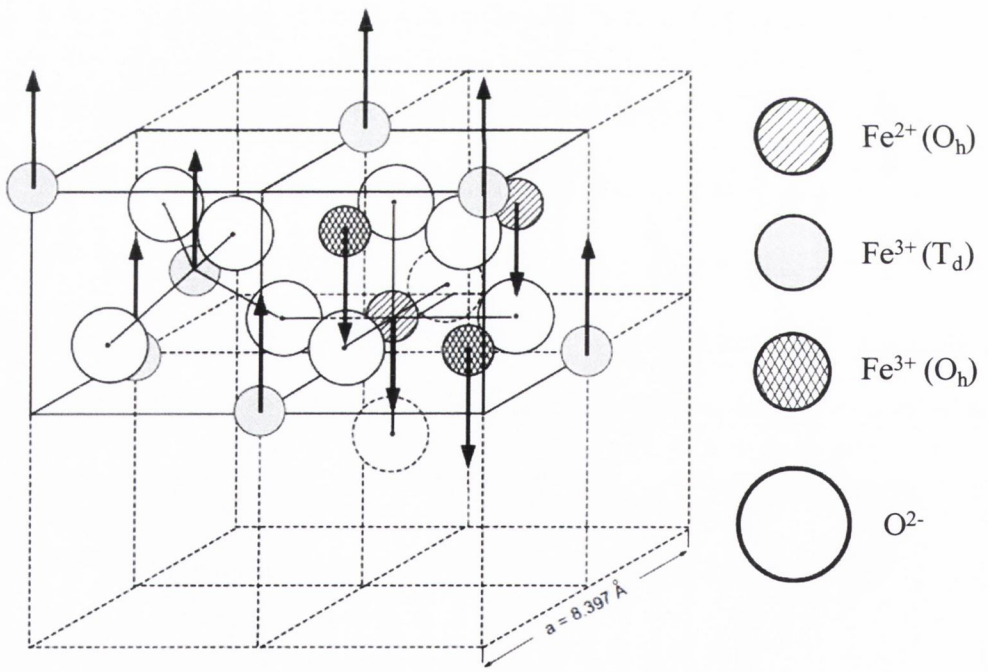

Figure 6.2 Inverse spinel structure of magnetite. Unit cell consists of fcc lattice of O^{2-} ions with the tetrahedral and octahedral sites containing the iron ions. Adapted from reference 281.

The magnetic state of magnetite depends on the size of the material. On going from the bulk to the nano realm, there is a transition from ferrimagnetism to superparamagnetism. The Curie temperature of magnetite is 570 °C. Superparamagnetism[284] is the phenomenon by which magnetic materials exhibit behaviour similar to paramagnetism at temperatures below the Curie temperature. Magnetite shows high conductivity, which is based on the electron exchange between Fe^{2+} and Fe^{3+} (figure 6.3). The conductivity is thermally activated and undergoes a first-order transition at the Verwey temperature of 120 K. The conductivity increases by orders of magnitude at this temperature. Even though the temperature is below the Curie temperature and the thermal energy is not sufficient to overcome the coupling forces between neighbouring atoms, the thermal energy is sufficient to change the direction of magnetization of the entire crystallite. The resulting fluctuations in the direction of magnetization cause the magnetic field to average to zero and each particle acts as a big 'spin' with suppressed exchange interaction between the particles.[285]

As the crystallite size decreases, the crystalline anisotropy energy also decreases - that being the energy required to change the direction of magnetization. The result is a decrease in the temperature at which the material becomes superparamagnetic.

The magnetisation near the surface is generally lower than in the interior. With increasing reduction in size, the surface effects become more predominant. Reduction in particle size leads to a reduction in magnetic transition temperature.[280]

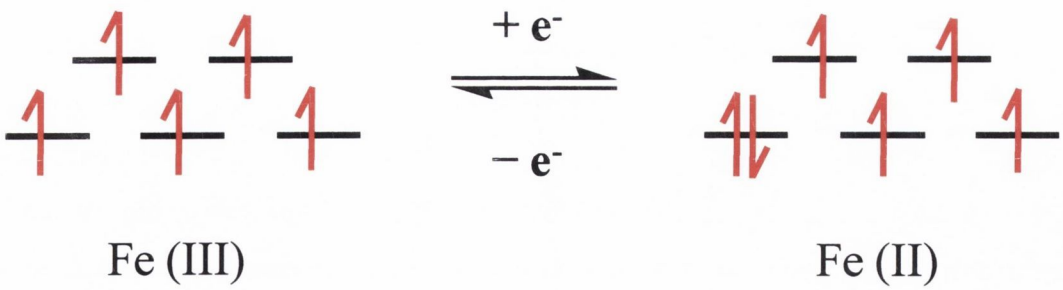

Figure 6.3 Electron hopping process between Fe^{3+} and Fe^{2+} ions in the O_h sites.

6.1.3 Synthetic Methods for the Preparation of Magnetite

There are numerous accounts on the synthesis of micro- and nanosized magnetite particles, ranging from bacterial aerobic synthesis[286], sonochemical[285], reverse micelle[287], sol-gel techniques[288], laser pyrolysis[289], dendrimer mediated self assembly[290] and both seeded[291] and direct co-precipitation methods.[292] A common thread that runs through the literature in all of the techniques listed above is a desire for the control of the size and shape of the particles. This is of paramount interest to the researcher, as these variables are intrinsically linked to the overall properties of the resulting material and are fundamental to any potential application(s).

Control of the size and morphology of the particles is achieved by controlling the experimental conditions of the particular technique. Temperature, ionic strength, concentration of reactants, solvent, reaction time, and pH all have an influence on the product that is obtained. The scope of synthetic procedures and experimental conditions are far too expansive to discuss in detail here, but some considerations relating to the experimental parameters of the co-precipitation reaction follow.

There are several reports in the literature in which researchers studied the effect of ionic strength, pH and temperature on the co-precipitation reaction. All of the reports agree that high ionic strength, low temperature and high pH favour the formation of smaller particles. The ionic strength ideally should be in the region $0.5 \leq I \leq 3$ where I is the ionic strength in mol L^{-1}.

Smaller particles are formed at lower temperature, but at higher temperatures, the rate of precipitation of magnetite is greater[293] and increased crystallinity of samples is reported.[294] With regards to pH, the accepted optimal range for magnetite formation is $8.5 \leq pH \leq 12$.[282] The isoelectric point of magnetite[283] occurs at pH 7 so the particles are expected to carry a net zero charge at this pH. At pH values lower than 9, colloids coagulate due to neutralization of their charges making the formation of stable aqueous sols impossible.[291] Formation of magnetite is reported to be suppressed at high pH (pH~13) with goethite (α-FeOOH) being the main iron oxide phase formed.[293]

6.1.3.1 Co-precipitation Method

With the co-precipitation method being both the most widely studied and the method employed in this work, a brief overview of the theory is warranted. Co-precipitation reactions involve the simultaneous occurrence of nucleation, growth, ripening/coarsening, and/or agglomeration processes. Ideally, for the production of nanoparticles, a relatively fast nucleation process with a relatively slow growth process is desirable. It is impossible to study each of these processes independently and as a consequence the fundamental mechanisms of co-precipitation are still not fully understood.

Nucleation and growth are the two processes that govern the particle size and morphology. When precipitation begins, numerous small crystallites initially form (nucleation) and tend almost instantaneously to aggregate together to form larger and more thermodynamically stable particles (growth).

Take the simple precipitate reaction:

$$A^{x+}_{(aq)} + B^{x-}_{(aq)} \leftrightarrow AB_{(s)} \qquad \textbf{(6.1)}$$

The equilibrium relationship between the product and its reactants can be expressed as the solubility product, K_{sp}:

$$K_{sp} = (a_A a_B)_{eq} \qquad \textbf{(6.2)}$$

where a_A and a_B are the activities of A and B in solution. The degree of supersaturation, S, is critical to any precipitation process and is given by:

$$S = a_A a_B / K_{sp} \qquad \textbf{(6.3)}$$

The difference in the concentrations of the solute at saturation (C) and at equilibrium (C_{eq}), $\Delta C = C - C_{eq}$ is referred to in the literature as the "driving force" for precipitation.

As nucleation begins in a supersaturated solution, there exists an equilibrium critical radius R*. Nucleated particles with R>R* will continue to grow, while those with R<R* will dissolve. If the nucleation rate per unit area is isotropic at the growth face, spherical particles will result. Ostwald ripening or coarsening, which is essentially the consumption of smaller particles by larger ones during the growth process, is a secondary process that can occur. Clusters continue to grow so as to minimize the free energy (ΔG) of the system until all reactants are consumed and equilibrium is attained.[295]

6.1.4 Coating and Stabilization of Particles

For a stable dispersion, forces due to thermal motion and interparticle repulsion in the ferrofluid must be stronger than the attractive van der Waals and magnetic forces in order to stabilize the ferrofluid. Due to their small size and large surface area, magnetic nanoparticles will tend to aggregate to reduce their surface energy.[296] The stability of a ferrofluid is not only determined by the inhomogeneous particle size distribution, but is also affected by the surface charge of the particles in solution.[297]

To prevent the inevitable agglomeration of particles some method of stabilisation is required. There are two main types of stabilization that may be employed, namely steric and electrostatic stabilization. Coating of surfaces can often change the intrinsic physical and chemical properties of the nanoparticles. The study of coatings on the surface of nanostructured powders is of great interest, because the coating can alter the charge, functionality, and reactivity of the surface, and enhance the stability and dispersibility of the nanoparticles.[298]

Steric stabilisation involves employing bulky or sterically demanding molecules. When particles are formed with coatings that provide robust stabilization such as those that repel each other sterically and provide thermodynamic stability the particles do not cluster. Ditsch *et al.* reported the controlled clustering and enhanced stability of polymer coated magnetic nanoparticles and found that low molecular weight polymers result in thin coatings that do not sufficiently screen van der Waals attractive forces, while high molecular weight polymers bridge between particles and bare magnetite.[296]

Long chain acids (oleic, lauric, hexanoic, decanoic acids) can be used to stabilize particles.[298,299] Strong binding occurs between the acid and the nanoparticle surface. Farrell *et al.* have reported the control of interparticle distance using oleic acid (OA) and oleylamine (OY), with the oleylamine being used to reduce the oxidation reactivity of the acid.[299] Replacing the OA/OY with hexanoic acid and hexylamine (HA/HY) can shorten the interparticle distance and particles remain apart even when dry.

Electrostatic stabilization utilises Coulombic repulsion forces. Once the surface of the particle is charged, the counterions in solution are in thermal motion, balancing the electrical attractive force to form a diffuse double layer around the particles. The electric double layer is dependent on dispersion of the particles in the polar medium, pH, concentration, and ionic strength of the suspension. Stabilisers such as tetramethylammonium hydroxide[276,282] (see figure 6.4) create such an electric double layer and result in stable ferrofluids.[297] Hydrophilic groups such as hydroxides, carboxylic acids, thiols and amines can generate a surface charge on particles.

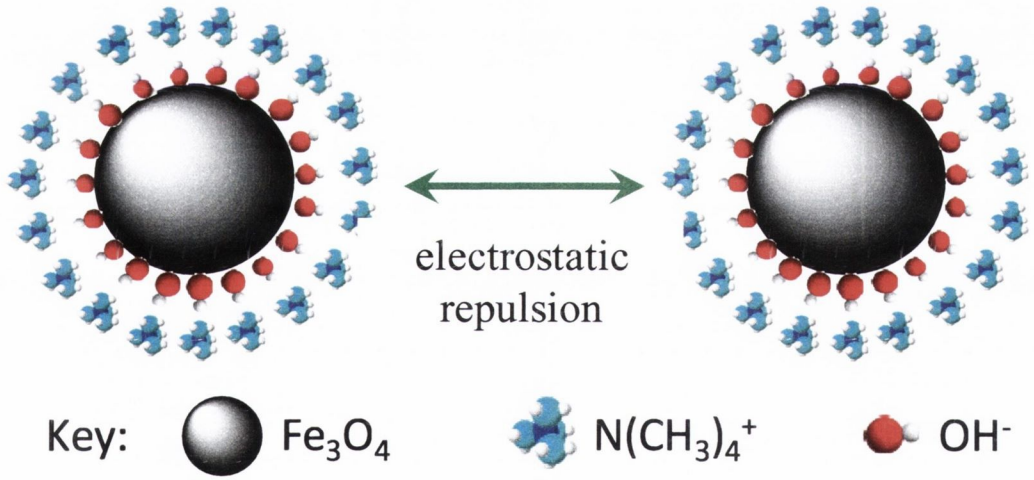

Figure 6.4 Example of electrostatic repulsion using tetramethylammonium hydroxide.

Ferrofluids for use in biomedical applications can be coated so as to increase their efficacy. Increasing the hydrophilicity of nanoparticles as has been shown by Gupta *et al.*, where magnetite was coated with pullulan, a non-ionic polysaccharide (primarily used as a food additive), resulted in reduced particle toxicity, increased blood retention time and allowed for increased cellular uptake of particles.[300] Rapid elimination of nanoparticles from the

blood stream after their injection is due to their recognition by macrophages of the mononuclear phagocyte system. Uncoated nanoparticles tend to agglomerate and absorb plasma proteins, after which the particles are quickly cleared by macrophages before they can reach target cells. Coating particles so that they will no longer have the tendency to aggregate, and therefore minimize or eliminate protein absorption, increases their circulation time in the blood stream.

Folic acid/PEG coated particles have been synthesized by Zhang *et al.* for use in targeted cancer therapies.[274] The folate receptor is frequently overexpressed on the surface of cancer cells. The receptor is not only a tumour marker but is known to efficiently internalise molecules coupled to folate, and therefore increase cellular uptake. This method overcomes many of the problems with nanoparticle cancer therapies: aggregation of particles, low intercellular uptake, short blood retention times and non-specific targeting.

Silica coating is routinely applied to magnetite nanoparticles for a number of reasons. It lowers the isoelectric point to pH 3, and in so doing results in an increased stability of the particles at neutral/physiological pH.[282,297] Silica coated particles are less susceptible to microbial attack, aggregate less than uncoated particles and functionality can be added to the particle surface, using for example amino- or thio- silane derivatives, allowing for subsequent modifications. In functionalising magnetite with flurophores, the problem of quenching can be overcome with an 'insulating' silica layer around the iron core. Silica coating reduces the cytotoxicity of the nanoparticles and therefore increases the blood retention time.

6.1.5 Labelling Biological Materials with Luminophores

Fluorescent labelling of biological materials using small organic dyes is widely employed in the life sciences, and has been used in a variety of applications that include diagnostics and biological imaging.[301] Organic fluorophores however have characteristics that limit their effectiveness for such applications. These include narrow excitation bands and broad emission bands with many exhibiting low resistance to photodegradation.[302] Metal polypyridyl complexes offer an excellent alternative as their photophysical properties can be tuned by ligand and or metal variation. Other advantages of such ruthenium systems

include long-lived emission for the excited state and their suitability towards binding with bio-macromolecules. Ruthenium metal complex chemistry is well established and as the group had expertise in this area[303] it was decided that such complexes would make for ideal luminescent labels for the development of novel 'two in one' magnetic and fluorescent nanocomposites.

6.1.6 'Two in One' Iron Oxide Nanocomposites to Date

Attachment of gold nanograins to magnetite,[304] gold coated iron nanoparticles,[287] nanoparticle heterodimers comprised of silver and magnetite, texas red labelled magnetite,[277] silica encapsulated CdSe/maghemite,[305] fluorescein thioisocyanate labelled maghemite,[306] silica coated particles for tumour targeting,[273] glucose sensing particles[307] and methotrexate-modified magnetite,[275] are all examples of iron oxide nanocomposites that have been reported in the literature in recent years, proving that the area is an active and relatively newly emerging one.

Lu *et al.* have prepared multi-functional nanoparticles possessing magnetic up-conversion fluorescence and bio-affinity properties by covering a magnetite core with ytterbium and erbium co-doped sodium yttrium fluoride (NaYF4:Yb,Er) which is an efficient infrared-to-visible up-conversion phosphor.[302] Electrostatic attachment of Prussian blue to magnetite was achieved by Zhao *et al.* and was studied with regards to the electrocatalytic reduction of H_2O_2.[308]

Both red- and green-emitting CdSe/ZnS quantum dots embedded in a mesoporous silica sphere that encapsulated magnetite nanoparticles (150 nm) have been reported.[309] Absorption and release of ibuprofen was analysed and it was found that 3-aminopropyltriethoxy silane (APTES) coated particles released the ionically attached drug at a much slower rate than tetraethyl orthosilicate (TEOS) coated particles due to the interaction of the amino group with the carboxylic acid on the drug.

6.1.7 Applications of Iron Oxide Nanocomposites

Iron oxide nanoparticles lend themselves to a very wide range of potential applications. High-density magnetic storage devices, sensor applications such as oligonucleotide sequence detection,[310] temperature humidity sensors[288], magnetic switches, and magnetically recoverable catalyst carriers.[311]

But perhaps the most widely researched and explored applications of iron oxide nanoparticles are of biological nature. Particles can be used in magnetic separation and cell sorting. The magnetically amplified DNA assay (MADA), which is the sensing of viral DNA and single-base mismatch by using nucleic acid modified magnetic nanoparticles has been shown to have a detection limit of single-base mismatch of 8.3×10^{-18} M (50 copies per 10 μL).[312] Cancer therapeutic agents allowing for targeted drug delivery based on iron oxide nanoparticles are currently under development[306] and some magnetic resonance imaging (MRI) contrast agents based on magnetite nanoparticles are currently commercially available. Nanoparticles can be used in the hyperthermia treatment of cancers,[278] with particles becoming entrapped in the capillary bed of the tumours. Taking advantage of the hysteresis loss of particles in an alternating magnetic field, the tumours are locally heated and perish at 43 °C due to insufficient oxygen supply.[282]

6.1.8 Aims and Objectives of this Work

The main aim of this work was to develop routes towards novel "two in one" fluorescent and magnetic nanocomposites of controlled size and morphology for intracellular visualisation, manipulation and diagnostics. Magnetic separation and fluorescent labelling are the two most widely used techniques used in bioscience today, and this work aims to combine facets from both techniques to futher the development of the next generation of nanocomposites (see figure 6.5). Main objectives include:

- Preparation and stabilisation of magnetite (Fe_3O_4) nanoparticles of controlled size and morphology
- Development of silica coating procedures with the aim of producing stable particles with increased biocompatibility and suitability toward further modification by virtue of an introduced functionality on the surface of the particles

- Preparation of ruthenium polypyridyl metal complexes as suitable luminophores for immobilization on nanoparticle surface
- Conjugation of luminophores with modified nanoparticles to result in novel "2 in 1" nanocomposites
- Preparation of novel oligonucleotide nanocomposites
- Photophysical characterization of all prepared nanocomposites

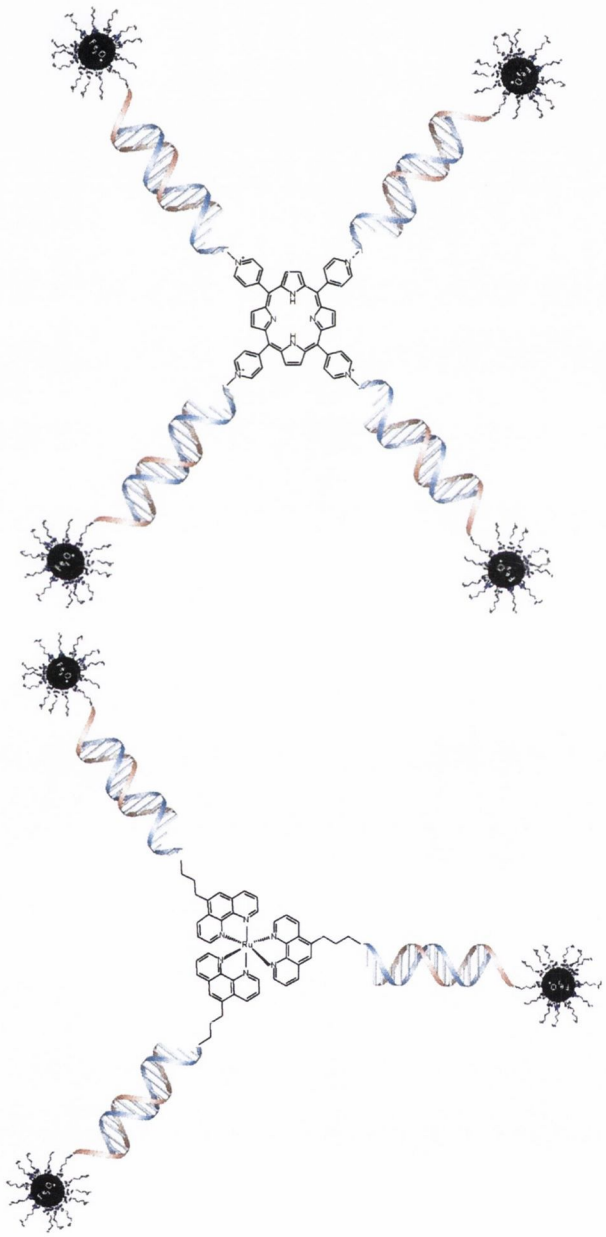

Figure 6.5 Example of possible two dimensional (2D) (using porphyrin) and three dimensional (3D) (using metal complex) magnetic and fluorescent nanoarrays.

6.2 Synthesis of Iron Oxide Nanoparticles

6.2.1 Preparation of Fe_3O_4 Nanoparticles

Magnetite nanoparticles were prepared according to the method of Philipse *et al.*[282] which itself is an adaptation of the aqueous co-precipitation method developed by Massart (see scheme 6.1).[292] Briefly, iron chlorides (Fe^{III}:Fe^{II} ; 2:1) were added to a vigorously stirred ammonia solution. The resulting particles instantaneously precipitate out of solution and were collected using an external magnet. Resuspension in a tetramethylammonium (TMA) hydroxide solution resulted in a stable ferrofluid suspension. Stabilization of the particles was required as the isoelectric point of magnetite occurs at pH 7, and without such stabilization the undesirable aggregation of particles is inevitable.

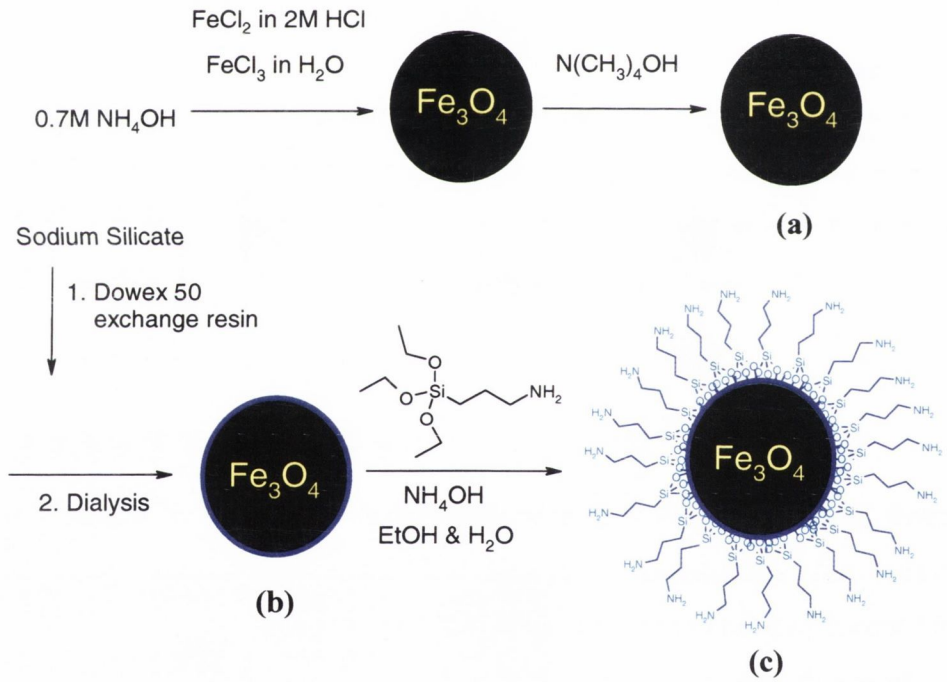

Scheme 6.1 Schematic for the preparation of (a) TMA stabilized, (b) silica coated particles and (c) 3-aminopropyltriethoxy silane (APTES) particles.

6.2.2 Preparation of Silica Coated and APTES Modified Fe_3O_4 Nanoparticles

Next, silica coating of the particles was carried out. This fulfils certain criteria required for the development of bimodal magnetic and fluorescent nanoparticles, namely: (i) the isoelectric point of silica occurs at pH 2-3, therefore coating the magnetite with silica results in stable suspensions at neutral and physiological pH, (ii) functionalities such as thio or amino can be introduced to the nanoparticles to allow for the subsequent coupling of fluorophore to the nanoparticle and (iii) if the particles are to be used for biomedical applications silica coating may help prevent their aggregation and increase their retention time in a biological environment.

A thin silica layer was deposited on the particles (scheme 6.1). A 0.58 wt % SiO_2 solution of pH 12 was prepared by dilution of a sodium silicate stock solution. The solution had a pH of 5 after passing through an acid exchange column (Dowex 50 Wx4 resin with sulfonic acid as functional groups). The pH was raised immediately to pH 9.5 by the addition of a few drops of silicate stock solution in order to avoid silica nucleation which may occur at acidic pH where silica has a low solubility. This silicate solution was mixed with the ferrofluid, the pH was adjusted to 10 and the resulting solution was stirred vigorously for 2 hours. Dialysis of the resulting dispersion was carried out so as to avoid flocculation of the particles, which may occur as a result of excess silicates in solution. There are two key parts to this procedure. Firstly, coating without the exchange of the Na^+ for H^+ ions resulted in samples that were not stable and tended to aggregate over time. Secondly, if the dialysis procedure was not performed, aggregation of the particles resulted. This is presumably due to excess silica that upon hydrolysis cross links the particles and ultimately resulted in their aggregation.

The Stoeber condensation of silica was used to further coat the nanoparticles (scheme 6.1).[313] Base condensation of an amino silane derivative was carried out in ethanol:water (4:1) mix. The resulting particles were washed several times to remove any excess silane species. This process involved the use of a strong (0.5 T) magnet to attract the particles so that the supernatant could be removed, and then resuspension of the particles in the absence of the magnetic field.

6.2.3 Preparation of Dopamine Modified Fe_3O_4 Nanoparticles

The binding of dopamine to the surface of iron oxides has been shown to be very strong and stable.[268,278,314,315] Dopamine modified magnetite was prepared following the procedure illustrated in scheme 6.2. This involved the precipitation of magnetite following the Philipse preparation as before, but this time the particles were resuspended by sonication in the presence of dopamine hydrochloride. Catechol binding to the iron surface is strong and resulted in very stable suspensions. Such particles may offer an additional route to the attachment of fluorophores as will be shown later.

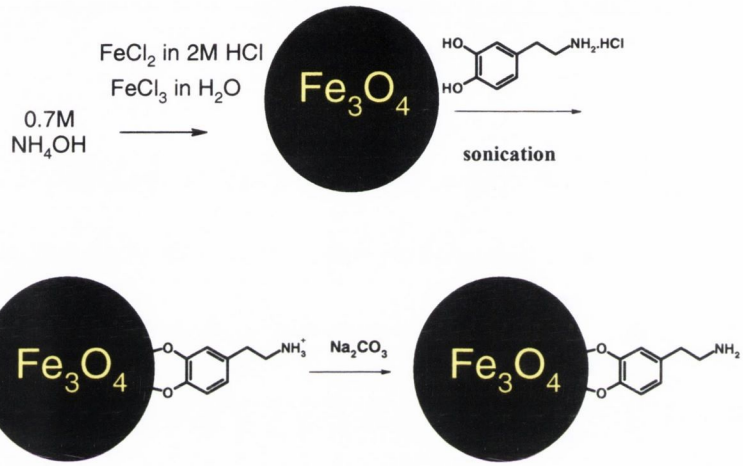

Scheme 6.2 Preparation of dopamine modified magnetite nanoparticles.

6.3 Characterization of Iron Oxide Nanoparticles

6.3.1 Characterization of Fe_3O_4 Nanoparticles

To confirm the presence of magnetite, powder X-ray diffraction (XRD) and infrared spectra were recorded. This was to discriminate between magnetite and maghemite, and confirm that the correct phase of iron oxide was present. Maghemite, Fe_2O_3, is formed upon oxidation of magnetite. Infrared (IR) analysis showed the characteristic Fe-O stretching frequency at 571 cm^{-1} with a band for the surface absorbed hydroxides at 3360 cm^{-1}. The XRD analysis is shown in figure 6.6. The spectrum of the particles (red line) was compared to known peak positions for magnetite (green lines, database file JCPDS No. 19-0629) and maghemite (blue lines, database file JCPDS No. 39-1346). As can be seen from table 6.1, the theoretical and experimentally obtained peak positions

correlate quite well, confirming that magnetite is the predominant phase of iron oxide present in the sample.

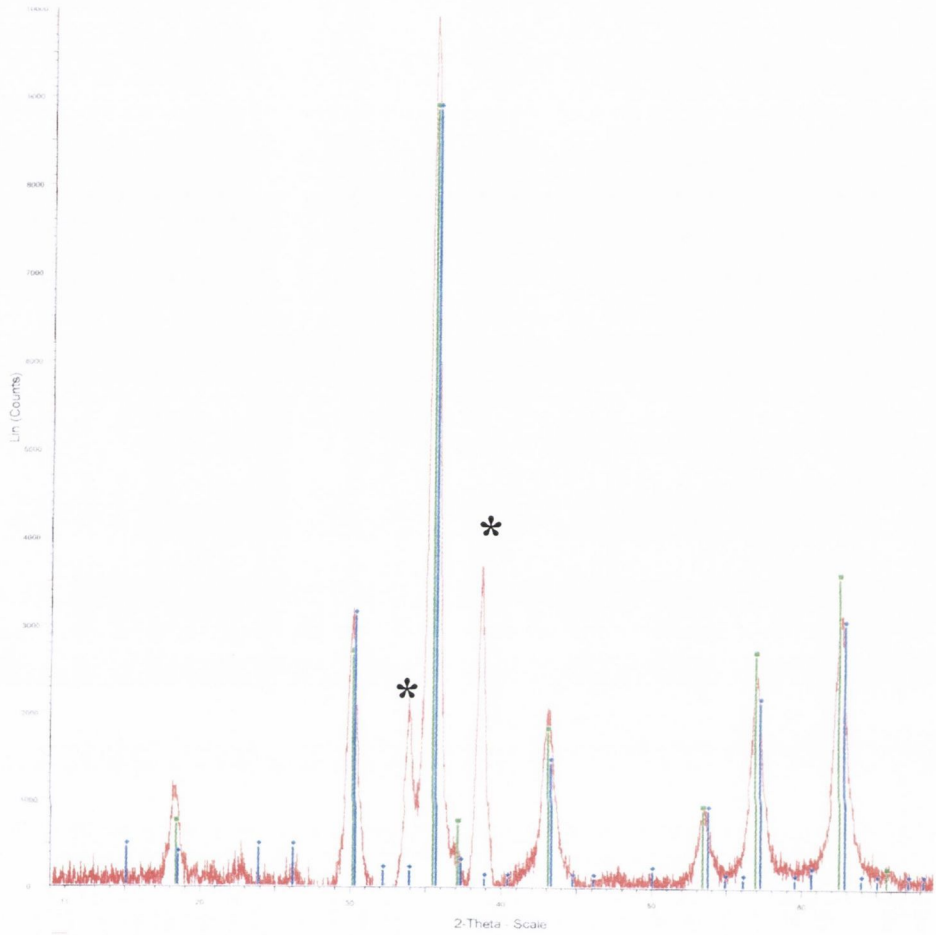

Figure 6.6 XRD of magnetite nanoparticles (red line). Expected peak positions for magnetite (green lines) and maghemite (blue lines) are also shown.
Peaks labelled * are Tungsten impurities from the instrument.

(h,k,l)	(111)	(220)	(311)	(222)	(400)	(422)	(511)	(440)
Theoretical 2Θ peak positions	18.27	30.10	35.42	37.05	43.05	53.39	59.94	65.52
Experimental 2Θ peak positions	18.23	30.32	35.74	37.10	43.39	54.19	55.81	62.90

Table 6.1 Comparison of theoretical and experimental XRD peak positions for Fe_3O_4.

Particles were also characterised by transmission electron microscopy (TEM) and typically showed a narrow size distribution with a mean diameter of 12 nm and standard deviation of 2 nm. As can be seen from figure 6.7, the particles appear aggregated on the TEM grid. The aggregation could be due to one or more of the following: (i) the particles are magnetic and are attracted to each other by magnetic interactions, (ii) the large surface area of the nanoparticles accelerates the agglomeration process in order to decrease the free energy (ΔG) of the system, and/or (iii) it could be a result of the rate and manner at which the solvent evaporated from the TEM grid.

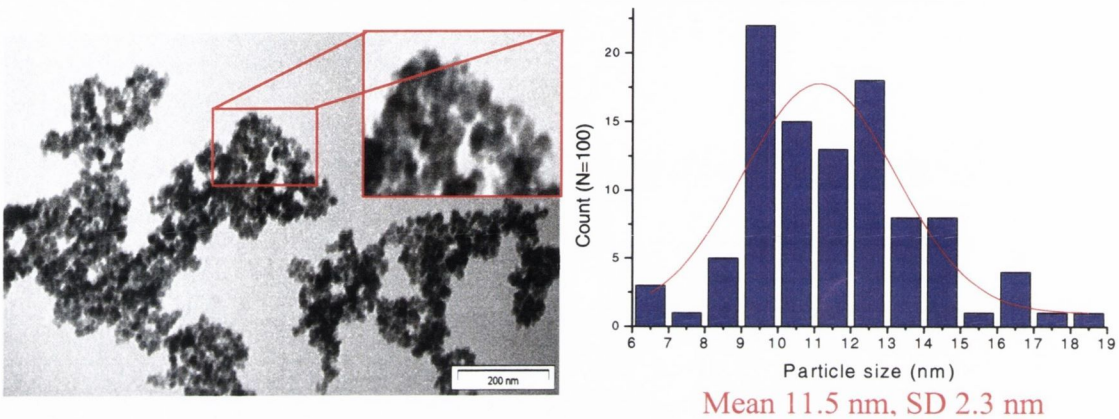

Figure 6.7 TEM image of magnetite nanoparticles with particle size distribution.

6.3.2 Characterization of APTES Modified Fe_3O_4

Particles were characterised by TEM and showed a Gaussian type distribution with a mean diameter of 19 nm and a standard deviation of 3 nm. A typical example is shown in figure 6.8 revealing there is a definite core/shell structure with the contrast between the magnetite core and silica shell clearly visible. However, the particles are somewhat aggregated and this may arise from any of the reasons as outlined above or in this case may also be due to interparticle cross-linking via siloxane bridges. IR analysis confirmed the coating with vibrations at 574 (Fe-O), 806 (Si-C), 1088 (Si-O), 1637 (C-N), 3450 (N-H) cm^{-1}.

APTES was used as it fulfils a few important requirements, namely: (i) the nanoparticle should be less prone to aggregation in solution as magnetic interactions are shielded and

the isoelectric point of the magnetite is lowered from pH 7 to 3, and therefore particles will be similarly charged and repel each other, (ii) coating with a silica layer may prevent quenching of luminophores (at least to a greater degree than the uncoated particles) and (iii) the nanoparticle now has a terminal amino functionality that can be used for subsequent modification and covalent attachment of luminophores.

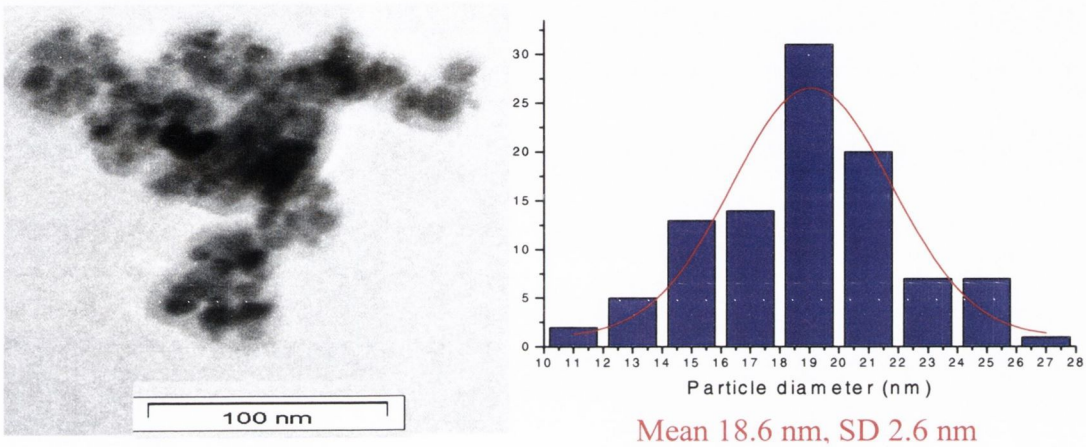

Figure 6.8 TEM image of silica coated (APTES) magnetite nanoparticles with particle size distribution.

The reaction is catalyzed in the presence of base but is also autocatalysed by the APTES itself due to the basic nature of the amino group, as noted by Bruce and Sen.[316] During the surface activation, there are two reactions taking place simultaneously with respect to the silane. Hydrolysis of the silane alkoxy groups to the highly reactive silanol species and the condensation of the resultant silanols with the free OH groups occurs on the surface to render stable Si-O-Si bonds. Oligomerisation in solution can occur as a competing reaction with covalent binding to the surface. Choice of solvent also affects the rate of reaction. Alcohols, being hydrophilic and protic solvents usually accelerate hydrolysis and condensation kinetics thus promoting the surface modification. Temperature also plays an important role in the kinetics. Not surprisingly, raising the temperature accelerates the condensation kinetics, both onto the nanoparticle surface and in solution, leading to the undesirable formation of silane aggregates. Particle aggregation phenomena and interparticle cross-linking through siloxane bridges may appear as a consequence of uncontrolled reaction conditions. Another important consideration with respect to silica coating is the concentration of the silane species. We found that the concentration of the

silane species was critical to the coating process. Too low a concentration resulted in incomplete coating of nanoparticles, while if the silane species was vastly in excess, the formation of silica nanoparticles was observed. Therefore, when coating nanoparticles with such species, the concentration of silane required was calculated by geometrical considerations of coating species and the size of particles to be coated.

The surface coverage of an APTES molecule ($S.C._{APTES}$) was calculated via simple geometry, and the surface area of a magnetite nanoparticle ($S.A._{magnetite}$) was calculated once the mean diameter of a sample of particles was known (obtained from TEM). The number of APTES molecules (N_{APTES}) required for a complete monolayer coating on each individual particle is given by:

$$\frac{S.A._{Fe_3O_4}}{S.C._{APTES}} = N_{APTES} \qquad \textbf{(6.4)}$$

The volume (V_{total}) of nanoparticles in any given sample of mass (M_{Fe3O4}) was calculated simply using:

$$\frac{M_{Fe_3O_4}}{\rho_{Fe_3O_4}} = V_{total} \qquad \textbf{(6.5)}$$

given the density of magnetite (5.2 g/cm^3). The number of particles (N_{par}) in a sample was obtained by:

$$\frac{V_{total}}{V_{particle}} = N_{par} \qquad \textbf{(6.6)}$$

Therefore, knowing the number of particles in a sample and the number of APTES molecules required to coat each particle, the concentration of APTES required was calculated.

6.3.3 Dynamic Light Scattering – Sizing and Zeta Potential Measurement of Fe_3O_4, Fe_3O_4@SiO_2 and Fe_3O_4@APTES

The particles were characterized using dynamic light scattering to determine the hydrodynamic radius. Zeta potential measurements were made to determine the charge on the surface of the particles and therefore provide an indication of their stability.

Light scattering results showed that the particle size increased on going from the tetramethylammonium hydroxide stabilized particles (16 ± 7 nm), to the silica coated (18 ± 8 nm) and finally (3-aminopropyl)triethoxy silane coated particles (87 ± 23 nm (37%) and 235 ± 89 nm (63%) (figure 6.9). It is noteworthy that the observed diameter is the hydrodynamic diameter and not the absolute diameter of the nanoparticles, and therefore these results are in excellent agreement with that of the TEM characterization. The results of the APTES sample would suggest that the particles are aggregated in solution or at least they are clumped so closely together they scatter the light in a similar manner to that of a large particle.

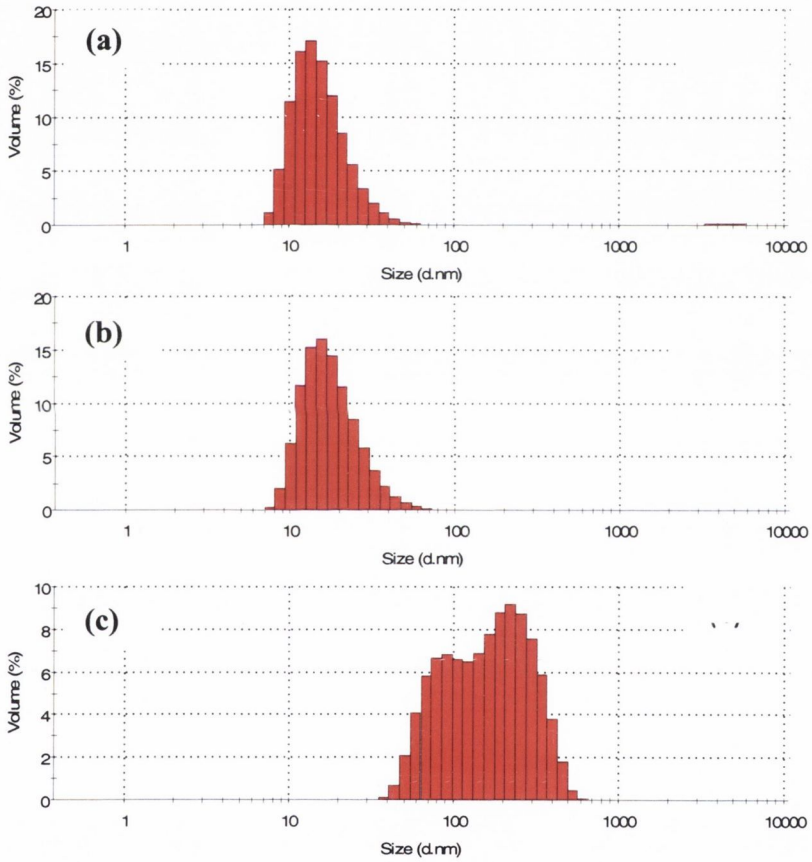

Figure 6.9 Dynamic light scattering histogram results for (a) tetramethylammonium hydroxide stabilized magnetite, (b) silica coated magnetite and (c) (3-aminopropyl)triethoxy silane coated magnetite. Measurements shown were carried out in water at neutral pH.

Zeta potential measurements on the particles confirmed the charge present on the surface of the particle, and hence gave an indication of the stability of the prepared particles

(figure 6.10). Measurements were carried out in water at neutral pH. Generally it is accepted that for nanoparticles to be considered stable they must possess a charge that is more positive than + 30 mV or more negative than − 30 mV. The results show that the tetramethylammonium hydroxide stabilized particles and the silica coated particles both possessed negative charges (− 46 ± 8 mV and − 43 ± 7 mV respectively). In the first case, the charge arises from the hydroxide ions on the surface of the nanoparticles. In the second case the negative zeta potential result arises from the presence of the silica layer on the particle which has shifted the isoelectric point of the particles (originally pH 7, now pH 2-3). The (3-aminopropyl)triethoxy silane coated particles carry a positive charge (+ 49 ± 7 mV), indicating that the particles were stable in solution. The positive charge that the APTES particles possess is due to protonation of the amino groups.

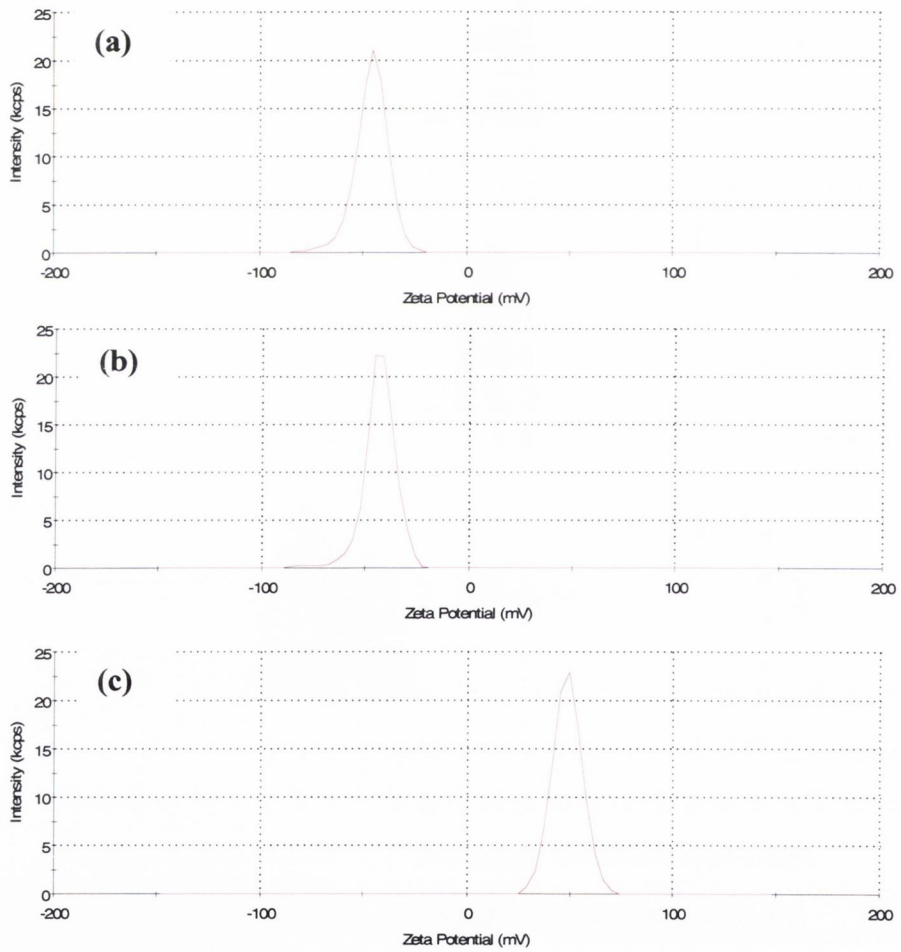

Figure 6.10 Zeta potential measurement results for (a) tetramethylammonium hydroxide stabilized magnetite, (b) silica coated magnetite and (c) (3-aminopropyl)treithoxy silane coated magnetite.

6.3.4 Dynamic Light Scattering – Sizing and Zeta Potential Measurement of Dopamine-Modified Fe_3O_4 Nanoparticles

Light scattering results revealed that the hydrodynamic diameter of the particles changed from 37 ± 12 nm for the hydrochloride salt of dopamine modified particles to 1000 ± 400 nm after treatment with Na_2CO_3 to remove the salt and furnish the free primary amine (figure 6.11). The reason for this dramatic change is that the particles are losing their stability in solution and agglomerating together. Zeta potential measurements reinforce this reasoning and reveal that before treatment with Na_2CO_3 the stable particles had a charge of + 36 ± 12 mV but after treatment with the base the charge at the slipping plane has decreased to just + 5 ± 5 mV. This has implications for the subsequent reaction of the particles, as poor stability of the particles with free primary amine functionality will mean decreased loading of fluorophore if the particles are tending to aggregate.

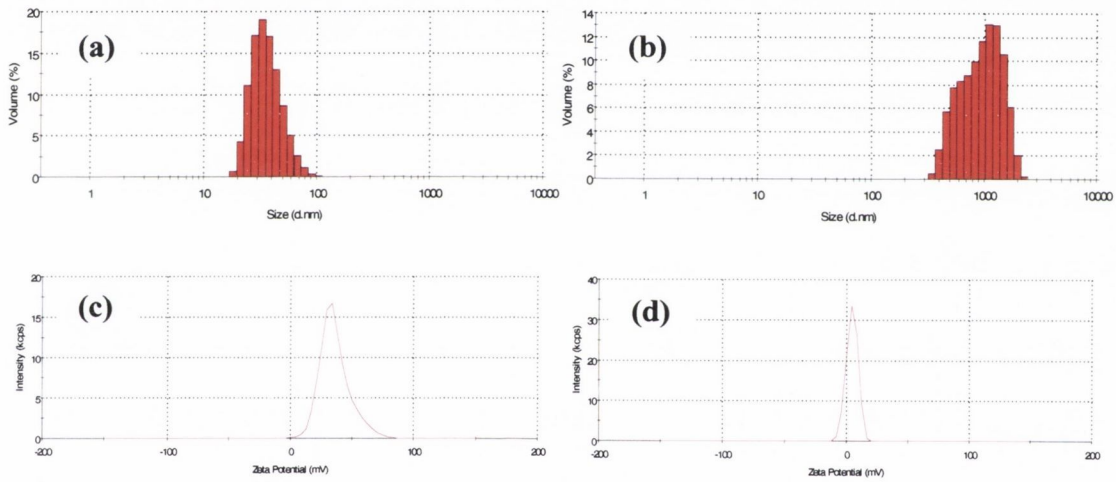

Figure 6.11 Light scattering histogram results for (a) dopamine modified magnetite with hydrochloric salt, and (b) after after removal of the salt.
Zeta potential measurements (c) with hydrochloric salt (d) after removal of the salt.
All measurements were recorded in water at neutral pH.

6.3.5 Reactivity of the Amino Modified Particles – The Kaiser Test

The Kaiser test,[317] more routinely employed to assess the completeness of solid phase peptide syntheses, was used to ascertain if the prepared particles had reactive free primary amines. This test is not only qualitative[318] but can be used quantitatively[319] to aid in the determination of the concentration of reactive amine present and hence the concentration of fluorophore needed for the coupling procedure can be more accurately estimated.

Scheme 6.3 outlines the test which involves the reaction of ninhydrin with a free primary amine. The procedure involves taking a few milligrams of particles and washing them three times with ethanol. Phenol ~ 80% in ethanol, KCN in H_2O / pyridine, and ninhydrin ~ 6% in ethanol is added to the particles and the resulting mixture is shaken and then heated to 120 °C for 5 minutes. The formation of an intense blue colour, Ruhemann's Blue, can be monitored using a UV/vis spectrometer and a concentration determined using the Beer-Lambert law.

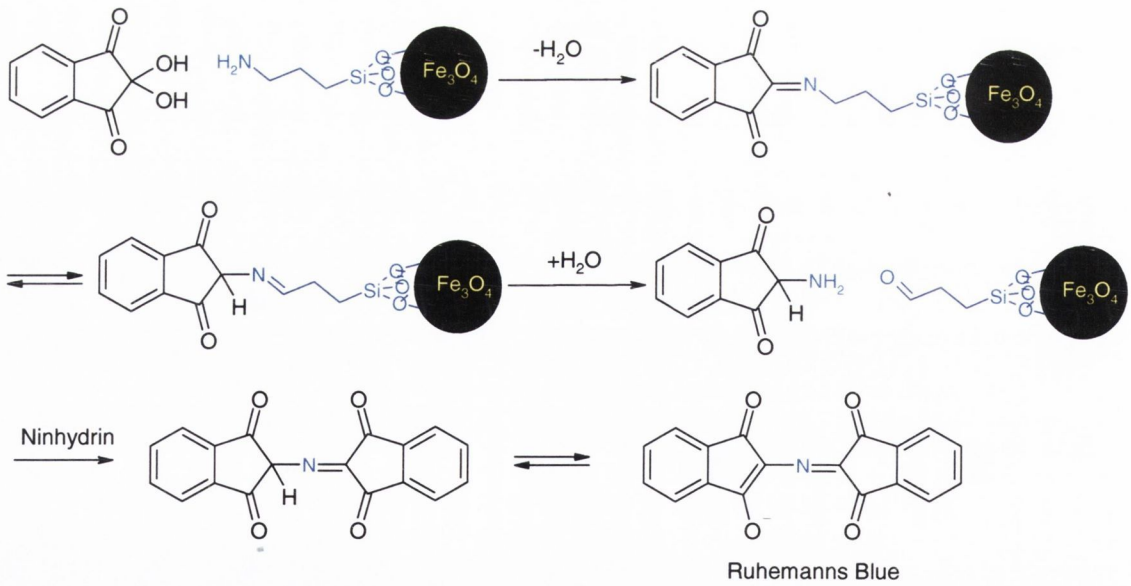

Scheme 6.3 Schematic representation the Kaiser test where an amino modified nanoparticle reacts with ninhydrin to produce Ruhemann's blue.

The test when applied to the (3-aminopropyl)triethoxy silane particles revealed that there were 139 nmoles of free primary amines per milligram of particles, while the dopamine modified particles had 74 nmoles of free primary amines per milligram of particles. The results of the test are given in figure 6.12 and correlate well with the light scattering data which suggested that the dopamine modified particles were agglomerating after treatment with base. This agglomeration process obviously decreases the surface area that is exposed and results in less free amines for reaction.

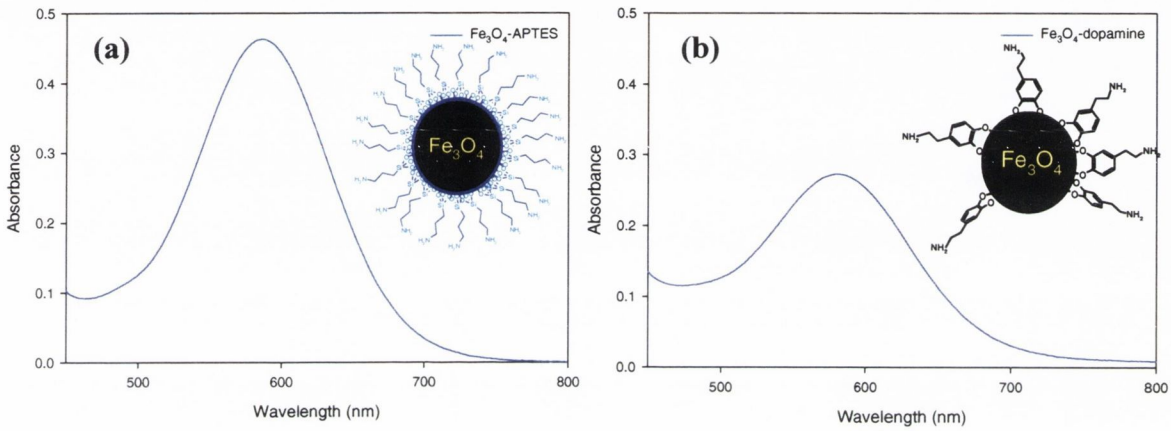

Figure 6.12 UV/vis spectra of the formation of Ruhemann's blue after the reaction of ninhydrin with (a) (3-aminopropyl)triethoxy silane coated magnetite and (b) dopamine modified magnetite. Absorption at 580 nm was used to calculate the number of free primary amines on the surface of the nanoparticles.

6.4 Ligand and Complex Syntheses

6.4.1 Synthesis of Phenanthroline Derivatives

For covalent attachment of a metal complex to the amino functionalized nanoparticles, it was necessary to introduce a functionality, on one of the three bidentate polypyridyl ligands, that could be coupled to the particle. The schematic below (scheme 6.4) illustrates the different ligands that were isolated. The synthesis of **1** was attempted following a *Merck* patent[320] which involved the reaction of 1,10-phenanthroline with fuming sulphuric and nitric acids but analysis showed that the preparation was unsuccessful, so commercially available 5-nitro 1,10-phenanthroline (**1**) was used in all phenanthroline derivative preparations.

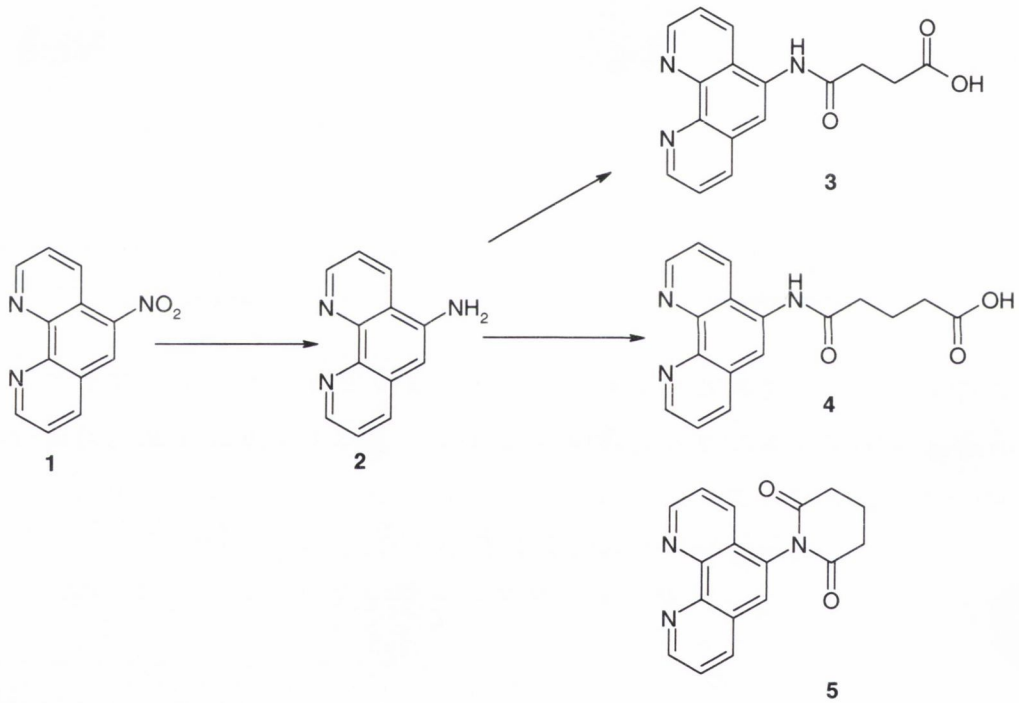

Scheme 6.4 Schematic representation of phenanthroline derivative ligands 1-5.

5-amino 1,10-phenanthroline (**2**) was prepared following a palladium-catalysed hydrogenation.[321] Palladium on charcoal (10%) was used as a reducing agent and hydrazine monohydrate was added dropwise. The resulting reaction mixture was refluxed overnight. After removal of the charcoal with celite, the filtrate was rotary evaporated, resulting in a yellow solid that was washed with ether several times.

Synthesis of 4-oxo-4-(1,10-phenanthroline-5-ylamino)butanoic acid, ligand **3,** was carried out following the method of Ramiro *et al.* by reacting **2** in the presence of succinic anhydride in chloroform with the reaction being catalysed by *p*-toluenesulfonic acid (PTSA).[322] The product precipitated out of solution after 3 days and was recrystallised from methanol in a modest yield of 50%.

5-(4-carboxybutanamido)-1,10-phenanthroline (phen′) ligand **4** was synthesized according to a method reported by the Barton group.[323] It involved the reflux of **2** with glutaric anhydride in pyridine. Thin layer chromatography (T.L.C.) analysis revealed that the starter had been consumed with two products present. The desired product **4** was precipitated out upon concentration of the reaction mixture and addition of acetonitrile. Conveniently, a side-product of the reaction, ligand **5**, was found to be soluble in acetonitrile so separation of the two products was straightforward. The intramolecular cyclisation resulting in the formation of **5** was found to increase with increasing reaction times.

Preparation of phen′ (**4**) was also carried out following the procedure of Ramiro *et al.*[322] As with the synthesis of **3**, the amino phenanthroline in chloroform was reacted with the corresponding anhydride, in this case glutaric anhydride, with the product being precipitated out of solution after 3 days. Interestingly, no evidence was found for the formation of **5** with this preparation suggesting that the intramolecular cyclisation might be driven by the presence of pyridine.

All ligands (**2, 3, 4** and **5**) were characterised by ^{1}H NMR, IR and mass spectrometries.

6.4.2 Complex Syntheses

$Ru(phen)_2Cl_2$ **6** was synthesized according to the method of Sullivan *et al.* (scheme 6.5).[324] The starting chloride was refluxed in DMF in the presence of LiCl and after cooling to room temperature precipitation of the product was induced by the addition of acetone. The product was filtered and washed with copious amounts of water to remove the by-product $Ru(phen)_3Cl_2$ that is often formed in small yield.

The complex $[Ru(phen)_2phen'](PF_6)_2$ **7** was prepared according to the method of Ellis *et al.*.[325] The metal complex, $Ru(phen)_2Cl_2$, was dissolved in hot water, with the phen′ ligand (**4**) dissolved in hot absolute ethanol being added. The resulting mixture was refluxed for 3 hours. Excess NH_4PF_6 was added and the product precipitated out of solution following concentration on the rotary evaporator. Size exclusion chromatography on a sephadex (LH-20) column eluting with methanol was used to purify the crude product.

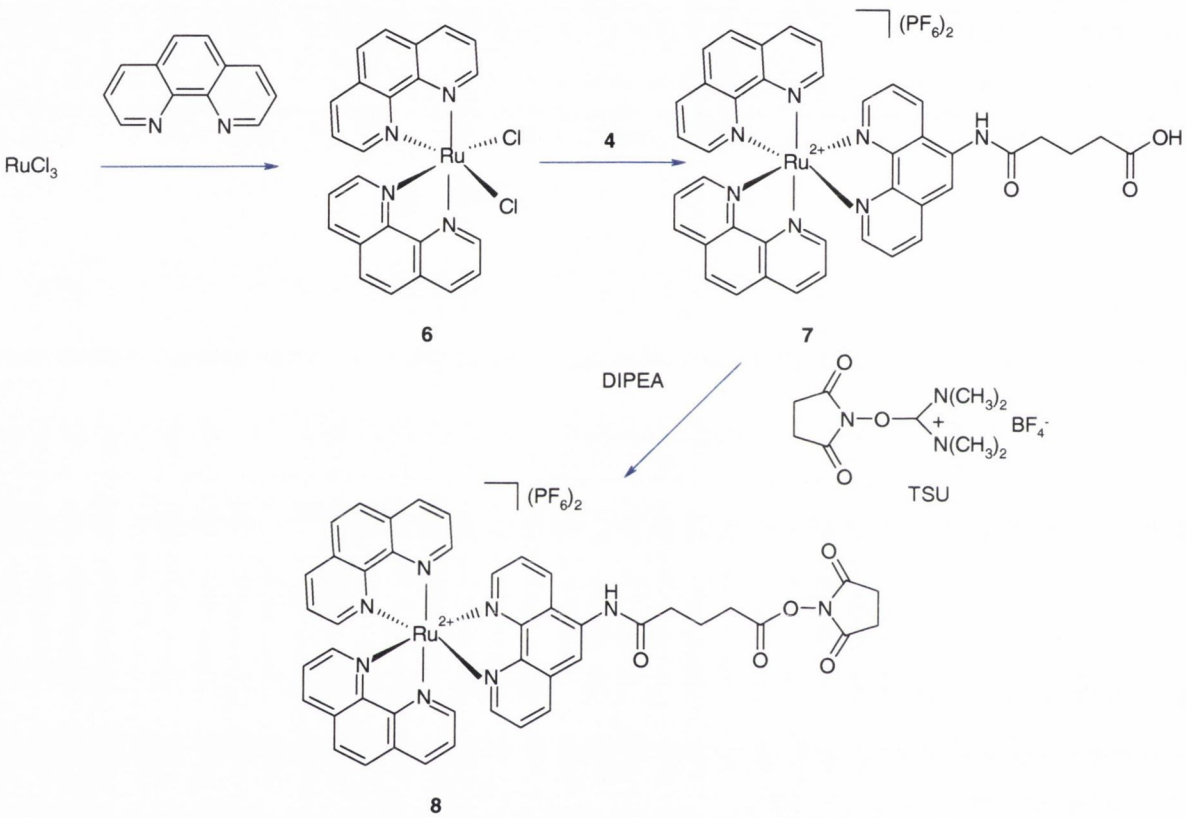

Scheme 6.5 Schematic representation for the synthesis and activation of $Ru(phen)_2phen'(PF_6)_2$.

The absorption spectrum of $Ru(phen)_2phen'$ was recorded and is given in figure 6.13. It consists of intra-ligand $\pi \rightarrow \pi^*$ transitions (LC) below 300 nm with $d \rightarrow \pi^*$ transitions (MLCT) above 300 nm. Excitation of the MLCT band (λ_{ex} = 450 nm) resulted in emission centred at 600 nm.

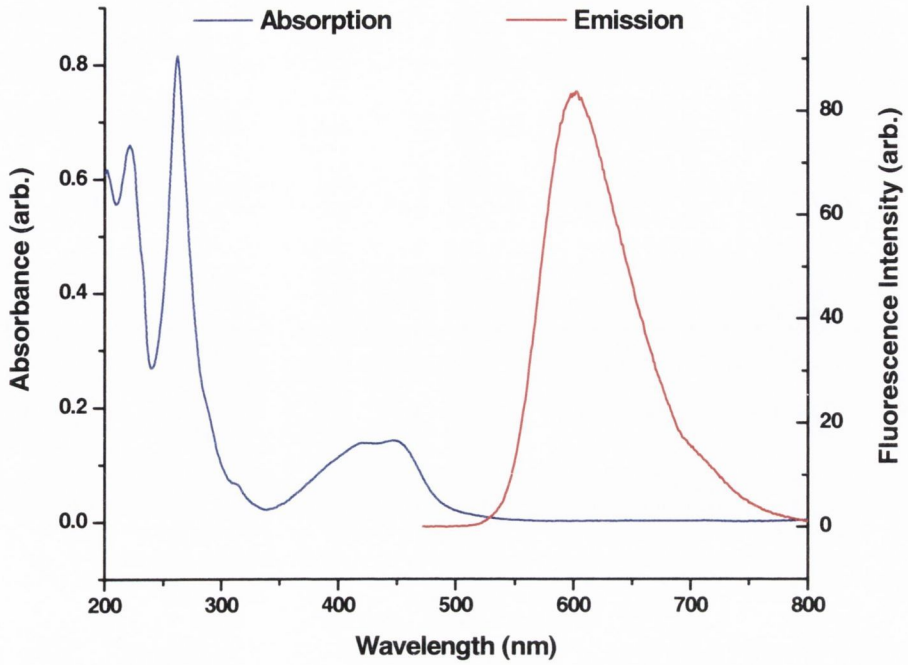

Figure 6.13 UV-vis absorption spectrum (blue line) and emission spectrum (red line, λ_{ex} = 450 nm) of $Ru(phen)_2phen'(PF_6)_2$.

6.4.3 Activation of Complex 7 for Conjugation

Activation of **7** to its corresponding N-hydroxysuccinimido ester **8** (scheme 6.5) was carried out following a procedure developed within the group that is an adaptation of a procedure reported by Bannwarth *et al.*[326] This was achieved by adding N,N,N′,N′-tetramethyl(succinimido)uronium tetrafluoroborate (TSU) and diisopropylethylamine (DIPEA) to the starting complex in DMF, followed by reaction at room temperature (scheme 6.5). T.L.C. analysis confirmed the quantitative formation of the activated ester, as the acid and ester have distinct R_f values.

Another route explored to make the complex more reactive toward conjugation was to synthesize the acid chloride derivative of **7**, something that has thus far proven unsuccessful (scheme 6.6). Route A, which involved the addition of thionyl chloride to the complex dissolved in DCM under an inert atmosphere followed by reflux for several hours was attempted first. No evidence for the formation of the acid chloride formation was found, with only the ring cyclized product being isolated. With this route, it is likely that the acid chloride did indeed form but owing to its greater reactivity over the acid derivative, intramolecular cyclization occurred very quickly. After some consideration a

milder route, route B was attempted (scheme 6.6). This method involved the addition of phosphorus trichloride to the complex dissolved in chloroform.[327] The solubility of **7** in chloroform is relatively poor and this method also failed to yield the desired product, with analysis showing that the starter complex had not reacted at all.

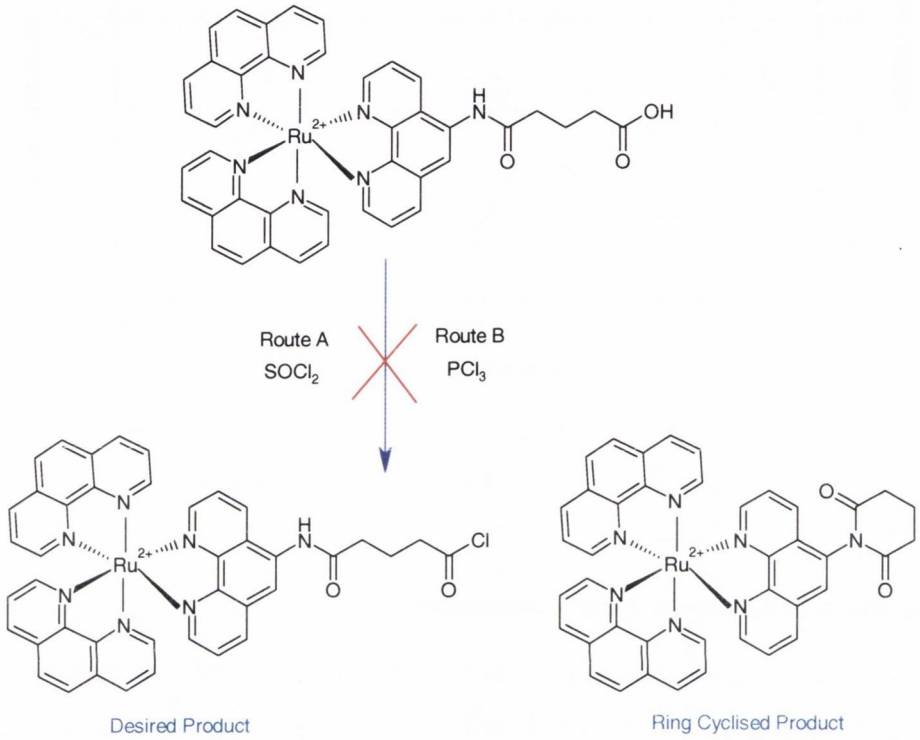

Scheme 6.6 Schematic summary of the routes attempted for the preparation of acid chloride derivatives of $Ru(phen)_2phen'(PF_6)_2$.

6.4.4 Conjugation Experiments

Several conjugation experiments were attempted for the preparation of 'two in one' nanocomposites. Attempts were made to conjugate APTES modified nanoparticles and the activated ester (TSU method) of both the phen′ ligand **4** and the $Ru(phen)_2phen'$ metal complex **7**. Formation of the activated esters in quantitative yield was confirmed by TLC analysis. Reaction of the particles and the esters was carried out in DMF with the esters being vastly in excess. However, following repeated washing of the particles to remove unreacted species, no evidence was seen in the UV and photoluminescence (PL) spectra to confirm successful conjugation. This would suggest that either the conjugation did not occur at all or has occurred at such low concentrations as to be considered insignificant. Two problems that contribute to the confirmation of conjugation to the iron oxide

nanoparticles are: (i) as previously mentioned, the phen′ ligand, either in isolation or when coordinated to the ruthenium metal centre, has a propensity toward intramolecular cyclisation, and in doing so will diminish any potential conjugation yields and (ii) monitoring the conjugation efficiency by UV and PL is made difficult by the fact that the particles absorb and scatter the light all across the UV-vis spectrum, and iron ions are possibly quenching any luminescence of conjugated luminophores.

Classic aqueous coupling strategies with 1-Ethyl-3-(3-dimethylaminopropyl) carbodiimide hydrochloride (EDC) were attempted for both the phen′ ligand and the $Ru(phen)_2phen'$ complex. In the case of the metal complex, the counterions were exchanged from PF_6^- ions to Cl^- using Amberlite exchange resin, to confer water solubility of the complex. When the resulting reaction mixture was analysed there was no indication from either UV/vis or PL that any complex had bound to the particles.

Some EDC coupling reactions were carried out with the metal complex **7** (Cl form) and cysteamine stabilised CdTe nanoparticles in water (with Bertrand Le Bon and Stephen Byrne from the Gun'ko group, T.C.D.). These experiments appear to have been more successful with the best results achieved when a 20-fold excess of complex:quantum dot ratio was used. This would suggest that the APTES stabilised nanoparticles have poor reactivity when compared with the cysteamine stabilised CdTe. Two possible sources of this poor reactivity are: (i) the tendency of the magnetite nanoparticles to aggregate limits the surface area available for the complex to react with and (ii) the terminal amine is either not very reactive or possibly not accessible due to siloxane cross linking of particles. The first problem can be addressed by having the particles very dilute in solution when carrying out conjugation reactions, so as to have a disperse solution that is free from agglomerates. This was not a consideration with the CdTe experiments because there are no magnetic interactions between particles, and hence little aggregation, in contrast to the case of magnetite nanoparticles. The second point is a more complex issue, with the problem of cross-linking being hard to control. As previously mentioned, this problem is best avoided by careful calculation of the concentration of APTES to be used when coating, along with the removal of any unreacted silane species after coating.

6.5 New Coupling Strategy Utilizing Dopamine

Following the relatively poor success of the previous strategies, we sought to investigate an alternative route that did not involve the $Ru(phen)_2phen'$ complex. Strong binding to the iron oxide surface and a complex that would not undergo side reactions (and hence decrease coupling efficiencies) were key requirements for this new strategy. Dopamine, and other enediols, had been shown in the literature to have a keen affinity for iron oxide surfaces (and indeed other oxides such as TiO_2).[328-331] A somewhat laborious synthetic strategy was devised to generate the complex shown in figure 6.14 below. However, if the final complex were to be isolated, this would most definitely attach to the nanoparticle surface. Two approaches were envisaged. Firstly, synthesis of the large bipyridine (bipy) derivative ligand followed by reaction with $Ru(phen)_2Cl_2$. The second approach involved assembly of the nanoparticle chelating ligand while all three ligands were complexed to the ruthenium centre.

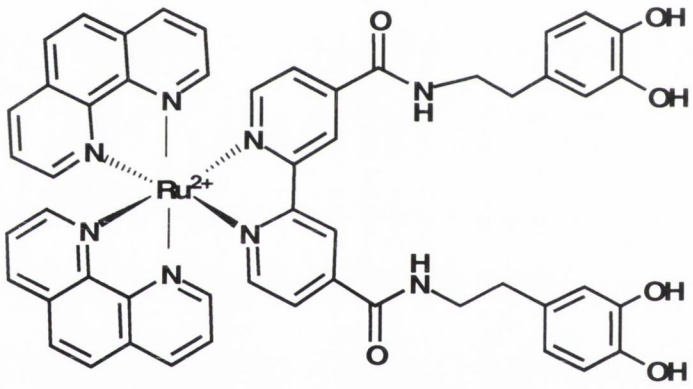

Figure 6.14 New synthetic target complex with dopamine functionality.

6.5.1 Approach 1 – Synthesis of a Dopamine Modified Bipyridine Derivative

It was initially envisaged that coupling of an activated bipyridine (bipy) ligand with the hydrochloric salt of dopamine would be the easiest route. However, when this was attempted, it was not successful. A paper by Xu *et al.*[315] utilizing dopamine for the very same purpose as ours, a strong anchor to a nanoparticle surface, was found. The authors outlined a relatively straightforward scheme of protections and deprotections on the dopamine moiety before attempting a coupling reaction. The strategy is summarized in scheme 6.7.

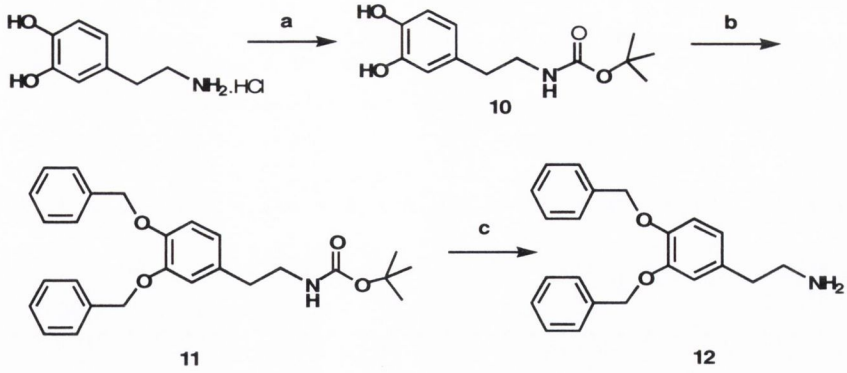

Scheme 6.7 Synthesis of a modified dopamine synthon. Conditions: (a) NaOH, *tert*-butyl dicarbonate, dioxane, H_2O 24 hrs ;(b) BnBr, K_2CO_3 DMF, rt, 24 hrs ; (c) 10% CF_3COOH, DCM, rt, 5 hrs.

Firstly, the animo group of the hydrochloride salt of dopamine was deprotonated with NaOH and this group was then protected using *tert*-butyl dicarbonate. Upon workup the product, **10**, was obtained in good yield (84%). Next the hydroxide groups were bonzoyl protected and the resulting product, **11**, was afforded in 58% yield after recrystallization from hexane/ethyl acetate. The final step, resulting in **12,** was the removal of the BOC protecting group and this was achieved in a quantitative yield by treatment of **11** with trifluoroacetic acid (TFA).

The next synthetic target was a bipyridine ligand that could be coupled with the modified dopamine compound (scheme 6.8). Chloride activated carbonyls are extremely reactive (as was seen earlier for the metal complex **7**) and it was decided that they would enable high efficiency coupling for our system. Commercially available 4-picoline was refluxed with Pd/C for several days after which time hot toluene was added to cleave the product, 4,4′-dimethyl-2,2′-bipyridine (**13**), from the solid surface.[332] After filtration the crude product was recrystallized from ethyl acetate. Treatment with potassium dichromate and subsequent reflux with nitric acid following the preparation of Oki *et al.* provided the dicarboxylic acid modified bipy compound, **14**.[333] Finally, the ligand was activated by refluxing in thionyl chloride for several hours under an inert atmosphere, with the excess thionyl chloride being removed by distillation.[334] Care was taken to maintain an inert atmosphere throughout the process.

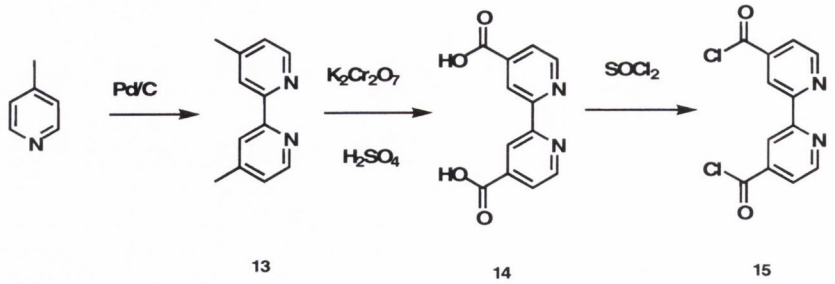

Scheme 6.8 Synthesis of a modified bipyridine ligand.

Reaction of **15,** with an excess of ligand **12** (2.2 equivalents) in dry DCM, afforded the desired ligand, **16** (in scheme 6.9 below) as a pink precipitate. The formation was confirmed by nmr and electrospray mass spectrometries. A number of efforts were made to react this ligand with $Ru(phen)_2Cl_2$ but all proved unfruitful. It is unclear as to why the reaction did not work, but possibly the orientation of the large ligand, if it is rotating about the central bipy bond, prevents the bipy nitrogens from coordinating to the metal centre.

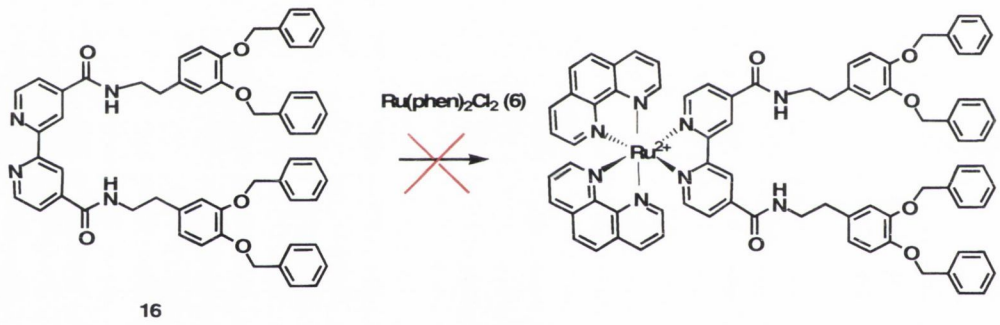

Scheme 6.9 Attempted preparation of a dopamine modified ruthenium complex.

6.5.2 Approach 2 – Synthesis of the Dopamine Modified Complex via a Metal Complex Precursor

As previously mentioned, an alternative route to afford the complex is to assemble the large dopamine modified bipy ligand while it is coordinated to the metal centre. This involved a synthetic route that is outlined in scheme 6.10 below.

Compound **17** was afforded in excellent yield (94%) by the reaction of $Ru(phen)_2Cl_2$ and 4,4′-carboxy-2,2′-bipyridine in an ethanol/water mix following the preparation of Uppadine *et al.*[334] Activation of the complex was achieved by reflux in thionyl chloride and **18** was assumed to have formed in a quantitative yield.

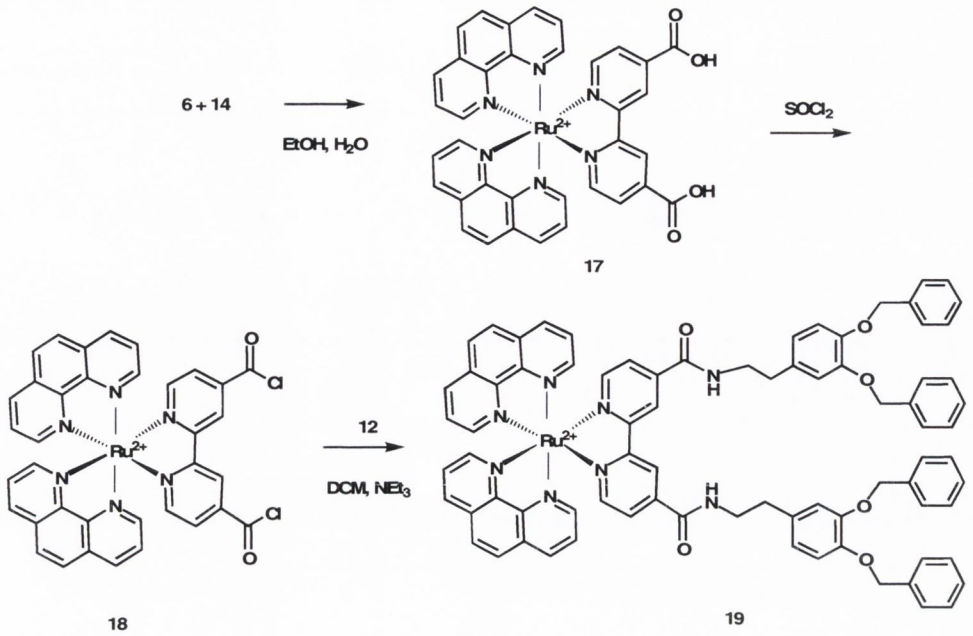

Scheme 6.10 Synthesis of compound **19** via a metal complex precursor.

An excess (~4 equivalents) of freshly prepared compound **12** in dry DCM, together with triethylamine was added dropwise to a stirred solution of **18** in dry DCM. An inert atmosphere was strictly maintained throughout. TLC analysis after 12 hours revealed a mixture of compounds. The solvent was removed and the compound was passed through a sephadex LH-20 column eluting with methanol. Electrospray mass spectroscopy analysis confirmed that the complex had indeed formed, however proton nmr characterization indicated that a mixture of compounds still existed. Further evidence for **19** was seen in the photoluminescence spectrum. The emission had redshifted from 610 nm (complex **18**) to 645 nm (complex **19**). The mixture was passed down a second column, this time a flash silica column, eluting with DMF : H_2O : NH_4OH (2 M) ; 1 : 1 : 2. Unfortunately, the product was not recovered from this column, even though good separation had been seen on TLC plates. Nonetheless, we have proven that the complex can be made. The synthesis was attempted a number of times and was only found to be successful once. Further tuning of the experimental conditions is clearly needed.

The mass spectroscopy result for the compound is shown in figure 6.15. Excellent agreement was found with that of the predicted spectrum, evidenced by the almost identical isotopic distribution.

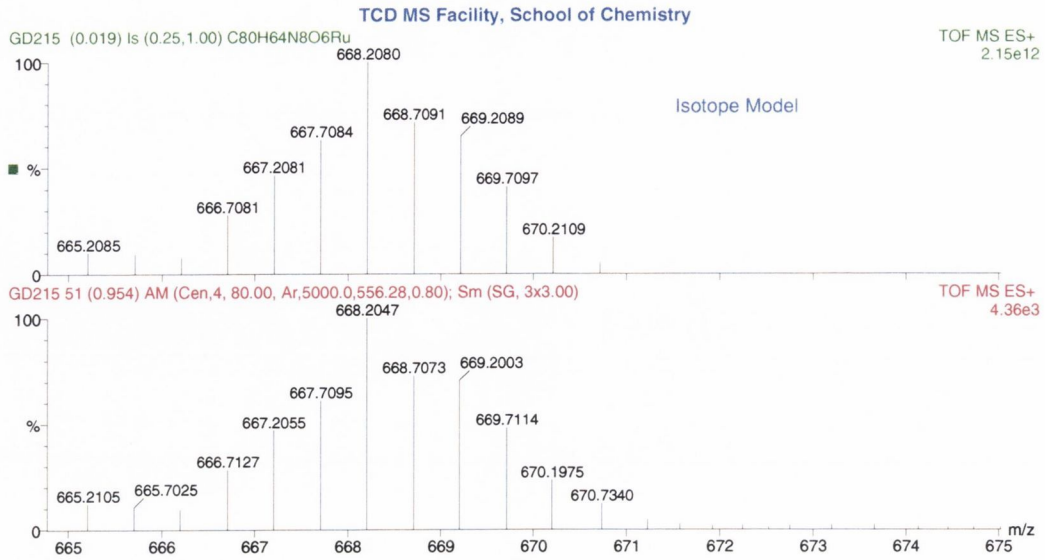

Figure 6.15 Comparison of the predicted and experimental electrospray mass spectra of compound **19**.

6.6 Linker for the Attachment of Oligonucleotides to Nanoparticle Surfaces

Another aspect of this project was to develop a method to anchor oligonucleotide sequences to the surface of metal oxide nanoparticle surfaces. Attachment of oligonucleotides to nanoparticle surfaces has been extensively investigated for gold and silver nanoparticles. Such modified particles are synthesized with relative ease as both gold and silver form strong bonds to thiol (or sometimes dithiol) modified oligonucleotides.[270-272] Such strategies are not applicable to Fe_3O_4 or TiO_2 particles. We envisaged a nanoparticle-to-oligonucleotide linker that would involve catechol binding to the nanoparticle surface (see scheme 6.11). In the design of such a linker, two important factors were necessary to consider: (i) the linker should have a strong affinity for the nanoparticle surface and (ii) the synthesis of the modified oligonucleotide should proceed with high efficiency so as to minimize the waste of expensive oligonucleotide samples. Taking this criteria on board, we designed a modified dopamine linker, that is expected to have excellent binding affinity for particles such as Fe_3O_4 or TiO_2, and can be conjugated to aldehyde-terminated oligonucleotides, by taking advantage of established oxime bond formation chemistry. Oxime conjugation involves the reaction of an oxyamine with an

aldehyde, and has been shown to be highly efficient for the synthesis of modified oligonucleotides.[335-337]

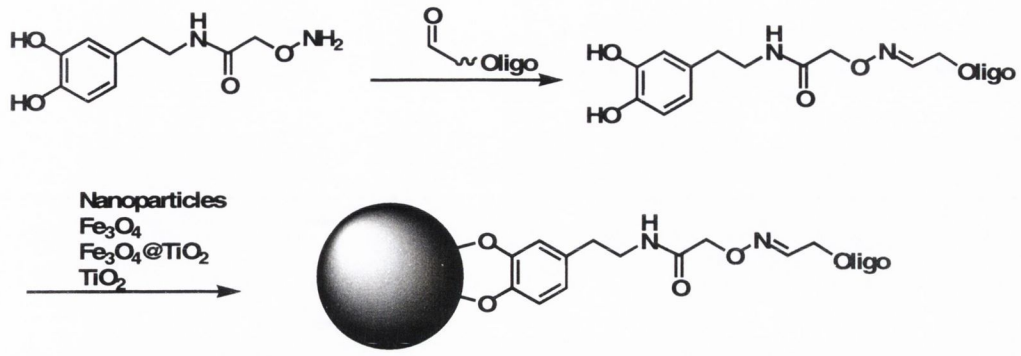

Scheme 6.11 Proposed scheme for the attachment of oligonucleotides to metal oxide nanoparticles such as Fe_3O_4 and TiO_2.

The synthetic approach taken toward the dopamine linker is outlined in scheme 6.12. The first step involved the protection of commercially available carboxymethylamine hemihydrochloride with *tert*-butyl dicarbonate and the procedure that was followed was similar to that of Xu *et al.*, the procedure that was employed earlier in the dopamine protection work.[315] The product was isolated as white crystals in good yield (77%) after recrystallization. The carboxylic acid was activated using N,N'-dicyclohexylcarbodiimide (DCC) and N-hydorxysuccinimide (NHS) in DCM with the crystalline product isolated after recrystallization from carbon tetrachloride. Compound **22** was synthesized by reacting a dopamine molecule with the succinic ester **21**. The protected oxyamine was not deprotected as this should be performed just before the oligonucleotide conjugation as the unprotected oxyamine is extremely reactive.

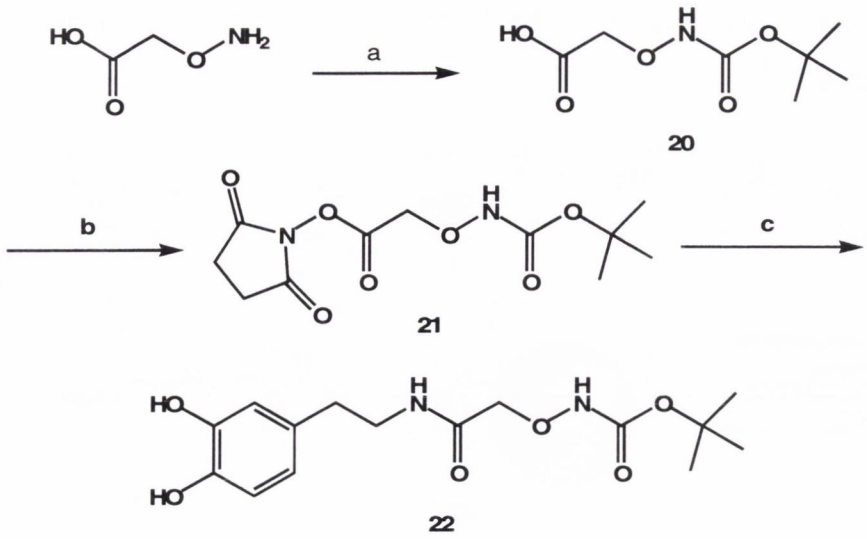

Scheme 6.12 Synthesis of modified dopamine linker for the conjugation of oligonucleotides to nanoparticle surfaces. Conditions: (a) NaOH, *tert*-butyl dicarbonate, dioxane, H_2O 24 hrs ; (b) DCC, NHS, DCM, rt, 24 hrs and (c) dopamine hydrochloride, DIPEA, DMF, rt, overnight.

6.7 'Two in One' Magnetic and Fluorescent Photophysical Studies

6.7.1 Conjugation of Amino Modified Fe_3O_4 and Ruthenium Complex 18

Some preliminary conjugation experiments were carried out with complex **18** and amino modified nanoparticles. Similar strategies were employed for the coupling of both (3-aminopropy)triethoxy silane and dopamine modified particles to the ruthenium fluorophore **18**. This is illustrated for the APTES modified Fe_3O_4 case in scheme 6.13. Amino-modified particles were dried and dispersed in dry DCM. This was necessary as any water remaining in the nanoparticle sample would decrease the coupling efficiency, by hydrolysing the acid chloride back to the carboxylic acid complex. The ruthenium complex was dissolved in dry DCM and added to the particles. The resulting mixture was sonicated for 2 hours. Magnetic stirring was avoided, as the magnetic particles become attracted to the stirring bar and this would hamper the reaction. The particles were washed several times to remove unbound complex.

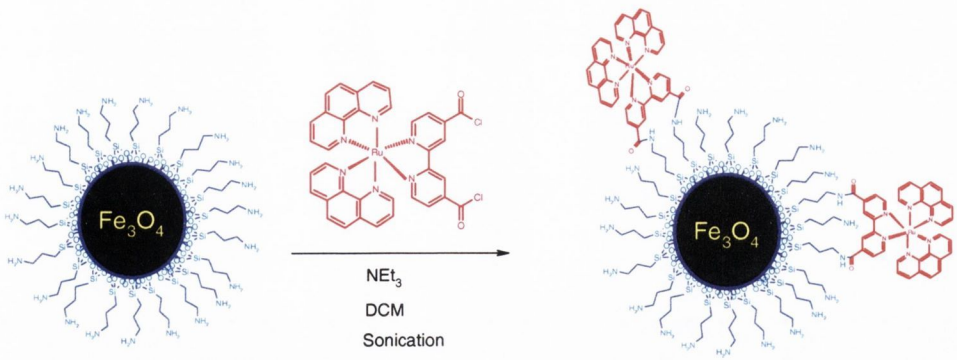

Scheme 6.13 Synthetic approach to couple APTES modified particles with ruthenium fluorophore **18**.

6.7.1.1 Lifetime Analysis

Single photon counting (SPC) lifetime analysis was carried out on the prepared nanocomposites, and a weak signal was detected. The decay profiles were fitted to monoexponential kinetics. The (3-aminopropyl)triethoxy silane modified particles displayed a lifetime of 273 ± 3 ns (figure 6.16 (b)). To put this lifetime into perspective the lifetime of the $Ru(phen)_2$(4,4′-dicarboxy-2,2′-bipyridine) complex (**17**) was recorded and this showed single exponential kinetics with a lifetime of 418 ± 2 ns (figure 6.16 (a)). Therefore, it is evident that the lifetime of the complex was being quenched when it was on the nanoparticles surface. On examining the dopamine modified particles the quenching was found to be even more pronounced with a lifetime of 1.9 ± 0.01 ns being found. (figure 6.16 (c)). This lifetime is very similar to the instrument response function (IRF) and so it is likely that the ruthenium emission from the dopamine particles is completely quenched. This may not be entirely unexpected as there is no protective or buffer layer between the complex and the iron as in the case of the silica coated nanoparticles.

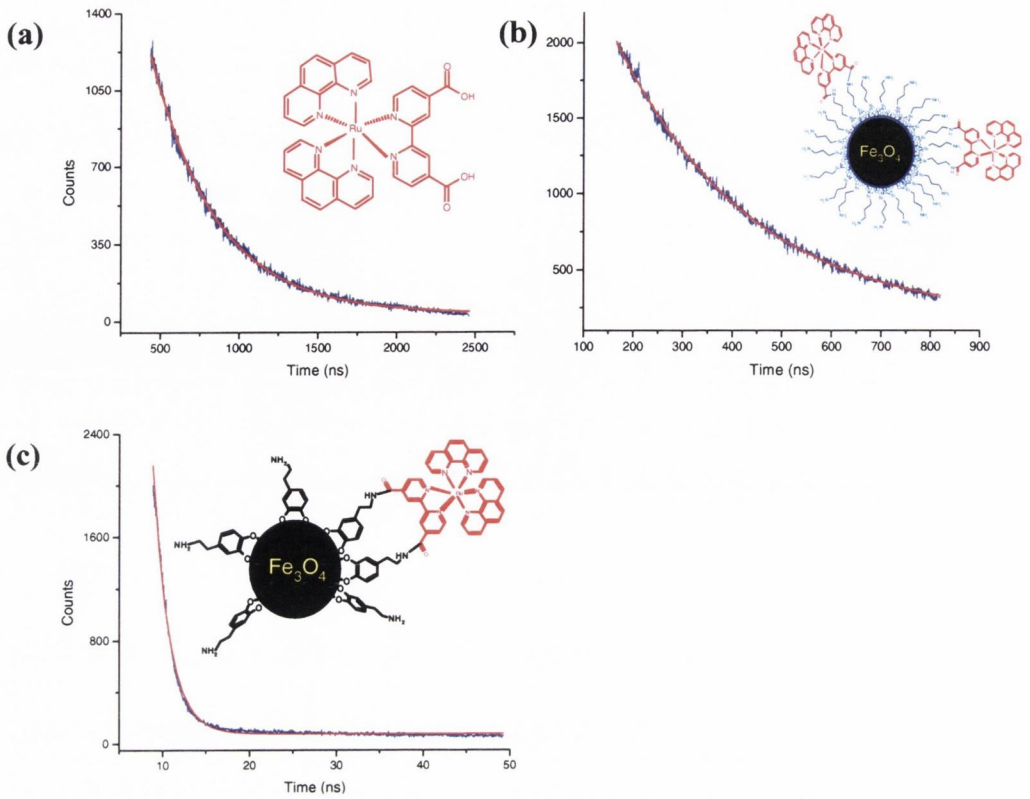

Figure 6.16 Single photon counting results for (a) $Ru(phen)_2$(4,4′-dicarboxy-2,2′-bipyridine) (b) (3-aminopropyl)triethoxy silane modified particles and (c) dopamine modified particles.

6.7.2 Magnetic and Fluorescent DNA Strings

Magnetic and fluorescent DNA strings were prepared by precipitating iron chlorides with ammonia (the Massart procedure), in the presence of denatured Herring sperm DNA (with Serena Corr of the Gun'ko group T.C.D.).[292] The resulting reaction mixture was washed several times with water (using magnetic decantation) until pH 7 was achieved. At neutral pH, stable suspensions were found and the light switch complex, $Ru(phen)_2dppz$ was titrated into the reaction mixture. Emission was observed from the complex, indicating intercalation with the DNA. Samples were prepared for confocal microscopy by allowing a sample to evaporate on a confocal microscopy slide in a 0.5 T magnetic field. The result is elongated DNA strings, where the magnetite particles have aligned with the magnetic field and due to their interaction with the DNA, have stretched the DNA into a linear arrangement. Confocal microscopy images of the sample are given in figure 6.17

(with Dr. Yurii Rakovich, School of Physics, T.C.D.). A large excess of the light switch complex was used in the preparation of the sample as it was very difficult to estimate the amount of DNA present in the sample. The colour image is an indication of different emission lifetimes. It can be clearly seen that there are different emission lifetimes from the parallel strings and the surrounding areas. We propose that there are bundles of DNA in each string and that the DNA is interacting with the particles through the phosphate backbone.

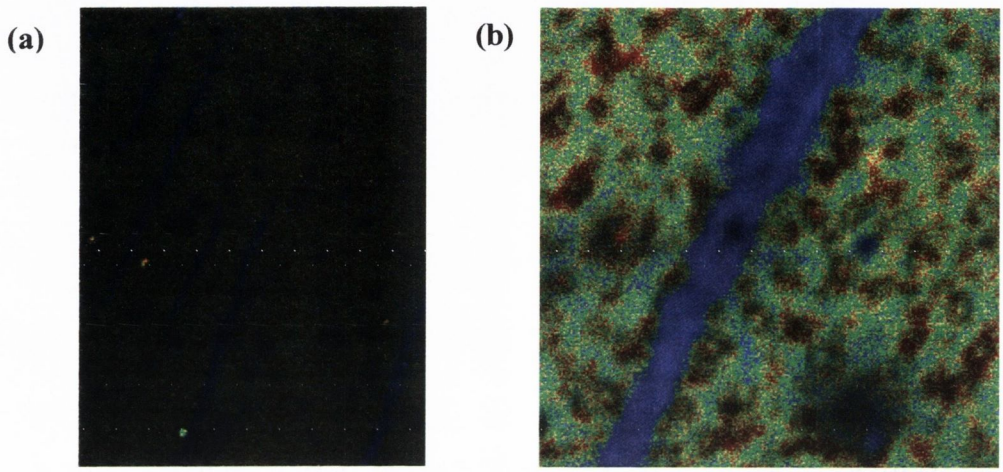

Figure 6.17 (a) Confocal microscopy image of DNA-Fe_3O_4-$Ru(phen)_2dppz$ strings and (b) enlargement of the fourth string from the left in image (a).

Further refinement of image 6.17 (b) resulted in figure 6.18. A lifetime histogram of the image shows an average lifetime of approximately 30 ns (figure 6.18 (b). Along the string there is a clearly identifiable region where the lifetime is shorter (dark blue circle). This could possibly be due to a higher concentration or agglomeration of nanoparticles at this site. The dark black circles are presumably regions of particles and the fluorescence of the complex is completely quenched at these positions. Interestingly, this sample shows emission throughout, but the reader is reminded this is in the solid state, and that the behaviour in solution may not be the same as that of the solid state.

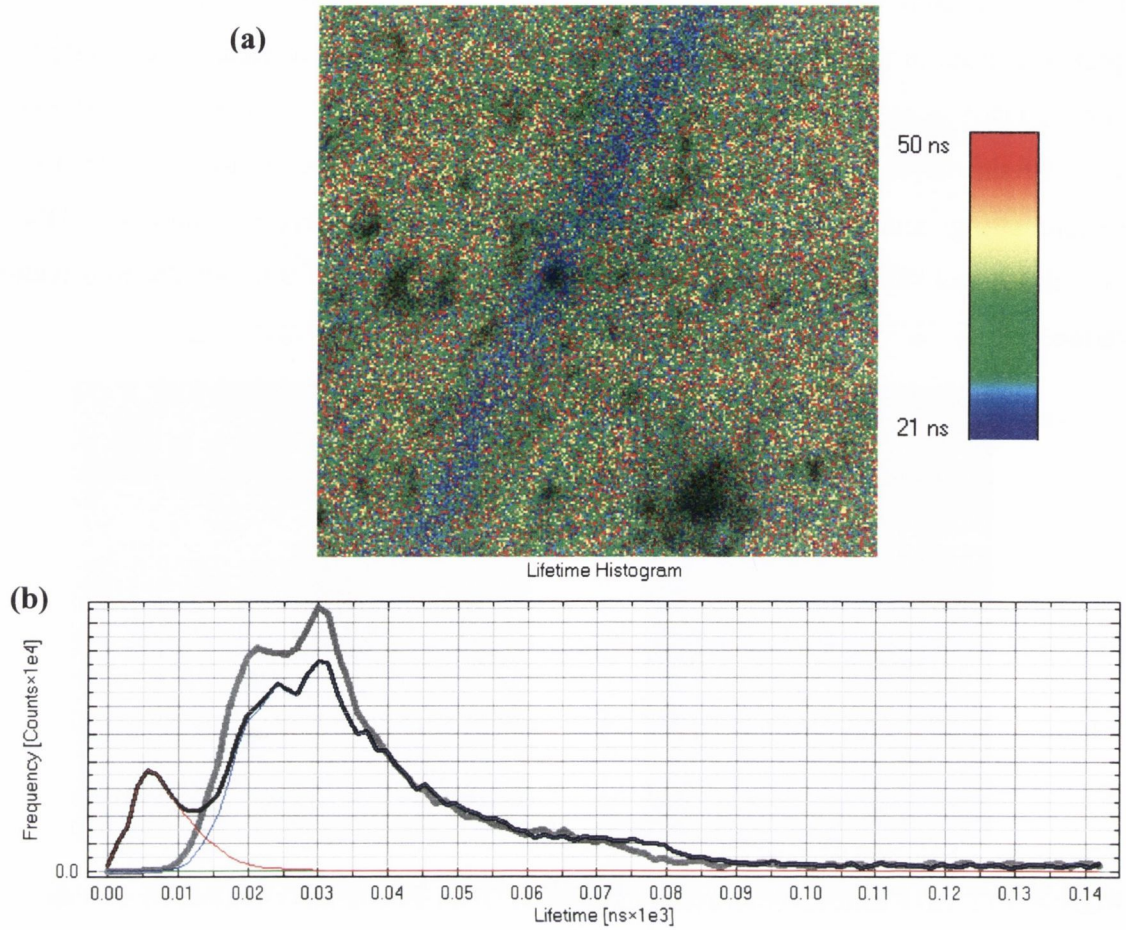

Figure 6.18 (a) Refinement of image (b) in figure 6.17 and (b) lifetime histogram analysis for image (a).

The lifetime of the solution was recorded using the SPC apparatus and the resulting decay is given in figure 6.19. Analysis revealed that the decay fitted well to a biexponential model. Lifetimes of 2.2 ± 0.03 and 23.7 ± 0.3 ns were found. Moon *et al.* have reported the enhancement in luminescent intensity when $Ru(phen)_2dppz$ binds to single stranded oligonucleotides,[338] indicating the light switch effect does not require the intercalation of the dppz ligand into a true double helical arrangement. The authors reported a short lifetime of 1-2 ns, together with two longer components (~120 and ~700 ns). Coates *et al.* also noted that full "intercalation" of the dppz ligand was not a necessary requirement for operation of the light-switch effect.[339] They suggested that other forms of protection, such as enclosure within the helical structure, in conjunction with the shielding ancillary ligands created a protective cavity for the dppz, providing the necessary stabilization for the emitting ^{3}MLCT state involved in the light switch mechanism. Another very recent report

on a light switch complex, though admittedly not the same light switch as in our system, also suggests that intercalation is not required for light switch behaviour.[340]

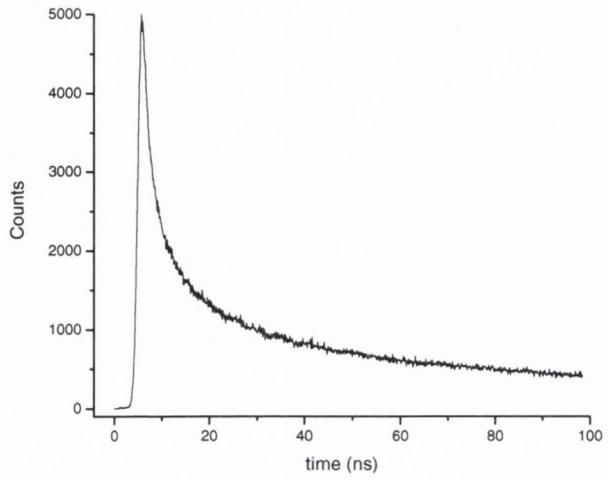

Figure 6.19 SPC lifetime decay of the DNA-Fe_3O_4-Ru(phen)$_2$dppz strings in solution.

6.8 Conclusions and Future Work

Magnetite nanoparticles of controlled size and morphology, with a narrow size distribution have been synthesized and characterized by a number of techniques. Particle stabilization has been achieved using electrostatic stabilisers such as tetramethylammonium hydroxide and APTES. Silica coating of the particles was successfully performed and characterized. Modification of the particles to introduce a potential coupling functionality was achieved using both APTES and dopamine, taking advantage of both molecules' strong binding affinity for the iron oxide surface. The presence of reactive primary amines was confirmed using the Kaiser test.

With respect to the syntheses of luminophores for the attachment to the nanoparticles, the initial strategy involved the preparation of the metal complex $Ru^{II}(phen)_2phen'$. Ligands **2, 3, 4,** and **5** together with complexes **6** and **7** were successfully synthesized, isolated and characterized. Activation of the complex has been achieved in the form of the activated ester complex **8.** While this approach appeared sound on paper, it proved to have too many complications with respect to side-reactions that interfered with coupling efficiencies.

An alternative route was devised, involving the use of dopamine as an anchor for the complex to the nanoparticles surface. Two sub-strategies were explored within this route, those being the preparation of the dopamine modified bipy ligand **16**, pre-coordination to the ruthenium metal complex and the assembly of **16** while the bipy was coordinated to the metal centre. Ligands **10-16** were successfully prepared and characterized as were metal complexes **17-19** toward this end. Coordination of **16** to $Ru(phen)_2Cl_2$ (sub-route one) has thus far been unsuccessful. However, the other path (sub-route two) did furnish the desired complex **19**. Further tuning of the purification is needed with the use of preparative high performance liquid chromatography (HPLC) being an avenue that will be explored. Future work will also involve the attachment of the catechol modified ruthenium complex to nanoparticles of Fe_3O_4 and TiO_2 coated Fe_3O_4 particles which have been prepared and characterized (see scheme 6.14 (a)).

Preparation of a linker capable of conjugating oligonucleotides to nanoparticles surfaces was another goal of this research. This was achieved by designing a ligand (**22**) that combined a moiety that is known to have a high affinity for oxide nanoparticles (enediol) [268,278,314,315,328-331] and a functionality that has been shown to provide facile conjugation to modified oligonucleotides without the need for high loadings, resulting in high conjugation efficiencies (oxyamine).[335-337] En route to ligand **22**, precursor ligands **20** and **21** were successfully isolated and characterized. Conjugation of ligand **22** to nanoparticles has at this point not been attempted but as mentioned above, Fe_3O_4 and TiO_2 coated Fe_3O_4 particles have been prepared and characterized for this purpose. Aldehyde modified short oligonucleotide sequences have been prepared using a glyceryl support[341] on a Beckmann Oligo 1000 DNA synthesizer. Future work will involve the conjugation of the ligand firstly to both the particles and oligonucleotide separately and then secondly all three components will be linked together. An oxyamine modified phenanthroline derivative has been prepared[337] and will be complexed to ruthenium, and conjugated to modified oligonucleotides following a previously reported procedure. Strategies such as that outlined in scheme 6.14 (b), where complementary strands are attached to particle and ruthenium complex respectively, with subsequent hybridization of the strands can then be realized.

Finally, initial experiments for the preparation of 'two in one' bifunctional nanoparticles showed that the emission of the complex on the surface of the dopamine modified particles was quenched while the analogous approach with APTES modified particles was found to undergo partial quenching. This was presumably due to the APTES layer acting as a buffer between the iron and the fluorophore. Future work will involve the study of the distance dependence of this quenching through variation of the silica shell thickness.

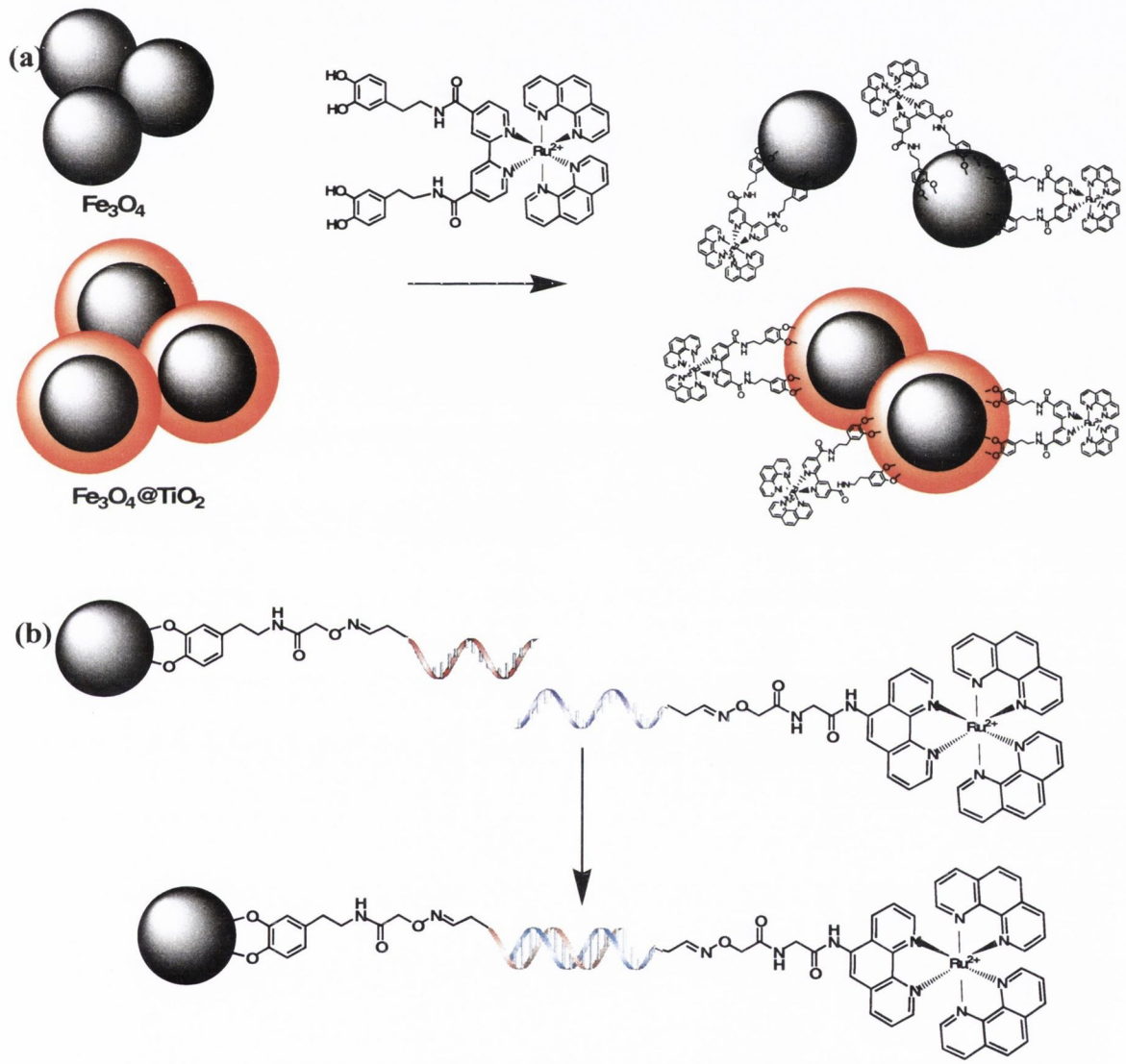

Scheme 6.14 Future directions for this work. (a) Attachment of dopamine modified ruthenium metal complex to Fe_3O_4 and $Fe_3O_4@TiO_2$ particles and (b) Single strand oligonucleotide modification of nanoparticles and metal complexes with subsequent hybridization of the complementary strands.

Chapter 7

Conclusions and Future Perspectives

7.1 Introduction

This work described in this thesis encompasses two exciting areas of chemistry that are both currently experiencing growth and as such are constantly evolving. The first of these involved the time resolved study of ultrafast relaxation processes in DNA following UV excitation (chapters 1-5). Comprehending how the nucleobases cope with and dispose of potentially harmful energy may lead to a greater understanding of the inherent photoprotection mechanisms in DNA and in doing so unravel some of the mysteries of the photostability of DNA. The second described synthetic approaches toward new bifunctional nanoparticles for biomedical applications. Nanoparticle science since its birth has been heralded as the way forward in a number of areas. There is a need for focussed thought to develop the next generation of 'smart' nanoparticles, and the work described in this thesis (chapter 6) represented our contribution toward that goal.

7.2 Conclusions from the TRIR Work

In chapter 2 the relaxation dynamics of a family of cytosine derivatives was probed using ps-TRIR. The deactivation of 5′-dCMP and dCyd was found to proceed by at least two routes (on a ps timescale). The first of these was the cooling of the vibrationally hot ground state (τ = 2.6 ps) and this was already known to occur on a picosecond timescale for the mononucleotides. The second process, had a lifetime of 33/37 ps for 5′-dCMP /dCyd respectively, and was characterized by a strong transient absorption band at 1574 cm^{-1}. Interestingly, the long-lived species was not found for 1-MeCyt and Cyt, suggesting that substitution at the 1-position by 2′-deoxyribose had a major effect on the photophysical properties of the nucleobase. All possible origins for the state were considered. Computational calculations on tautomeric forms of substituted cytosine were performed and ruled out the imino-carbonyl isomer, but could not fully exclude the possibility of the imino-enol isomer without higher level calculations. Given the region in which the transient absorption occurred we assigned the species as the dark $^1n_N\pi^*$ state. Such states are immensely important to DNA photostability, when one considers that the vast majority of DNA excited states are deactivated by non-emissive means. This study represented the first direct measurement of a dark state for a nucleobase. Future work will involve the search for this state in di- and polynucleotide systems.

The next study, chapter 3, encompassed a comprehensive study of A-T containing systems, from mono- to di- and finally polynucleotide systems. Stacking interactions between bases are instrumental in the production of long-lived states. Long-lived species (hundreds of picoseconds) were found in dApdA and TpT that are most likely due to excimer-like states, possibly non-emissive in the case of TpT. Intriguingly, a long-lived state was found for dApdA when monitoring the ground state repopulation, but the transient absorption contained only fast species. A comprehensive and detailed study of the structural isomers dApT and TpdA was undertaken, including, for the first time, variable temperature time resolved infrared measurements. Circular dichroism and variable temperature NMR were used to study the difference in stacking in the dinucleotides and complement the ps-TRIR data. Long-lived species' lifetimes of 70 and 50 ps were found for dApT and TpdA respectively (at 20 °C), and the contribution from the long-lived state was found to increase with increased stacking. Most significantly in the mixed dinucleotides, dApT and TpdA, the thymine dominated regions were found to have a higher contribution from the long-lived species than the adenine dominated regions, and at long time delays the TRIR profile of the dinucleotides resembled that of thymine. Using the fingerprint information afforded with infrared spectroscopy, we hypothesize that the long-lived state is localized on thymine. Long-lived states were also found in the polymeric structures poly(dA).poly(dT) and poly(dA-dT).poly(dA-dT), with the latter polymer displaying the longer lifetime. The results suggest that the excess energy dissipation is dependent on the base-base stacking overlap. Interestingly, the TRIR profile of the poly(dA).poly(dT) did not resemble the constituent dinucleotides dApdA and TpT, whereas in the poly(dA-dT).poly(dA-dT) the profile was similar to that of dApT and TpdA. Future work will involve the investigation of dark thymine states and the use of designed short oligonucleotide sequences to study the hypothesis of energy transfer from adenine to thymine.

A study of DNA secondary structure of $[poly(dG\text{-}dC)]_2$ was described in chapter 4. Two relaxation processes were found for the B form, with the first having a lifetime of 7 ps and being assigned to cooling of the vibrationally hot ground state. The second transient (τ = 30 ps) was found to have a well-defined absorption band at 1597 cm^{-1} and was assigned to the $^1n_N\pi^*$ state of the cytidine moiety. Sensitivity of the G-C base-pairs in the polymer to secondary structure was confirmed when only one lifetime, having a broad

transient absorption at 1600 cm^{-1} was found for the Z form. A single lifetime of 16 ps was evident and taking account of the dinucleotide-like repeating unit of the Z polymer, this species was assigned to a localized exciplex state. This work showed that transient species formed in G-C systems are more rapidly deactivated than their A-T counterparts, and this may be directly linked to the increased interbase hydrogen-bonding in the G-C system (3 hydrogen bonds) versus the A-T (2 hydrogen bonds). In the future, undertaking of a study of G-C dinucleotides, dCpdC, dGpdG, dCpdG and dGpdC, and also poly(dG).poly(dC) may further our understanding of G-C systems.

Chapter 5 described ps-TRIR investigations of three biologically relevant DNA systems, and a full understanding of which represents an ambitious undertaking. The first study was concerned with mixed-base oligonucleotides in both the single- and double-stranded forms. The paucity of literature relating to mixed-base studies speaks to the difficult nature of the interpretation of the results of such a study. Our work was to our knowledge, the first such examination of mixed-base duplex DNA. Two lifetimes were evident upon excitation of the duplex, the first of which is assigned to vibrational cooling. The second process is due to an electronic excited state or more likely a mixture of states from the four bases. Perhaps of greater importance were the fundamental results arising from this study. The presence of a long-lived component in a mixed-base system confirmed that electronic delocalization occurs between stacked bases and possibly even across hydrogen-bonded structures (as the bases, with the exception of 5′-dCMP do not have a long-lived species when studied in isolation) and that relaxation dynamics are heavily dependent on such delocalization and secondary structure. Further studies will involve investigation of a lower wavenumber window where individual vibrations of the bases are better resolved and hence base-dependent relaxation behaviour may be observed.

The next section involved probing the ultrafast relaxation mechanisms in triple-stranded DNA. This represented a comprehensive review of the basic single strand elements, to the higher order double-stranded B-form helix and finally the triplex structure. Both short oligonucleotides (18 bases long) and polymer strands (average ~2000 bases long) were studied. Surprising results were found for stacked adenine systems, implying that identical samples under the same conditions but possessing different secondary structures have different excited states as evidenced by different UV/vis spectra and hence these systems displayed different relaxation dynamics. This may perhaps in part explain the

discrepancies between reported lifetimes between different studies in the literature. The key result from this chapter was that the triple-stranded form displayed monoexponential kinetics. When one considers that both the single- and double-stranded structures display a long-lived species, it is remarkable that the triplex does not. Incorporation of the third strand introduces extra hydrogen bonding in the structure and this may be the reason for the increased rate of energy dissipation. Interestingly, the oligonucleotide sample was found to be more robust toward laser exposure than the polymeric analogue. Another major consequence from this study was the photosusceptibility toward photodamage that thymine residues normally display was somehow lessened in the multistranded arrangements, possibly suggesting that interstrand energy transfer aids the removal of the potentially harmful energy from the thymine residue before damage can take place. For follow-up studies it would be highly desirable to repeat all measurements on a system such as the new ULTRA development at RAL, which has enhanced sensitivity compared to the PIRATE apparatus and would therefore allow for milder pumping conditions to be used. Perhaps then our observations (which are currently the only such measurements that we are aware of) can be corroborated and our hypotheses confirmed.

The third and final study was a TRIR investigation of the human telomeric sequence, a sequence that has been directly linked with the immortality of cancerous cells. We undertook a cation-dependent study of the quadruplex structure, using Na^+, K^+ and Sr^{2+}. The relaxation dynamics were found to be biphasic, with the lifetimes being assigned to cooling of the vibrationally hot ground state and an electronic state or more likely states, probably excimer/exciplex in character. Interestingly, the sample containing the divalent Sr^{2+} cations was the only one to display differential long-lived relaxation times between bleaching bands. Future studies will involve the acquisition of improved measurements, with a focus on the 1537 cm^{-1} mode, which is the characteristic quadruplex mode.

Finally, all the studies described herein illustrate how ps-TRIR provides direct information relating structure and dynamics. The goal was to undertake a comprehensive study from simple to complex units and this has been achieved. We have demonstrated how ps-TRIR is an invaluable tool for the investigation of the structural nuances and photophysical behaviour of DNA systems.

7.3 Conclusions from the Bimodal Nanoparticle Work

The synthesis of magnetite, silica coated magnetite, APTES modified magnetite and dopamine modified magnetite were all described herein. Characterization results from TEM and dynamic light scattering confirmed a narrow size distribution of particles. Zeta potential measurements were performed to access the stability of the particles in solution. The use of APTES and dopamine introduced a potential coupling functionality on the particle surface, the presence of which was confirmed by the Kaiser test.

Synthesis of a ruthenium metal complex capable of conjugation to the particles was achieved, however this initial strategy was not without its difficulties – that is to say side reactions detracted from the successful coupling. Re-evaluation of the situation resulted in a new synthetic target. Two approaches were taken toward this compound, one of which proved fruitful. Further tuning of the purification of this compound is needed with the use of preparative high performance liquid chromatography (HPLC) being an option that will be explored. Future work will involve attachment of the catechol modified ruthenium complex to nanoparticles of Fe_3O_4 and TiO_2 coated Fe_3O_4 particles which have been prepared and characterized.

A novel linker capable of conjugating oligonucleotides to nanoparticles surfaces was designed and realized. This molecule combined a functionality capable of strong binding to metal oxide nanoparticles - an enediol, and a functionality that affords high conjugation efficiencies in conjugation reactions - an oxyamine. Future work will involve the conjugation of this ligand to aldehyde modified short oligonucleotide sequences. The linker will also be explored as a robust anchor of oligonucleotides to nanoparticles surfaces, such as Fe_3O_4 and TiO_2 coated Fe_3O_4.

Chapter 8

Experimental

8.1 TRIR Section

8.1.1 The TRIR Aparatus

The PIRATE instrument (figure 8.1) at the LSF in the Rutherford Appleton Laboratories was described briefly in the introduction. The following description details each individual component that is used to generate the final TRIR spectrum.

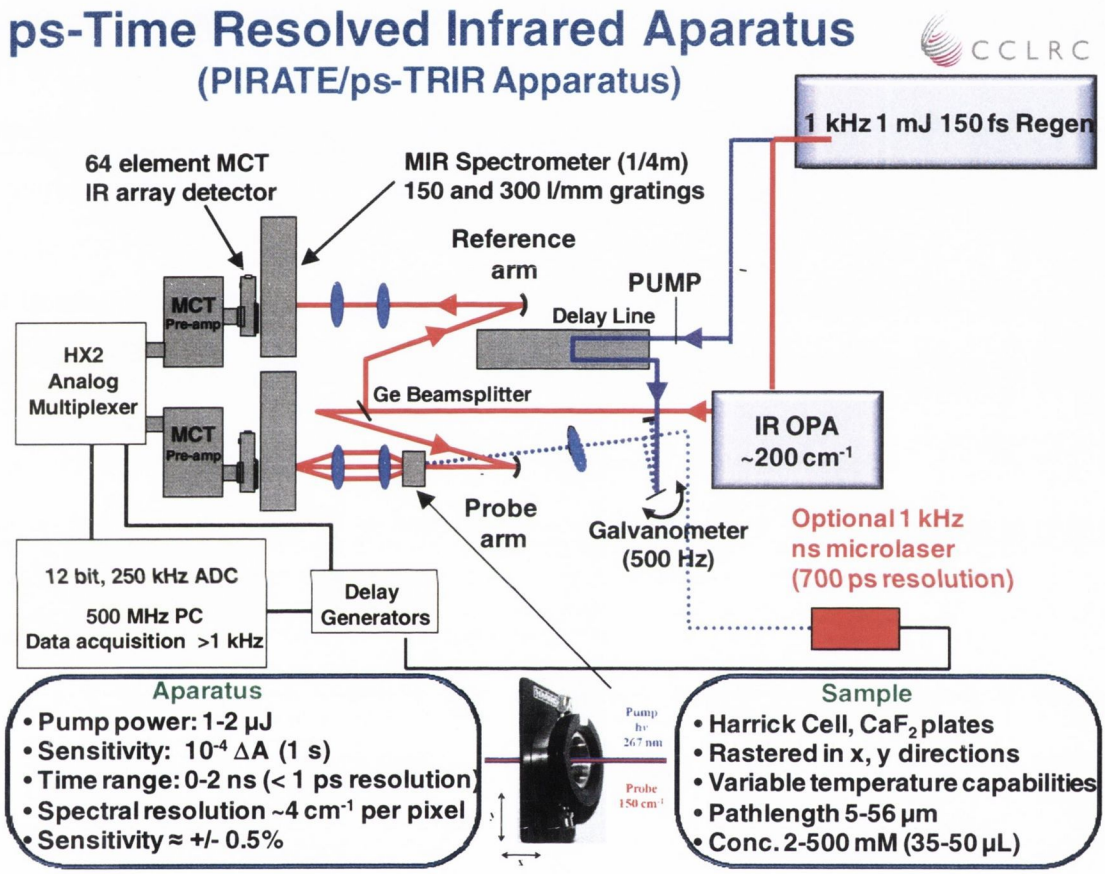

Figure 8.1 Setup of the ps-TRIR apparatus at the Rutherford Appleton Laboratory.

8.1.1.1 The Pump Beam

DNA bases absorb strongly in the UV and this requires harmonic generation of the pump pulse from the initial laser output. The third harmonic of part of the output from a 1 kHz, 800 nm, 150 fs, 1 mJ regenerative amplifer (Spectra Physics Tsunami/Spitfire) is used to generate the pump beam. The resulting pulses at 267 nm (150 fs) have energies of 1-2 µJ at a 0.5 kHz repetition rate. An optical delay line (controlled by the PC) on the pump beam line allows for optical delays between 1 ps and 2 ns. The size of the pump beam at the

sample is attenuated to ~200 μm. Pump laser energy was kept below the threshold for sample degradation through sample window interface effects, two photon ionization and non-linear processes (typically 1-2 μJ).

8.1.1.2 The Probe Beam

Stable broadband mid infrared (MIR) radiation (~150 cm^{-1} at FWHM) is produced using difference frequency generation (DFG) methods. The pulses are generated using an optical parametric amplifier (OPA) scheme that was originally described by Kaindl *et al.*.[342] The mid IR pulses are generated by difference frequency mixing the 800 nm regenerative amplifer output with the signal and idler outputs, obtained from a white light continuum seeded 800 nm pumped BBO (β-BaB_2O_4) optical parametric amplifer in a $AgGaS_2$ crystal at 1 kHz. IR pulse energy and spectral stability are obtained through careful control of the amplifier gain characteristics and use of a highly stable pump laser source of good beam quality. The infrared beams were dispersed by 150 l/mm, 4000 nm blaze, gold grating monochromators and imaged onto 64 element mercury cadmium telluride (MCT) array. The size of the probe beam at the sample was attenuated to ~150 μm. All IR probe and reference beams and optics are enclosed within nitrogen-purged beam pipes and boxes to reduce absorption by atmospheric water vapour to an acceptable level and to remove signal intensity variations caused by fluctuations from air currents and dust particles.

8.1.1.3 The Detectors, Multiplexer and Analogue to Digital Converter

The detectors are 64-element mid-IR sensitive (MCT) arrays. These detectors allow for sensitive measurements at the high repetition rates. From here the wavelength dispersed probe and reference beam signals are fed simultaneously into HX2 analog multiplexer boards based on a unique Rutherford Appleton Laboratory (RAL) design. The multiplexer boards were carefully engineered to minimize electromagnetic field (emf) noise pickup from laboratory sources that would interfere with the sample signal and hence result in a poor signal-to-noise ratio. Two channels of a 12 bit analogue-to-digital converter (ADC) handle the multiplexer signals and a third channel on the ADC is used to monitor the pump off signal.

8.1.1.4 Data Acquisition and Processing

The signal is then streamed to the personal computer (PC) memory where data analysis involving signal discrimination, normalization, and averaging between detector channels is carried out on a shot-by-shot basis at the 1 kHz acquisition rate. A third channel of the ADC is used to monitor the pump-on/off status of the laser. Analysis of the pump-on/pump-off data pairs creates a rolling average for the change in transmission, ΔT_N using the following equation:

$$\Delta T_N = \frac{\left[\left(\frac{I_{probe}}{I_{ref}}\right)pump\ on - \left(\frac{I_{probe}}{I_{ref}}\right)pump\ off\right] + \Delta T_{N-1}(N-1)}{N} \quad (1.1)$$

The average change in absorbance, ΔA_N is then given by:

$$\Delta A_N = -\log\left(1 + \frac{I_R}{I_P}\Delta T_N\right) \quad (1.2)$$

where I_R and I_P are the final averages of the pump-off spectra on the reference and probe side, respectively, and N is the total number of acquisitions. Further discrimination by the software removes large fluctuations in the signal, such as laser 'drop outs', or other large variations in signal, that may result from scattering of the probe beam by atmospheric or sample particulates or from a bubble in the sample, on a shot-by-shot basis. The normalization of probe and reference signal, allied with the real-time pulse-to-pulse signal processing, results in a highly sensitive apparatus, even though the stability of the laser source is relatively low (10%). Sensitivity is estimated to be as good as ΔOD ~10^{-4} with one second acquisition time, corresponding to an effective shot-to-shot stability of ~1%. A file containing the difference spectrum, probe and reference beam signals and statistics of the experiment is stored on a server before being processed through RAL designed software (Feitan). After processing, the spectrum is stored as a Microsoft Excel document.

8.1.1.5 Sample Considerations

A commercial cell from Harrick Scientific Corporation was used. The instrument has flow cell capabilities, however, with our systems the volume of sample needed would make our experiments extremely expensive, due to the necessity to maintain the concentration in the mM range – this concentration is needed to afford a good signal. Therefore, we use static samples of low-volume (typically 35-50 μL) together with a commercial teflon spacer (typically 6-56 μm from Harrick Scientific, U.S.) between two 25 mm diameter CaF_2 plates (Krystron Limited, U.K.). To minimize sample degradation, the cell is randomly oscillated in both x and y directions (i.e. perpendicular to the direction of the laser beam) using an in-house built x-y stage and electric motors at an approximate rate of 100 mm/ms. Variable temperature measurements were carried out in a Harrick Scientific temperature cell. The number of delays is user defined as are the delay times themselves. Acquisition time for each delay is also variable and in our experiments data acquisitions were over 30 seconds. Within a cycle the delay times are randomized by the software, and a typical spectrum will consist of 4 accumulations, that is four full cycles of all delay times. A negative delay time(s) is necessary so as to provide a baseline.

8.1.1.6 Sample Preparation

Samples were purchased from Sigma Aldrich, with the exceptions of dApdA which was kindly donated by Prof. R. J. H. Davies, Queens University Belfast, and 1-methycytosine which was purchased from Synchem, Germany and recrystallized according to the method of Hosmane and Leonard.[343] All oligonucleotide samples were purchased from Sigma Genosys and required further purification with NAP-5 columns (Amersham Biosciences), as traces of a buffer from previous purification steps that absorbed in the mid infrared remained. Sample concentrations were determined by UV measurement and for TRIR experiments the concentrations used were typically 10 mM in 50 mM potassium phosphate buffer, pH 7. All samples were prepared in D_2O as H_2O absorbs strongly in the mid infrared. UV and FTIR spectra were routinely recorded before and after each ps-TRIR experiment to ascertain if sample decomposition/degradation had occurred.

8.1.1.7 Spectrum Calibration

The monochromator setting (PC controlled, given in tenths of angstroms) is converted to wavenumbers to give an initial estimate of the centre of the window. The probe and reference beam profiles are examined and any apparent spikes are noted (see figure 8.2 (a)). The FTIR spectrum of atmospheric water (figure 8.2 (b)) is compared to the beam profile and pixel positions that can be identified as water absorptions are noted. The values of the water absorptions are then converted into the monochromator scale (i.e. tenths of angstroms) and plotted against the pixel number (figure 8.2 (c)). Successful peak identification in the beam profile will be confirmed if a good fit straight line is obtained. Linear regression provides the equation of the line for that particular spectral window. Pixel numbers 1 to 64 are then substituted into the equation of the line resulting in the full 64 point spectral window in tenths of angstroms. The final step is to convert these figures back into wavenumbers and the result is the calibrated window.

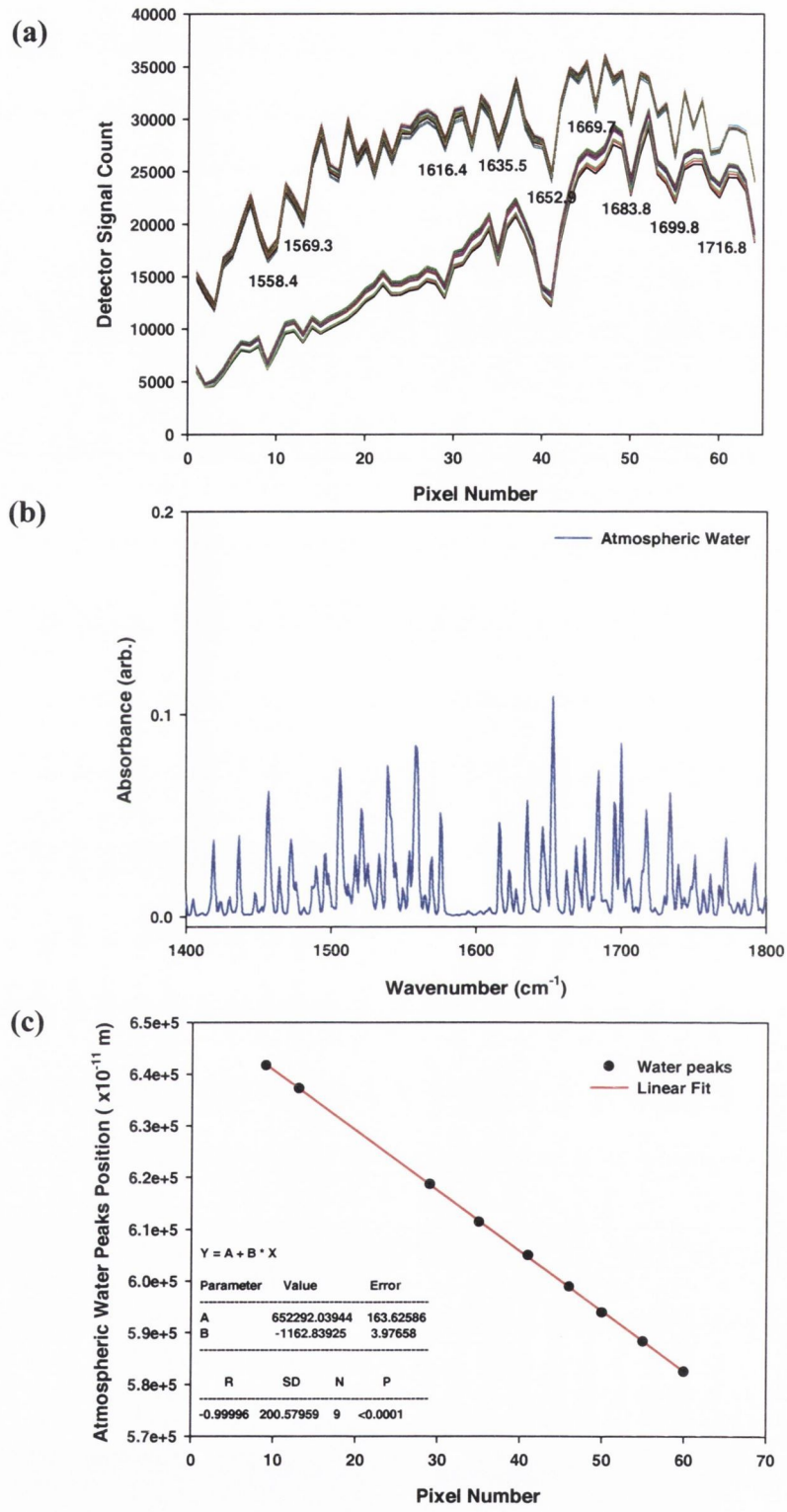

Figure 8.2 (a) Probe and reference beam signal profiles with the positions of atmospheric water absorptions marked, (b) FTIR spectrum of atmospheric water and (c) calibration result for the 64 pixel window in part (a).

8.2 Bimodal Nanoparticles Section

8.2.1 Nanoparticle Preparations

8.2.1.1 Preparation of TMA Stabilized Magnetite Nanoparticles

A 20 mL portion of a 1 M $FeCl_3$ solution in water was mixed with 5 mL of a 2 M $FeCl_2$ solution in 2 M HCl. The chlorides were mixed and quickly added to 250 mL of 0.7 M ammonia solution under vigorous shaking, and immediately a black gelatinous precipitate was formed. Shaking was continued for 30 mins, after which the precipitate was collected with an external magnet. The supernatant was removed and tetramethylammonium hydroxide (TMA, 30 mL) and water (220 mL) were then added to redisperse the precipitate, resulting in a stable ferrofluid. IR (CsI, cm^{-1}) 3387, 3018, 1654, 1569, 1487, 1439, 1403, 948, 665 583 (Fe-O) TEM – Size distribution (N=100), diameter 11 ± 2 nm DLS: hydrodynamic diameter 16 ± 7 nm. Zeta potential: − 46 ± 8 mV.

8.2.1.2 Preparation of Silica Coated Magnetite Nanoparticles

TMA stabalized particles were prepared as per **8.2.1.1**. Next, a 0.58 wt % SiO_2 solution. pH 12, was prepared by dilution of a sodium silicate stock solution. The solution had a pH of 5 after passing through an acid exchange column (Dowex 50 Wx4 resin with sulfonic acid as functional groups). The pH of the eluate was raised immediately to pH 9.5 by the addition of a few drops of silicate stock solution to avoid silica nucleation which may occur at acidic pH where silica has a low solubility. This silicate solution was mixed with the ferrofluid, the pH was adjusted to 10 and the resulting solution was stirred vigorously for 2 hours. Dialysis of the resulting dispersion was carried out so as to avoid flocculation of the particles, which may occur as a result of excess silicates. DLS: hydrodynamic diameter 18 ± 8 nm. Zeta potential: − 43 ± 7 mV.

8.2.1.3 Preparation of APTES Modified Magnetite Nanoparticles

Magnetite nanoparticles (300 mg) and 3-aminopropyltriethoxysilane (350 μL, 1.5 mmol) were reacted in ethanol (30 mL) with triethylamine (210 μL ; 1.5 mmol). The reaction mixture was stirred for 18 hours under an inert atmosphere. The particles were washed

with ethanol (30 mL x 5). The particles were collected with a magnet and dried under vacuum. IR (CsI, cm^{-1}) 574 (Fe-O), 806 (Si-C), 1088 (Si-O), 1637 (C-N), 3450 (N-H) cm^{-1} TEM Size distribution (N = 100), diameter 19 ± 3 nm. TGA: 1.6% weight loss from 30-140 °C, absorbed water and 3% weight loss, 140-800 °C, organic APTES layer. DLS: hydrodynamic diameter 87 ± 23 nm (37%) and 235 ± 89 nm (63%). Zeta potential: + 49 ± 7 mV.

8.2.1.4 Preparation of Dopamine Modified Magnetite Nanoparticles

A 20 mL portion of a 1 M $FeCl_3$ solution in water was mixed with 5 mL of a 2 M $FeCl_2$ solution in 2 M HCl. The chlorides were mixed and quickly added to 250 mL of 0.7 M ammonia solution under vigorous shaking, and immediately a black gelatinous precipitate was formed. Shaking was continued for 30 mins, after which the precipitate was collected with an external magnet. The supernatant was removed and dopamine hydrochloride (0.4 g ; 2.5 mmol) and water (250 mL) were then added to redisperse the precipitate. The resulting mixture was sonicated for 2 hours resulting in very stable particles. DLS: hydrodynamic diameter 37 ± 12 nm. Zeta potential: + 36 ± 12 mV.

8.2.2 Ligand and Complex Syntheses for $Ru(phen)_2phen'$ approach

8.2.2.1 Preparation of 5-amino 1,10-phenanthroline (2)[321]

Ethanol (30 mL) was degassed by bubbling a constant stream of nitrogen through the solution for approximately half an hour. 5-nitro 1,10-phenanthroline (1 g ; 4.44 mmol) and palladium on charcoal (Pd/C 10%) (292 mg ; 2.7 mmol) were added to the ethanol and this solution was allowed to stir for half an hour with nitrogen bubbling through. Hydrazine monohydrate (0.8 mL ; 826 mg ; 16.5 mmol) was added drop-wise via syringe. The mixture was brought to reflux (~80 °C) and left overnight. The solution was filtered while still hot through a glass-sintered funnel containing celite. The solvent was removed from the filtrate under reduced pressure, resulting in a yellow/light brown solid. The solid was washed with ether (5 x 20 mL). Yield: 90%. ES-MS ($CHCl_3$): calculated ($C_{12}H_9N_3$; M) 195.08, found ($C_{12}H_{10}N_3$; $M+H^+$) 196.09. ^1H NMR (400 MHz, DMSO–d_6) : δ ppm : 9.05 (dd, 1H, J = 4.5, 1.5 Hz, CH), 8.67 (m, 2H, 2 x CH),

8.04 (dd, 1H, J = 8.0, 1.5 Hz, CH), 7.74 (dd, 1H, J = 8.5, 4.0 Hz, CH), 7.51 (dd, 1H, J = 8.0, 4.0 Hz, CH), 6.86 (s, 1H, CH), 6.16 (s, 2H, NH_2) IR (KBr, cm^{-1}): 3417, 3320, 3216, 3059, 1636, 1611, 1594, 1562, 1505, 1489, 1455, 1428, 1407, 1335, 1303, 1272, 1219, 1128, 1107, 1035, 885, 841, 826, 812.

8.2.2.2 Preparation of 4-oxo-4-(1,10-phenanthroline-5-ylamino)butanoic acid (3)[322]

A mixture of 1,10-phenanthroline-5-amine (195 mg ; 1 mmol), succinic anhydride (500 mg ; 5 mmol) and *p*-toluenesulfonic acid (38 mg ; 0.2 mmol) were placed in a 100 mL round bottom flask equipped with a stirring bar and a condenser. Chloroform (40 mL) was added and the solution was refluxed for 3 days. An insoluble precipitate was evident in the reaction vessel after the reflux and this precipitate was filtered, washed with chloroform and dried. The isolated solid was yellow in colour and after recrystallisation with methanol a cream/off-white product was isolated. Yield of recrystallised product: 49% ES-MS (H_2O): calculated ($C_{16}H_{13}N_3O_3$; M) 295.09, found ($C_{16}H_{14}N_3O_3$; M + H^+) 296.10. ^1H NMR (400 MHz, DMSO–d_6): δ ppm : 12.17 (s, br, 1H, OH), 10.45 (s, br, 1H, NH), 9.13 (s, 1H, CH), 9.03 (s, 1H, CH), 8.70 (d, 1H, J = 8.0 Hz, CH), 8.44 (d, 1H, J = 8.0 Hz, CH), 8.19 (s, 1H, CH), 7.82 (dd, 1H, J = 8.0, 4.0 Hz, CH), 7.74 (dd, 1H, J = 8.0, 4.5 Hz, CH), 2.78 (t, 2H, J = 6.5 Hz, CH_2), 2.60 (t, 2H, J = 6.5 Hz, CH_2). IR (KBr, cm^{-1}): 3277, 1724, 1654, 1532, 1483, 1424, 1389, 1234, 1184, 902, 828, 805.

8.2.2.3 Preparation of 5-(4-carboxybutanamido)-1,10-phenanthroline (4) – route 1[322]

A mixture of 5-amino 1,10-phenanthroline (195 mg ; 1 mmol), glutaric anhydride (685 mg ; 6 mmol) and *p*-toluenesulfonic acid (PTSA) (38 mg ; 0.2 mmol) was dissolved in $CHCl_3$ (~35 mL) at room temperature under an inert atmosphere of nitrogen. The reaction mixture was refluxed for 6 days after which an insoluble precipitate was evident. This precipitate was filtered, washed with chloroform and dried. The resulting crude product (off white/cream) will be recrystallised from methanol. Yield: 59%. ES-MS (CH_3CN): calculated ($C_{17}H_{15}N_3O_3$; M) 309.11, found ($C_{17}H_{16}N_3O_3$; M + H^+) 310.12 . ^1H NMR: (400 MHz, DMSO–d_6) : δ ppm: 10.21 (s, 1H, NH),

9.13 (dd, 1H, J = 4.0, 1.5 Hz, CH), 9.03 (dd, 1H, J = 4.0, 1.5 Hz, CH), 8.62 (dd, 1H, J = 8.5, 1.5 Hz, CH), 8.45 (dd, 1H, J = 8.0, 1.5 Hz, CH), 8.19 (s, 1H, CH), 7.83 (dd, 1H, J = 8.5, 4.5 Hz), 7.75 (dd, 1H, J = 8.0, 4.0 Hz, CH), 2.59 (t, 2H, J = 7.5 Hz, CH_2), 2.36 (t, 2H, J = 7.0 Hz, CH_2), 1.91 (t, 2H, J = 7.0 Hz, CH_2). IR (KBr, cm^{-1}): 3274, 3049, 2960, 2498, 1703, 1658, 1591, 1567, 1530, 1481, 1459, 1458, 1424, 1411, 1389, 1317, 1301, 1281, 1262, 1230, 1187, 1149, 1099, 1023, 975, 898, 883, 865, 807.

8.2.2.4 Preparation of 5-(4-carboxybutanamido)-1,10-phenanthroline (4) – route 2[323]

5-amino-1,10-phenanthroline (0.5 g ; 2.56 mmol) was dissolved in anhydrous pyridine (25 mL) and heated to 70 °C. Glutaric anhydride (1.46 g ; 12.81 mmol) was added and the mixture was brought to and maintained at reflux (~115 °C) for 3 hours. After reflux the reaction mixture was concentrated down to approximately 5 mL. Acetonitrile (130 mL) was added and the resulting solution was allowed to stir for 2 hours. The product being insoluble in acetonitrile was precipitated out of solution and was collected by suction filtration. The ring-closed ligand was isolated from the filtrate by addition of water, which caused it to be precipitated out of solution. Yield: 43% ES-MS (CH_3CN): calculated ($C_{17}H_{15}N_3O_3$; M) 309.11, found ($C_{17}H_{16}N_3O_3$; M + H^+) 310.12. ^1H NMR: (400 MHz, DMSO–d_6) : δ ppm: 10.21 (s, 1H, NH), 9.13 (dd, 1H, J = 1.5, 4.0 Hz, CH), 9.03 (dd, 1H, J = 2.0, 4.5 Hz, CH), 8.62 (dd, 1H, J = 1.5, 8.5 Hz, CH), 8.45 (dd, 1H, J = 1.5, 8.5 Hz, CH), 8.19 (s, 1H, CH), 7.83 (dd, 1H, J = 4.0, 8.5 Hz, CH), 7.75 (dd, 1H, J = 4.5, 8.0 Hz, CH), 2.59 (t, 2H, J = 7.5 Hz, CH_2), 2.36 (t, 2H, J = 7.5 Hz, CH_2), 1.91 (t, 2H, J = 7.5 Hz, CH_2). IR (KBr, cm^{-1}): 3287, 3049, 2969, 2458, 1916, 1696, 1663, 1591, 1569, 1528, 1480, 1458, 1404, 1322, 1281, 1259, 1210, 1186, 1148, 1114, 1095, 1064, 977, 918, 868, 832, 806.

Isolated the ring-closed product **(5)**: ES-MS (CH_3CN): calculated ($C_{17}H_{13}N_3O_2$; M) 291.10, found ($C_{17}H_{14}N_3O_2$; M + H^+) 292.11. ^1H NMR: (400 MHz, DMSO–d_6) : δ ppm: 9.16 (dd, 1H, J = 2.0, 4.5 Hz, CH), 9.14 (dd, 1H, J = 1.5, 4.5 Hz, CH), 8.50 (dd, 1H, J = 2.0, 8.0 Hz, CH), 8.30 (dd, 1H, J = 1.5, 8.5 Hz, CH), 7.94 (s, 1H, CH), 7.82 (dd, 1H, J = 4.5, 8.0 Hz, CH), 7.77 (dd, 1H, J = 4.0, 8.5 Hz, CH), 2.99 (m, 1H, CH_2), 2.84 (m, 1H, CH_2), 2.19 (m, 1H, CH_2). IR (KBr, cm^{-1}): 3242, 3079, 2970, 1735, 1680, 1631, 1589,

1569, 1515, 1489, 1459, 1424, 1354, 1334, 1247, 1175, 1134, 1097, 1075, 1002, 954, 926, 906, 884, 828, 814.

8.2.2.5 Preparation of $Ru(phen)_2Cl_2$ (6)[324]

A solution of $RuCl_3$ (503 mg ; 2.4 mmol), 1,10-phenanthroline (868 mg ; 4.8 mmol) and LiCl (681 mg ; 16 mmol) in reagent grade DMF (30 mL) was brought to reflux under an inert atmosphere of nitrogen. After 8 hours refluxing the reaction mixture was allowed to cool to room temperature. Reagent grade acetone was added and the resulting mixture was cooled and stored at 0 °C overnight. Filtering yielded a red/orange filtrate and a dark green/black microcrystalline product. The product was washed with water until the washings ran clear. Yield: 55%. IR (KBr, cm^{-1}): 3031, 2161, 1954, 1626, 1592, 1566, 1499, 1446, 1422, 1407, 1339, 1284, 1247, 1196, 1148, 1141, 1096, 1049, 964, 914, 840, 770, 716, 556. UV-vis (CH_2Cl_2, nm): 229, 268, 452.

Also isolated $[Ru(phen)_3]Cl_2$: ^1H NMR: (400 MHz, D_2O) : δ ppm: 8.45 (d, 1H, J = 8.0 Hz, CH), 8.10 (s, 1H, CH), 7.97 (d 1H, J = 5.0 Hz, CH), 7.46 (dd, 1H, J = 5.5 , 7.0 Hz, CH). IR (KBr, cm^{-1}): 3343, 3045, 2160, 1981, 1629, 1600, 1577, 1512, 1493, 1451, 1426, 1411, 1341, 1294, 1254, 1225, 1205, 1143, 1094, 1055, 845, 772, 720. UV-vis (H_2O, nm): 220, 262, 447. ES-MS (H_2O): calculated ($RuC_{36}N_6H_{24}$; M) 642.11, found ($RuC_{36}N_6H_{24}$; M/z) 642.11 / 2 = 321.06.

8.2.2.6 Preparation of $[Ru(phen)_2phen']$$(PF_6)_2$ (7)[344]

A 10% molar excess of phen′ (100 mg ; 0.32 mmol) dissolved in hot ethanol (30 mL) was added to a hot solution of $Ru(phen)_2Cl_2$ (156 mg ; 0.29 mmol) in water (20 mL). The solution was stirred and deaerated with nitrogen for 30 mins and then refluxed for 3 hours under nitrogen. A 5-fold molar excess of NH_4PF_6 (264 mg ; 1.63 mmol) dissolved in ~1 mL of water was added to produce an orange/brown precipitate. The solution was allowed to cool somewhat and then most of the solvent was removed by rotary evaporation. The resulting mixture was filtered yielding a orange/rusty coloured solid which was dried under vacuum to give crude $[Ru(phen)_2phen']$$(PF_6)_2$ in a yield of 83%, which was purified using size exclusion chromatography on a Sephadex LH-20 column

eluting with methanol. ES-MS (H_2O): calculated ($RuC_{41}H_{31}N_7O_3$; M) 771.15, found ($RuC_{41}H_{31}N_7O_3$; M/z) 771.15 / 2 = 385.58 ^1H NMR: (400 MHz, CD_3CN) : δ ppm: 9.76 (s, br, 1H, OH), 8.85 (d, 1H, *J* = 9.0 Hz, CH), 8.64 (s, 1H, NH), 8.57 (m, 4H, 4 x CH), 8.43 (d, 1H, *J* = 8.7 Hz, CH), 8.23 (s, 4H, 4 x CH), 8.01 (m, 5H, 5 x CH), 7.89 (dd, 1H, *J* = 1.0, 5.0 Hz, CH), 7.61 (m, 5H, 5 x CH), 7.52 (dd, 1H, *J* = 5.0, 8.0 Hz, CH), 2.63 (t, 2H, *J* = 7.0 Hz, CH_2), 2.39 (t, 2H, *J* = 7.5 Hz, CH_2), 1.99 (d, 2H, *J* = 7.5 Hz, CH_2). UV-vis (CH_3CN, nm) 223, 263, 448. IR (KBr, cm^{-1}): 3388, 1979, 1698, 1630, 1600, 1579, 1528, 1480, 1461, 1426, 1387, 1340, 1317, 1235, 1206, 1185, 1147, 1095, 1058, 827, 720, 555.

8.2.2.7 Activation of (4) to give the corresponding N-hydroxysuccinimido ester[344]

Anhydrous DMF (600 μL) and phen′ (25 mg ; 80.82 μmol) were placed in a 1.5 mL eppendorf and the mixture was vortexed for three minutes. N,N,N',N'-tetramethyl(succinimido)uranium tetrafluoroborate (TSU) (30 mg ; 99.65 μmol) and diisopropylethylamine (DIPEA) (20 μL ; 0.11 mmol) were added to a second eppendorf and this mixture was also vortexed. The contents of the first eppendorf were added to the second and the entire mixture was vortexed for 3 minutes and left shaking in the dark for 3 hours. Yield = 100% (by TLC) T.L.C: (Silica plates) ($DMF:H_2O:NH_4Cl$ (2 M) ; 1:1:2) Co-spotted the starter and product: R_f 0.43 (acid) R_f 0.66 (ester).

8.2.2.8 Activation of (7) to give the corresponding N-hydroxysuccinimido ester[344]

Anhydrous DMF (600 μL) and $[Ru(phen)_2phen']$$(PF_6)_2$ (35 mg ; 0.03 mmol) were added to a 1.5 mL eppendorf. The mixture was vortexed for three minutes. N,N,N',N'-tetramethyl(succinimido)uranium tetrafluoroborate (TSU) (15 mg ; 0.05 mmol) and diisopropylethylamine (DIPEA) (11 μL ; 0.06 mmol) were added to a second eppendorf and this mixture was also vortexed for three minutes. The contents of the first eppendorf were added to the second and the entire mixture was vortexed for three minutes, centrifuged (3 mins @ 2,000 rpm) and left shaking in the dark for three hours. Yield = 100% (by TLC) T.L.C: (Silica plates) ($DMF:H_2O:NH_4Cl$ (2 M) ; 1:1:2) Co-spotted the starter and product: R_f 0.30 (acid) R_f 0.42 (ester). UV-vis: (DMF, nm) 225, 263, 450.

8.2.3 Ligand and Complex Syntheses Toward a Dopamine Modified Ruthenium Complex

8.2.3.1 Preparation of N-*tert*-butoxycarbonyl-3,4-dihydroxyiphenylethylamine(10)[315]

To a mix solvent of dioxane (5 mL) and H_2O (2.5 mL) was added dopamine hydrochloride (0.48 g, 2.54 mmol) and NaOH (1 M, 2.54 mL, 2.54 mmol). The solution was degassed for 3 times and stirred for 10 min, then tert-butyl dicarbonate (0.555 g, 2.54 mmol) in 5 mL of dioxane was dropped into the solution. After stirring for 20 hrs under an inert atmosphere, the solution was cooled in an ice bath. After adding 50 mL ethyl acetate, the mixture was acidified with dilute HCl solution (1 M) to pH 3. The aqueous phase was washed with ethyl acetate (2 × 30 mL), and all organic fractions were combined. The organic phase was sequentially washed by H_2O (3 × 30 mL), brine (3 × 30 ml) and dried over anhydrous Na_2SO_4. After the organic phase was condensed to 10 mL, the product was purified by flash column (eluent:- hexane : ethyl acetate : MeOH ; 3 : 1 : 0.5) to give 0.502 g of pure product (yield = 84%). ^{1}H NMR (400 MHz, DMSO–d_6): 6.61 (d, 1H), 6.56 (d, 1H), 6.41 (dd, 2H), 3.03 (q, 2H), 2.48 (t, 2H), 1.37 (s, 9H). ES-MS: calculated ($C_{13}H_{19}NO_4$; M) 253.1314, found ($C_{13}H_{19}NO_4Na$; M + Na^+) 276.1223. IR (ATR, cm^{-1}): 3486, 3375, 2968, 2941, 2862, 1676, 1611, 1519, 1473, 1461, 1448, 1411, 1365, 1348, 1294, 1276, 1244, 1201, 1186, 1166, 1154, 1129, 1113, 1055, 1023, 978, 953, 929, 861, 816, 795, 775, 752, 717, 668.

8.2.3.2 Preparation of N-*tert*-butoxycarbonyl-3,4-dibenzyloxyphenylethylamine (11)[315]

After the mixture of (**10**) (0.45 g, 1.78 mmol) in anhydrous DMF (15 mL) containing K_2CO_3 (1.8 g, 13.0 mmol) was degassed for three times, benzyl bromide (0.262 mL, 2.2 mmol) was added dropwise to the mixture under N_2 atomsphere. The reaction was stirred at room temperature for 24 hrs. Then, the mixture was filtered through celite, and the solid was washed with ethyl ether (3 × 20 mL). The combined filtrate and washing solution were washed with ice-water (3 × 25 mL) and brine. The organic layer was dried over anhydrous Na_2SO_4 and concentrated to give a residue, which was purified by recrystallization (ethyl acetate/hexane). **2** was obtained as a white solid. (0.508 g, yield = 58%). ^{1}H NMR (400 MHz, DMSO–d_6): 7.29-7.47 (m, 10H), 6.95 (d, 1H), 6.93 (s, 1H),

6.69 (d, 1H), 5.09 (d, 4H), 3.09 (d, 2H), 2.60 (t, 2H), 1.37 (s, 9H). ES-MS: calculated ($C_{27}H_{31}NO_3$; M) 433.2253, found ($C_{27}H_{31}NO_4Na$; M + Na^+) 456.2135. IR (ATR, cm^{-1}): 3380, 3069, 2971, 2922, 1679, 1593, 1518, 1462, 1454, 1442, 1427, 1388, 1365, 1334, 1265, 1239, 1206, 1163, 1139, 1080, 1062, 1046, 1036, 1027, 1011, 989, 921, 902, 885, 847, 805, 792, 782, 757, 730, 694.

8.2.3.3 Preparation of 2-(3,4-bis-benzyloxy-phenyl)-ethylamine (12)[315]

After **2** (0.200 g, 0.46 mmol) was treated with 5% TFA in CH_2Cl_2 (30 mL) at room temperature for 5 hours, after which the solvent was removed under vacuum to obtain **3** as an oil in a quantitative yield. ^1H NMR (400 MHz, DMSO–d_6): 7.42-7.31 (m, 10H), 7.01 (d, 2H), 6.76 (d, 1H), 5.12 (d, 4H), 3.0 (m, 2H), 2.76 (t, 2H). ES-MS: calculated ($C_{22}H_{23}NO_2$; M) 333.1729, found ($C_{22}H_{23}NO_2$; M + H^+) 334.1793.

8.2.3.4 Preparation of 4,4′-dimethyl-2,2′-bipyridine (13)[332]

Freshly distilled 4-picoline (300 mL) and palladium on charcoal (12 g, 10% Pd/C) were refluxed for 4 days. After the addition of hot toluene (120 mL) the reflux was continued for a further hour. The mixture was filtered from the catalyst while still hot and the solvent was removed under vacuum. The crude product was recrystallized from ethyl acetate. ^1H NMR (400 MHz, DMSO–d_6): 8.58 (d, 1H), 8.32 (s, 1H), 7.20 (d, 1H), 2.49 (s, 3H). ES-MS: calculated ($C_{12}H_{12}N_2$; M) 184.1000, found ($C_{12}H_{13}N_2$; M + H^+) 185.1080. IR (ATR, cm^{-1}): 3056, 1591, 1560, 1551, 1458, 1366, 1249, 1103, 1072, 1044, 991, 912, 824, 670.

8.2.3.5 Preparation of 4,4′-dicarboxy-2,2′-bipyridine (14)[333]

To a stirring solution of sulphuric acid (98%, 125 mL) was added 4,4′-dimethyl-2,2′-bipyridine (5.0 g ; 20.5 mmol). Potassium dichromate (24 g ; 81.5 mmol) was added in small portions under vigorous stirring, and a temperature of 70-80 °C was maintained through careful addition. Occasional cooling in an ice bath was necessary during the addition of the dichromate. The reaction was stirred at room

temperature until the temperature of the mixture had fallen below 40 °C. The deep green reaction mixture was poured into 800 mL of ice water and filtered. The solid was washed with water until the filtrate was colourless, and then allowed dry. The resulting light yellow solid was then further purified by refluxing it in nitric acid (170 mL, 50%) for 4 hours. The solution was poured over ice, diluted with 1 L of water and cooled to 5 °C. The precipitate was filtered, washed with water (5 x 50 mL) and acetone (2 x 20 mL) and dried resulting in 4.936 g (99% yield) of a fine white powder. ^{1}H NMR (400 MHz, DMSO–d_6): 8.93 (d, 1H), 8.86 (s, 1H), 7.93 (d, 1H). ES-MS: calculated ($C_{12}H_8N_2O_4$; M) 244.0484, found ($C_{12}H_7N_2O_4$; M - H^+) 243.0396. IR (ATR, cm^{-1}): 3113, 2424, 1885, 1707, 1604, 1563, 1459, 1364, 1281, 1265, 1240, 1140, 1070, 1011, 992, 931, 914, 865, 822, 765, 722, 679, 662.

8.2.3.6 Preparation of 4,4′-bis(chlorocarbonyl)-2,2′-bipyridine (15)[334]

4,4′-dicarboxy-2,2′-bipyridine (0.869 g ; 3.56 mmol) was refluxed in thionyl chloride (25 mL) for 16 hours under an inert atmosphere. The excess thionyl chloride was removed by distillation and the resulting yellow residue was dried under vacuum for 4 hours. The acid chloride was assumed to have formed in quantitative yield and was used immediately in subsequent reaction.

8.2.3.7 Preparation of N4,N4′-bis(3,4-bis(benzyloxy)phenethyl)-2,2′-bipyridine-4,4′-dicarboxamide (16)

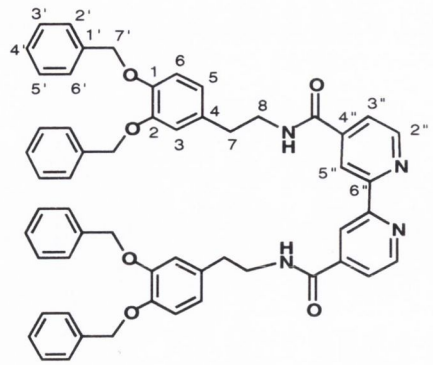

Compound **15** from above (1 mmol) was dissolved in dry DCM, under an inert atmosphere. Triethyamine (0.1 mL) and compound **12** (2.2 mmol) in dry DCM were added dropwise to the stirring solution. The resulting mixture was left refluxed for 4 hours after which time a pink precipitate that had formed was filtered off. ^{1}H NMR (600 MHz, DMSO–d_6): 9.03 (t, 2H, 2 x NH), 8.84 (dd, 2H, bipy 2 x 2′′), 8.80 (s, 2H, bipy 2 x 5′′), 7.82 (dd, 2H, bipy 2 x 3′′), 7.42 (m, 8H, 4 x 2′ and 4 x 6′), 7.36 (m, 8H, 4 x 3′ and 4 x 5′), 7.31 (t, 4H, 4 x 4′), 6.99 (m, 4H, 2 x 6 and 2 x 3), 6.78 (dd, 2, 2 x 5), 5.09 (d, 8, 4 x 7′), 3.51 (dd, 4H, 4 x 8), 2.81 (t, 4H, 2 x 7). ES-MS: calculated ($C_{56}H_{50}N_4O_6$; M) 874.3730, found ($C_{56}H_{51}N_4O_6$; M + H^+) 875.3782. IR (ATR, cm^{-1}): 3313, 3059, 2951, 2877, 1675, 1643, 1590, 1553, 1532, 1511, 1454, 1428, 1381, 1365, 1314, 1249, 1222, 1192, 1157, 1134, 1062, 1035, 1000, 938, 917, 907, 860, 845, 803, 746, 696.

8.2.3.8 Preparation of [4,4′-dicarboxy-2,2′-bipyridine]bis(1,10-phenanthroline)-ruthenium (II) dichloride (17)[334]

A solution of $[Ru(phen)_2Cl_2]$ (0.70 g, 1.31 mmol) in 1 : 1 EtOH : H_2O (130 mL) was added to a suspension of 4,4′-dicarboxy-2,2′-bipyridine (0.340 g, 1.39 mmol) in 1 : 1 EtOH : H_2O (650 mL). The mixture was refluxed for 3 days under nitrogen and was then cooled and filtered to remove unreacted 4,4′-dicarboxy-2,2′-bipyridine. The solvent was evaporated from the red filtrate to give the product as a brown solid, which was dried under vacuum (0.98 g ; 94%). ^{1}H NMR (400 MHz, DMSO–d_6): 9.22 (s, 2H, bipyH3,3′), 8.85 (d, 2H, J = 8.8 Hz, bipyH6,6′), 8.76 (d, 2H, J = 8.8 Hz, bipy5,5′), 8.40 (m, 4H, phen2,2′), 7.93 (m, 4H, phen4,4′), 7.74 (m, 4H, phen3,3′) IR (ATR, cm^{-1}): 3338, 1713, 1628, 1551, 1509, 1483, 1427, 1407, 1314, 1266, 1227, 1142, 1027, 900, 843, 769, 740, 721.

8.2.3.9 Preparation of [4,4′-dichlorocarbonyl-2,2′-bipyridine]bis(1,10-phenanthroline)-ruthenium (II) dichloride (18)[334]

4,4′-Dicarboxy-2,2′-bipyridine]bis(1,10-phenanthroline)-ruthenium(II) dichloride (0.050 g, 0.64 μmol) was refluxed in thionyl chloride (15 mL) for 15 h under nitrogen. The excess thionyl chloride was then removed by distillation and the brown/dark red residue dried under vacuum for 2 hours, then heated under vacuum (60–70 °C) for a further 45 minutes. The acid chloride was assumed to have formed in quantitative yield and was used immediately in subsequent reaction.

8.2.3.10 Preparation of [N4,N4′-bis(3,4-bis(benzyloxy)phenethyl)-2,2′-bipyridine-4,4′-dicarboxamide]bis(1,10-phenanthroline)-ruthenium (II) dichloride (19)

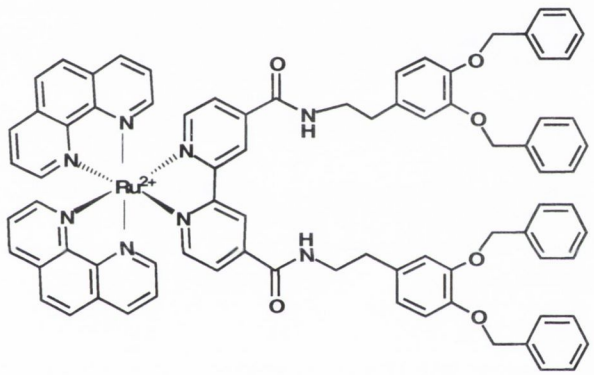

Freshly prepared compound **18** from above (64 μmol) was dissolved in dry DCM, under an inert atmosphere. Triethyamine (0.05 mL) and freshly prepared compound **12** (264 μmol) in dry DCM were added dropwise to the stirring solution. The resulting mixture was left stirring for 12 hours. TLC analysis after this time showed three spots. The solvent was removed and the crude product was passed down a Sephadex LH-20 column. After this time, proton NMR and TLC confirmed that the product as still impure. A second column, flash silica was attempted but the product was not recovered off the column. Mass spec analysis of the crude product was obtained. ES-MS: calculated ($C_{56}H_{50}N_4O_6$; M) 1336.4138, found ($C_{56}H_{51}N_4O_6$; M/z) 1336.4149/2 = 668.2047.

8.2.4 Syntheses Toward a Modified Dopamine Linker for Nanoparticles and Oligonucleotides

8.2.4.1 Preparation of 2-(*tert*-butoxycarbonylaminooxy) acetic acid (20)

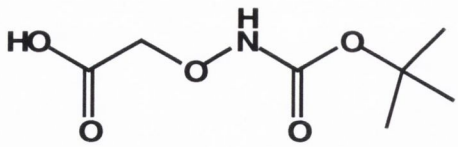

To a mix solvent of dioxane (10 mL) and H_2O (5 mL) carboxymethylamine hemihydrochloride (0.5456 g ; 5 mmol) and NaOH (1 M, 5 mL ; 5 mmol) were added. The solution was degassed and then *tert*-butyl dicarbonate (1.09 g ; 5 mmol) in dioxane (5 mL) was added dropwise to the stirring solution. After stirring for 24 hours the solution was cooled in an ice bath. After the addition of ethyl acetate (80 mL), the mixture was acidified with HCl solution (1 M) to pH 2. The aqueous phase was washed with ethyl acetate (2 x 50 mL) and all organic fractions were combined. The organic phase was sequentially washed with H_2O (3 x 50 mL), brine (3 x 50 mL) and then dried over anhydrous Na_2SO_4. The solvent was removed and the resulting white solid was recrystallized from ethyl acetate:hexane (50:50) to give 0.713 g ; 77% yield) of white crystals. ^{1}H NMR (400 MHz, DMSO – d_6): 12.85 (s(br), 0.8H, OH), 10.14 (s, 1H, NH), 4.27 (s, 2H, CH_2), 1.41 (s, 9H, 3 x CH_3). ^{13}C NMR (100 MHz, DMSO–d_6): 170.66 (C=O (COOH)), 156.91 (C=O), 80.51 (q, O-C-$(CH_3)_3$), 72.46 (CH_2), 28.45 (3 x CH_3). ES-MS: calculated ($C_7H_{13}NO_5$; M) 191.0794, found ($C_7H_{13}NO_5Na$; M + Na^+) 214.0691. IR (ATR, cm^{-1}): 3375, 2986, 2958, 2575, 1747, 1719, 1438, 1414, 1395, 1369, 1285, 1236, 1162, 1119, 1056, 976, 908, 853, 776, 758, 694.

8.2.4.2 Preparation of 2,5-dioxopyrrolidin-1-yl 2-(*tert*-butoxycarbonylaminooxy) acetate (21)

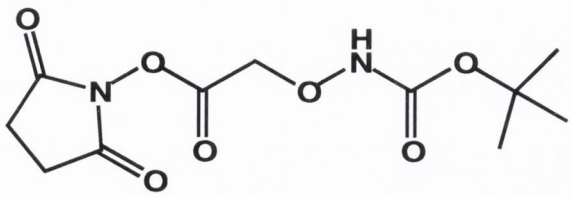

To 2-(tert-butoxycarbonylaminooxy) acetic acid (0.669 g ; 3.5 mmol) in DCM (20 mL) under nitrogen was added N,N'-dicyclohexylcarbodiimide (DCC) (0.7576 g ; 3.675 mmol) in DCM (5 mL) via syringe. After 30 minutes of stirring, N-hydorxysuccinimide (0.4230 g ; 3.675 mmol) in DCM (50 mL) was added. The reaction mixture was left stirring overnight at room temperature. The precipitated side product, DCU, was removed by filtration. The filtrate was dissolved in hot carbon tetrachloride and filtered. The filtrate was stored at 4 °C, resulting in 0.737 g (73%) of white crystals. ^{1}H NMR (400 MHz, DMSO–d_6): 10.39 (s, 1H, NH), 4.83 (s, 2H, CH_2), 2.84 (s, 4H, 2 x CH_2 ($CO(CH_2)CO$), 1.42 (s, 9H, 3 x CH_3). ^{13}C NMR (100 MHz, DMSO–d_6): 169.98 (2 x C=O), 165.17 (C=O, O-CO-CH_2), 156.58 (C=O, NH-CO-O), 80.59 ($C(CH_3)$), 69.88 (CH_2, O-CH_2-CO) 27.93 (3 x CH_3). ES-MS: calculated ($C_{11}H_{16}N_2O_7$; M) 288.0958, found ($C_{11}H_{16}N_2O_7Na$; M + Na^+) 311.0866. IR (ATR, cm^{-1}): 3375, 3324, 2928, 1747, 1700, 1625, 1574, 1436, 1414, 1369, 1232, 1161, 1119, 1086, 1055, 976, 894, 853, 775, 758, 691.

8.2.4.3 Preparation of *tert*-butyl-2-(3,4-dihydroxyphenethylamino)-2-oxoethoxycarbamate (22)

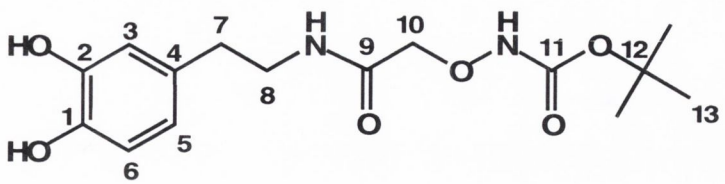

Dopamine hydrochloride (0.291g ; 2.85 mmol) and diisopropylethylamine (DIPEA) (0.392 cm^3 ; 2.25 mmol) were vigorously stirred in anhydrous dimethylformamide (DMF) for 2 hours under an inert atmosphere. Compound **21** (0.589g ; 2.05 mmol) in anhydrous DMF was added via syringe and the resulting mixture was stirred overnight solution. The

solvent was removed resulting in a brown oil. Attempts were made to crystallize the product but the compound remained as a viscous oil. ^{1}H NMR (600 MHz, DMSO–d_6): 10.29 (s, 1H, NH, O-NH-CO), 8.04 (s, 1H, NH, H_2C-NH-CO), 6.64 (d, 1H, C_5H, J = 8.0 Hz), 6.60 (d, 1H, C_6H, J = 1.6 Hz), 6.44 (dd, 1H, C_3H, J = 1.8, 8.0 Hz), 4.13 (s, 2H, CH_2, CO-CH_2-O), 3.58 (m, 2H, CH_2, -CH_2NH-), 2.55 (t, 2H, CH_2, J = 7.7 Hz), 1.42 (s, 9H, 3 x CH_3). ^{13}C NMR (150 MHz, DMSO–d_6): 168.09 (C_9), 157.12 (C_{11}), 145.41 (C_2), 143.90 (C_1), 130.21 (C_4), 119.44 (C_5), 116.28 (C_6), 115.90 (C_3), 80.90 (C_{12}), 75.06 (C_{10}), 53.48 (C_8), 28.24 (C_{13}), 25.53 (C_7). ES-MS: calculated ($C_{15}H_{22}N_2O_6$; M) 326.1478, found ($C_{15}H_{22}N_2O_6Na$; M + Na^+) 349.1371. IR (ATR, cm^{-1}): 2981, 2700, 1781, 1708, 1649, 1519, 1434, 1393, 1368, 1282, 1252, 1211, 1161, 1112, 1073, 975, 847, 814, 782, 713.

8.2.5 Preparation of '2 in 1' Nanocomposites

8.2.5.1 Preparation of APTES Modified Fe_3O_4 –Ru Metal Complex Nanocomposites

APTES coated magnetite (20 mg as per **8.2.1.3**) particles were dried on a vac line and redispersed several times (using a magnet to attract the particles between redispersions) in dry DCM. Excess freshly prepared [4,4′-dichlorocarbonyl-2,2′-bipyridine]bis(2,2′-bipyridine)-ruthenium(II) dichloride (0.2 mmol) was added via syringe and the resulting mixture was sonicated for 1 hour. The particles were collected using a permanent magnet and washed with water. SPC lifetime analysis: $\tau = 273 \pm 3$ ns.

8.2.5.2 Preparation of Dopamine Modified Fe_3O_4 –Ru Metal Complex Nanocomposites

Dopamine stabilized particles (20 mL) were prepared as per **8.2.1.4**. The hydrochloric salt was removed by washing the particles with sodium carbonate solution. The partices were washed with water several times until the pH was ~7. The particles were then dried on a vac line and redispersed several times (using a magnet to attract the particles between redispersions) in dry DCM. Excess freshly prepared [4,4′-dichlorocarbonyl-2,2′-bipyridine]bis(2,2′-bipyridine)-ruthenium(II) dichloride (0.2 mmol) in dry DCM was added via syringe to a solution containing 25 mg of dispersed particles in dry DCM. The

resulting mixture was sonicated for 1 hour. The particles were collected using a permanent magnet and washed with water. SPC lifetime analysis: $\tau = 1.9 \pm 0.01$ ns.

8.2.5.3 Preparation of Fe_3O_4 –Ru Dye – DNA Nanocomposites

$FeCl_3.6H_2O$ (1.1g ; 4 mmol) and $FeCl_2.4H_2O$ (0.4 g ; 2 mmol) were dissolved in deoxygenated millipore water (100 mL). Herring sperm DNA (0.006 g) was dissolved in millipore water (10 mL) via shaking for 10 minutes. Heated to boiling and cooled rapidly in ice. This solution was then added to 10 mL of the above prepared iron(II)/(III) solution under argon. Ammonia solution (2 mL) was added to the stirring solution to precipitate the magnetite nanoparticles. The resulting suspension was allowed to stir for 15 minutes at room temperature under argon. The particles were then separated using a magnet. The supernatant was removed and the particles washed 5 times with millipore water (10 mL). Each washing was kept and labelled (washings 1-5). The final 3 washings were found to be stable suspensions of magnetite/DNA composite material. Washing number five (360 μL) was added to Millipore water (3ml). $Ru(phen)_2dppz$ (10 μL ; 7.5 μmoles) was added to the DNA-magnetite solution. A 50 μL portion of this sample was dropped onto a confocal slide in a 0.5 T magnetic field and the drop was allowed to evaporate before imaging. Confocal results: $\tau_{average} = 30$ ns, $\tau_{on\ the\ string} = 20$ ns. SPC lifetime biexponential fitting: $\tau_1 = 2.2 \pm 0.03$ ns, $\tau_1 = 23.7 \pm 0.3$ ns.

8.3 Experimental Procedures and Techniques

8.3.1 Reagents and Solvents

All solvents were reagent grade except where otherwise stated. All chemicals were purchased from Sigma Aldrich, Sigma Genosys, and Fluka. Millipore water was used in all aqueous preparations. Samples of $[poly(dA\text{-}dT)]_2$ and $[poly(dG\text{-}dC)]_2$ were purchased from Amersham Biosciences.

8.3.2 Thin Layer Chromotography

Thin layer chromatography (TLC) plates of silica and alumina were purchased from Merck and Sigma Aldrich respectively.

8.3.3 Size exclusion Chromotography

Sephadex LH-20 (Fluka) was used as size exclusion resin. The compound, which was loaded onto the top of the column, was eluted using either acetonitrile or methanol, with the largest compound being eluted first.

8.3.4 ^{1}H and ^{13}C Nuclear Magnetic Resonance Spectroscopy

Samples were recorded on Bruker 400/600 MHz machines in appropriate deuterated solvents.

8.3.5 UV-vis Absorption Spectroscopy

Absorption spectra and optical density were recorded on a Varian Cary 300 spectrophotometer or a Shimadzu UV-2401 PC UV-Vis spectrophotometer in an appropriate range. Solutions were measured in 4 cm^3 (10 mm x 10 mm) cuvettes.

8.3.6 Steady State Excitation and Emission Spectroscopy

Steady state emission spectra were recorded using an LS-50B Perkin Elmer Luminescence spectrometer or Varian Cary Eclipse spectrometer.

8.3.7 Fourier Transform Infrared Spectroscopy

Fourier transform infrared spectra were recorded on a Mattson Genesis II FTIR spectrophotometer where solid samples were dispersed in KBr or CsI and recorded as clear pressed discs. A Perkin Elmer spectrometer with an ATR sampling accessory was also used for the characterization of some samples, where spectra of neat samples were recorded.

8.3.8 Electrospray Mass Spectrometry

Mass spectra were recorded on a Micromass LCT time of flight mass spectrometer using electrospray injection in both positive and negative modes where appropiate.

8.3.9 Circular Dichroism Spectroscopy

Corcular dichroism spectra were recorded on a Jasco 810 spectrometer in an appropriate range with an appropriate scan rate. Spectra were typically accumulated over eight cycles.

8.3.10 X-Ray Diffraction Analysis

X-ray diffraction measurements were carried out on a Siemens diffractometer. Samples were either evaporated onto the XRD slide or were adhered to the slide using a small amount of vacuum grease. Samples were scanned for 2Θ values in the range 10-70° at a rate of 0.02° per second.

8.3.11 Transmission electron Microscopy

The average particles size, size distribution and morphology of particles were examined using a Hitachi H-7000 electron microscope at a voltage of 100 kV. Dispersions of particles were drop-cast onto a formvar copper grid and the grid was air dried at room temperature before viewing under the microscope.

8.3.12 Dynamic Light Scattering and Zeta Potential Measurements

Dymanic light scattering and zeta potential measurements were recorded on a Malvern Nano ZS instrument. Samples were passed through 0.45 μm syringe filters (Roth Ltd. Germany) before measurement. Data were typically recorded over at least five accumulations.

8.3.13 Time Correlated Single Photon Counting (SPC) Spectroscopy

Time correlated single photon counting was used for the measurement of the metal complex lifetime in solution. The photomultiplier triggers the excitation pulse, generating an electronic and optical pulse simultaneously. The time-to-amplitude (TAC) receives the electronic pulse, the START signal at time t = 0. The optical pulse excited the sample, a photon is emitted and the signal from the photon stops the charging of the capacitor in the TAC and is essentially the STOP signal. The time difference between start and stop pulses is measured over thousands/hundreds of thousands of events and an average lifetime results.

Chapter 9

References

(1) Watson, J. D.; Crick, F. H. C. *Nature* **1953**, *171*, 737-738.

(2) Mouret, S.; Charveron, M.; Favier, A.; Cadet, J.; Douki, T. *DNA Repair* **2008**, *7*, 704-712.

(3) Masson, F.; Laino, T.; Tavernelli, I.; Rothlisberger, U.; Hutter, J. *J. Am. Chem. Soc.* **2008**, *13*, 3443-3450.

(4) Marrot, L.; Meunier, J.R. *J. Am. Acad. Derm.* **2008**, *58*, S139-S148.

(5) Kwok, W.-M.; Ma, C.; Phillips, D. L. *J. Am. Chem. Soc.* **2008**, *130*, 5131-5139.

(6) Mouret, S.; Baudouin, C.; Charveron, M.; Favier, A.; Cadet, J.; Douki, T. *Proc. Natl. Acad. Sci. (USA)* **2006**, *103*, 13765-13770.

(7) Cadet, J.; Sage, E.; Douki, T. *Mutat. Res., Fundam. Mol. Mech. Mutagen* . **2005**, *571*, 3-17.

(8) Cadet, J.; Courdavault, S.; Ravanat, J. L.; Douki, T. *Pure Appl. Chem.* **2005**, *77*, 947-961.

(9) Douki, T.; Cadet, J. *Biochemistry* **2001**, *40*, 2495-2501.

(10) Cadet, J.; Berger, M.; Douki, T.; Morin, B.; Raoul, S.; Ravanat, J. L.; Spinelli, S. *Biol. Chem.* **1997**, *378*, 1275-1286.

(11) Neidle, S. *Principles of Nucleic Acid Structure*; Academic Press, Elsevier, **2008**.

(12) Neidle, S.; Balasubramanian, S.; (eds.) *Quadruplex Nucleic Acids*; Royal Society of Chemistry, Cambridge, UK., **2006**.

(13) Blancafort, L.; Cohen, B.; Hare, P. M.; Kohler, B.; Robb, M. A. *J. Phys. Chem. A* **2005**, *109*, 4431-4436.

(14) Ismail, N.; Blancafort, L.; Olivucci, M.; Kohler, B.; Robb, M. A. *J. Am. Chem. Soc.* **2002**, *124*, 6818-6819.

(15) Daniels, M.; Hauswirth, W. *Science* **1971**, *171*, 675-677.

(16) Crespo-Hernandez, C. E.; Cohen, B.; Hare, P. M.; Kohler, B. *Chem. Rev.* **2004**, *104*, 1977-2020.

(17) Pecourt, J. M. L.; Peon, J.; Kohler, B. *J. Am. Chem. Soc.* **2001**, *123*, 10370-10378.

(18) Sharonov, A.; Gustavsson, T.; Carré, V.; Renault, E.; Markovitsi, D. *Chem. Phys. Lett.* **2003**, *380*, 173-180.

(19) Onidas, D.; Markovitsi, D.; Marguet, S.; Sharonov, A.; Gustavsson, T. *J. Phys. Chem. B* **2002**, *106*, 11367-11374.

(20) Roca-Sanjuán, D.; Merchán, M.; Serrano-Andrés, L. *Chem. Phys.* **2008**, *349*, 188-196.

(21) Gustavsson, T.; Bányász, Á.; Sarkar, N.; Markovitsi, D.; Improta, R. *Chem. Phys.***2008**, *350*, 186-192.

(22) Groenhof, G.; Schafer, L. V.; Boggio-Pasqua, M.; Goette, M.; Grubmuller, H.; Robb, M. A. *J. Am. Chem. Soc.* **2007**, *129*, 6812-6819.

(23) Blancafort, L.; Migani, A. *J. Photochem. Photobiol., A* **2007**, *190*, 283-289.

(24) Blancafort, L.; Migani, A. *J. Am. Chem. Soc.* **2007**, *129*, 14540-14541.

(25) Santoro, F.; Barone, V.; Gustavsson, T.; Improta, R. *J. Am. Chem. Soc.* **2006**, *128*, 16312-16322.

(26) Perun, S.; Sobolewski, A. L.; Domcke, W. *J. Phys. Chem. A* **2006**, *110*, 13238-13244.

(27) Gustavsson, T.; Sarkar, N.; Lazzarotto, E.; Markovitsi, D.; Barone, V.; Improta, R. *J. Phys. Chem. B* **2006**, *110*, 12843-12847.

(28) Tomic, K.; Tatchen, J.; Marian, C. M. *J. Phys. Chem. A* **2005**, *109*, 8410-8418.

(29) Pancur, T.; Schwalb, N. K.; Renth, F.; Temps, F. *Chem. Phys.***2005**, *313*, 199-212.

(30) Matsika, S. *J. Phys. Chem. A* **2005**, *109*, 7538-7545.

(31) Marian, C. M. *J. Chem. Phys.* **2005**, *122*, 104314.

(32) Canuel, C.; Mons, M.; Piuzzi, F.; Tardivel, B.; Dimicoli, I.; Elhanine, M. *J. Chem. Phys.***2005**, *122*, 074316.

(33) Sobolewski, A. L.; Domcke, W. *Phys. Chem. Chem. Phys.***2004**, *6*, 2763-2771.

(34) Schultz, T.; Samoylova, E.; Radloff, W.; Hertel, I. V.; Sobolewski, A. L.; Domcke, W. *Science* **2004**, *306*, 1765-1768.

(35) Blancafort, L.; Robb, M. A. *J. Phys. Chem. A* **2004**, *108*, 10609-10614.

(36) Kang, H.; Jung, B.; Kim, S. K. *J. Chem. Phys.* **2003**, *118*, 6717-6719.

(37) Pecourt, J. M. L.; Peon, J.; Kohler, B. *J. Am. Chem. Soc.* **2000**, *122*, 9348-9349.

(38) Cohen, B.; Crespo-Hernandez, C. E.; Kohler, B. *Faraday Discuss.* **2004**, *127*, 137-147.

(39) Hare, P. M.; Crespo-Hernandez, C. E.; Kohler, B. *Proc. Natl. Acad. Sci. (USA)* **2007**, *104*, 435-440.

(40) Hare, P. M.; Crespo-Hernandez, C. E.; Kohler, B. *J. Phys. Chem. B* **2006**, *110*, 18641-18650.

(41) Cadet, J.; Vigny, P. *Bioorganic Photochemistry*; Morrison, H. (ed.), Wiley, New York **1990**; Vol. 1 Pages 1-37.

(42) Rahn, R. O.; Shulman, R. G.; Longworth, J. W. *Proc. Natl. Acad. Sci. (USA)* **1965**, *53*, 893-896.

(43) Gut, I. G.; Wood, P. D.; Redmond, R. W. *J. Am. Chem. Soc.* **1996**, *118*, 2366-2373.

(44) Hare, P. M.; Middleton, C. T.; Mertel, K. I.; Herbert, J. M.; Kohler, B. *Chem. Phys.***2008**, *347*, 383-392.

(45) Climent, T.; González-Luque, R.; Merchán, M.; Serrano-Andrés, L. *Chem. Phys. Lett.* **2007**, *441*, 327-331.

(46) Zhang, R. B.; Eriksson, L. A. *J. Phys. Chem. B* **2006**, *110*, 7556-7562.

(47) Noguera, M.; Blancafort, L.; Sodupe, M.; Bertran, J. *Mol. Phys.* **2006**, *104*, 925-931.

(48) Kuimova, M. K.; Dyer, J.; George, M. W.; Grills, D. C.; Kelly, J. M.; Matousek, P.; Parker, A. W.; Sun, X. Z.; Towrie, M.; Whelan, A. M. *Chem. Commun.* **2005**, 1182-1184.

(49) Middleton, C. T.; Cohen, B.; Kohler, B. *J. Phys. Chem. A* **2007**, *111*, 10460-10467.

(50) Wu, R.; McMahon, T. B. *J. Am. Chem. Soc.* **2007**, *129*, 569-580.

(51) Kabelac, M.; Hobza, P. *Phys. Chem. Chem. Phys.* **2007**, *9*, 903-917.

(52) Ten, G. N.; Baranov, V. I. *J. Appl. Spectrosc.* **2005**, *72*, 155-163.

(53) Sobolewski, A. L.; Domcke, W.; Hattig, C. *Proc. Natl. Acad. Sci. (USA)* **2005**, *102*, 17903-17906.

(54) Shukla, M. K.; Leszczynski, J. *J. Phys. Chem. A* **2005**, *109*, 7775-7780.

(55) Sahu, P. K.; Mishra, R. K.; Lee, S. L. *J. Phys. Chem. A* **2005**, *109*, 2887-2893.

(56) Marian, C.; Nolting, D.; Weinkauf, R. *Phys. Chem. Chem. Phys.* **2005**, *7*, 3306-3316.

(57) Choi, M. Y.; Dong, F.; Miller, R. E. *Philos. Trans. R. Soc. London, Ser. A* **2005**, *363*, 393-413.

(58) Brauer, B.; Gerber, R. B.; Kabelac, M.; Hobza, P.; Bakker, J. M.; AboRiziq, A. G.; deVries, M. S. *J. Phys. Chem. A* **2005**, *109*, 6974-6984.

(59) Blancafort, L.; Bertran, J.; Sodupe, M. *J. Am. Chem. Soc.* **2004**, *126*, 12770-12771.

(60) Podolyan, Y.; Gorb, L.; Leszczynski, J. *Int. J. Mol. Sci.* **2003**, *4*, 410-421.

(61) Hanus, M.; Ryjacek, F.; Kabelac, M.; Kubar, T.; Bogdan, T. V.; Trygubenko, S. A.; Hobza, P. *J. Am. Chem. Soc.* **2003**, *125*, 7678-7688.

(62) Cohen, B.; Hare, P. M.; Kohler, B. *J. Am. Chem. Soc.* **2003**, *125*, 13594-13601.

(63) Trygubenko, S. A.; Bogdan, T. V.; Rueda, M.; Orozco, M.; Luque, F. J.; Sponer, J.; Slavicek, P.; Hobza, P. *Phys. Chem. Chem. Phys.* **2002**, *4*, 4192-4203.

(64) Shukla, M. K.; Leszczynski, J. *J. Phys. Chem. A* **2002**, *106*, 11338-11346.

(65) Fogarasi, G. *J. Phys. Chem. A* **2002**, *106*, 1381-1390.

(66) Podolyan, Y.; Gorb, L.; Leszczynski, J. *J. Phys. Chem. A* **2000**, *104*, 7346-7352.

(67) Mishra, S. K.; Shukla, M. K.; Mishra, P. C. *Spectrochim. Acta Part A* **2000**, *56*, 1355-1384.

(68) Gorb, L.; Podolyan, Y.; Leszczynski, J. *J. Mol. Struct., Theochem* **1999**, *487*, 47-55.

(69) Broo, A. *J. Phys. Chem. A* **1998**, *102*, 526-531.

(70) Broo, A.; Holmen, A. *J. Phys. Chem. A* **1997**, *101*, 3589-3600.

(71) Florian, J.; Leszczynski, J. *J. Am. Chem. Soc.* **1996**, *118*, 3010-3017.

(72) Colominas, C.; Luque, F. J.; Orozco, M. *J. Am. Chem. Soc.* **1996**, *118*, 6811-6821.

(73) Douhal, A.; Kim, S. K.; Zewail, A. H. *Nature* **1995**, *378*, 260-263.

(74) Purrello, R.; Molina, M.; Wang, Y.; Smulevich, G.; Fossella, J.; Fresco, J. R.; Spiro, T. G. *J. Am. Chem. Soc.* **1993**, *115*, 760-767.

(75) Gould, I. R.; Vincent, M. A.; Hillier, I.; Lapinski, L.; Nowak, M. J. *Spectrochim. Acta Part A* **1992**, *48*, 811-818.

(76) Wilson, R. W.; Callis, P. R. *Photochem. Photobiol.* **1980**, *31*, 323-327.

(77) Johnson, W. C.; Vipond, P. M.; Girod, J. C. *Biopolymers* **1971**, *10*, 923-933.

(78) Sundstrom, V. *Annu. Rev Phys. Chem.* **2008**, *59*, 53-77.

(79) Banerjee, D.; Pal, S. K. *J. Phys. Chem. A* **2008**, *112*, 7314-7320.

(80) Gorb, L.; Podolyan, Y.; Dziekonski, P.; Sokalski, W. A.; Leszczynski, J. *J. Am. Chem. Soc.* **2004**, *126*, 10119-10129.

(81) Bertran, J.; Oliva, A.; Rodriguez-Santiago, L.; Sodupe, M. *J. Am. Chem. Soc.* **1998**, *120*, 8159-8167.

(82) Colson, A. O.; Sevilla, M. D. *Int. J. Radiat. Biol.* **1995**, *67*, 627-645.

(83) Florian, J.; Hrouda, V.; Hobza, P. *J. Am. Chem. Soc.* **1994**, *116*, 1457-1460.

(84) Elias, B.; Creely, C.; Doorley, G. W.; Feeney, M. M.; Moucheron, C.; Kirsch-DeMesmaeker, A.; Dyer, J.; Grills, D. C.; George, M. W.; Matousek, P.; Parker, A. W.; Towrie, M.; Kelly, J. M. *Chem. Eur. J.* **2008**, *14*, 369-375.

(85) Schwalb, N. K.; Temps, F. *J. Am. Chem. Soc.* **2007**, *129*, 9272-9273.

(86) Schreier, W. J.; Schrader, T. E.; Koller, F. O.; Gilch, P.; Crespo-Hernandez, C. E.; Swaminathan, V. N.; Carell, T.; Zinth, W.; Kohler, B. *Science* **2007**, *315*, 625-629.

(87) Towrie, M.; Grills, D. C.; Dyer, J.; Weinstein, J. A.; Matousek, P.; Barton, R.; Bailey, P. D.; Subramaniam, N.; Kwok, W. M.; Ma, C. S.; Phillips, D.; Parker, A. W.; George, M. W. *Appl. Spectrosc.* **2003**, *57*, 367-380.

(88) Levenberg, K. *Q. Appl. Math.* **1944**, *2(2)*, 164–168.

(89) Marquardt, D. W. SIAM *J. Appl. Math.* **1963**, *11*, 431-441.

(90) Kelley, C. T. *Iterative Methods for Optimization*; SIAM Press: Philadelphia, **1999**.

(91) Lampton, M. *Comput. Phys.* **1997**, *11*, 110-115.

(92) Nocedal, J.; Wright, S. J. *Numerical Optimization*; Springer: New York, **1999**.

(93) Taboury, J. A.; Liquier, J.; Taillandier, E. *Can. J. Chem.* **1985**, *63*, 1904-1909.

(94) Taillandier, E.; Liquier, J., Vibrational Spectroscopy of the Nucleic Acids, in the Handbook of Vibrational Spectroscopy , ed. J.M. Chalmers and P. R. Griffiths, Wiley, Chichester, **2002**.

(95) Hamm, P.; Helbing, J.; Bredenbeck, J. *Annu. Rev. Phys. Chem.* **2008**, *59*, 291-317.

(96) Krummel, A. T.; Zanni, M. T. *J. Phys. Chem. B* **2006**, *110*, 13991-14000.

(97) Kuimova, M. K.; Cowan, A. J.; Matousek, P.; Parker, A. W.; Sun, X. Z.; Towrie, M.; George, M. W. *Proc. Natl. Acad. Sci. (USA)* **2006**, *103*, 2150-2153.

(98) Peon, J.; Zewail, A. H. *Chem. Phys. Lett.* **2001**, *348*, 255-262.

(99) Zuo, Z.; Yao, S.; Luo, J.; Wang, W.; Zhang, J.; Lin, N. *J. Photochem. Photobiol., B* **1992**, *15*, 215-222.

(100) Malone, R. J.; Miller, A. M.; Kohler, B. *Photochem. Photobiol.* **2003**, *77*, 158-164.

(101) Harshica, F.; Papadantonakis, G. A.; Kim, N. S.; LeBreton, P. R. *Proc. Natl. Acad. Sci. (USA)* **1998**, *95*, 5550-5555.

(102) Crespo-Hernandez, C. E.; Arce, R.; Ishikawa, Y.; Gorb, L.; Leszczynski, J.; Close, D. M. *J. Phys. Chem. A* **2004**, *108*, 6373-6377.

(103) Carlos E. Crespo-Hernández, R. A. *Photochem. Photobiol.* **2002**, *76*, 259-267.

(104) Glickman, B. W.; Schaaper, R. M.; Haseltine, W. A.; Dunn, R. L.; Brash, D. E. *Proc. Natl. Acad. Sci. (USA)* **1986**, *83*, 6945-6949.

(105) Ritze, H. H.; Hobza, P.; Nachtigallova, D. *Phys. Chem. Chem. Phys.***2007**, *9*, 1672-1675.

(106) DeBoer, G.; Johns, H. E. *Biochim. Biophys. Acta* **1970**, *204*, 18-30.

(107) Deboer, G.; Klinghoffer, O.; Johns, H. E. *Biochim. Biophys. Acta* **1970**, *213*, 253-268.

(108) Liu, F. T.; Yang, N. C. *Biochemistry* **1978**, *17*, 4877-4885.

(109) Szczesniak, M.; Szczepaniak, K.; Kwiatkowski, J. S.; KuBulat, K.; Person, W. B. *J. Am. Chem. Soc.* **1988**, *110*, 8319-8330.

(110) Leulliot, N.; Ghomi, M.; Jobic, H.; Bouloussa, O.; Baumruk, V.; Coulombeau, C. *J. Phys. Chem. B* **1999**, *103*, 10934-10944.

(111) Frisch, M. J. *et al.*, **2003**, Gaussian 03 Revission C.02; Gaussian, Inc.: Pittsburgh.

(112) Andersson, M. P.; Uvdal, P. *J. Phys. Chem. A* **2005**, *109*, 2937-2941.

(113) Merchan, M.; Serrano-Andres, L. *J. Am. Chem. Soc.* **2003**, *125*, 8108-8109.

(114) Blancafort, L. *Photochem. Photobiol.* **2007**, *83*, 603-610.

(115) Santoro, F.; Barone, V.; Improta, R. *Proc. Natl. Acad. Sci. (USA)* **2007**, *104*, 9931-9936.

(116) He, Y. G.; Wu, C. Y.; Kong, W. *J. Phys Chem. A* **2003**, *107*, 5145-5148.

(117) Gustavsson, T.; Sarkar, N.; Lazzarotto, E.; Markovitsi, D.; Improta, R. *Chem. Phys. Lett.* **2006**, *429*, 551-557.

(118) Rachofsky, E. L.; Ross, J. B. A.; Krauss, M.; Osman, R. *J. Phys. Chem. A* **2001**, *105*, 190-197.

(119) Merchan, M.; Serrano-Andres, L.; Robb, M. A.; Blancafort, L. *J. Am. Chem. Soc.* **2005**, *127*, 1820-1825.

(120) Lee, C.; Park, K.-H.; Cho, M. *J. Chem. Phys.* **2006**, *125*, 114508.

(121) Lee, C.; Cho, M. *J. Chem. Phys.* **2006**, *125*, 114509.

(122) Shukla, M. K.; Kuramshina, G. M.; Leszczynski, J. *Chem. Phys. Lett.* **2007**, *447*, 330-334.

(123) Cadet, J.; Douki, T.; Ravanat, J.-L. *Acc. Chem. Res.* **2008**, *41*, 1075-1083.

(124) Crespo-Hernandez, C. E.; Cohen, B.; Kohler, B. *Nature* **2005**, *436*, 1141-1144.

(125) Markovitsi, D.; Talbot, F.; Gustavsson, T.; Onidas, D.; Lazzarotto, E.; Marguet, S. *Nature* **2006**, *441*, E7-E7.

(126) Crespo-Hernandez, C. E.; Cohen, B.; Kohler, B. *Nature* **2006**, *441*, E8-E8.

(127) Onidas, D.; Gustavsson, T.; Lazzarotto, E.; Markovitsi, D. *Phys. Chem. Chem. Phys.* **2007**, *9*, 5143-5148.

(128) Crespo Hernandez, C. E.; de La Harpe, K.; Kohler, B. *J. Am. Chem. Soc.* **2008**, *130*, 10844-10845.

(129) Markovitsi, D.; Gustavsson, T.; Talbot, F. *Photochem. Photobiol. Sci.* **2007**, *6*, 717-724.

(130) Doorley, G. W.; McGovern, D. A.; George, M. W.; Towrie, M.; Parker, A. W.; Kelly, J. M.; Quinn, S. *Angew. Chem. Int. Ed.* **2009**, *48*, 123-127.

(131) McGovern, D. A.; Quinn, S.; Doorley, G. W.; Whelan, A. M.; Ronayne, K. L.; Towrie, M.; Parker, A. W.; Kelly, J. M. *Chem. Commun.* **2007**, 5158-5160.

(132) Cohen, B.; Larson, M. H.; Kohler, B. *Chem. Phys.* **2008**, *350*, 165-174.

(133) Hariharan, M.; Lewis, F. D. *J. Am. Chem. Soc.* **2008**, *130*, 11870-11871.

(134) Zhang, X. S.; Rosenstein, B. S.; Wang, Y.; Lebwohl, M.; Mitchell, D. M.; Wei, H. C. *Photochem. Photobiol.* **1997**, *65*, 119-124.

(135) Mitchell, D., L. *Photochem. Photobiol.* **2000**, *71*, 162-165.

(136) Markovitsi, D.; Sharonov, A.; Onidas, D.; Gustavsson, T. *ChemPhysChem* **2003**, *4*, 303-305.

(137) Takaya, T.; Su, C.; de La Harpe, K.; Crespo-HernÃ¡ndez, C. E.; Kohler, B. *Proc. Natl. Acad. Sci. (USA)* **2008**, *105*, 10285-10290.

(138) Kwok, W. M.; Ma, C.; Phillips, D. L. *J. Am. Chem. Soc.* **2006**, *128*, 11894-11905.

(139) Kang, H.; Lee, K. T.; Jung, B.; Ko, Y. J.; Kim, S. K. *J. Am. Chem. Soc.* **2002**, *124*, 12958-12959.

(140) Eisinger, J.; GuÃ©ron, M.; Shulman, R. G.; Yamane, T. *Proc. Natl. Acad. Sci. (USA)* **1966**, *55*, 1015-1020.

(141) Gueron, M.; Shulman, R. G.; Eisinger, J. *Proc. Natl. Acad. Sci. (USA)* **1966**, *56*, 814-818.

(142) Helene, C.; Douzou, P.; Michelson, A. M. *Proc. Natl. Acad. Sci. (USA)* **1966**, *55*, 376-381.

(143) Quinn, S.; Doorley, G. W.; Watson, G. W.; Cowan, A. J.; George, M. W.; Parker, A. W.; Ronayne, K. L.; Towrie, M.; Kelly, J. M. *Chem. Commun.* **2007**, 2130-2132.

(144) Isaksson, J.; Acharya, S.; Barman, J.; Cheruku, P.; Chattopadhyaya, J. *Biochemistry* **2004**, *43*, 15996-16010.

(145) Rinkel, L. J.; Altona, C. *J. Biomol. Struct. Dyn.* **1987**, *4*, 621-649.

(146) Ezra, F. S.; Lee, C.-H.; Kondo, N. S.; Danyluk, S. S.; Sarma, R. H. *Biochemistry* **1977**, *16*, 1977-1987.

(147) Fornasiero, D.; Kurucsev, T. *Eur. J. Biochem.* **1984**, *143*, 1-7.

(148) Kadhane, U.; Holm, A. I. S.; Hoffmann, S. V.; Nielsen, S. B. *Phys. Rev. E: Stat. Nonlinear, Soft Matter Phys.* **2008**, *77*, 021901.

(149) Kononov, A. I.; Bakulev, V. M.; Rapoport, V. L. *J. Photochem. Photobiol. B: Biol.* **1993**, *19*, 139-144.

(150) Takaya, T.; Su, C.; de La Harpe, K.; Crespo-Hernandez, C. E.; Kohler, B. *Proc. Natl. Acad. Sci. (USA)* **2008**, *105*, 10285-10290.

(151) Cantor, C. R.; Warshaw, M. M.; Shapiro, H. *Biopolymers* **1970**, *9*, 1059-1077.

(152) Johnson, W. C. J.; Tinoco, I. J. R. *Biopolymers* **1969**, *7*, 727-749.

(153) Johnson, N. P.; Switkes, E. *Biopolymers* **1978**, *17*, 857-872.

(154) Bose, S. N.; Kumar, S.; Davies, R. J. H.; Sethi, S. K.; McCloskey, J. A. *Nucl. Acids Res.* **1984**, *12*, 7929-7947.

(155) Clark, C. L.; Cecil, P. K.; Singh, D.; Gray, D. M. *Nucl. Acids Res.* **1997**, *25*, 4098-4105.

(156) Tsankov, D.; Krasteva, M.; Andrushchenko, V.; van de Sande, J. H.; Wieser, H. *Biophys. Chem.* **2006**, *119*, 1-6.

(157) Gottarelli, G.; Lena, S.; Masiero, S.; Pieraccini, S.; Spada, G. P. *Chirality* **2008**, *20*, 471-485.

(158) Kadhane, U.; Holm, A. I. S.; Hoffmann, S. V.; Nielsen, S. B. *J. Photochem. Photobiol. A* **2008**, *197*, 110-114.

(159) Fang, K. N.; Kondo, N. S.; Miller, P. S.; Ts'o, P. O. P. *J. Am. Chem. Soc.* **1971**, *93*, 6647-6656.

(160) Evans, F. E.; Lee, C.H.; Sarma, R. H. *Biochem. Biophys. Res. Commun.* **1975**, *63*, 106-114.

(161) A. E. Kister, V. G. D. *Biopolymers* **1976**, *15*, 1009-1013.

(162) Cozzone, P. J.; Jardetzky, O. *Biochemistry* **1976**, *15*, 4860-4865.

(163) Kondo, N. S.; Danyluk, S. S. *Biochemistry* **1976**, *15*, 756-768.

(164) Lee, C.-H.; Ezra, F. S.; Kondo, N. S.; Sarma, R. H.; Danyluk, S. S. *Biochemistry* **1976**, *15*, 3627-3639.

(165) Cheng, D. M.; Sarma, R. H. *J. Am. Chem. Soc.* **1977**, *99*, 7333-7348.

(166) Hart, P. A. *Biophys. J.* **1978**, *24*, 833-848.

(167) Neumann, J. M.; Guschlbauer, W.; Tran-Dinh, S. *Eur. J. Biochem.* **1979**, *100*, 141-148.

(168) Kan, L. S.; Cheng, D. M.; Miller, P. S.; Yano, J.; Ts'o, P. O. P. *Biochemistry* **1980**, *19*, 2122-2132.

(169) Isaacs, R. J.; Spielmann, H. P. *J. Mol. Biol.* **2001**, *307*, 525-540.

(170) Arnold, J. R. P.; Baker, J. M.; Beevers, A. P. G.; Elliot, M.; Fisher, J. *Magn. Reson. Chem.* **2001**, *39*, 109-112.

(171) Nordlund, T. M. *Photochem. Photobiol.* **2007**, *83*, 625-636.

(172) Trifonov, A.; Raytchev, M.; Buchvarov, I.; Rist, M.; Barbaric, J.; Wagenknecht, H. A.; Fiebig, T. *J. Phys. Chem. B* **2005**, *109*, 19490-19495.

(173) Bittner, E., R. *J. Chem. Phys.* **2006**, *125*, 094909.

(174) Bittner, E. R. *J. Photochem. Photobiol., A* **2007**, *190*, 328-334.

(175) Crespo-Hernandez, C. E.; Kohler, B. *J. Phys. Chem. B* **2004**, *108*, 11182-11188.

(176) Emanuele, E.; Markovitsi, D.; Millié, P.; Zakrzewska, K. *ChemPhysChem* **2005**, *6*, 1387-1392.

(177) Lange, A. W.; Rohrdanz, M. A.; Herbert, J. M. *J. Phys. Chem. B* **2008**, *112*, 6304-6308.

(178) Hyeon-Deuk, K.; Tanimura, Y.; Cho, M. *J. Chem. Phys.* **2008**, *128*, 135102.

(179) Scholes, G. D.; Ghiggino, K. P. *J. Phys. Chem.* **1994**, *98*, 4580-4590.

(180) Buchvarov, I.; Wang, Q.; Raytchev, M.; Trifonov, A.; Fiebig, T. *Proc. Natl. Acad. Sci. (USA)* **2007**, *104*, 4794-4797.

(181) Czader, A.; Bittner, E., R. *J. Chem. Phys.* **2008**, *128*, 035101.

(182) Miannay, F. A.; Banyasz, A.; Gustavsson, T.; Markovitsi, D. *J. Am. Chem. Soc.* **2007**, *129*, 14574-14575.

(183) Rich, A.; Zhang, S. *Nat Rev Genet* **2003**, *4*, 566-572.

(184) Pohl, F. M.; Jovin, T. M. *J. Mol. Biol.* **1972**, *67*, 375-396.

(185) Gessner, R. V.; Frederick, C. A.; Quigley, G. J.; Rich, A.; Wang, A. H. J. *J. Biol. Chem.* **1989**, *264*, 7921-7935.

(186) Daniels, M.; Hart, L. P.; Ho, P. S.; Ballini, J. P.; Vigny, P.; Brochon, J. C. *Photochem. Photobiol. Sci.* **2007**, *6*, 883-893.

(187) Bouvier, B.; Gustavsson, T.; Markovitsi, D.; Millié, P. *Chem. Phys.* **2002**, *275*, 75-92.

(188) Emanuele, E.; Zakrzewska, K.; Markovitsi, D.; Lavery, R.; Millie, P. *J. Phys. Chem. B* **2005**, *109*, 16109-16118.

(189) Lee, C.; Cho, M. *J. Chem. Phys.* **2007**, *126*, 145102.

(190) Markovitsi, D.; Gustavsson, T.; Sharonov, A. *Photochem. Photobiol.* **2004**, *79*, 526-530.

(191) Markovitsi, D.; Onidas, D.; Gustavsson, T.; Talbot, F.; Lazzarotto, E. *J. Am. Chem. Soc.* **2005**, *127*, 17130-17131.

(192) Onidas, D.; Gustavsson, T.; Lazzarotto, E.; Markovitsi, D. *J. Phys. Chem. B* **2007**, *111*, 9644-9650.

(193) Gustavsson, T.; Sharonov, A.; Onidas, D.; Markovitsi, D. *Chem. Phys. Lett.* **2002**, *356*, 49-54.

(194) Felsenfeld, G.; Rich, A. *Biochim. Biophys. Acta* **1957**, *26*, 457-468.

(195) Dervan, P. B. *Science* **1986**, *232*, 464-471.

(196) Dagle, J. M.; Weeks, D. L. *Differentiation* **2001**, *69*, 75-82.

(197) Roberts, R. W.; Crothers, D. M. *Science* **1992**, *258*, 1463-1466.

(198) Jain, A.; Wang, G.; Vasquez, K. M. *Biochimie* **2008**, *90*, 1117-1130.

(199) Simon, P.; Cannata, F.; Concordet, J. P.; Giovannangeli, C. *Biochimie* **2008**, *90*, 1109-1116.

(200) Benfield, A. P.; Macleod, M. C.; Liu, Y.; Wu, Q.; Wensel, T. G.; Vasquez, K. M. *Biochemistry* **2008**, *47*, 6279-6288.

(201) Fox, K. R. *Curr. Med. Chem.* **2000**, *7*, 17-37.

(202) Duca, M.; Vekhoff, P.; Oussedik, K.; Halby, L.; Arimondo, P. B. *Nucl. Acids Res.* **2008**, *36*, 5123-5138.

(203) Wells, R. D. *FASEB J.* **2008**, *22*, 1625-1634.

(204) Hebert, M. D. *Biochimie* **2008**, *90*, 1131-1139.

(205) Ruan, H.; Wang, Y.-H. *J. Mol. Biol.* **2008**, *383*, 292-300.

(206) Lee, H.-T.; Olsen, C. M.; Waters, L.; Sukup, H.; Marky, L. A. *Biochimie* **2008**, *90*, 1052-1063.

(207) Shchyolkina, A. K.; Kaluzhny, D. N.; Arndt-Jovin, D. J.; Jovin, T. M.; Zhurkin, V. B. *Nucl. Acids Res.* **2006**, *34*, 3239-3245.

(208) Shigemori, Y.; Oishi, M. *DNA Res* **2005**, *12*, 441-449.

(209) Rosu, F.; Gabelica, V.; Houssier, C.; Colson , P.; De Pauw, E. *Rapid Commun. Mass Spectrom.* **2002**, *16*, 1729-1736.

(210) Polak, M.; Hud, N. V. *Nucl. Acids Res.* **2002**, *30*, 983-992.

(211) Lewis, F. D.; Wu, Y.; Hayes, R. T.; Wasielewski, M. R. *Angew. Chem. Int. Ed.* **2002**, *41*, 3485-3487.

(212) Dingley, A. J.; Masse, J. E.; Peterson, R. D.; Barfield, M.; Feigon, J.; Grzesiek, S. *J. Am. Chem. Soc.* **1999**, *121*, 6019-6027.

(213) Shields, G. C.; Laughton, C. A.; Orozco, M. *J. Am. Chem. Soc.* **1997**, *119*, 7463-7469.

(214) Noll, D. M.; Miller, A. F.; Miller, P. S. *J. Am. Chem. Soc.* **1996**, *118*, 8979-8980.

(215) Dagneaux, C.; Gousset, H.; Shchyolkina, A. K.; Ouali, M.; Letellier, R.; Liquier, J.; Florentiev, V. L.; Taillandier, E. *Nucl. Acids Res.* **1996**, *24*, 4506-4512.

(216) Fox, K. R.; Polucci, P.; Jenkins, T. C.; Neidle, S. *Proc. Natl. Acad. Sci. (USA)* **1995**, *92*, 7887-7891.

(217) Radhakrishnan, I.; Patel, D. J. *Biochemistry* **1994**, *33*, 11405-11416.

(218) Pilch, D. S.; Levenson, C.; Shafer, R. H. *Biochemistry* **1991**, *30*, 6081-6087.

(219) Henderson, E.; Hardin, C. C.; Walk, S. K.; Tinoco, I.; Blackburn, E. H. *Cell* **1987**, *51*, 899-908.

(220) Williamson, J. R.; Raghuraman, M. K.; Cech, T. R. *Cell* **1989**, *59*, 871-880.

(221) Lundblad, V.; Wright, W. E. *Cell* **1996**, *87*, 369-375.

(222) Wang, Y.; Patel, D. J. *Structure* **1993**, *1*, 263-282.

(223) Oulton, R.; Harrington, L. *Curr. Opin. Oncology* **2000**, *12*, 74-81.

(224) Qin, Y.; Hurley, L. H. *Biochimie* **2008**, *90*, 1149-1171.

(225) Verdun, R. E.; Karlseder, J. *Cell* **2006**, *127*, 709-720.

(226) Cech, T. R. *Cell* **2004**, *116*, 273-279.

(227) Masutomi, K.; Yu, E. Y.; Khurts, S.; Ben-Porath, I.; Currier, J. L.; Metz, G. B.; Brooks, M. W.; Kaneko, S.; Murakami, S.; DeCaprio, J. A.; Weinberg, R. A.; Stewart, S. A.; Hahn, W. C. *Cell* **2003**, *114*, 241-253.

(228) Zakian, V. A. *Cell* **1997**, *91*, 1-3.

(229) Hardin, C. C.; Watson, T.; Corregan, M.; Bailey, C. *Biochemistry* **1992**, *31*, 833-841.

(230) Guzman, M. R.; Liquier, J.; Brahmachari, S. K.; Taillandier, E. *Spectrochim. Acta Part A* **2006**, *64*, 495-503.

(231) Viscardi, V.; Clerici, M.; Cartagena-Lirola, H.; Longhese, M. P. *Biochimie* **2005**, *87*, 613-624.

(232) Davis, J., T. *Angew. Chem. Int. Ed.* **2004**, *43*, 668-698.

(233) Ying, L.; Green, J. J.; Li, H.; Klenerman, D.; Balasubramanian, S. *Proc. Natl. Acad. Sci. (USA)* **2003**, *100*, 14629-14634.

(234) Zhang, R. B.; Xu, H.; Qu, Z. W.; Zhang, X. K.; Ai, X. C.; Zhang, Q. Y. *J. Mol. Struct. Theochem* **2002**, *586*, 167-175.

(235) Parkinson, G. N.; Lee, M. P. H.; Neidle, S. *Nature* **2002**, *417*, 876-880.

(236) Kankia, B. I.; Marky, L. A. *J. Am. Chem. Soc.* **2001**, *123*, 10799-10804.

(237) Walmsley, J. A.; Burnett, J. F. *Biochemistry* **1999**, *38*, 14063-14068.

(238) Gilbert, D. E.; Feigon, J. *Curr. Opin. Struct. Biol.* **1999**, *9*, 305-314.

(239) Dai, J.; Punchihewa, C.; Ambrus, A.; Chen, D.; Jones, R. A.; Yang, D. *Nucl. Acids Res.* **2007**, *35*, 2440-2450.

(240) da Silva, M., Webba *Chem. Eur. J.* **2007**, *13*, 9738-9745.

(241) Bates, P.; Mergny, J. L.; Yang, D. *EMBO Reports* **2007**, *8*, 1003-1010.

(242) Xu, Y.; Sugiyama, H. *Angew. Chem. Int. Ed.* **2006**, *45*, 1354-1362.

(243) Xue, Y.; Kan, Z..; Wang, Q.; Yao, Y.; Liu, J.; Hao, Y.; Tan, Z. *J. Am. Chem. Soc.* **2007**, *129*, 11185-11191.

(244) Vorlícková, M.; Bednárová, K.; Kejnovská, I.; Kypr, J. *Biopolymers* **2007**, *86*, 1-10.

(245) Phan, A. T.; Kuryavyi, V.; Luu, K. N.; Patel, D. J. *Nucl. Acids Res.* **2007**, *35*, 6517-6525.

(246) Oganesian, L.; Bryan, T. M. *BioEssays* **2007**, *29*, 155-165.

(247) Hurley, L. H. *Nat. Rev. Cancer* **2002**, *2*, 188-200.

(248) Shirude, P. S.; Balasubramanian, S. *Biochimie* **2008**, *90*, 1197-1206.

(249) Olsen, C. M.; Lee, H. T.; Marky, L. A. *J. Phys. Chem. B* **2009**, *113*, 2587-2595.

(250) Neidle, S.; Parkinson, G. N. *Biochimie* **2008**, *90*, 1184-1196.

(251) Monchaud, D.; Allain, C.; Bertrand, H.; Smargiasso, N.; Rosu, F.; Gabelica, V.; De Cian, A.; Mergny, J. L.; Teulade-Fichou, M. P. *Biochimie* **2008**, *90*, 1207-1223.

(252) Lane, A. N.; Chaires, J. B.; Gray, R. D.; Trent, J. O. *Nucl. Acids Res.* **2008**, *36*, 5482-5515.

(253) Huppert, J. L. *Biochimie* **2008**, *90*, 1140-1148.

(254) Gray, R. D.; Chaires, J. B. *Nucl. Acids Res.* **2008**, *36*, 4191-4203.

(255) Gaynutdinov, T. I.; Neumann, R. D.; Panyutin, I. G. *Nucl. Acids Res.* **2008**, *36*, 4079-4087.

(256) Dai, J.; Carver, M.; Yang, D. *Biochimie* **2008**, *90*, 1172-1183.

(257) Chakraborty, S.; Krishnan, Y. *Biochimie* **2008**, *90*, 1088-1095.

(258) Law, Y. K.; Azadi, J.; Crespo-Hernandez, C. E.; Olmon, E.; Kohler, B. *Biophys. J.* **2008**, *94*, 3590-3600.

(259) Krummel, A. T.; Mukherjee, P.; Zanni, M. T. *J. Phys. Chem. B* **2003**, *107*, 9165-9169.

(260) Hu, L.; Zhao, Y.; Wang, F.; Chen, G.; Ma, C.; Kwok, W. M.; Phillips, D. L. *J. Phys. Chem. B* **2007**, *111*, 11812-11816.

(261) Schwalb, N. K.; Temps, F. *Science* **2008**, *322*, 243-245.

(262) Plessow, R.; Brockhinke, A.; Eimer, W.; Kohse-Hoinghaus, K. *J. Phys. Chem. B* **2000**, *104*, 3695-3704.

(263) Rezac, J.; Hobza, P. *Chem. Eur. J.* **2007**, *13*, 2983-2989.

(264) Gray, R. D.; Chaires, J. B. *Nucl. Acids Res.* **2008**, *36*, 4191-4203.

(265) Miyoshi, D.; Sugimoto, N. *Biochimie* **2008**, *90*, 1040-1051.

(266) Kelley, S. O.; Barton, J. K. *Science* **1999**, *283*, 375-381.

(267) O'Neill, P.; Parker, A. W.; Plumb, M. A.; Siebbeles, L. D. A. *J. Phys. Chem. B* **2001**, *105*, 5283-5290.

(268) Gu, H. W.; Xu, K. M.; Xu, C. J.; Xu, B. *Chem. Commun.* **2006**, 941-949.

(269) Sun, S.; Zeng, H.; Robinson, D. B.; Raoux, S.; Rice, P. M.; Wang, S. X.; Li, G. *J. Am. Chem. Soc.* **2004**, *126*, 273-279.

(270) Nam, J. M.; Thaxton, C. S.; Mirkin, C. A. *Science* **2003**, *301*, 1884-1886.

(271) Park, S. J.; Taton, T. A.; Mirkin, C. A. *Science* **2002**, *295*, 1503-1506.

(272) Rosi, N. L.; Giljohann, D. A.; Thaxton, C. S.; Lytton-Jean, A. K. R.; Han, M. S.; Mirkin, C. A. *Science* **2006**, *312*, 1027-1030.

(273) Dormer, K.; Seeney, C.; Lewelling, K.; Lian, G.; Gibson, D.; Johnson, M. *Biomaterials* **2005**, *26*, 2061-2072.

(274) Zhang, Y.; Kohler, N.; Zhang, M. *Biomaterials* **2002**, *23*, 1553-1561.

(275) Kohler, N.; Sun, C.; Wang, J.; Zhang, M. *Langmuir* **2005**, *21*, 8858-8864.

(276) Cheng, F. Y.; Su, C. H.; Yang, Y. S.; Yeh, C. S.; Tsai, C. Y.; Wu, C. L.; Wu, M. T.; Shieh, D. B. *Biomaterials* **2005**, *26*, 729-738.

(277) Nitin, N.; LaConte, L. E. W.; Zurkiya, O.; Hu, X.; Bao, G. *J. Biol. Inorg. Chem.* **2004**, *9*, 706-712.

(278) Gu, H.; Xu, K.; Yang, Z.; Chang, C. K.; Xu, B. *Chem. Commun.* **2005**, 4270-4272.

(279) Glasser, M. L.; Milford, F. J. *Phys. Rev.* **1963**, *130*, 1783-1789.

(280) Thapa, D.; Palkar, V. R.; Kurup, M. B.; Malik, S. K. *Mater. Lett.* **2004**, *58*, 2692-2694.

(281) Walz, F. *J. Phys.: Condens. Matter* **2002**, *14*, R285-R340.

(282) Philipse, A. P.; van Bruggen, M. P. B.; Pathmamanoharan, C. *Langmuir* **1994**, *10*, 92-99.

(283) Jolivet, J. P.; Chaneac, C.; Tronc, E. *Chem. Commun.* **2004**, 481-487.

(284) Kumar, R. V.; Koltypin, Y.; Cohen, Y. S.; Cohen, Y.; Aurbach, D.; Palchik, O.; Felner, I.; Gedanken, A. *J. Mater. Chem.* **2000**, *10*, 1125-1129.

(285) Vijayakumar, R.; Koltypin, Y.; Felner, I.; Gedanken, A. *Mater. Sci. Eng., A* **2000**, *A286*, 101-105.

(286) Bharde, A.; Wani, A.; Shouche, Y.; Joy, P. A.; Prasad, B. L. V.; Sastry, M. *J. Am. Chem. Soc.* **2005**, *127*, 9326-9327.

(287) Cho, S. J.; Idrobo, J.-C.; Olamit, J.; Liu, K.; Browning, N. D.; Kauzlarich, S. M. *Chem. Mater.* **2005**, *17*, 3181-3186.

(288) Tongpool, R.; Jindasuwan, S. *Sens. Actuators, B* **2005**, *B106*, 523-528.

(289) Bomati-Miguel, O.; Leconte, Y.; Morales, M. P.; Herlin-Boime, N.; Veintemillas-Verdaguer, S. *J. Magn. Magn. Mater.* **2005**, *290-291*, 272-275.

(290) Frankamp, B. L.; Boal, A. K.; Tuominen, M. T.; Rotello, V. M. *J. Am. Chem. Soc.* **2005**, *127*, 9731-9735.

(291) Klokkenburg, M.; Vonk, C.; Claesson, E. M.; Meeldijk, J. D.; Erne, B. H.; Philipse, A. P. *J. Am. Chem. Soc.* **2004**, *126*, 16706-16707.

(292) Massart, R. *IEEE Trans. Magn.* **1981**, *MAG-17*, 1247-1248.

(293) Qiu, X.-P. *Chin. J. Chem.* **2000**, *18*, 834-837.

(294) Wang, J.; Deng, T.; Dai, Y. *J. Alloys Compd.* **2005**, *390*, 127-132.

(295) Cushing, B. L.; Kolesnichenko, V. L.; O'Connor, C. J. *Chem. Rev.* **2004**, *104*, 3893-3946.

(296) Ditsch, A.; Laibinis, P. E.; Wang, D. I. C.; Hatton, T. A. *Langmuir* **2005**, *21*, 6006-6018.

(297) Kim, D. K.; Mikhaylova, M.; Zhang, Y.; Muhammed, M. *Chem. Mater.* **2003**, *15*, 1617-1627.

(298) Fu, L.; Dravid, V. P.; Johnson, D. L. *Appl. Surf. Sci.* **2001**, *181*, 173-178.

(299) Farrell, D.; Cheng, Y.; McCallum, R. W.; Sachan, M.; Majetich, S. A. *J. Phys. Chem. B* **2005**, *109*, 13409-13419.

(300) Gupta Ajay, K.; Gupta, M. *Biomaterials Biomaterials* **2005**, *26*, 1565-1573.

(301) Schrock, E.; de Manoir, S.; Veldman, T.; Schoell, B.; Wienberg, J.; Ferguson-Smith, M. A.; Ning, Y.; Ledbetter, D. H.; Bar-Am, I.; et al. *Science* **1996**, *273*, 494-497.

(302) Lu, H.; Yi, G.; Zhao, S.; Chen, D.; Guo, L. H.; Cheng, J. *J. Mater. Chem.* **2004**, *14*, 1336-1341.

(303) Crean, C. W.; Kavanagh, Y. T.; O'Keeffe, C. M.; Lawler, M. P.; Stevenson, C.; Davies, R. J. H.; Boyle, P. H.; Kelly, J. M. *Photochem. Photobiol. Sci.* **2002**, *1*, 1024-1033.

(304) Caruntu, D.; Cushing, B. L.; Caruntu, G.; O'Connor, C. J. *Chem. Mater.* **2005**, *17*, 3398-3402.

(305) Yi, D. K.; Selvan, S. T.; Lee, S. S.; Papaefthymiou, G. C.; Kundaliya, D.; Ying, J. Y. *J. Am. Chem. Soc.* **2005**, *127*, 4990-4991.

(306) Choi, H.; Choi Seok, R.; Zhou, R.; Kung Hank, F.; Chen, I. W. *Acad. Radiol.* **2004**, *11*, 996-1004.

(307) Rossi, L. M.; Quach, A. D.; Rosenzweig, Z. *Anal. Bioanal. Chem.* **2004**, *380*, 606-613.

(308) Zhao, G.; Feng, J. J.; Zhang, Q. L.; Li, S. P.; Chen, H. Y. *Chem. Mater.* **2005**, *17*, 3154-3159.

(309) Kim, J.; Lee, J. E.; Lee, J.; Yu, J. H.; Kim, B. C.; An, K.; Hwang, Y.; Shin, C.-H.; Park, J.-G.; Kim, J.; Hyeon, T. *J. Am. Chem. Soc.* **2006**, *128*, 688-689.

(310) Josephson, L.; Perez, J. M.; Weissleder, R. *Angew. Chem. Int. Ed.* **2001**, *40*, 3204-3206.

(311) Hu, A.; Yee, G. T.; Lin, W. *J. Am. Chem. Soc.* **2005**, *127*, 12486-12487.

(312) Patolsky, F.; Weizmann, Y.; Katz, E.; Willner, I. *Angew. Chem. Int. Ed.* **2003**, *42*, 2372-2376.

(313) Stoeber, W.; Fink, A.; Bohn, E. *J. Colloid Interface Sci.* **1968**, *26*, 62-69.

(314) Gu, H.; Yang, Z.; Gao, J.; Chang, C. K.; Xu, B. *J. Am. Chem. Soc.* **2005**, *127*, 34-35.

(315) Xu, C.; Xu, K.; Gu, H.; Zheng, R.; Liu, H.; Zhang, X.; Guo, Z.; Xu, B. *J. Am. Chem. Soc.* **2004**, *126*, 9938-9939.

(316) Bruce, I. J.; Sen, T. *Langmuir* **2005**, *21*, 7029-7035.

(317) Kaiser, E.; Colescott, R. L.; Bossinger, C. D.; Cook, P. I. *Anal. Biochem.* **1970**, *34*, 595-598.

(318) Sarin, V. K.; Kent, S. B. H.; Tam, J. P.; Merrifield, R. B. *Anal. Biochem.* **1981**, *117*, 147-57.

(319) Fontenot, J. D.; Ball, J. M.; Miller, M. A.; David, C. M.; Montelaro, R. C. *Peptide Research* **1991**, *4*, 19-25.

(320) *United States Patent 5185447.*

(321) Lecomte, J. P.; Kirsch-De Mesmaeker, A.; Demeunynck, M.; Lhomme, J. *J. Chem. Soc., Faraday Trans.* **1993**, *89*, 3261-3269.

(322) Ramiro, P.; Garcia-Fresnadillo, D.; Orellana, G. *Tetrahedron* **2005**, *61*, 9478-9483.

(323) Sardesai, N. Y.; Lin, S. C.; Zimmerman, K.; Barton, J. K. *Bioconjugate Chem.* **1995**, *6*, 302-12.

(324) Sullivan, B. P.; Salmon, D. J.; Meyer, T. J. *Inorg. Chem.* **1978**, *17*, 3334-3341.

(325) Ellis, C. D.; Margerum, L. D.; Murray, R. W.; Meyer, T. J. *Inorg. Chem.* **1983**, *22*, 1283-1291.

(326) Bannwarth, W.; Schmidt, D.; Stallard, R. L.; Hornung, C.; Knorr, R.; Mueller, F. *Helv. Chim. Acta* **1988**, *71*, 2085-2099.

(327) Grayson, D. H.; McCarthy, U.; Roycroft, E. D. *Org. Biomol. Chem.* **2003**, *1*, 1930-1937.

(328) Rajh, T.; Chen, L. X.; Lukas, K.; Liu, T.; Thurnauer, M. C.; Tiede, D. M. *J. Phys. Chem. B* **2002**, *106*, 10543-10552.

(329) Chen, L. X.; Liu, T.; Thurnauer, M. C.; Csencsits, R.; Rajh, T. *J. Phys. Chem. B* **2002**, *106*, 8539-8546.

(330) Rajh, T.; Saponjic, Z.; Liu, J.; Dimitrijevic, N. M.; Scherer, N. F.; Vega-Arroyo, M.; Zapol, P.; Curtiss, L. A.; Thurnauer, M. C. *Nano Lett.* **2004**, *4*, 1017-1023.

(331) delaGarza, L.; Saponjic, Z. V.; Dimitrijevic, N. M.; Thurnauer, M. C.; Rajh, T. *J. Phys. Chem. B* **2006**, *110*, 680-686.

(332) Sprintschnik, G.; Sprintschnik, H. W.; Kirsch, P. P.; Whitten, D. G. *J. Am. Chem. Soc.* **1977**, *99*, 4947-4954.

(333) Oki, A. R.; Morgan, R. J. *Synth. Commun.* **1995**, *25*, 4093-4097.

(334) Uppadine, L. H.; Keene, F. R.; Beer, P. D. *Dalton Trans.* **2001**, 2188-2198.

(335) Herman, L.; Ghosh, S.; Defrancq, E.; Kirsch-De Mesmaeker, A. *J. Phys. Org. Chem.* **2008**, *21*, 670-681.

(336) Villien, M.; Deroo, S.; Gicquel, E.; Defrancq, E.; Moucheron, C.; Kirsch-De Mesmaeker, A.; Dumy, P. *Tetrahedron* **2007**, *63*, 11299-11306.

(337) Deroo, S.; Defrancq, E.; Moucheron, C.; Kirsch-De Mesmaeker, A.; Dumy, P. *Tetrahedron Lett.* **2003**, *44*, 8379-8382.

(338) Moon, S. J.; Kim, J. M.; Choi, J. Y.; Kim, S. K.; Lee, J. S.; Jang, H. G. *J. Inorg. Biochem.* **2005**, *99*, 994-1000.

(339) Coates, C. G.; McGarvey, J. J.; Callaghan, P. L.; Coletti, M.; Hamilton, J. G. *J. Phys. Chem. B* **2001**, *105*, 730-735.

(340) Lutterman, D. A.; Chouai, A.; Liu, Y.; Sun, Y.; Stewart, C. D.; Dunbar, K. R.; Turro, C. *J. Am. Chem. Soc.* **2008**, *130*, 1163-1170.

(341) Urata, H.; Akagi, M. *Tetrahedron Lett.* **1993**, *34*, 4015-4018.

(342) Kaindl, R. A.; Wurm, M.; Reimann, K.; Hamm, P.; Weiner, A. M.; Woerner, M. *J. Opt. Soc. Am. B: Opt. Phys.* **2000**, *17*, 2086-2094.

(343) Hosmane, R. S.; Leonard, N. J. *Synthesis-Stuttgart* **1981**, 118-119.

(344) Kavanagh, Y. T., *PhD* Thesis, University of Dublin, Trinity College, **2001**.

Appendices for ps-TRIR Investigations of DNA Systems and Toward Bimodal Nanoparticles for Biomedical Applications

A thesis submitted to the University of Dublin for the degree of Doctor of Philosophy

by

Gerard W. Doorley B.A. (Mod.), P. Grad. Dip. Stat.

Under the supervision of

Prof. John M. Kelly

School of Chemistry
Trinity College Dublin

2009

Contents

Chapter 3 – ps-TRIR Study of a Family of Adenine and Thymine Containing Dinucleotides

Chapter 5 – ps-TRIR Study of Biologically Relevant Systems

Appendix for Chapter 3

ps-TRIR Study of a Family of Adenine and Thymine Containing Dinucleotides

1. Figures

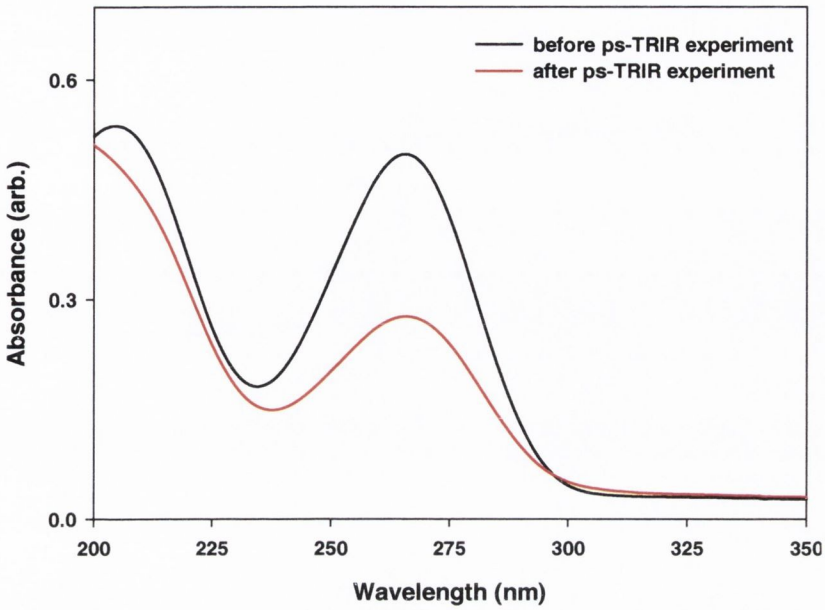

Figure A3.1 UV absorbance of 10 mM 5′-TMP in 50 mM potassium phosphate D_2O buffer (pH 7) before (black) and after the ps-TRIR experiment (red).

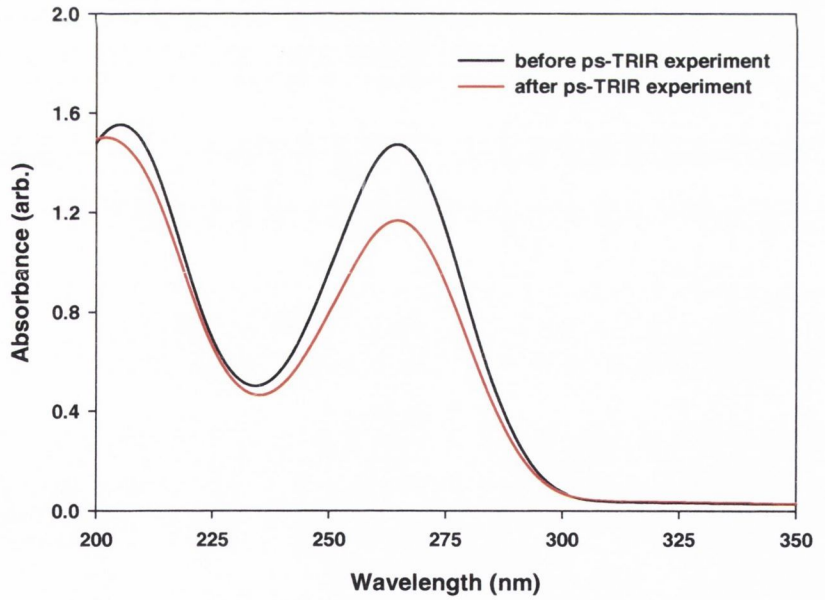

Figure A3.2 UV absorbance of 10 mM TpT in 50 mM potassium phosphate D_2O buffer (pH 7) before (black) and after the ps-TRIR experiment (red).

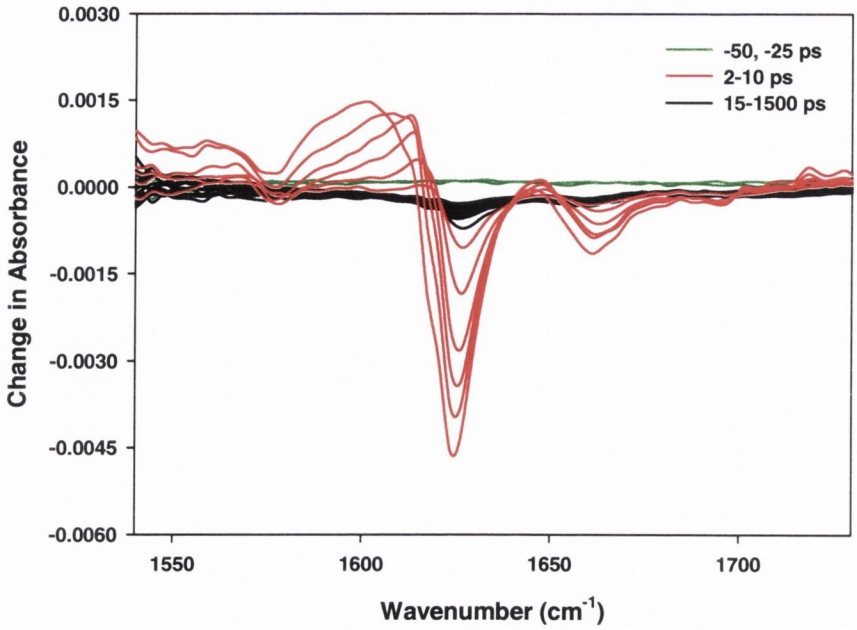

Figure A3.3 ps-TRIR of an equimolar mixture (10 mM each) of 5′-dAMP and 5′-TMP in 50 mM potassium phosphate D_2O buffer (pH 7). Delays are at -50, -25 (green), 2, 3, 4, 5, 7, 10 (red), 15, 20, 35, 50, 65, 80, 100, 150, 225, 325, 450, 650, 850, 1000 and 1500 ps (black).

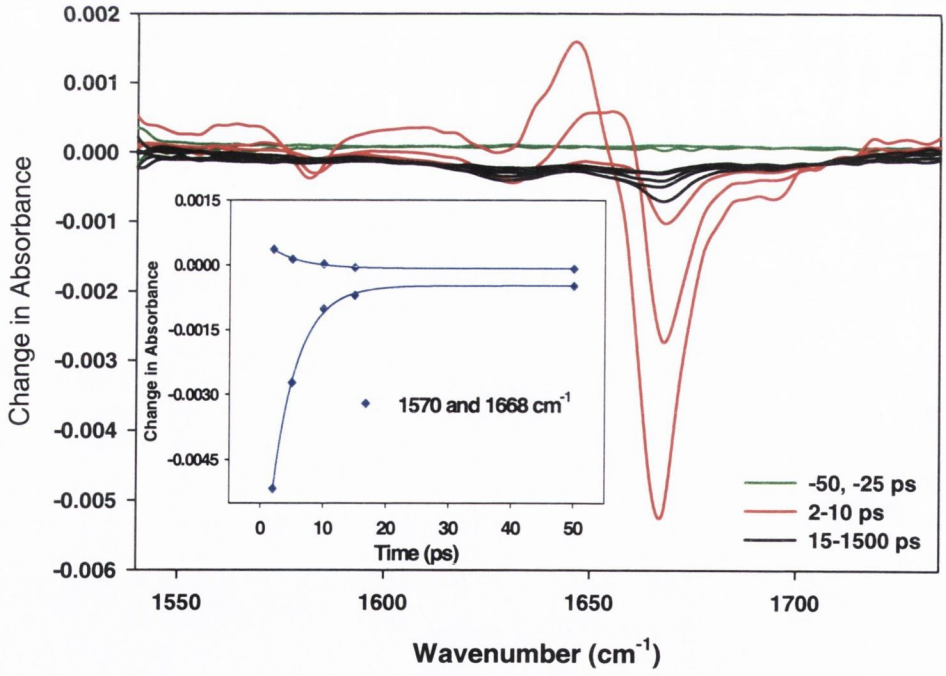

Figure A3.4 ps-TRIR of 10 mM dApT in 0.132 M H_3PO_4 in D_2O (pH 2). Delays are at -50, -25 (green), 2, 5, 10 (red), 15, 50, 100, 500, 1000 and 1500 ps (black). Inset: Kinetic analysis at 1570 and 1668 cm^{-1}.

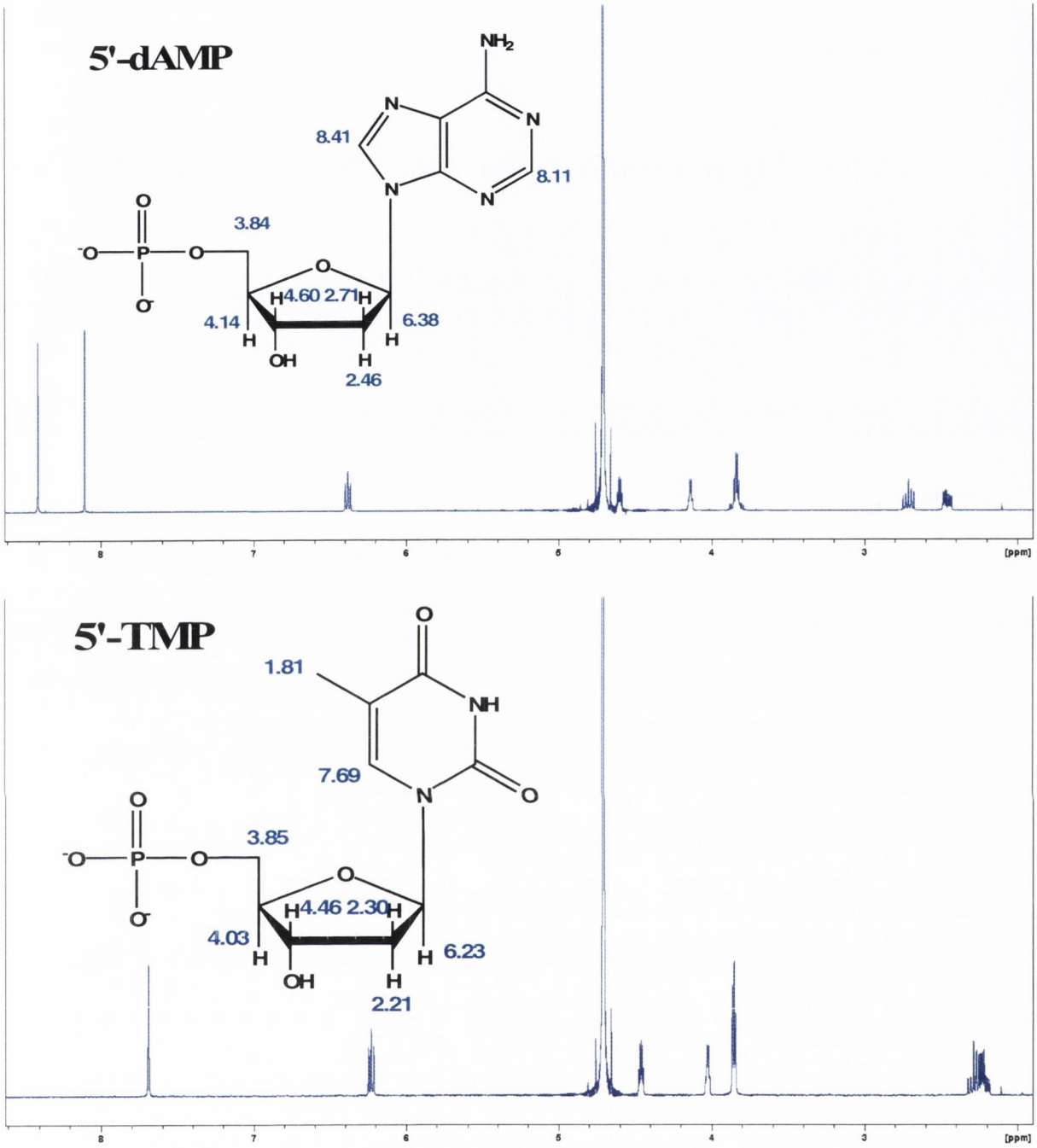

Figure A3.5 ^{1}H NMR spectrum and signal assignment for 5′dAMP and 5′-TMP. Conditions were as the ps-TRIR experiments, 10 mM nucleotide in 50 mM potassium phosphate D_2O buffer, pH 7.

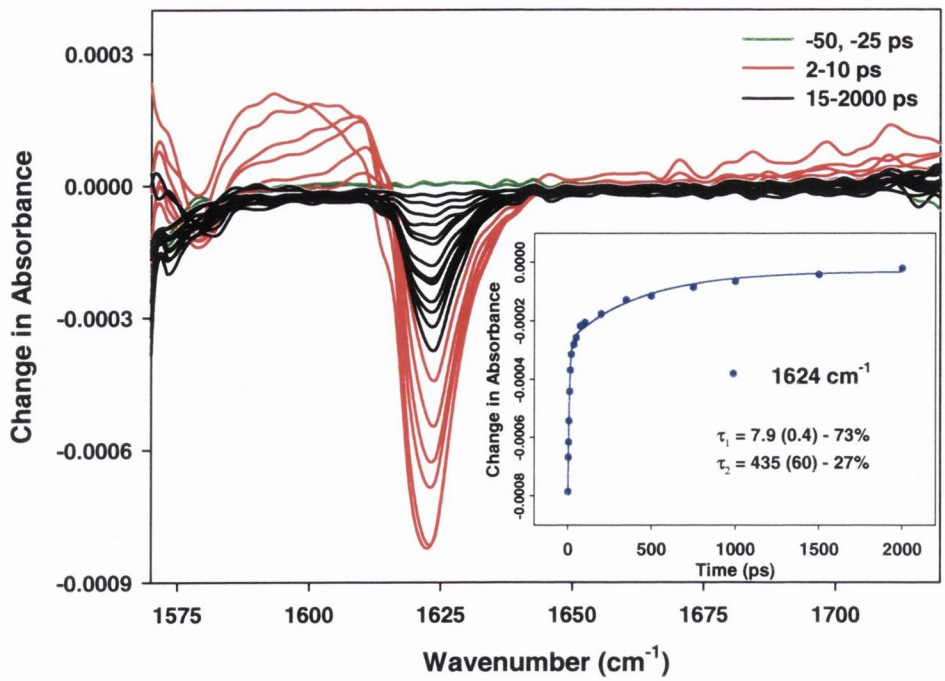

Figure A3.6 ps-TRIR of $(dA)_6$ in 50 mM potassium phosphate D_2O buffer (pH 7). Delays are at -50, -25 (green), 2, 3, 4, 5, 7, 10 (red), 15, 20, 35, 75, 100, 150, 200, 350, 500, 750, 1000, 1500 and 2000 ps (black). Inset: Kinetic analysis at 1624 cm^{-1}.

2. Kinetic Analysis Tables

Focus on the long-lived species in multiple dApT samples.

Single pixel analysis with time delays from 20 ps onwards being fitted to a single exponential (T = transient, B = bleach).

Table A3.1

		jkapt2		sgapt2		sgapt5		gsapt3		gsapt5	
B or T	cm^{-1}	τ (ps)	+/-	τ (ps)	+/-	τ (ps)	+/-	τ (ps)	+/-	τ (ps)	+/-
T	1534	59	12								
T	1537	67	11								
T	1540	64	11								
T	1543	64	8								
T	1546	64	7								
T	1549	61	6								
T	1551	64	9								
T	1554	70	6								
T	1557	69	6					50	5	74	9
T	1560	65	6	77	18	73	5	50	5	80	8
T	1563	66	6	74	18	70	4	56	3	75	6
T	1566					71	4				
T	1575							66	5	80	5
T	1578	74	5	73	12	78	5	64	3	80	5
T	1581	68	4	73	12	77	5	60	4	79	4
T	1584	66	5	70	11	74	4	60	4	76	5
T	1587	64	4	66	10	72	3	58	4	76	4
T	1590	63	4	65	11	71	5	56	4	72	5
Average		**66**	**7**	**71**	**13**	**73**	**4**	**58**	**4**	**77**	**6**
B	1617							65	7	58	5
B	1620	65	8	65	10			59	7	51	5
B	1623	58	9	62	10	75	12	60	6	55	5
B	1627	64	8	70	9	80	11				
B	1630	71	7	75	9	83	10				
Average		**65**	**8**	**68**	**10**	**79**	**11**	**61**	**7**	**55**	**5**
B	1655	87	3	84	6			80	3	75	1
B	1659	83	3	82	6	93	5	77	3	72	2
B	1662	81	3	80	6	92	6	76	3	71	2
B	1665	81	4	81	7	90	6				
B	1682	81	3	86	6			74	4	69	3
B	1685	85	4	84	8			75	4	70	3
B	1689	80	4	83	7	93	6	70	5	70	3
B	1692	80	6					77	7	65	3
Average		**82**	**4**	**83**	**7**	**92**	**6**	**76**	**4**	**70**	**2**

Area analysis in multiple dApT samples.

Single pixel analysis with time delays from 20 ps onwards being fitted to a single exponential (S = single exponential fitting of delays from 20 ps onwards, B = biexponential fitting of all delays).

Table A3.2

		jkapt2			sgapt2			sgapt5			gsapt3			gsapt5		
cm^{-1}	S or B	τ (ps)	+/-	%	τ (ps)	+/-	%	τ (ps)	+/-	%	τ (ps)	+/-	%	τ (ps)	+/-	%
1540-1563	B	2.6 68	0.3 6	71 29				3.2 74	0.3 5	57 43						
	S	66	6	-				72	4	-						
1581-1593	B				2.8 77	0.3 12	77 23	1.8 75	0.1 4	80 20	1.5 58	0.2 3	73 27	1.9 76	0.3 5	66 34
	S				70	11	-	74	4	-	59	4	-	78	6	-
1620-1630	B	6.3 110	0.3 20	76 24	6.6 120	0.8 30	76 24	7.3 148	0.7 23	71 29	3.6 88	0.2 6	73 27	5.2 81	0.2 5	71 29
	S	63	8	-	67	9	-	79	11	-	75	6	-	59	5	-
1655-1665	B	4.7 88	0.7 5	41 59	4.4 88	0.7 8	52 48	4.8 101	0.6 7	48 52	2.3 81	0.3 3	52 48	2.5 75	0.2 2	50 50
	S	82	3	-	82	6	-	91	6	-	79	3	-	74	2	-
1682-1692	B	6.4 85	3.3 8	22 78	4.3 86	1.8 9	32 68				2.9 76	0.9 5	35 65	5.3 74	1.1 4	34 66
	S	82	4	-	84	7	-				75	4	-	70	3	-
1655-1692	B	5.7 87	1.6 7	31 69							2.5 79	0.4 4	46 54	3.0 74	0.2 2	44 56
	S	83	3	-							78	4	-	73	2	-

Focus on the long-lived species in multiple TpdA samples.

Single pixel analysis with time delays from 20 ps onwards being fitted to a single exponential (T = transient, B = bleach).

Table A3.3

		sgtpa1		sgtpa3		sgtpa4		gstpa5	
B or T	cm^{-1}	τ (ps)	+/-	τ (ps)	+/-	τ (ps)	+/-	τ (ps)	+/-
T	1549			42	10				
T	1551			34	9			51	9
T	1554			41	8			49	7
T	1557							47	7
T	1560							45	5
T	1563							42	4
Average				**39**	**9**			**47**	**6**
T	1578	36	9			41	10	54	5
T	1581	34	6	44	7	36	8	49	6
T	1584	34	7	41	7			46	5
T	1587	36	6	35	7				
T	1590							34	7
Average		**35**	**7**	**40**	**7**	**39**	**9**	**46**	**6**
B	1617							38	5
B	1620			54	13	40	9	32	5
B	1623	41	10	57	14	49	10	36	5
B	1627	47	11	66	15	60	11	42	5
B	1630	55	12	76	17	69	13	48	5
B	1633	67	14						
Average		**53**	**16**	**63**	**15**	**55**	**11**	**39**	**5**
B	1655					68	7	52	3
B	1659	61	8	68	9	59	7	49	3
B	1662	55	7	63	9	57	7	45	3
B	1665	54	7	63	8	55	6		
B	1669	48	6						
B	1682			62	6				
B	1685	49	5	67	8	59	6	42	2
B	1689	49	5	67	9	58	6	38	3
B	1692					71	10	40	3
B	1695					68	11		
Average		**53**	**6**	**65**	**8**	**62**	**8**	**44**	**3**

Area analysis in multiple TpdA samples.

Single pixel analysis with time delays from 20 ps onwards being fitted to a single exponential (S = single exponential fitting of delays from 20 ps onwards, B = biexponential fitting of all delays).

Table A3.4

		sgtpa1			sgtpa3			sgtpa4			sgtpa5		
cm^{-1}	S or B	τ (ps)	+/-	%	τ (ps)	+/-	%	τ (ps)	+/-	%	τ (ps)	+/-	%
1549-1554	B				3.0 42	0.6 14	78 22						
	S				37	9	-						
1580-1590	B	1.6 34	0.1 6	90 10	2.3 47	0.2 9	88 12				2.0 50	0.2 6	81 19
	S	34	6	-	43	8	-				49	5	-
1620-1630	B	7.8 296	0.5 82	83 17	7.6 319	0.6 92	72 28	7.1 159	0.5 36	81 19	6.0 84	0.5 19	82 18
	S	51	11	-	62	15	-	54	11	-	41	5	-
1655-1665	B	5.2 78	0.6 12	68 32	5.3 90	0.7 14	67 33	4.7 77	0.4 8	31 69	4.4 55	0.3 4	65 35
	S	55	7	-	65	9	-	60	7	-	46	3	-
1685-1695	B				 71	1.1 10	50 50	5.4 77	1.0 12	59 41	3.0 41	0.7 3	45 55
	S				64	7	-	64	8	-	40	2	-
1655-1692	B										4.8 49	0.8 5	55 45
	S										43	2	-

Tabular Analysis for Variable Temperature Experiments

The tabular analyses on the following pages for dApT and TpdA, have been divided into regions corresponding to those marked in the figure below. This is to highlight the varying kinetics, that arise from predominant contributions from one base rather than the other in a particular regions. Regions I, IIIB, IV and V are predominately T based, whereas regions II and IIIA are for the most part A based.

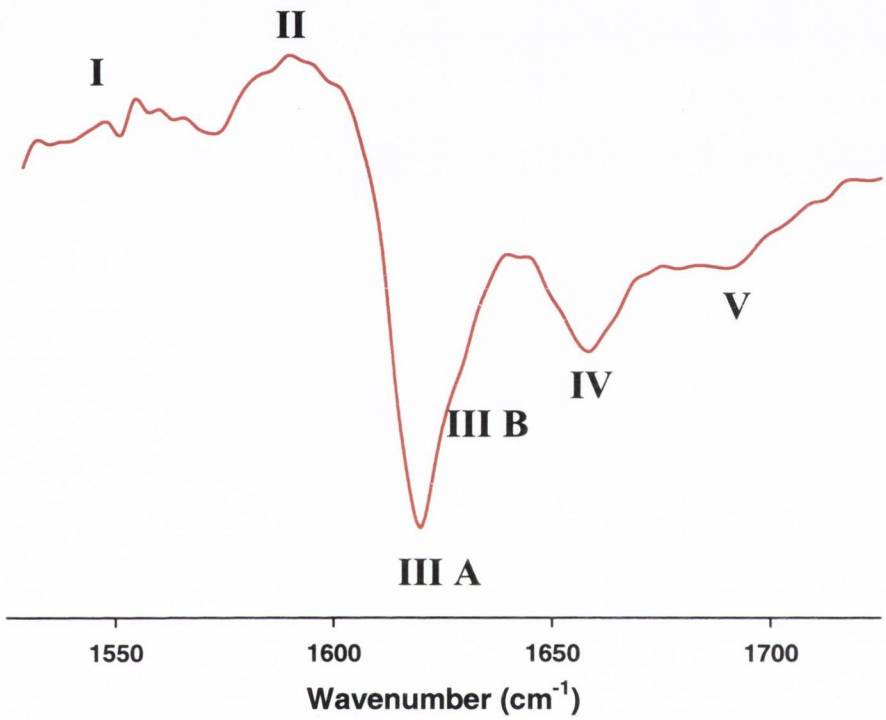

Tabular Analyis A3.5 - dApT at 20 °C

Region I					
cm^{-1}	τ_1 (ps)	±	τ_2 (ps)	±	% (τ_1 : τ_2)
1563	**2.3**	0.2	**74**	12	**81 : 19**
1566	**2.7**	0.3	**82**	15	**79 : 21**
1568	**3.0**	0.3	**82**	10	**73 : 27**
1571	**3.3**	0.4	**79**	11	**68 : 32**
1573	**3.9**	0.4	**80**	8	**63 : 37**
1575	**4.3**	0.7	**81**	9	**56 : 44**
1578	**2.9**	0.7	**73**	8	**51 : 49**
Average	**3.2**	0.4	**79**	10	**67 : 33**

Region II					
cm^{-1}	τ_1 (ps)	±	τ_2 (ps)	±	% (τ_1 : τ_2)
1588	**1.3**	0.1	**73**	4	**85 : 15**
1591	**1.7**	0.1	**70**	5	**83 : 17**
1593	**2.0**	0.1	**70**	5	**82 : 18**
1596	**2.3**	0.1	**73**	6	**83 : 17**
1598	**2.5**	0.1	**75**	6	**83 : 17**
1601	**3.0**	0.1	**84**	8	**84 : 16**
Average	**2.1**	0.1	**74**	6	**83 : 17**

Region III					
cm^{-1}	τ_1 (ps)	±	τ_2 (ps)	±	% (τ_1 : τ_2)
1624	**5.3**	0.5	**88**	22	**83 : 17**
1627	**6.2**	0.6	**87**	19	**78 : 22**
1629	**6.6**	0.7	**85**	14	**70 : 30**
1632	**7.0**	1.0	**81**	12	**59 : 41**
Average	**6.3**	0.7	**85**	17	**73 : 27**

Region IV					
cm^{-1}	τ_1 (ps)	±	τ_2 (ps)	±	% (τ_1 : τ_2)
1654	**2.3**	0.2	**70**	4	**60 : 40**
1656	**3.4**	0.3	**71**	5	**56 : 44**
1659	**4.1**	0.4	**72**	5	**53 : 47**
1662	**4.5**	0.5	**74**	5	**49 : 51**
Average	**3.6**	0.4	**72**	5	**54 : 46**

Region V					
cm^{-1}	τ_1 (ps)	±	τ_2 (ps)	±	% (τ_1 : τ_2)
1673	**1.6**	0.3	**68**	3	**50 : 50**
1681	**1.8**	0.4	**68**	4	**47 : 53**
1678	**1.9**	0.3	**68**	3	**49 : 51**
1681	**2.3**	0.3	**68**	3	**49 : 51**
1684	**2.9**	0.5	**67**	4	**46 : 54**
1687	**3.6**	0.5	**67**	4	**46 : 54**
1690	**4.2**	0.9	**66**	6	**45 : 55**
Average	**2.6**	0.5	**67**	4	**47 : 53**

Tabular Analyis A3.5 - dApT at 70 °C

Region I					
cm^{-1}	τ_1 (ps)	±	τ_2 (ps)	±	% (τ_1 : τ_2)
1566	**2.7**	0.2	**32**	5	**84 : 16**
1568	**3.6**	0.3	**44**	11	**83 : 17**
1571	**3.9**	0.3	**44**	10	**80 : 20**
1573	**5.1**	0.4	**51**	14	**79 : 21**
1575	**5.2**	1.3	**38**	18	**71 : 29**
Average	**4.1**	0.5	**42**	12	**80 : 20**

Region II					
cm^{-1}	τ_1 (ps)	±	τ_2 (ps)	±	% (τ_1 : τ_2)
1588	**1.5**	0.1	**44**	6	**91 : 9**
1591	**1.9**	0.1	**38**	7	**90 : 10**
1593	**2.1**	0.1	**37**	10	**91 : 9**
1596	**2.4**	0.2	**39**	15	**92 : 8**
1598	**2.8**	0.2	**57**	15	**94 : 6**
1601	**2.3**	0.1	**52**	19	**95 : 5**
Average	**2.2**	0.1	**45**	12	**92 : 8**

Region III A					
cm^{-1}	τ_1 (ps)	±	τ_2 (ps)	±	% (τ_1 : τ_2)
1621	**4.4**	0.7	**49**	36	**93 : 7**
1624	**4.1**	1.7	**41**	16	**92 : 8**
1627	**5.9**	1.3	**50**	31	**86 : 14**
1629	**5.8**	1.7	**45**	18	**75 : 25**
Average	**5.1**	1.4	**46**	25	**87 : 13**

Region III B					
cm^{-1}	τ_1 (ps)	±	τ_2 (ps)	±	% (τ_1 : τ_2)
1632	6.6	1.9	42	11	59 : 41
1635	3.7	2.3	38	3	26 : 74
Average	5.2	2.1	40	7	42 : 58

Region IV					
cm^{-1}	τ_1 (ps)	±	τ_2 (ps)	±	% (τ_1 : τ_2)
1654	2.4	0.6	45	7	71 : 29
1656	3.8	0.8	48	8	68 : 32
1659	4.4	0.9	46	8	67 : 33
1662	4.4	1.0	43	8	63 : 37
1665	4.5	1.4	40	7	56 : 44
Average	3.9	0.9	44	8	65 : 35

Region V					
cm^{-1}	τ_1 (ps)	±	τ_2 (ps)	±	% (τ_1 : τ_2)
1678	2.2	0.7	36	6	68 : 32
1681	2.6	0.8	36	6	67 : 33
1684	3.4	1.0	40	7	64 : 36
1687	3.6	1.2	39	8	62 : 38
1690	3.7	1.4	36	8	60 : 40
Average	3.1	1.0	37	7	64 : 36

Tabular Analyis A3.6 - TpdA at 20 °C

Region I					
cm^{-1}	τ_1 (ps)	±	τ_2 (ps)	±	% (τ_1 : τ_2)
1550	**2.3**	0.5	**46**	14	**80 : 20**
1553	**2.3**	0.4	**51**	13	**81 : 19**
1555	**2.3**	0.4	**57**	14	**82 : 18**
1558	**3.6**	0.4	**64**	15	**81 : 19**
1561	**4.0**	0.5	**62**	11	**75 : 25**
1564	**5.5**	0.7	**64**	15	**75 : 25**
Average	**3.3**	0.5	**57**	14	**79 : 21**

Region II					
cm^{-1}	τ_1 (ps)	±	τ_2 (ps)	±	% (τ_1 : τ_2)
1581	**1.2**	0.1	**42**	5	**89 : 11**
1584	**1.6**	0.1	**40**	6	**75 : 25**
1587	**1.8**	0.1	**35**	6	**88 : 12**
1590	**2.1**	0.1	**37**	6	**89 : 11**
1593	**2.4**	0.1	**39**	11	**92 : 8**
Average	**1.8**	0.1	**39**	7	**87 : 13**

Region III					
cm^{-1}	τ_1 (ps)	±	τ_2 (ps)	±	% (τ_1 : τ_2)
1623	**5.1**	0.4	**80**	29	**89 : 11**
1626	**5.4**	0.3	**72**	12	**88 : 12**
1630	**7.1**	0.7	**86**	27	**83 : 17**
1633	**7.5**	0.8	**83**	22	**78 : 22**
Average	**6.3**	0.6	**80**	23	**84 : 16**

Region IV					
cm^{-1}	τ_1 (ps)	±	τ_2 (ps)	±	% (τ_1 : τ_2)
1661	**2.8**	0.2	**56**	3	**71 : 29**
1664	**4.0**	0.3	**58**	4	**67 : 33**
1668	**5.0**	0.3	**58**	4	**68 : 32**
1671	**6.1**	0.9	**54**	7	**59 : 41**
Average	**4.5**	0.4	**57**	5	**66 : 34**

Region V					
cm^{-1}	τ_1 (ps)	±	τ_2 (ps)	±	% (τ_1 : τ_2)
1688	**2.4**	0.8	**41**	3	**37 : 63**
1691	**2.8**	0.6	**43**	3	**45 : 55**
1694	**2.8**	0.6	**39**	3	**49 : 51**
1698	**4.3**	1.1	**43**	5	**48 : 52**
Average	**3.1**	0.8	**42**	4	**45 : 55**

Tabular Analyis A3.6 - TpdA at 70°C

Region I					
cm^{-1}	τ_1 (ps)	±	τ_2 (ps)	±	% (τ_1 : τ_2)
1563	**2.4**	0.5	**73**	42	**84 : 16**
1566	**2.7**	0.8	**48**	34	**80 : 20**
1568	**3.5**	0.8	**60**	43	**81 : 19**
1571	**4.2**	1.0	**61**	53	**82 : 18**
Average	**3.2**	0.8	**61**	43	**82 : 18**

Region II					
cm^{-1}	τ_1 (ps)	±	τ_2 (ps)	±	% (τ_1 : τ_2)
1588	**1.4**	0.2	**28**	15	**93 : 7**
1591	**1.6**	0.1	**19**	6	**91 : 9**
1593	**1.8**	0.2	**19**	7	**92 : 8**
1596	**2.1**	0.2	**22**	11	**93 : 7**
1598	**2.4**	0.1	**36**	13	**95 : 5**
Average	**1.9**	0.2	**25**	10	**93 : 7**

Region III A					
cm^{-1}	τ_1 (ps)	±	τ_2 (ps)	±	% (τ_1 : τ_2)
1621	**3.7**	0.2	**65**	28	**94 : 6**
1624	**4.4**	0.1	**73**	15	**94 : 6**
1627	**4.6**	0.3	**67**	20	**91 : 9**
Average	**4.2**	0.2	**68**	21	**93 : 7**

Region III B					
cm^{-1}	τ_1 (ps)	±	τ_2 (ps)	±	% (τ_1 : τ_2)
1629	**4.9**	0.5	**74**	21	**86 : 14**
1632	**5.0**	0.7	**71**	21	**82 : 18**
1635	**6.2**	1.2	**69**	21	**73 : 27**
Average	**5.4**	0.8	**71**	21	**80 : 20**

Region IV					
cm^{-1}	τ_1 (ps)	±	τ_2 (ps)	±	% (τ_1 : τ_2)
1654	**1.9**	0.2	**57**	11	**83 : 17**
1656	**2.9**	0.2	**55**	8	**79 : 21**
1659	**3.5**	0.3	**50**	9	**78 : 22**
1662	**3.6**	0.4	**60**	14	**76 : 24**
Average	**3.0**	0.3	**56**	11	**79 : 21**

Region V					
cm^{-1}	τ_1 (ps)	±	τ_2 (ps)	±	% (τ_1 : τ_2)
1684	**2.4**	0.4	**48**	12	**79 : 21**
1687	**2.5**	0.4	**51**	13	**77 : 23**
1690	**2.8**	0.5	**64**	18	**77 : 23**
1693	**2.4**	0.6	**57**	21	**77 : 23**
1696	**2.3**	0.7	**56**	23	**76 : 24**
1698	**1.8**	0.8	**63**	35	**78 : 22**
Average	**2.4**	0.6	**57**	20	**77 : 23**

Area Analysis					
cm^{-1}	τ_1 (ps)	±	τ_2 (ps)	±	% (τ_1 : τ_2)
1563-1578	**4.1**	1.2	**26**	20	**83 : 17**
1621-1632	**5.6**	0.4	**127**	55	**92 : 8**
1656-1690	**2.9**	0.4	**36**	8	**76 : 24**

Tabular Analyis A3.6 - TpdA at 70 °C

Focus on the long-lived species in multiple TpdA at 70 °C

Single pixel analysis with time delays from 20 ps onwards being fitted to a single exponential

Region I		
cm^{-1}	τ (ps)	±
1566	**22**	10
1571	**30**	7
1575	**23**	3
Average	**25**	7

Region II		
cm^{-1}	τ (ps)	±
1591	**25**	4
1593	**28**	3
1596	**19**	7
1598	**22**	12
1601	**16**	8
Average	**22**	7

Region III A		
cm^{-1}	τ (ps)	±
1621	23	7
1624	22	6
1627	23	7
Average	23	7

Region III B		
cm^{-1}	τ (ps)	±
1629	25	7
1632	31	12
1635	29	8
Average	28	9

Region IV		
cm^{-1}	τ (ps)	±
1654	40	9
1656	39	7
1659	34	7
1662	32	7
Average	36	8

Region V		
cm^{-1}	τ (ps)	±
1681	29	6
1684	27	4
1687	30	2
1690	32	6
1693	32	5
1696	29	2
1698	30	3
Average	30	4

Tabular Analyis A3.6 - TpdA at 90 °C

Region I		
cm^{-1}	τ (ps)	±
1571	12	6
Average	12	6

Region II		
cm^{-1}	τ (ps)	±
1591	1.1	0.3
1593	1.4	0.3
1596	1.6	0.3
1598	2.3	0.4
1601	2.2	0.3
1603	2.8	0.3
Average	1.9	0.3

Region III A		
cm^{-1}	τ (ps)	±
1621	3.2	0.3
1624	3.5	0.3
1627	3.9	0.4
1629	3.8	0.5
Average	3.6	0.4

Region III B		
cm^{-1}	τ (ps)	±
1632	2.7	0.5
1635	2.1	0.6
1637	2.3	0.7
Average	2.4	0.6

Region IV		
cm^{-1}	τ (ps)	±
1659	3.8	0.3
1662	4.3	0.8
1665	4.2	0.6
Average	4.1	0.6

Region V		
cm^{-1}	τ (ps)	±
1684	2.3	0.3
1687	2.2	0.5
1690	3.0	0.4
1693	3.3	0.6
1696	2.9	0.2
Average	2.7	0.4

Appendix for Chapter 5

ps-TRIR Study of Biologically Relevant Systems

Study 1: Mixed-Base Duplex DNA

5'-TACGAGTTGAGAATCCTGAATGCG-3'					
Transient (2-1500 ps)					
cm^{-1}	τ_1 (ps)	±	τ_2 (ps)	±	% (τ_1 : τ_2)
1584	**3.4**	1.0	**93**	69	**71:29**
1587	**4.1**	0.9	**70**	33	**71:29**
1590	**3.8**	0.9	**54**	21	**70:30**
1593	**3.8**	0.9	**57**	29	**74:26**
1596	**4.3**	0.9	**64**	34	**77:23**
Average	**3.9**	0.9	**68**	37	**73:27**
Bleach (2-1500 ps)					
cm^{-1}	τ_1 (ps)	±	τ_2 (ps)	±	% (τ_1 : τ_2)
1620	**4.3**	2.2	**39**	27	**68:32**
1623	**5.0**	3.5	**37**	22	**57:43**
1627	**4.5**	6.1	**31**	25	**50:50**
1630	**3.6**	5.0	**35**	21	**43:57**
1633	**3.1**	4.7	**42**	22	**42:58**
1636	**2.2**	2.4	**43**	14	**44:56**
1639	**3.5**	2.2	**41**	10	**43:57**
1642	**3.9**	3.9	**40**	14	**38:62**
1646	**3.5**	3.6	**41**	11	**32:68**
1649	**2.4**	2.0	**41**	10	**42:58**
1652	**4.1**	2.9	**53**	13	**40:60**
1655	**3.3**	2.0	**45**	13	**50:50**
1659	**4.2**	2.1	**53**	16	**53:47**
1662	**4.7**	1.6	**62**	15	**54:46**
1665	**6.3**	1.9	**74**	24	**59:41**
1669	**7.2**	1.9	**83**	27	**61:39**
1672	**8.9**	2.5	**102**	48	**66:34**
1675	**7.6**	1.9	**63**	15	**57:43**
1679	**9.7**	2.4	**112**	66	**71:29**
1682	**7.6**	4.3	**60**	32	**55:45**
1685	**6.8**	3.2	**59**	24	**54:46**
1689	**6.5**	2.6	**54**	21	**58:42**
1692	**6.5**	3.0	**62**	33	**61:39**
1695	**4.4**	2.9	**42**	20	**54:46**
Average	**5.2**	3.0	**55**	23	**52:48**

5'-TACGAGTTGAGAATCCTGAATGCG-3'					
Area analysis (2-1500 ps)					
cm^{-1}	τ_1 (ps)	±	τ_2 (ps)	±	% (τ_1 : τ_2)
1584-1614	**3.5**	0.9	**77**	40	**77:23**
1614-1633	**3.1**	0.9	**76**	18	**74:26**
1633-1709	**9.1**	1.5	**160**	31	**56:44**
1614-1709	**10.3**	2.1	**172**	56	**60:40**

5'-CGCATTCAGGATTCTCAACTCGTA-3'					
Transient (2-200 ps)					
cm^{-1}	τ_1 (ps)	±	τ_2 (ps)	±	% (τ_1 : τ_2)
1590	**7.1**	2.1	-	-	-
1593	**7.1**	1.5	-	-	-
1596	**6.6**	1.1	-	-	-
1599	**6.0**	0.7	-	-	-
1602	**5.5**	0.6	-	-	-
1605	**6.1**	0.5	-	-	-
1608	**7.1**	0.8	-	-	-
Average	**6.5**	1.0	-	-	-
Bleach (2-1500 ps)					
cm^{-1}	τ_1 (ps)	±	τ_2 (ps)	±	% (τ_1 : τ_2)
1623	**1.9**	0.7	**84**	51	**85:15**
1626	**2.8**	0.8	**64**	22	**74:26**
1629	**2.6**	1.0	**52**	14	**63:37**
1632	**1.7**	0.5	**46**	10	**66:34**
1635	**2.8**	0.8	**64**	22	**74:26**
Average	**2.4**	0.8	**62**	24	**72:28**
1657	**1.8**	0.3	**56**	7	**71:29**
1660	**2.2**	0.3	**54**	6	**67:33**
1664	**3.0**	0.5	**57**	7	**63:37**
1667	**3.5**	0.6	**58**	8	**61:39**
1670	**3.7**	0.8	**57**	9	**60:40**
1673	**3.0**	0.6	**46**	6	**57:43**
1676	**4.8**	1.1	**62**	11	**55:45**
1680	**3.3**	0.8	**53**	7	**55:45**
1683	**1.7**	0.5	**38**	6	**66:34**
1686	**1.9**	0.6	**43**	6	**68:32**
1690	**2.4**	0.8	**44**	8	**59:41**

1693	**1.9**	0.6	**36**	8	**68:32**
Average	**2.8**	0.6	**50**	7	**62:38**
Area analysis (2-1500 ps)					
1620-1638	**1.5**	0.6	**64**	19	**77:23**
1638-1710	**1.8**	0.4	**50**	6	**69:31**
1620-1710	**1.8**	0.4	**48**	6	**68:32**

5'-TACGAGTTGAGAATCCTGAATGCG-3' 3'-ATGCTCAACTCTTAGGACTTACGC-5'					
Bleach (2-200 ps)					
cm^{-1}	**τ_1 (ps)**	±	**τ_2 (ps)**	±	**% (τ_1 : τ_2)**
1645	**1.9**	0.4	**28**	8	**70:30**
1648	**2.8**	0.7	**32**	6	**58:42**
1651	**3.3**	0.9	**36**	8	**55:45**
1654	**1.7**	0.4	**32**	6	**65:35**
1657	**1.9**	1.0	**25**	8	**65:35**
1660	**2.0**	0.8	**31**	10	**71:29**
1664	**2.2**	0.6	**40**	10	**69:31**
1667	**2.7**	0.6	**37**	8	**66:34**
1670	**3.8**	0.6	**42**	8	**61:39**
1673	**4.7**	0.8	**45**	10	**60:40**
1676	**4.9**	0.7	**45**	7	**58:42**
1680	**5.4**	1.2	**42**	11	**58:42**
1683	**5.8**	1.7	**40**	15	**61:39**
1686	**5.0**	1.0	**36**	6	**54:46**
1690	**5.2**	1.0	**39**	10	**62:38**
1693	**5.5**	1.3	**41**	17	**69:31**
1696	**5.1**	0.8	**38**	9	**67:33**
1699	**5.6**	1.0	**49**	19	**71:29**
1703	**5.0**	1.1	**36**	16	**73:27**
1706	**5.5**	2.2	**33**	43	**81:19**
1710	**4.9**	2.4	**32**	31	**76:24**
Average	**4.0**	1.0	**37**	13	**65:35**

5'-TACGAGTTGAGAATCCTGAATGCG-3' 3'-ATGCTCAACTCTTAGGACTTACGC-5'					
Transient (2-1000 ps)					
cm^{-1}	τ_1 (ps)	±	τ_2 (ps)	±	% (τ_1 : τ_2)
1590	**4.0**	3.2	**79**	73	**67:33**
1593	**4.4**	2.5	**90**	84	**75:25**
1596	**4.6**	2.2	**95**	94	**78:22**
1599	**4.3**	1.6	**95**	82	**79:21**
1602	**4.1**	1.3	**79**	56	**80:20**
1605	**4.5**	1.2	**77**	53	**81:19**
1608	**5.3**	1.5	**97**	79	**82:18**
1611	**6.2**	2.0	**92**	76	**80:20**
Average	**4.7**	1.9	**88**	75	**78:22**
Bleach (2-1000 ps)					
cm^{-1}	τ_1 (ps)	±	τ_2 (ps)	±	% (τ_1 : τ_2)
1645	**3.6**	1.3	**58**	22	**67:33**
1648	**7.1**	1.7	**83**	38	**73:27**
1651	**7.2**	2.2	**76**	43	**70:30**
1654	**2.1**	1.1	**33**	10	**61:39**
1657	**4.1**	1.5	**74**	27	**63:37**
1660	**2.8**	0.9	**71**	21	**68:32**
1664	**2.7**	0.7	**81**	18	**68:32**
1667	**3.8**	0.9	**89**	20	**66:34**
1670	**5.0**	0.8	**88**	16	**65:35**
1673	**6.2**	1.0	**97**	18	**64:36**
1676	**5.9**	0.8	**72**	11	**61:39**
1680	**6.9**	1.1	**81**	17	**64:36**
1683	**7.9**	1.4	**111**	32	**69:31**
1686	**7.2**	1.2	**82**	18	**65:35**
1690	**6.8**	1.0	**88**	20	**68:32**
1693	**6.9**	1.1	**126**	38	**72:28**
1696	**6.5**	0.8	**101**	23	**73:27**
1699	**6.4**	0.8	**108**	25	**74:26**
1703	**6.4**	0.9	**141**	46	**74:26**
1706	**6.5**	1.1	**243**	148	**79:21**
1710	**6.2**	1.5	**156**	92	**76:24**
Average	**5.6**	1.1	**98**	33	**69:31**

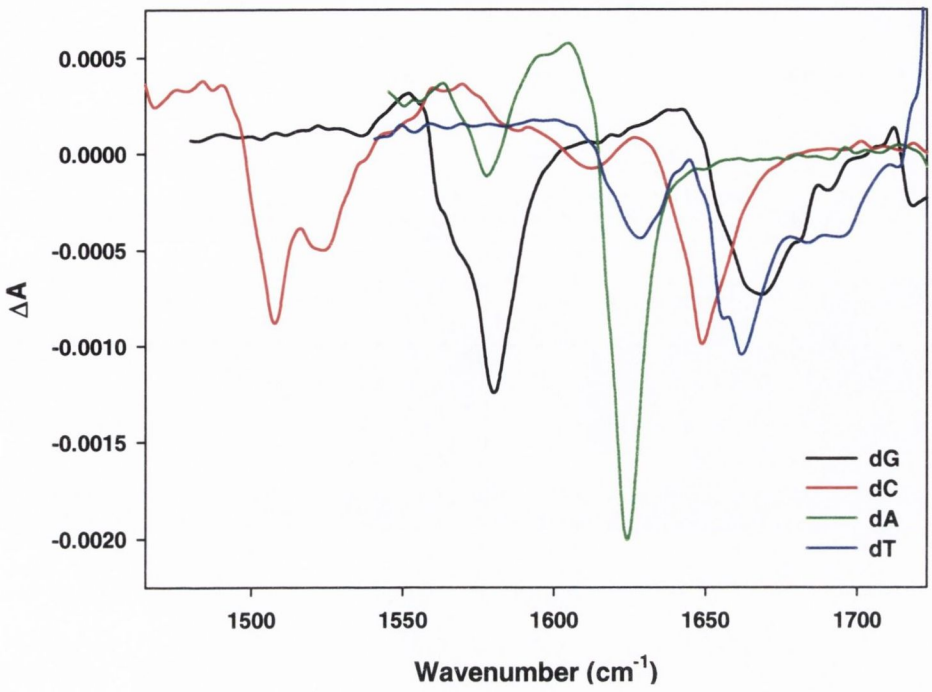

Contributions in 1580-1723 cm^{-1} window		
cm^{-1}	Ground state bleaching	Excited state absorption
1460-1495	-	dC
1495-1540	dC	-
1540-1555	-	dG, dA, dC(s)
1555-1570	dG	dA, dC
1570-1580	dG, dA(s)	dC
1580-1600	dG	dA, dC(s), dT(s)
1600-1615	dC(s)	dA, dT(s)
1615-1635	dA, dT	dG(s), dC(s)
1635-1655	dC, dT(s)	dG
1655-1680	dT, dG, dC(s)	-
1680-1723	dT, dG	-
s = small		

Figure A5.1 ps-TRIR band positions of the mononucleotides (10 mM) in 50 mM potassium phosphate D_2O buffer (pH 7) at 2 ps for the spectral window (1460-1723 cm^{-1}) of the single- and double-stranded mixed base oligonucleotide experiments. Table below summarizes the contributions in various regions of the spectrum.

Study 2: Triplex DNA

A5.1 poly(dA)

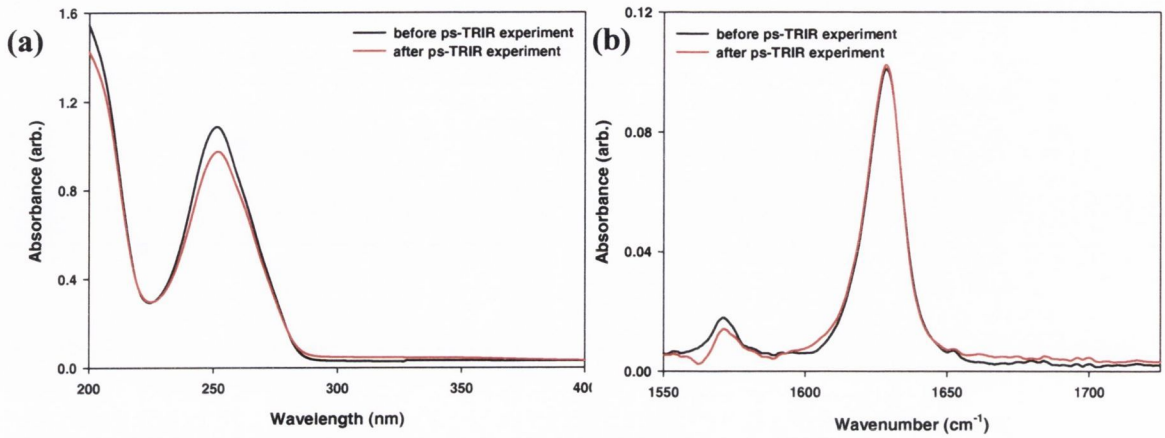

Figure A5.1.1 (a) UV and (b) FTIR spectra of 10 mM poly(dA) in 50 mM potassium phosphate D_2O buffer (pH 7) before (black) and after (red) 4 cycles of ps-TRIR measurements.

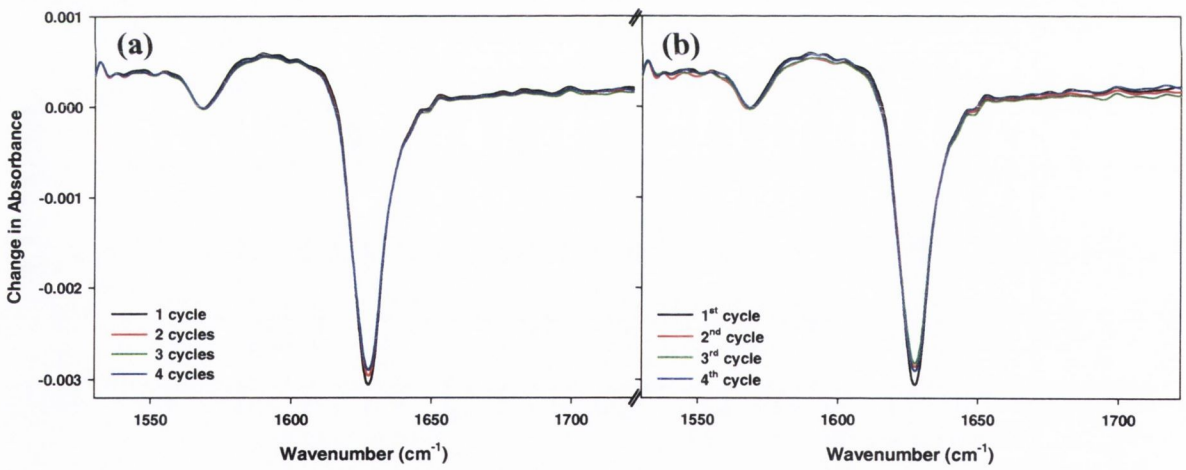

Figure A5.1.2 Comparison of the 2 ps delay for (a) accumulated and (b) individual cycles of 10 mM poly(dA) in 50 mM potassium phosphate D_2O buffer (pH 7).

Transient (2-2000 ps)					
cm^{-1}	τ_1 (ps)	±	τ_2 (ps)	±	% (τ_1 : τ_2)
1532	**3.4**	0.4	**236**	76	**83:17**
1534	**2.8**	0.5	**231**	103	**84:16**
1537	**2.7**	0.3	**240**	69	**86:14**
1540	**2.9**	0.4	**276**	107	**85:15**
1546	**3.0**	0.4	**301**	138	**88:12**
1549	**3.3**	0.4	**285**	153	**89:11**
1551	**3.5**	0.4	**313**	210	**91:9**
1554	**4.7**	0.5	**226**	114	**89:11**
1557	**4.7**	0.5	**307**	196	**90:10**
Average	**3.4**	0.4	**268**	130	**87:13**
1581	**2.1**	0.2	**317**	218	**96:4**
1587	**2.8**	0.1	**244**	130	**96:4**
1590	**3.1**	0.2	**289**	224	**96:4**
Average	**2.7**	0.2	**283**	191	**96:4**
Bleach (2-2000 ps)					
cm^{-1}	τ_1 (ps)	±	τ_2 (ps)	±	% (τ_1 : τ_2)
1623	**3.8**	0.2	**308**	45	**86:14**
1627	**5.8**	0.3	**268**	40	**83:17**
1630	**7.2**	0.4	**257**	47	**82:18**
1633	**8.7**	0.6	**249**	56	**80:20**
1636	**10**	1.0	**255**	83	**81:19**
1639	**9.8**	1.4	**201**	88	**81:19**
Average	**7.6**	0.7	**256**	60	**82:18**
Area 1620-1639 cm^{-1}					
2-2000 ps	**6.0**	0.3	**251**	42	**82:18**
20-1000 ps	-	-	**157**	33	-

Bleach (20-2000 ps)		
cm^{-1}	τ_1 (ps)	±
1623	**261**	40
1627	**191**	32
1630	**152**	30
1633	**128**	26
1636	**102**	26
1639	**81**	28
Average	**153**	30

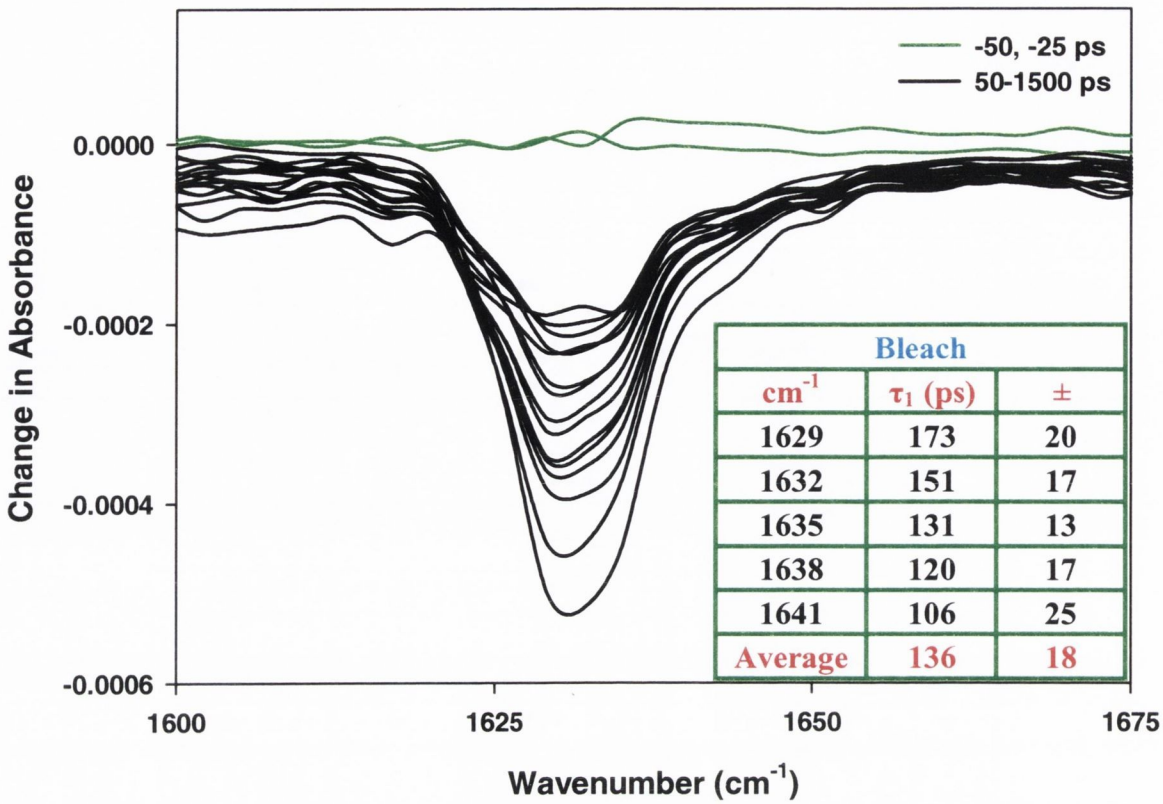

Figure A5.1.3 ps-TRIR of 10 mM poly(dA) in 50 mM potassium phosphate D_2O buffer (pH 7). Delays are at -50, -25 (green), 50, 75, 100, 125, 150, 175, 200, 250, 300, 350, 400, 500, 700, 1000 and 1500 ps (black). Inset: Single exponential kinetic fits to data.

A5.2 poly(dT)

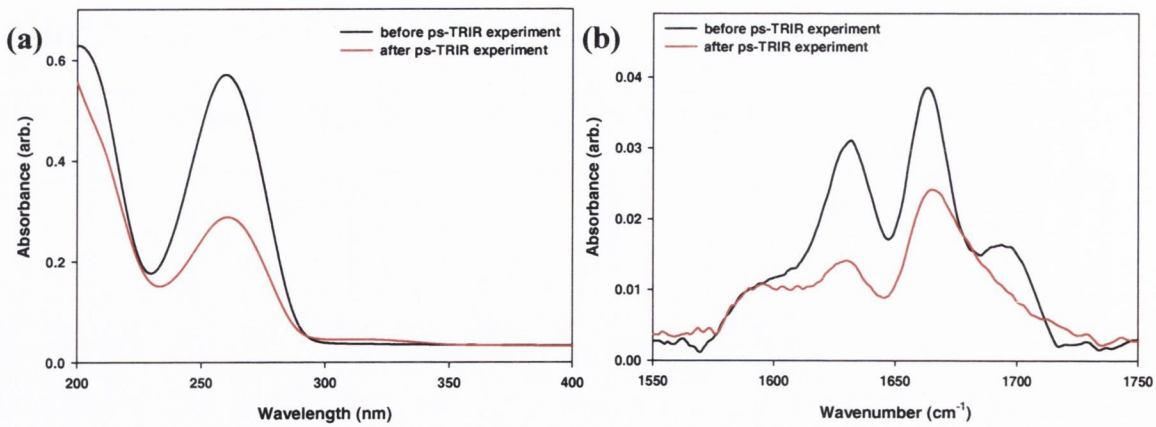

Figure A5.2.1 (a) UV and (b) FTIR spectra of 10 mM poly(dT) in 50 mM potassium phosphate D_2O buffer (pH 7) before (black) and after (red) 3 cycles of ps-TRIR measurements.

1 cycle (2-1000ps)					
cm^{-1}	τ_1 (ps)	±	τ_2 (ps)	±	% (τ_1 : τ_2)
1659	**1.7**	0.5	**88**	70	**90:10**
1662	**1.7**	0.3	**83**	42	**89:11**
1665	**1.8**	0.4	**82**	47	**89:11**
1692	**1.3**	0.5	**172**	144	**90:10**
1695	**1.3**	0.6	**69**	57	**90:10**
1698	**1.6**	0.9	**45**	41	**85:15**
Average	**1.6**	0.5	**90**	67	**89:11**

1 cycle (2-200ps)					
cm^{-1}	τ_1 (ps)	±	τ_2 (ps)	±	% (τ_1 : τ_2)
1662	**1.7**	0.4	**50**	40	**90:10**
1665	**1.8**	0.4	**53**	45	**90:10**
1669	**1.9**	0.4	**55**	54	**90:10**
1672	**2.2**	0.7	**33**	37	**85:15**
1675	**3.3**	0.6	**37**	40	**84:16**
1698	**1.9**	0.3	**79**	73	**90:10**
Average	**2.1**	0.5	**51**	48	**88:12**

A5.3 poly(dA).poly(dT)

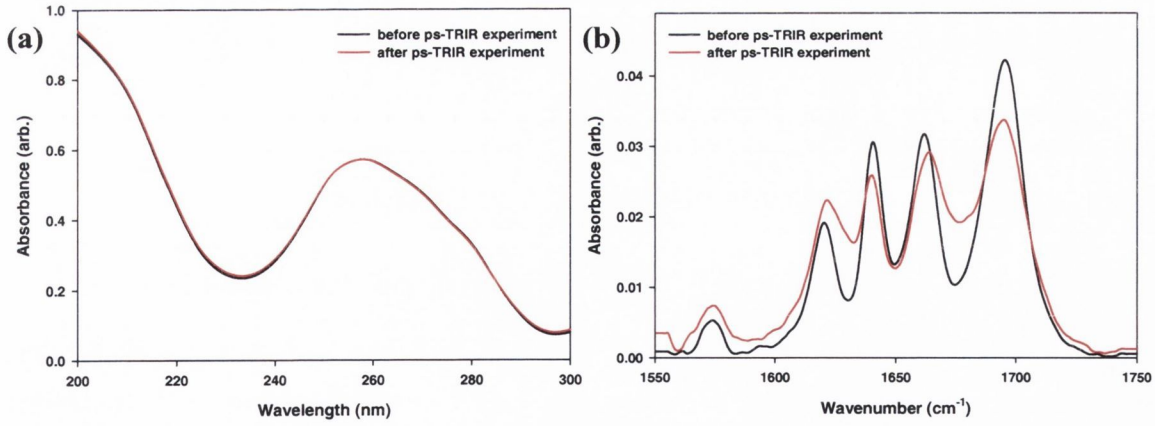

Figure A5.3.1 (a) UV and (b) FTIR spectra of 6.1 mM poly(dA).poly(dT) in 50 mM potassium phosphate D_2O buffer (pH 7) before (black) and after (red) 4 cycles of ps-TRIR measurements.

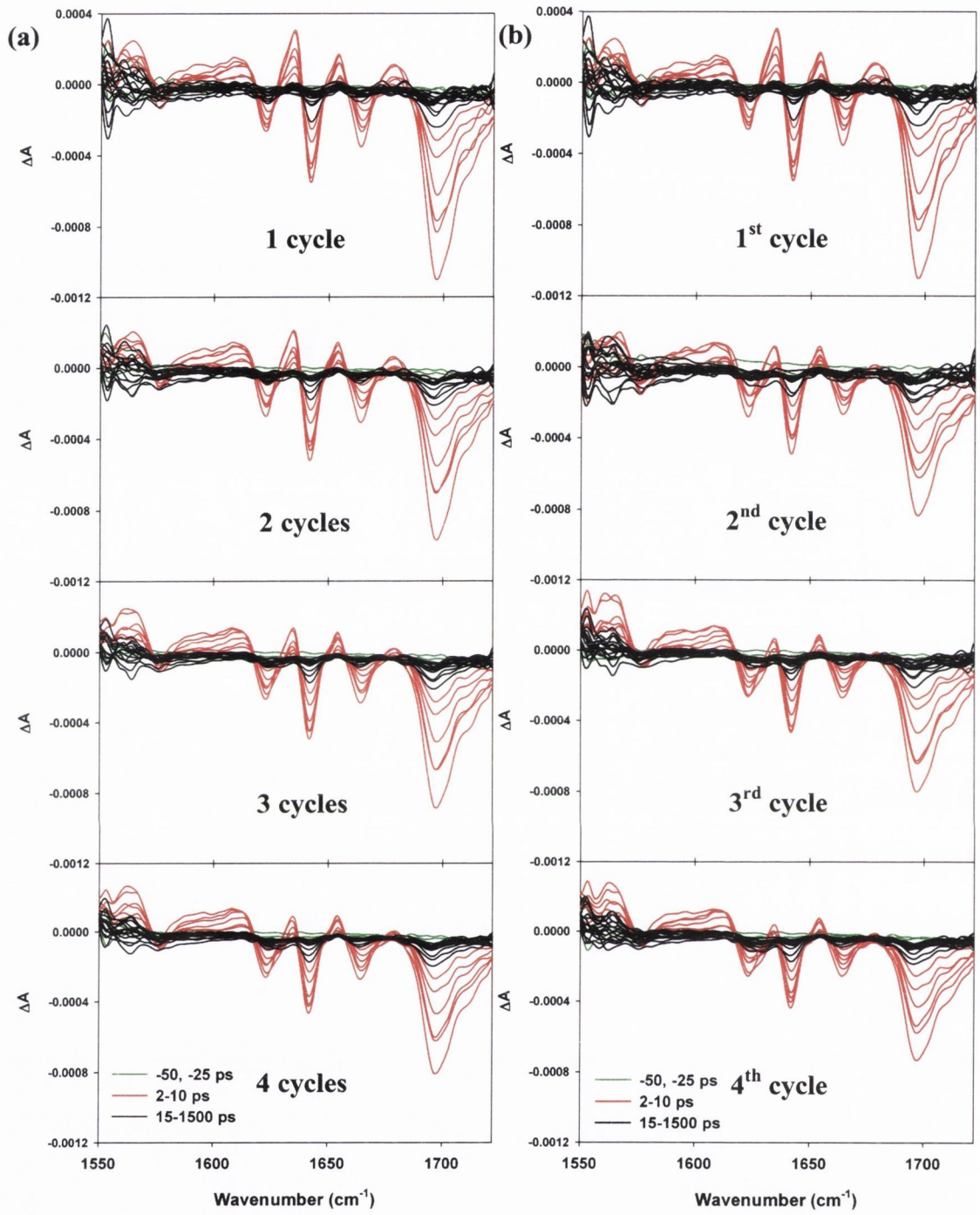

Figure A5.3.2 Accumulated (a) and separated (b) cycles of 6.1 mM poly(dA).poly(dT) in 50 mM potassium phosphate D_2O buffer (pH 7) with 250 mM NaCl (annealed). Delays are at -50, -25 (green), 2, 3, 4, 5, 7, 10 (red), 15, 20, 35, 50, 75, 100, 150, 175, 200, 250, 300, 350, 500, 700, 1000 and 1500 ps (black).

4 cycles (2-2000 ps)					
cm^{-1}	τ_1 (ps)	±	τ_2 (ps)	±	% (τ_1 : τ_2)
1620	**2.2**	0.9	**17**	19	**87:13**
1623	**4.0**	1.7	**20**	19	**78:22**
1626	**5.6**	4.5	**33**	35	**69:31**
1641	**7.7**	1.1	**46**	34	**88:12**
1645	**10.1**	2.1	**49**	87	**91:9**
1660	**1.4**	0.3	**31**	14	**93:7**
1664	**2.9**	0.5	**17**	5	**76:24**
1667	**4.2**	3.5	**10**	9	**58:42**
1693	**3.0**	0.5	**22**	8	**81:19**
1696	**3.9**	0.5	**32**	14	**86:14**
1699	**4.3**	0.4	**39**	19	**90:10**
1703	**4.0**	0.6	**22**	11	**85:15**
1706	**3.7**	0.5	**26**	15	**88:13**
Average	**3.8**	0.5	**28**	13	**86:14**

4 cycles (2-2000 ps)		
cm^{-1}	τ_1 (ps)	±
1620	**3.4**	0.5
1623	**6.5**	0.7
1626	**12**	2.2
1641	**9.6**	0.5
1645	**10.5**	0.7
1664	**5.7**	0.4
1667	**6.8**	0.4
1693	**5.6**	0.5
1696	**5.7**	0.4
1699	**5.7**	0.3
1703	**5.8**	0.3
1706	**5.2**	0.4
Average	**5.6**	0.4

1st cycle (2-2000 ps)					
cm^{-1}	τ_1 (ps)	±	τ_2 (ps)	±	% (τ_1 : τ_2)
1602	**3.3**	1.4	**24**	50	**87:13**
1623	**2.7**	1.6	**31**	30	**87:13**
1641	**8.2**	4.7	**28**	98	**89:11**
1693	**2.3**	1.3	**12**	7	**70:30**
1696	**3.9**	0.9	**31**	29	**88:12**
1699	**3.4**	1.2	**16**	13	**80:20**
1703	**3.1**	2.0	**10**	9	**69:31**
1706	**3.3**	1.6	**12**	12	**78:22**
1710	**3.1**	2.2	**11**	13	**74:26**
Average	**3.2**	1.5	**15**	14	**77:23**

1st cycle (2-2000 ps)		
cm^{-1}	τ_1 (ps)	±
1602	**3.3**	4.4
1623	**6.5**	1.7
1641	**9.5**	0.9
1693	**5.3**	0.6
1696	**5.4**	0.5
1699	**5.4**	0.5
1703	**5.2**	0.4
1706	**5.0**	0.4
1710	**5.0**	0.5
Average	**5.2**	0.5

4th cycle (2-2000 ps)		
cm^{-1}	τ_1 (ps)	±
1602	**4.4**	0.6
1623	**6.5**	1.7
1641	**9.5**	0.9
1693	**5.8**	0.5
1696	**5.9**	0.4
1699	**5.8**	0.3
1703	**6.0**	0.3
1706	**5.3**	0.3
1710	**5.9**	0.5
Average	**5.8**	0.4

4th cycle (2-2000 ps)					
cm^{-1}	τ_1 (ps)	±	τ_2 (ps)	±	% (τ_1 : τ_2)
1623	**2.9**	1.8	**17**	13	**73:27**
1626	**3.7**	3.0	**29**	21	**62:38**
1641	**7.4**	1.5	**31**	21	**81:19**
1641s	**8.3**	0.5	**106**	47	**88:12**
1645	**10.4**	4.7	**32**	77	**87:13**
1645s	**10.7**	0.9	**108**	65	**87:13**
1660	**1.2**	0.4	**28**	16	**92:8**
1664	**2.5**	0.8	**15**	5	**72:28**
1667	**2.7**	3.8	**9**	4	**38:62**
1693	**2.8**	0.6	**18**	7	**77:23**
1696	**3.8**	0.5	**26**	10	**84:16**
1699	**4.3**	0.4	**34**	14	**89:11**
1703	**3.9**	0.7	**18**	8	**80:20**
1706	**3.8**	0.8	**18**	14	**85:15**
1710	**0.9**	0.7	**8**	1	**66:34**
Average	**3.3**	0.6	**20**	9	**80:20**
s = selected delays, i.e. outliers were not included in the fit					

A5.4 poly(dA).poly(dT) .poly(dT)

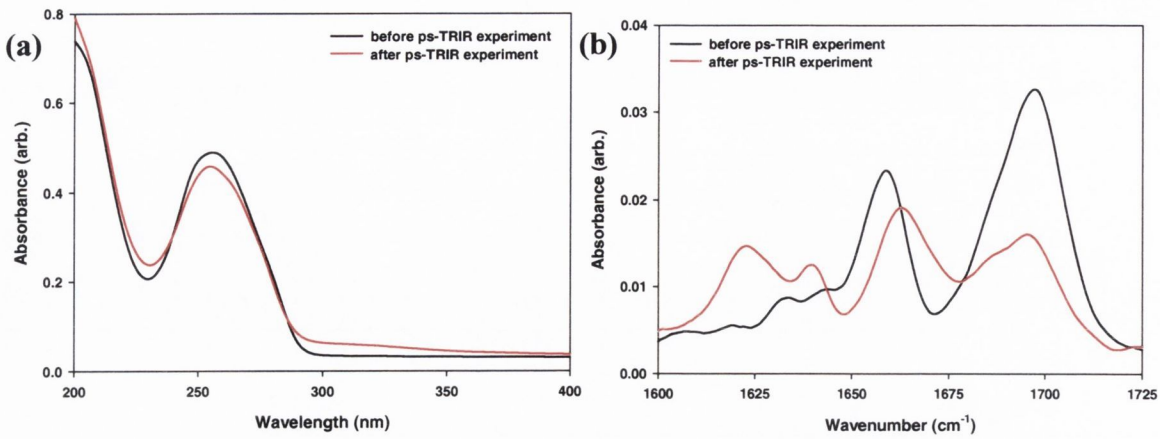

Figure A5.4.1 (a) UV and (b) FTIR spectra of 6.1 mM poly(dA).poly(dT).poly(dT) in 50 mM potassium phosphate D_2O buffer (pH 7) with 250 mM NaCl (annealed) before (black) and after (red) 5 cycles of ps-TRIR measurements.

1590 cm^{-1}					
cm^{-1}	τ_1 (ps)	±	τ_2 (ps)	±	% (τ_1 : τ_2)
1st	**4.6**	0.8	**-**	-	-
2nd	**1.6**	0.5	**12**	4	**77:23**
3rd	**2.4**	0.4	**81**	30	**83:17**
4th	**2.9**	0.7	**28**	24	**89:11**
5th	**2.7**	0.6	**18**	11	**83:17**

1620 cm^{-1}					
cm^{-1}	τ_1 (ps)	±	τ_2 (ps)	±	% (τ_1 : τ_2)
1st	-	-	-	-	-
2nd	**3.9**	0.9	**127**	58	**80:20**
3rd	**6.3**	1.8	**268**	197	**74:26**
3rd *	**5.9**	1.3	**233**	34	**73:27**
4th	**5.1**	1.1	**58**	43	**78:22**
5th	**6.6**	0.8	**376**	126	**73:27**
5th *	**8.4**	0.3	**110**	38	**73:27**
* outliers were omitted from the fit					

1633 cm^{-1}					
cm^{-1}	τ_1 (ps)	±	τ_2 (ps)	±	% (τ_1 : τ_2)
1st	**4.3**	1.2	**-**	-	-
2nd	**7.3**	1.2	**201**	140	**82:18**
3rd	**6.3**	1.0	**87**	43	**80:20**
4th	**5.8**	1.1	**136**	60	**76:24**
5th	**7.4**	0.9	**218**	101	**79:21**

1659 cm^{-1}					
cm^{-1}	τ_1 (ps)	±	τ_2 (ps)	±	% (τ_1 : τ_2)
1st	**3.4**	0.3	**53**	20	**85:15**
2nd	**4.2**	0.4	**118**	40	**87:13**
3rd	**3.4**	0.4	**56**	28	**86:14**
4th	**3.0**	0.4	**45**	24	**85:15**
5th	**3.9**	0.2	**134**	33	**87:13**

1695 cm^{-1}					
cm^{-1}	τ_1 (ps)	±	τ_2 (ps)	±	% (τ_1 : τ_2)
1st	**5.3**	0.3	**189**	151	**94:6**
2nd	**4.2**	0.4	**67**	26	**87:13**
3rd	**4.4**	0.5	**132**	95	**90:10**
4th	**4.3**	0.5	**46**	27	**87:13**
5th	**4.4**	0.4	**71**	35	**87:13**

Area 1689-1702 cm^{-1}					
cm^{-1}	τ_1 (ps)	±	τ_2 (ps)	±	% (τ_1 : τ_2)
1st	**5.3**	0.3	**213**	187	**96:4**
2nd	**4.3**	0.5	**68**	30	**88:12**
3rd	**3.6**	0.4	**70**	35	**88:12**
4th	**4.0**	0.4	**89**	49	**87:13**
5th	**4.0**	0.3	**114**	39	**88:12**

A5.4.2 poly(dA).poly(dT) .poly(dT)

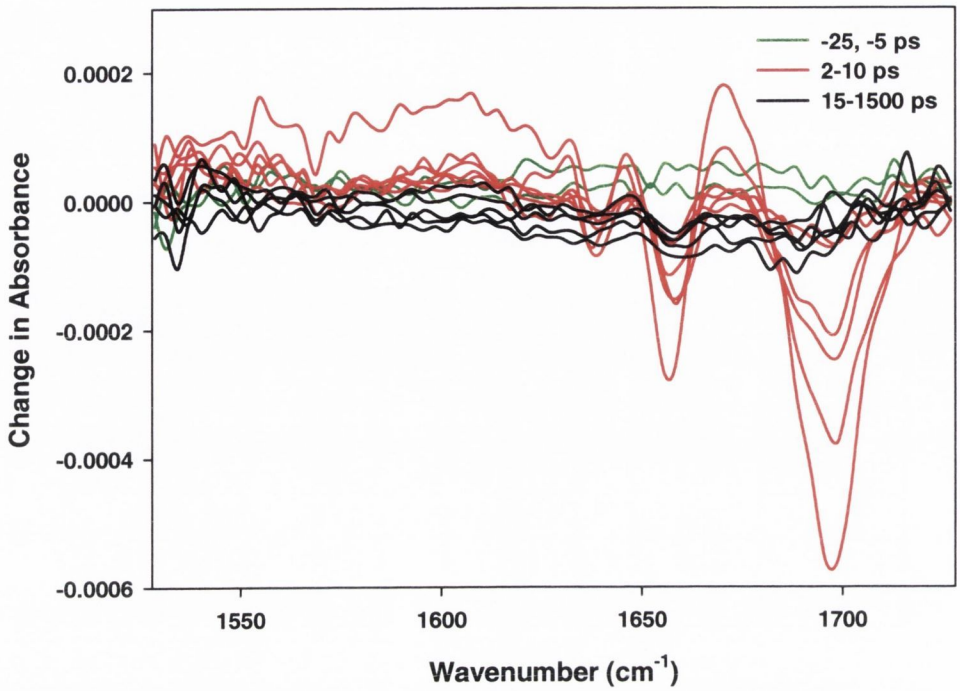

Figure A5.4.2 ps-TRIR (1 cycle) of 6.1 mM poly(dA).poly(dT).poly(dT) in 50 mM potassium phosphate D_2O buffer (pH 7) with 200 mM NaCl (annealed). Delays are at -50, -25 (green), 2, 4, 7, 10 (red), 20, 50, 100, 200, 500, 1000 and 1500 ps (black).

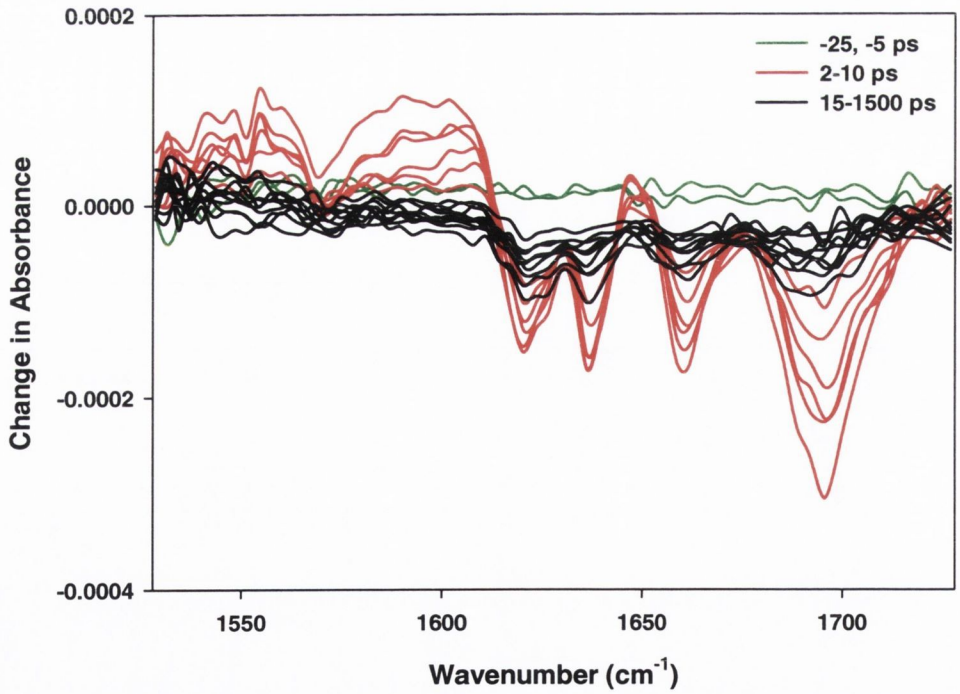

Figure A5.4.3 ps-TRIR (4 cycles) of 6.1 mM poly(dA).poly(dT).poly(dT) in 50 mM potassium phosphate D_2O buffer (pH 7) with 200 mM NaCl (annealed). Delays are at -50, -25 (green), 2, 3, 4, 5, 7, 10 (red), 15, 20, 35, 50, 75, 100, 200, 500, 1000 and 1500 ps (black).

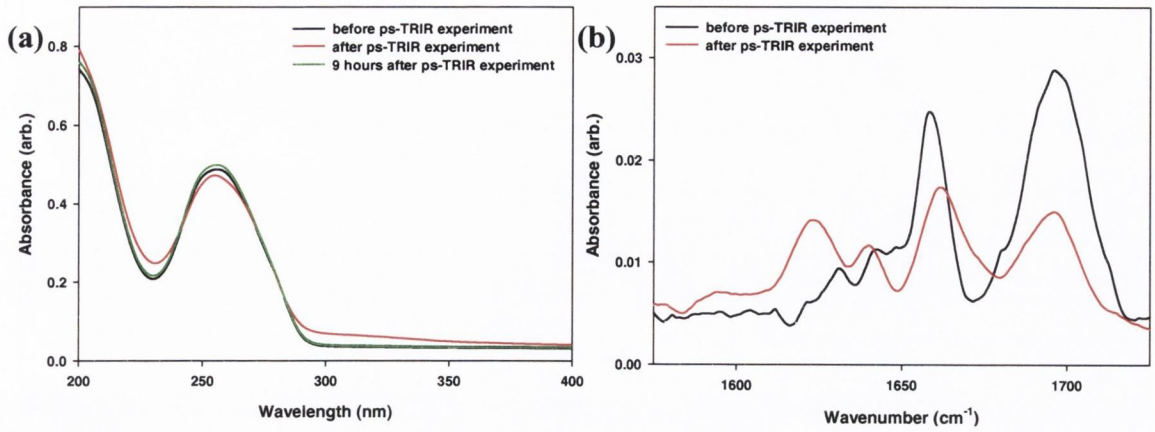

Figure A5.4.4 (a) UV and (b) FTIR spectra of 6.1 mM poly(dA).poly(dT).poly(dT) in 50 mM potassium phosphate D_2O buffer (pH 7) with 250 mM NaCl (annealed) before (black) and after (red) 5 cycles of ps-TRIR measurements. UV was also recorded 9 hours after the experiment (green).

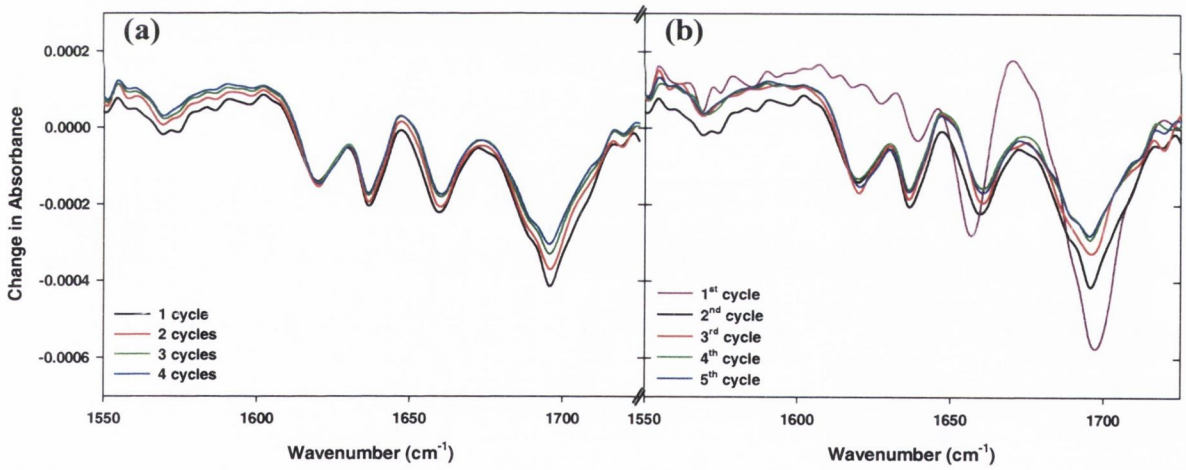

Figure A5.4.5 Comparison of the 2 ps delay for (a) accumulated and (b) individual cycles of 6.1 mM poly(dA).poly(dT).poly(dT) in 50 mM potassium phosphate D_2O buffer (pH 7) with 200 mM NaCl (before annealing).

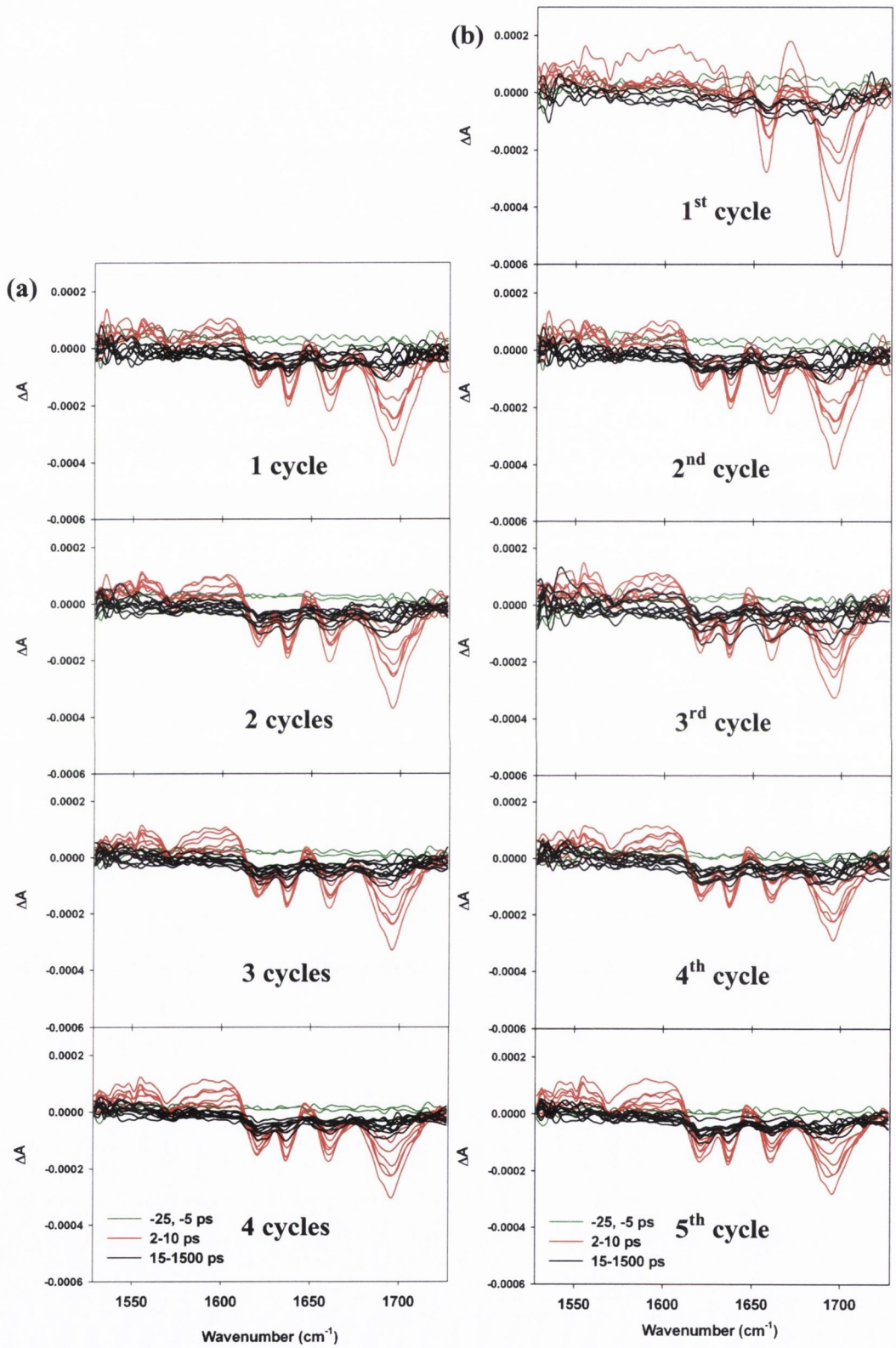

Figure A5.4.6 Accumulated (a) and separated (b) cycles of 6.1 mM poly(dA).poly(dT) .poly(dT) in 50 mM potassium phosphate D_2O buffer (pH 7) with 200 mM NaCl (before annealing).

A5.5 $(dA)_{18}$

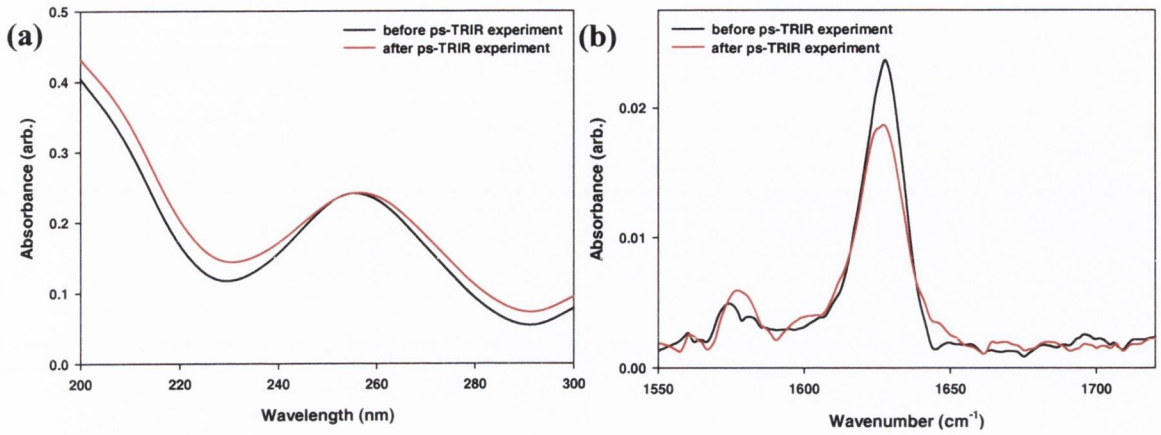

Figure A5.5.1 (a) UV and (b) FTIR spectra of 5 mM $(dA)_{18}$ in 50 mM potassium phosphate D_2O buffer (pH 7) before (black) and after (red) 4 cycles of ps-TRIR measurements.

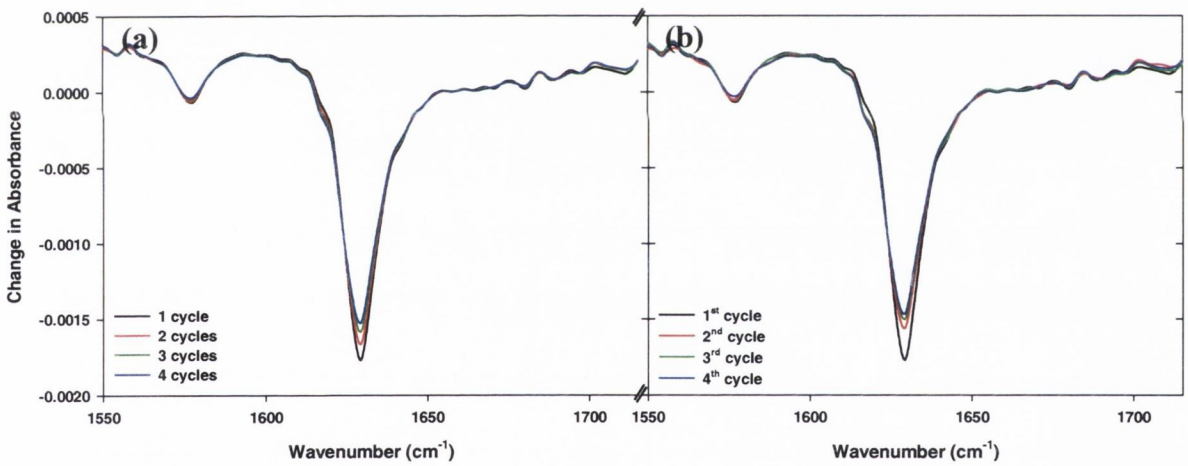

Figure A5.5.2 Comparison of the 2 ps delay for (a) accumulated and (b) individual cycles of 5 mM $(dA)_{18}$ in 50 mM potassium phosphate D_2O buffer (pH 7).

4 cycles $(dA)_{18}$ (2-2000 ps)					
cm^{-1}	τ_1 (ps)	±	τ_2 (ps)	±	% (τ_1 : τ_2)
1596	**3.6**	0.2	-	-	-
1626	**5.1**	0.2	**558**	86	**79:21**
1629	**7.0**	0.4	**515**	95	**75:25**
1633	**7.9**	0.5	**528**	100	**74:26**
1636	**8.3**	0.5	**635**	105	**74:26**
1639	**8.3**	0.5	**778**	153	**76:24**
Average	**7.3**	0.4	**603**	108	**76:24**

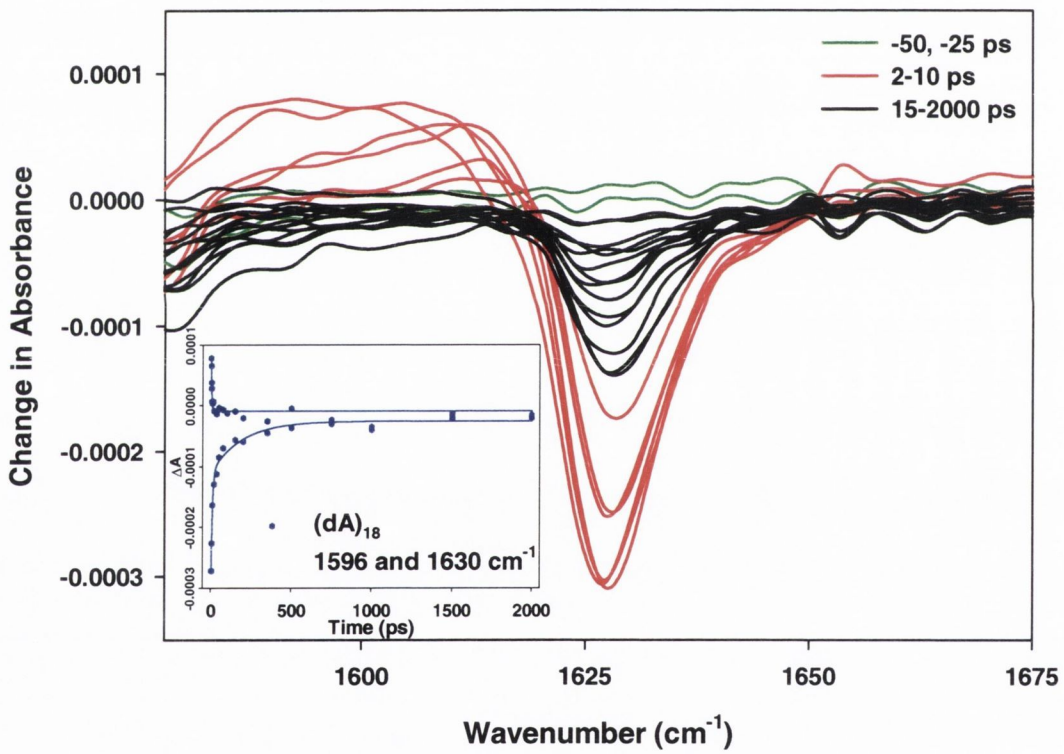

Figure A5.5.3 ps-TRIR of 2.5 mM $(dA)_{18}$ in 50 mM potassium phosphate D_2O buffer (pH 7). Delays are at -50, -25 (green), 2, 3, 4, 5, 7, 10 (red), 15, 20, 35, 50, 75, 100, 150, 200, 350, 500, 750, 1000, 1500 and 2000 ps (black).
Inset: Kinetic analysis at 1596 and 1630 cm^{-1}.

4 cycles $(dA)_{18}$ (2-2000 ps)					
cm^{-1}	τ_1 (ps)	±	τ_2 (ps)	±	% (τ_1 : τ_2)
1596	**3.6**	0.6	-	-	-
1627	**5.8**	1.1	**215**	72	**81:19**
1630	**7.5**	1.7	**189**	72	**78:22**
1634	**13.0**	2.3	**708**	552	**81:19**
1637	**6.2**	2.1	**131**	78	**80:20**
Average*	**6.5**	1.6	**178**	74	**80:20**
*** Average calculated excluding 1634cm^{-1} fit.**					

A5.6 $(dT)_{18}$

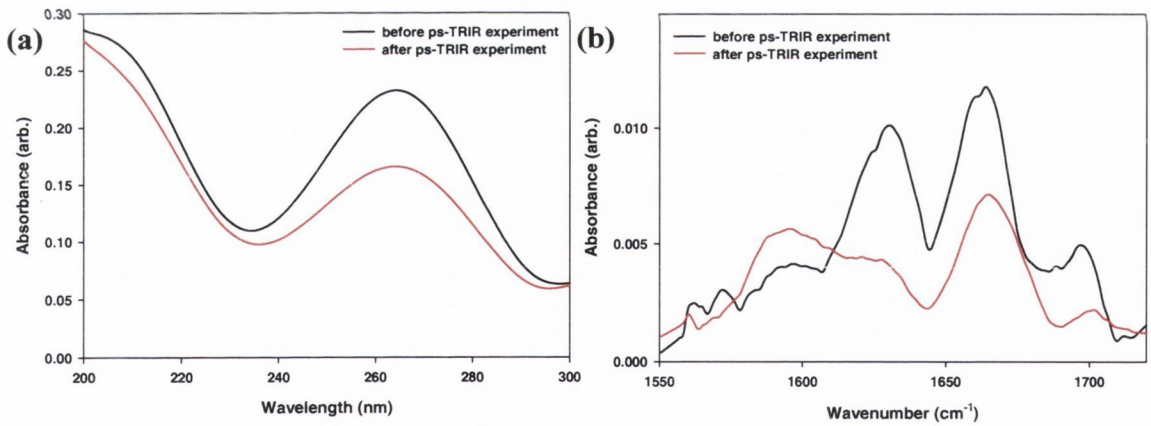

Figure A5.6.1 (a) UV and (b) FTIR spectra of 5 mM $(dT)_{18}$ in 50 mM potassium phosphate D_2O buffer (pH 7) before (black) and after (red) 4 cycles of ps-TRIR measurements.

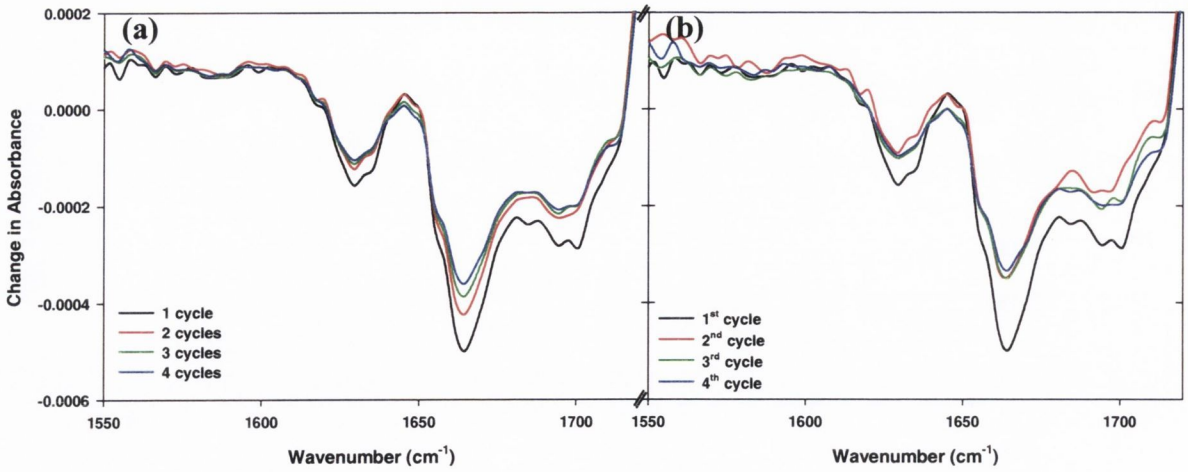

Figure A5.6.2 Comparison of the 2 ps delay for (a) accumulated and (b) individual cycles of 5 mM $(dT)_{18}$ in 50 mM potassium phosphate D_2O buffer (pH 7).

1st cycle (2-20 ps)		
cm^{-1}	τ_1 (ps)	±
1587	**1.8**	0.8
1590	**3.3**	1.3
1593	**3.0**	0.9
Area 1569-1608	**2.5**	0.5
1664	**3.9**	1.2

1st cycle (2-1000 ps)					
cm^{-1}	τ_1 (ps)	±	τ_2 (ps)	±	% (τ_1 : τ_2)
1587	**0.7**	0.5	**17**	7	**94:6**
1590	**0.7**	0.5	**14**	4	**90:10**
1593	**0.6**	0.4	**9**	2	**94:6**
Average	**0.7**	0.4	**12**	4	**93:7**
Area 1569-1608	**0.2**	0.8	**6**	1	**99:1**
1629	**1.4**	0.1	**215**	64	**94:6**
1633	**1.2**	0.5	**144**	88	**93:7**
1664	**1.7**	0.3	**46**	29	**94:6**
1671	**1.9**	0.2	**27**	12	**94:6**

A5.7 $(dA)_{18}.(dT)_{18}$

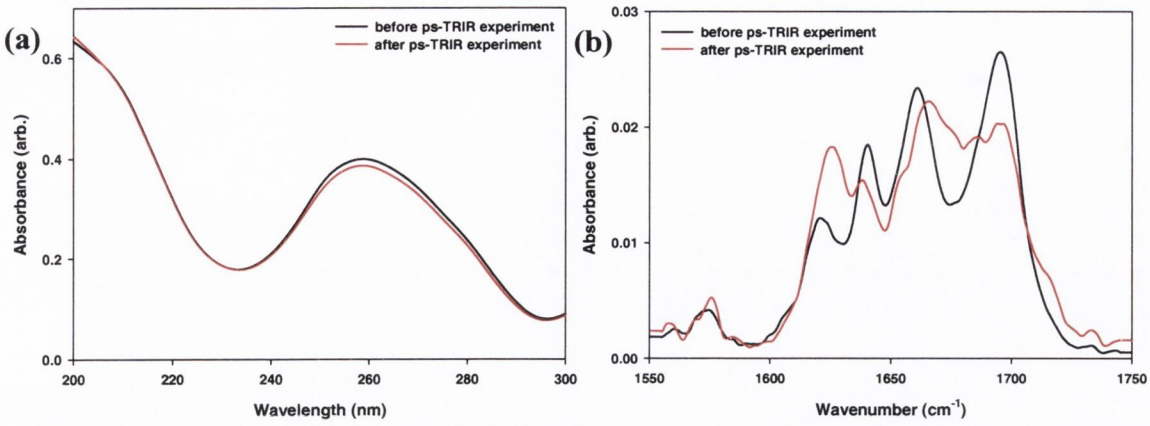

Figure A5.7.1 (a) UV and (b) FTIR spectra of 2.5 mM $(dA)_{18}.(dT)_{18}$ in 50 mM potassium phosphate D_2O buffer (pH 7) with 50 mM $MgCl_2$ before (black) and after (red) 4 cycles of ps-TRIR measurements.

1st cycle (2-1500 ps)					
cm^{-1}	τ_1 (ps)	±	τ_2 (ps)	±	% (τ_1 : τ_2)
1593s	**3.0**	3.7	**15**	8	**45:55**
1596s	**3.3**	3.5	**20**	16	**55:45**
Average	**3.2**	3.6	**18**	12	**50:50**
1623	**1.4**	0.9	**42**	37	**82:18**
1641s	**1.9**	0.8	**21**	4	**52:48**
1654s	**2.4**	0.6	**81**	103	**97:3**
1660s	**2.0**	1.3	**21**	18	**82:18**
1664s	**2.6**	1.6	**15**	9	**70:30**
Average	**2.3**	1.5	**18**	14	**76:24**
1693	**1.3**	1.0	**12**	5	**75:25**
1696	**3.8**	1.1	**17**	11	**80:20**
1699	**4.4**	0.8	**30**	21	**86:14**
1703	**4.4**	1.5	**20**	26	**87:13**
Average	**3.5**	1.1	**20**	16	**82:18**

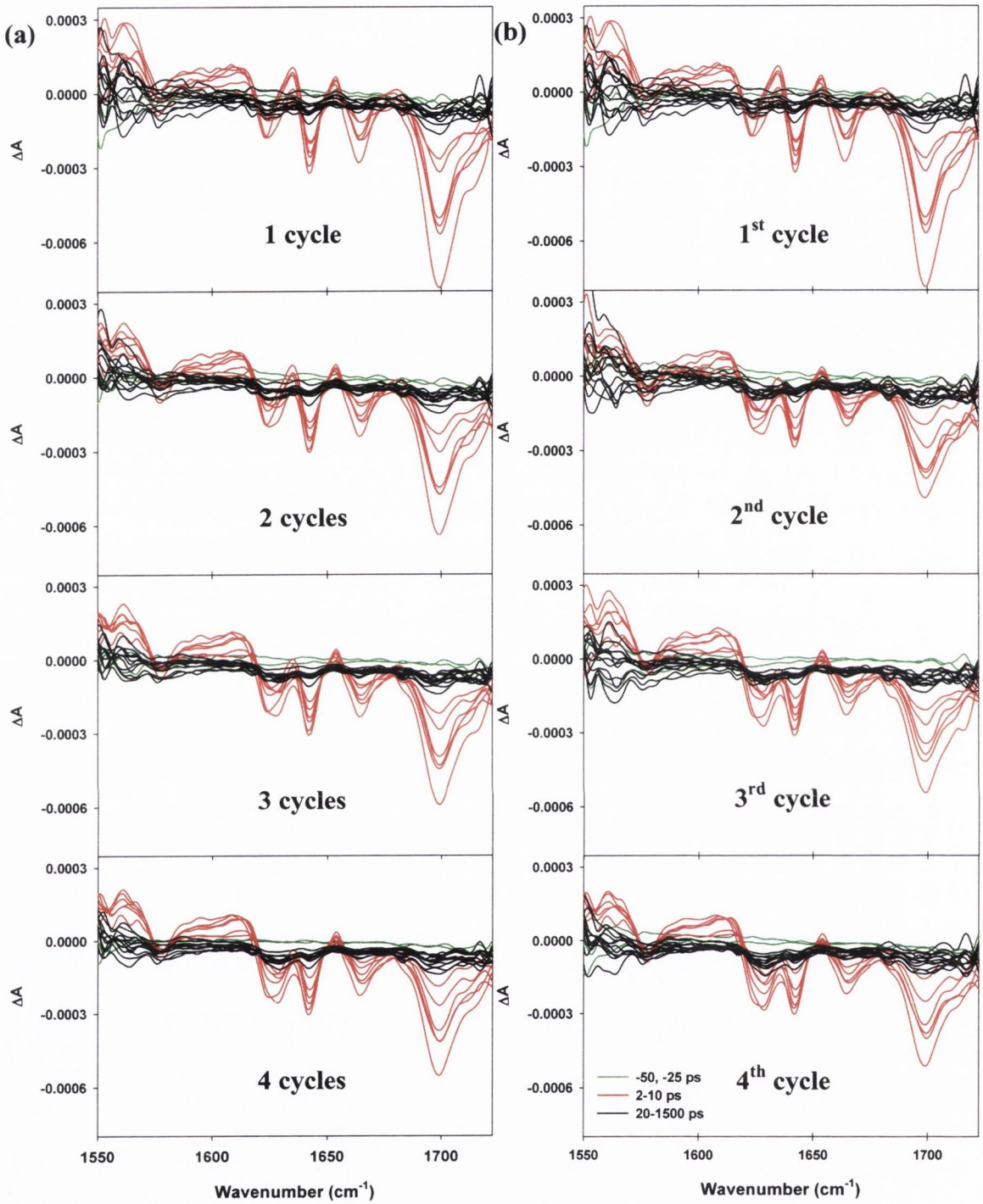

Figure A5.7.2 Accumulated (a) and separated (b) cycles of 2.5 mM $(dA)_{18}.(dT)_{18}$ in 50 mM potassium phosphate D_2O buffer (pH 7) with 50 mM $MgCl_2$. Delays are at -50, -25 (green), 2, 3, 4, 5, 7, 10 (red), 15, 20, 35, 50, 75, 100, 200, 350, 500, 700, 1000 and 1500 ps (black).

1st cycle (2-1500 ps)		
cm^{-1}	τ_1 (ps)	±
1593s	**8.6**	1.3
1596s	**8.9**	2.0
Average	**8.8**	1.7
1623	Definite double	
1641s	**13.0**	2.0
1654s	**3.4**	0.6
1660s	**3.5**	0.8
1664s	**5.2**	0.7
Average	**4.4**	0.8
1693	**5.3**	0.9
1696	**5.7**	0.5
1699	**6.0**	0.5
1703	**5.6**	0.5
Average	**5.7**	0.6

4th cycle (2-1500 ps)		
cm^{-1}	τ_1 (ps)	±
1629	Definite double	
1641s	**7.6**	0.9
1641s2	**8.1**	1.1
1641s3	**492**	248
1660s	**3.5**	0.8
1664s	**5.2**	0.7
Average	**4.4**	0.8
1699s	**5.6**	0.8
1699s2	**5.5**	0.8
1699s3	**5.4**	0.6
Average	**5.5**	0.7
1702s	**5.9**	0.9
1702s	**534**	234
1702s	**508**	17

4th cycle (2-1500 ps)					
cm^{-1}	τ_1 (ps)	±	τ_2 (ps)	±	% (τ_1 : τ_2)
1593	**4.2**	2.0	**103**	68	**67:33**
1593s	**1.1**	0.7	**16**	4	**72:28**
1629s	**3.6**	0.5	**507**	218	**78:22**
1641s	**5.5**	2.0	**35**	50	**84:16**
1641s2	**6.3**	1.1	**105**	161	**91:9**
1699s	**4.5**	0.9	**104**	198	**92:8**
1699s2	**4.2**	1.2	**46**	49	**88:12**
1699s3	**4.6**	0.5	**323**	249	**91:9**
Average	**4.4**	0.9	**158**	165	**90:10**
1702s	**4.9**	0.6	**409**	358	**91:9**

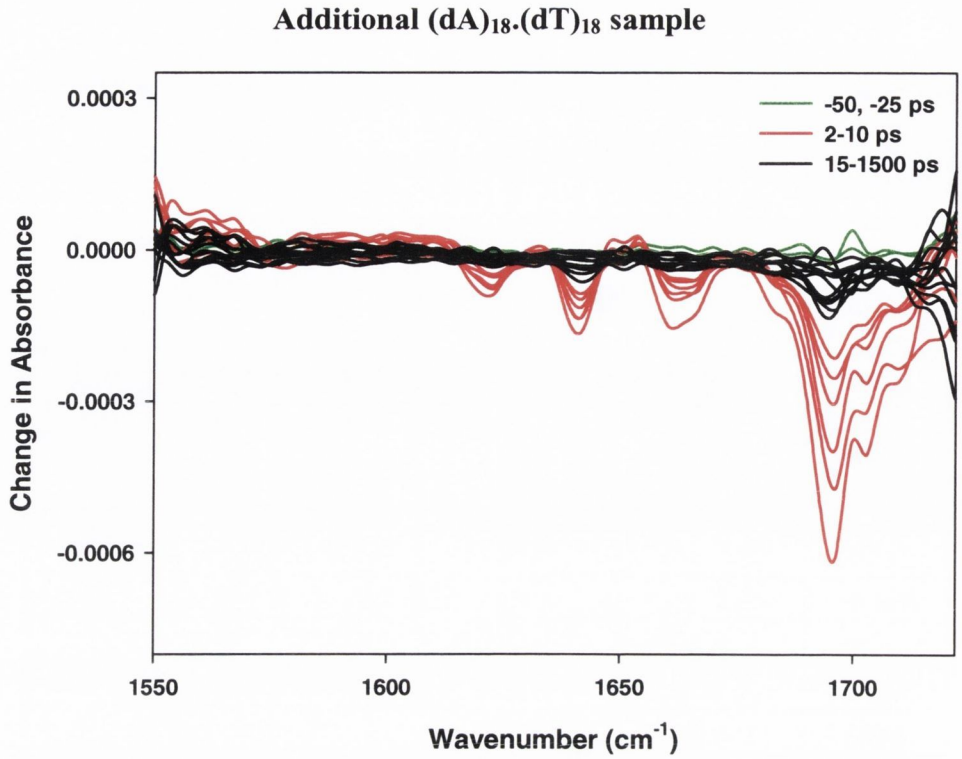

Figure A5.7.3 ps-TRIR of 2.5 mM $(dA)_{18}.(dT)_{18}$ in 50 mM potassium phosphate D_2O buffer (pH 7) with 50 mM $MgCl_2$. Delays are at -50, -25 (green), 2, 3, 4, 5.5, 7.5, 10 (red), 15, 20, 35, 50, 75, 100, 200, 350, 500, 750, 1000, and 1500 ps (black).

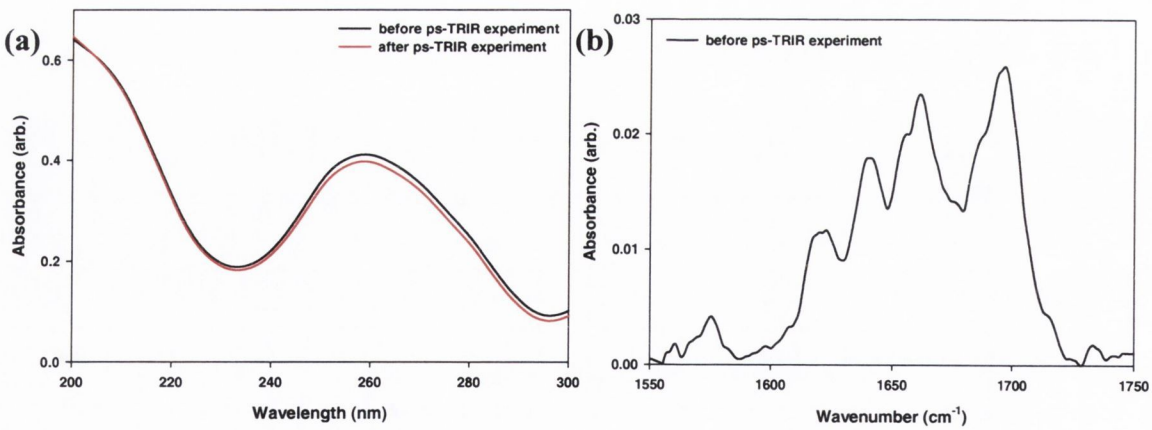

Figure A5.7.4 (a) UV spectra of 2.5 mM $(dA)_{18}.(dT)_{18}$ in 50 mM potassium phosphate D_2O buffer (pH 7) with 50 mM $MgCl_2$ before (black) and after (red) 4 cycles of ps-TRIR measurements and (b) FTIR spectrum before the experiment.

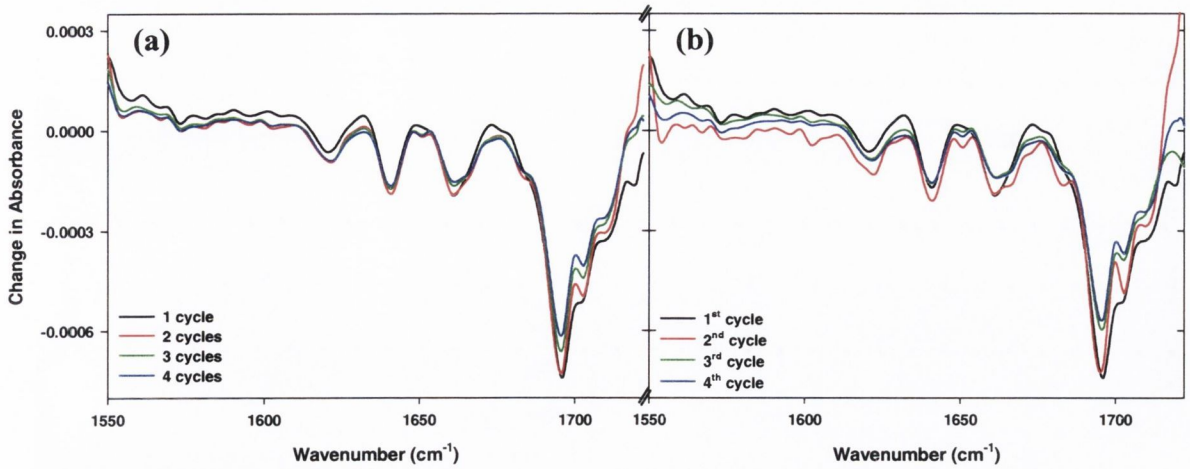

Figure A5.7.5 Comparison of the 2 ps delay for (a) accumulated and (b) individual cycles of 2.5 mM $(dA)_{18}.(dT)_{18}$ in 50 mM potassium phosphate D_2O buffer (pH 7) with 50 mM $MgCl_2$.

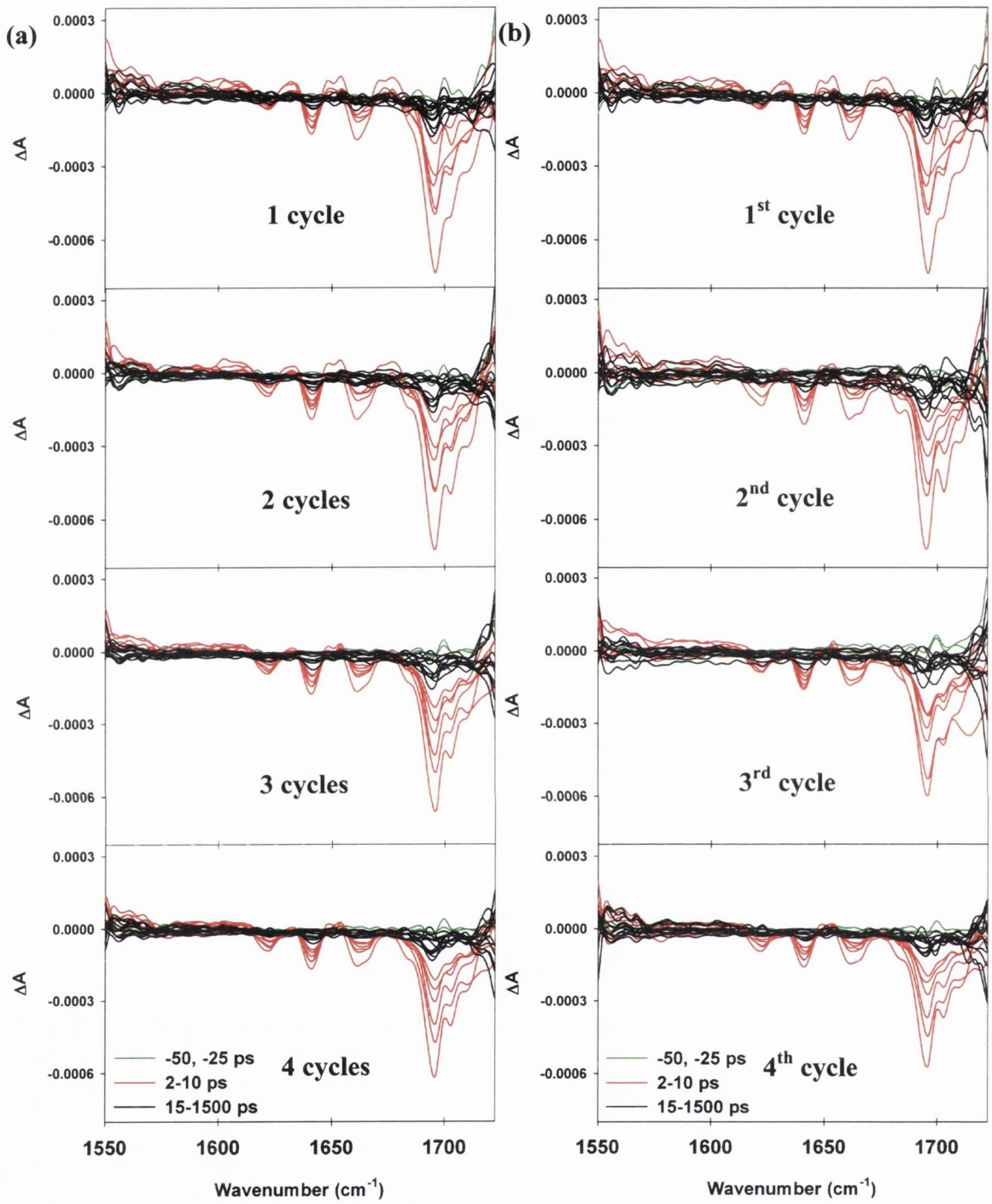

Figure A5.7.5 Accumulated (a) and separated (b) cycles of 2.5 mM $(dA)_{18}.(dT)_{18}$ in 50 mM potassium phosphate D_2O buffer (pH 7) with 50 mM $MgCl_2$. -50, -25 (green), 2, 3, 4, 5.5, 7.5, 10 (red), 15, 20, 35, 50, 75, 100, 200, 350, 500, 750, 1000, and 1500 ps (black).

A5.8 $(dA)_{18}.(dT)_{18}.(dT)_{18}$

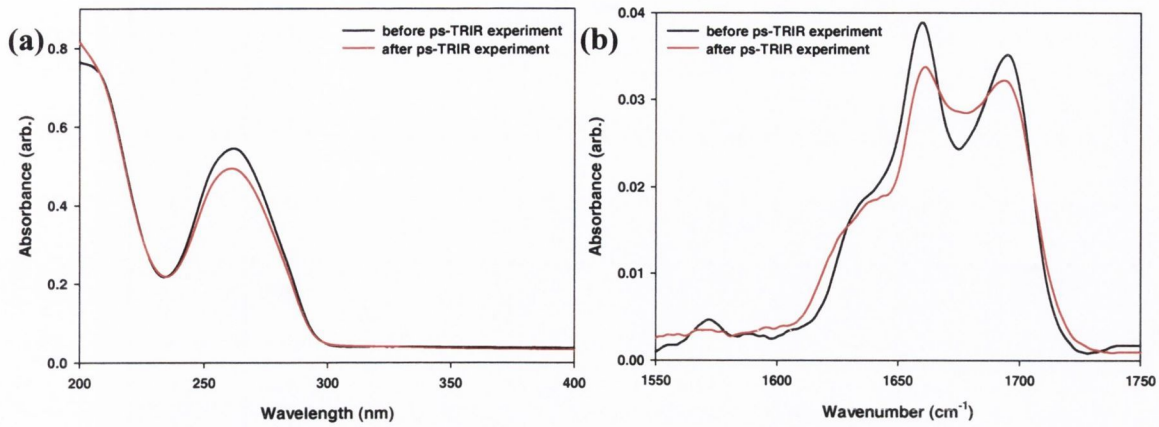

Figure A5.8.1 (a) UV and (b) FTIR spectra of 5 mM $(dA)_{18}.(dT)_{18}.(dT)_{18}$ in 50 mM potassium phosphate D_2O buffer (pH 7) with 50 mM $MgCl_2$ before (black) and after (red) 4 cycles of ps-TRIR measurements.

4 cycles (2-1000 ps)					
cm^{-1}	τ_1 (ps)	±	τ_2 (ps)	±	% (τ_1 : τ_2)
1584	**2.6**	0.6	**33**	21	**82:18**
1590	**3.0**	0.7	**52**	48	**90:10**
1611	**3.5**	0.9	**27**	49	**89:11**
Average	**3.0**	0.7	**37**	39	**87:13**
1660	**4.9**	0.5	**335**	355	**89:11**
1686	**4.2**	0.4	**180**	98	**99:12**
1690	**4.8**	0.3	**99**	41	**91:9**
1693	**4.8**	0.4	**88**	46	**90:10**
1696	**5.3**	0.4	**95**	62	**93:7**
1703	**6.1**	0.4	**220**	338	**96:4**
1706	**5.7**	0.6	**126**	233	**95:5**
1710	**4.7**	2.8	**16**	55	**91:9**
Average	**5.1**	0.8	**118**	125	**92:8**

4 cycles (2-1000 ps)		
cm^{-1}	τ_1 (ps)	±
1584	4.1	0.6
1587	3.8	0.5
1590	4.0	0.6
1593	4.6	0.8
1596	4.7	0.6
1599	4.6	0.9
1602	3.8	0.9
1605	4.5	1.0
1608	4.6	0.8
1611	4.0	0.4
Average	4.3	0.7
1657	4.0	0.4
1660	5.6	0.6
1664	5.7	0.6
Average	5.1	0.5
1686	4.7	0.4
1690	5.7	0.4
1693	5.8	0.5
1696	5.9	0.3
1699	6.0	0.4
1703	6.2	0.3
1706	6.0	0.5
1710	5.4	0.6
Average	5.7	0.4

4 cycles (2-20 ps)		
cm^{-1}	τ_1 (ps)	±
1584	2.5	0.8
1587	2.1	0.5
1590	2.6	0.7
1593	3.0	0.9
1596	2.9	0.4
1599	2.1	0.6
1602	1.6	0.4
1605	2.0	0.4
1608	2.1	0.3
1611	3.0	0.3
Average	2.4	0.5
1657	3.9	0.3
1660	5.1	0.5
1664	6.2	0.8
Average	5.1	0.5
1686	4.4	0.6
1690	4.8	0.3
1693	4.9	0.5
1696	5.1	0.4
1699	6.5	0.8
1703	6.1	0.7
1706	6.1	0.7
1710	4.7	1.1
Average	5.3	0.6

1st cycle (2-1000 ps)		
cm^{-1}	τ_1 (ps)	±
1590	**6.4**	1.7
1660	**6.4**	1.7
1690	**5.5**	0.8
1693	**5.5**	0.7
1696	**6.4**	0.7
1699	**7.4**	0.9
1703	**6.7**	0.8
1706	**5.8**	0.9
1710	**5.5**	0.9
Average	**6.1**	0.8

4th cycle (2-1000 ps)		
cm^{-1}	τ_1 (ps)	±
1590	**4.0**	0.6
1660	**5.4**	0.6
1690	**5.8**	0.4
1693	**6.0**	0.6
1696	**6.1**	0.5
1699	**6.8**	0.3
1703	**6.3**	0.4
1706	**6.6**	0.5
1710	**5.5**	0.7
Average	**6.2**	0.5

4th cycle (2-1000 ps)					
cm^{-1}	τ_1 (ps)	±	τ_2 (ps)	±	% (τ_1 : τ_2)
1590	**3.1**	0.7	**69**	67	**90:10**
1660	**5.4**	0.3	**553**	793	**92:8**
1690	**4.4**	0.5	**39**	21	**88:12**
1693	**5.0**	0.6	**93**	74	**91:9**
1696	**5.2**	0.7	**62**	65	**93:7**
1699	**6.1**	0.8	**34**	48	**94:6**
Average	**5.2**	0.7	**57**	52	**91:9**

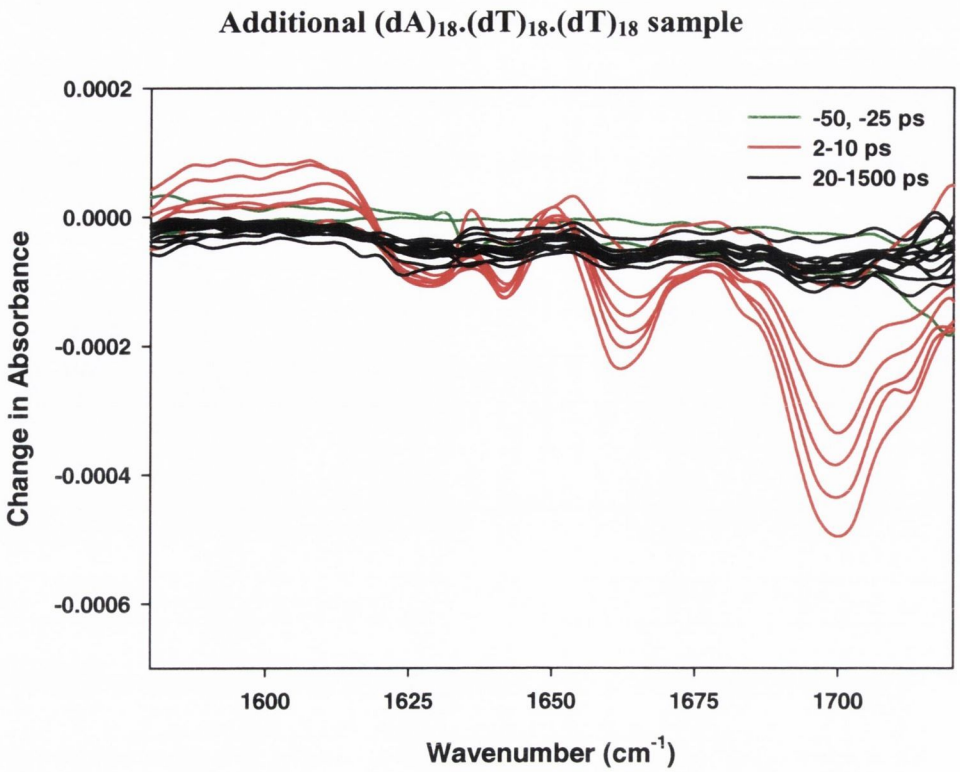

Figure 5.8.2 ps-TRIR of 5 mM $(dA)_{18}.(dT)_{18}.(dT)_{18}$ in 50 mM potassium phosphate D_2O buffer (pH 7) with 50 mM $MgCl_2$ (annealed). Delays are at -50, -25 (green), 2, 3, 4, 5, 7, 10 (red), 20, 35, 50, 75, 100, 150, 200, 350, 500, 750, 1000 and 1500 ps (black).

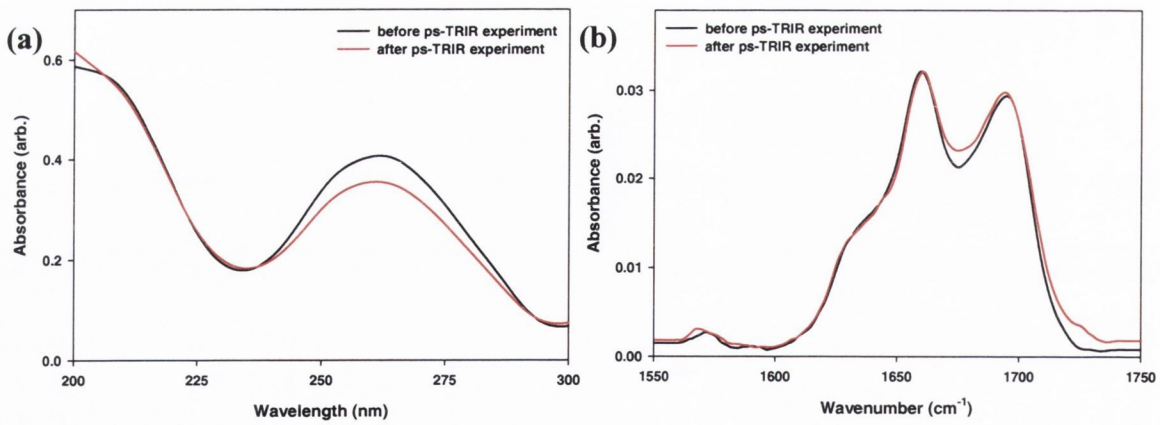

Figure A5.8.3 (a) UV and (b) FTIR spectra of 5 mM $(dA)_{18}.(dT)_{18}.(dT)_{18}$ in 50 mM potassium phosphate D_2O buffer (pH 7) with 50 mM $MgCl_2$ before (black) and after (red) 4 cycles of ps-TRIR measurements.

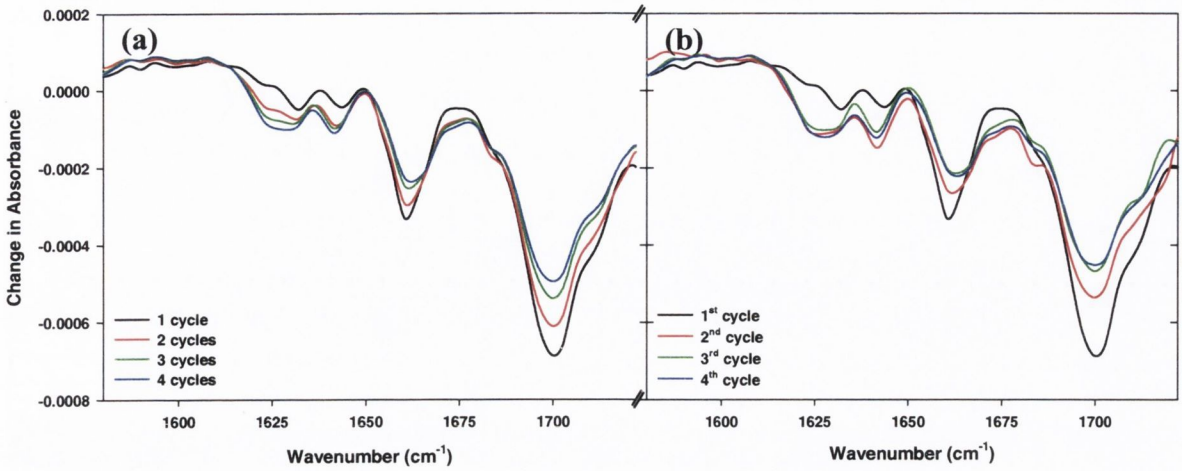

Figure A5.8.4 Comparison of the 2 ps delay for (a) accumulated and (b) individual cycles of 5 mM $(dA)_{18}.(dT)_{18}.(dT)_{18}$ in 50 mM potassium phosphate D_2O buffer (pH 7) with 50 mM $MgCl_2$.

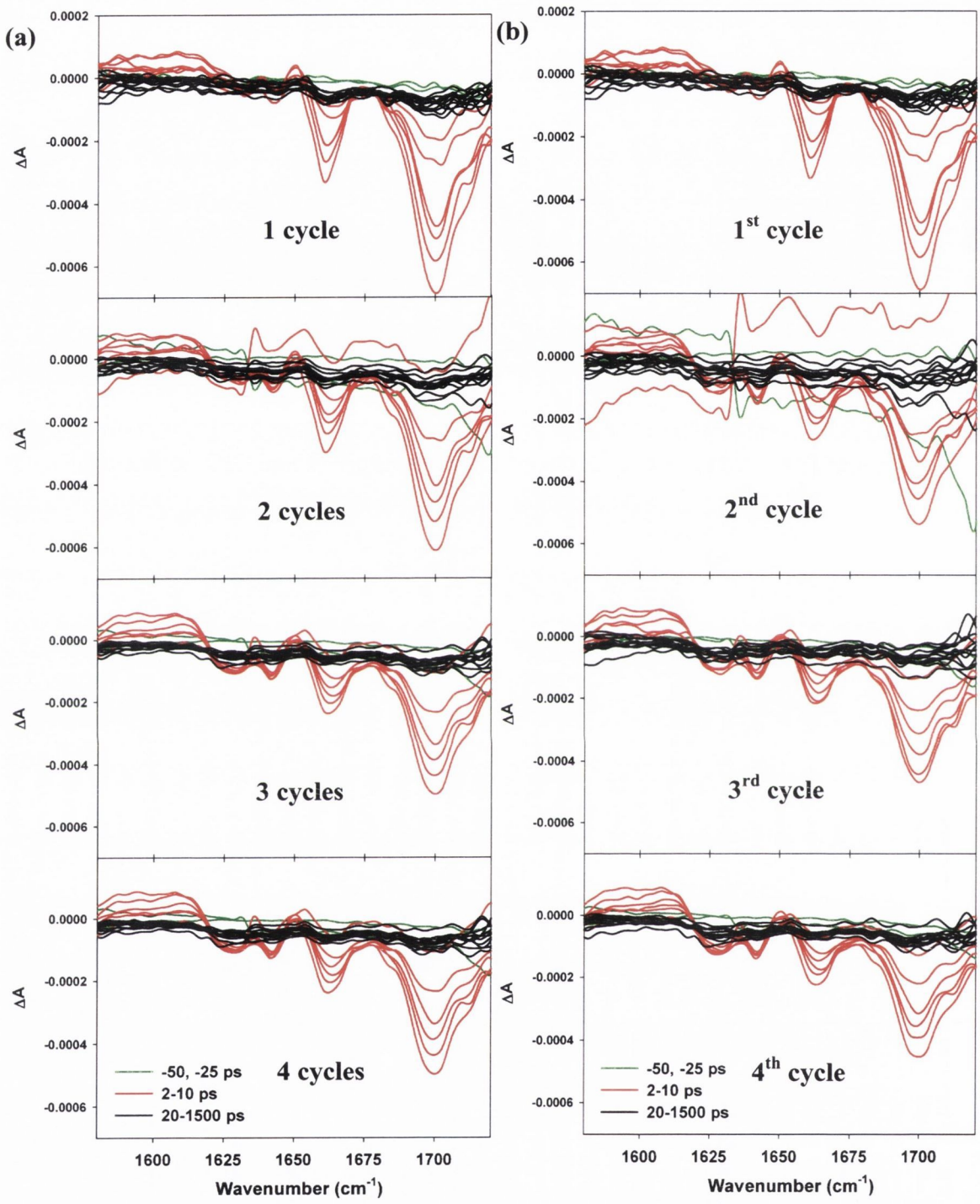

Figure A5.8.5 Accumulated (a) and separated (b) cycles of 5 mM $(dA)_{18}.(dT)_{18}.(dT)_{18}$ in 50 mM potassium phosphate D_2O buffer (pH 7) with 50 mM $MgCl_2$ (annealed). Delays are at -50, -25 (green), 2, 3, 4, 5, 7, 10 (red), 20, 35, 50, 75, 100, 150, 200, 350, 500, 750, 1000 and 1500 ps (black).

1st cycle (2-1000 ps)		
cm^{-1}	τ_1 (ps)	±
1602	**5.0**	1.1
1657	**2.6**	0.4
1660	**3.5**	0.4
1664	**4.6**	0.5
1667	**5.7**	0.8
Average	**4.1**	0.5
1686	**4.6**	0.7
1690	**4.4**	0.4
1693	**4.5**	0.4
1696	**4.9**	0.3
1699	**5.0**	0.4
1703	**5.3**	0.4
1706	**4.8**	0.5
1710	**4.4**	0.6
1713	**4.9**	0.7
Average	**4.8**	0.5

1st cycle (2-50 ps)		
cm^{-1}	τ_1 (ps)	±
1602	**4.7**	1.4
1657	**2.4**	0.4
1660	**3.2**	0.5
1664	**4.2**	0.6
1667	**5.3**	0.7
Average	**3.8**	0.6
1686	**4.1**	0.8
1690	**4.1**	0.4
1693	**4.5**	0.4
1696	**4.6**	0.3
1699	**4.8**	0.6
1703	**4.9**	0.5
1706	**4.8**	0.6
1710	**4.4**	0.6
1713	**5.2**	0.8
Average	**4.6**	0.6

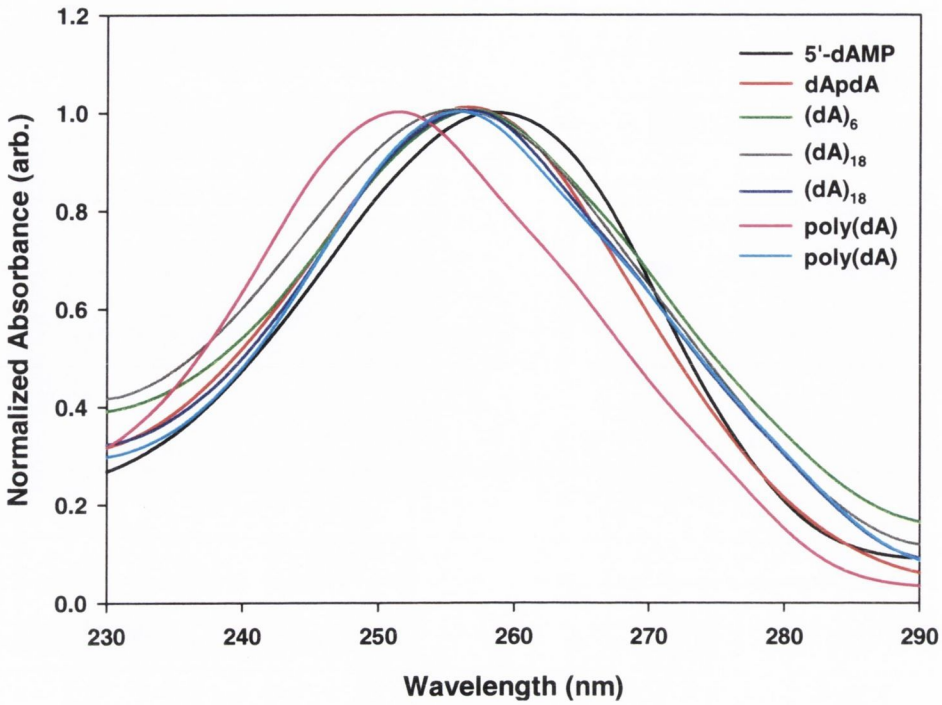

cm^{-1}	λ_{max} (nm)	τ (ps)
dAMP	**258.5**	**3.3** ± 0.2
dApdA	**256.6**	**5.0** ± 0.5 (85%) **700** ± 0.5 (15%)
$(dA)_6$	**256.9**	**7.9** ± 0.4 (73%) **435** ± 60 (27%)
$(dA)_{18}$ (1)	**255.8**	**5.1** ± 0.2 (79%) **558** ± 86 (21%)
$(dA)_{18}$ (2)	**256.1**	**5.8** ± 1.1 (81%) **215** ± 72 (19%)
poly(dA) (1)	**251.2**	**3.4** ± 0.4 (83%) **236** ± 76 (17%)
poly(dA) (2)	**256.0**	- **173** ± 20

Figure A5.8.5 Normalized UV absorption spectra adenine systems studied in this thesis: 5′-dAMP (black), dApdA (red), $(dA)_6$ (green), $(dA)_{18}$ sample 1 (gray), $(dA)_{18}$ sample 2 (blue), poly(dA) sample 1(purple) and poly(dA) sample 1(cyan). Table summarizes the maxima of absorption and the kinetics obtained from the main bleaching maxima in the TRIR spectrum.

Study 3: Human Telomeric Sequence DNA

No additional salt					
cm^{-1}	τ_1 (ps)	±	τ_2 (ps)	±	% (τ_1 : τ_2)
1546s	**4.4**	1.2	**60**	85	**92:8**
1549s	**4.0**	0.9	**50**	23	**82:18**
Average	**4.2**	1.1	**55**	54	**87:13**
1575s	**6.9**	1.3	**134**	60	**95:5**
1578	**4.8**	1.0	**101**	45	**77:23**
1581	**6.9**	1.0	**103**	32	**74:26**
1584	**7.0**	1.6	**80**	27	**67:33**
Average	**6.4**	1.2	**105**	41	**78:22**
1596	**3.2**	1.3	**70**	33	**70:30**
1599	**6.5**	1.8	**204**	145	**75:25**
1659	**3.5**	0.9	**91**	14	**52:48**
1662	**5.7**	1.1	**128**	21	**53:47**
1665	**7.3**	1.7	**141**	31	**54:46**
1669	**9.0**	1.8	**173**	39	**56:44**
1672	**8.2**	1.7	**155**	36	**56:44**
1675	**8.5**	1.4	**148**	31	**59:41**
1679	**7.1**	1.2	**127**	28	**62:38**
1682	**8.4**	0.8	**156**	25	**67:33**
1685	**6.2**	0.7	**131**	23	**66:34**
1689	**5.4**	0.8	**91**	15	**61:39**
Average	**6.9**	1.2	**134**	26	**58:42**

100 mM NaCl					
cm^{-1}	τ_1 (ps)	±	τ_2 (ps)	±	% (τ_1 : τ_2)
1578	**4.7**	1.7	**91**	48	**72:28**
1581	**4.1**	1.2	**74**	26	**69:31**
1584	**4.1**	1.4	**93**	26	**62:38**
1587	**3.4**	1.6	**105**	27	**55:45**
Average	**4.1**	1.5	**91**	32	**65:35**
1596s	**7.3**	1.4	**235**	93	**71:29**
1599s	**8.8**	1.7	**200**	132	**79:21**
1605s	**8.5**	1.7	**107**	18	**54:46**
Average	**8.2**	1.6	**181**	81	**68:32**
1630	**2.4**	0.7	**177**	105	**85:15**
1633	**2.0**	0.6	**125**	53	**84:16**
1636	**2.8**	0.8	**109**	43	**79:21**
1639	**4.4**	0.9	**126**	73	**85:15**
Average	**2.9**	0.8	**134**	69	**83:17**
1655	**2.7**	0.8	**152**	19	**56:44**
1659	**2.4**	0.9	**119**	17	**55:45**
1662	**3.0**	0.9	**106**	15	**55:45**
1665	**3.9**	1.1	**94**	16	**56:44**
1669	**6.4**	1.5	**99**	23	**62:38**
1672s	**9.2**	1.4	**164**	66	**74:26**
1675s	**9.0**	2.5	**101**	52	**71:29**
1679s	**11.9**	3.1	**175**	89	**69:31**
Average	**6.1**	1.5	**126**	37	**62:38**

100 mM KCl					
cm^{-1}	τ_1 (ps)	±	τ_2 (ps)	±	% (τ_1 : τ_2)
1554	**3.7**	3.3	**150**	83	**56:44**
1578	**10.3**	2.0	**122**	120	**87:13**
1581s	**9.5**	1.2	**78**	24	**78:22**
Average	**9.9**	1.6	**100**	72	**82:18**
1593	**3.2**	0.7	**426**	182	**75:25**
1596	**3.2**	0.5	**215**	73	**69:31**
1599	**4.2**	1.0	**147**	70	**72:28**
1602	**4.6**	1.0	**110**	84	**68:32**
1608	**3.6**	0.9	**139**	35	**73:27**
Average	**3.8**	0.8	**207**	89	**71:29**
1630	**3.3**	0.5	**176**	77	**84:16**
1633	**3.9**	1.0	**152**	70	**78:22**
1636	**4.0**	0.8	**167**	74	**79:21**
1639	**5.4**	0.8	**266**	151	**81:19**
1642	**6.3**	1.7	**233**	160	**74:26**
1646	**7.5**	4.1	**136**	114	**67:33**
Average	**5.1**	1.5	**188**	108	**77:23**
1662	**7.8**	3.2	**124**	39	**53:47**
1665	**5.0**	2.1	**89**	24	**51:49**
1669	**5.2**	2.3	**86**	26	**52:48**
1672	**5.4**	2.4	**83**	28	**56:44**
1675	**7.7**	2.7	**95**	38	**63:37**
1679	**8.1**	2.0	**99**	29	**64:36**
1682	**6.6**	1.9	**96**	39	**68:32**
1685	**9.9**	0.9	**132**	33	**81:19**
1689	**7.4**	3.5	**79**	39	**61:39**
Average	**7.0**	2.3	**98**	33	**61:39**

50 mM $SrCl_2$					
cm^{-1}	τ_1 (ps)	±	τ_2 (ps)	±	% (τ_1 : τ_2)
1575	**2.8**	0.6	**75**	28	**80:20**
1578	**3.6**	0.7	**87**	33	**78:22**
1581	**4.5**	0.7	**87**	27	**76:24**
Average	**3.6**	0.7	**83**	29	**78:22**
1605s	**1.1**	1.2	**53**	16	**70:30**
1633	**5.0**	0.8	**248**	128	**81:19**
1636	**7.4**	3.4	**59**	27	**58:42**
1639	**7.4**	1.3	**83**	31	**74:26**
1642	**7.8**	1.3	**58**	31	**82:18**
Average	**6.9**	1.7	**112**	54	**74:26**
1655	**8.1**	1.2	**164**	29	**56:44**
1659	**8.5**	1.1	**166**	29	**59:41**
1662	**8.3**	1.1	**160**	31	**63:37**
1665	**7.8**	1.0	**152**	31	**65:35**
1669	**7.2**	0.9	**142**	28	**65:35**
1672	**6.9**	1.0	**123**	23	**63:37**
1675	**5.5**	1.0	**113**	21	**59:41**
1679	**6.3**	1.0	**186**	37	**59:41**
1682	**7.5**	1.8	**137**	33	**55:45**
1685	**7.2**	1.8	**190**	64	**62:38**
1689	**6.6**	1.1	**185**	41	**64:36**
1672	**7.2**	1.5	**202**	63	**63:37**
Average	**7.3**	1.2	**160**	36	**61:39**